PROBABILITY-BASED ASSESSMENT OF POST-LIQUEFACTION SHEAR STRENGTH: AN EFFECTIVE STRESS APPROACH

A THESIS SUBMITTED TO
THE GRADUATE SCHOOL OF NATURAL AND APPLIED SCIENCES
OF
MIDDLE EAST TECHNICAL UNIVERSITY

BY

SATUK BUĞRAHAN SARİ

IN PARTIAL FULFILLMENT OF THE REQUIREMENTS
FOR
THE DEGREE OF MASTER OF SCIENCE
IN
CIVIL ENGINEERING

JUNE 2022

Approval of the thesis:

PROBABILITY-BASED ASSESSMENT OF POST-LIQUEFACTION SHEAR STRENGTH: AN EFFECTIVE STRESS APPROACH

submitted by **SATUK BUĞRAHAN SARİ** in partial fulfillment of the requirements for the degree of **Master of Science** i**n Civil Engineering, Middle East Technical University** by,

Prof. Dr. Halil Kalıpçılar
Dean, Graduate School of **Natural and Applied Sciences** _____

Prof. Dr. Erdem Canbay
Head of the Department, **Civil Engineering** _____

Prof. Dr. Kemal Önder Çetin
Supervisor, **Civil Engineering, METU** _____

Examining Committee Members:

Prof. Dr. Erdal Çokça
Civil Engineering, METU _____

Prof. Dr. Kemal Önder Çetin
Civil Engineering, METU _____

Prof. Dr. Nihat Sinan Işık
Civil Engineering, Gazi Uni. _____

Assoc. Prof. Dr. Nejan Huvaj Sarıhan
Civil Engineering, METU _____

Assoc. Prof. Dr. Nabi Kartal Toker
Civil Engineering, METU _____

Date: 17.06.2022

I hereby declare that all information in this document has been obtained and presented in accordance with academic rules and ethical conduct. I also declare that, as required by these rules and conduct, I have fully cited and referenced all material and results that are not original to this work.

Name Last name : Satuk Buğrahan Sari

Signature :

ABSTRACT

PROBABILITY-BASED ASSESSMENT OF POST-LIQUEFACTION SHEAR STRENGTH: AN EFFECTIVE STRESS APPROACH

Sari, Satuk Buğrahan
Master of Science, Civil Engineering
Supervisor : Prof. Dr. Kemal Önder Çetin

June 2022, 664 pages

Although post-liquefaction shear strengths of soils are very small, their accurate estimations are critical for post-liquefaction stability assessments. Due to the large strain nature of the liquefaction problem and difficulties in preparing re-constituted soil samples representing field conditions, laboratory testing-based assessments are not commonly used. Instead, semi-empirical residual strength assessments based on back analyses of liquefaction-induced failure cases are used for the purpose. Earlier studies suggest estimating the undrained residual shear strength of liquefied soils based on the SPT-based capacity parameter of $(N_1)_{60}$. Within the scope of this thesis, available post-liquefaction failure case histories were compiled and studied. A liquefaction state-like framework is introduced to assess the effective stress-based post-liquefaction shear strength of cohesionless soils in the void ratio-mean effective stress domain. Descriptive parameters of the problem are selected as mean grain size (D_{50}), fines content (FC), coefficient of uniformity (C_u), roundness (R), and sphericity (S) along with stress and density state parameters. A probabilistically defined liquefaction state curve is defined in the ln(e) – ln(p') domain, addressing the nonlinearity in small to larger stress ranges including the crushing responses in

very large stresses. The resulting probability-based liquefaction state curves to assess residual shear strength of liquefied soils are shown to be a superior alternative to existing models, founded on a theoretically sounder critical state-like framework.

Keywords: Post-liquefaction Shear Strength, Residual Shear Strength

ÖZ

ZEMİN SIVILAŞMASI SONRASI KAYMA MUKAVEMETİNİN EFEKTİF GERİLME YAKLAŞIMI İLE OLASILIKSAL BELİRLENMESİ

Sari, Satuk Buğrahan
Yüksek Lisans, İnşaat Mühendisliği
Tez Yöneticisi: Prof. Dr. Kemal Önder Çetin

Haziran 2022, 664 sayfa

Sıvılaşmış zeminlerin kayma dayanımları çok düşük olmasına rağmen bu mukavemet değerlerinin doğru tahmin edilmesi duraylılık değerlendirmeleri için kritik öneme sahiptir. Zemin sıvılaşması davranışının büyük deformasyon problemi olması ve saha ve zemin koşullarını temsil eden zemin numunelerinin hazırlanmasındaki zorluklar nedeniyle, laboratuvar testlerine dayalı değerlendirmeler yerine vaka analizlerine dayalı yarı-görgül bağıntıların kullanımı tercih edilmektedir. Mevcut çalışmalar sıvılaşmış zeminlerin drenajsız artık kayma mukavemetlerinin tahmin edilmesi için SPT$(N_1)_{60}$ kapasite parametresini kullanmaktadır. Bu tez kapsamında, mevcut sıvılaşma sonrası yenilme vaka örnekleri derlenmiş ve yeniden incelenmiştir. Kohezyonsuz zeminlerin sıvılaşma sonrası kayma mukavemetinin belirlenmesi için boşluk oranı-ortalama efektif gerilme uzayında sıvılaşma-durum eğrisi tariflenmiştir. Problemin tanımlayıcı parametreleri gerilme ve relatif yoğunluk durum parametrelerine ek olarak ortalama dane boyutu (D_{50}), ince dane içeriği (FC), uniformite katsayısı (C_u), yuvarlaklık (R) ve küresellik (S) olarak seçilmiştir. Küçükten büyüğe gerilme aralıklarındaki doğrusal olmayan davranışı gözeten ve çok büyük gerilmelerdeki dane parçalanma

tepkisini de modelleyebilen bir sıvılaşma durum eğrisi, ln(e)-ln(p') uzayında olasılığa dayalı olarak tanımlanmıştır. Sıvılaşmış zeminlerin kayma mukavemetini değerlendirmek için sunulan bu durum eğrilerinin mevcut modellerden daha üstün bir tahmin doğruluğu sunduğu, ve daha doğru bir teorik çerçeve üzerine kurulduğu gösterilmiştir.

Anahtar Kelimeler: Zemin Sıvılaşması, Sıvılaşma Sonrası Kayma Mukavemeti

To my family…

ACKNOWLEDGMENTS

The completion of this thesis would not have been possible without the generous assistance, guidance, and support of many colleagues and friends.

First of all, I would like to express my deepest gratitude and sincere thanks to my research supervisor, Dr. Kemal Önder Çetin, for his endless guidance, support, patience, insight, and encouragement throughout this tough journey. He clarified my every question throughout this study with great patience and understanding. His continuous motivation, energy, determination, and resolution contributed a lot to my academic, professional, and personal development. In fact, he has been a mentor to me that I can consult on any topic without any hesitation.

I would also like to thank the members of my examining committee: Dr. Erdal Çokça, Dr. Nejan Huvaj, Dr. Nabi Kartal Toker, and Dr. Nihat Sinan Işık, for their comments and insightful recommendations.

I owe further thanks to other professors that I learned a lot during their graduate courses and one-by-one personal conversations: Dr. Bahadır Sadık Bakır, Dr. Zeynep Gülerce, Dr. Onur Pekcan, Dr. Özgür Kurç, and Dr. Yalın Arıcı.

I would also like to express my gratitude to a number of researchers who provided special guidance in gathering and providing data for post-liquefaction case histories. It requires a significant effort to prepare a case history database, and back-analyze them for residual strengths. Therefore, special thanks are due to Drs. Weber, Olson, Stark, Kramer, Wang, Seed, Harder, and many other researchers for their guiding works on this topic. Their studies shed light on my research on many points, and encouraged me to put one more piece to the entire puzzle.

I am especially grateful to my Middle East Technical University fellows and friends: Elife Çakır, Makbule Ilgaç, Gizem Can, Mehmet Türkezer, Amirahmad Vakilinezhad, Eray Caceoğlu, Berkan Söylemez, Moutasem Zarzour, Emre Duman,

Yılmaz Emre Sarıçiçek, Ahmed El Suheyli, Alaa As-Sayed, Muhammet Durmaz, and Eray Altıncı for all the fun and positive energy that they bring to the Geotechnical Engineering division. Furthermore, it is also my debt to thank Baki Aykut Bilginer, Pınar Arıkoğlu, Güralp Aydemir, and Murat Altun for showing me that there also exists perfect friends in other civil engineering branches besides geotechnical engineering. I feel fortunate to have their friendship and support. In fact, I owe special thanks to Elife Çakır at this point for patiently enduring my problems and helping me at every step during this process.

Further appreciation is for my friends for life: Elif Didem Özer, Muhammed Ferhat Arslan, Mehmet Ali Tuncer, Mahmut Cihad Arslan, Esma Selek, Alperen Ünal, Cemal Kılıç, Mehmet Berat Arslan, and Eren Vural. Every time I was stressed, they motivated me by being by my side without complaining about what time it was.

Last but not least, I would also like to express my deepest love and appreciation to my family. I am sincerely grateful to my dear mother, Filiz Sari, dear brother, Farabi Sina Sari, and dear father, Davut Sari, for their immeasurable support and love. In fact, I especially thank my brother for being much smarter and cooler than me. It gives me peace of mind knowing that he will complete everything when I fail or leave something unfinished. Also, it is obviously great to know that my grandfather, grandmothers, aunts, uncles, and cousins are always there for me. Thanks to all.

TABLE OF CONTENTS

LIST OF TABLES

TABLES

LIST OF FIGURES

FIGURES

LIST OF ABBREVIATIONS

ABBREVIATIONS

2D	Two-Dimensional
3D	Three-Dimensional
ASTM	American Society for Testing Materials
BPT	Becker Penetration Test
BS EN	British and European Standard Specifications
CCW	Counterclockwise Direction
COG	Center Of Gravity
CPT	Cone Penetration Test
CSC	Critical State Curve
CSL	Critical State Line
CW	Clockwise Direction
C&I	Cubrinovski and Ishihara
DSS	Direct Simple Shear Test
D/S	Downstream
DCPT	Dutch Cone Penetration Test
FS	Factor of Safety
GSD	Grain Size Distribution
ICC	Isotropic Compression Curve
ICL	Isotropic Compression Line
IC-U	Isotropically Consolidated Undrained Triaxial Compression Test
i.e.	In other words
K&M	Kulhawy and Mayne
LSC	Liquefaction State Curve
LSL	Liquefaction State Line
METU	Middle East Technical University
MLE	Maximum Likelihood Estimation
MS	Master of Science

NC	Normally Consolidated
OC	Overconsolidated
OCR	Overconsolidation Ratio
Ph.D.	Doctor of Philosophy
RPI	Rensselaer Polytechnic Institute and State University
SCPT	Swedish Cone Penetration Test
SPT	Standard Penetration Test
SPT-N	Standard Penetration Test Penetration Resistance
TS	Turkish Standards
TXC	Triaxial Compression Test
TXE	Triaxial Extension Test
U.S.	United States
U/S	Upstream
USCS	Unified Soil Classification System
WES	Waterways Experiment Station
ZIF	Zero Inertial Force, Zero Inertial Factor

LIST OF SYMBOLS

SYMBOLS

a	Acceleration
A_{2D}	Two-dimensional angularity
c'	Cohesion
C_A	Correction factor for aging effects in relative density estimations of Kulhawy and Mayne (1990) method
C_B	Correction factor for borehole diameter in SPT
C_c	Compression index
C_D	Coefficient for grain size characteristics of soils in relative density estimations of Cubrinovski and Ishihara (1999) method
C_E	Correction factor for hammer energy efficiency in SPT
C_{fines}	Correction factor fines content in SPT
C_N	Correction factor for overburden stress in SPT
C_N	Correction factor for particle size effects in relative density estimations of Kulhawy and Mayne (1990) method
C_{OCR}	Correction factor for overconsolidation effects in relative density estimations of Kulhawy and Mayne (1990) method
C_P	Correction factor for particle size in relative density estimations
C_R	Correction factor for short rod length in SPT
$C_{R,Auto}$	Updated correction factor for short rod length in SPT
$C_{R,Safety}$	Updated conservative correction factor for short rod length in SPT
C_S	Correction factor for sampler configuration in SPT
C_u	Coefficient of uniformity, undrained shear strength
$C_{u,clay}$	Shear strength of the clayey zone
$C_{u,initial}$	Shear strength of the liquefied zone evaluated by Weber (2015)
$C_{u,modified}$	Shear strength of the liquefied zone evaluated by this study
$C_{u,modified,post}$	Shear strength of the liquefied zone evaluated by this study considering post-failure geometry

$C_{u,modified,pre}$	Shear strength of the liquefied zone evaluated by this study considering pre-failure geometry
D_{10}	Diameter of the 10% of the sample to be finer
D_{30}	Diameter of the 30% of the sample to be finer
D_{50}	Diameter of the 50% of the sample to be finer, mean grain size
D_{60}	Diameter of the 60% of the sample to be finer
e	Void ratio
e_{c0}	Void ratio at a known mean effective stress p'_{c0} on the liquefaction state curves
e_{ICC}	Void ratio corresponding to isotropic states, in-situ void ratio
e_{lim}	Minimum limit void ratio that the isotropic compression curves become asymptomatic at very high stresses
e_{max}	Maximum void ratio
e_{min}	Minimum void ratio
e_0	Initial void ratio
E	Elastic modulus, Young's modulus
FC	Fines content
g	Gravitational acceleration, functional form
I_1, I_2, I_3	Stress invariants
J_1, J_2, J_3	Stress invariants
K_0	Lateral earth pressure coefficient at rest
L	Rod length for SPT depth
L_{clay}	Failure plane length remaining in the clayey zone
L_i	Failure plane length of i^{th} slice/sub-section
L_{liq}	Failure plane length remaining in the liquefied portion
$L_{non-liq}$	Failure plane length remaining in the non-liquefied portion
L_t, L_{total}	Total failure plane length
m	Mass
M	Slope of the stress path in q vs. p' domain
M_i	Slope of the stress path in q vs. p' domain for i^{th} slice/sub-section

M_{tc}	Slope of the stress path in q vs. p' domain for triaxial compression test
N	Raw SPT resistance, void ratio on the isotropic compression curves or lines corresponding to unit stress
N_{sw}	Number of half-revolutions in rotating phase of SCPT
N_{60}	Equipment, energy (60%) and procedure corrected SPT resistance
$(N_1)_{60}$	Equipment, energy (60%), procedure and overburden stress corrected SPT resistance
$(N_1)_{78}$	Equipment, energy (78%), procedure and overburden stress corrected SPT resistance
$(N_1)_{60,cs}$	Equipment, energy (60%), procedure, overburden stress and fines content corrected SPT resistance
O_p	Pole of the Mohr's circle, origin of the planes
P	Initial vertical effective stress
P, P( )	Probability
p_a, p_{atm}	Atmospheric pressure
p'	Mean effective stress
p'_{cr}	Shifting stress controlling the curvature of the liquefaction state curves
p'_{c0}	Reference mean effective stress corresponding to e_{c0} on the liquefaction state curves
p'_{ls}	Liquefaction state mean effective stress
$p'_{ls,i}$	Liquefaction state mean effective stress of i^{th} slice/sub-section
p'_r	Shifting stress controlling the curvature of the isotropic compression curves
p'_0	Initial mean effective stress
q	Deviatoric stress
q_{ls}	Deviatoric stress for liquefaction state
q_c	Cone tip resistance
r_i	Radius of i^{th} circle which fits inside the grain

$r_{max\text{-}in}$	Maximum circle radius which fits inside the grain
$r_{min\text{-}cir}$	Minimum circle radius which encircled the grain
R	Roundness
RD, D_R, D_r	Relative Density
R^2	Least squares regression
S	Sphericity
S_d	Drained strength for non-liquefied materials
S_r, S_u	Overall post-liquefaction strength
$S_{r,backanalyzed}$	Post-liquefaction shear strength based on back-analysis
$S_{r,drained}$	Drained residual strength
$S_{r,predicted}$	Predicted post-liquefaction shear strength
$S_{r,resid/geom}$	Apparent residual stress based on the post-failure geometry evaluated by assigning the static Factor of Safety equal to 1.0 for residual post-geometry
$S_{r,yield}$	Apparent pre-failure yield stress based on the pre-failure geometry evaluated by assigning the static Factor of Safety equal to 1.0 for pre-geometry
S_u(LIQ)	Post-liquefaction strength for liquefied materials
S_{us}	Undrained steady state shear strength
u	Pore water pressure
V_s	Shear wave velocity
W	Total weight of failure mass
W_{sw}	Weight used in static phase of SCPT
x_c	x-coordinate of the center of the circle
y_c	y-coordinate of the center of the circle
#	Number
γ	Unit weight
γ_{dry}	Dry unit weight
γ_{sat}	Saturated unit weight
Δe	Change in void ratio

$\Delta(N_1)_{60}$	Additional SPT resistance with respect to fines content
Δu	Change in pore water pressure, excess pore water pressure
ν, μ	Poisson's ratio
σ'	Effective normal stress
σ'_f	Final effective stress
σ'_i	Initial effective stress
σ'_N, $\sigma'_{N,0}$	Effective normal stress acting on the failure plane
σ'_v	Vertical effective stress
σ'_{v0}	Initial vertical effective stress
$\sigma'_{v,ave}$	Average vertical effective stress
$\sigma'_{v,i}$	Vertical effective stress of i^{th} slice/sub-section
σ'_{xx}	Cartesian effective normal stress in x direction
σ'_{xy}	Cartesian effective shear stress on xz plane in y direction
σ'_{yy}	Cartesian effective normal stress in y direction
σ'_{zz}	Cartesian effective normal stress in z direction
σ'_1	Major principal effective stress
σ'_2	Intermediate principal effective stress
σ'_3	Minor principal effective stress
τ	Shear stress
τ_{liq}, $\tau_{liq,overall}$	Post-liquefaction shear strength
$\tau_{liq,i}$	Post-liquefaction shear strength of i^{th} slice/sub-section
$\tau_{liq,predicted}$	Predicted post-liquefaction shear strength
τ_{static}	Static shear stress acting on the failure plane
α	Failure plane inclination
α_i	Failure plane inclination for i^{th} slice/sub-section
ϕ, ϕ'	Internal friction angle
$\phi'_{initial}$	Internal friction angle used by Weber (2015)
ϕ'_{ls}	Liquefaction state friction angle
$\phi'_{modified}$	Internal friction angle used by this study
Φ	Cumulative standard normal distribution

θ	Lode angle
$\theta_{initial}$	Initial slope angle of failure plane
θ_{final}	Final slope angle of failure plane
θ_1, θ_2, etc.	Model parameters
θ_ε	Standard deviation of model error
λ	Slope of the isotropic compression curves or lines
λ_{ls}	Slope of the liquefaction state lines
Γ	Void ratio on the liquefaction state curves or lines corresponding to unit stress
Γ_1	Void ratio on the liquefaction state curves or lines corresponding to 1 kPa mean effective stress
ξ	Runout distance coefficient
$\sum r_i/N$	Average radius of the circles which fit the grain's protrusion

CHAPTER 1

INTRODUCTION

Soil liquefaction is known as the significant reduction in shear strength and stiffness of soils resulting from a rapid type of loading such as earthquake shaking or vibration. This phenomenon is observed in saturated soils in which groundwater fills the space between individual soil grains and particles. A rapid (undrained) type of loading such as an earthquake cycle can cause an increase in water pressures in these pores up to a point where the soil particles can readily move with respect to each other. Consequently, the strength of soil reduces with increasing pore water pressures, and the soil itself cannot resist and support the superstructures or infrastructures. In addition, increased water pressures can also trigger slope stability problems and landslides.

The history of soil liquefaction dates back to the 1960s such that significant liquefaction-induced damages and failures were observed in two severe earthquakes that occurred in the mid-1960s, the 1964 Great Alaskan Earthquake ($M_W = 9.2$) and 1964 Niigata Earthquake ($M_W = 7.7$). Although the term “soil liquefaction” and the mechanism behind this phenomenon were already known in those years, these two major earthquakes had made the geotechnical engineering profession realize that earthquakes should not only be the natural disasters concerned by structural engineers dealing with superstructures but also they should be investigated by the geotechnical engineers researching the soil and ground.

These two events initiated the development of well-established engineering methods for handling soil liquefaction and its consequences. As a first step, the effects of seismic loading on the risk of soil liquefaction triggering were evaluated. These evaluation techniques have further developed over the years, and numerous well-established methods including empirical methods based on laboratory and in-situ

tests, advanced fully nonlinear constitutive models using finite elements or finite difference computer analysis frameworks are proposed.

Historical earthquake events damaged several dams, starting with the Lower San Fernando Dam during the 1971 San Fernando Earthquake (M_W = 6.6), showed that liquefaction-induced deformations and failures are likely to be observed on slopes of dams, levees or embankments. Accordingly, the effect of soil liquefaction on also other critical structures such as transportation facilities (roads, bridges, tunnels, airports, harbors, etc.), energy production facilities (nuclear power plants, hydroelectric power plants, industrial buildings, waste impoundments, etc.), in-ground lifelines (water, gas, telecommunications, etc.) and daily structures (homes, schools, hospitals, businesses, etc.) are examined in detail over the decades, and liquefaction risk and mitigation techniques are beginning to be developed.

These developments also initiated the investigation of the resulting performances; in other words, the consequences of potential liquefaction in terms of deformations, displacements, and damages. During the first times of the liquefaction phenomenon, evaluation of initiation, triggering, and risk was the only concern of geotechnical engineers. The post-liquefaction strengths and stiffnesses were commonly assumed to be negligible for liquefied materials. On the other hand, it is obvious that this approach was over-conservative. With further understanding of the mechanics of soil liquefaction and critical state soil mechanics, as well as the development of advanced laboratory techniques for large strain tests, engineering evaluation of post-liquefaction strengths, stiffnesses, deformations, and displacements is also improved in addition to the initiation and triggering of soil liquefaction. As a result, more accurate and less over-conservative assessments of post-liquefaction strengths and performances are achieved, and continuing development of these assessments has been ongoing over the past four decades.

Evaluation of post-liquefaction strength, or namely residual strength, of soils requires a significant amount of research involving laboratory testing, and analytical and numerical studies. Due to the difficulties and challenges in physical laboratory-

scale large strain cyclic testing, empirical and semi-empirical relationships founded on back-analyses of full-scale field liquefaction failure case histories have become the more preferred approach in engineering practice for the evaluation of residual strengths. Developing relationships for the post-liquefaction shear strength requires the compilation of high-quality case histories from liquefaction-induced failure sites. Then, these case histories need to be analyzed with the intent of identifying and estimating the governing factors behind the post-liquefaction response.

Previous studies on this topic are perfect efforts to understand the essential pieces of the entire liquefaction engineering puzzle. Older studies contain significant clues and lessons about the topic, and they shed light to further studies to guide them. They developed new methods including the contribution of momentum effects to perform more accurate and reliable back-analyses, and these efforts resulted in a high-qualified case history database at the end. Accordingly, they have performed probabilistic regressions to evaluate the uncertainties in these case histories and developed new predictive relationships for engineering evaluation of post-liquefaction strength. As a common approach, these studies recommend residual strength relationships as a function of equipment, energy, and procedure corrected (also some include fines content correction) SPT resistance, and initial in-situ effective vertical stress. Even though these studies contribute a lot to literature in terms of the assessment of residual strength relationships, the use of the term "undrained" without any reference to the induced excess pore pressures can be misleading for practicing engineers, who are used to performing effective stress-based stability assessments for cohesionless soils under monotonic loading conditions. Hence, inspired from the earlier work in the literature, a critical state-like framework in the void ratio versus effective stress domain will be implemented to assess the post-liquefaction strength of soils on the basis of back-analyses of available case histories. In addition to the equipment, energy, procedure, and fines corrected SPT resistance ($(N_1)_{60,cs}$) and initial in-situ effective vertical stress (σ'_{v0}), new descriptive key parameters correlating with the physical nature and state of the soil such as mean grain size (D_{50}), fines content (FC), coefficient of uniformity (C_u),

roundness (R) and sphericity (S) will be implemented in the post-liquefaction (residual) strength relationships. Instead of the undrained shear strength versus penetration resistance domain suggested by previous studies on this topic, this study recommends a void ratio versus effective stress domain, which is a well-known domain in geotechnical engineering in performing effective stress-based stability assessments for cohesionless soils, to represent the residual strength of soils.

The recommended relationships agree well with recent suggestions of Olson and Stark (2002), Wang (2003), Kramer (2008) and Weber (2015). In fact, they are shown to be viable alternatives to previous studies due to their relatively more accurate and precise predictive capability. Therefore, it is possible to say that these new relationships offer potentially significant advantages over previously available recommendations.

1.1 Research Statement

As discussed in the previous section, there exist numerous studies on the engineering evaluation of post-liquefaction, or namely residual, strength of soils. In general, these studies recommend their undrained residual strength (S_r or S_u) prediction relationships as a function of equipment, energy and procedure corrected (also some include fines content correction) SPT resistance, and initial in-situ effective vertical stress. Nevertheless, the use of the term "undrained" without any reference to the induced excess pore pressures can be misleading for practicing engineers, who are used to performing effective stress-based stability assessments for cohesionless soils under monotonic loading conditions. Therefore, this study will introduce a new effective stress approach based on a critical state framework compatible methodology to assess the post-liquefaction strength of soils on the basis of back-analyses of available case histories.

The critical state framework includes void ratio versus effective stress domain, and this study shows that each case history has its unique data point on this domain with

a specific initial mean effective stress and void ratio. This new framework is theoretically advantageous as initial in-situ effective vertical stress (σ'_{v0}) is the only stress component in previous studies to represent the confining effects. On the other hand, it is obvious that other stress components including the horizontal stresses in out-of-plane and on-plane directions also have effects on the mean confining stress. Neglecting these impacts and imposing all confining effects to initial effective vertical stress theoretically weakens other studies. Furthermore, the in-situ void ratio, and therefore the in-situ relative density, is one of the critical parameters for soil to determine its susceptibility to liquefaction. Previous studies also consider this effect indirectly by implementing an in-situ test index metric (e.g., $(N_1)_{60}$, q_c, V_s, etc.) in their residual strength relationships to represent the capacity of the soil. This parameter is commonly the SPT resistance due to the wide usage of this test all around the world and the abundance of conversions available in the literature to convert other types of penetration resistances to SPT resistance. On the other hand, it is always a problem to convert other types of resistances to an equivalent SPT resistance. Luckily, this new framework takes this effect into account directly such that the in-situ relative densities and void ratios of the cases are presented in the void ratio versus mean effective stress domain. Therefore, the differences in in-situ tests are automatically eliminated as the in-situ void ratio is unique for all tests, and it is possible to estimate it by using correlations developed by all types of experiments. This convenience also explains well that the new framework sounds theoretically more correct.

This study also claims that there exists a post-liquefaction state curve similar to the critical state curve in void ratio versus mean effective stress domain, and all data points on this domain follow this curve after the liquefaction. In other words, the initial location of these points shifts horizontally in the void ratio versus the mean effective stress domain as a result of changing pore water pressures and mean effective stresses during seismic earthquake shaking or vibration. Since liquefaction is an “undrained” condition due to a rapid type of loading, the void ratios remain the same during cyclic loading, which proves that this movement of data points is also

theoretically stable and valid. In fact, the liquefaction state curve can be considered as a critical state “like” curve as very large deformations reaching 20-30% strains are observed for liquefaction-induced case histories. Hence, the implementation of a critical state framework for the engineering evaluation of post-liquefaction shear strength is reasonable and theoretically logical.

Since a new framework and domain for residual strength are introduced in this study, new promising descriptive material parameters in addition to SPT resistance used to estimate in-situ void ratios and relative densities are also implemented into the probabilistic relationships. These parameters are selected as the ones corresponding to the physical nature and physical state of the soil, and directly correlated with the limit and in-situ void ratios such as mean grain size (D_{50}), fines content (FC), coefficient of uniformity (C_u), roundness (R) and sphericity (S). Moreover, the confining effect of the liquefied layer is well better implemented into the relationships by considering three-dimensional (3D) stress components. The effects of major, intermediate, and minor effective principal stresses are all included in the evaluation of residual strengths.

Although totally different approaches are followed in this study, the predictions have shown a good agreement with previous studies. Significant advantages of the new framework are observed, and the void ratio versus mean effective stress domain is judged to be more favorable and technically sound for representing the post-liquefaction shear strengths. In fact, this study provides relatively more accurate and precise models thanks to its stronger theoretical background. Since the recommended models are presented in a fully probabilistic form, they can be considered for probabilistic risk studies. Also, it is quite advantageous to use recommended relationships in the design of routine and sophisticated projects.

1.2 Research Objectives

The research objectives of this study are described as follows:

- To introduce a liquefaction state framework compatible methodology to evaluate post-liquefaction strength of soils on the basis of back-analyses of available case histories,
- To present void ratio versus effective stress domain for representing the post-liquefaction strength and eliminate the confusion between different types of penetration resistances,
- To recommend a liquefaction state curve in void ratio versus mean effective stress domain, which all cases reach at their residual strengths,
- To implement new material parameters correlating with the physical nature and physical states of the soil, such as mean grain size (D_{50}), fines content (FC), coefficient of uniformity (C_u), roundness (R), and sphericity (S) into the post-liquefaction strength relationships,
- To include the effect of the third-dimensional stress component, i.e., the intermediate effective principal stress, in confining effect of the liquefied layer,
- To implement the usage of a new failure criterion including the effect of all effective principal stresses in three dimensions on residual strength.

1.3 Scope of the Thesis

Following this introduction, a summary and history of the development of post-liquefaction prediction relationships are presented in Chapter 2. Essential studies and methods including both laboratory testing and empirical/semi-empirical relationships based on back-analyses of full-scale liquefaction-induced failures are reviewed, and their approaches are discussed. The challenges in full-scale laboratory testing for the assessment of residual strength are explained. Advantages and

disadvantages, as well as strengths and weaknesses, of previous studies for engineering evaluation of in-situ post-liquefaction strength are assessed.

In Chapter 3, detailed explanations of the selection of liquefaction case histories for the development of residual strength relationships are presented. The case history database developed by previous research teams and the database used in this study is explained. The evaluation of new descriptive material parameters correlating with the physical nature and physical state of the soil for case histories is discussed in detail. The sub-sectioning procedure of overall failure planes and cross-sections for case histories is explained in order to consider confining effect better at different points along the failure surface. Elastic modeling of selected case histories for evaluation of effective principal stresses, mean effective stresses, and deviatoric stresses are declared. Methods, assumptions, cross-sections, modeling details, soil parameters, etc., involved in the modeling process are discussed. The stress rotation procedure and estimation method of normal effective stress and static shear stress acting on the inclined failure planes corresponding to each sub-section are explained step by step. Evaluation of representative SPT resistance for each sub-section is clarified, and equipment, energy, procedure, and fines content correction techniques applied to these resistances are explained. Studies followed in the evaluation of limit void ratios, void ratio ranges, and in-situ relative densities are presented, and the importance of these processes for the new framework and void ratio versus mean effective stress domain is stated.

In Chapter 4, the new critical state framework compatible methodology to evaluate post-liquefaction strength of soils on the basis of back-analyses of available case histories is introduced. The volume stress models are presented in void ratio versus mean effective stress domain. Evaluation of Isotropic Compression Curves, Limit Compression Curves, and Liquefaction State Curves are discussed in detail with their definitions, corresponding equations, and required model parameters. The probabilistic regression process is presented for the evaluation of model parameters. Estimation of liquefaction state friction angles for the case histories is explained. A new failure criterion including the effect of all effective principal stresses in three

dimensions on residual strength is introduced, and the advantages and theoretical background of this criterion are discussed. The fully probabilistic semi-empirical relationships for the engineering evaluation of in-situ post-liquefaction (residual) strengths based on mean grain size, fines content, coefficient of uniformity, roundness, sphericity, penetration resistance, and effective principal stresses are developed.

In Chapter 5, the comparison of this study with the previous ones for the same case histories based on the residual strength relationships is presented. Advantages and disadvantages, as well as strengths and weaknesses, of this study compared to previous ones for engineering evaluation of in-situ post-liquefaction strength are discussed. Comparison of predicted residual strengths with the ones obtained from back-analyses are presented. Residual plots for the relationships are provided for each model parameter to understand their effect and significance in predictions.

In Chapter 6, an overall summary of the findings is presented. Major conclusions and recommendations for future works are listed.

CHAPTER 2

LITERATURE REVIEW

This chapter presents a summary and historical progression of the development of post-liquefaction prediction relationships. Existing methods available in the literature for engineering evaluation of residual strengths are reviewed. Laboratory-based and empirical/semi-empirical methods based on back-analyses of full-scale liquefaction-induced failures are discussed in separate sections. Advantages and disadvantages, as well as strengths and weaknesses, of previous studies for engineering evaluation of in-situ post-liquefaction strength are assessed.

2.1 Laboratory-Based Methods

Laboratory-based methods for engineering evaluation of post-liquefaction strength are not many as the number of available empirical/semi-empirical relationships. This is because physical laboratory-scale large strain cyclic testing is quite difficult for the evaluation of residual strengths due to a variety of reasons. The complexity of required test setup and apparatus, uncertainties in sampling, obstacles in sample saturation procedure, scaling of actual field conditions, high level of strains representing large deformations that occur in the field, etc., are some of these challenging factors. In addition to these common difficulties for many types of experimental studies, there are three sets of additional challenges that complicate the laboratory-based methods for engineering evaluation of post-liquefaction strength of soils. They render the use of laboratory test data potentially unconservative when compared to field-scale applications giving in-situ post-liquefaction strengths. These additional challenges complicating the laboratory-based methods for the engineering assessment of post-liquefaction strength are summarized below.

Void redistribution:

It is obvious that a "flow" occurs from the zone with higher pressures to the zone with lower pressures. In liquefaction cases, this flow is typically towards the upwards direction as pore water pressure increases at the liquefied layer below the ground, and excess pore pressures force groundwater to "flow" towards the ground surface in the upwards direction. During this flow process, the void ratio of the corresponding layers changes with the transportation of soil particles and pore water. Therefore, void redistribution is called the process of the movement of solid particles with pore fluids within a soil zone of constant overall volume so that the in-situ void ratio and relative density may change locally at some portions of the saturated material. These minor changes in void ratio and relative density can cause dramatic changes in post-liquefaction strength as post-liquefaction behavior is controlled by the void ratio that appeared after the void redistribution process, not by the pre-event in-situ void ratio. Moreover, a weaker zone may occur as a result of the void redistribution process. Therefore, although the engineering evaluation of void redistribution is studied by many researchers and the mechanism behind it is understood, it is very challenging to analytically model them since it is tough to determine the absolute amount of void redistribution occurring at the site. Hence, the void redistribution cannot be predicted adequately yet. The void redistribution process is simply illustrated within a confined soil stratum in Figure 2.1.

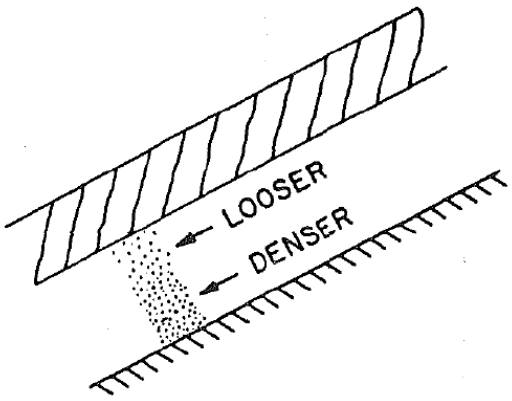

Figure 2.1. Simplified illustration of void redistribution process within a confined soil stratum (National Research Council, 1985)

Partial drainage:

Partial drainage can be considered as a second type of void redistribution case, which occurs over a larger period of time than the more localized type of void redistribution illustrated in Figure 2.1. During rapid loading, cyclic loading, or undrained monotonic loading, initially pore pressures increase, and effective stresses decrease. Then, these pore pressures start to dissipate by the flow of fluids in pores from the zone of higher pressures to lower ones. Although this dissipation is an advantageous process for the increase of effective stresses and therefore, the shear strengths in most cases, it may also have disadvantageous effects in some cases such that these flowing fluids may be impeded at impervious or less pervious layers temporarily. The blocking of flowing fluids may result in local increases of pore pressures at impervious or low pervious zones. Thus, continuing dissipation of pore pressures can also cause void redistribution effects in some cases. It is again complicated to analytically model partial drainage because it is challenging to determine the amount of ongoing pore pressure dissipation at the site. Hence, the partial drainage also cannot be predicted adequately yet.

Inter-layer mixing:

During the shearing along with the interface between two materials, such as the soil above and below the failure plane, fine particles located in one material may be mixed up with the other material and be placed between the coarser particles. This type of transition may occur as a result of chaotic interactions such as grinding, rubbing, etc. When fine particles in a material are located between the coarser particles of the other material, more efficient packing of the particles is achieved, and the resulting mixture has less volume than either of the two materials per unit weight of solids. This type of efficient packing cannot be taken into account yet either experimentally or analytically since the amount of mixture and the way it affects the residual strength are still indefinite.

Even though these three sets of additional challenges are significant obstacles to the development of the laboratory-based methods for the engineering evaluation of post-

liquefaction strength, there are numerous laboratory investigations and scale model experimental studies both on shaking tables and on centrifuges available in the literature focusing on these issues. Nevertheless, there is still no universally accepted laboratory-based approach exists for the evaluation of post-liquefaction strengths for in-situ soils. Luckily, one of the most qualified and valuable in effort study for the laboratory-based assessment of post-liquefaction strength is explained below in detail.

2.1.1 Poulos et al. (1985)

As already discussed, laboratory-based methods for engineering evaluation of post-liquefaction shear strengths requires careful field sampling and high-qualified laboratory testing. Poulos et al. (1985) exhibited significant efforts on these challenges and produced a method based upon principles of critical state soil mechanics.

In critical state, the soil continues to shear under constant volume, constant effective stress, and constant shear strength. In other words, it is defined as the ability to deform for a soil under constant volume and stress. Principals of critical state soil mechanics declare that a soil's state can be explained by its location with respect to the critical state curve in void ratio versus effective stress domain. This effective stress is commonly represented by effective confining stress or mean effective stress. When soil is sheared, it may produce a dilative or contractive behavior depending on its current state with respect to the critical state curve in that domain. While soils whose states are located above the critical state curve (CSC) are classified as loose soils and show contractive behavior when sheared, soils whose states are located below the CSC are classified as dense soils and show dilative behavior when sheared. The contractive or dilative response of these soils continues until the new state reaches critical state, i.e., the location of the point touches the CSC in void ratio versus the effective stress domain. For undrained conditions, the initial state of soils follows a horizontal path in this domain (towards the right and left for dense and

loose soils, respectively) as no volume change occurs and the void ratio remains the same. Oppositely, for drained conditions, the initial state of soils follows a vertical path in this domain (towards upwards and downwards for dense and loose soils, respectively) as no effective stress change occurs. Consequently, all soils that sheared sufficiently will reach critical state condition, which is not unique but different for each soil, in theory. It should be remarked that a "steady state" is also defined in the same domain by Castro and Poulos (1977) and Poulos (1981). The difference between this state and the critical state is that strain rate is also constant in addition to constant shearing resistance, effective stress, and volume. On the other hand, the constant strain rate is generally ignored, and the two states are assumed to be the same mostly.

In literature, there is still a hot debate available about the shape of the critical state curve, whether it is a line or a curve. Steady-state and critical state curves are generally plotted in semi-logarithm space where the vertical and horizontal axes represent void ratio and logarithm of effective confining stress, respectively. In this semi-log domain, steady-state and critical state curves are approximately obtained as log-linear over the void ratio and effective stress ranges that geotechnical engineers are interested in liquefiable soils.

To be able to use the laboratory-based steady-state method proposed by Poulos et al. (1985) for the engineering assessment of post-liquefaction shear strengths of in-situ soils, fully disturbed bulk samples should be obtained such that these samples should be reconstituted in the laboratory to be able to obtain different relative densities and void ratios. Accordingly, these reconstituted samples should be subjected to isotropically consolidated undrained (IC-U) triaxial compression tests in order to estimate their critical state, i.e., steady-state curves. On the other hand, these steady-state curves (or lines) are not directly used to estimate in-situ strengths because they are obtained from disturbed samples. Actual results should be received by testing high-quality undisturbed samples. The results obtained from disturbed samples should only be used just to examine the effect of sampling disturbance during the

sampling process, transportation, extrusion, mounting, and reconsolidation prior to undrained shearing in the laboratory, and provide a correction factor accordingly.

Unfortunately, high-quality undisturbed sampling is challenging for cohesionless soils, but there are some ways to minimize the disturbance effects during soil sampling. One way to decrease the sample disturbance is to use sharp-edged thin-walled samplers, which is a commonly used method in engineering practice. These samplers must be pushed into the soil instead of driving with hammers in order to avoid vibratory densification of soils. Another way is to excavate a large diameter shaft that a man fits in it easily, and then lower an engineer or technician into this shaft with a cylindrical sampling tube fixed on a tripod to get samples. The engineer or technician can obtain less disturbed samples by hand carving at the base of the shaft.

After the sampling, the changes in volume, and therefore in void ratio, should be tracked very carefully and accurately to obtain precise results at the end. The length of the sampler, the radius of the cutting edge, the interior radius of the sampler tube, and the length of the recovered sample should be measured precisely to calculate the volume and corresponding void ratio. The length of the sample should be measured one more time in the laboratory to detect the volume change during transportation. When the sample is trimmed, and a membrane is put around it, the corresponding volume should be calculated again to track any further void ratio change of the sample. Finally, void ratio change during reconsolidation should also be reported to compute the void ratio of the final, consolidated sample subjected to undrained shearing.

An example of a laboratory-based evaluation of the post-liquefaction shear strength of the Lower San Fernando dam hydraulic fill is shown in Figure 2.2. In this figure, while the horizontal axis represents the undrained steady-state shear strength, the vertical axis gives the corresponding void ratios. The bold, nearly straight line is the steady-state line for this soil, obtained from disturbed reconstituted samples. The

nearly straight but thinner parallel line above it is the actual corrected steady-state line for this soil, obtained from high-qualified nearly undisturbed samples.

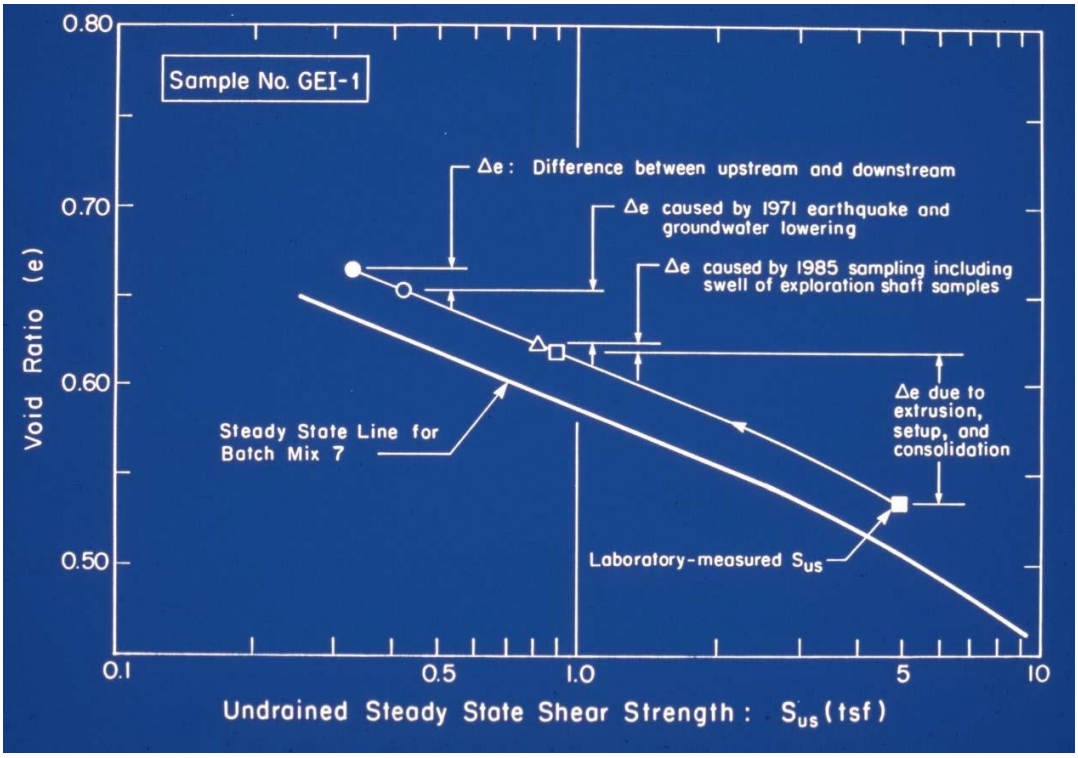

Figure 2.2. Illustration of the steady-state method proposed by Poulos et al. (1985) for laboratory-based engineering evaluation of post-liquefaction shear strengths for Lower San Fernando Dam hydraulic fill (Castro et al., 1992)

Referring to Figure 2.2, initially the solid square located at the lower right corner is defined with respect to final, laboratory consolidated void ratio. This S_{us} value obtained with respect to the laboratory void ratio is then corrected back to the initial in-situ void ratio, which is located as a solid dot at the upper left corner. While performing this correction, it is assumed that the actual steady-state line based on high-quality undisturbed samples is parallel to the steady-state line obtained from disturbed reconstituted samples. Therefore, a path is followed from the solid square with the same slope of the steady-state line obtained from disturbed reconstituted samples (bold line below) until the in-situ void ratio is reached. Then, the solid dot is put there, giving the corrected S_{us} value.

There are several gaps in this approach, such that there is no reasonable explanation for obtaining a lower steady-state line for disturbed reconstituted samples than high-quality undisturbed samples. In addition, assuming these two steady-state lines for disturbed reconstituted samples and high-quality undisturbed samples perfectly parallel is again not clearly explained.

To be able to examine the viability and reliability of the laboratory-based steady-state methodology proposed by Poulos et al. (1985) for assessment of the in-situ post-liquefaction strengths of soils, the Lower San Fernando Dam case history is re-studied by four different investigation teams having laboratories with good reputations on high-level testing, GEI Consultants, the U.S. Army Corps of Engineers Waterways Experiment Station (WES), Rensselaer Polytechnic Institute and State University (RPI), and Stanford University working jointly with U.C. Berkeley. The consensus steady-state line developed by these four teams is shown in Figure 2.3.

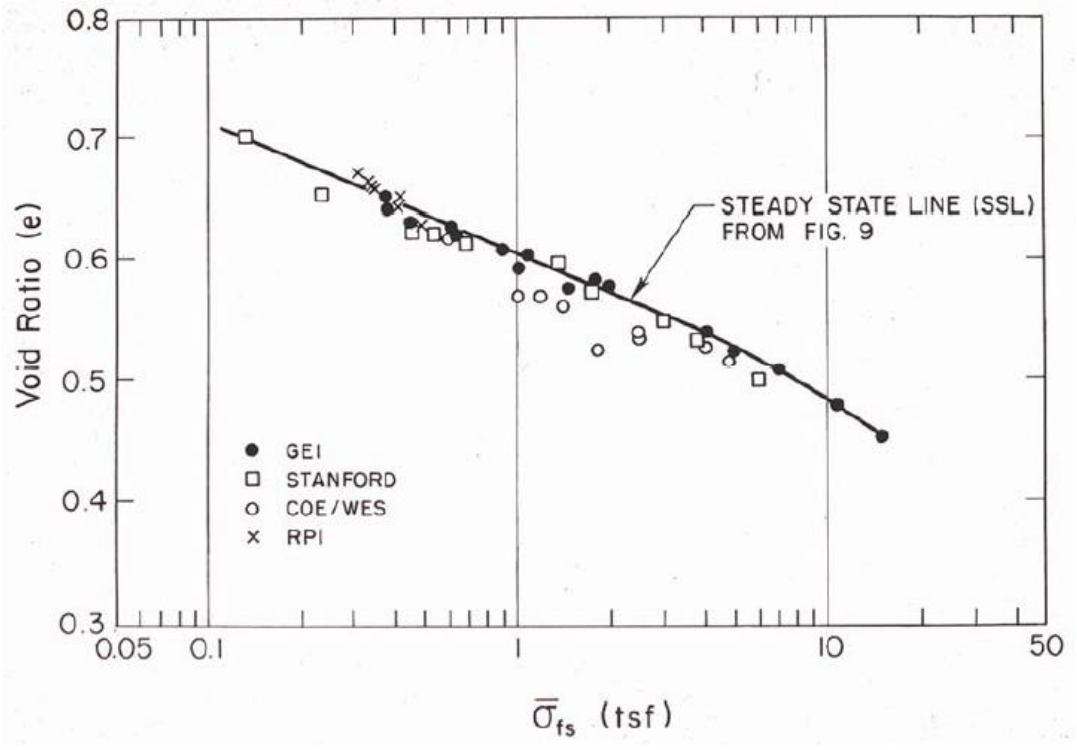

Figure 2.3. Consensus steady-state line for the Lower San Fernando Dam hydraulic fill developed by four investigation teams (Castro et al., 1992)

The samples used in the process of developing this consensus steady-state line presented in Figure 2.3 were disturbed reconstituted samples. A series of IC-U triaxial tests were then conducted by these teams using high-quality undisturbed samples. Accordingly, S_{us} values were corrected by assuming the parallelism between two steady-state lines obtained from disturbed and undisturbed samples. The resulting corrected estimates of in-situ S_{us} values (solid black dots) and their corresponding laboratory S_{us} values (solid black squares) are presented in Figure 2.4.

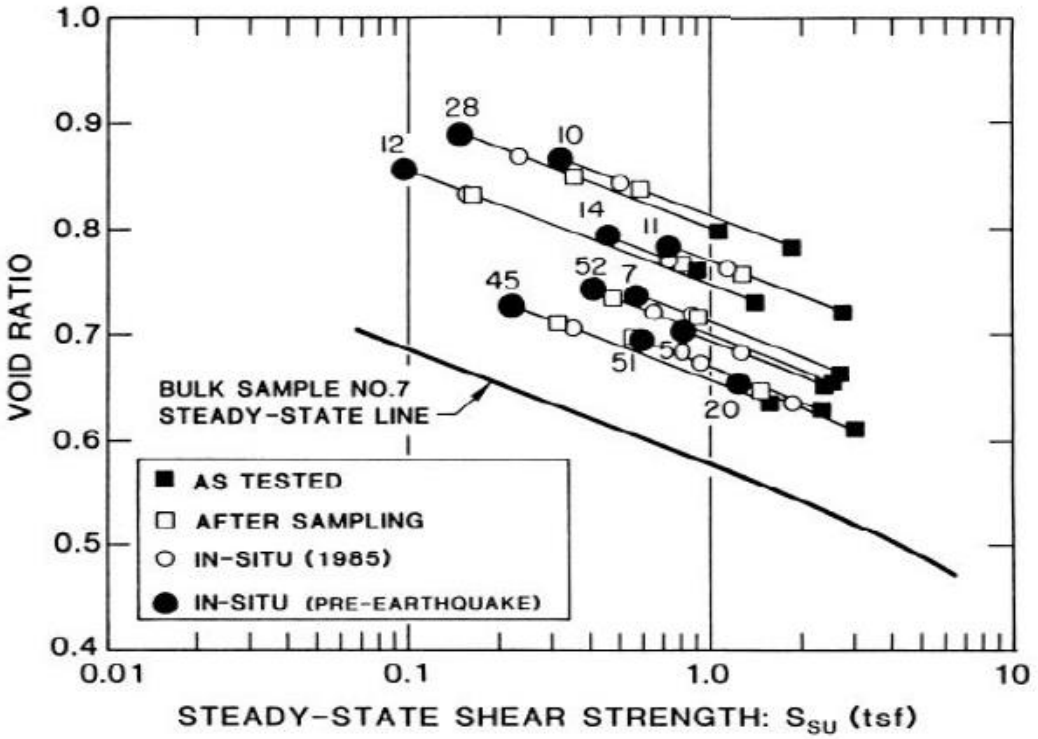

Figure 2.4. Corrected estimates of in-situ S_{us} values and their corresponding laboratory S_{us} values for the Lower San Fernando Dam (Seed et al., 1988)

As it can be observed in Figure 2.4, this method includes extensive corrections from laboratory S_{us} values to the estimated in-situ S_{us} values. When the assumption of parallelism between the steady-state lines obtained from disturbed reconstituted samples and high-quality undisturbed samples is taken into account, these large correction factors may result in some problems in estimated shear strengths.

Further studies are also developed to validate the laboratory-based method proposed by Poulos et al. (1985) for the engineering evaluation of the in-situ post-liquefaction strengths of soils. For five different dams in the U.S. (O'Neill Forebay Dam, Wickiup Dam, Anderson Ranch Dam, Casitas Dam, and Jackson Lake Dam), the in-situ post-liquefaction strengths of soils are estimated by the laboratory-based method proposed by Poulos et al. (1985). The corresponding residual strengths for these dams are also estimated by the empirical relationship suggested by Seed (1987) based on available case histories. The comparison of the results is shown in Figure 2.5. As it can be seen from this figure, in-situ S_{us} values estimated by Poulos et al. (1985) laboratory-based method are generally higher than the S_r values suggested by empirical Seed (1987) relationship.

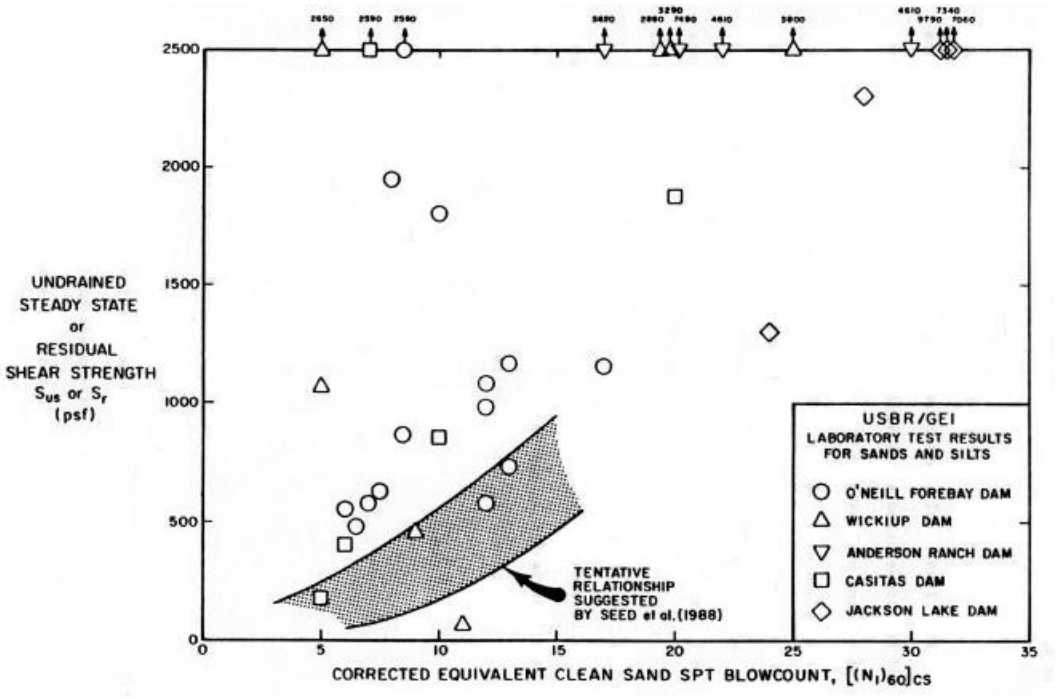

Figure 2.5. Comparison of in-situ post-liquefaction shear strengths obtained by Poulos et al. (1985) laboratory-based method and Seed (1987) empirical relationship for five different dams (Harder, 1988, after Von Thun, 1986)

Further laboratory-based techniques are also developed inspired by the steady-state method proposed by Poulos et al. (1985). These methods clarified some of the

reasons behind obtaining unconservative in-situ S_{us} values as shown in Figure 2.5. First of all, it is realized by several researchers that the type of the test and shearing affect the final S_{us} value. While higher S_{us} values are obtained at the end of undrained triaxial compression (TXC) tests, lower values are evaluated for undrained direct simple shear (DSS) tests or undrained triaxial extension (TXE) tests. When a slope failure is considered, it is common to observe compression and extension behavior at the back heel and toe of the landslide, respectively. Thus, while TXC tests are more suitable for the back heels of the landslides where compressions are observed, TXE tests are better in representing the behaviors of the toes of the landslides showing extensional behavior. Additionally, DSS tests are better for representing the base, i.e., the middle portion with belly, of the landslide. Since the method proposed by Poulos et al. (1985) only includes TXC tests, it is highly possible to overestimate the shear strengths of the toe and base of the landslides with that method. Fortunately, this issue can be handled by replacing TXC tests of the original steady-state procedure with more representative tests such as TXE or DSS with respect to the relative location of the failure surface along the landslide.

Further laboratory studies on post-liquefaction shear strength assessments also revealed a new state called quasi-steady state for some soils. It is seen that contractive behavior is observed for sands and low plasticity silts with very low relative densities, and very low undrained residual strength values are achieved for these types of soils at large strains. On the contrary, it is found that dilative behavior is observed for dense soils, and higher undrained residual strength values are achieved for these types of soils at large strains. Interestingly, the soils of intermediate relative density between loose and dense soils showed a very different type of behavior after shearing. First, they produced a contractive type of behavior, i.e., strain softening, up to a point, but then they experienced a phase transformation and showed a dilative behavior, i.e., strain hardening, resulting in shear strength increase at larger strains. The corresponding undrained stress-strain behaviors and stress paths for these three types of soils are explained in Figure 2.6.

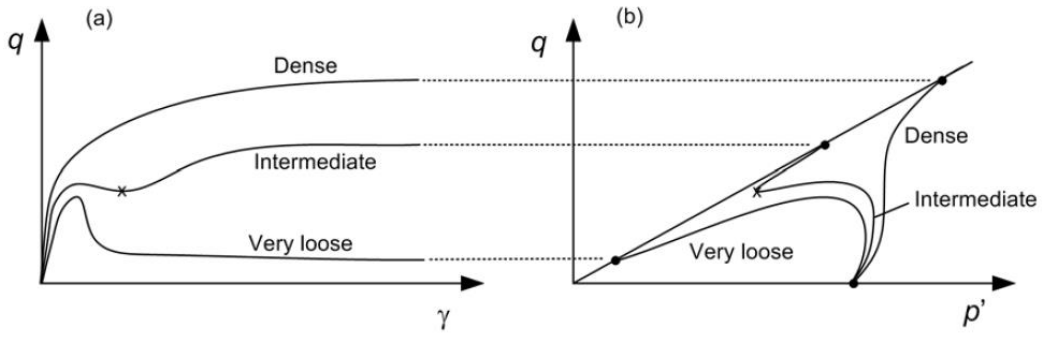

Figure 2.6. Schematic plots of undrained stress-strain behaviors and stress paths for dense, intermediate, and loose soils under monotonic loading (Kramer, 2008)

For the soils with intermediate relative density, the point that the local minimum value of strength is observed is marked with x in Figure 2.6. Alarcon-Guzman (1988) defined the state at this point as the quasi-steady state. As it can be seen in this figure, the ultimate steady-state reached at very large strains may give larger undrained shear strengths than the quasi-steady state. This type of behavior is also validated by various researchers such as Yoshimine and Ishihara (1998) and Yamamuro and Convert (2001). On the other hand, still a debate exists in the literature about whether the quasi-steady state strength or ultimate steady-state strength is better in representing the actual post-liquefaction shear strength for soils with intermediate relative density.

Furthermore, further experimental studies also pointed out that the initial effective confining stress affects the post-liquefaction shear strengths in the field as well. Riemer and Seed (1997) claimed that when two identical samples consolidated to exactly the same post-consolidation void ratios, the one with higher initial effective confining stress produces a higher S_{us} value but a lower S_{us}/P ratio (P represents initial vertical effective confining stress) in undrained TXC tests. The study also showed that the increase of S_{us} values with increasing initial effective confining stresses was nonlinear.

It should be noted that although numerous additional laboratory investigations by shaking tables etc. and scale model experiments have been performed these days, a

universally accepted laboratory-based engineering evaluation method for post-liquefaction shear strengths of in-situ soils has not been developed yet due to challenges mentioned throughout this section. Hence, empirical and semi-empirical relationships are much preferred approaches in practice to predict the residual shear strengths of soils.

2.2 Empirical and Semi-empirical Methods

It is already discussed that experimental evaluation of post-liquefaction strength includes a lot of difficulties as laboratory-scale large strain cyclic test is extremely grueling to be conducted. The fundamental challenges faced during laboratory-based methods are summarized as void redistribution, partial drainage, and inter-layer mixing. Because of these challenges faced during experimental investigation of post-liquefaction strengths, empirical and semi-empirical relationships for the evaluation of S_r based on full-scale field case histories are developed. A brief history of these methods is provided below.

2.2.1 Seed (1987)

This study can be considered as the first well-established study in developing post-liquefaction strength relationships. As it is the initiator in this topic, it also presented the difficulties and challenges in evaluating post-liquefaction strength and shed light on the upcoming studies. The study presents a post-liquefaction strength prediction relationship, which is described as a tentative relationship by Prof. H. Bolton Seed, given in Figure 2.7 based on 12 case histories.

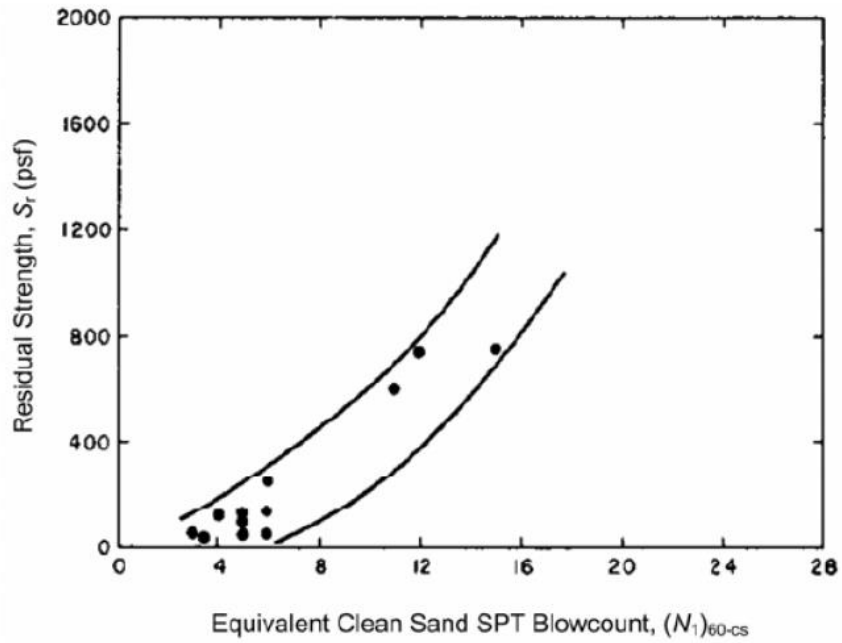

Figure 2.7. Post-liquefaction strength relationship proposed by Seed (1987)

Right after the publication of this study, it was realized that a small detail had been overlooked for the data point located at the rightest in Figure 2.7 with $S_r \approx 750$ psf and $(N_1)_{60,cs} \approx 15$ blows/ft, which corresponds to Lower San Fernando Dam case history. The residual strength value for this case was evaluated with an unconservative approach as only the pre-failure geometry was considered during the back-analysis. In fact, an erroneous assumption was made by the research team for this case history such that the momentum effects were assumed to be minor. Prof. H. Bolton Seed's son, Prof. Raymond B. Seed, who was a Ph.D. student in those years, corrected this error, and the repaired data point is published in Seed and Harder (1990) with the updated residual strength relationship.

At the time when this study was performed, the number of case histories was few, and the back-analysis methods were not developed much yet. Thus, various assumptions, approaches, and techniques were applied to this small number of case histories. The cases other than dams, such as levees and embankments, were considered "small" case histories with low penetration resistances, and they were analyzed with relatively approximate techniques. Furthermore, these case histories

were not documented in detail, so available information about soil stratigraphy, site geology, and in-situ penetration tests was not clear for some cases.

As presented in Figure 2.7, the residual strength values back-calculated from 12 liquefaction case histories were correlated as a function of equipment, energy, procedure, overburden stress, and fines content corrected SPT resistance, $(N_1)_{60,cs}$, only. A closed-form solution to the relationship was not provided. Prof. H. Bolton Seed proposed a slightly different fines content adjustment form in Seed (1987) than the previous correlations used in SPT-based liquefaction triggering correlations. This fines content correlation recommended specifically for residual strength relationships is given in Equation 2-1.

$$(N_1)_{60,cs} = (N_1)_{60} + \Delta(N_1)_{60} \qquad \text{Equation 2-1}$$

In this equation, $\Delta(N_1)_{60}$ represents the additional SPT resistance due to the fines content of the soil, and it increases with increasing fines content. The recommended values for $\Delta(N_1)_{60}$ can be obtained using Table 2.1 provided by Seed (1987).

Table 2.1 Recommended values for fines content adjustment for SPT resistance, $\Delta(N_1)_{60}$ (Seed, 1987)

Fines Content (%)	**$\Delta(N_1)_{60}$ (blows/ft)**
0	0
10	1
25	2
50	4
75	5

2.2.2 Seed and Harder (1990)

This study can be considered as the updated version of Seed (1987) study with five more additional case histories, and corrected value of S_r for the Lower San Fernando

Dam failure case history. The corresponding residual strength relationship presented in Figure 2.8 is developed by the back-analyses of 17 case histories in total.

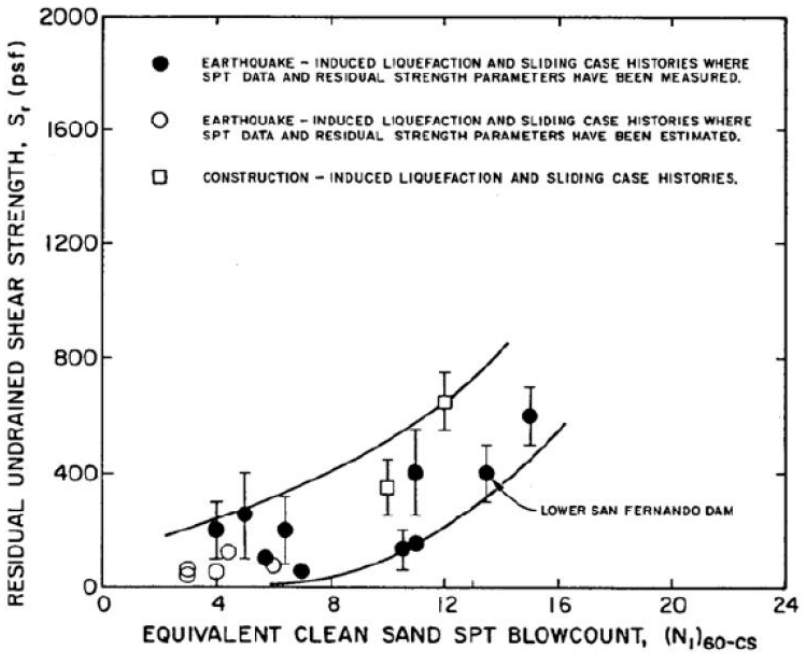

Figure 2.8. Post-liquefaction strength relationship proposed by Seed and Harder (1990)

Since this paper was published very close to Seed (1987) study within three years, the back-analysis methods were not still developed much yet. However, this study succeeded in including five more case histories into the database. Again, a variety of assumptions, approaches, and techniques were applied to these seventeen case histories, and the cases whose SPT penetration resistance was estimated instead of measuring were specified in the relationship given in Figure 2.8 by empty dots. One of the case histories added later than Seed (1987), the Upper San Fernando Dam damaged during the 1971 San Fernando Earthquake (M_w=6.6), was not failed during the event. Therefore, the residual strength value evaluated for this case history was higher than the residual strength values of the cases in which a major flow-type failure was observed.

In addition to that, Seed and Harder (1990) also incorporated momentum effects, i.e., inertial effects, for three of the most extensive liquefaction-induced failures also

included in Seed (1987) database. These three case histories are Fort Peck Dam, Lower San Fernando Dam, and Calaveras Dam. For these three significant cases, both $S_{r,yield}$ value corresponding to the residual strength based on pre-failure geometry, and $S_{r,resid/geom}$ value corresponding to the residual strength based on post-failure geometry are evaluated separately. $S_{r,yield}$ is defined as the apparent pre-failure yield stress based on the pre-failure geometry that gives the theoretical strength along the failure plane remaining in the liquefied portion of the soil. It is evaluated by assigning the static Factor of Safety equal to 1.0 for pre-geometry, and assessing the strength along the liquefied portions of the eventual slide surfaces. $S_{r,resid/geom}$, on the other hand, is defined as the apparent residual stress based on the post-failure geometry that gives the theoretical strength along the failure plane remaining in the liquefied portion of the soil. It is evaluated by assigning the static Factor of Safety equal to 1.0 for residual post-geometry, and assessing the strength along the liquefied portions of the eventual slide surfaces. Seed and Harder (1990) states that the actual residual strength value, S_r, should be selected between $S_{r,yield}$ and $S_{r,resid/geom}$ values such that these two values are the lower and upper boundaries of the residual strength.

It is obvious that the moving failure mass would accumulate some momentum, and this momentum should be eliminated by the failure mass to be decelerated and brought back to rest at its final resting position. Therefore, the actual post-liquefaction strength should be greater than the residual strength evaluated based on post-failure geometry ($S_{r,resid/geom}$) as it under-estimates the actual value of S_r by neglecting the shear strength required to slow down (decelerate) the moving failure mass and overcome the momentum effects. Consequently, $S_{r,resid/geom}$ can be considered as the lower bound for actual post-liquefaction strength, S_r.

A similar case is also valid for $S_{r,yield}$ such that the actual post-liquefaction strength, S_r, should be less than the apparent pre-failure yield stress based on the pre-failure geometry, $S_{r,yield}$. Otherwise, the failure mass during the event would remain statically stable at its initial position, and no failure would be observed. In fact, only

small displacements may occur as a result of cyclic lurching. Hence, $S_{r,yield}$ can be considered as the upper bound for actual post-liquefaction strength, S_r.

Seed and Harder (1990) realized that the actual value of post-liquefaction strength should exist between these two boundaries, $S_{r,yield}$ in the upper and $S_{r,resid/geom}$ in the lower, with respect to the runout distances of the failure mass. For the cases where the runout distance of the failure mass (or center of gravity of failure mass) is very large such as for the major failures Fort Peck Dam, Lower San Fernando Dam, and Calaveras Dam cases mentioned above, the actual post-liquefaction strength values are evaluated closer to the lower bound, $S_{r,resid/geom}$. For several other case histories added later than Seed (1987) with smaller runout distances, such as the La Marquesa Dam U/S and D/S Slopes and the La Palma Dam case histories, the actual post-liquefaction strength values are assumed to be close to the average of upper and lower bounds, $S_{r,yield}$ and $S_{r,resid/geom}$ respectively. Furthermore, some additional strength is also added to these cases in order to consider cyclic inertial effects. These effects are mainly caused by strong shakings with high seismic loading intensity.

As represented in Figure 2.8, this study provides a post-liquefaction strength as a function of equipment, energy, procedure, overburden stress, and fines content corrected SPT resistance ($(N_1)_{60,cs}$) as well similar to Seed (1987). The fines content adjustment suggested by Seed (1987) given in Equation 2-1 is also employed for this study. A closed-form solution to the relationship was not provided. Weber (2015) evaluates the least-squares regression (R-square) value as R^2=0.64 for the relationship given in Figure 2.8, which indicates a moderately good overall fit. It should be noted that the post-liquefaction strength estimations of Seed and Harder (1990) are more reasonable than Seed (1987) because momentum and inertial effects are included in the back-analyses, both pre-failure and post-failure geometries and corresponding strengths are considered with respect to runout distances of the failure mass, and S_r values are adopted accordingly.

2.2.3 Stark and Mesri (1992)

Another guiding study in the engineering evaluation of post-liquefaction strength is Stark and Mesri (1992). This study considers all 17 case histories used by Seed and Harder (1990), and adds three more case histories to this database. Consequently, the relationship presented in Figure 2.9 is provided based on 20 case histories in overall. Back-analyses results of Seed and Harder (1990) are exactly used for the case histories during the development of residual strength relationships. Again, numerous assumptions, approaches, and techniques were applied to these twenty case histories, and the cases whose SPT penetration resistance was estimated instead of measuring were specified in the relationship given in Figure 2.9 by empty dots and squares. A closed-form solution of the relationship was provided as given in Equation 2-2.

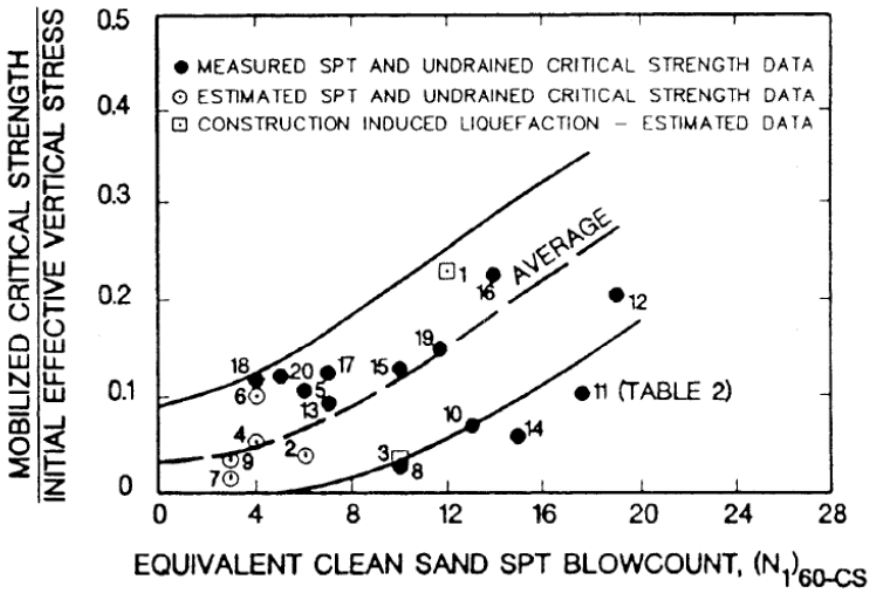

Figure 2.9. Post-liquefaction strength relationship proposed by Stark and Mesri (1992)

$$\frac{S_u(critical)}{\sigma'_{v0}} = 0.0055 \cdot (N_1)_{60,cs} \qquad \text{Equation 2-2}$$

Different than the previous studies, this study was also including the effect of initial vertical effective stress, σ'_{v0}. As presented in Equation 2-2, the post-liquefaction

strength increases linearly with increasing equipment, energy, procedure, overburden stress, and fines content corrected SPT resistance ($(N_1)_{60,cs}$) and initial vertical effective stress (σ'_{v0}). The initial vertical effective stress values are evaluated by taking the average of σ'_{v0} values along the entire failure plane for each case history. It should be remarked that only the region remaining in the liquefied layer is taken into account for average initial vertical effective stress calculations. The corresponding relationship is given in S_u/σ'_{v0} form such that the vertical axis presented in Figure 2.9 represents the ratio of mobilized critical strength and initial effective vertical stress, S_u/σ'_{v0}, while the horizontal axis still gives the equipment, energy, procedure, overburden stress, and fines content corrected SPT resistance, $(N_1)_{60,cs}$.

Weber (2015) performed a variety of linear and nonlinear least-squares regressions on the case history database provided by Stark and Mesri (1992) given in Figure 2.9. The least-squares regression (R-square) value was evaluated as R^2=0.22 for both linear and second-order polynomial curves fitting the corresponding relationship. This circumstance indicates that the regression did not provide a well fit for the data provided, and therefore it can be defined as randomly scattered or poorly behaved.

It is obvious that the main difference between this study and the previous ones is that previous studies such as Seed (1987) and Seed and Harder (1990) claim constant post-liquefaction strength (S_r) for any given relative density as the relationship is only a function of SPT resistance. This approach is parallel to the classical critical state theory. On the other hand, the relationship proposed by Stark and Mesri (1992) also considers the effect of initial vertical effective stress and suggests a constant residual strength-initial vertical effective stress ratio (S_u/σ'_{v0}). Despite the fact that the relationship recommended by Stark and Mesri (1992) provides a lower R^2 value and higher scattered data than Seed and Harder (1990), a correlation between post-liquefaction strength and initial effective vertical stress is implemented in a theoretically correct way in this study. Hence, it is a great guide for further studies to give a clue about examining the relationship between post-liquefaction strength

and initial vertical effective stress. One can only criticize this study by suggesting a better relationship between SPT resistance and the S_u/σ'_{v0} ratio.

2.2.4 Olson (2001) and Olson and Stark (2002)

Olson (2001) is the doctoral thesis of Prof. Scott Michael Olson in the Graduate College of the University of Illinois at Urbana-Champaign, and it is one of the most detailed and pioneer studies in this field. It includes the back-analyses of 33 case histories in total, which makes it one of the studies in this field with the most expanded case history database. Olson and Stark (2002), on the other hand, is the paper published based on this Ph.D. thesis with the same database.

Two types of different approaches are performed in the study based on the quality of the information available for case histories. For 10 of these 33 field failure case histories, kinetics analyses are applied such that these analyses include the inertial and momentum effects. These 10 cases are selected with respect to the amount of available information to consider the momentum effects. This required information for kinetics analyses is generally the step-by-step progression of the failure mass from its pre-failure position at rest to the post-failure position at rest. This approach used by Olson (2001) is mainly adapted from the methodology proposed by Davis et al. (1988) given in Figure 2.10.

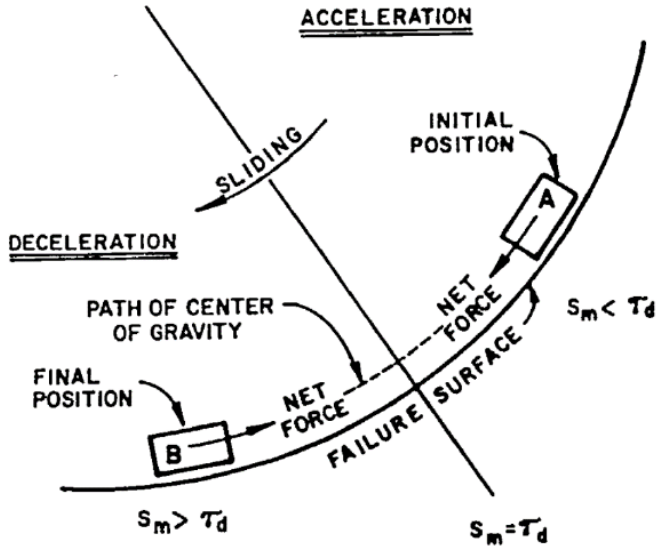

Figure 2.10. Schematic illustration of the progression of a failure mass and the net forces acting on it to decelerate and come to rest (Davis et al., 1988)

Davis et al. (1988) states that a failure mass initially gains velocity and momentum with acceleration, and then loses them with a declaration. Eventually, it comes to rest when accumulated velocity and momentum reduce totally. Inspired by this phenomenon, the study claims that the progressive development and change in acceleration, velocity, displacement, and momentum of the failure mass can be tracked and monitored. With a basic assumption, the movement of the whole mass can be examined by tracking its center of gravity.

Theoretically, at the moment when the failure mass passes from accelerating to decelerating, no net shear force transfer of inertial force to the base of the moving slide mass would be observed. This moment is defined as the zero inertial force moment, and the residual strength evaluated exactly at that moment is claimed to be the actual residual strength value including the momentum and inertia effects. Although this methodology is theoretically correct for estimating a residual strength value involving the effects of momentum and inertia, it is extremely challenging to assess the geometry of failure mass at this moment. Therefore, Seed and Harder (1990), for example, considers both $S_{r,yield}$ value corresponding to the residual strength based on pre-failure geometry, and $S_{r,resid/geom}$ value corresponding to the

residual strength based on post-failure geometry, and assigns the best estimate of S_r value between these two boundaries with respect to corresponding runout distance of the failure mass.

Olson (2001) takes this method forward and performs a full progressive inertial analysis by tracking the changes in acceleration, velocity, displacement, and momentum of the center of gravity of the failure mass. As a first step, the initial and final locations of the center of gravity of the failure mass are estimated. Then, a third-order polynomial function is fitted between these initial and final points of the center of gravity (COG) of the failure mass in order to approximate the route of the COG. Olson (2001) states that the third-order polynomial function should be parallel as much as possible to the actual sliding surface. An example of Olson (2001)'s study for the Wachusett Dam case history is presented in Figure 2.11 schematically. The uppermost sketch represents the shape of the third-degree polynomial curve for this case history that the COG of the failure mass used as moving path. The following plots represent the change of total shear stress along the failure surface, acceleration and deceleration of the COG, velocity of the COG, and displacement of the COG of the failure mass, respectively. While negative acceleration values in the second plot correspond to the acceleration period, positive values correspond to the deceleration period due to the sign convention of the directions. Also, the velocity values are given in negative signs due to same reason. It should be remarked that the velocity value reaches zero at the final point when failure mass comes to rest totally.

In Figure 2.11, the angle θ represents the slope angle of the fitted third-order polynomial function at any point. Therefore, the weight of the failure mass (W) multiplied by $\sin\theta$ gives the overall driving force acting on the COG of the failure mass. As it can be understood from this figure, it is better to fit a polynomial that represents the inclination slope correctly than to fit a polynomial that represents the correct path of the COG of the failure mass. In other words, the polynomial fitted between the initial and final points of the COG of the failure mass should have a similar angle of slopes at any point on the curve with the same point on the actual

sliding surface. Mimicking the slopes is more critical than mimicking the correct path of the COG of the failure mass.

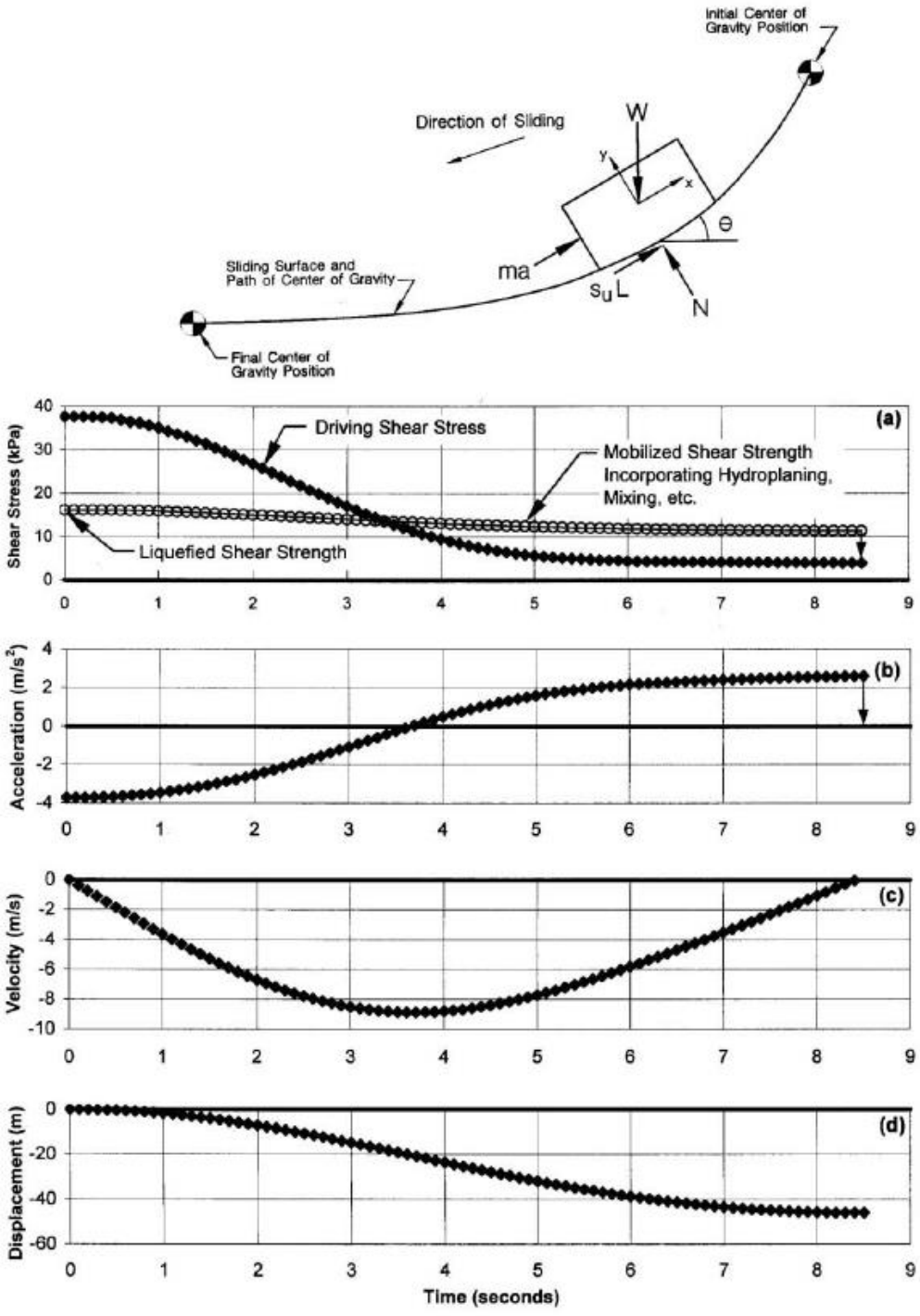

Figure 2.11. An example of Olson (2001)'s kinetic analysis representation for the Wachusett Dam case (Olson, 2001)

It should be noted that although evaluation of multiple failure stages between the pre-failure geometry and post-failure geometry is required to estimate correct values of θ, Olson (2001) did not prepare any failure stages for this purpose. To be able to compare their results with Olson (2001), Weber (2015) estimates initial and final slope angles, $\theta_{initial}$ and $\theta_{final,}$ respectively, and compares its initial and residual driving forces by considering these angles. It is stated that suitably good matches are achieved between the values of S_r estimated by Olson (2001) and Wang (2003), Kramer (2008), and Weber (2015) for 9 of the 10 cases (except Shibecha-Cho Embankment case history) that kinetics analyses are performed by Olson (2001).

The final resisting force acting on the COG of the failure mass was evaluated by multiplying the single residual strength value assigned for the whole failure surface in the full-scale cross-section with the overall length of the failure plane. The final driving force was evaluated by multiplying the weight of the failure mass with the sinus of the slope of the polynomial curve. The difference between these two resulting forces in upslope and downslope directions, respectively, gives the surplus force that produces an acceleration or deceleration. The corresponding acceleration value was evaluated referring to Newton's second law given in Equation 2-3.

$$F = m \cdot a \qquad \text{Equation 2-3}$$

Then, the progressive changes in acceleration, velocity, displacement, and momentum of the COG of the failure mass were tracked by solving the system incrementally with the help of a time-step algorithm. The value of S_r used in calculations is incrementally changed until the same displacement is obtained for COG of the failure mass with the actually observed displacement of this COG in the field. Consequently, the post-liquefaction strength for liquefied materials is obtained by using Equation 2-4.

$$S_u(LIQ) = \frac{S_u - \left(\frac{L_d}{100} \cdot S_d\right)}{1 - \frac{L_d}{100}} \qquad \text{Equation 2-4}$$

In this equation, while S_u represents the post-liquefaction strength coming from the portion of the failure plane controlled by liquefied materials, S_d represents the drained strength coming from the portion of the failure plane controlled by non-liquefied materials.

It should be noted that potential hydroplaning effects which occur when the toe of the failure mass enters the water, and overall buoyancy effects that occur when the failure mass enters the water are also taken into account by Olson (2001) for these 10 case histories that kinetics analyses are performed. The study reduces the shear strengths by half for the soils which showed an excessive sliding by passing the initial location of the toe of the slope and reaching the reservoir. Olson (2001) defines these hydroplaning effects as reservoir mixing. Although a sensitivity analysis between 0% and 100% is performed in the study to evaluate the strength reduction for these types of soils, the main approximation of 50% reduction is logical.

The thesis of Olson (2001) showed that as the displacements proceed for the failure mass, the overall residual strength changes along the entire failure plane. Thus, the studies considering the incremental progress of failure mass, and momentum (inertial) effects possibly provide more correct post-liquefaction strength values. Even though Olson (2001) performs a great effort to include these effects in its kinetics analyses, several challenges exist for this analytical approach.

First of all, it is sometimes quite difficult to create a reasonable third-degree polynomial that fits between the initial and final points of the COG of the failure mass, and follows the path that actual COG also followed in the field. If the difference between pre-failure and post-failure geometries is large, then it becomes challenging to define the translation path of the COG. In those cases, it is also difficult to assign a polynomial curve that is parallel to this overall failure surface. As a result, the calculated driving shear stresses along the fitted polynomial curve may not match with the actual driving shear stresses in the field along the failure plane for some steps of the displacement progressions.

Secondly, the drained strength coming from the portion of the failure plane controlled by non-liquefied materials, S_d, is a function of effective normal stresses evaluated on those portions of the field failure plane. On the other hand, effective normal stresses change as the failure mass slides along the failure plane. Therefore, it is really compelling to evaluate these stresses along the failure plane as movement occurs.

Thirdly, for the regions where two different soil materials contact along the failure plane as movements occur, it is again difficult to assign a shear strength to these regions. In order to stay on the conservative and safe side, the material with lower shear strength should control the overall strength in these contact regions in theory, but this approach is also questionable.

Fourthly, the residual undrained shear strengths should be employed instead of peak undrained shear strengths for cohesive soils for the cases in which large deformations are observed. A transition from peak strength to residual strength may also be challenging during the modeling of shear strengths of soil materials.

Finally, some cases include several slope failures in it such that initially a smaller portion begins to slide close to the toe of the overall slope. Then, the movement of this smaller piece triggers another failure plane, and a larger piece begins to slide. This process continues for a while, and these preceding small failure surfaces trigger the overall failure plane at the end. For these kinds of incrementally progressive, i.e., retrogressive failure modes, each of these sliding slices can be considered as a separate failure mass with a different center of gravity. Therefore, it is required to deal with several COGs of several failure masses for one case. In these cases, it is difficult to use this analytical kinetics approach since it is capable of tracking only a single failure mass, not multiple masses.

Unfortunately, these major challenges are not explained clearly in Olson (2001). On the other hand, it is quite probable that Olson (2001) treats these issues well as the overall best estimation S_r values are reasonable and logical for these 10 cases. Most importantly, the theory behind the study is correct as the apparent pre-failure yield

stress based on the pre-failure geometry that is evaluated by assigning the static Factor of Safety equal to 1.0 for pre-geometry, $S_{r,yield}$, overestimates the actual value of S_r because large displacements would not have occurred otherwise. Similarly, the apparent residual stress based on the post-failure geometry that is evaluated by assigning the static Factor of Safety equal to 1.0 for residual post-geometry, $S_{r,resid/geom}$, underestimates the actual value of S_r because it does not include momentum effects causing the moving mass coming to rest. Hence, as long as a reasonable polynomial curve is fitted between the initial and final points of the COG movement path, the overall driving shear stresses would be evaluated logically, and therefore the overall value of S_r would fall between these two bound limits. Once better assumptions and judgments are made, better answers could be expected.

Although Olson (2001)'s efforts in kinetics analyses are great, and it evaluates very accurate S_r values consistent with Wang (2003), Kramer (2008), and Weber (2015) for 9 of the 10 cases, it estimates a significantly lower S_r value than the other studies for the remaining one case history, Shibecha-Cho Embankment. The reason behind this difference may arise from the modeling procedure of the case history. As explained earlier, it is difficult to model retrogressive failures that a smaller piece of failure triggers larger failures. Shibecha-Cho Embankment case can be considered as one of these retrogressive failure cases as a small slice of failures reach to overall failure plane step by step. Unfortunately, the kinetics analysis method proposed by Olson (2001) cannot handle these types of failure modes. Therefore, Prof. Olson made assumptions and simplifications in his doctoral thesis for this case history and only considered the movements of the first failure slice closest to the front of the overall failure plane. Accordingly, accelerations, velocities, and displacements were only tracked for this initial failure mass. Due to the fact that only the initial slice was taken into account, the overall scale of the failure, and therefore the overall driving forces acting on the entire failure mass, were underestimated. This underestimation also resulted in the under-estimation of the post-liquefaction strength of this case history.

These 10 case histories were adequately documented, and therefore it was possible to apply kinetics analyses to them. For the remaining 23 case histories, kinetics analyses cannot be performed due to the lack of information available. For most of these cases, the representative post-liquefaction strength was evaluated with respect to the apparent residual stress based on the post-failure geometry that gives the theoretical strength along the failure plane remaining in the liquefied portion of the soil. In other words, the residual strength is assigned equal to $S_{r,resid/geom}$, which is evaluated by assigning the static Factor of Safety equal to 1.0 for residual post-geometry, and assessing the strength along the liquefied portions of the eventual slide surfaces. For some of these 23 case histories, an infinite slope analysis which also gives approximate $S_{r,resid/geom}$ value was employed. The results evaluated for these 23 poorly documented case histories are judged to be over-conservative as it only considers the residual strength obtained based on post-failure geometry ($S_{r,resid/geom}$), and do not include the inertial and momentum effects. As a result, the relationship recommended by Olson (2001) and Olson and Stark (2002) suffered significantly due to the use of $S_{r,resid/geom}$ directly equal to actual S_r for these 23 cases.

For 12 of these 23 case histories, $S_{r,resid/geom}$ is evaluated by assigning the static Factor of Safety equal to 1.0 for residual post-geometry directly, and this value is taken as the best estimate of S_r. For the remaining 11 case histories, again $S_{r,resid/geom}$ is evaluated by assigning the static Factor of Safety equal to 1.0 for residual post-geometry without considering the momentum effects, i.e., inertial forces are equal to zero. However, an infinite slope analysis is employed for these cases in order to approximate the actual field geometry additionally. Both of these approaches are approximate and over-conservative for the assessment of the best estimate of S_r as they ignore the inertial effects and only consider $S_{r,resid/geom}$ value obtained with respect to post-failure geometry. In other words, these methods do not consider the deceleration of the failure mass and reaching zero velocity at the end of the movement. Hence, Olson (2001) underestimates the overall S_r values for these less well-documented 23 case histories.

Similar to Stark and Mesri (1992), Olson (2001) also includes the effect of initial vertical effective stress in post-liquefaction strength relationships. It evaluated the average representative initial vertical effective stresses along the portion of failure planes remaining within the liquefied materials, and divided its back-calculated S_r values to these stress values to obtain S_r/σ'_{v0} ratios for case histories. In parallel with the previous studies, the relationship proposed by Olson (2001) was also a function of SPT resistance. Nevertheless, this study does not apply any fines content adjustment to its SPT resistances by claiming that the fines content correction recommended by Seed (1987) given in Equation 2-1 was not well-founded. Therefore, Olson (2001) directly uses $(N_1)_{60}$ values instead of $(N_1)_{60,cs}$ values in its relationship. On the other hand, fines content adjustment for most of these post-liquefaction case histories is actually important and necessary because liquefied soils generally consist of silty sands and sandy silts. Thus, a reasonable fines content correction is required for the SPT resistances of these cases.

The post-liquefaction strength relationship proposed by Olson (2001) and Olson and Stark (2002) is presented in Figure 2.12. In this figure, while the horizontal axis represents the equipment, energy, procedure, and overburden stress corrected SPT resistance $(N_1)_{60}$ (no fines adjustment), the vertical axis gives the corresponding mobilized critical strength-initial effective vertical stress ratio, S_u/σ'_{v0}, for 33 case histories. The relationships recommended by Stark and Mesri (1992) and Davies and Campanella (1994) are also presented in the same figure. While the straight, bold lines show the boundaries of Olson (2001) study, the dashed bold line between them gives the average relationship for the best estimate of S_r. Closed-form solution of the relationship was also provided as given in Equation 2-5.

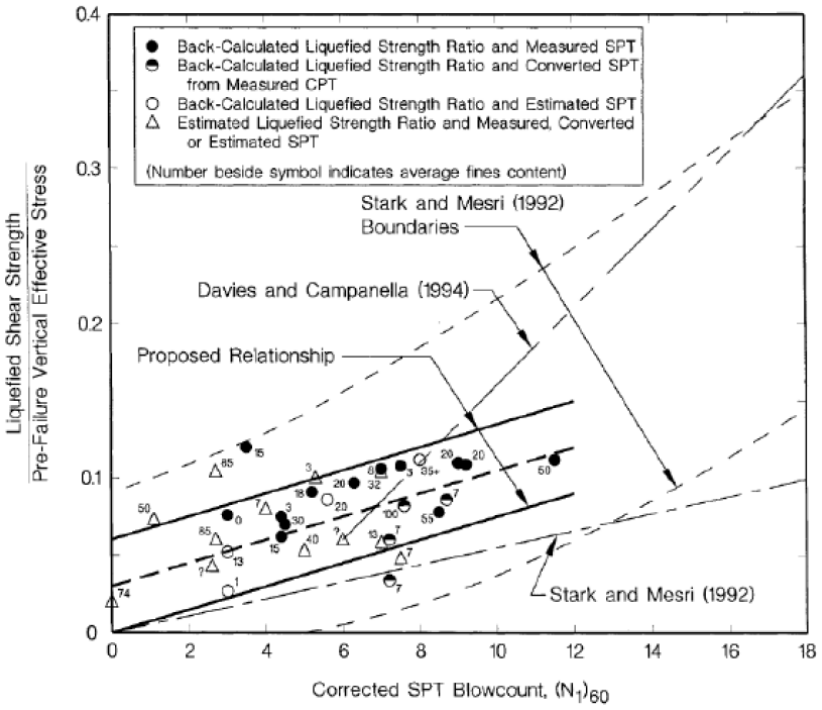

Figure 2.12. Post-liquefaction strength relationship proposed by Olson and Stark (2002)

$$\frac{S_u(LIQ)}{\sigma'_{v0}} = 0.03 + 0.0075 \cdot (N_1)_{60} \pm 0.03 \qquad \text{Equation 2-5}$$

As it can be observed from this figure, some cases have not been taken into account for the proposed relationship as some data points remain outside of the recommended range. Weber (2015) performed several linear least squares regressions on the case history database provided by Olson (2001) given in Figure 2.12. The least-squares regression (R-square) value was evaluated as R^2=0.23 for the line fitting the corresponding relationship. Weber (2015) also recognized that the slope obtained from the regressed relationship with R^2=0.23 was slightly flatter than the slope of the average line of the relationship published by Olson (2001), somehow. In the end, this fit showed that the regression did not provide a well fit for the data provided, and therefore it can be defined as randomly scattered or poorly behaved. The reason behind this poor fit may possibly be the accuracy rate between the well-documented 10 case histories and less well-documented 23 case histories. While well-

documented 10 cases were analyzed in detail with kinetics analyses considering the inertia and momentum effects, the remaining 23 cases were analyzed with an over-conservative approach by considering the residual strength values obtained based on the post-failure geometries ($S_{r,resid/geom}$) instead of the overall residual strength (S_r) values. Another reason behind this poor fit can also be the lack of fines content adjustment for the SPT resistances. Since most of these liquefaction-induced failures consist of silty sand or sandy silt type of soils, a fines content adjustment may have increased the quality of the proposed relationship.

It should be noted that the same criticism made for Stark and Mesri (1992) is also valid for this study. Similar to Stark and Mesri (1992), Olson (2001) and Olson and Stark (2002) also consider the effect of initial vertical effective stress in their relationship, and suggest a constant residual strength-initial vertical effective stress ratio (S_u/σ'_{v0}). However, even though this ratio should change with effective overburden stress, a constant ratio was used in both of these studies.

It should be noted that Olson (2001) also evaluated $S_{r,yield}$, the apparent pre-failure yield stress based on the pre-failure geometry that gives the theoretical strength along the failure plane remaining in the liquefied portion of the soil by assigning the static Factor of Safety equal to 1.0 for pre-geometry, for its case histories. However, these values have not been used in the development of post-liquefaction strength relationships. Instead of using $S_{r,resid/geom}$ values directly as the overall residual strength value for 23 less well-documented case histories, the average of $S_{r,yield}$ and $S_{r,resid/geom}$ could have been used for better estimation. In fact, it is already explained that the actual post-liquefaction strength remains between $S_{r,yield}$ and $S_{r,resid/geom}$ values; therefore, taking the average of them as a best-estimated value gives better results than using $S_{r,resid/geom}$ value directly as the post-liquefaction strength.

In summary, Olson (2001) and Olson and Stark (2002) are important studies in engineering evaluation of post-liquefaction strength. The doctoral thesis of Prof. Olson is one of the most detailed works in this field in terms of documentation of the analyses such as case history database, engineering judgments, assumptions,

calculations, cross-sections, failure planes, soil stratigraphy, and material descriptions, soil properties, etc. In most cases, it is a transparent study, and each step can be followed easily and consistently. No study earlier than Olson (2001) documented this information in such a clear and understandable way. Hence, it is a pioneer study in this field that sheds light to further studies in many ways.

2.2.5 Wang (2003), Kramer (2008) and Wang and Kramer (2015)

Wang (2003) is the doctoral thesis of Prof. Chwen-Huan Wang at the University of Washington, and it is again one of the guiding and pioneer studies in this field. It includes the back-analyses of 31 case histories in total, which makes it one of the studies in this field with the most expanded case history database. Kramer (2008), on the other hand, is the paper published based on this Ph.D. thesis with the same database to develop new probabilistic relationships for in-situ post-liquefaction strengths based on SPT resistance. Seven years later, the obtained regressed relationship is re-published in Kramer and Wang (2015) with minor corrections and improvements over Kramer (2008).

The main difference between Prof. Wang's Ph.D. thesis and the papers published accordingly, Kramer (2008) and Kramer and Wang (2015), is that while Wang (2003) used fines content corrected SPT resistance ($(N_1)_{60,cs}$) in corresponding residual strength relationships, subsequent studies employed non-fines-corrected SPT resistance ($(N_1)_{60}$). On the other hand, Kramer (2008) presents $(N_1)_{60,cs}$ values instead of $(N_1)_{60}$ values for case histories as input parameters for corresponding relationships. Weber (2015) explains this confusion such that the input parameters presented in Kramer (2008) include typographical errors, and the wrong parameters were published in the paper. In other words, the published prediction relationship was actually based on $(N_1)_{60}$ values. Kramer and Wang (2015) fixes this error and publishes $(N_1)_{60}$ values for the corresponding relationship.

Wang (2003) selected 31 case histories in total to be used in the study. Based on the quality of available data, these case histories are divided into two classifications as Primary Case Histories and Secondary Case Histories. While more well-documented and reported 9 case histories are named as Primary Case Histories, the remaining 22 less well-documented cases are considered as Secondary Case Histories. For 9 Primary Case Histories, separate individual back-analyses are performed for each case, and three indices of residual strength relationship, S_r, $(N_1)_{60,cs}$ and σ'_{v0}, are evaluated with the assessment of the level of uncertainty or variance. For 22 Secondary Case Histories, individual back-analyses have not been performed, and average S_r and σ'_{v0} values published by previous investigation teams are used instead. However, $(N_1)_{60,cs}$ values are again evaluated separately for these 22 Secondary Case Histories also.

9 Primary Case Histories were back-analyzed based on a new method proposed in the study, called Zero Inertial Force (ZIF) method. These well-documented 9 cases were also the same as the 9 of 10 case histories that Olson (2001) performed kinetics analyses. The theoretical background of the ZIF method also comes from Davis et al. (1988) explained in the previous section, and presented by a simple sketch in Figure 2.10. A failure mass initially gains velocity and momentum with acceleration, and then loses them with declaration. Eventually, it comes to rest when accumulated velocity and momentum reduce totally. At the moment when the failure mass passes from accelerating to decelerating, no net shear force transfer of inertial force to the base of the moving slide mass would be observed. This moment is defined as the zero inertial force moment, and the residual strength evaluated exactly at that moment is claimed to be the actual residual strength value including the momentum and inertia effects.

The post-liquefaction geometry is evaluated based on this zero inertial force moment. A factor called Zero Inertial Factor (ZIF) is defined which gives the percentage of final displacement necessary to reach this post-failure geometry evaluated based on zero inertial force moment. The pre-failure geometry was then transitioned towards the post-failure geometry with respect to this ZIF, and the residual strength required

to obtain a static Factor of Safety equal to 1.0 at this ZIF geometry was back-calculated. Unfortunately, evaluation of deformed cross-section geometry exactly at this ZIF moment is extremely challenging because it is a random geometry between the pre-failure and post-failure geometries. In most cases, Wang (2003) claims that this geometry representing the moment passing from acceleration to deceleration was achieved before the mid-way between the initial and final geometries, which indicates ZIF<50%.

Wang (2003) uses the kinetics displacement analyses of Olson (2001) for these 9 Primary Case Histories to estimate the ZIF fraction, i.e., the percentage of overall displacement observed at the ZIF moment passing from acceleration to deceleration. A point cloud is defined on pre-failure geometry, and these points are translated incrementally to their locations in post-failure geometry. The ZIF geometry and fraction were evaluated with several engineering judgments in an iterative approach. An example for evaluation of ZIF geometry is illustrated in Figure 2.13 presented below for the Wachusett Dam North Dike case history.

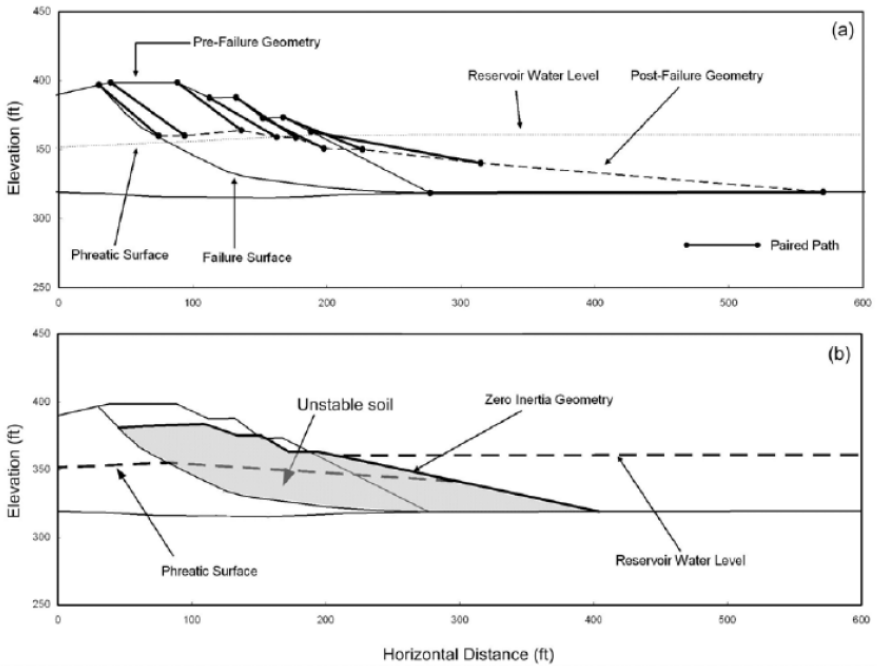

Figure 2.13. Evaluation of ZIF geometry for Wachusett Dam North Dike (Kramer, 2008, after Wang, 2003)

In Figure 2.13a, the translation of points located in pre-failure geometry to their corresponding locations in post-failure geometry is presented. While the solid lines represent the pre-failure geometry, the dashed lines give the post-failure geometry. Olson (2001) estimated ZIF as 43.3% for this case history; therefore, 43.3% of the overall displacements were targeted from initial to final cross-sections. Accordingly, the ZIF geometry is obtained as presented in Figure 2.13b for Wachusett Dam North Dike.

Obviously, several issues exist with the ZIF method. First of all, Wang (2003) uses the kinetics displacement analyses of Olson (2001) for these 9 Primary Case Histories to estimate the ZIF fraction. Therefore, its results are dependent on the accuracy of Olson (2001) study. Secondly, it is still questionable whether this method can be used to evaluate ZIF geometry perfectly or not. Furthermore, it is not clear yet whether these developed ZIF geometries can be used further to estimate the post-liquefaction geometries actually observed at the site. Nevertheless, it can be said that the back-calculated S_r values by Wang (2003) with this ZIF method for these 9 well-documented case histories are accurate and reasonable compared to other milestone studies such as Olson (2001) and Weber (2015).

It is stated that more than 50,000 Monte Carlo simulations were performed for each case history for the combination of several parameters in analyses such as cross-section details, locations of failure planes and groundwater tables, soil properties, etc. It should also be noted that hydroplaning effects were also considered by Wang (2003) when the toes of the failure masses entered the water. The sliding velocity of the failure mass was used to evaluate the extent of hydroplaning at the toe of the slope. On the other hand, the details of the ZIF methods including engineering assumptions and judgments, cross-sections, failure surfaces, soil properties, etc., were not reported for 8 of these 9 Primary Case Histories. The method was only illustrated for the Wachusett Dam North Dike case history as presented in Figure 2.13; therefore, it was not possible to track the steps followed in Wang (2003) for the remaining 8 cases.

For these 9 Primary Case Histories, evaluated σ'_{v0} and $(N_1)_{60,cs}$ values generally, but not perfectly, agree with estimated values by previous studies. For the evaluation of $(N_1)_{60,cs}$ values, Wang (2003) uses the fines content correction proposed by Seed (1987), which provides a high amount of penetration increase with high fine contents even for low penetration resistance ranges. Therefore, the differences between penetration resistances may rise from the method used in fines content adjustments.

For the remaining 22 Secondary Case Histories, the ZIF method and corresponding back-analyses were not performed due to lack of information. Therefore, S_r values and S_r/σ'_{v0} ratios were estimated by using the studies of previous investigation teams considering the same case histories as shown in Table 2.2 and Table 2.3, respectively. Similarly, $(N_1)_{60}$ or $(N_1)_{60,cs}$ values were also evaluated based on previous studies as well. Although best estimates of SPT resistances generally fit well and agree with other studies in most cases, there exist some differences between the selected values of other studies and Wang (2003). As explained earlier, these differences mainly arise from the fines content correction approaches followed by researchers such that the methods using Seed (1987) approach for fines adjustments may end up with larger penetration resistances due to higher penetration increase with higher fines content. Moreover, some cases do not include any information regarding the penetration resistances. Thus, researchers estimate those values based on various assumptions and judgments with respect to available documentation. As a result, some differences may also be obtained based on these assumptions and judgments.

Unfortunately, the evaluation procedure of representative initial vertical effective stress values for these 22 less well-documented case histories was not explained transparently in Wang (2003) or Kramer (2008). In fact, the mean and standard deviations for σ'_{v0} values were not stated in these sources even. Those values were finally published in Kramer and Wang (2015) individually for each case. One of the most significant studies in the post-liquefaction shear strength field examining previous studies for cross-comparison, Weber (2015), states that significant errors were observed when these σ'_{v0} values were back-tracked. Even, the poor evaluation

of these values was causing some problems in the predictive relationships provided by Kramer (2008) and Kramer and Wang (2015). For these 22 Secondary Case Histories, S_r/σ'_{v0} ratios estimated from several previous studies were used to evaluate σ'_{v0} values. The best estimate of residual strength values obtained from previous studies, S_r, were divided by these S_r/σ'_{v0} ratios to determine σ'_{v0} values. On the other hand, the ways that these S_r values and S_r/σ'_{v0} ratios evaluated were not compatible with each other because they were developed by different investigation teams using different back-analyses methods, technical opinions, and failure mechanisms. Hence, obtained representative σ'_{v0} values in Wang (2003) study were not reasonable totally. In fact, while σ'_{v0} values estimated by Olson (2001) and Weber (2015) were in a good agreement, the values reported by Wang (2003) do not agree with those values totally due to the reason explained above. Even, nearly half of the σ'_{v0} values estimated by Wang (2003) are less or greater than the values reported by Olson (2002) or Weber (2015) by a factor of 1.5. Moreover, this factor increases up to 2 for six case histories. This factor increases more and more for the case histories with a high level of uncertainty in parameters such as unit weights, groundwater table level, etc. In general, Wang (2003) estimates higher σ'_{v0} values, which indicates conservative under-predictions of S_r for any actual σ'_{v0} value. Therefore, relationships developed for post-liquefaction shear strength by Wang (2003) study suffer from these erroneous estimations of initial vertical effective stress values.

It should be noted that the differences in initial vertical effective stress values may also rise from the selection of failure planes for case histories such that while Olson (2001) selects slightly shallower failure planes for some cases, Weber (2015) tends to analyze deeper failure surfaces for them.

Nevertheless, the differences in residual strength evaluations of Wang (2003) and other studies were not only caused by differences in selected representative initial vertical effective stress values, but also due to other conflicts. Similar to σ'_{v0} values, representative S_r values and S_r/σ'_{v0} ratios were estimated by using the studies of previous investigation teams considering the same case histories as presented in Table 2.2 and Table 2.3, respectively.

Table 2.2 Evaluation of representative residual strengths for 22 Secondary Case Histories based on previous studies (Wang, 2003)

Case	References	S_r Values (psf)	Mean S_r (psf)
Asele Road	Konrad and Watts (1995)	11	
	Olson (2001)	241	164
Chonan Middle School	Ishihara et al (1990)	167	
	Ishihara (1993)	194	
	Olson (2001)	178	179
El Cobre	Olson (2001)	195	195
Helsinki Harbor	Olson (2001)	53	53
Hokkaido Tailings	Ishihara et al. (1990a)	408	
	Olson (2001)	172	251
Kawagishi-cho	Seed (1987)	120	
	Seed and Harder (1990)	120	
	Stark and Mesri (1992)	120	120
Koda Numa	Lucia (1981); Lucia et al. (1982)	25	
	Seed (1987)	50	
	Seed (1987)	50	
	Olson (2001)	66	48
La Marquesa Downstream	De Alba et al. (1987)	423	
	Seed and Harder (1990)	400	
	Stark and Mesri (1992)	400	
	Olson (2001)	190	344
La Marquesa Upstream	De Alba et al. (1987)	208	
	Seed and Harder (1990)	200	
	Stark and Mesri (1992)	200	
	Olson (2001)	129	181
Lake Merced	Seed (1987)	100	
	Seed and Harder (1990)	100	
	Stark and Mesri (1992)	100	
	Olson (2001)	257	139
La Palma Dam	De Alba et al. (1987)	210	
	Seed and Harder (1990)	200	
	Stark and Mesri (1992)	200	
	Olson (2001)	156	189

Table 2.2 (cont'd) Evaluation of representative residual strengths for 22 Secondary Case Histories based on previous studies (Wang, 2003)

Case	References	S_r Values (psf)	Mean S_r (psf)
Metoki Road	Olson (2001)	113	133
Mochi Koshi Dike 1	Poulos (1988)	60	
	Davis et al. (1988)	60	
	Olson (2001)	258	159
Mochi Kosho Dike 2	Lucia (1981); Lucia et al. (1982)	210	
	Seed (1987)	210	
	Seed (1987)	210	
	Poulos (1988)	250	
	Seed and Harder (1990)	250	
	Stark and Mesri (1992)	250	
	Olson (2001)	223	234
Nalband	Yegian et al.(1994)	117	
	Olson (2001)	152	140
Nerlerk Berm 1	Sladen et al (1985a)	42	
	Jeffries et al. (1990)	308	
	Stark and Mesri (1992)	300	
	Olson (2001)	54	179
Sheffield Dam	Seed (1987)	50	
	Seed and Harder (1990)	75	
	Stark and Mesri (1992)	75	
	Olson (2001)	198	100
Snow River	Seed (1987)	50	
	Seed and Harder (1990)	50	
	Stark and Mesri (1992)	50	50
Solfatara Canal	Seed (1987)	130	
	Seed and Harder (1990)	50	
	Stark and Mesri (1992)	50	
	Olson (2001)	88	77
Soviet Tajik - May 1 Slide	Ishihara et al (1990b)	167	
	Olson (2001)	418	334
Tar Island Dike	Plewes et al. (1989)	305	
	Konrad and Watts (1995)	80	
	Olson (2001)	500	346
Zeeland	Olson (2001)	226	226

Table 2.3 Evaluation of representative residual strength-initial vertical effective stress ratios for 22 Secondary Case Histories based on previous studies (Wang, 2003)

Case	References	S_r/σ'_{vo} Values	Mean S_r/σ'_{vo}
Asele Road	Olson and Stark (2002)	0.104	0.104
Chonan Middle School	Olson and Stark (2002)	0.091	0.091
El Cobre	Olson and Stark (2002)	0.020	0.020
Helsinki Harbor	Olson and Stark (2002)	0.060	0.060
Hokkaido Tailings	Olson and Stark (2002)	0.074	0.074
Kawagishi-cho	Stark and Mesri (1992) Olson and Stark (2002)	0.098 0.075	0.087
Koda Numa	Stark and Mesri (1992) Wride et al. (1999) Olson and Stark (2002)	0.032 0.032 0.040	0.045
La Marquesa Downstream	Stark and Mesri (1992) Wride et al. (1999) Olson and Stark (2002)	0.224 0.223 0.110	0.186
La Marquesa Upstream	Stark and Mesri (1992) Wride et al. (1999) Olson and Stark (2002)	0.125 0.125 0.070	0.107
Lake Merced	Stark and Mesri (1992) Wride et al. (1999) Olson and Stark (2002)	0.105 0.105 0.108	0.106
La Palma Dam	Stark and Mesri (1992) Olson and Stark (2002)	0.120 0.120	0.120
Metoki Road	Olson and Stark (2002)	0.043	0.043
Mochi Koshi Dike 1	Stark and Mesri (1992) Wride et al. (1999) Olson and Stark (2002)	0.092 0.015 0.060	0.091
Mochi Kosho Dike 2	Stark and Mesri (1992) Wride et al. (1999) Olson and Stark (2002)	0.092 0.048 0.104	0.081
Nalband	Olson and Stark (2002)	0.109	0.109
Nerlerk Berm	Jeffries et al (1990) Stark and Mesri (1992) Olson and Stark (2002)	0.150 0.148 0.086	0.124
Sheffield Dam	Stark and Mesri (1992) Wride et al. (1999) Olson and Stark (2002)	0.038 0.038 0.053	0.043
Snow River	Stark and Mesri (1992)	0.024	0.024
Solfatara Canal	Stark and Mesri (1992) Wride et al. (1999) Olson and Stark (2002)	0.052 0.052 0.080	0.063
Soviet Tajik - May 1 Slide	Olson and Stark (2002)	0.082	0.082
Tar Island Dike	Olson and Stark (2002)	0.058	0.058
Zeeland	Olson and Stark (2002)	0.048	0.048

As it can be seen in Table 2.2, the representative S_r value was directly selected same as the value reported by Olson (2001) as 195 psf = 9.34 kPa. However, this value was reported as 40 psf = 1.92 kPa by Olson (2001), actually. Similarly, S_r value was taken as a value between the values provided by Ishihara et al. (1990) and Olson (2001) (408 psf = 19.54 kPa and 172 psf = 8.24 kPa, respectively) for the Hokkaido Tailings Dam case history, but again the actual value reported by Ishihara et al. (1990) was 137 psf = 6.56 kPa instead of 408 psf = 19.54 kPa. These erroneous values may have affected the post-liquefaction shear strength prediction relationships of Wang (2003), Kramer (2008), and Kramer and Wang (2015).

On the other hand, it should be noted that the values reported in Table 2.2 for Olson (2001) study are not the exact final S_r values reported by Prof. Olson. As already discussed in the previous section, Olson (2001) directly used $S_{r,resid/geom}$ values, the apparent post-failure residual strength values based on the post-failure geometry that was evaluated by assigning the static Factor of Safety equal to 1.0, as the overall residual strength values for 23 less well-documented case histories. Fortunately, Wang (2003) realizes that it is an over-conservative approach and takes the average of $S_{r,yield}$, the apparent pre-failure yield stress based on the pre-failure geometry that gives the theoretical strength along the failure plane remaining in the liquefied portion of the soil by assigning the static Factor of Safety equal to 1.0 for pre-geometry, and $S_{r,resid/geom}$ values to represent the overall S_r values of Olson (2001). As already explained, it is a much better approach than directly using $S_{r,resid/geom}$ values as final representative S_r values as Olson (2001) have done because the actual residual strength lies between $S_{r,yield}$ and $S_{r,resid/geom}$ values.

Another problem with Wang (2003)'s residual strength values is that while considering various previous studies to evaluate the representative S_r values, it did not check the dependency between those values. In some cases, the study both considers two methods that are dependent on each other, i.e., one evaluated its value based on the other study. An example of this situation is Nerlerk Embankment Slide 1 case history. As already presented in Table 2.2, Wang (2003) used the values of Sladen et al. (1985), Jeffries et al. (1990), Stark and Mesri (1992), and Olson (2001)

to evaluate the representative S_r value. However, Stark and Mesri (1992) adopted its value based on Jeffries et al. (1990); in other words, these two values are dependent on each other. Therefore, considering these two studies separately is misleading for the final result. In fact, the residual strength value suggested by Jeffries et al. (1990) for this case history is far greater than the values provided by the original source Sladen et al. (1985), Olson (2001), and Weber (2015). Thus, it is possible that an error exists for that value. However, since the details were not presented clearly in the study, the result cannot be checked. Hence, it seems that the reliability of those values was not properly checked by Wang (2003) in residual strength estimations of 22 less well-documented case histories.

Weber (2015) also reports a similar problem for the La Marquesa Dam D/S slope case history. Referring to Table 2.2, Wang (2003) again averages four different studies to obtain a single representative post-liquefaction shear strength value. On the other hand, three of these four studies are actually dependent. De Alba et al. (1987) and Seed and Harder (1990) were actually involved in the same investigation team. Therefore, their values are parallel to each other and very close. Additionally, Stark and Mesri (1992) does not perform any independent back-analyses for their case histories, and directly uses the values provided by Seed and Harder (1990) as already discussed. Therefore, their value is also dependent on previous ones. Consequently, the value provided by Olson (2001) (actually the average of $S_{r,yield}$ and $S_{r,resid/geom}$ values provided) is the only independent value other than these three studies, in fact. Moreover, Weber (2015) states that it is highly possible that De Alba et al. (1987) probably took additional potential cyclic inertial effects for this case, and therefore resulted in a high unconservative residual strength value. Considering that biased value three times obviously affected the overall estimate of S_r for Wang (2003), and concluded by an unconservative high result. Weber (2015) also claims that the same kind of unconservative high result also exists for the La Marquesa Dam U/S slope case history due to the same reasons.

In summary, Wang (2003) unconservatively overestimates the residual strength values (10-20%) for these 22 Secondary Case Histories due to the issues

abovementioned. Therefore, the post-liquefaction shear strength prediction relationships developed by Kramer (2008) and Kramer and Wang (2015) suffer from these results.

Each case history is assigned with a weighting factor in Kramer (2008) and Kramer and Wang (2015) for the development of residual strength prediction relationships. These weighting factors were developed to be able to take the uncertainties and variabilities in information and documentation of case histories into account. While qualified documentation results in a low level of uncertainty and a high weighting factor (~1.00), poor documentation results in the opposite (~0.20). These weighting factors were developed based on engineering judgment, and details of the development procedures were not presented. The corresponding weighting factors are tabulated in Table 2.4.

Table 2.4 Regression parameters and corresponding weighting factors for case histories (Kramer and Wang, 2015)

Case history type	Case history	Weighting factor	SPT resistance	Fines content (%)	Initial vertical effective stress (atm)	Residual strength (atm)
Primary	Calaveras Dam	0.55	7.9	34	3.237	0.311
	Fort Peck Dam	0.85	11.7	54	3.528	0.322
	Hashiro-Gata	0.55	4.4	15	0.188	0.030
	Lake Ackerman	1.00	4.8	0	0.396	0.045
	Lower San Fernando Dam	1.00	12.6	25	1.672	0.240
	Route 272	0.70	6.6	33	0.493	0.061
	Shibeca-Cho	0.70	3.7	20	0.495	0.099
	Uetsu	0.55	3.0	0	0.433	0.021
	Wachusett Dam	1.00	7.3	8	1.209	0.164
Secondary	Asele road	0.20	8.9	32	0.310	0.060
	Chonan	0.74	5.1	18	0.930	0.085
	El Cobre Tailings Dam	0.60	1.2	95	4.608	0.092
	Helsinki Harbor	0.39	6.1	0	0.417	0.025
	Hokkaido	0.31	1.1	50	1.603	0.119
	Kawagishi-cho	0.50	4.3	2	0.646	0.058
	Koda Numa	0.44	3.05	40	0.504	0.023
	La Marquesa D/S	0.72	8.2	20	0.874	0.163
	La Marquesa U/S	0.76	4.1	30	0.795	0.087
	La Palma Dam	0.80	2.9	15	0.745	0.092
	Lake Merced	0.39	6.1	0	0.620	0.066
	Metoki road	0.39	2.1	0	1.246	0.055
	Mochi-Koshi 1	0.34	4	73	0.826	0.075
	Mochi-Koshi 2	0.67	5.2	73	1.365	0.111
	Nalbland	0.51	4	30	0.607	0.066
	Nerlerk Berm	0.41	10.6	10	0.682	0.085
	Sheffield Dam	0.37	5	40	1.099	0.047
	Snow River	0.50	7	20	0.984	0.024
	Solfatara	0.42	5.1	0	0.578	0.036
	Soviet Tajik	0.22	7.6	15	1.948	0.158
	Tar Island	0.32	8.2	13	2.966	0.172
	Zeeland	0.39	7.7	11	2.225	0.107

Kramer (2008) performed a variety of nonlinear least-squares regressions to the case history dataset of Wang (2003) to develop well-fitted residual strength relationships.

Following that, fully probabilistic Bayesian regressions using the maximum likelihood method were utilized to improve the relationships in terms of the probability of uncertainties. The resulting model depending on SPT resistance ($(N_1)_{60}$) and initial vertical effective stress (σ'_{v0}) was classified as a hybrid model by Prof. Kramer. On the other hand, it is observed that the resulting model predicted very low residual strengths at low initial vertical effective values. Kramer (2008) claimed that it was due to differences between lateral spreading and flow slide cases. The study declared that the residual strength value for lateral spreading cases should have been at least large as the static driving shear stress, because otherwise these cases were also classified as flow failure case histories. Hence, a fitting parameter is implemented into the prediction relationships to slightly increase the predicted S_r values at very low confining stresses. However, details of the evaluation of this fitting parameter have not been presented in the study.

The resulting post-liquefaction shear strength prediction relationship is developed as in the closed-form solution of Equation 2-6 by the Maximum Likelihood Method. The uncertainties and variations were evaluated based on the First Order Second Moment analyses.

$$\ln(S_r) = -8.444 + 0.109 \cdot N + 5.379 \cdot S^{0.1} \qquad \text{Equation 2-6}$$

In this equation, while S_r represents the post-liquefaction shear strength in the units of atm, N and S represent equipment, energy, procedure, and overburden stress corrected SPT resistance ($(N_1)_{60}$) and initial vertical effective stress (σ'_{v0}) in the units of atm, respectively.

Prof. Kramer decided that 40^{th} percentile values would be appropriate for deterministic values of residual strengths. As a result, the values and curves presented in Figure 2.14 are developed by the study.

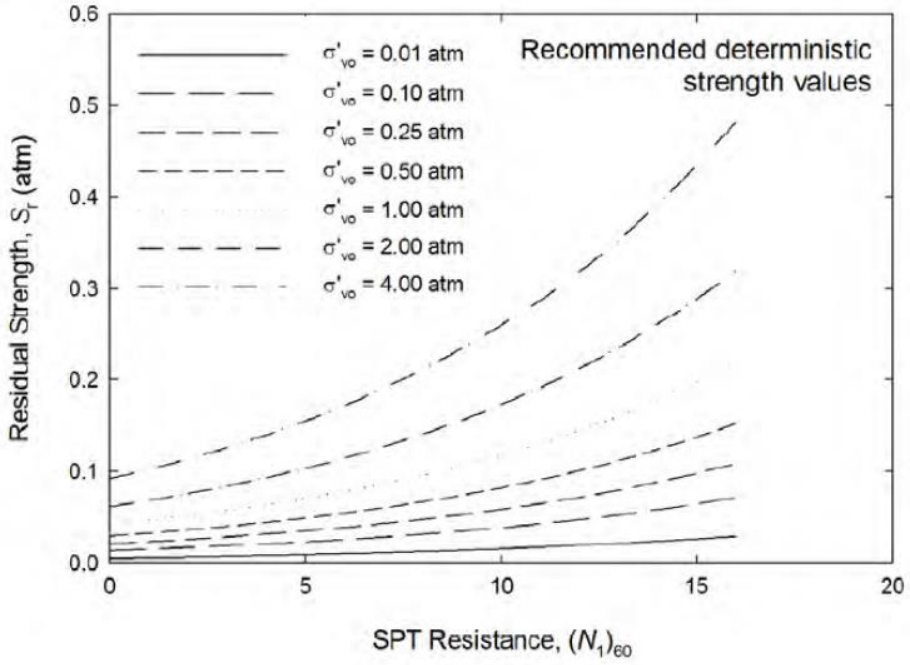

Figure 2.14. Recommended deterministic post-liquefaction shear strength curves based on $(N_1)_{60}$ and σ'_{v0} (Kramer, 2008)

2.2.6 Weber (2015)

Weber (2015) is the doctoral thesis of Joseph Patrick Weber in the Graduate Division of the University of California, Berkeley, and it is one of the latest studies in this field. It is definitely one of the most detailed and transparent works in terms of documentation of the case histories and back-analyses. It includes the back-analyses of 33 case histories (including the sub-cases for Mochi-Koshi Tailings Dam and Nerlerk Embankment Slide) in total, which makes it one of the studies with the most expanded case history database.

Similar to the previous pioneer studies such as Olson (2001) and Wang (2003), it divided its case history database into classifications based on the quality of the information available to them. It classified the case histories into three divisions as Group A (13 cases), Group B (19 cases), and Group C (1 case), where Group A cases are the ones with high-quality documentation. It is interesting that the single Group

C case history, Calaveras Dam, was also a high-qualified case history based on the available data and information, and back-analyses were also performed to estimate its post-liquefaction shear strength. On the other hand, it was not used during the development of empirical relationships for the engineering assessment of in-situ post-liquefaction shear strengths for several reasons. The dam failed in 1918 during the construction process, but the corresponding penetration tests, SPT and BPT, were performed approximately 80 years later than the failure. Therefore, it is quite possible that the materials comprised of sufficient clay were subjected to significant consolidation during that period. Hence, it is judged that the corresponding SPT and BPT resistances were not able to represent the conditions at the time of failure. Moreover, it is challenging to estimate the amount of additional consolidation over the 80 years of duration and the aging effects. In summary, the SPT and BPT resistances could not be correlated with the back-analyzed estimates of residual strength for this special case history by Weber (2015). As a result, it was separated from the other 13 cases of the Group A case histories. It should be noted that the study also defines Group D case histories for six cases. These cases are the ones that had been analyzed by one or more studies previously, but not considered in Weber (2015) due to lack of information availability and high levels of uncertainty.

For 13 Group A case histories, a new method called the incremental momentum back-analysis method was performed to evaluate the best estimates of residual strengths. The pre-failure and post-failure geometries, penetration resistances of the liquefied materials, soil stratigraphies, material properties, groundwater table elevations, etc., were clearly documented for these cases. The proposed method is illustrated for the Lower San Fernando Dam case history in Figure 2.15 and Figure 2.16. While Figure 2.15 shows the pre-failure and post-failure geometries of the case history, Figure 2.16 shows the step-by-step incremental cross-sections (first four steps) used by Weber (2015) to back-analyze it.

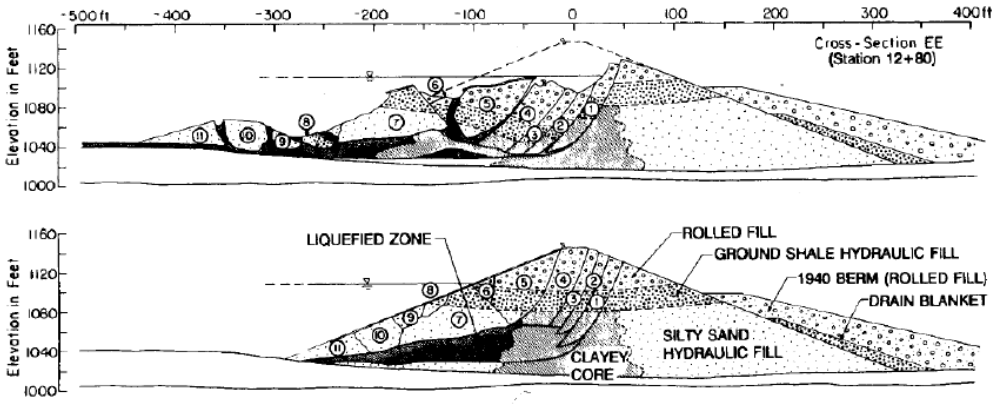

Figure 2.15. Documented pre-failure and post-failure cross-sections of the Lower San Fernando Dam (Castro et al., 1992)

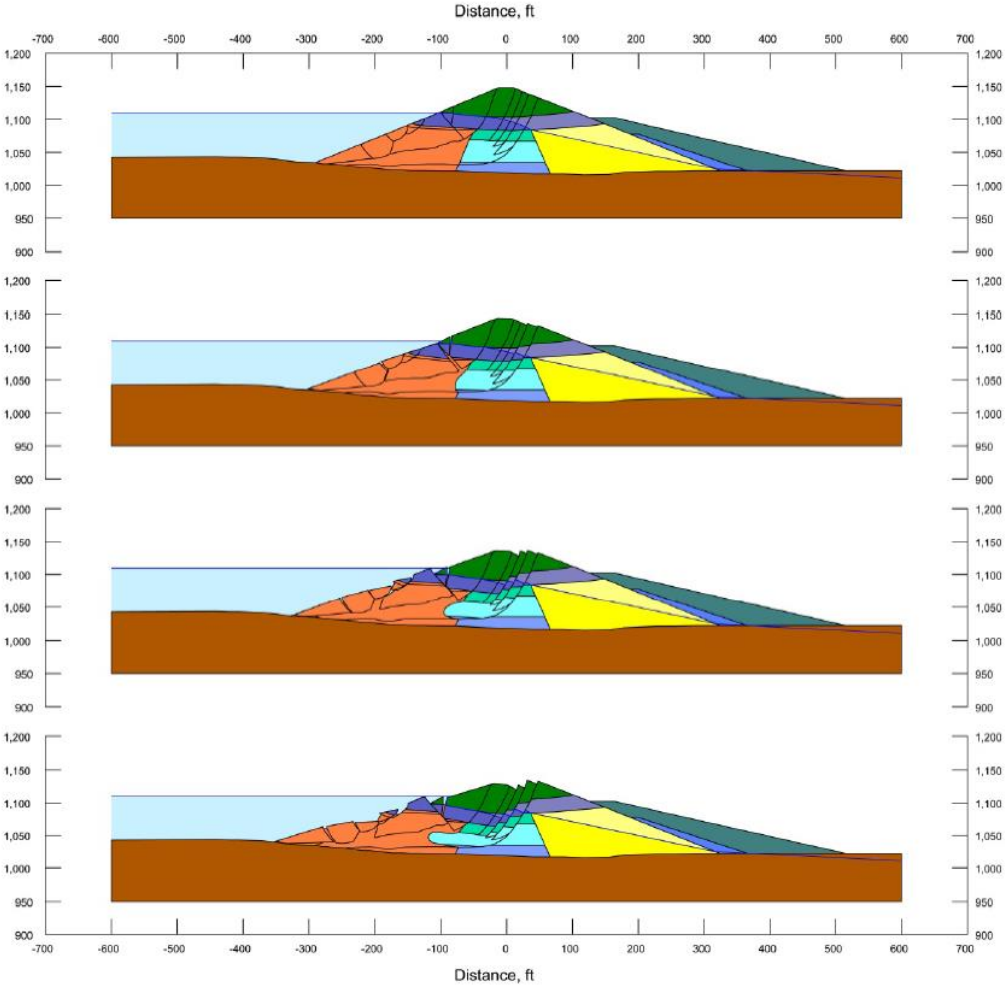

Figure 2.16. Incremental cross-sections used to back-analyze the Lower San Fernando Dam (Weber, 2015)

The incremental momentum method proposed by Weber (2015) involves incremental proceedings of the cross-sections from pre-failure geometry to post-failure geometry, as shown in Figure 2.16. In other words, a step-by-step progression of the failure should be tracked and modeled in order to perform a successful back-analysis with the incremental momentum method. It is obviously very challenging, even more challenging than the ZIF method proposed by Wang (2003), because only the failure geometry at the ZIF moment (the moment that zero inertial force is transferred) was required in that method. Additionally, it is more time-consuming than the other methods due to the numerous iterations performed between the analyses and cross-sections. Furthermore, it requires significant engineering judgment, imagination, and artistic vision capability to track the progression of a failure without seeing it. Nevertheless, it claimed to be better than the previous methods proposed by Olson (2001) and Wang (2003) in estimating the post-liquefaction shear strength of soils based on back-analyses of case histories.

As explained in the previous sections of this chapter, Olson (2001) proposes the kinetics analysis for its well-documented high-quality case histories and performs its back-analysis according to this method. Similarly, Wang (2003) presents the ZIF method, which is also similar to Olson (2001)'s kinetics analysis, and uses it in its back-analyses of well-documented Primary Case Histories. Weber (2015), on the other hand, claims several benefits of its incremental momentum analysis relative to these previous methods. First of all, it is stated that the incremental geometries forced to converge on the observed post-failure geometries in this method, which provides a more reasonable and reliable progression path for failure masses. Secondly, step-wise animations showing the entire failure process can be obtained for the failures such that the previous or next steps of the failure masses can be followed easily by this method. Thirdly, incremental progression of the failure masses can increase the accuracy in evaluating the driving shear stresses along the failure plane. Moreover, the failure plane details, such as the length of the proportion controlled by the liquefied and non-liquefied materials, inclination angles, etc., can also be evaluated more precisely by this method. Accordingly, the hydroplaning effects which are

observed when the toes of the failure masses enter bodies of water can be evaluated more easily. Fourthly, since the analyses proceed from pre-failure geometries to post-failure geometries continuously, no additional effort is necessary to estimate any partial displacement stage between these two geometries, such as the Wang (2003)'s ZIF geometry observed at the moment when zero inertial force is transferred. Fifthly, there is also no requirement for fitting higher-order curvilinear polynomials to the displacement paths of the failure masses, as done in Olson (2001)'s kinetics method, because the driving shear stresses are calculated at each incremental step. Hence, approximating the driving shear forces at random partial displacement moments is not necessary at this moment, which increases the level of accuracy for those forces. Finally, this method is also applicable for the incrementally developing (retrogressive) failures in which smaller slices of failures trigger successive larger failure surfaces.

In incremental momentum analysis, the best estimate of the driving shear forces towards the downslope and the resisting shear forces towards the upslope are evaluated and compared for each incremental step. Any overall force imbalance is then applied to the overall failure mass by using Newton's Second Law given in Equation 2-3. Accordingly, the resulting acceleration or deceleration value, a, is computed by dividing this net force by the overall mass of the failure body. As a result, the corollary resulting increase (for acceleration case) or decrease (for deceleration case) in velocities and cumulative displacements are estimated. Figure 2.17 illustrates the evolution of acceleration, velocity, and displacement of the center of gravity (COG) of the overall failure mass for the Lower San Fernando case history. The empty circle dots in this figure represent the moments of incremental steps of the cross-sections shown in Figure 2.16.

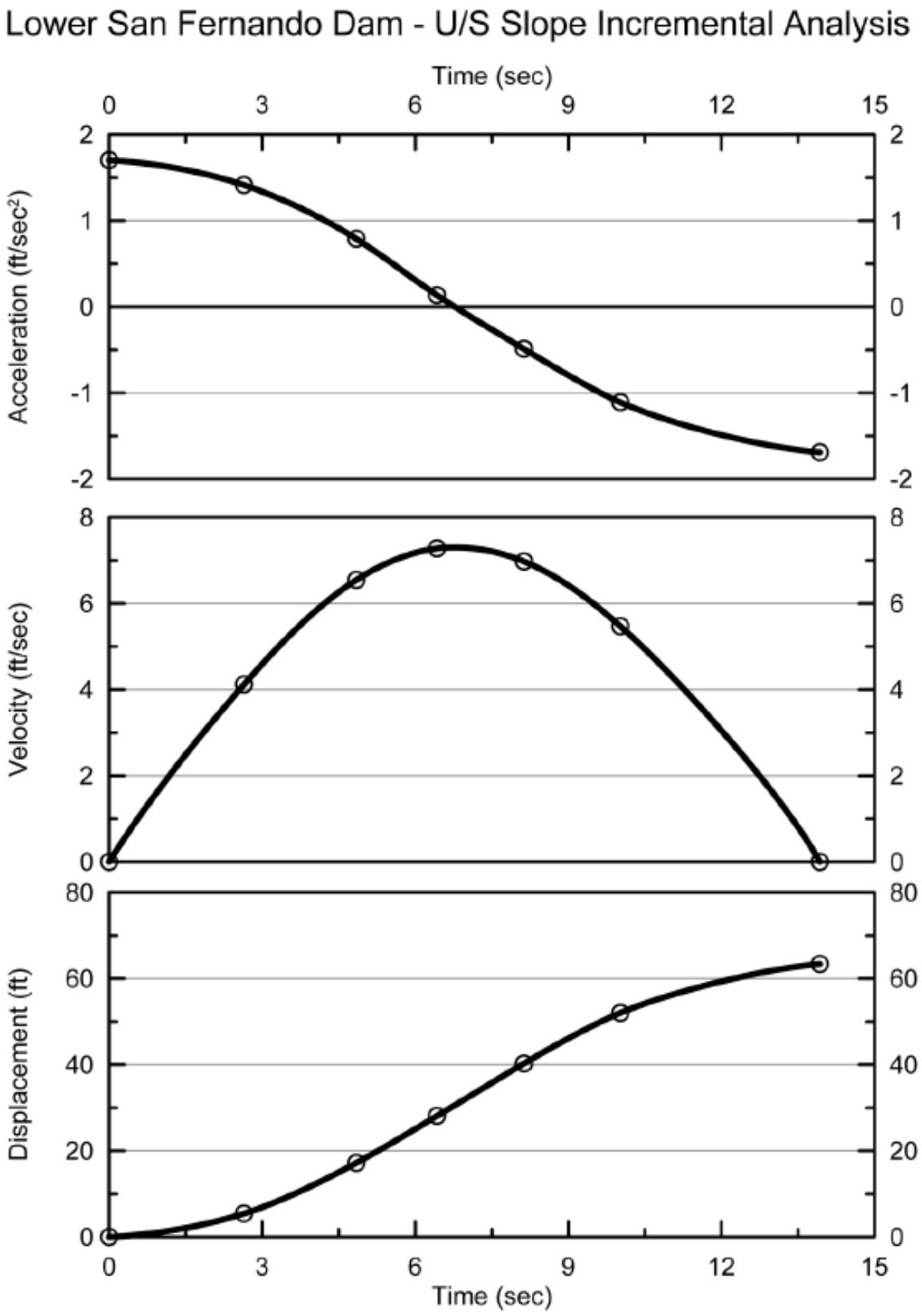

Figure 2.17. Incremental evolution of (a) acceleration vs. time, (b) velocity vs. time, (c) displacement vs. time of the COG of the overall failure mass of the Lower San Fernando Dam (Weber, 2015)

During the modeling process, the shear strength parameters are estimated for non-liquefied soils along with the soil profile based on available data and information in the primary sources of references. For the liquefied zones, on the other hand, the post-liquefaction shear strength of S_r is assigned, and this value is iterated until the final displacements obtained at the end of the progression match with the actual ones observed at the site. As it can be understood, it is an iterative process that requires additional effort. Once the model is prepared, parameter and assumption sensitivity analyses are performed, and the uncertainties are evaluated based on the variations in properties, assumptions, and modeling details in this context. Consequently, the best estimate of the residual strengths with acceptable ranges was reported for each of these high-qualified 14 case histories (13 Group A and 1 Group C). Based on the factors contributing to uncertainty or variance of the case histories, the residual strength ranges were commonly represented by approximately ±2 standard deviations. However, this range was generally not symmetrical to the best estimate value.

Typical uncertainties and variances regarding the case histories are the shape and location of the overall failure planes, the location of the ground water table at the time of failure, the possibility of incrementally progressive (retrogressive) failure, the shear strength parameters of the non-liquefied materials, the soil material properties such as unit weights.

It should be noted that Weber (2015) also considered the hydroplaning effects on the toes of the failure masses. As discussed earlier, hydroplaning is the entrapment of water beneath the toe portion of the failure sliding mass by definition. For the cases in which hydroplaning effects are observed, the strength of water controls the shear strength beneath some portion of the sliding toe since the toe portion of the failure mass rides out atop the entrapped water. While some of the previous studies considered this effect in their back-analyses, some of them did not consider or discuss it. Olson (2001) reduced the strength of the toes that enter bodies of water by half, and then examined the variation of strength reduction between 0-100% by sensitivity analysis. Wang (2003) and Kramer (2008) developed a quantitative and

semi-probabilistic procedure for hydroplaning effects acting on the toes of the failure masses entering into water such that they allowed a maximum lateral penetration beneath the toes of slide masses of up to ten times the thickness of the soils entering into the bodies of water. Weber (2015) followed a different approach for evaluating the hydroplaning effects, and the velocities of the advancing toes were considered to obtain some guidance. Available research states that the hydroplaning would occur only to some limited depth of penetration beneath advancing toes of slopes, which is ten times the thickness of the soils entering into the bodies of water for Wang (2003), for example. Weber (2015) evaluated each case history separately in terms of hydroplaning effects and judged that if some portion of the toe of the sliding mass is separated from the main failure body and enters into a body of water, then the corresponding toe section likely hydroplaned and displaced farther than the remaining overall mass. Similar to Olson (2001), a strength reduction ranging from 20% to 80% was applied for the toe portions that hydroplaning effects were observed based on the runout distances. However, due to the high level of uncertainties about the hydroplaning effects, these evaluations were performed based on a variety of engineering assumptions and judgments.

The incrementally progressive failures were also sufficiently back-analyzed with Weber (2015)'s incremental momentum method. As already discussed, the kinetics method proposed by Olson (2001) was not able to back-analyze these retrogressive failures such that it is just capable of analyzing a single failure mass with a single center of gravity. On the other hand, in incrementally progressive types of failures, the movement of smaller pieces triggers another failure plane, and a larger piece begins to slide. This process continues for a while, and these preceding small failure surfaces trigger the overall failure plane at the end. Therefore, it is required to deal with several COGs of several failure masses for one case.

An example of retrogressive failure back-analyzed by Weber (2015) is presented in Figure 2.18 for the Shibecha-Cho Embankment case history. The incremental analyses of acceleration, velocity, and displacement of this case history are also

given in Figure 2.19. In this figure, while the solid lines represent the behavior of overall failure mass, the dashed lines show the behavior of partial failure masses.

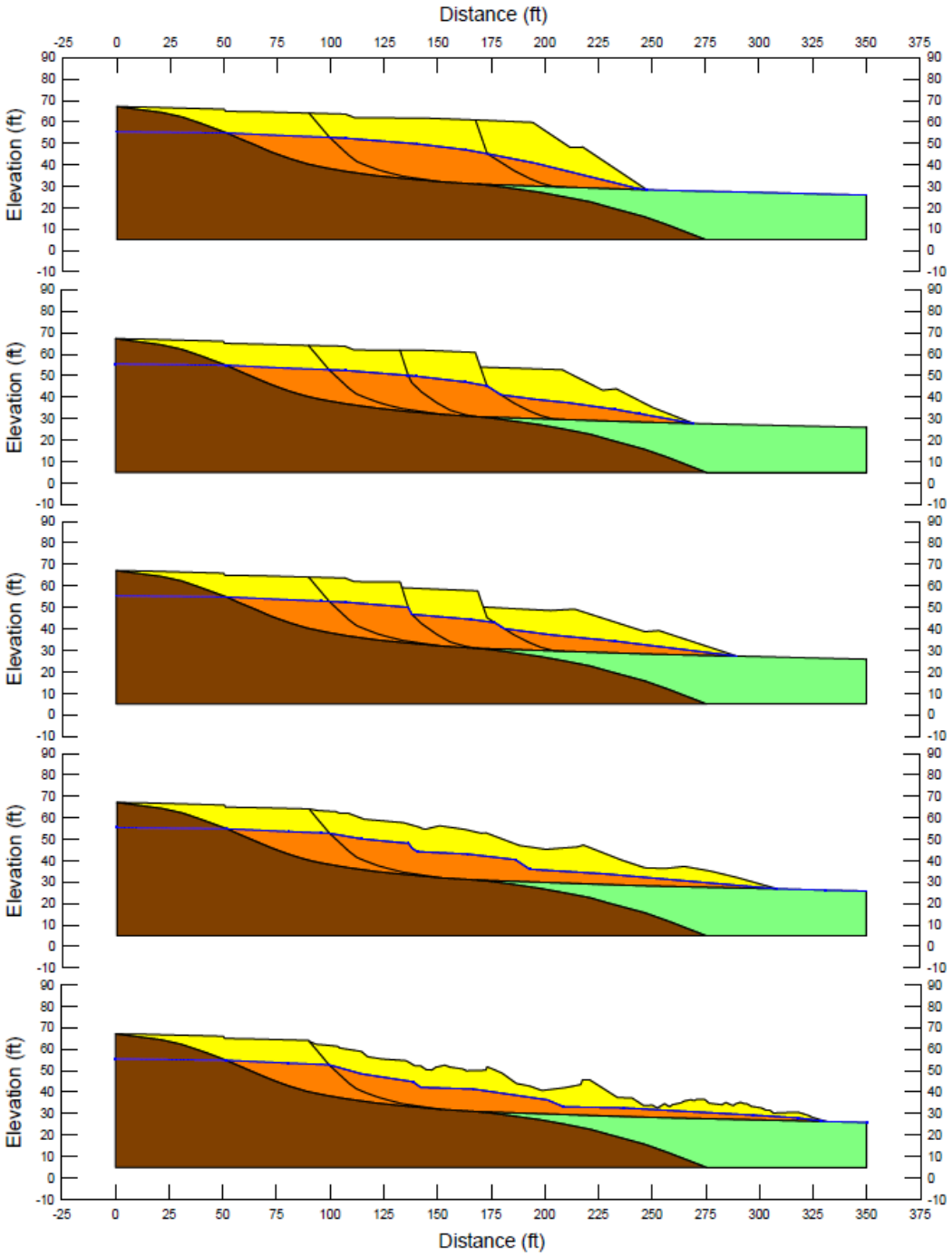

Figure 2.18. Illustration of an incrementally progressive (retrogressive) failure for Shibecha-Cho Embankment case history (Weber, 2015)

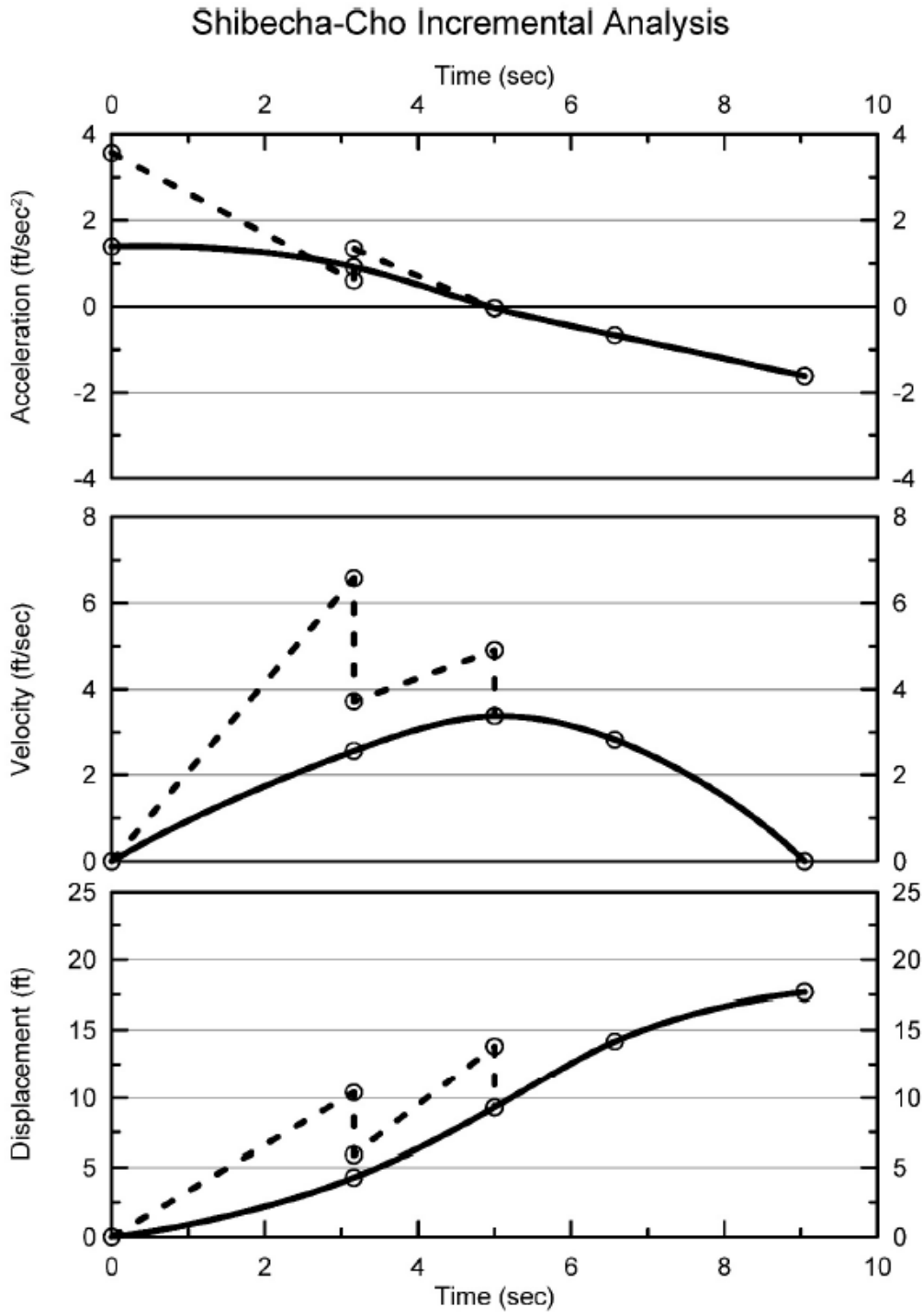

Figure 2.19. Incremental evolution of (a) acceleration vs. time, (b) velocity vs. time, (c) displacement vs. time of the COG of the overall failure mass (solid lines), and incremental partial failure masses (dashed lines) of the Shibecha-Cho Embankment fill (Weber, 2015)

In the back-analyses of these incrementally progressive failures, initially the movement of the first slice that is closest to the toe is examined. Following that, the movements of the subsequent slices were modeled step-by-step. For the Shibecha-Cho Embankment case history, the incremental changes in the acceleration, velocity, and displacement are shown with dashed lines in Figure 2.19. Simultaneously, the corresponding acceleration, velocity, and displacement values for the eventual overall failure mass are also calculated by taking the weighted average of the mass of the sliding portions, and these values are shown with solid lines in Figure 2.19. As it can be observed from this figure, retrogressive modeling of this case history resulted in a decrease in overall peak velocities, and therefore also a reduction in corollary overall momentum. As a result, a lower post-liquefaction shear strength value is evaluated for this retrogressive failure than would have been produced by the monolithic inception of failure. For this case history, Weber (2015) reported the best estimate of S_r as 224 lbs/ft^2 = 10.73 kPa and S_r as 263 lbs/ft^2 = 12.59 kPa for incrementally progressive failure modeling and monolithically initiated failure modeling, respectively. Hence, it can be judged that the post-liquefaction shear strength reduces by 15% approximately for the incrementally progressive (retrogressive) failure case histories when they are modeled with Weber (2015)'s incremental momentum method.

For 19 Group B case histories, information regarding the pre-failure and post-failure geometries, penetration resistances of the liquefied materials, soil stratigraphies, material properties, groundwater table elevations, etc., were not clearly documented. Thus, the fully incremental momentum analyses were not performed for them. Instead, a different approach was being followed for these less well-documented cases instead of using the values reported by previous investigators.

It should be noted that Weber (2015) actually reported 16 case histories as Group B case histories such that it considered Mochi-Koshi Tailings Dam and Nerlerk Embankment Slide case histories as single cases, similar to Seed and Harder (1990) and Stark and Mesri (1992). On the other hand, some of the previous studies, such as Olson (2001), Wang (2003), and Kramer (2008), consider two and three sub-cases

for these case histories, respectively, and evaluate each sub-failure that occurred for these case histories separately. In other words, they divide the Mochi-Koshi Tailings Dam case history into two as Mochi-Koshi Tailings Dam 1 and Dam 2, and analyze them independently from each other. Similarly, they divide Nerlerk Embankment Slide case history into three as Nerlerk Embankment Slide 1, Slide 2, and Slide 3 since three independent slope failures occurred for that embankment. Weber (2015) also analyzed these sub-cases independently and assigned separate residual strength values for those sub-cases; however, it reported a final single value as the best estimate of post-liquefaction shear strength. Nevertheless, since separate residual strength values were developed and documented for the sub-cases, they are judged to be separate case histories in this study, and therefore the case number is taken as 19 instead of 16 for Group B case histories.

A considerable effort was also expanded for these less well-documented Group B case histories to evaluate their best estimated residual shear strengths. It is better to remember that Olson (2001) directly uses the value of $S_{r,resid/geom}$, which is evaluated by assigning the static Factor of Safety equal to 1.0 for residual post-geometry, as the best estimate of S_r for these less well-documented case histories. It is already discussed that it is an approximate and over-conservative approach for the assessment of the best estimate of S_r as it ignores the inertial effects. Wang (2003), on the other hand, uses the values provided by previous investigators for these cases and averages them to evaluate the best-estimated value. Weber (2015) moves these approaches one step further and estimates the overall S_r values based on pre-failure geometries, post-failure geometries, approximate runout features and characteristics, $S_{r,yield}$ values, and $S_{r,resid/geom}$ values.

The study follows two different approaches for the engineering evaluation of the post-liquefaction shear strength values of these Group B case histories. In the first approach, the pre-failure and post-failure analyses are calibrated based on the runout characteristics using the relationship given in Equation 2-7.

$$S_r = \xi \cdot \frac{S_{r,yield} + S_{r,resid/geom}}{2} \qquad \text{Equation 2-7}$$

In this equation, $S_{r,yield}$ and $S_{r,resid/geom}$ represent the apparent pre-failure stress along the liquefied portions of the failure plane required to provide a static Factor of Safety equal to 1.0 for pre-failure geometry and the apparent residual stress required to provide a post-failure Factor of Safety equal to 1.0 for post-failure geometry, respectively. The term ξ, on the other hand, represents the coefficient related to the runout characteristics and overall failure mechanism of the failure.

It is already explained that $S_{r,yield}$ gives the upper bound for the post-liquefaction shear strength as it over-estimates the actual value by considering the initial geometry. On the contrary, $S_{r,resid/geom}$ gives the lower bound for the post-liquefaction shear strength as it under-estimates the actual value by considering the final geometry. Therefore, taking the arithmetic average of these two boundaries is a reasonable approach for achieving a good starting point for estimating the actual post-liquefaction shear strength value. Then, it is also quite logical to modify this average value by a coefficient (ξ) related to the runout characteristics and overall failure mechanism of the failure.

The runout characteristics and overall failure mechanism coefficient, ξ, varies between the range 0 and 1. For the cases in which the slide displacements are negligible or very small, $S_{r,yield}$ and $S_{r,resid/geom}$ values become very close to each other, and the inertial momentum effects would also be small. Therefore, ξ can be taken as nearly 1 for these cases. On the other hand, for the cases in which runout distances and slide displacements are infinitely large, there would be a large difference between $S_{r,yield}$ and $S_{r,resid/geom}$ values, and the inertial momentum effects would be very large. In fact, the actual post-liquefaction shear strength would be very close to zero for these cases. Thus, ξ can be taken as nearly 0 for these cases.

Consequently, the value of ξ is made a function of runout distance such that it decreases with increasing runout distance. To evaluate the corresponding function of ξ, the residual strength values obtained from the back-calculation of well-

documented 14 case histories (Group A and C) by the incremental momentum analyses are used. These values are compared with the residual strength values obtained by Equation 2-7 for these cases. The comparison of these results is shown in Figure 2.20, where the vertical and horizontal axes represent the residual strength values obtained by the incremental momentum method and Equation 2-7, respectively.

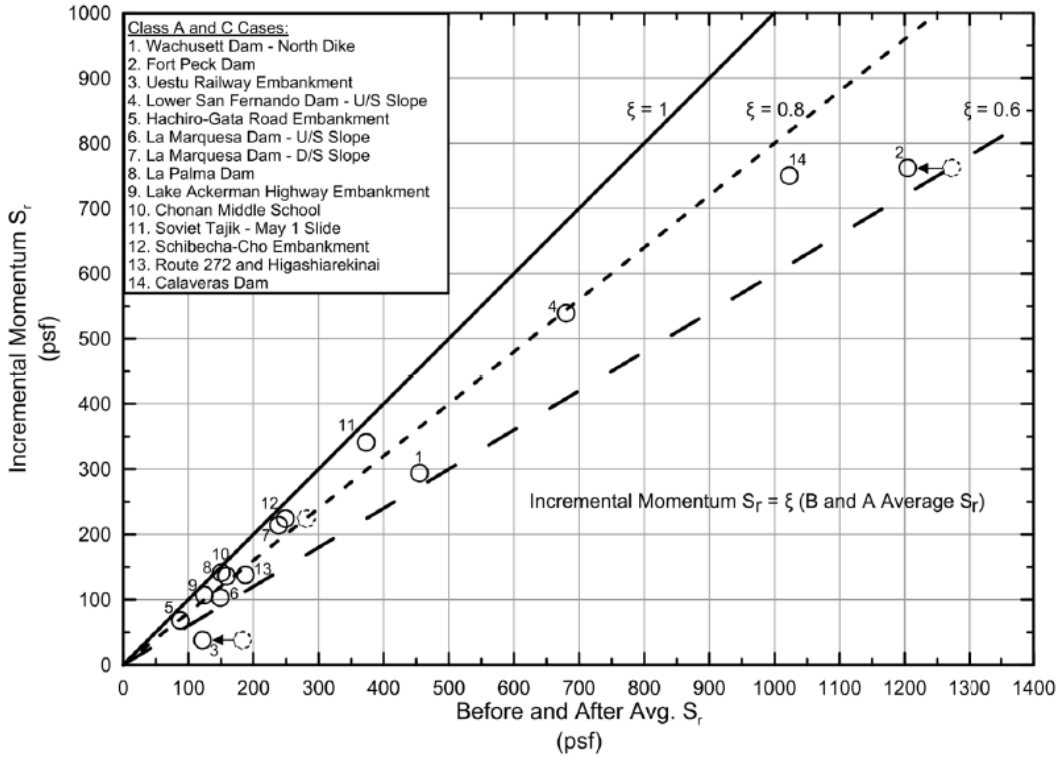

Figure 2.20. Comparison of the residual strength values obtained by incremental momentum method and average $S_{r,yield}$ and $S_{r,resid/geom}$ method for well-documented Group A and C case histories (Weber, 2015)

In Figure 2.20, $\xi = 1$ line gives the 1 vs. 1 line for the comparison of the results. The slope of this line decreases with decreasing ξ value, as shown in this figure. Referring to these results, it is judged that the value of ξ ranges between 0.6 and 1.0 for a majority of the back-calculated data.

Accordingly, these ξ values are plotted against different measures of runout distance, and the best relationship is achieved by correlating them with the ratio of the total

distance traveled by the COG of the overall failure mass and the initial slope height as measured from the toe of the failure to the top of the eventual back heel of the overall failure. This ratio is defined as the runout distance ratio or the travel path ratio, and the corresponding ξ relationship is obtained as given in Figure 2.21. As it can be seen from this figure, ξ = 0.8 is fairly reasonable for the cases where runout characteristics and failure mechanisms are unknown or unclear.

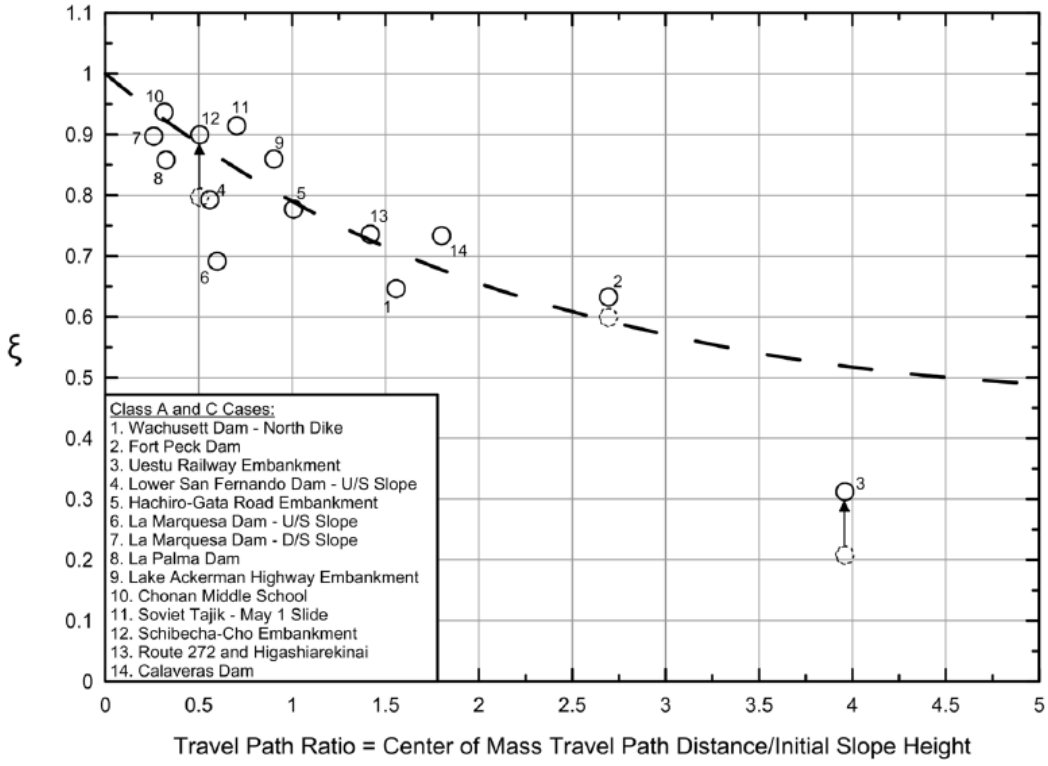

Figure 2.21. The relationship between ξ and the travel path (runout) ratio (Weber, 2015)

In the second approach followed by Weber (2015) to evaluate the post-liquefaction shear strength of less-well documented Group B case histories, initial and final factor of safeties were used. Here, the initial factor of safety is defined as the apparent factor of safety calculated for pre-failure geometry when the back-calculated value of S_r is assigned to the liquefied soils. Similarly, the final factor of safety is defined as the static factor of safety calculated for post-failure geometry when the back-calculated value of S_r is assigned to the liquefied soils.

The initial and final factor of safeties of the well-documented 14 Group A and Group C case histories are plotted as shown in Figure 2.22. The corresponding runout distance ratios, i.e., the travel path ratios, of these cases are also written next to each data point in parenthesis.

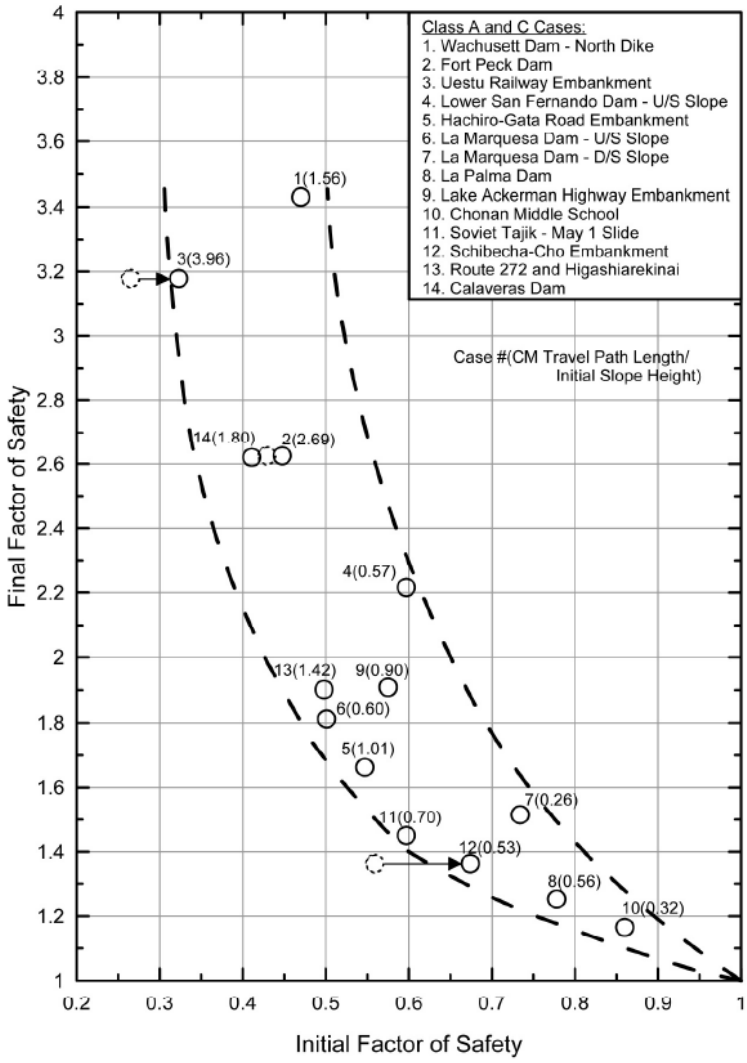

Figure 2.22. The initial and final factor of safety values of well-documented 14 Group A and C case histories with their corresponding runout distance ratios in parenthesis (Weber, 2015)

For less well-documented Group B case histories, an initial factor of safety is estimated referring to Figure 2.22 based on the runout distance ratio of the corresponding case history. Then, this FS value is multiplied by the $S_{r,yield}$ value,

which gives the apparent pre-failure stress along the liquefied portions of the failure plane for pre-failure geometry, and the result is reported as the best estimate of S_r obtained with the second approach.

For Group B case histories, the overall post-liquefaction shear strengths are evaluated with both of these two approaches abovementioned. Then, the arithmetic average of these two values is judged to represent the overall final post-liquefaction shear strength. Since two very similar failures were observed for Moshi-Koshi Tailings Dam Dikes 1 and 2, these best estimated residual strength values of these cases were averaged to a single value in order to avoid any over-contribution of these similar cases to the probabilistic regressions of residual strength relationships. In parallel to that, the three Nerlerk Embankment slides, Slides 1, 2, and 3, were also averaged to a single value due to the same reason.

Similar to previous studies, SPT resistance is utilized in this study as an in-situ test index matric to estimate the post-liquefaction shear strengths of liquefied materials. The equipment, energy, procedure, and effective overburden stress corrected SPT resistance values, $(N_1)_{60}$, were primarily evaluated using the corrections proposed by Cetin et al. (2004), which are pretty similar to those of Seed et al. (1984), and of Idriss and Boulanger (2008). In addition to it, the method proposed in Deger (2014) is used for the effective overburden stress effects as the relationships suggested by Deger (2014) fall between the normalization curves recommended by Cetin et al. (2004) and Idriss and Boulanger (2008). In addition, short rod length corrections at shallow depths were also made by the method proposed in the same reference, where negligibly reduced corrections compared to Cetin et al. (2004) are obtained.

It should be noted that to include the effect of fines content in penetration resistances, a fines content adjustment is also performed to $(N_1)_{60}$ values to obtain corresponding $(N_1)_{60,cs}$ values. In fact, these fines content corrected $(N_1)_{60,cs}$ values were used in the development of resulting residual strength relationships. Again, the relationship suggested by Cetin et al. (2004) was used for the fines correction of the SPT resistances of the case histories since it falls between the relationships recommended

by Seed et al. (1984) and Seed (1987) for fines adjustments. Despite the fact that different investigation teams studying post-liquefaction shear strength of liquefied soils follow different methods for fines content adjustments, and these methods vary slightly relative to each other, they do not produce significant differences. It is better to remark at this point that Olson (2001) and Olson and Stark (2002) do not perform any fines content correction for their representative SPT resistances. In other words, they employ $(N_1)_{60}$ values instead of $(N_1)_{60,cs}$ values in their relationships. Considering that the selected case histories are usually comprised of silty soils, this choice of them causes some differences between the representative SPT resistances of case histories containing high fines content. Weber (2015) also applied additional corrections for aging effects for two case histories, Wachusset Dam and Fort Peck Dam, because these failures occurred several decades ago.

It should be noted that usually the filtered (spurious high penetration resistances are eliminated) median values of penetration resistances are used as the representative penetration resistances to characterize the liquefiable soils because it is beneficial to use median values for more stable characterization when data are sparse. However, for the cases in which mean and median values differ significantly, the average value of these two is selected as the best estimate of representative $(N_1)_{60,cs}$ value. While performing regressions to develop empirical relationships between SPT resistance and residual strength, $(N_1)_{60,cs}$ values were assumed to be normally distributed. The variances generally appeared to be due to uncertainties during the conversion of other types of penetration resistances to equivalent SPT resistances. In fact, some variances were also due to approximation of $(N_1)_{60,cs}$ values for the cases where no information was available about the penetration resistances.

Similar to previous studies in this field, the representative initial vertical effective stress values for the case histories were estimated by averaging the pre-failure effective vertical stresses along the failure plane remaining in the portion comprised of liquefied materials. The representative σ'_{v0} values estimated by Weber (2015) agreed well with the ones evaluated by Olson (2001), Olson and Stark (2002) and Wang (2003), and Kramer (2008). It is better to remark that Wang (2003) (and

therefore Kramer (2008)) performed independent assessments of σ'_{v0} only for 9 Primary Case Histories that available information exists for pre-failure geometries, locations of failure planes and groundwater table levels, soil material properties, etc.

The overall results of the back analyses of all 30 Group A, B, and C cases (33 cases when sub-cases for Mochi-Koshi Tailings Dam and Nerlerk Embankment Slides are included) are tabulated in Table 2.5. This table includes the best-estimate mean and standard deviation values for S_r, $\sigma'_{v0,}$ and $(N_1)_{60,cs}$ values that are used to develop residual strength relationships. It should be noted that for the case histories that kinetics analyses were not performed by Olson and Stark (2002) due to lack of information, the representative post-liquefaction strength was evaluated with respect to the apparent residual stress based on the post-failure geometry that gives the theoretical strength along the failure plane remaining in the liquefied portion of the soil. In other words, the residual strength is assigned equal to $S_{r,resid/geom}$, which is evaluated by assigning the static Factor of Safety equal to 1.0 for residual post-geometry. Since it is an over-conservative approach giving lower residual strength values, these cases are modified in Table 2.5 with Equation 2-7 by taking $\xi = 0.8$ approximately. While using this equation, the $S_{r,yield}$ and $S_{r,resid/geom}$ values are taken as the ones reported by Olson (2001). Only the best-estimate residual strength value of El Cobre Tailings Dam case history (written between triangular parenthesis) was not modified by this method because the necessary $S_{r,yield}$ and $S_{r,resid/geom}$ values were not reported by Olson (2001). Therefore, the over-conservative value of $S_{r,resid/geom}$ is directly implemented only for this case.

Table 2.5 Back-analyses results for all case histories and their cross-comparisons with Seed and Harder (1990), Olson and Stark (2002) [modified], and Wang and Kramer (2003, 2008) (Weber, 2015)

Group	Case	Seed and Harder (1990)		Olson and Stark (2002)				Wang (2003) + Kramer (2008)				This Study			
		S_r (psf)	$N_{1,60,CS}$	S_{u}(Liq) (psf) [1]	S_{u}(Liq)/σ'_{vo}	σ'_{vo} (psf)	$N_{1,60}$ [2]	$\tilde{S}_r$ (psf) [3]	$\tilde{S}_r/\tilde{\sigma}'_{vo}$	$\tilde{\sigma}'_{vo}$ (psf) [4]	$\tilde{N}_{1,60,CS}$	$\tilde{S}_r$ (psf)	$\tilde{S}_r/\tilde{\sigma}'_{vo}$	$\tilde{\sigma}'_{vo}$ (psf)	$\tilde{N}_{1,60,CS}$
A	Wachusett Dam - North Dike			334	0.106	3158	7	348	0.136	2559	7.3	294	0.094	3142	7.5
	Fort Peck Dam	350	10	570	0.078	7341	8.5	671.6	0.091	7360	15.8	762	0.105	7258	12.5
	Uetsu Railway Embankment	40	3	36	0.027	1280	3	43.7	0.048	910	2.9	38	0.026	1448	3
	Lower San Fernando Dam - U/S Slope	400	13.5	390	0.120	3482	11.5	484.7	0.133	3644	14.5	539	0.170	3174	13.5
	Hachiro-Gata Road Embankment			42	0.062	670	4.4	65	0.164	396	5.7	68	0.101	673	7
	La Marquesa Dam - U/S Slope	200	6	[104]	0.114	911	4.5	(185.1)	0.110	1683	6.5	103	0.105	981	6.5
	La Marquesa Dam - D/S Slope	400	11	[152]	0.152	1000	9	(343.5)	0.186	1847	9.9	214	0.176	1215	10.5
	La Palma Dam	200	4	[125]	0.158	789	3.5	(193.3)	0.123	1572	4.2	136	0.177	767	5
	Lake Ackerman Highway Embankment			82	0.076	1076	3	98	0.114	860	4.8	107	0.118	909	3.5
	Chonan Middle School			[142]	0.127	1119	5.2	(178.7)	0.091	1964	6.4	141	0.137	1032	6.5
	Sowiet Tajik - May 1 Slide			[334]	0.154	2170	7.6	(334.3)	0.082	4077	8.9	341	0.179	1907	10.5
	Shibecha-Cho Embankement			117	0.086	1351	5.6	208.9	0.200	1045	5.6	224	0.158	1416	7.5
	Route 272 at Higashiarekinai			100	0.097	1030	6.3	130.5	0.125	1044	8.5	138	0.107	1285	8
B	Zeeland - Vlietepolder			[180]	0.075	2396	7.5	(226.0)	0.048	4708	8.5	156	0.063	2488	8
	Sheffield Dam	75	6	[159]	0.111	1429	5	(100.0)	0.072	1389	8.2	138	0.106	1308	7
	Helsinki Harbor			[44]	0.084	522	6	(53.2)	0.060	887	5.9	48	0.057	846	6
	Solfatara Canal Dike	50	4	[71]	0.114	624	4	(77.1)	0.063	1224	4.9	64	0.096	669	4.5
	Lake Merced Bank	100	6	[205]	0.149	1372	7.5	(139.5)	0.106	1316	5.9	136	0.163	834	8.5
	El Cobre Tailings Dam			<40>	0.020	1946	0	(195.2)	0.020	9760	6.8	96	0.046	2075	2
	Metoki Road Embankment			[90]	0.103	875	2.6	(116.8)	0.044	2655	2	92	0.106	871	2.5
	Hokkaido Tailings Dam			[138]	0.100	1376	1.1	(250.6)	0.074	3386	5.1	131	0.109	1203	4
	Upper San Fernando Dam - D/S Slope	600	15									726	0.231	3138	15
	Tar Island Dyke			[401]	0.093	4300	7	(364.2)	0.058	6279	8.9	516	0.123	4197	11
	Mochi-Koshi Tailings Dam, Dikes 1 and 2	250	5	[207]	0.165	1251	2.7	(158.9)	0.091	1746	8.9	211	0.138	1532	6
				[180]	0.165	1090	2.7	(233.6)	0.081	2884	10				
	Nerlerk Embankment, Slides 1, 2 and 3			[44]	0.071	616	8.7								
				[50]	0.077	650	7.2	(178.5)	0.1239	1440	11.4	68	0.058	1171	7.5
				[52]	0.056	925	7.2								
	Asele Road Embankment			[192]	0.163	1251	7	(183.6)	0.104	1573	11	137	0.132	1037	9.5
	Nalband Railway Embankment			[121]	0.110	1101	9.2	(139.9)	0.109	1283	6.3	167	0.138	1209	7.5
	Sullivan Tailings											277	0.114	2422	9.5
	Jamuna Bridge											175	0.125	1404	10.5
C	Calaveras Dam	650	12	721	0.112	6422	8	636.9	0.099	6433	10.5	749	0.106	7097	15

Notes :
(1) Where noted in brackets, S_u(Liq) and S_u(Liq)/σ'_{vo} for Olson (2001) reinterpreted using reported values of Su Yield and S_u Residual in Olson (2001) and the equation S_u(Liq) = 0.8 (S_u Yield + S_u Residual)/2. Reinterpretation of S_u(Liq) performed for cases not calculated using the Kinetic procedure in Olson (2001). Where noted in triangular brackets, no S_u Yield value reported in Olson (2001).
(2) No fines content correction utilized in Olson and Stark (2002).
(3) Where noted in parentheses, $S_{u,r}$ values are for secondary cases in Wang (2003) and were not fully reanalyzed.
(4) σ'_{vo} not explicitly reported in Wang (2003) or Kramer (2008). Values shown were back calculated from reported S_r and S_r/σ'_{vo}.

As discussed earlier, Wang (2003) assigned weighting factors for each of its case histories during the probabilistic regression process to include the effect of uncertainties. However, since all factors contributing to uncertainties of case histories, such as poor quality of data and documentation, unclear pre-failure and post-failure geometries, uncertain ground water table levels, etc., are considered together for each parameter, and standard deviations are computed accordingly in Weber (2015), a natural self-weighting has occurred for all case histories during the probabilistic regressions process. This approach is preferred by Weber (2015) as no subjective engineering judgment is required to evaluate weighting factors.

For well-documented 14 Group A and C case histories, the obtained overall post-liquefaction shear strength results agree well with the ones reported by previous studies in general because each of them includes the momentum and inertia effects. For the remaining 16 less well-documented Group B case histories, also good agreements are caught when the residual strength values of Olson and Stark (2002) are modified with Equation 2-7 by taking $\xi = 0.8$ approximately. For some cases, different residual strength values are back-calculated by Weber (2015) still; however, the reasons behind these differences are already explained in previous sections during the discussions of the drawbacks and errors of the previous studies.

Based on this case history database, both deterministic and probabilistic regressions were performed by Weber (2015). While the deterministic (non-probabilistic) regressions were performed by the least-squares method, the probabilistic regressions were performed by the Maximum Likelihood Method. These fully probabilistic regressions incorporated all kinds of uncertainties dealt with during the back-analyses process. The representative median and standard deviation values of S_r, $\sigma'_{v0,}$ and $(N_1)_{60,cs}$ for all 29 cases (excluding Group C Calaveras Dam case history) are tabulated in Table 2.6.

Table 2.6 Representative median and standard deviation values of S_r, σ'_{v0}, and $(N_1)_{60,cs}$ for all 29 Group A and B case histories (Weber, 2015)

Group	Case	This Study					
		$\bar{S}_r$ (psf)	$\sigma_{\bar{S}}$	$\bar{\sigma}'_{vo}$ (psf)	$\sigma_{\bar{\sigma}}$	$\bar{N}_{1,60,CS}$	$\sigma_{\bar{N}}$
A	Wachusett Dam - North Dike	294	31	3142	132	7.5	1.6
	Fort Peck Dam	762	118	7258	687	12.5	2.7
	Uetsu Railway Embankment	38	8	1448	116	3	0.8
	Lower San Fernando Dam - U/S Slope	539	47	3174	281	13.5	1.8
	Hachiro-Gata Road Embankment	68	12	673	41	7	1.2
	La Marquesa Dam - U/S Slope	103	33	981	134	6.5	1.8
	La Marquesa Dam - D/S Slope	214	57	1215	103	10.5	2.2
	La Palma Dam	136	23	767	42	5	1.2
	Lake Ackerman Highway Embankment	107	19	909	61	3.5	0.7
	Chonan Middle School	141	35	1032	82	6.5	2.1
	Soviet Tajik - May 1 Slide	341	57	1907	177	10.5	2.7
	Shibecha-Cho Embankement	224	37	1416	95	7.5	1.7
	Route 272 at Higashiarekinai	138	17	1285	104	8	1.6
B	Zeeland - Vlietepolder	156	37	2488	431	8	2.1
	Sheffield Dam	138	23	1308	71	7	2.3
	Helsinki Harbor	48	14	846	105	6	2.0
	Solfatara Canal Dike	64	22	669	59	4.5	1.5
	Lake Merced Bank	136	21	834	102	8.5	2.2
	El Cobre Tailings Dam	95	31	2075	183	2	1.0
	Metoki Road Embankment	92	20	871	85	2.5	0.9
	Hokkaido Tailings Dam	131	45	1203	191	4	1.1
	Upper San Fernando Dam - D/S Slope	726	138	3138	278	15	1.8
	Tar Island Dyke	516	119	4197	484	11	2.3
	Mochi-Koshi Tailings Dam, Dikes 1 and 2	211	38	1532	165	6	1.7
	Nerlerk Embankment, Slides 1 ,2 and 3	68	19	1171	129	7.5	1.8
	Asele Road Embankment	137	27	1037	77	9.5	2.0
	Nalband Railway Embankment	167	15	1209	94	7.5	2.5
	Sullivan Tailings	277	24	2422	142	9.5	2.4
	Jamuna Bridge	175	22	1404	210	10.5	2.5

After regressing a variety of candidate equational forms, the most promising form is obtained as given in Equation 2-8.

$$S_r = \exp\left(\theta_1 \cdot (N_1)_{60,cs} + \theta_2 \cdot \sigma'^{\theta_3}_{v0}\right) \quad \text{Equation 2-8}$$

Accordingly, the result is obtained as given in Equation 2-9 following the non-probabilistic (deterministic) regression, with R^2=0.911.

$$S_r = \exp\left(0.1625 \cdot (N_1)_{60,cs} + 4.004 \cdot \sigma'^{0.120}_{v0}\right) \quad \text{Equation 2-9}$$

In Equation 2-9, while S_r represents the post-liquefaction shear strength in the units of lbs/ft^2, $\sigma'_{v0,}$ and $(N_1)_{60,cs}$ represent the initial vertical effective stress in atmospheres, and equipment, energy, procedure, overburden stress, and fines content corrected SPT resistance in blows/ft, respectively. The corresponding plot of the best fit to this relationship is shown in Figure 2.23 in $(N_1)_{60,cs}$ versus S_r domain. Different curves representing different initial effective vertical stress values are also plotted on the same figure.

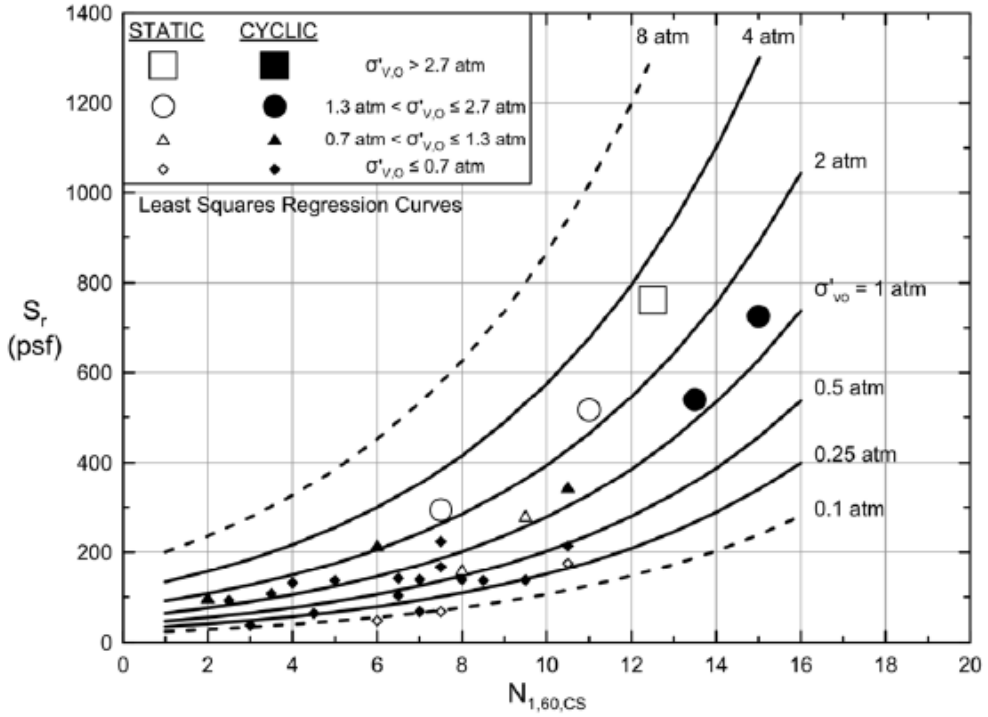

Figure 2.23. The final relationship that is obtained at the end of the deterministic regression (Weber, 2015)

In order to include the variances and uncertainties in the evaluation of post-liquefaction failure case histories, probabilistic regressions are also performed by the Maximum Likelihood Method, a Bayesian procedure, to determine the relationship between residual strength and penetration resistance and initial effective vertical stress. Table 2.6 shows the input variables, i.e., means and standard deviations, for 29 liquefaction field case histories. Since these standard deviations represent all sources of uncertainties and variances for these case histories, a natural weighting is

obtained for each of them, and no additional weighting factors were applied separately. In other words, the cases having higher uncertainties, and therefore higher standard deviations, contribute less to the regressed relationships than the cases with lower standard deviations.

A similar functional form given in Equation 2-8 was again implemented in a Bayesian regression by the Maximum Likelihood Method, and the median values of S_r, which indicates a 50% probability of exceedance, are treated to be equal to the linear least-squares regression trend relationship. The results are obtained in the form given in Equation 2-10.

$$P \cong \Phi\left(\frac{g - S_r}{\theta_\varepsilon}\right) \qquad \text{Equation 2-10}$$

In this form, P, Φ, g, S_r, and θ_ε represent probability, cumulative standard normal distribution, functional form $= \exp\left(\theta_1 \cdot (N_1)_{60,cs} + \theta_2 \cdot {\sigma'}_{v0}^{\theta_3}\right)$, post-liquefaction shear strength in lbs/ft^2, and the error term, respectively.

By rearranging Equation 2-10 and solving for the dependent variable S_r, the form given in Equation 2-11 can be obtained.

$$S_r \cong g + \theta_\varepsilon \cdot \Phi^{-1}(P) \qquad \text{Equation 2-11}$$

In this form, Φ^{-1} and P represent the inverse cumulative standard normal distribution and probability of exceedance, respectively.

Putting the functional form g in its place, the predictive equation is obtained as given in Equation 2-12.

$$S_r \cong \exp\left(\theta_1 \cdot (N_1)_{60,cs} + \theta_2 \cdot {\sigma'}_{v0}^{\theta_3}\right) + \theta_\varepsilon \cdot \Phi^{-1}(P) \qquad \text{Equation 2-12}$$

It is stated that setting P = 0.50 results in a median curve very similar, but not identical, to the deterministic predictive relationship given in Equation 2-9. Once the best fit for the error term distribution was determined, the overall resulting fully probabilistic best-fit relationship was evaluated as shown in Equation 2-13.

$$S_r \cong \exp\left(0.1407 \cdot (N_1)_{60,cs} + 4.2399 \cdot \sigma'^{0.120}_{v0}\right) +\cdot \Phi(\theta_\varepsilon) \qquad \text{Equation 2-13}$$

where

$$\theta_\varepsilon = (N_1)^{1.45}_{60,cs} + 0.2 \cdot (N_1)_{60,cs} \cdot \sigma'^{2.48}_{v0} + 41.13 \qquad \text{Equation 2-14}$$

Weber (2015) claims that 33rd percentile values (33% of values would be expected to be lower) are reasonable for typical design applications, and this one-third level of conservatism is commonly used in geotechnical engineering. Consequently, the recommended resulting residual strength prediction relationship is given in Equation 2-15 for 33rd percentile values.

$$S_r\ (33^{rd} precentile) = \exp\left(0.1407 \cdot (N_1)_{60,cs} + 4.2399 \cdot \sigma'^{0.120}_{v0}\right) - 0.43991 \cdot \left((N_1)^{1.45}_{60,cs} + 0.2 \cdot (N_1)_{60,cs} \cdot \sigma'^{2.48}_{v0} + 41.13\right) \qquad \text{Equation 2-15}$$

The corresponding plot of the best fit to this 33rd percentile probabilistic relationship is shown in Figure 2.24 in $(N_1)_{60,cs}$ versus S_r domain. Different curves representing different initial effective vertical stress values are also plotted on the same figure.

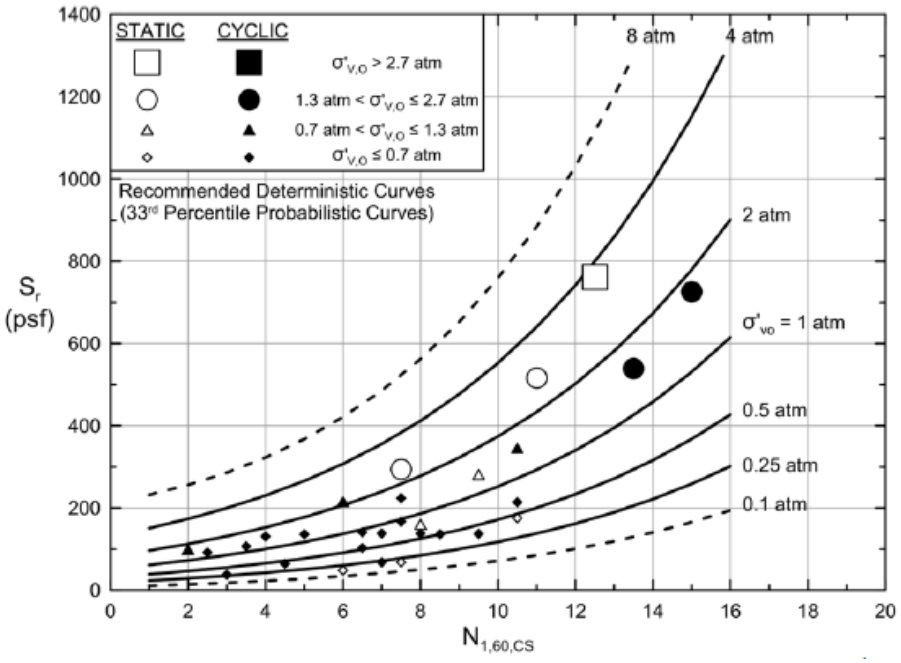

Figure 2.24. The final relationship that is obtained at the end of the 33rd percentile probabilistic regression (Weber, 2015)

Weber (2015) also declares that the post-liquefaction shear strength should be taken as the lower of either the undrained post-liquefaction shear strength (S_r), or the fully drained residual strength ($S_{r,drained}$), where the fully drained residual strength can be evaluated as given in Equation 2-16.

$$S_{r,drained} = \sigma'_{N,0} \cdot tan\phi' \qquad \text{Equation 2-16}$$

In this equation, $\sigma'_{N,0}$ and ϕ' represent the initial normal effective stress acting on the failure plane and residual effective friction angle, respectively.

The residual effective friction angle ranges between 28°-31° typically for cohesionless soils and silty soils of low plasticity. When a representative value of 30° is selected for it, the corresponding relationship occurs as given in Equation 2-17 for horizontal failure surfaces that effective vertical stress is approximately equal to the normal effective stress.

$$S_{r,drained} = \sigma'_{N,0} \cdot \tan(30) \approx \sigma'_{v0} \cdot \tan(30) = 0.577 \cdot \sigma'_{v0} \qquad \text{Equation 2-17}$$

This equation implies that the approximate upper bound of the drained frictional cut-off range becomes $S_r/\sigma'_{v0} = 0.577$.

For steeply inclined failure surfaces, the effective normal stress can be evaluated roughly by multiplying this value with the lateral earth pressure coefficient at rest, K_0. Although K_0 is dependent on internal friction angle, which is a function of relative density, its value can be approximated roughly as 0.5 in general. Then, the corresponding relationship occurs as given in Equation 2-18.

$$\begin{aligned} S_{r,drained} &= \sigma'_{N,0} \cdot \tan\phi' \approx \sigma'_{v0} \cdot K_0 \cdot \tan\phi' \\ &= \sigma'_{v0} \cdot 0.5 \cdot \tan(30) = 0.29 \cdot \sigma'_{v0} \end{aligned} \qquad \text{Equation 2-18}$$

Referring to this equation, the approximate lower bound of the drained frictional cut-off range becomes $S_r/\sigma'_{v0} = 0.29$.

The relationship showing the approximate range of drained frictional cut-off for 33rd percentile probabilistic values of S_r/σ'_{v0} is presented in Figure 2.25 in $(N_1)_{60,cs}$ versus

S_r/σ'_{v0} domain. Different curves representing different initial effective vertical stress values are also plotted on the same figure.

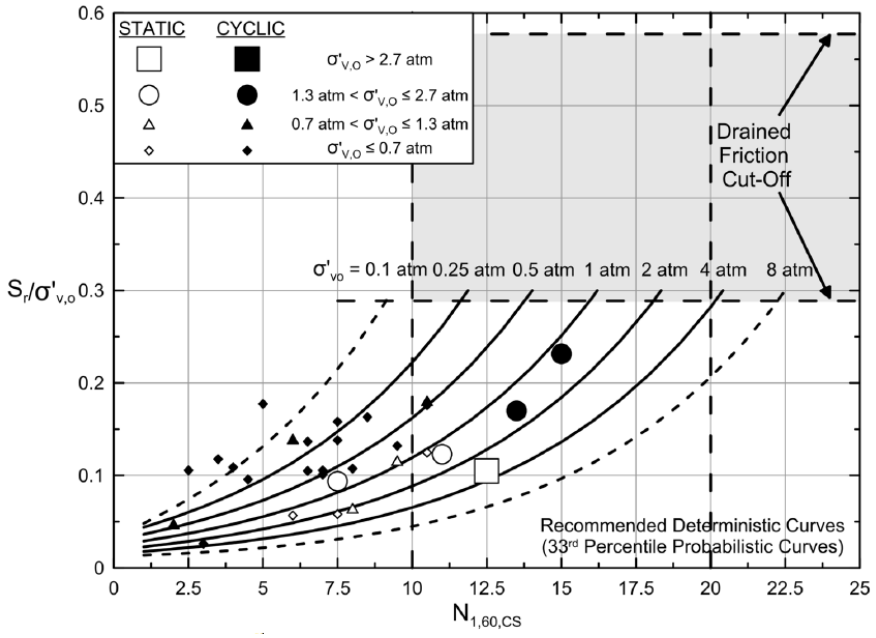

Figure 2.25. The final S_r/σ'_{v0} relationship obtained at the end of the 33rd percentile probabilistic regression showing the approximate range of drained frictional cut-off (Weber, 2015)

In summary, Weber (2015) performs perfect efforts in all of its selected case histories to evaluate best-estimate of post-liquefaction shear strengths, and it is the most comprehensive study for sure at this moment on this topic. Each parameter used in the residual strength prediction relationship is evaluated by the investigation team individually, and no value is directly taken from the previous studies. The momentum effects are considered for each case history, and advanced incremental momentum analyses are conducted for well-documented 14 Group A and C case histories. The best estimates of the residual strengths are evaluated by taking the runout characteristics and failure mechanisms into account for the remaining less well-documented Group B case histories. Additional efforts are also performed for the incrementally progressive (retrogressive) failures and hydroplaning effects. Considering all of these, this study can be considered one of the most important pieces of the overall post-liquefaction shear strength puzzle.

CHAPTER 3

REVIEW AND EVALUATION OF LIQUEFACTION CASE HISTORIES

Previous studies on post-liquefaction shear strength showed that the general approach is to use an in-situ test index metric (e.g., $(N_1)_{60}$, q_c, V_s, etc.) to represent the capacity of the soil. Although available studies explained in Chapter 2 are listed as perfect efforts to determine "undrained residual strength" values, S_r or S_u namely, the use of the term "undrained" without any reference to the induced excess pore pressures can be misleading for practicing engineers, who are very much used to performing effective stress-based stability assessments for cohesionless soils under monotonic loading conditions. As discussed earlier in Chapter 1, this study aims to introduce a new framework for evaluation of post-liquefaction shear strength, such that instead of representing post-liquefaction strength, or namely residual strength, in the undrained shear strength versus penetration resistance domain, it suggests void ratio versus effective stress domain, which is a well-known domain in geotechnical engineering in performing effective stress-based stability assessments for cohesionless soils.

In this study, a critical state-like methodology will be introduced to assess post-liquefaction-induced excess pore pressures on the basis of back analyses of available case histories. Although the details of the methodology will be discussed in Chapter 4, the descriptive parameters of the methodology are explained in this chapter. As void ratio versus effective stress domain is used as a new framework for evaluation of residual shear strength, estimation of the in-situ void ratio with its limits (e_{max} and e_{min}) and maximum range (e_{max}-e_{min}) is a crucial part of the critical state concept in addition to the determination of the initial mean effective stresses. In this context, parameters that can be used in estimating the limit void ratios, void ratio range, and in-situ relative density are selected as the potential descriptive parameters of the

problem. Accordingly, the key parameters corresponding to the physical nature and physical state of the soil are selected as mean grain size (D_{50}), fines content (FC), coefficient of uniformity (C_u), roundness (R), sphericity (S), and penetration resistance (SPT-N). The parameters other than the penetration resistance are then used to evaluate the limit void ratios and void ratio range with some semi-empirical models that will be discussed in Section 3.6. Following that, the in-situ relative densities of the case histories are evaluated by some semi-empirical models as well based on these void ratio limits, void ratio ranges, and penetration resistance recordings, as will be discussed in Section 3.7. In the end, the initial void ratios are evaluated for the case histories with the help of limit void ratios and in-situ relative densities as also discussed in Section 3.7.

As already mentioned, estimation of the mean effective stress is also a crucial part of the critical state concept as well as the in-situ void ratios. Therefore, the initial mean effective stresses for the case histories are also evaluated in detail as explained in Section 3.4. It should strongly be noted that assigning a single mean effective stress value for a slip surface might be illogical and misleading as stresses are changing significantly along the failure surfaces due to the fact that some of these failures include tens of meters, even hundreds of meters of sliding soil mass. For these types of large deformations, the lateral length and vertical height of the failure mass can be extremely long, which proves that the local and principal stresses may differ dramatically along with the different points of the failure surface. Therefore, the failure surfaces are divided into smaller failure segments in length to allow assigning different mean effective stress values for different parts of the slip surface. This approach also leads to obtaining multiple "sub-case histories" from a single case history such that although the material properties such as fines content, mean grain size, coefficient of uniformity, roundness, sphericity, and penetration resistance are considered to be the same along the whole failure surface, the confining stress, or mean effective stress in this case, is different along the slip surface. This also means that the location of the corresponding data points of these "sub-case histories" are also different on void ratio versus effective stress domain, which actually increases

the resolution of case histories for modeling purposes. The procedure of the sub-sectioning of case history failure surfaces and evaluation of initial mean effective stresses for these "sub-case histories" are explained in detail in Sections 3.3 and 3.4, respectively.

3.1 Selection of Liquefaction Case Histories

As discussed in Chapter 2, there are several important studies available in the literature on residual strength, such as Seed (1987), Seed and Harder (1990), Stark and Mesri (1992), Olson (2001), Olson and Stark (2002), Wang (2003), Kramer (2008) and Weber et al. (2015). All of these researchers perform their studies based on the semi-empirical relationships founded on back-analyses of field liquefaction failure case histories. Therefore, compilation and examination of high-quality case histories from liquefaction-induced failure sites are crucial to developing correlations for the engineering evaluation of residual shear strength.

As the years progressed and more detailed studies began to be carried out, the number of case histories used in the development of relationships for the engineering evaluation of post-liquefaction shear strength has increased. One of the first research studies on this topic, Seed (1987), considers only 12 case histories to develop residual strength relationships of liquefied sands. This number increases up to 17 in Seed and Harder (1990) by adding five more case histories to the dataset of Seed (1987). Then, Stark and Mesri (1992) uses 20 case histories to develop their own post-liquefaction shear strength relationship. 9 years later, Olson (2001) performs a great effort in his Ph.D. thesis to increase the number of these case histories, and published 33 cases with their detailed information. Olson and Stark (2002) also follows this study and uses the same 33 case histories to develop its residual strength relationship. Following that, Wang (2003) considers 31 case histories in total to develop its residual strength relationship. It divides its case histories into two categories as primary (9 cases) and secondary case histories (22 cases) based on the quality of data documented for them. Similarly, Kramer (2008) also uses the same

31 cases in its study and provides a post-liquefaction shear strength relationship based on the same case histories. In 2015, these two researchers combined their efforts by merging their databases, and publish Kramer and Wang (2015) for the same 31 case histories. Again, they divide their database into primary and secondary case histories (9 to 22 cases, respectively) based on the quality of data. Finally, Weber (2015) considers 33 case histories in total (including the sub-cases) to develop its residual strength relationship, and again divides its database into three categories as Group A (13 cases), Group B (19 cases), and Group C (1 case) based on the quality of data. Since this study is also a Ph.D. thesis similar to Olson (2001) and Wang (2003), it again includes much detailed information about the cases and their properties.

In this study, a combination of these case histories is taken into account while developing a residual strength relationship for liquefied soils. Due to the fact that there is a limited number of case histories available in the literature for post-liquefaction, these cases are examined with certain care and attention. To be able to avoid losing any valuable data, all convenient and appropriate cases are tried to be included in the study. Accordingly, all 33 case histories included in Weber (2015) are also studied as part of this study. 30 of these case histories excluding Upper San Fernando Dam Downstream Slope, Sullivan Tailings, and Jamuna Bridge cases were also studied by Olson and Stark (2002), Wang (2003), Kramer (2008), and Kramer and Wang (2015). In addition to these 33 case histories, three more cases, Koda Numa Railway Embankment, Whiskey Springs Fan, and San Fernando Valley Juvenile Hall, are also considered in this study.

The first of these cases added later, Koda Numa Railway Embankment, was also studied by many research groups including Seed (1987), Seed and Harder (1990), Stark and Mesri (1992), Olson and Stark (2002), Wang (2003), Kramer (2008) and Wang and Kramer (2015). Weber (2015) eliminated this case history from his database and back-analyses by claiming that the available information and documentation regarding the post-failure geometry and runout characteristics were

not reliable. It is stated that the mass of the displaced material evaluated from the post-failure geometry appears to be more than twice the failed mass estimated from the pre-failure geometry, and this disagreement cannot be resolved. On the other hand, this case is included in this study as Mishima and Kimura (1970), the main source of reference for this case history, documented both the pre-failure and post-failure geometries of this case with a sketch. Furthermore, the exact locations of the Swedish soundings performed at the site following the failure were placed along the critical cross-section on this sketch. Therefore, the representative penetration resistance, which is a piece of very valuable information in residual strength relationships, was easy to be evaluated for this case history. As a result, this case history is included in this study as the 34th case.

The other two cases added later, Whiskey Springs Fan and San Fernando Valley Juvenile Hall, were only studied by relatively earlier research groups, Seed and Harder (1990) and Stark and Mesri (1992). The Whiskey Springs Fan case was eliminated from further consideration as the cyclic lurching forces were contributing significantly to the observed displacements, and the analytical assessment of these cyclic lurching forces was really challenging. However, similar to the Koda Numa Railway Embankment case, the pre-failure and post-failure geometries were provided clearly by a sketch in the main source of reference of this case history, Andrus and Youd (1987). Moreover, the exact locations of the Standard Penetration Tests and Cone Penetration soundings performed at the site before the failure were placed along the critical cross-section on this sketch. Thus, the representative penetration resistance, which is a piece of very valuable information in residual strength relationships, was again easy to be evaluated for this case history. As a result, this case history is included in this study as the 35th case.

San Fernando Valley Juvenile Hall case was also eliminated by recent studies due to the same issues as the Whiskey Springs Fan case, such that it was a lateral spreading case, and the cyclic lurching forces were contributing significantly to the observed displacements, and the analytical assessment of these cyclic lurching forces was

really challenging. Nevertheless, similar to the previous two cases added later, Koda Numa Railway Embankment and Whiskey Springs Fan, the pre-failure and post-failure geometries were provided clearly by a sketch in the main source of reference of this case history, Bennett (1989). Additionally, the exact locations of the Standard Penetration Tests and Cone Penetration surroundings performed at the site before the failure were placed along the critical cross-section on this sketch. Consequently, the representative penetration resistance, which is a piece of very valuable information in residual strength relationships, was again easy to be evaluated for this case history. As a result, this case history is included in this study as the 36th case.

It should be noted that although totally 36 case histories were selected as valuable and reliable cases for the engineering evaluation of post-liquefaction shear strength, the first 32 of them are taken into account during the development of residual strength prediction relationships as it will be further discussed in Chapter 5. The reason behind this decision is that the residual strength results obtained in this study are validated by comparing them with the back-analysis post-liquefaction shear strength results reported by Weber (2015) as it is decided to be one of the most reliable and accurate studies in terms of engineering approaches and evaluations. Since Weber (2015) developed its post-liquefaction shear strength prediction relationships based on 32 Group A and Group B case histories (this value is reported as 29 in Weber (2015) since it considers Mochi-Koshi Tailings Dam 1 and 2, and Nerlerk Embankment Slide 1, 2 and 3 cases as single cases due to high similarity between them), same case histories are also used in this study during the development of residual strength prediction relationships. On the other hand, details of the remaining 4 case histories are also presented in this study in order to provide helpful documentation for them.

In addition to these 36 case histories, there were also several case histories available in the literature studied by previous research groups, such as Kawagishi-Cho Building, Snow River Bridge Fill, Fraser River Delta, and Heber Road. Kawagishi-Cho Building case was investigated by many research groups such as Seed (1987),

Seed and Harder (1990), Stark and Mesri (1992), Olson and Stark (2002), Wang (2003), Kramer (2008) and Wang and Kramer (2015), and only eliminated by Weber (2015). This case is also put out of action for this study as the cyclic inertial forces and moments were unknown, and the post-failure geometry was not clear due to the non-symmetric and non-uniform bearing pressures at the base of the structure that contributed to the failure. Snow River Bridge Fill case was also studied by many research groups and only eliminated by Olson and Stark (2002) and Weber (2015). This case history also has not been considered in this study as both the pre-failure and post-failure geometries were unknown, and there were significant uncertainties about the actual failure mode of the structure, such as depth and length of the failure, etc. Fraser River Delta case was only studied by Olson and Stark (2002), but not in detail, such that the study only reported representative SPT resistance and S_r/σ'_{v0} value for this case. Furthermore, S_r/σ'_{v0} value was not evaluated separately in the study, and the ratio provided by Chillarige et al. (1997) from the laboratory tests conducted on reconstituted Fraser River Delta sand was reported as representative liquefied strength ratio. This case history also has not been taken into account in this study as well because both the pre-failure and post-failure geometries were not documented clearly, and there was no study available in the literature to compare the residual strength estimations. Heber Road case was only studied by Stark and Mesri (1992), and other research groups have not considered it due to lack of documentation. Similar to the majority of these investigation teams, this case history has not been considered in this study also since post-failure geometry was not documented in any of the main sources of references.

In the end, totally 36 case histories compatible with the literature are documented in this study, and 32 of them are employed to develop relationships for post-liquefaction (residual) shear strength of soils. These case histories are numbered from 1 to 36, and the corresponding case history numbers are frequently used inside of the thesis instead of their full names for simplicity. Selected case histories with their corresponding case numbers, failure dates, and failure reasons are tabulated in Table 3.1. It should be noted that these cases are numbered with respect to the quality

of data such that while case histories 1-13 represent higher-quality cases with good documentation, 14-36 represent lower quality cases with poorer documentation.

Table 3.1 Selected case histories for this study

#	Case History	Failure Date
1	Wachusett Dam - North Dike	1907 Reservoir Filling
2	Fort Peck Dam	1938 Construction
3	Uetsu Railway Embankment	1964 Niigata Eq (M=7.5)
4	Lower San Fernando Dam - U/S Slope	1971 San Fernando Eq (M_w=6.6)
5	Hachiro-Gata Road Embankment	1983 Nihon-Kai-Chubu Eq (M=7.7)
6	La Marquesa Dam - U/S Slope	1985 Chilean Eq (M_s=7.8)
7	La Marquesa Dam - D/S Slope	1985 Chilean Eq (M_s=7.8)
8	La Palma Dam	1985 Chilean Eq (M_s=7.8)
9	Lake Ackerman Highway Embankment	1987 Seismic Survey
10	Chonan Middle School	1987 Chiba-Toho-Oki Eq (M=6.7)
11	Soviet Tajik - May 1 Slide	1989 Tajik, Soviet Union Eq (M_L=5.5)
12	Shibecha-Cho Embankment	1993 Kushiro-Oki Eq (M_L=7.8)
13	Route 272 at Higashiarekinai	1993 Kushiro-Oki Eq (M_L=7.8)
14	Zeeland - Vlietepolder	1889 High Tide
15	Sheffield Dam	1925 Santa Barbara Eq (M_L=6.3)
16	Helsinki Harbor	1936 Construction
17	Solfatara Canal Dike	1940 El Centro Eq (M=7.2)
18	Lake Merced Bank	1957 San Francisco Eq (M=5.7)
19	El Cobre Tailings Dam	1965 Chilean Eq (M_L=7 to 7.25)
20	Metoki Road Embankment	1968 Tokachi-Oki Eq (M=7.9)
21	Hokkaido Tailings Dam	1968 Tokachi-Oki Eq (M=7.9)
22	Upper San Fernando Dam - D/S Slope	1971 San Fernando Eq (M_w=6.6)
23	Tar Island Dyke	1974 Construction
24	Mochi-Koshi Tailings Dam 1	1978 Izu-Ohshima Eq (M=7.0)
25	Mochi-Koshi Tailings Dam 2	1978 Izu-Ohshima Eq (M=7.0)
26	Nerlerk Embankment Slide 1	1983 Construction
27	Nerlerk Embankment Slide 2	1983 Construction
28	Nerlerk Embankment Slide 3	1983 Construction
29	Asele Road Embankment	1983 Pavement Repairs
30	Nalband Railway Embankment	1988 Armenian Eq (M_s=6.8)

Table 3.1 (cont'd) Selected case histories for this study

31	Sullivan Tailings	1991 Dyke Raising, British Columbia
32	Jamuna Bridge	1994 Construction, Bangladesh
33	Calaveras Dam	1918 Construction
34	Koda Numa Railway Embankment	1968 Tokachi-Oki Eq (M=7.9)
35	Whiskey Springs Fan	1983 Borah Peak Eq (M=7.3)
36	San Fernando Valley Juvenile Hall	1971 San Fernando Eq (M_w=6.6)

3.2 Evaluation of Material Properties

Estimation of the in-situ void ratio with its limits (e_{max} and e_{min}) and maximum range (e_{max}-e_{min}) is an integral part of the critical (liquefaction) state concept as the location of a point in the critical state domain is determined by its void ratio under the corresponding mean effective stress. Hence, parameters that can be used in estimating the limit void ratios and void ratio range are selected as the promising descriptive parameters of the problem.

It will be further discussed in Section 3.6, but undisturbed sampling of cohesionless soils is known to be extremely challenging. Although there are several standard testing procedures available in the literature for estimating the densest and the loosest states of soil for the case when soil samples are available, different values for limiting void ratios may be obtained depending on the method used during estimation. The reason behind these differences is that these tests are extremely sensitive to sample preparation, equipment-used, energy-delivered, and inevitable human effects during testing, as also claimed by Blaker et al. (2015) and Tavenas et al. (1973). Therefore, significant variability in limiting void ratios is common even when soil samples are available, and standard laboratory tests are performed. Additionally, the confining stress on the sample during the time when the test is performed is generally not reported, or even unknown in many cases. As a result, soil sampling and laboratory testing may be misleading for limit void ratio estimations.

Based on these uncertainties in laboratory-estimated void ratio limits, a number of semi-empirical, probability-based relationships are proposed in the literature to evaluate e_{max}, e_{min} and e_{max}-e_{min}. The main objective of these research studies is to correlate the index properties of soils and their particle morphology (surface texture, roundness, sphericity) with their mechanical responses under monotonic or cyclic loading conditions. Yang and Wei (2012, 2014), Belkhatir et al. (2012, 2013), Cherif et al. (2016, 2018), Xiao et al. (2019), and Xie et al. (2017) are some of the qualified studies related to mechanical responses of soils under monotonic loading conditions. Yilmaz et al. (2008), on the other hand, is one of the research studies on mechanical responses of soils under cyclic loading conditions. These studies also examine the effects of index properties and particle morphology of soils on minimum or maximum void ratio states. The vast majority of these studies correlate mean grain size (D_{50}), fines content (FC), coefficient of uniformity (C_u), roundness (R), and sphericity (S), with e_{min}, e_{max} and e_{max}-e_{min} of cohesionless soils. Thus, these material parameters are estimated for all selected case histories. The standard procedures followed in this study while estimating these parameters are explained below.

Mean grain size (D_{50}):

By definition, the letter D represents the diameter of soil particles, and the mean grain size (D_{50}), or median particle diameter, median particle size, etc., is the corresponding particle size when the cumulative percentage in a standard Sieve Analysis Test reaches 50%. In simpler terms, it means that 50% of particles are larger and 50% of them are smaller than D_{50} value. It is a typical material characteristic used to represent the average particle size in a soil sample.

To be able to determine D_{50} value, the cumulative grain/particle size distribution curve of the corresponding soil sample, which can be obtained as a result of a standard Sieve Analysis Test, is required. Sieve Analysis Test is the laboratory experiment used to determine the grain size distribution of the coarse fraction of a soil sample. To be able to develop the entire grain size distribution curve of a soil, Hydrometer (i.e. Sedimentation) Test should also be performed on the fines of the

same sample, where the fines fraction is defined as the fraction smaller than the openings of No.200 sieve of Sieve Analysis Test. The details of the Sieve Analysis Test are out of the scope of this study; hence, they are not mentioned here to avoid straying from the main research topic. However, the detailed explanations of the equipment, calibration, sample preparation, test procedure, and calculations of the test can be reached from the standardized testing specifications such as ASTM D6913 and TS 1900.

An example grain size distribution curve developed for Lake Ackerman Highway Embankment case history is given in Figure 3.1. As shown in this figure, the mean grain size (D_{50}) value is estimated as 0.390 mm on average, with a range of 0.320-0.470 mm.

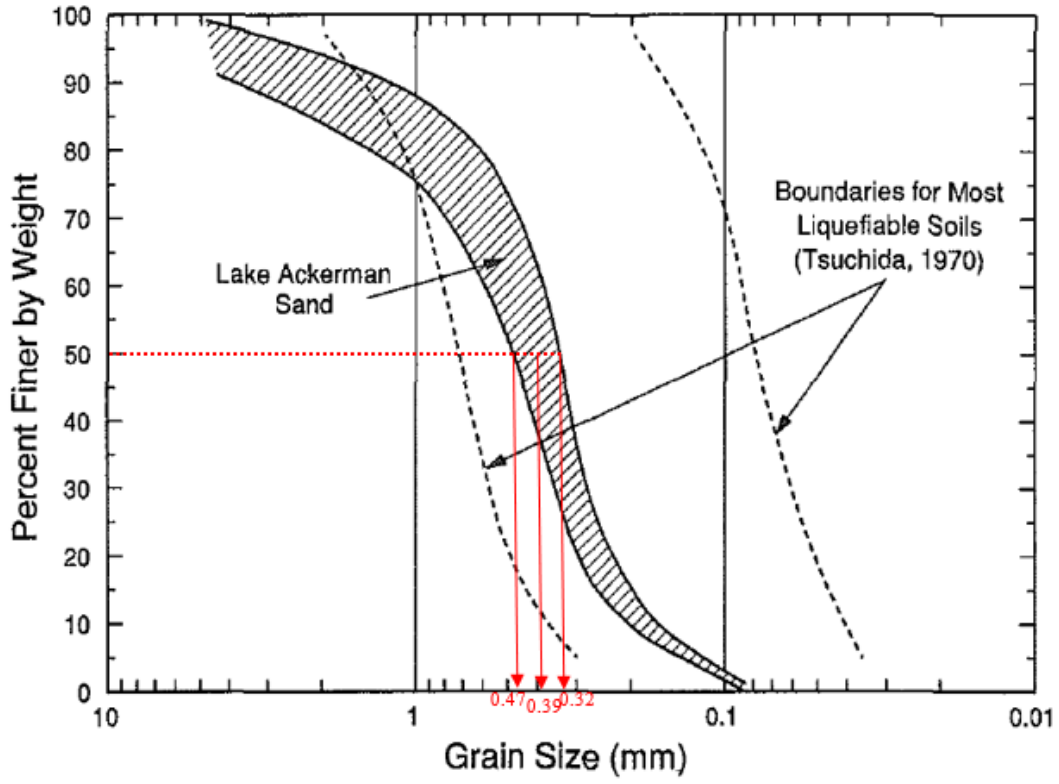

Figure 3.1. Example grain size distribution curve and D_{50} evaluation

The mean grain size provides important clues about the soil such that it basically tells the classification of soil as whether it is gravel, sand, even fine sand, or coarse

sand. In addition, it is one of the fundamental material properties in estimating limit void ratios and void ratio range such that many empirical and semi-empirical correlations that will be discussed in Section 3.6 use D_{50} as an input parameter. An example correlation suggested by Cubrinovski and Ishihara (1999) is provided in Figure 3.2 to initiate a better understanding of the effect of D_{50} on limit void ratios and void ratio range.

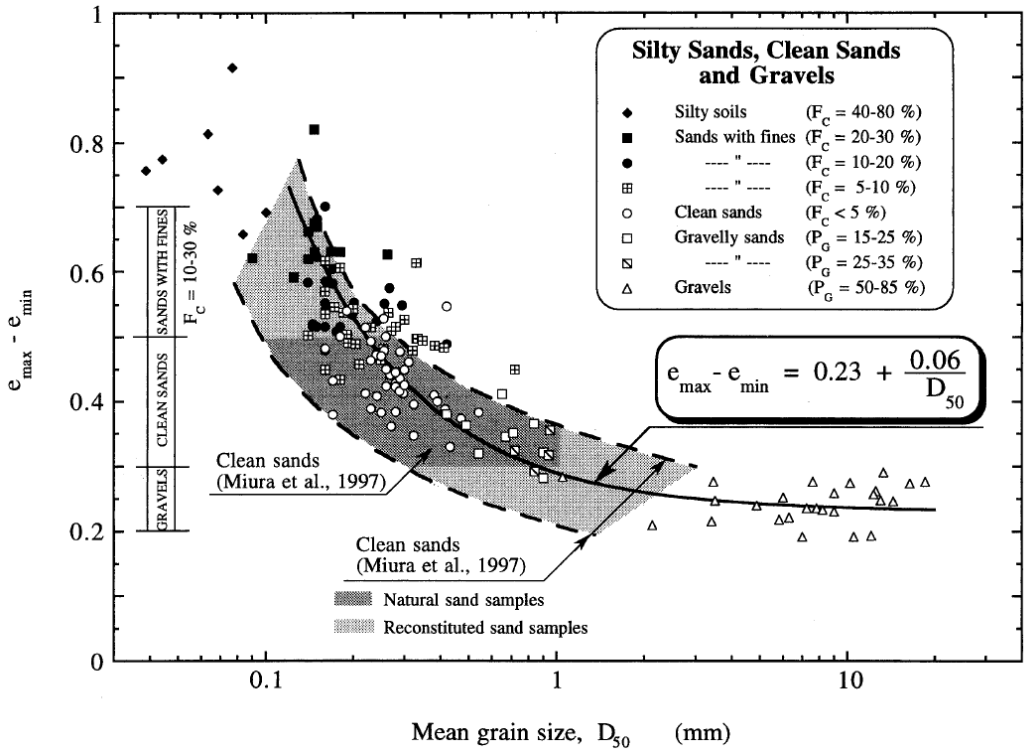

Figure 3.2. Relationship between void ratio range and mean grain size (Cubrinovski and Ishihara, 1999)

Figure 3.3 also shows the results of Cetin and Ilgac (2021) study, which examines the effect of mean grain size (D_{50}) on limit void ratios and void ratio range. As clearly observed in Figure 3.2 and Figure 3.3, the limit void ratios (e_{max}, e_{min}) and void ratio range (e_{max}-e_{min}) decreases with increasing mean grain size (D_{50}) value.

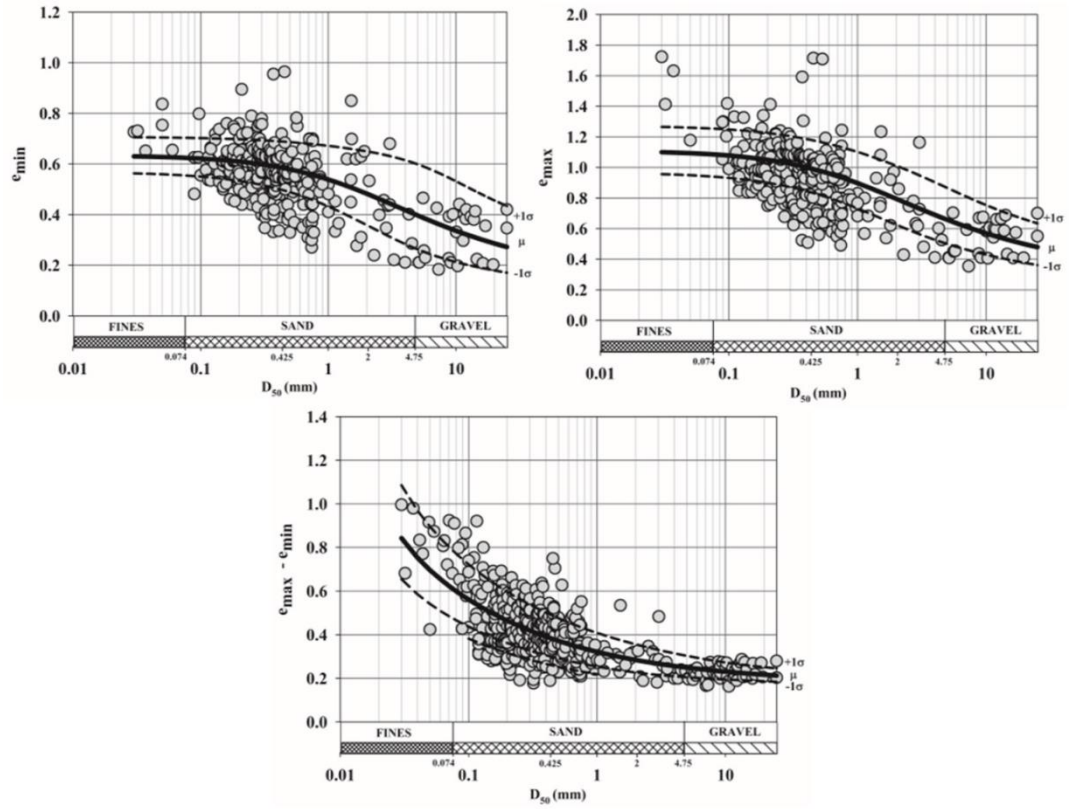

Figure 3.3. Relationship between (a, b) limit void ratios and (c) void ratio range and mean grain size (Cetin and Ilgac, 2021)

As a result, D_{50} value of each selected case history is determined with significant effort and attention. On the other hand, many of these case histories belong to very old years as already discussed; therefore, they are not well-documented, and much valuable information is not reported. Moreover, some of the laboratory and in-situ testing techniques were not developed at the times when some of these failures occurred. Even, the liquefaction phenomenon was not understood totally at the times of them. Hence, the grain size distribution curve, and therefore the mean grain size value, was not reported in the main sources of some case histories.

For 20 of the 36 case histories (Case history #: 2, 3, 4, 9, 11, 12, 14, 17, 18, 22, 24, 25, 26, 27, 28, 29, 30, 34, 35, 36), the grain size distribution curves were reported clearly by the main sources of the failure case histories. Therefore, the mean grain size values for these well-reported case histories are read individually from the

corresponding curves in this study. The estimated values are reported in Appendix A for each of these 20 case histories with their gradation curves taken from the main sources. It is observed that the estimated values are in perfect agreement with the reported ones by other sources and investigation teams.

For 11 of the 36 case histories (Case history #: 1, 5, 6, 7, 8, 10, 13, 15, 19, 23, 32), only the exact value of D_{50} or a narrow range of it was reported in the main sources instead of the entire grain size distribution curve. Therefore, the mean grain size values for these case histories are selected as the same as the reported values in this study due to lack of available information. The estimated values are reported in Appendix A for each of these 11 case histories by referring to their main sources.

For the remaining 5 case histories (Case history #: 16, 20, 21, 31, 33), neither the grain size distribution curve nor the D_{50} value itself was reported in the main sources. Therefore, a representative mean grain size value is assigned for these case histories. For case histories #20 (Metoki Road Embankment) and #21 (Hokkaido Tailings Dam), Olson (2001) suggests representative D_{50} values based on the D_{50} values of similar soil types. For these 2 case histories, the same values as Olson (2001) are selected in this study as well. For the remaining 3 of these 5 poorly-documented case histories, the dataset compiled by Ilgac et al. (2019) is used while selecting the representative D_{50} values based on the reported soil classifications in main sources. This dataset consists of maximum and minimum void ratio limits and their range, particle size, distribution, and shape characteristics of 636 natural cohesionless soils and reconstituted grained material mixtures. Maximum void ratio (e_{max}), minimum void ratio (e_{min}), void ratio range (e_{max}-e_{min}), mean grain size (D_{50}), fines content (FC), coefficient of uniformity (C_u), roundness (R) and sphericity (S) information of 19 silts and clays, 527 sands (357 fine sands, 153 medium sands, 17 coarse sands) and 47 gravels (44 fine gravels, 3 coarse gravels) are well-reported in the dataset. For these remaining 3 cases that neither the grain size distribution curve nor the D_{50} value was reported, the average D_{50} value in the dataset for the corresponding soil type is selected as representative. For instance, the average D_{50} values are evaluated as 0.090 mm and 0.732 mm for silty soils with 30%<FC<70% and for gravelly sands

with FC<6%, respectively, based on the reported soils in the dataset. Thus, these values are selected as the representative D_{50} values for case histories #31 and #33, respectively, where the zone of liquefaction consisted of silty sands for case history #31 (Sullivan Tailings) and gravelly sands for case history #33 (Calaveras Dam).

Fines content (FC):

By definition, fines content is the amount of silts and clays, in percentage, in soil, which also means the amount of soil particles passing from No.200 sieve in Sieve Analysis Test. While the American Society for Testing and Materials (ASTM) considers 74 μm (0.074 mm) as the boundary between coarse and fine particles, the Turkish Standards (TS) and the British and European Standard Specifications (BS EN) takes this value as 63 μm (0.063 mm). The ASTM boundary, which is 74 μm (0.074 mm), is chosen as the reference in this study, and the fines contents of the case histories were determined accordingly.

In addition to affecting the liquefaction susceptibility of sandy soils, fines content also has a significant effect on limit void ratio and void ratio range models similar to mean grain size. As it will be further discussed in Section 3.6, many empirical and semi-empirical correlations on e_{max}, e_{min} and e_{max}-e_{min} use fines content as an input parameter. An example correlation suggested by Cubrinovski and Ishihara (2002) is provided in Figure 3.4 to initiate a better understanding of the effect of fines content on limit void ratios and void ratio range. As clearly observed in Figure 3.4, the limit void ratios (e_{max}, e_{min}) and void ratio range (e_{max}-e_{min}) increases with increasing fines content (FC) value.

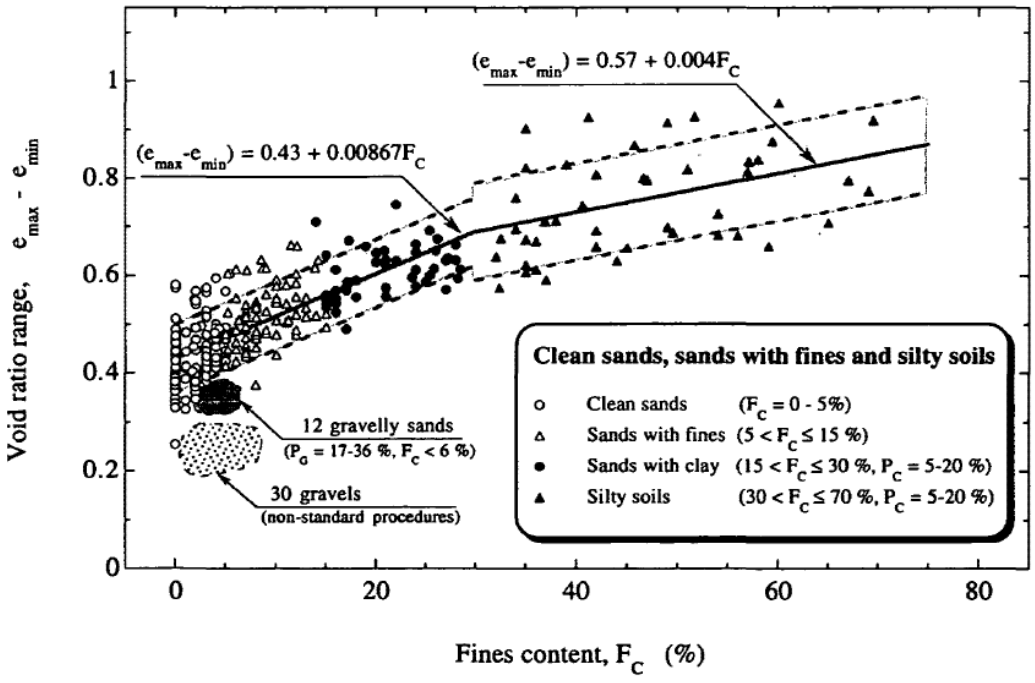

Figure 3.4. Relationship between void ratio range and fines content (Cubrinovski and Ishihara, 2002)

In addition to that, the penetration resistance is also affected by the fines content such that there are lots of fines correction methods and techniques available in the literature for Standard Penetration Test (SPT). The effect of fines on penetration resistance will be further discussed in Section 3.5 during the explanation of SPT resistances for case histories, but it is valuable to remark at this point that the penetration resistance has a crucial impact on the in-situ relative densities of the soils. Therefore, fines content also has an indirect effect on the relative density, and therefore in-situ void ratio, as well. Hence, the fines content value of each selected case history is evaluated with a significant effort and attention in the scope of this study that focuses on implementing a new critical state framework compatible methodology in void ratio versus effective strain domain.

Similar to mean grain size, the cumulative grain/particle size distribution curve of the corresponding soil sample is again required to evaluate the fines content. The cumulative passing percentage from the No.200 sieve (0.074 mm for ASTM) gives

the amount of fines in a standard Sieve Analysis Test, and the ratio of this amount to the entire sample by mass gives the fines content in percentage. On the other hand, the same issues in evaluating D_{50} values are also present in fines content case such that many of these case histories are not very well-documented as they belong to old times. Thus, much valuable information including the fines content is not reported in some cases.

For 20 of the 36 case histories (Case history #: 2, 3, 4, 9, 11, 12, 14, 17, 18, 22, 24, 25, 26, 27, 28, 29, 30, 34, 35, 36), the grain size distribution curves were reported clearly by the main sources of the failure case histories. Therefore, the fines content values for these well-reported case histories are read individually from the corresponding curves in this study. The estimated values are reported in Appendix A for each of these 20 case histories with their gradation curves taken from the main sources. It is observed that the estimated values are in perfect agreement with the reported ones by other sources and investigation teams.

For 14 of the 36 case histories (Case history #: 1, 5, 6, 7, 8, 10, 13, 15, 19, 20, 23, 31, 32, 33), only the exact value of fines content or a narrow range of it was reported in the main sources instead of the entire grain size distribution curve. Therefore, the fines content values for these case histories are selected similarly to the reported values in this study due to the lack of available information. The estimated values are reported in Appendix A for each of these 14 case histories by referring to their main sources.

For the remaining 2 case histories (Case history #: 16, 21), neither the grain size distribution curve nor the fines content value itself were reported in the main sources. For case history #21 (Hokkaido Tailings Dam), Olson (2001) suggests a representative FC value based on the FC values of similar soil types; therefore, the same value as Olson (2001) is selected in this study as well for this case history. For case history #16 (Helsinki Harbor), no information about the fines content was reported in the main sources of the case history since the failure was observed in 1936 during the construction, and it was not documented properly at those years.

Due to the fact that a reliable penetration resistance was also not reported for this case history, a representative fines content value is not assigned for it, and corresponding void ratio models including the effect of fines content are not used in estimating the limit void ratios and void ratio range for this case history.

Another example grain size distribution curve developed for Asele Road Embankment case history is given in Figure 3.5. As shown in this figure, the fines content value is estimated as 30% on average, with a range of 23-37%.

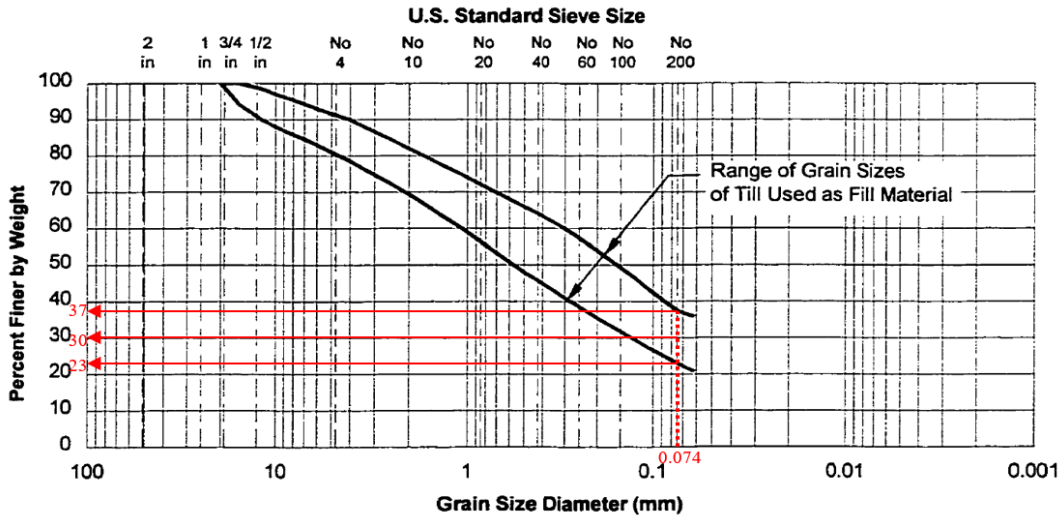

Figure 3.5. Example grain size distribution curve and fines content evaluation

Coefficient of uniformity (C_u):

By definition, the coefficient of uniformity (C_u) is the ratio of D_{60} value to D_{10} value of soil, and it measures the soil gradation and uniformity of grain size in soil. D_{60} value of soil indicates that 60% of the particles are finer and 40% of the particles are coarser than that value. Similarly, D_{10} value of soil indicates that 10% of the particles are finer and 90% of the particles are coarser than that value. It is a geometric property of a grain size distribution curve that describes a particular type of soil. Typically, the Unified Soil Classification System (American Society of Testing of Materials, ASTM D2487) states that while a value of C_u greater than 4 to 6 classifies the soil as well-graded, a value less than 4 classifies it as poorly-graded or uniformly-graded soil. Uniformly graded soil has identical particles with C_u value

approximately close to or equal to 1. A coefficient of uniformity value of 2 or 3 typically classifies the soil as poorly-graded. A higher value of C_u indicates that the soil mass contains soil particles with different size ranges.

The coefficient of uniformity provides valuable clues about the soil such that while a uniformly-graded soil has larger voids, higher permeability, and higher compressibility, a well-graded soil has smaller voids, lower permeability, and lower compressibility as smaller soil particles fill the spaces between the larger ones. In addition to that, the particle size range increases with increasing coefficient of uniformity; therefore, it has an important effect on the void ratio range similar to D_{50} and fines content. Hence, it is also another fundamental material property in estimating limit void ratios and void ratio range, and many empirical and semi-empirical correlations that will be discussed in Section 3.6 use C_u as an input parameter. On the other hand, most of these limit void ratio and void ratio range correlation models have an upper limit for C_u since the value of it can reach extremely great numbers for gap-graded soils, which have a significant difference between D_{60} and D_{10} values. In the case of gap-graded (or step-graded) soils, while the particles of large and small sizes are present, the proportion of intermediate-sized particles is low. Accordingly, D_{60} and D_{10} values differ from each other dramatically, which reveals extremely great C_u values. These types of large values may bias the accuracy of void ratio prediction models; therefore, the prediction models including the coefficient of uniformity as an input parameter should not be used for the soils exceeding the limit C_u value.

An example correlation suggested by Cetin and Ilgac (2021) is provided in Figure 3.6 to initiate a better understanding of the effect of the coefficient of uniformity on limit void ratios and void ratio range. As clearly observed in Figure 3.6, the limit void ratios (e_{max}, e_{min}) and void ratio range (e_{max}-e_{min}) decreases with increasing coefficient of uniformity (C_u) value.

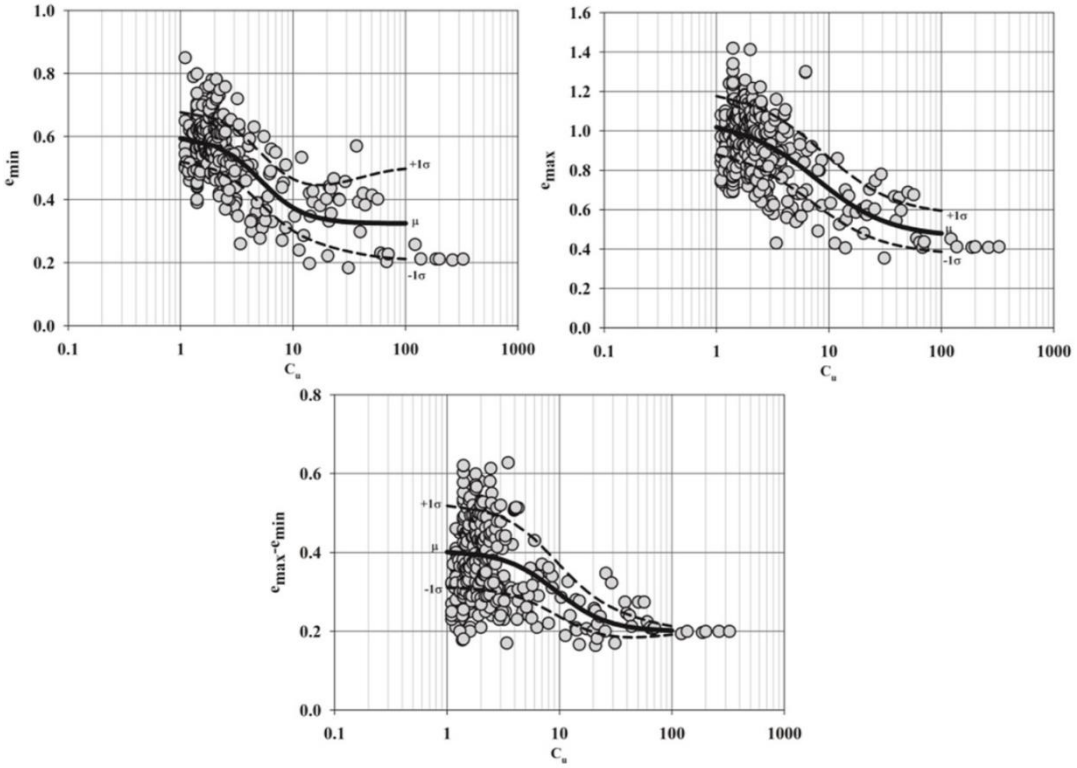

Figure 3.6. Relationship between (a, b) limit void ratios and (c) void ratio range and coefficient of uniformity (Cetin and Ilgac, 2021)

In this context, the coefficient of uniformity value of each selected case history is determined with significant effort and attention. Similar to mean grain size and fines content, the cumulative grain/particle size distribution curve of the corresponding soil sample is required to evaluate the coefficient of uniformity. However, the same trouble in evaluating D_{50} and FC values is also present in C_u case, such that many of these older case histories are not documented well. Thus, much valuable information including the grain size distribution curve and coefficient of uniformity is not reported in some cases.

For 20 of the 36 case histories (Case history #: 2, 3, 4, 9, 11, 12, 14, 17, 18, 22, 24, 25, 26, 27, 28, 29, 30, 34, 35, 36), the grain size distribution curves were reported clearly by the main sources of the failure case histories. Therefore, D_{60}, D_{10}, and the coefficient of uniformity values for these well-reported case histories are evaluated individually from the corresponding curves in this study. The estimated values are

reported in Appendix A for each of these 20 case histories with their gradation curves taken from the main sources. Extremely large C_u values, which exceed the upper limit boundaries of void ratio estimation models, are evaluated for 2 of these 20 case histories (Case history #: 30, 35) due to the reasons explained previously. Hence, the void ratio prediction models using the coefficient of uniformity as an input parameter are used with special care and attention in estimating the limit void ratios and void ratio range for these two cases. The maximum allowable coefficient of uniformity value to be used in these models is selected as the representative C_u value for them. It is observed that the estimated values are in perfect agreement with the reported ones by other sources and investigation teams.

For the remaining 16 case histories (Case history #: 1, 5, 6, 7, 8, 10, 13, 15, 16, 19, 20, 21, 23, 31, 32, 33), neither the grain size distribution curve nor the coefficient of uniformity value itself was reported in the main sources. Therefore, a representative C_u value cannot be assigned for these case histories, with an exception to one of them. For Hokkaido Tailings Dam case (Case history #: 21), the value of the coefficient of uniformity is estimated as 1.50 by assuming that very uniformly-graded artificial synthetic soil particles are used in the construction of tailing type of dams. Since the value of C_u depends on two other parameters, D_{60} and D_{10}, an assumption also has not been made for the remaining case histories to protect the quality of the dataset. Accordingly, the corresponding void ratio prediction models including the effect of coefficient of uniformity are not used in estimating the limit void ratios and void ratio range for them.

Another example grain size distribution curve developed for Soviet Tajik – May 1 Slide case history is given in Figure 3.7. As shown in this figure, D_{60} and D_{10} values are estimated as 0.015 mm and 0.0025 mm, respectively. As a result, the coefficient of uniformity is evaluated as C_u=0.015/0.0025=6.00.

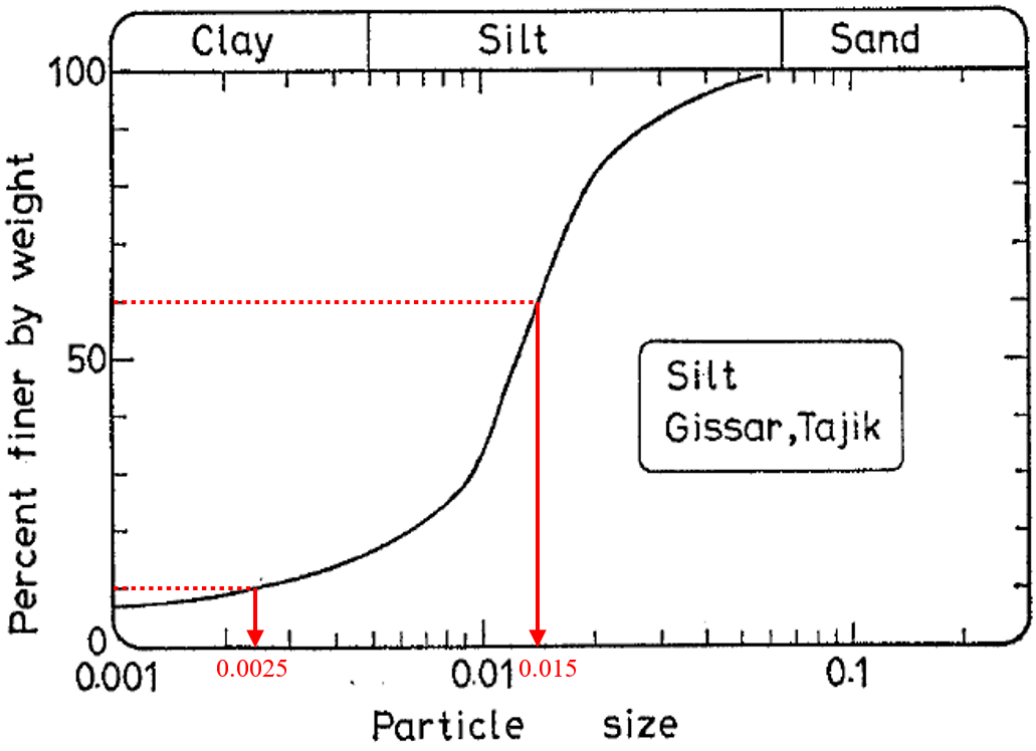

Figure 3.7. Example grain size distribution curve and coefficient of uniformity evaluation

Roundness (R):

The formation history of grains depends on the size and shape of soil particles, which means that the particle level interactions governed by particle shape affect the macroscale behavior of the soil mass. Although there are different definitions of roundness available in the literature, and an accurate differentiation among these available definitions could not be made due to lack of documentation in the source of references, Cho et al. (2006) provides one of the most common and well-known definitions of roundness as a dimensionless parameter of the average radius of surface feature curvatures relative to the radius of the maximum sphere that can be inscribed in the particle. In other words, roundness is defined as the ratio of the average radius of the circles that fit in the grain's protrusion ($\sum r_i/N$) and the maximum circle radius that fits inside the grain ($r_{max\text{-}in}$). This definition and

estimation method of roundness given in Equation 3-1 is modified from Krumbein and Sloss (1963) method.

$$Roundness: R = \frac{\sum r_i / N}{r_{max-in}} \qquad \text{Equation 3-1}$$

Figure 3.8 shows a sketch that illustrates these parameters, r_i and $r_{max\text{-}in}$ for a better understanding. Additionally, it also provides a particle shape determination chart for the visual examination, which is proposed by Cho et al. (2006), and is a modified version of Krumbein and Sloss (1963). According to this definition, roundness is a dimensionless parameter that ranges between 0.1-1.0.

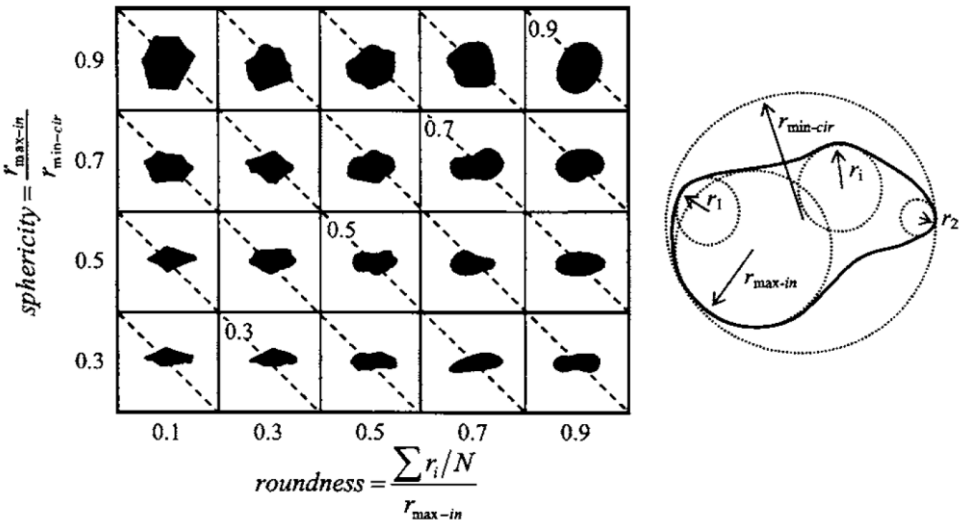

Figure 3.8. Particle shape determination chart for visual examination, Cho et al. (2006), modified from Krumbein and Sloss (1963)

Nevertheless, although the definition provided by Cho et al. (2006) used in this study for roundness, there are also different definitions of roundness are available in the literature. Powers (1953) provides Table 3.2, which summarizes the roundness grades according to Russell and Taylor (1937) and Pettijohn (1949). The same study also suggests additional roundness ranges given in Table 3.3 in addition to these studies.

Table 3.2 Roundness grades according to Russell and Taylor (1937) and Pettijohn (1949), summarized by Powers (1953)

	Russell and Taylor (1937)		*Pettijohn (1949)*	
Classification	*Class limit*	*Arithmetic midpoint*	*Class limit*	*Geometric midpoint*
Angular	0.00 – 0.15	0.075	0.00 – 0.15	0.150
Subangular	0.15 – 0.30	0.225	0.15 – 0.25	0.200
Subrounded	0.30 – 0.50	0.400	0.25 – 0.40	0.315
Rounded	0.50 – 0.70	0.600	0.40 – 0.60	0.500
Well rounded	0.70 – 1.00	0.850	0.60 – 1.00	0.800

Table 3.3 Roundness classification by Powers (1953)

Classification	*Class intervals*	*Geometric mean*
Very angular	0.12 – 0.17	0.14
Angular	0.17 – 0.25	0.21
Subangular	0.25 – 0.35	0.30
Subrounded	0.35 – 0.49	0.41
Rounded	0.49 – 0.70	0.59
Well rounded	0.70 – 1.00	0.84

Despite the fact that there are different definitions and estimation methods of roundness are present in literature, most of these studies including Cho et al. (2006), Wadell (1932), Krumbein (1941), Powers (1953), Krumbein and Sloss (1963), Barrett (1980), etc. proved that roundness has an essential effect on limit void ratios as shown in Figure 3.9, such that e_{max} and e_{min} values increase with increasing angularity or eccentricity.

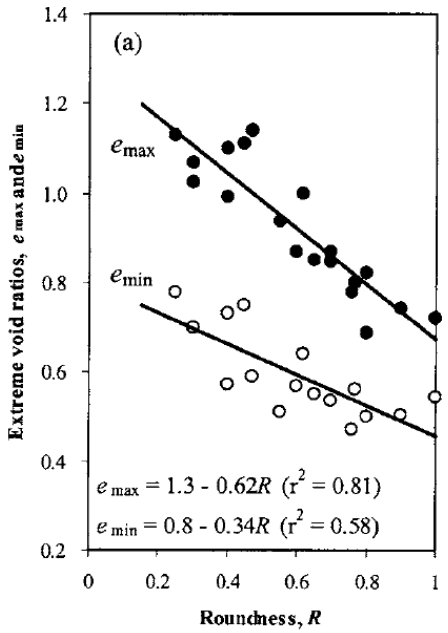

Figure 3.9. Effect of roundness (R) on limit void ratios (Cho et al., 2006)

Similarly, Figure 3.10 provided by Cubrinovski and Ishihara (2002) also shows that the limit void ratios (e_{max}, e_{min}) and void ratio range (e_{max}-e_{min}) decrease with increasing roundness (R) value.

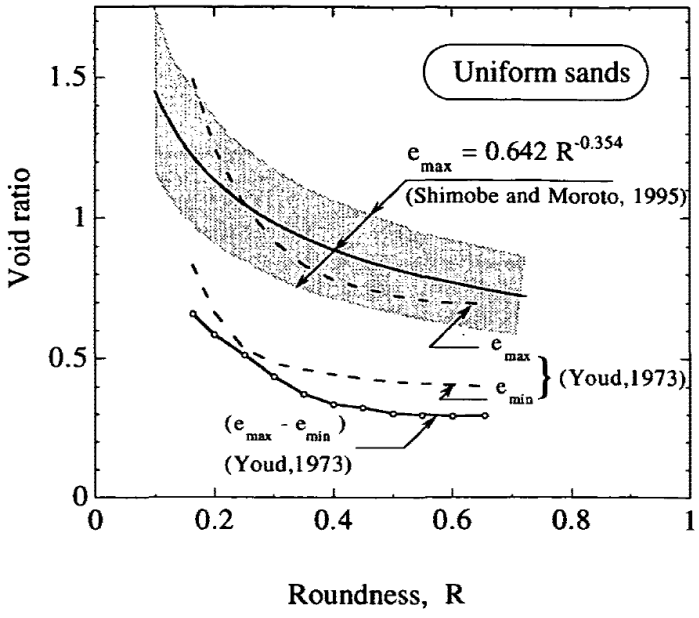

Figure 3.10. Effect of roundness (R) on limit void ratios and void ratio range (Cubrinovski and Ishihara, 2002)

Consequently, roundness (R) is also another fundamental material property in estimating limit void ratios and void ratio range, and many empirical and semi-empirical correlations that will be discussed in Section 3.6 use it as an input parameter.

In this context, the roundness value of each selected case history is tried to be determined with significant effort and attention. On the other hand, the documentation of these case histories has not been kept properly in those years, or even they have not been reported detailly. Furthermore, the importance of fabric and particle shape was not well-understood in the years when some liquefaction-triggered failures occurred; therefore, the fabric information for most of the cases was not reported adequately.

For 34 of the 36 case histories (Case history #: 1, 2, 3, 4, 5, 6, 7, 6, 9, 10, 11, 12, 13, 14, 15, 16, 17, 18, 19, 20, 21, 22, 24, 26, 27, 28, 29, 30, 31, 32, 33, 34, 35, 36), the roundness values or related information about the fabric and angularity were not reported in the main source of references. Therefore, the corresponding void ratio prediction models including the effect of roundness are not used in estimating the limit void ratios and void ratio ranges for them. However, the roundness values are representatively assumed to be 0.50 for these cases as the angularity of the soil particles, and therefore the roundness, has an effect on the critical state friction angle of the soils referring to the literature. This representative value is wisely selected such that it falls in the middle of the limits determined by Cho et al. (2006) well given in Equation 3-66 (0.1-1.0). Since critical state friction angle, or namely liquefaction state friction angle in this study, has a significant effect on the predicted post-liquefaction shear strength values in this suggested new framework, it is defined as a function of roundness. The details of the correlation between the roundness and liquefaction state friction angle of the soil will be discussed detailly in Chapter 4.

For the remaining 2 case histories (Case history #: 23, 35), the liquefied zones were reported as consisting of mainly “subangular” materials in main source references. Several research studies on surface roughness and shape of soil particles recommend

common roundness ranges for subangular materials. Russell and Taylor (1937) suggests a roundness range of 0.15-0.30 for subangular materials. Similarly, Pettijohn (1949) also recommends a roundness range of 0.15-0.25 for subangular types of materials. A more popular and commonly used study, Powers (1953), provides a range of 0.25-0.35 for the roundness of subangular materials. Cho et al. (2006), the article that taken into account in this study, also suggests a roundness range of 0.20-0.40 for subangular materials. Referring to these sources, the roundness values of these two special cases are estimated as 0.30, and the corresponding void ratio prediction models including the effect of roundness are considered in order to award the documented roundness information.

Sphericity (S):

Similar to roundness, there are different definitions of sphericity available in the literature, and an accurate differentiation among these available definitions could not be made due to lack of documentation in the source of references. Again, Cho et al. (2006) provides one of the most common and well-known definitions of sphericity as the global form of the particle that reflects the similarity between the length, height, and width of the particle. It can be quantified as a dimensionless parameter that indicates the diameter of the largest inscribed sphere relative to the diameter of the smallest circumscribed sphere. In other words, it is defined as the ratio of the maximum circle radius which fits inside the grain ($r_{max\text{-}in}$) and the minimum circle radius which encircles the grain ($r_{min\text{-}cir}$). This definition and estimation method of sphericity given in Equation 3-2 is modified from Krumbein and Sloss (1963) method.

$$Sphericity: S = \frac{r_{max-in}}{r_{min-cir}} \qquad \text{Equation 3-2}$$

As also described with roundness, Figure 3.8 shows a sketch that illustrates these parameters, $r_{max\text{-}in}$ and $r_{min\text{-}cir}$ for a better understanding. In addition, it also provides a particle shape determination chart for the visual examination, which is proposed by Cho et al. (2006), and is a modified version of Krumbein and Sloss (1963).

According to this definition, sphericity is a dimensionless parameter that ranges between 0.25-1.0.

Despite the fact that there are different definitions and estimation methods of sphericity are present in literature, most of these studies including Cho et al. (2006), Wadell (1932), Krumbein (1941), Powers (1953), Krumbein and Sloss (1963), Barrett (1980), etc. proved that sphericity has an essential effect on limit void ratios as shown in Figure 3.11, such that e_{max} and e_{min} values increase with increasing angularity or eccentricity.

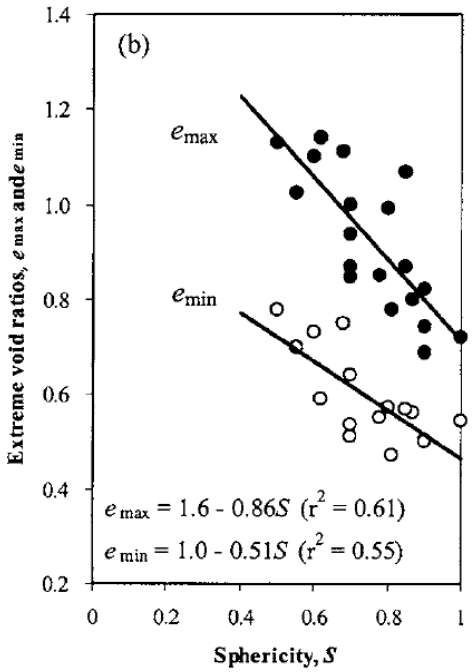

Figure 3.11. Effect of sphericity (S) on limit void ratios (Cho et al., 2006)

Similarly, Figure 3.12 provided by Cetin and Ilgac (2021) also shows that the limit void ratios (e_{max}, e_{min}) and void ratio range (e_{max}-e_{min}) decrease with increasing sphericity (S) value.

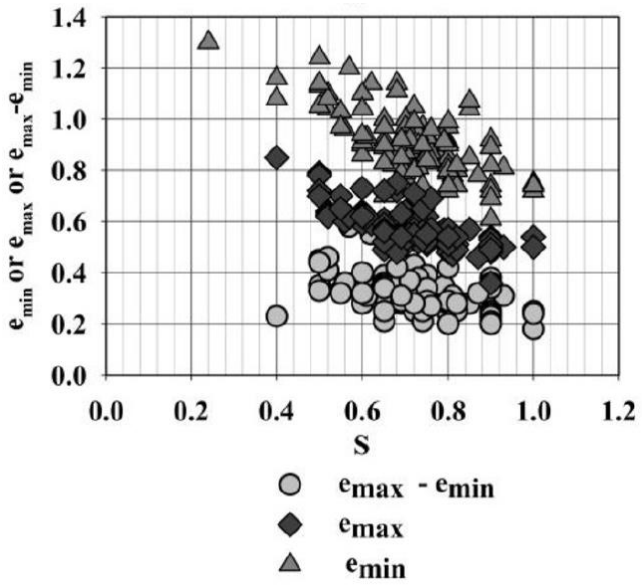

Figure 3.12. Effect of sphericity (S) on limit void ratios and void ratio range (Cetin and Ilgac, 2021)

As a result, it is also another fundamental material property in estimating limit void ratios and void ratio range, and many empirical and semi-empirical correlations that will be discussed in Section 3.6 use sphericity (S) as an input parameter.

In this context, the sphericity value of each selected case history is tried to be determined with significant effort and attention. However, the documentation of these case histories has not been kept properly in those years, or even they have not been reported detailly. Furthermore, the importance of fabric and particle shape was not well-understood in the years when some liquefaction-triggered failures occurred; therefore, the fabric information for most of the cases was not reported adequately.

For all of the 36 case histories (Case history #: 1, 2, 3, 4, 5, 6, 7, 6, 9, 10, 11, 12, 13, 14, 15, 16, 17, 18, 19, 20, 21, 22, 23, 24, 25, 26, 27, 28, 29, 30, 31, 32, 33, 34, 35, 36), the sphericity values or related information about it were not reported in the main source of references. Therefore, the corresponding void ratio prediction models including the effect of sphericity are not used in estimating the limit void ratios and void ratio ranges for them. However, the sphericity values are representatively assumed to be 0.60 for these cases as the angularity of the soil particles, and therefore

the sphericity, has an effect on the critical state friction angle of the soils referring to the literature. This representative value is wisely selected such that it falls in the middle of the limits determined by Cho et al. (2006) well given in Equation 3-66 (0.25-1.0). Since critical state friction angle, or namely liquefaction state friction angle in this study, has a significant effect on the predicted post-liquefaction shear strength values in this suggested new framework, it is also defined as a function of sphericity in addition to the roundness. The details of the correlation between the sphericity and liquefaction state friction angle of the soil will be discussed detailly in Chapter 4.

In the end, the database represented in Table 3.4, which consists of available material parameters for grain size and distribution (mean grain size, fines content, and coefficient of uniformity) and particle morphology (roundness and sphericity), is compiled for case histories.

Table 3.4 Summary of available material properties for grain size and distribution and particle morphology for case histories

#	Case History	FC (%)	D_{50} (mm)	C_u	R*	S*
1	Wachusett Dam - North Dike	7.5	0.420		0.50	0.60
2	Fort Peck Dam	4	0.280	2.31	0.50	0.60
3	Uetsu Railway Embankment	1	0.340	2.57	0.50	0.60
4	Lower San Fernando Dam - U/S Slope	53	0.070	31.49	0.50	0.60
5	Hachiro-Gata Road Embankment	18	0.181		0.50	0.60
6	La Marquesa Dam - U/S Slope	30	0.150		0.50	0.60
7	La Marquesa Dam - D/S Slope	20	0.150		0.50	0.60
8	La Palma Dam	15	0.200		0.50	0.60
9	Lake Ackerman Highway Embankment	1	0.390	2.50	0.50	0.60
10	Chonan Middle School	18	0.200		0.50	0.60
11	Soviet Tajik - May 1 Slide	100	0.013	6.00	0.50	0.60
12	Shibecha-Cho Embankment	20	0.200	9.71	0.50	0.60

Table 3.4 (cont'd) Summary of available material properties for grain size and distribution and particle morphology for case histories

13	Route 272 at Higashiarekinai	20	0.200		0.50	0.60
14	Zeeland - Vlietepolder	7	0.130	1.81	0.50	0.60
15	Sheffield Dam	40	0.100		0.50	0.60
16	Helsinki Harbor		0.100		0.50	0.60
17	Solfatara Canal Dike	7	0.170	2.22	0.50	0.60
18	Lake Merced Bank	3	0.210	1.92	0.50	0.60
19	El Cobre Tailings Dam	93	0.080		0.50	0.60
20	Metoki Road Embankment	15	0.120		0.50	0.60
21	Hokkaido Tailings Dam	50	0.075	1.50	0.50	0.60
22	Upper San Fernando Dam - D/S Slope	47.5	0.070	31.49	0.50	0.60
23	Tar Island Dyke	12.5	0.150		0.30	0.60
24	Mochi-Koshi Tailings Dam 1	81	0.038	16.97	0.50	0.60
25	Mochi-Koshi Tailings Dam 2	74	0.042	18.15	0.50	0.60
26	Nerlerk Embankment Slide 1	7.5	0.220	1.85	0.50	0.60
27	Nerlerk Embankment Slide 2	7.5	0.220	1.85	0.50	0.60
28	Nerlerk Embankment Slide 3	7.5	0.220	1.85	0.50	0.60
29	Asele Road Embankment	30	0.276	3.51	0.50	0.60
30	Nalband Railway Embankment	28	1.629	909.10	0.50	0.60
31	Sullivan Tailings	50	0.090		0.50	0.60
32	Jamuna Bridge	6	0.150		0.50	0.60
33	Calaveras Dam	30	0.732		0.50	0.60
34	Koda Numa Railway Embankment	13	0.180	8.70	0.50	0.60
35	Whiskey Springs Fan	31.5	1.613	455.33	0.30	0.60
36	San Fernando Valley Juvenile Hall	63	0.055	17.10	0.50	0.60

** If no information was reported in the main sources of references, Roundness (R) and Sphericity (S) values are assumed as 0.50 and 0.60, respectively, to be able to evaluate critical (liquefaction) state friction angles.*

Accordingly, the mean grain size, fines content, and coefficient of uniformity distributions of the case history database are obtained as given in Figure 3.13, Figure 3.14, and Figure 3.15, respectively.

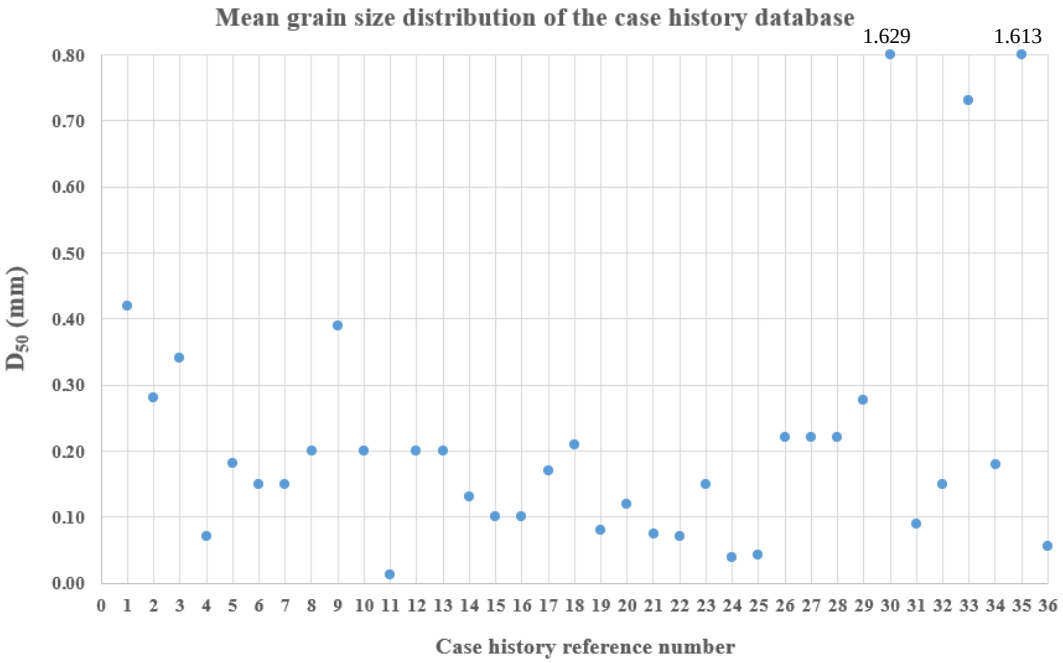

Figure 3.13. Mean grain size distribution of the case history database

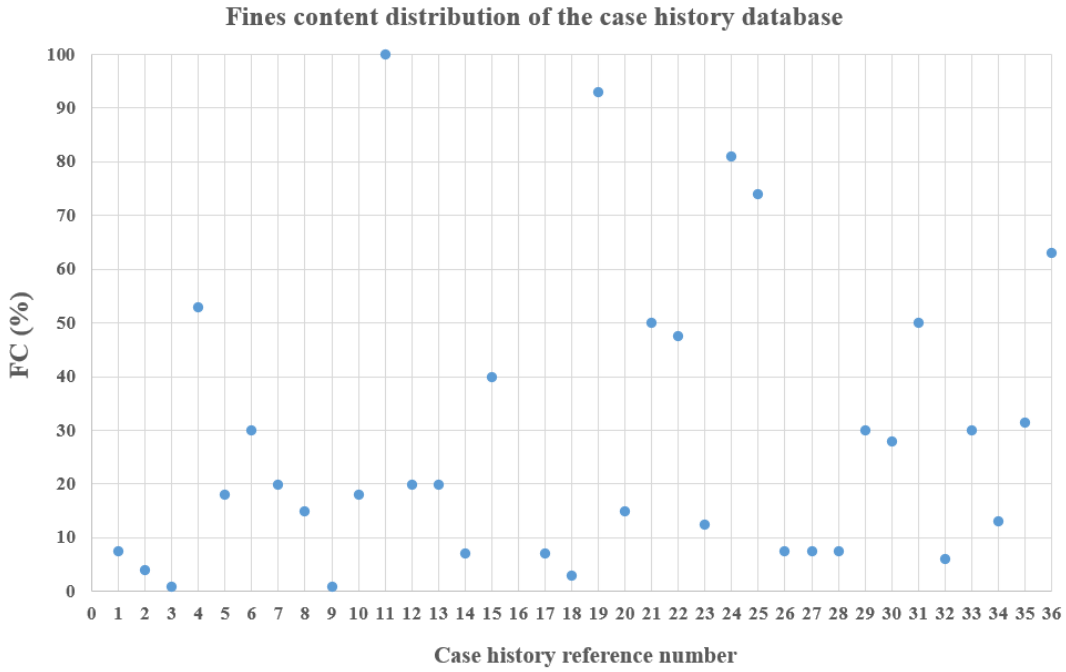

Figure 3.14. Fines content distribution of the case history database

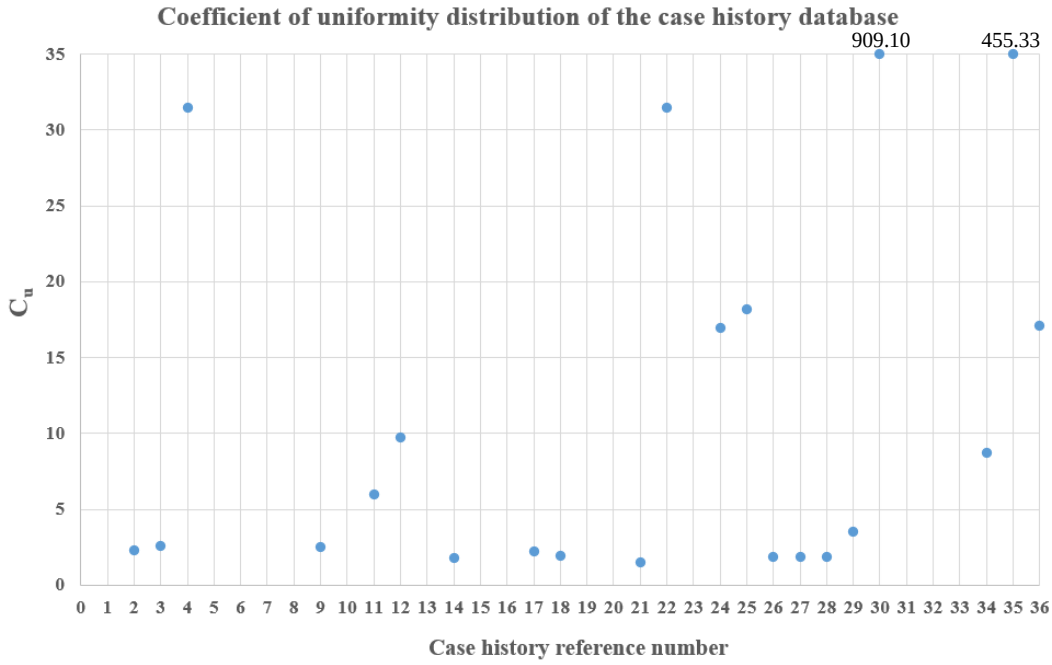

Figure 3.15. Coefficient of uniformity distribution of the case history database

3.3 Sub-sectioning of Cross-section and Failure Surfaces

As discussed in Chapter 2, most of the previous studies, such as Olson and Stark (2002), Wang (2003), Kramer (2008), and Weber et al. (2015), use initial vertical effective stress (σ'_{v0}) as a normalization parameter for post-liquefaction shear strength, S_r. In other words, these studies divide their estimated post liquefaction shear strength values to their initial vertical effective stress values to normalize the results. Furthermore, they claim that the post-liquefaction strength, or the residual strength, depends on the initial vertical effective stress of the soil as well as the SPT resistance. It is proven to be true that residual strength is related to confining stress of the liquefied soil layer, and previous studies use initial vertical effective stress to represent this confining stress effect in practice.

Although there are differences available between the estimation methods of initial vertical effective stresses for the case histories, all of the previous studies mentioned above assign a single initial vertical effective stress value for each case history, i.e.,

each liquefaction triggered failure. Although it might be practical in engineering to use a single representative σ'_{v0} value while estimating the residual strength, it is quite misleading to use a single stress value for the whole failure as liquefaction-triggered failures generally include failure surfaces of hundreds of meters long as a result of large strains. Moreover, it is fairly uncertain to use which initial vertical effective stress value as a representative for these kinds of large failures. Similar confusion also exists for assigning a single penetration resistance value for the case history such that although there are numerous penetration tests performed along with the different locations of the cross-section, previous studies tend to assign a single representative resistance value for the whole soil profile. On the other hand, the penetration resistance differs from point to point along the overall failure plane, similar to the vertical effective stress value. As a result of these unclear issues in assigning a representative σ'_{v0} and penetration resistance values for case histories, this study focused on "sub-dividing" the failure surfaces into smaller pieces and assigning separate confining stress and penetration resistance values for each of these "sub-sections" along the main overall failure surface.

Considering the initial vertical effective stress as the only representative stress value for confining effects is another questionable approach in previous studies abovementioned. It is evident that the horizontal force acting on the failure surface is the governing driving force in liquefaction-triggered slope failures. Therefore, it is illogical to use only initial vertical effective stress for representing the confining effects and neglect the horizontal stress components. Thus, this study also focused on including the effects of horizontal stress components in confining effect in addition to initial vertical effective stresses.

As a common approach in previous studies, the representative initial vertical effective stress value for each case history is evaluated by averaging the pre-failure effective vertical stresses along the failure plane located in liquefied materials, as shown in Equation 3-3.

$$\sigma'_{v,ave} = \frac{\sum_{i=1}^{n} \sigma'_{v,i} \cdot L_i}{L_{total}} \qquad \text{Equation 3-3}$$

In this equation, while n represents the total number of slices, i.e., sub-sections, along the failure plane, i represents each of these slices from number 1 to n. $\sigma'_{v,i}$ corresponds to the initial vertical effective stress of slice number i evaluated at its mid-point, L_i gives the failure plane length of slice number i, and L_{total} represents the total length of failure plane located in liquefied materials. Although taking the weighted average of initial effective vertical stresses of slices is a correct approach in terms of mathematical perspective to obtain a single representative value for the whole failure plane, it may be fallacious in terms of an engineering point of view. Some of these liquefaction-triggered slope stability failures include hundreds of meters of failure planes passing from different elevations along with the soil profile. Therefore, the effective vertical stresses change dramatically along the failure surfaces. Hence, using the vertical effective stress value of each slice separately instead of merging them might be a more sensible approach than taking the weighted average of them. In fact, it also increases the number of case points in the study such that since each slice is treated as a separate case with a different confining stress value, a single case history may provide several data points with different confining stress values.

In this context, each overall large failure surface is sub-divided into smaller pieces, and a separate σ'_{v0} value for each of these "sub-sections" is assigned. In addition to σ'_{v0}, other stress components including the horizontal stress and effective principal stresses are also evaluated for these sub-sections in order to include the effect of all stress components in confining. During the sub-dividing process of case histories, a stable template is followed for consistency. In the case that penetration tests are performed on the site, and their exact locations are known along the cross-section, sub-division is made based on the locations of these penetration tests. A territory length is assigned for each of these penetration tests along the overall failure plane and sub-division is performed according to these territory lengths. The overall failure plane is divided from the mid-points of the regions between these penetration tests,

and each test is assigned (names of the boreholes are directly assigned as the name of the sub-section) for the corresponding territory length. These territory lengths, L_i, (length of the failure plane remaining in the corresponding sub-section) for each sub-section are also evaluated. By this approach, it is also possible to assign separate penetration resistance values for each of these sub-sections along the failure plane instead of assigning a single representative resistance value for the whole overall failure plane.

An example is shown below in Figure 3.16 for Case history #1: Wachusett Dam North Dike. The exact locations of four Standard Penetration Tests were known along the cross-section; therefore, the overall failure plane remaining in the liquefied zone was divided into smaller pieces from the mid-points of these penetration test locations. Then, each borehole is assigned for a single sub-section, and SPT resistances are evaluated separately for each of these four pieces. Additionally, all stress components including the effective vertical stresses, effective horizontal stresses, and principal effective stresses, are evaluated at four points where boreholes and failure plane intersect. Consequently, different penetration resistances and confining effects are obtained for each of these sub-sections along the overall failure plane, which means that four different case data points are obtained from the single case history. Considering that there is a limited number of case histories available in residual strength studies, it is very useful to increase the number of data points in this way.

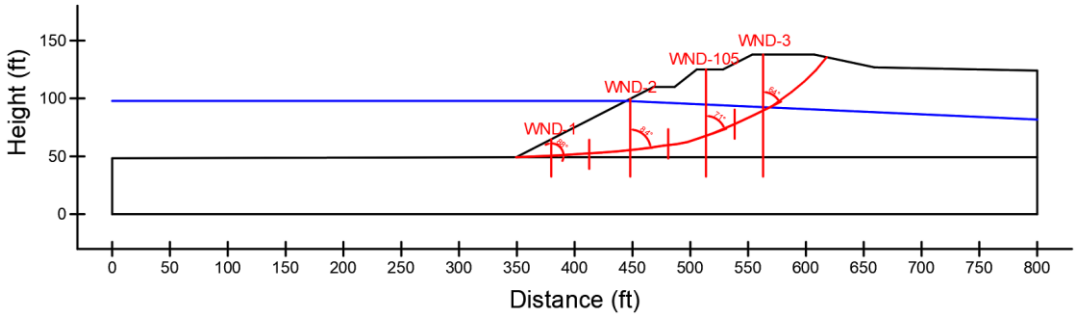

Figure 3.16. Segmenting (sub-sectioning) of Case history #1: Wachusett Dam North Dike

The cartesian and principal effective stresses for sub-sections are evaluated by elastic modeling of these cross-sections in PLAXIS 2D Ultimate Connect Edition V22.00.00.1733 software, and the details of the modeling process are further explained in Section 3.4 in particular. It should also be noted that the stresses we are dealing with at this point are the initial effective stresses obtained from the pre-failure geometry. However, some of the penetration tests are performed on post-failure geometries following the failure. Therefore, the locations of these boreholes opened in post-failure geometries cannot be used directly in the analyses performed on pre-geometries. For the cases in which penetration tests are performed after the failure on post-failure geometries, the locations of the boreholes are relocated approximately on the pre-failure geometry, and the sub-sectioning is performed according to these new assumed borehole locations. The procedure for overburden correction also differs for the cases where tests are performed before the failure or after the failure. The overburden effect correction should be done according to the stresses at the time when the test is performed. Therefore, if the tests are performed on pre-failure geometry (before the failure occurs), the overburden correction should also be performed based on the pre-failure effective stresses. Similarly, if the tests are performed on post-failure geometry (after the failure occurs), the overburden correction should be performed based on the post-failure effective stresses. Hence, although the boreholes are always located on pre-failure geometries for initial effective vertical stress and SPT resistance evaluations, the overburden corrections for penetration resistances are performed based on the time when tests are performed. Evaluation of the penetration resistances for case histories and sub-sections will further be discussed in Section 3.5 in detail.

The procedure explained up to this point was applicable for 17 cases (Case history #: 1, 2, 4, 6, 7, 8, 10, 12, 13, 18, 20, 22, 30, 31, 34, 35, 36) that penetration tests are performed in the site, and their exact locations are known along the cross-section. For the remaining 19 cases (Case history #: 3, 5, 9, 11, 14, 15, 16, 17, 19, 21, 23, 24, 25, 26, 27, 28, 29, 32, 33), unfortunately the locations of the penetration tests were unknown along the critical cross-section, or even no penetration test data was

available. Therefore, a different template is followed for these cases such that the overall failure plane is sub-divided into 3-4 pieces (namely S1, S2, S3, etc.) with similar lengths. While dividing into smaller pieces, the change in effective vertical stresses along the soil profile is also taken into account so that each piece represents a region with different confining stress. In other words, the regions on the failure plane where the effective vertical stresses do not change significantly remained in the same sub-section. In addition to that, the change in the inclination of the failure plane is also taken into account while sub-dividing the entire failure plane into smaller pieces. The zones where major changes in the slope of the failure planes are observed are considered to be separate sub-sections. The importance of these inclination differences will further be discussed in Section 3.4 during the explanation of stress rotation and evaluation of normal effective stresses acting on the failure surfaces. The corresponding territory lengths, L_i, (length of the failure plane remaining in the corresponding sub-section) of the sub-sections are also evaluated separately. For the case histories where exact locations of the penetration tests were known, it was also possible to assign a separate penetration resistance value for each sub-section in addition to the cartesian and principal effective stresses. On the other hand, for these cases where the locations of the penetration tests are missing, it is only possible to assign separate cartesian and principal effective stresses for each sub-section, and a single representative penetration resistance value is assumed to be valid for all sub-sections. For these cases, it is assumed that the penetration resistance, and therefore the in-situ relative density, is almost equal along the entire failure plane, but the confining stress differs significantly at different points. Therefore, sub-sectioning is still necessary for also these cases to include the effect of confining stress in residual strength evaluations more accurately.

An example is shown below in Figure 3.17 for Case history #9: Lake Ackerman Highway Embankment. Although the representative penetration resistance values for the soil profile were reported by the main source of references, the exact locations of the tests along the critical cross-section were not reported clearly. Thus, the overall failure plane remaining in liquefied materials is divided into three smaller sub-

sections based on the change of effective vertical stresses. Then, imaginary three boreholes are assigned for each of these sub-sections, and the same representative SPT resistance is assumed for each of these three pieces. However, all stress components including the effective vertical stresses, effective horizontal stresses, and principal effective stresses, are evaluated at three points separately where these imaginary boreholes and failure plane intersect. Consequently, the same penetration resistance but different confining effects are obtained for each of these sub-sections along the overall failure plane, which means that three different case data points are obtained from the single case history. Considering that there is a limited number of case histories available in residual strength studies, it is beneficial to increase the number of data points in this way.

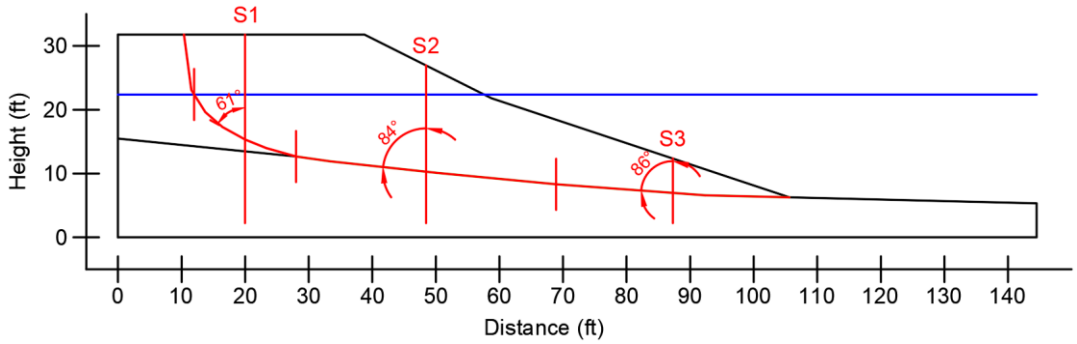

Figure 3.17. Sub-sectioning of Case history #9: Lake Ackerman Highway Embankment

For 7 case histories (Case history #: 12, 14, 16, 21, 23, 30, 31), two different initial failure planes (typically small and large) are considered based on the information available about the failure modes on the main sources of references and post-failure geometries of the cases. These two separate failure surfaces are generally different initial yield surfaces observed on the pre-failure geometry, and both have an effect on the overall failure of the slope. Usually, while the smaller initial yield surfaces locate near the toe of the main slopes, the larger ones represent the overall failure scarp. Based on the geometry of the cross-section, causing effects of these two initial yield surfaces may be different on the overall failure of the slope. Weber (2015) also considers these separate initial yield surfaces for the same case histories

abovementioned and applies a weighting function for them based on the cross-section geometry to evaluate a single representative post-liquefaction initial yield strength, $S_{r,yield}$, value. In this study, instead of weighting these initial yield strength values corresponding to different initial yield surfaces to obtain a single representative strength value, these surfaces are taken into account separately, and each failure plane is considered as a different slope failure. Furthermore, these separate failure planes are sub-divided into sub-sections individually so that they can be analyzed totally independently. As a result, two main cases are obtained from a single case for these 7 case histories. Hence, the total number of major case histories (major means without considering the sub-sections) become 36+7=43 for this study.

To better illustrate the procedure followed for these 7 case histories, an example is provided in Figure 3.18 for Case history #12: Shibecha-Cho Embankment. The exact locations of four Swedish Cone Penetration Tests were known along the cross-section; therefore, the overall cross-section remaining in the liquefied zone was divided into smaller pieces from the mid-points of these penetration test locations. Then, each borehole is assigned to a single sub-section, where the rightest sub-section assigned to Borehole B-5 located closest to the toe of the slope is shared by both small and large initial failure surfaces. Therefore, this sub-section is used for both small and large failure surfaces. Consequently, three and two sub-sections are (the rightest one is common) defined for large and small failure surfaces, respectively. While Boreholes B-2, B-3, and B-5 represent the large initial yield surface, Boreholes B-4 and B-5 represent the small initial yield surface.

As explained above, these two surfaces are considered totally independently in the computations and analyses of the post-liquefaction strength prediction relationships. All stress components including the effective vertical stresses, effective horizontal stresses, and principal effective stresses, are evaluated at four points where boreholes and failure plane intersect. Consequently, different penetration resistances and confining effects are obtained for each of these three and two sub-sections (one of them is common) along the large and small failure surfaces, respectively. This means that five different case data points are obtained from the single case history.

Considering that there is a limited number of case histories available in residual strength studies, it is advantageous to increase the number of data points in this way.

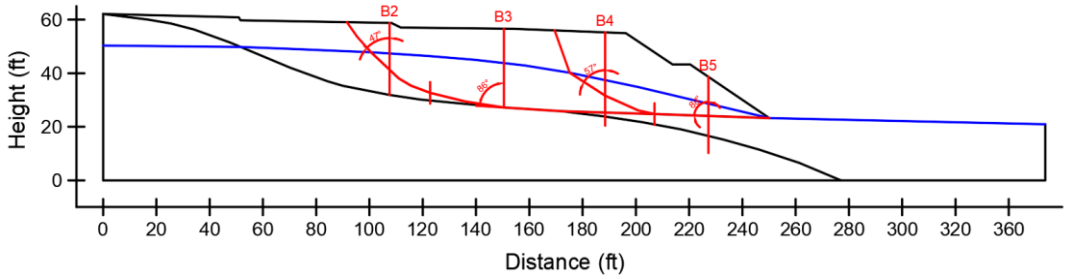

Figure 3.18. Sub-sectioning of two different initial yield surfaces of Case history #12: Shibecha-Cho Embankment

It should be noted that similar to confining stresses and penetration resistances, other material properties such as mean grain size (D_{50}), fines content (FC), coefficient of uniformity (C_u), roundness, and sphericity (R and S) of grains may also differ along the critical cross-section. However, these material properties are not reported detailly for these residual strength case histories such that generally a single representative value is assigned for the entire cross-section, or even no data is documented. Hence, these material properties are assumed to be the same along the overall failure plane for all case histories. On the other hand, once more detailed information is obtained for these material properties, it will definitely increase the quality of data points to assign different values for separate sub-sections, similar to confining stresses or penetration resistances.

In the end, the database represented in Table 3.5, which consists of finalized sub-sections, lengths, and inclination angles of failure planes corresponding to each sub-section, is compiled for case histories.

Table 3.5 Summary of finalized sub-sections, lengths, and inclination angles of failure planes corresponding to each sub-section for case histories

#	Case History	Section	Failure plane length, L_i (m)	Total failure plane length, L_t (m)	Failure plane inclination, α_i (degrees)
1	Wachusett Dam - North Dike	WND-1	19.29	68.87	2
		WND-2	20.92		6
		WND-105	18.45		19
		WND-3	10.20		26
2	Fort Peck Dam	Boring 3	200.25	389.30	0
		Boring 7	67.93		0
		Boring 6	79.37		21
		Boring 7	41.75		54
3	Uetsu Railway Embankment	S1	9.39	20.27	-11
		S2	10.88		-2
4	Lower San Fernando Dam - U/S Slope	S103&S111	54.84	103.82	0
		S101&S102& S104	16.94		5
		S105	16.77		10
		S105	15.28		60
5	Hachiro-Gata Road Embankment	S1	10.85	14.86	-1
		S2	4.01		31
6	La Marquesa Dam - U/S Slope	B-2	6.61	21.81	-87
		B-III	7.20		-1
		B-3	8.00		-1
7	La Marquesa Dam - D/S Slope	B-II	10.07	15.81	0
		B-1	5.75		0
8	La Palma Dam	B-3	6.06	15.91	-17
		B-4	9.85		-12
9	Lake Ackerman Highway Embankment	S1	5.90	29.65	-29
		S2	12.55		-6
		S3	11.20		-4
10	Chonan Middle School	No.4	6.65	15.40	-8
		No.3	8.75		0
11	Soviet Tajik - May 1 Slide	S1	44.85	68.84	7
		S2	23.99		61

Table 3.5 (cont'd) Summary of finalized sub-sections, lengths, and inclination angles of failure planes corresponding to each sub-section for case histories

12	Shibecha-Cho Embankment	B-2	8.32	47.32	-43
		B-3	25.85		-4
		B-5	13.14		-2
		B-4	10.87	24.02	-33
		B-5	13.14		-2
13	Route 272 at Higashiarekinai	Left	6.67	22.87	-24
		Right	16.21		-3
14	Zeeland - Vlietepolder	Small-S1	31.25	75.67	-30
		Small-S2	44.42		36
		Large-S1	100.22	318.60	4
		Large-S2	107.37		3
		Large-S3	111.00		3
15	Sheffield Dam	Right	14.88	14.88	0
16	Helsinki Harbor	Small-S1	6.72	15.97	-4
		Small-S2	9.25		34
		Large-S1	35.50	71.31	0
		Large-S2	35.81		5
17	Solfatara Canal Dike	S1	4.58	9.41	-8
		S2	4.83		25
18	Lake Merced Bank	Boring 2	30.35	30.35	-14
19	El Cobre Tailings Dam	S1	83.71	348.12	1
		S2	43.82		0
		S3	85.77		0
		S4	134.82		0
20	Metoki Road Embankment	S-19	6.81	14.04	-28
		S-13	7.23		19
21	Hokkaido Tailings Dam	Small-S1	18.26	23.23	6
		Small-S2	4.98		26
		Large-S1	18.26	48.61	6
		Large-S2	30.35		5
22	Upper San Fernando Dam - D/S Slope	A1&B1&C1	14.26	111.06	-29
		A2&B2&C2	10.02		-22
		A3	23.15		-3
		B4&C4	33.44		-3
		B5&C5	30.19		0

Table 3.5 (cont'd) Summary of finalized sub-sections, lengths, and inclination angles of failure planes corresponding to each sub-section for case histories

23	Tar Island Dyke	Large-S1	260.18	308.55	2
		Large-S2	48.37		3
		Small-S1	27.62	75.99	-33
		Small-S2	48.37		3
24	Mochi-Koshi Tailings Dam 1	S1	61.15	183.68	-7
		S2	60.98		-4
		S3	61.55		-3
25	Mochi-Koshi Tailings Dam 2	S1	34.81	70.94	1
		S2	36.13		12
26	Nerlerk Embankment Slide 1	S1	23.49	166.67	-29
		S2	71.73		-7
		S3	71.44		-5
27	Nerlerk Embankment Slide 2	S1	18.90	155.45	-25
		S2	68.49		-4
		S3	68.07		-1
28	Nerlerk Embankment Slide 3	S1	80.49	361.89	-16
		S2	140.49		-2
		S3	140.91		0
29	Asele Road Embankment	S1	20.08	26.51	9
		S2	6.43		48
30	Nalband Railway Embankment	NB-1	25.32	32.51	-2
		Small-S2	7.19		30
		NB-1	25.32	57.17	-2
		Large-S2	25.75		5
		Large-S3	6.09		64
31	Sullivan Tailings	Large-S1	13.79	38.63	-41
		CP91-29	10.68		-9
		CP91-31	14.16		2
		Small-S1	6.46	23.51	-46
		CP91-31	17.05		0
32	Jamuna Bridge	S1	44.86	88.27	-12
		S2	43.41		-2
33	Calaveras Dam	S1	83.00	277.27	-35
		S2	194.27		0

Table 3.5 (cont'd) Summary of finalized sub-sections, lengths, and inclination angles of failure planes corresponding to each sub-section for case histories

34	Koda Numa Railway Embankment	Left	3.84	10.57	-14
		Middle	2.95		-2
		Right	3.77		-2
35	Whiskey Springs Fan	SP 1	35.90	81.19	0
		SP 3	45.29		1
36	San Fernando Valley Juvenile Hall	Boring 2	89.87	284.87	-1
		Boring 4	86.62		0
		Boring 6	108.38		0

3.4 Elastic Modeling and Stress Rotation

As discussed earlier in Section 3.3, critical cross-sections and overall failure planes remaining in the liquefied material are sub-divided into smaller sub-sections to be able to take confining effect and penetration resistance into account separately along the failure surface. Although previous studies on residual strength were only considering initial vertical effective stress as representative stress for confining effects, this study also includes the effects of effective horizontal stresses in confining because the horizontal force acting on the failure surface is the governing driving force in liquefaction triggered slope failures.

To achieve a more accurate and precise evaluation of confining effects, all stress components including the effective vertical stresses, effective horizontal stresses, and principal effective stresses, are evaluated at the points where real or imaginary (explained in Section 3.3) boreholes and failure plane intersect. While evaluating these stress components, PLAXIS 2D Ultimate Connect Edition V22.00.00.1733 software is used, and pre-failure geometries of all 36 case histories are modeled linear elastically to eliminate redundant computation time and the hassle of soil parameter selection. The pre-failure geometries and estimated critical failure planes of the case histories are obtained either from the main source of references of the

case histories or from the previous studies performed back-analyses such as Olson (2001) and Weber (2015).

The soil stratigraphy of the cases is estimated in consistent with the previous studies and documented information. Similarly, dry and saturated unit weights of the soil layers are also evaluated with respect to the available information in the references. Soil bodies are modeled linear elastically, and the finite elements method is utilized for gravity loading as these liquefaction-triggered failures were observed usually in slopes of earth structures such as dams, levees, and embankments. Very fine mesh is used for element distribution in order to obtain more accurate results, and the groundwater table is assigned at its position just before the failure.

Since soil bodies are modeled linear elastically, some mechanical elastic parameters are required for soil materials to define their stiffnesses, such as elastic modulus and Poisson's ratio. Due to the fact that these parameters, especially the Poisson's ratio, have a dramatic effect on the stress components, they are arranged with significant attention and effort. The Poisson's ratio values are defined by Figure 3.19 with respect to their estimated internal friction angle values.

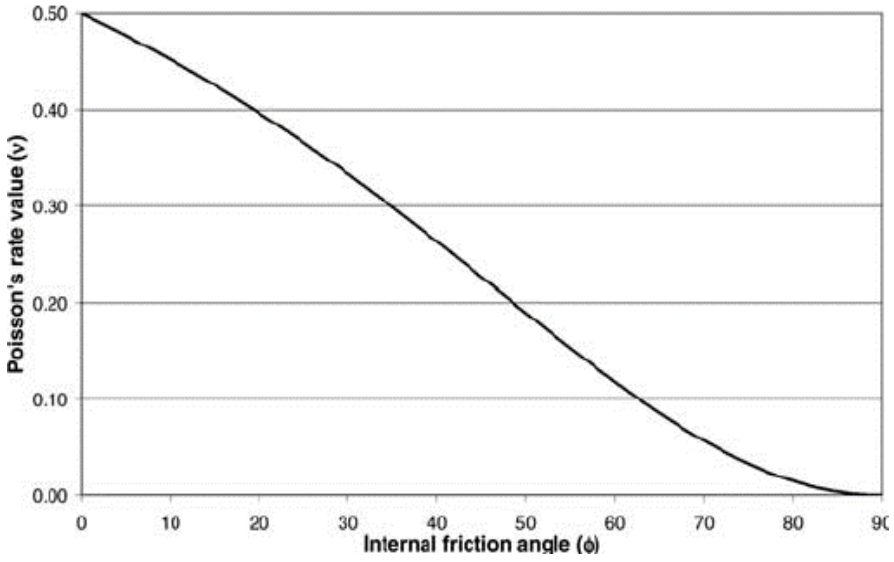

Figure 3.19. Poisson's ratio and internal friction angle relationship (Vásárhelyi, 2009)

To be able to use this figure, internal friction angles were required for the soil layers, and these values are evaluated by using their relative densities. The relative densities of the soil layers are determined with the relationships proposed by Kulhawy and Mayne (1990) and Cubrinovski and Ishihara (1999) by using average penetration resistance ($(N_1)_{60}$), limit void ratio (e_{max} and e_{min}), and mean grain size (D_{50}) values of the layers. These relationships are given in Equation 3-73 and Equation 3-82, respectively, and further detailed explanations are provided in Section 3.7. Once relative densities are estimated for the soil layers, their internal friction angle values are evaluated by Equation 3-4 given below. In this equation, ϕ and RD represent the internal friction angle of soil in degrees and relative density of soil in percentage, respectively.

$$\phi = 0.276 \cdot RD + 18.7 \qquad \text{Equation 3-4}$$

During the sensitivity analysis of elastic parameters on stress components, it is observed that although the Poisson's ratio has a significant effect on computed stress values, the elastic modulus does not have that much effect on the stresses. Even, its effect is observed to be negligibly small for almost all of the case histories. Therefore, a simpler approach is followed for the elastic modulus values of the soil layers. For the liquefied soil layers, the elastic modulus is assigned between 5000-8000 kPa by assuming that the contribution of elastic modulus to the stiffness of the soil is the least for liquefied materials. For non-liquefied fill materials, the elastic modulus is assigned between 10000-15000 kPa by assuming that the contribution of elastic modulus to the stiffness is higher for non-liquefied materials. For foundations, stiff core materials and rock-type of fill materials, the elastic modulus is assigned between 20000-30000 kPa by assuming that the contribution of elastic modulus to the stiffness is the highest for these stiff materials.

Once the elastic parameters and unit weights are defined for the soil layers, models are analyzed linear elastically to evaluate the representative stress components for each sub-section of case histories. For the points where real or imaginary (explained in Section 3.3) boreholes and failure plane intersect, effective cartesian stresses (σ'_{xx},

σ'_{yy}, σ'_{zz} and σ'_{xy}) and principal effective stresses (σ'_1, σ'_2 and σ'_3) are determined as the representative stress components for that sub-section. These principal effective stress components are further used in the development of the residual strength prediction models, which will be discussed in detail in Chapter 4. It should be noted that the territory length, L_i, corresponds to each borehole (length of the failure plane for the corresponding sub-section) is also evaluated separately for each sub-section, as explained in Section 3.3.

In addition to cartesian and principal effective stresses, the effective normal (σ'_N) and shear (τ_{static}) stresses acting on the inclined failure plane are also evaluated with the help of corresponding Mohr's circles. The inclination angle of the failure plane with horizontal axis, α, is also evaluated for each sub-section in a case history (positive for counterclockwise direction) to be able to determine the critical failure point having coordinates of σ'_N in the horizontal axis and τ'_{static} on the vertical axis on the Mohr's circle.

For each sub-section of a case history, corresponding Mohr's circles are plotted by using cartesian and principal effective stresses. The sign convention given in Figure 3.20 is used in reporting the results and plotting the Mohr's circles.

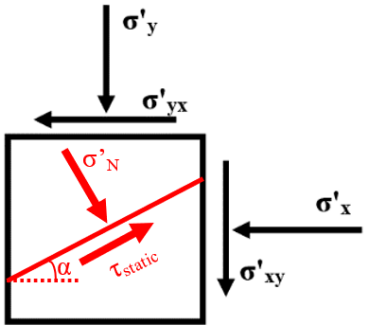

Figure 3.20. Sign convention for stress components

As a first step, two stress points corresponding to (σ'_{yy}, σ'_{xy}) and (σ'_{xx}, $-\sigma'_{xy}$) are defined in the effective normal stress (σ') and shear stress (τ) domain. Then, these two points are connected with a straight line, and a circle passing from these two points and having the diameter as the straight line drawn between those two stress

points is plotted as the corresponding Mohr's circle. Once the Mohr's circle is plotted on effective normal stress and shear stress space, the major and minor effective principal stresses (σ_1' and σ_3') are evaluated with simple analytical geometry. First, the center of the Mohr's circle, which is also the average of major and minor effective principal stresses, is evaluated by taking the average of the effective cartesian stresses in x and y directions. The corresponding geometrical relationship is given in Equation 3-5.

$$Center\ of\ the\ Mohr's\ circle: \frac{\sigma'_1 + \sigma'_3}{2} = \frac{\sigma'_{xx} + \sigma'_{yy}}{2} \qquad \text{Equation 3-5}$$

Then, the radius of the Mohr's circle, which is also the half of difference between major and minor effective principal stresses, is evaluated by using the cartesian effective stresses σ'_{xx}, σ'_{yy}, σ'_{xy}, and Pythagoras Theorem. The corresponding geometrical relationship is given in Equation 3-6.

$$Radius\ of\ the\ Mohr's\ circle: \frac{\sigma'_1 - \sigma'_3}{2} = \frac{\sqrt{\left(\left|\sigma'_{yy} - \sigma'_{xx}\right|\right)^2 + \left(2 \cdot \left|\sigma'_{xy}\right|\right)^2}}{2} \qquad \text{Equation 3-6}$$

Following that, the effective major and minor principal stresses (σ_1' and σ_3') are evaluated by solving these two equations. It should be noted that PLAXIS 2D Ultimate Connect Edition V22.00.00.1733 software also computes effective principal stresses at those points; therefore, these evaluated values for σ_1' and σ_3' are double-checked with the ones provided by the software. It should also be noted that it is not possible to evaluate effective intermediate principal stress (σ_2') from Mohr's circle; hence, this value is directly taken from the software. The evaluation of effective intermediate principal stress is crucially important for this study because it also has an effect on the confining stress at the corresponding point, and therefore it is required to include the effect of the third dimension (into the plane dimension for this sign convention) stresses in residual strength relationships, which will be discussed in Chapter 4 in detail.

Once the effective major, intermediate and minor principal stresses are evaluated, the mean effective stress (p') and deviatoric stress (q) values are evaluated by Equation 3-7 and Equation 3-8, respectively.

$$Mean\ effective\ stress: p' = \frac{\sigma'_1 + \sigma'_2 + \sigma'_3}{3} \qquad \text{Equation 3-7}$$

$$Deviatoric\ stress: q = \sqrt{\frac{(\sigma'_1 - \sigma'_2)^2}{2} + \frac{(\sigma'_2 - \sigma'_3)^2}{2} + \frac{(\sigma'_3 - \sigma'_1)^2}{2}} \qquad \text{Equation 3-8}$$

It should be noted that there are different definitions of mean effective stress and deviatoric stress available in the literature. However, since this study aims to include the effect of the third dimension (into the plane direction for this sign convention) in the confining stress, the intermediate principal stress (σ'_2) is also utilized in mean effective stress and deviatoric stress evaluations.

The evaluation of p' is crucially important for this study since it constitutes a crucial part of the critical state concept. As each case corresponding to each sub-section has its own data point in the void ratio and mean effective stress domain, initial mean effective stress is one of the major parameters for all cases in addition to the in-situ void ratios. Similarly, the evaluation of q is also significant for this study as well due to the fact that it includes the contribution of intermediate effective principal stress, and has a direct effect on the strength of the soil. Therefore, it will be used as a parameter in the development of the post-liquefaction strength prediction model, which will be discussed in Chapter 4 in detail.

Following the evaluation of effective principal stresses, mean effective stress, and deviatoric stress, the origin of the planes, i.e., the pole of the Mohr's circle (O_p), is determined. The origin of the planes is determined either by drawing a horizontal straight line from (σ'_{yy}, σ'_{xy}) point (because these stresses are acting on the horizontal plane referring to the sign convention) or drawing a vertical straight line from (σ'_{xx}, $-\sigma'_{xy}$) point (because these stresses are acting on vertical plane referring to the sign convention). The pole of the Mohr's circle is the point where these straight lines

drawn intersect with the Mohr's circle at another point. The origin of the planes is an essential and critical point for a Mohr's circle because when a line is drawn with a particular inclination starting from this point, the second intersection point of this line and the Mohr's circle gives the corresponding failure point for that inclined plane. In other words, the effective normal and shear stresses acting on any inclined failure plane can be evaluated by drawing a line starting from the origin of planes and intersecting this line with another point on the Mohr's circle. Therefore, the effective normal (σ'_N) and shear (τ_{static}) stresses acting on the inclined failure planes of the sub-sections are evaluated by considering the stress rotation, and drawing an inclined line (with the same inclination of the failure plane at that point) from the pole of the Mohr's circle and intersecting that line with a second point on the circle. While the horizontal stress component of that intersection point gives the effective normal stress (σ'_N) acting on the inclined failure plane, the vertical stress component of the same point gives the static (just before the failure) shear stress (τ_{static}) acting on the failure plane.

It should be remarked that these two values can be obtained analytically by equating the equations of Mohr's circle and the inclined line drawn starting from the pole. The equation of a circle in the x-y plane is given in Equation 3-9.

$$r^2 = (x - x_c)^2 + (y - y_c)^2 \qquad \text{Equation 3-9}$$

In this equation, while r represents the radius of the circle, x_c and y_c represent the coordinates of the center of the circle in the x and y axes, respectively. Hence, the analytical equation of the Mohr's circle can be written in the form of Equation 3-10.

$$\left(\frac{\sigma'_1 - \sigma'_3}{2}\right)^2 = \left(x - \frac{\sigma'_1 + \sigma'_3}{2}\right)^2 + (y - 0)^2 \qquad \text{Equation 3-10}$$

In this equation, while $\frac{\sigma'_1 - \sigma'_3}{2}$ term represents the radius of the Mohr's circle, $\frac{\sigma'_1 + \sigma'_3}{2}$ and 0 terms represent the coordinates of the center of the Mohr's circle in the x and y axes, respectively. Leaving y alone in this equation, the same equality can be rewritten in the form given in Equation 3-11.

$$y = \sqrt{\left(\frac{\sigma'_1 - \sigma'_3}{2}\right)^2 - \left(x - \frac{\sigma'_1 + \sigma'_3}{2}\right)^2} \qquad \text{Equation 3-11}$$

Similarly, the equation of the inclined line passing from the pole can be written analytically with a simple equation of a line given in Equation 3-12.

$$y = m \cdot x + n \qquad \text{Equation 3-12}$$

In this equation, while m represents the inclination, i.e., slope, of the line, n represents the intersection of this line with the vertical y-axis. For our case, the slope of the line can easily be obtained such that the tangent of the inclination angle of the failure plane directly gives this value. To be able to determine the intersection point n, the coordinates of a point located on this line should be known, which is the origin of planes in our case. Due to the fact that the origin of the planes is determined either by drawing a horizontal straight line from (σ'_{yy}, σ'_{xy}) point or drawing a vertical straight line from (σ'_{xx}, $-\sigma'_{xy}$) point, the coordinates of this point automatically become (σ'_{xx}, σ'_{xy}) for the case where $\sigma'_{yy} > \sigma'_{xx}$, and ($\sigma'_{xx}$, $-\sigma'_{xy}$) for the case where $\sigma'_{yy} < \sigma'_{xx}$. The second case is rare such that usually the effective vertical stress acting on a point is greater than the effective horizontal stress acting on that point for these cases. On the other hand, for the points close to the toe of the slopes, effective horizontal stress can be greater than the effective vertical stress. It should be noted that for the cases where cartesian effective shear force is acting in the reverse direction ($-\sigma'_{xy}$ instead of $+\sigma'_{xy}$), the coordinates of the pole become (σ'_{xx}, $-\sigma'_{xy}$) and (σ'_{xx}, σ'_{xy}), respectively for these two cases.

For more common $\sigma'_{yy} > \sigma'_{xx}$ and $\sigma'_{xy} > 0$ cases, the value of n can be evaluated by Equation 3-13 then.

$$n = \sigma'_{xy} - \tan(\alpha) \cdot \sigma'_{xx} \qquad \text{Equation 3-13}$$

Accordingly, the equation of the inclined line passing from the pole can be written in the form of Equation 3-14.

$$y = \tan(\alpha) \cdot x + \left(\sigma'_{xy} - \tan(\alpha) \cdot \sigma'_{xx}\right) \quad \text{Equation 3-14}$$

By equating Equation 3-11 and Equation 3-14, the numerical value of x can be solved analytically as shown in Equation 3-15.

$$\sqrt{\left(\frac{\sigma'_1 - \sigma'_3}{2}\right)^2 - \left(x - \frac{\sigma'_1 + \sigma'_3}{2}\right)^2} = \tan(\alpha) \cdot x + \left(\sigma'_{xy} - \tan(\alpha) \cdot \sigma'_{xx}\right) \quad \text{Equation 3-15}$$

This value of x directly gives the coordinate of the intersection point of the inclined line and Mohr's circle in the horizontal axis, which is the effective normal stress (σ'_N) acting on that inclined failure plane. Then, by putting the value of that x into Equation 3-11 or Equation 3-14, the corresponding value of y, which represents the static shear stress (τ_{static}) acting on the failure plane, can be obtained.

Example of stress rotation:

To better explain the evaluation of effective normal stress and static shear stress acting on an inclined failure plane, an example is provided below for Case history #1: Wachusett Dam North Dike. The sub-section corresponding to borehole WND-2 (see Appendix A.1 for detailed visualization) is illustrated. Cartesian effective stresses are obtained from PLAXIS 2D Ultimate Connect Edition V22.00.00.1733 software for this sub-section, as given in Table 3.6.

Table 3.6 Cartesian effective stresses for Case history #1: Wachusett Dam North Dike subsection WND-2

σ'_{xx} (kPa)	72.85
σ'_{yy} (kPa)	142.50
σ'_{zz} (kPa)	71.08
σ'_{xy} (kPa)	32.27

Then, the center (horizontal component) and radius of the Mohr's circle are evaluated by referring to Equation 3-16 and Equation 3-17, respectively.

$$Center: \frac{\sigma'_1 + \sigma'_3}{2} = \frac{\sigma'_{xx} + \sigma'_{yy}}{2} = \frac{72.85 + 142.50}{2} = 107.675 \quad \text{Equation 3-16}$$

$$Radius: \frac{\sigma'_1 - \sigma'_3}{2} = \frac{\sqrt{\left(\left|\sigma'_{yy} - \sigma'_{xx}\right|\right)^2 + \left(2 \cdot \left|\sigma'_{xy}\right|\right)^2}}{2} = \frac{\sqrt{(|142.50 - 72.85|)^2 + (2 \cdot |32.27|)^2}}{2} = 47.48 \quad \text{Equation 3-17}$$

By solving these two equations for σ'_1 and σ'_3, the major and minor effective principal stresses are evaluated as 155.20 kPa and 60.22 kPa, respectively. These values are also checked with the ones provided by the software. In addition to these two principal stresses, the intermediate effective principal stress, σ'_2, is obtained from the software as 71.10 kPa.

Accordingly, the mean effective and deviatoric stresses are evaluated by referring to Equation 3-18 and Equation 3-19, respectively.

$$p' = \frac{\sigma'_1 + \sigma'_2 + \sigma'_3}{3} = \frac{155.20 + 71.10 + 60.22}{3} = 95.51\ kPa \quad \text{Equation 3-18}$$

$$q = \sqrt{\frac{(\sigma'_1 - \sigma'_2)^2}{2} + \frac{(\sigma'_2 - \sigma'_3)^2}{2} + \frac{(\sigma'_3 - \sigma'_1)^2}{2}} = \sqrt{\frac{(155.20 - 71.10)^2}{2} + \frac{(71.10 - 60.22)^2}{2} + \frac{(60.22 - 155.20)^2}{2}} = 90.03\ kPa \quad \text{Equation 3-19}$$

Then, the effective normal stress (σ'_N) acting on the inclined failure plane is evaluated by solving x in Equation 3-20. It should be remarked that the inclination of the failure plane for this sub-section is estimated as +6 degrees with the horizontal, where the positive sign means counterclockwise direction.

$$\sqrt{\left(\frac{155.20 - 60.22}{2}\right)^2 - \left(x - \frac{155.20 + 60.22}{2}\right)^2} = \tan(6) \cdot x + (32.27 - \tan(6) \cdot 72.85) \quad \text{Equation 3-20}$$

$$\rightarrow x = \sigma'_N = 135.08\ kPa$$

Finally, by putting this value of that x into Equation 3-11 or Equation 3-14, the corresponding value of y, which represents the static shear stress (τ_{static}) acting on the failure plane, is obtained.

$$y = \tau_{static} = \sqrt{\left(\frac{155.20 - 60.22}{2}\right)^2 - \left(135.08 - \frac{155.20 + 60.22}{2}\right)^2} = 38.81\ kPa \qquad \text{Equation 3-21}$$

$$y = \tau_{static} = \tan(6) \cdot 135.08 + (32.27 - \tan(6) \cdot 72.85) = 38.81\ kPa \qquad \text{Equation 3-22}$$

The step-by-step development of the corresponding Mohr's circle for this example is also illustrated in Figure 3.21.

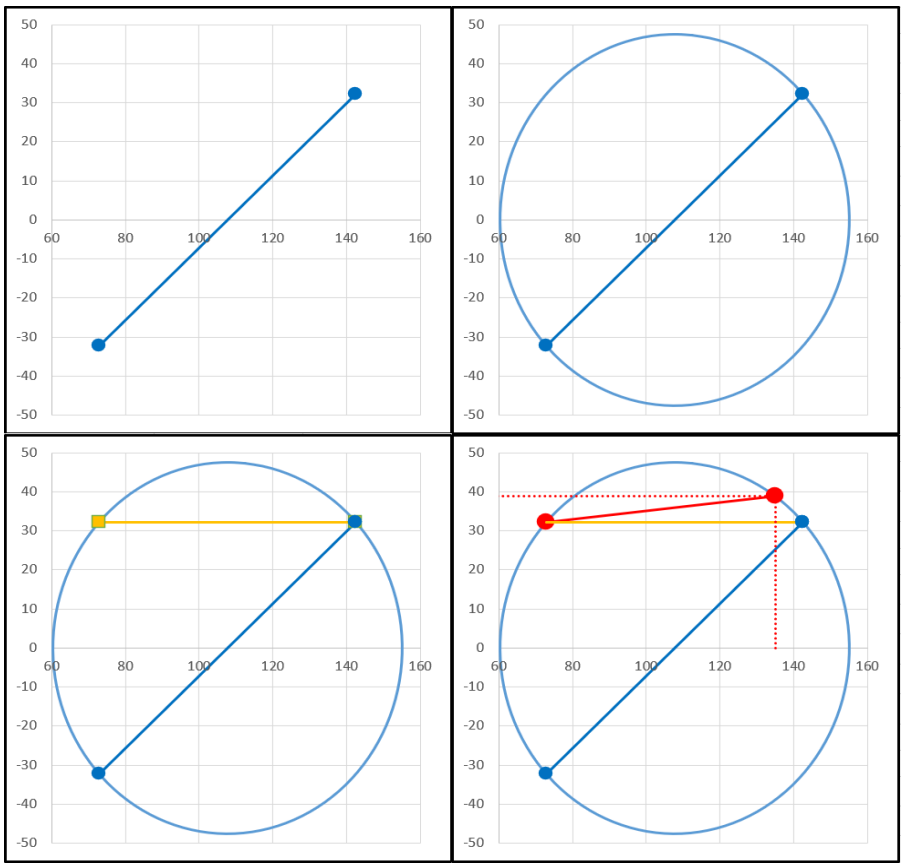

Figure 3.21. Step-by-step development of Mohr's circle for Case history #1: Wachusett Dam North Dike sub-section WND-2

In the end, the database represented in Table 3.7 that consists of effective principal stresses, mean effective stresses, deviatoric stresses, effective normal stresses, and static shear stresses acting on the corresponding failure planes of case history sub-sections is compiled.

Table 3.7 Summary of evaluated effective principal stresses, mean effective stresses, deviatoric stresses, effective normal stresses, and static shear stresses for case histories

#	Case History	Section	σ'_1 (kPa)	σ'_2 (kPa)	σ'_3 (kPa)	p_0' (kPa)	q (kPa)	σ'_N (kPa)	τ_{static} (kPa)	$\lvert\tau_{static}\rvert$ (kPa)
1	Wachusett Dam - North Dike	WND-1	64.0	27.5	19.4	37.00	41.14	49.60	20.90	20.90
		WND-2	155.2	71.1	60.2	95.50	90.03	135.10	38.80	38.80
		WND-105	234.1	108.7	95.4	146.10	132.53	202.10	58.40	58.40
		WND-3	233.0	106.5	89.8	143.10	135.65	200.40	60.10	60.10
2	Fort Peck Dam	Boring 3	475.0	219.3	188.6	294.50	272.35	440.80	92.80	92.80
		Boring 7	594.1	276.9	244.8	372.20	334.41	574.50	80.50	80.50
		Boring 6	531.8	243.7	206.8	327.40	308.21	493.50	104.80	104.80
		Boring 7	138.9	17.4	-81.1	25.10	190.87	-7.60	103.80	103.80
3	Uetsu Railway Embankment	S1	89.6	40.2	32.1	53.90	53.94	83.20	-18.00	18.00
		S2	48.1	21.8	17.9	29.30	28.45	40.80	-12.90	12.90
4	Lower San Fernando Dam - U/S Slope	S103&S111	194.1	91.7	83.6	123.20	106.72	183.60	32.40	32.40
		S101&S102 &S104	297.0	135.7	114.2	182.30	173.05	283.80	47.40	47.40
		S105	356.7	159.7	127.2	214.50	215.10	346.90	46.30	46.30
		S105	259.1	118.8	100.8	159.60	150.11	152.70	74.30	74.30
5	Hachiro-Gata Road Embankment	S1	31.5	14.3	11.7	19.20	18.65	28.80	6.80	6.80
		S2	56.9	26.8	24.3	36.00	31.47	46.50	15.20	15.20
6	La Marquesa Dam - U/S Slope	B-2	74.3	33.2	26.2	44.60	45.02	26.20	-0.40	0.40
		B-III	55.9	26.4	24.0	35.40	30.75	54.80	-5.80	5.80
		B-3	27.5	12.9	11.6	17.30	15.23	25.50	-5.20	5.20
7	La Marquesa Dam - D/S Slope	B-II	50.2	21.4	14.7	28.80	32.66	40.60	15.80	15.80
		B-1	100.0	47.2	43.0	63.40	54.98	98.00	10.50	10.50
8	La Palma Dam	B-3	75.3	34.6	29.6	46.50	43.36	67.00	-17.60	17.60
		B-4	30.1	12.5	7.8	16.80	20.39	24.20	-9.80	9.80
9	Lake Ackerman Highway Embankment	S1	74.5	34.3	29.4	46.00	42.86	66.30	-17.40	17.40
		S2	60.2	58.0	22.2	36.50	36.96	55.80	-12.10	12.10
		S3	17.6	8.1	6.9	10.90	10.13	16.00	-3.80	3.80
10	Chonan Middle School	No.4	19.1	11.4	10.1	13.60	8.46	12.30	3.90	3.90
		No.3	74.8	34.0	28.3	45.70	43.90	71.80	11.30	11.30
11	Soviet Tajik - May 1 Slide	S1	128.8	55.0	37.7	73.80	83.79	108.20	38.10	38.10
		S2	190.0	64.8	25.9	93.50	148.55	29.00	22.50	22.50

Table 3.7 (cont'd) Summary of evaluated effective principal stresses, mean effective stresses, deviatoric stresses, effective normal stresses, and static shear stresses for case histories

12	Shibecha-Cho Embankment	B-2	55.0	25.7	23.0	34.60	30.76	38.00	-16.00	16.00
		B-3	80.1	38.0	35.0	51.00	43.69	78.60	-7.90	7.90
		B-5	59.0	24.8	16.2	33.40	39.19	51.00	-16.70	16.70
		B-4	81.5	37.1	30.8	49.80	47.91	60.00	-25.10	25.10
		B-5	59.0	24.8	16.2	33.40	39.19	51.00	-16.70	16.70
13	Route 272 at Higashiarekinai	Left	66.1	31.1	28.0	41.70	36.72	62.70	-10.90	10.90
		Right	74.3	32.8	25.1	44.00	45.87	67.90	-16.50	16.50
14	Zeeland - Vlietepolder	Small-S1	86.5	40.2	35.3	54.00	48.91	85.90	-5.30	5.30
		Small-S2	135.8	63.4	56.3	85.20	76.16	101.40	39.40	39.40
		Large-S1	71.9	36.8	35.9	48.20	35.57	71.80	2.30	2.30
		Large-S2	196.9	97.0	96.9	130.30	99.95	196.40	7.10	7.10
		Large-S3	163.2	79.0	76.1	106.10	85.71	162.20	9.10	9.10
15	Sheffield Dam	Right	62.5	28.4	23.4	38.10	36.84	57.20	-13.40	13.40
16	Helsinki Harbor	Small-S1	18.4	8.7	8.0	11.70	10.00	17.80	2.40	2.40
		Small-S2	27.8	13.0	11.5	17.40	15.61	21.30	8.00	8.00
		Large-S1	46.7	22.8	22.3	30.60	24.21	46.60	1.70	1.70
		Large-S2	49.1	23.9	23.5	32.20	25.35	48.60	3.20	3.20
17	Solfatara Canal Dike	S1	26.9	13.2	13.2	17.80	13.70	26.00	3.50	3.50
		S2	43.3	19.1	14.7	25.70	26.62	35.20	12.90	12.90
18	Lake Merced Bank	Boring 2	58.0	25.7	19.9	34.50	35.49	53.90	-11.70	11.70
19	El Cobre Tailings Dam	S1	114.1	49.1	34.6	66.00	73.32	113.10	8.90	8.90
		S2	95.9	45.7	42.7	61.50	51.73	95.70	2.90	2.90
		S3	73.4	35.7	34.9	48.00	38.04	73.30	0.70	0.70
		S4	50.7	24.9	24.8	33.50	25.87	50.70	0.30	0.30
20	Metoki Road Embankment	S-19	61.9	27.7	21.9	37.20	37.40	47.70	-19.10	19.10
		S-13	24.8	11.0	8.5	14.80	15.21	22.40	-5.80	5.80
21	Hokkaido Tailings Dam	Small-S1	51.6	25.2	24.8	33.90	26.63	47.90	9.20	9.20
		Small-S2	72.2	32.5	26.1	43.60	43.24	62.20	19.00	19.00
		Large-S1	51.6	25.2	24.8	33.90	26.63	47.90	9.20	9.20
		Large-S2	42.3	20.2	18.9	27.10	22.75	42.00	2.20	2.20
22	Upper San Fernando Dam - D/S Slope	A1&B1&C1	76.0	30.4	16.2	40.90	54.08	64.70	-23.40	23.40
		A2&B2&C2	144.0	60.4	39.1	81.20	96.00	116.90	-45.90	45.90
		A3	200.5	85.1	83.1	122.90	116.45	194.20	-26.50	26.50
		B4&C4	209.9	99.2	90.8	133.30	115.14	203.00	-27.80	27.80

Table 3.7 (cont'd) Summary of evaluated effective principal stresses, mean effective stresses, deviatoric stresses, effective normal stresses, and static shear stresses for case histories

		B5&C5	131.5	60.5	51.9	81.30	75.66	116.80	-30.90	30.90
23	Tar Island Dyke	Large-S1	99.6	49.9	49.3	66.30	49.98	98.70	6.60	6.60
		Large-S2	318.7	143.2	115.2	192.40	191.05	313.40	32.40	32.40
		Small-S1	87.6	53.5	46.6	62.60	38.04	87.40	-3.20	3.20
		Small-S2	318.7	143.2	115.2	192.40	191.05	313.40	32.40	32.40
24	Mochi-Koshi Tailings Dam 1	S1	34.9	16.3	14.7	22.00	19.43	34.50	-2.60	2.60
		S2	83.1	38.1	32.5	51.20	48.06	82.40	-5.80	5.80
		S3	131.9	57.9	43.7	77.80	82.05	125.30	-23.30	23.30
25	Mochi-Koshi Tailings Dam 2	S1	108.7	49.3	40.7	66.20	64.16	102.30	19.90	19.90
		S2	60.4	25.6	17.1	34.40	39.77	57.30	11.10	11.10
26	Nerlerk Embankment Slide 1	S1	51.0	24.2	22.2	32.50	27.89	43.60	-12.60	12.60
		S2	78.2	37.4	35.1	50.20	41.96	73.40	-13.50	13.50
		S3	38.2	20.0	19.2	25.80	18.63	37.30	-4.00	4.00
27	Nerlerk Embankment Slide 2	S1	55.4	26.3	24.3	35.30	30.12	49.90	-11.90	11.90
		S2	97.3	47.0	45.0	63.10	51.37	96.00	-8.40	8.40
		S3	15.3	10.0	8.3	11.20	6.24	15.00	-1.20	1.20
28	Nerlerk Embankment Slide 3	S1	116.6	56.7	55.1	76.10	60.77	110.50	-18.40	18.40
		S2	72.3	37.2	36.1	48.60	35.64	70.90	-6.90	6.90
		S3	18.0	8.9	8.9	11.90	9.06	17.90	-0.10	0.10
29	Asele Road Embankment	S1	60.6	25.7	17.3	34.60	39.76	52.10	17.20	17.20
		S2	48.2	21.7	17.6	29.10	28.73	40.10	13.40	13.40
30	Nalband Railway Embankment	NB-1	46.7	22.6	21.9	30.40	24.38	46.10	3.50	3.50
		Small-S2	80.4	37.2	32.5	50.00	45.71	65.30	22.30	22.30
		NB-1	46.7	22.6	21.9	30.40	24.38	46.10	3.50	3.50
		Large-S2	87.1	42.1	40.5	56.60	45.83	86.20	6.40	6.40
		Large-S3	19.9	8.8	6.6	11.80	12.36	11.30	6.30	6.30
31	Sullivan Tailings	Large-S1	85.3	27.3	-2.7	36.60	77.45	57.00	-41.10	41.10
		CP91-29	165.3	71.8	52.2	96.40	104.68	157.60	-28.60	28.60
		CP91-31	105.5	49.2	43.4	66.00	59.44	92.40	-25.40	25.40
		Small-S1	126.7	57.3	47.0	77.00	75.10	73.70	-37.70	37.70
		CP91-31	131.8	61.5	54.5	82.60	74.06	116.30	-31.00	31.00
32	Jamuna Bridge	S1	74.9	40.2	38.0	51.00	35.92	68.00	-14.40	14.40
		S2	42.9	28.8	23.7	31.80	17.23	40.50	-6.30	6.30

Table 3.7 (cont'd) Summary of evaluated effective principal stresses, mean effective stresses, deviatoric stresses, effective normal stresses, and static shear stresses for case histories

33	Calaveras Dam	S1	357.3	133.1	46.0	178.80	278.16	281.80	-133.40	133.40
		S2	369.7	166.8	135.8	224.10	220.04	327.90	-89.60	89.60
34	Koda Numa Railway Embankment	Left	30.8	14.4	13.0	19.40	17.12	30.10	-3.40	3.40
		Middle	34.5	16.1	14.4	21.60	19.28	34.10	-2.70	2.70
		Right	23.1	9.8	6.6	13.20	15.19	19.80	-6.60	6.60
35	Whiskey Springs Fan	SP 1	23.9	13.4	12.3	16.50	11.10	23.70	1.70	1.70
		SP 3	123.5	60.4	59.5	81.10	63.59	123.00	5.60	5.60
36	San Fernando Valley Juvenile Hall	Boring 2	160.9	78.9	78.2	106.00	82.32	160.80	-2.70	2.70
		Boring 4	113.7	56.2	56.1	75.30	57.55	113.60	-1.90	1.90
		Boring 6	80.1	39.6	39.5	53.10	40.54	80.10	-0.90	0.90

3.5 Evaluation of SPT Resistance

As discussed in Chapter 2, previous studies performed on the post-liquefaction strength of soils tend to correlate an in-situ test index metric (e.g., $(N_1)_{60}$, q_c, V_s, etc.) to represent the capacity of the soil during and after the liquefaction. Among these in-situ test index metrics, the common approach is to use Standard Penetration Test resistance (SPT-N) as a key parameter to predict the residual strengths of soils. In addition, it is also prevalent to apply energy and overburden corrections to these SPT resistances before using them in the prediction models. Even, some of these studies apply clean sand correction to these resistances and develop their post-liquefaction strength relationships based on $(N_1)_{60,cs}$ values.

There are a couple of justifiable reasons behind using SPT resistance instead of other in-situ test index metrics in residual strength prediction correlations. First of all, it is one of the most widely used in-situ tests all around the world to measure many properties of the soil profile. It is easy to be conducted, recorded, and documented. Moreover, there are lots of empirical and semi-empirical correlations available in the literature to convert other types of penetration resistances to SPT resistances as much data exist for this test to develop correlations. Therefore, it is logical to use SPT

resistance as the in-situ test index metric in the development of residual strength relationships, as done by previous studies so far.

Previous studies use SPT resistance ($(N_1)_{60}$ or $(N_1)_{60,cs}$) as an essential key parameter to develop residual strength relationships for liquefied soils. On the other hand, since this study also aims to introduce a new framework for the evaluation of post-liquefaction shear strength, the importance of the SPT resistance is even higher. As discussed in Chapter 1, this study suggests representing post-liquefaction strength in void ratio versus mean effective stress domain instead of strength versus penetration resistance domain as done by previous studies so far. Although previous studies perform admirable efforts to evaluate the undrained residual strength of liquefied soils, the use of the term "undrained" without any reference to the induced excess pore pressures can be misleading for practicing engineers, who are very much used to performing effective stress-based stability assessments for cohesionless soils under monotonic loading conditions. Hence, this study recommends an effective stress approach for the assessment of post-liquefaction shear strength. Consequently, in addition to the initial mean effective stresses, the equipment, and the procedure corrected SPT blow counts along with fines content, roundness and sphericity, mean grain size, and coefficient of uniformity are selected as the promising descriptive parameters for the in-situ relative densities, or in other perspectives, the void ratios.

SPT penetration resistance and in-situ density state relationships for cohesionless soils are commonly used in literature. Cubrinovski and Ishihara (1999, 2001), Haldar and Miller (1984), Selig and Ladd (1973), Juang et al. (1996), and Igwe et al. (2012) are some of the common studies focused on these relationships. These previous studies have compromised that SPT resistance is a good representation of relative density, and it is reasonable to use SPT resistance versus relative density relationships for estimating in-situ density states of cohesionless soils as long as the relationship is well-prepared and trustworthy. In this context, the SPT resistance of each selected case history is determined with significant effort and attention to liquefied layers.

For 19 of the 36 case histories (Case history #: 1, 2, 4, 5, 6, 7, 8, 9, 13, 18, 19, 22, 23, 24, 25, 30, 33, 35, 36), Standard Penetration Tests were conducted at the site, and the results were documented properly. These cases were generally modern and well-documented cases such that some other penetration tests, such as CPT, were also conducted at some of these sites in addition to SPT. Evaluated representative SPT resistance values therefore checked with the other type of in-situ test results for consistency. While directly the raw SPT-N values were reported for most of the cases, equipment and overburden corrected resistance values were documented instead of raw SPT-N values for some cases. To achieve consistency in evaluating the representative penetration resistances for case histories and their sub-sections, all documented resistance values are converted into the raw SPT-N values initially, and then corrected for equipment and overburden with the same procedure and method. For the cases in which equipment and overburden corrected resistance values (N_{60} or $(N_1)_{60}$) were documented instead of raw SPT-N values, the back-calculations to evaluate raw SPT-N values are performed by considering the correction methods used by the reporters. In other words, raw SPT-N values are evaluated by back-analyzing the corrected N_{60} or $(N_1)_{60}$ values with the same correction methods used by the reporting teams.

Once the raw SPT-N values are evaluated for all these 19 case histories and their sub-sections, initially the equipment, energy, and procedure corrections are employed correspond largely to those recommended by Cetin et al. (2004) and the NCEER Working Group (NCEER 1997) as given in Table 3.8.

$$N_{60} = N \cdot C_R \cdot C_S \cdot C_B \cdot C_E \qquad \text{Equation 3-23}$$

In Equation 3-23, C_R, C_S, $C_{B,}$ and C_E represent corrections for short rod length, nonstandardized sampler configuration, borehole diameter, and hammer energy efficiency, respectively. The recommended values for these correction factors are summarized in Table 3.8.

Table 3.8 Recommended corrections for SPT equipment, energy, and procedures (NCEER 1997)

C_R (See Fig. 7 for Rod Length Correction Factors)

C_S For samplers with an indented space for interior liners, but with liners omitted during sampling,

$$C_S = 1 + \frac{N_{1,60}}{100} \qquad (Eq.T\text{-}1)$$

With limits as $1.10 \leq C_S \leq 1.30$

C_B

Borehole diameter	Correction (C_B)
65 to 115 mm	1.00
150 mm	1.05
200 mm	1.15

C_E

$$C_E = \frac{ER}{60\%} \qquad (Eq.T\text{-}2)$$

where ER (efficiency ratio) is the fraction or percentage of the theoretical SPT impact hammer energy actually transmitted to the sampler, expressed as %

- The best approach is to directly measure the impact energy transmitted with each blow. When available, direct energy measurements were employed.
- The next best approach is to use a hammer and mechanical hammer release system that has been previously calibrated based on direct energy measurements.
- Otherwise, ER must be estimated. For good field procedures, equipment and monitoring, the following guidelines are suggested:

Equipment	Approximate *ER* (see Note [c])	C_E (see Note [c])
-Safety Hammer[a]	0.4 to 0.75	0.7 to 1.2
-Donut Hammer[a]	0.3 to 0.6	0.5 to 1.0
-Donut Hammer[b]	0.7 to 0.85	1.1 to 1.4
-Automatic-Trip Hammer (Donut or Safety Type)	0.5 to 0.8	0.8 to 1.4

- For lesser quality fieldwork (e.g.: irregular hammer drop distance, excessive sliding friction of hammer on rods, wet or worn rope on cathead, etc.) further judgmental adjustments are needed.

[a]Based on rope and cathead system, two turns of rope around cathead, "normal" release (not the Japanese "throw"), and rope not wet or excessively worn.
[b]Rope and cathead with special Japanese "throw" release. (See also Note [d]).
[c]For the ranges shown, values roughly central to the mid-third of the range are more common than outlying values, but *ER* and C_E can be even more highly variable than the ranges shown if equipment and/or monitoring and procedures are not good.
[d]Common Japanese SPT practice requires additional corrections for borehole diameter and for frequency of SPT hammer blows. For "typical" Japanese practice with rope and cathead, donut hammer, and the Japanese "throw" release, the overall product of $C_B \times C_E$ is typically in the range of 1.0 to 1.3.

Instead of using the stepwise incremental values of the NCEER Workshop recommendations, or the nonlinear curve provided in Figure 3.22 suggested by further studies for the short rod length correction between the driving hammer and the penetrating sampler (C_R), the values obtained from Equation 3-24 and Equation 3-25 are employed.

$$ln(C_{R,Auto}) = ln(1.003) - 0.363 \cdot e^{-0.375 \cdot L} \qquad \text{Equation 3-24}$$

$$ln(C_{R,Safety}) = ln(0.983) - 0.363 \cdot e^{-0.375 \cdot L} \qquad \text{Equation 3-25}$$

In these equations, L symbolizes the rod length of the driving hammer in meters. As it can be observed from these two relationships, Equation 3-25 recommends lower C_R values than Equation 3-24 to be on the safer side. In this study, the arithmetic means of the C_R values obtained from these two equations are employed as the overall short rod length correction values.

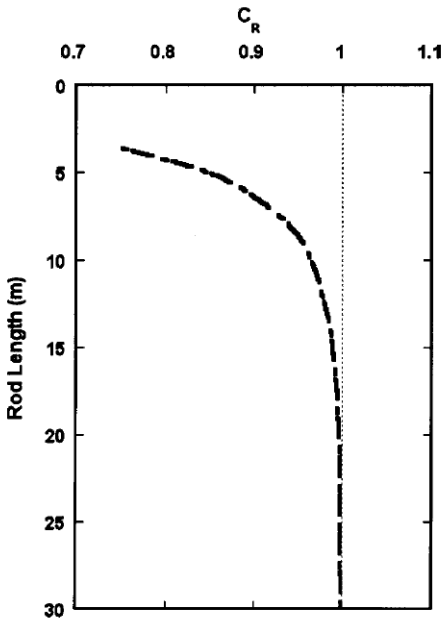

Figure 3.22. Recommended C_R values (rod length from the point of hammer impact to the tip of the sampler)

It should be noted that when C_R values obtained from Figure 3.22 are added by 1, and then divided by 2, the obtained results agree well with the ones evaluated by Equation 3-24 and Equation 3-25. This circumstance actually shows that for the cases where $C_R < 1$, higher C_R values than the ones recommended by Figure 3.22 are compatible with the most recent studies performed on C_R correction.

It is better to remark that due to the fact that most of these case histories suffered from liquefaction many decades ago, equipment, energy, and procedure details of Standard Penetration Tests were not documented properly for other correction factors, unfortunately. For these types of lack of information cases, the correction factors are assumed to be equal to unity. For instance, C_S values are recommended in 1.1-1.3 range referring to Table 3.8 for the samplers with an indented space for interior liners. On the other hand, no reliable information regarding the sampling method was documented for most of the case histories. Therefore, the correction factor C_S is assumed to be 1.0 for unknown cases by considering that a standard sampler is used.

Similar to the sampling methods, the borehole diameters were also not reported for most of the cases. Thus, the correction factor C_B is also assumed to be 1.0 for unknown cases by considering that a standard borehole with 65-155 mm diameter is used during the tests. It should be noted that the effect of borehole diameter correction is tiny as its value can reach up to 1.15 for 200 mm diameter boreholes; therefore, an assumption of 1.0 for poorly-documented cases is quite admissible.

For 5 of the 19 case histories (Case history #: 1, 6, 7, 13, 36) that Standard Penetration Tests were conducted at the site, the percent hammer energy efficiency ratios were reported clearly. Therefore, the energy efficiency correction factors (C_E) are evaluated individually for them. For the remaining 12 cases, no information was provided regarding the energy efficiency or type of hammer (safety, donut, or automatic-trip hammer). Consequently, the hammer energy efficiency ratio is assumed to be 60% for unknown cases, and the corresponding correction factor C_E is taken as 1.0.

Once the equipment, energy, and procedure corrected resistance values (N_{60}) are evaluated for all SPTs corresponding to these 19 case histories and their sub-sections, then the overburden correction is employed by the equation given in Equation 3-26.

$$(N_1)_{60} = C_N \cdot N_{60} \qquad \text{Equation 3-26}$$

In this form, C_N represents the correction for overburden stress. Although there are numerous methods available in literature as shown in Figure 3.29 to evaluate the overburden stress correction, it can be evaluated by the popular method recommended by Liao and Whitman (1986) as given in Equation 3-27.

$$C_N = \sqrt{\frac{1}{\sigma'_v\,(atm)}} \qquad \text{Equation 3-27}$$

In this equation, σ'_v is the actual effective overburden stress at the depth of the SPT drop in atmospheres. Once the effective overburden stress is converted into the

metric system with the unit of kilopascals, Equation 3-28 provided below can be used as the correction for overburden stress.

$$C_N = \frac{9.78}{\sqrt{\sigma'_v\ (kPa)}} \qquad \text{Equation 3-28}$$

It should be noted that this effective overburden stress correction is not only applied for these 19 case histories in which Standard Penetration Tests were conducted at the site, but also employed for the remaining cases that other types of penetration tests (Swedish Cone, Dutch Cone, etc.) are conducted at the site. The penetration resistances obtained from these different in-situ tests are also converted to equivalent SPT resistances by various correlations that exist in the literature, and effective overburden stress correction is also employed for them with respect to the depth of in-situ tests performed.

For 7 of the remaining 17 case histories (Case history #: 11, 14, 26, 27, 28, 31, 32), Cone Penetration Tests were conducted at the site, and the results were documented properly. For these cases, cone penetration resistances (generally tip resistances, q_c) are converted to representative equivalent SPT resistances by reliable correlations and relationships available in the literature. While converting CPT resistances to equivalent SPT resistances, the methods and correlations followed by previous studies on case history-based residual strength relationships are considered mainly. The latest of these studies, Weber (2015), usually divides tip resistances obtained from CPT (in the units of kg/cm^2) to a constant number between 2-6 to obtain a representative value for $(N_1)_{60}$ in the units of blow/feet. The study evaluates the constant ratio based on the type of the case history and geological conditions. Similarly, Olson (2001) also defines a constant ratio for q_c/N_{60} value (this time q_c is in the units of MPa), and evaluates its representative equivalent SPT resistance accordingly. It defines the constant value of this ratio by referring to the method proposed by Stark and Olson (1995), which provides a q_c/N_{60} ratio with respect to mean grain size value, D_{50}, in millimeters. It should be noted that these methods directly provide N_{60} or $(N_1)_{60}$ values by these constant ratios. However, if one wants

to evaluate raw SPT-N value from CPT tip resistance without any assumed correction, can use the ratios provided by Ishihara et al. (1990) for q_c/N. Similar to Weber (2015), Ishihara et al. (1990) also recommends a constant number between 2-6 to obtain a representative value for N in the units of blow/feet. Again, this method also employs q_c in the units of kg/cm^2.

In this study, instead of using a constant ratio for q_c/N_{60}, the relationship recommended by Kulhawy and Mayne (1990) given in Equation 3-29 is employed to convert CPT tip resistances to representative SPT resistances in order to include the effect of mean grain size in conversion.

$$N_{60} = \frac{{q_c}/{P_a}}{5.44 \cdot (D_{50})^{0.26}} \qquad \text{Equation 3-29}$$

Here, q_c, P_a and D_{50} represent cone tip resistance, atmospheric pressure and mean grain size value in millimeters, respectively. For the estimation of raw SPT-N values, the constant q_c/N ratios provided by Ishihara et al. (1990) is used. It should be remarked that the overburden corrected SPT resistances ($(N_1)_{60}$) are again evaluated by the method provided in Equation 3-26 for these 7 case histories. In other words, instead of passing $(N_1)_{60}$ value directly from the $q_c/(N_1)_{60}$ ratio as done by Weber (2015), representative equivalent N_{60} values are estimated by Equation 3-29, and $(N_1)_{60}$ values are then evaluated accordingly by using the effective overburden stress correction factor, C_N, provided in Equation 3-28.

For 1 of the remaining 10 case histories (Case history #: 21), the Dutch Cone Penetration Test sounding, which is a quite similar test to traditional CPT, was conducted at the site, and the results were documented properly. Similar to CPT performed cases, again previous studies such as Weber (2015) and Olson (2001) use a constant $q_c/(N_1)_{60}$ or q_c/N_{60} ratio to evaluate a representative equivalent SPT penetration resistance. In this study, the relationship provided in Equation 3-29 is employed to convert Dutch Cone Penetration Test tip resistances to representative SPT resistances instead of a constant $q_c/(N_1)_{60}$ or q_c/N_{60} ratio. For the estimation of raw SPT-N values, again the constant q_c/N ratios provided by Ishihara et al. (1990)

is used. The overburden corrected SPT resistances ($(N_1)_{60}$) are evaluated by the method provided in Equation 3-26 by using the effective overburden stress correction factor, C_N, provided in Equation 3-28.

For 3 of the remaining 9 case histories (Case history #: 10, 20, 34), Swedish Cone Penetration Tests were conducted at the site, and the results were documented properly. This is an out-of-date test and not applicable for geotechnical site investigations anymore; thus, correlations between Swedish Cone Penetration Test and SPT are very rare in literature. Weber (2015) employs the correlation proposed by Inada (1982) to convert Swedish Cone Penetration Test resistances to SPT resistances. Similarly, this study also uses the same method for these cases. The proposed SCPT-SPT conversion is given in Equation 3-30.

$$N = 0.02 \cdot W_{sw} + 0.067 \cdot N_{sw} \qquad \text{Equation 3-30}$$

In this empirical formula suggested by Inada (1982), while N represents the equivalent representative SPT resistance, W_{sw} and N_{sw} represent the amount of weight in kilograms used for the static phase of the penetration and the number of half-revolutions of the rod in the rotating phase of the penetration, respectively.

To be able to understand the correlation and parameters provided above, it is better to understand the test procedure for Swedish Cone Penetration Test. Initially, four weightings (25 kg each) are put on the penetration cone rod one by one until penetration is observed. In other words, initially one 25 kg weighting is put on the cone rod and examined to see whether penetration is observed or not. If penetration is monitored, then W_{sw} is recorded as 25 kg, and no N_{sw} value is reported. If not, a second 25 kg weighting is put on the cone rod (totally 50 kg), and again the penetration is examined. Until a penetration is observed for the cone, 25, 50, 75, and 100 kg weights are applied statically on top of the cone rod step by step. For the cases when penetration is observed, the weighting on top of the cone is reported as W_{sw} value, and N_{sw} is taken as equal to zero as the rotating phase of the experiment has not been performed. If penetration has not been observed even with 100 kg weighting, then the rotating phase of the experiment begins, and a rotation is applied

to the rod of the penetration cone while 100 kg was still on top of it. When penetration is monitored, W_{sw} value is directly reported as 100 kg, and the number of half-revolutions of the rod in the rotating phase of the penetration is reported as N_{sw} value.

Since the empirical correlation suggested by Inada (1982) gives an equivalent raw SPT-N value, this value is assumed to be almost equal to N_{60} as equipment, energy, and procedure corrections are not applicable for this test. On the other hand, the short rod length and overburden stress corrected SPT resistances ($(N_1)_{60}$) are again evaluated by the method provided in Equation 3-26 for these 3 case histories.

For the remaining 6 case histories (Case history #: 3, 12, 15, 16, 17, 29), no penetration test data was provided by the main source of references or previous studies. Therefore, the representative SPT penetration resistances are assumed in consistent with the SPT resistance or in-situ relative density values reported by previous studies. The estimated values showed well agreement with the average of the selected values by previous studies such as Seed (1987), Seed and Harder (1990), Stark and Mesri (1992), Olson and Stark (2002), Wang (2003), Kramer (2008) and Weber et al. (2015).

In addition to equipment, energy, procedure, and overburden stress corrections, fines (clean sand) correction to these resistance values ($(N_1)_{60,cs}$) are also employed further using the method recommended by Cetin et al. (2004) given in Equation 3-31 and Equation 3-32.

$$(N_1)_{60,cs} = C_{fines} \cdot (N_1)_{60} \qquad \text{Equation 3-31}$$

$$C_{fines} = (1 + \theta_{18} \cdot FC) + \theta_{19} \cdot \left(\frac{FC}{(N_1)_{60}}\right) \qquad \text{Equation 3-32}$$

In these equations, C_{fines}, FC, and $(N_1)_{60}$ represent fines correction factor, percent fines content (by dry weight) expressed as an integer, and equipment, energy, procedure, and overburden stress corrected SPT resistance, respectively. It should be noted that the fines content value is only allowed between the range 5%-35% for this

relationship. Therefore, for the fines content values less than 5% and greater than 35%, FC=0% and FC=35% should be used, respectively.

Cetin et al. (2004) recommends best-fit values for θ_{18} and θ_{19} as 0.004 and 0.05, respectively. On the other hand, lower fines content correction factors, i.e., lower additional penetration resistances, are suggested for residual strength predictions than liquefaction triggering relationships in the literature, such as stated by Seed (1987). Nevertheless, fines content correction for SPT resistances is not an important debate for this study because $(N_1)_{60}$ values are used in the evaluation of relative densities instead of $(N_1)_{60,cs}$ values, which will be discussed in Section 3.7 in detail. In fact, it is commonly known that the fines content of the soil has also an impact on the penetration resistances, and this impact should be considered during the evaluation of in-situ relative densities. However, a separate fines content correction to $(N_1)_{60}$ values is not required for relative density estimations as the effect of fines content is already included in the other parameters in relative density prediction relationships, such as mean grain size (D_{50}) and void ratio range (e_{max}-e_{min}), that will be discussed in Section 3.7. Hence, these two coefficients remained the same with the values recommended by Cetin et al. (2004), $\theta_{18} = 0.004$ and $\theta_{19} = 0.05$. However, they can be arranged accordingly to obtain lower C_{fines} values than the ones suggested by Cetin et al. (2004), if demanded.

Fines correction for SPT resistances is the point where minor differences exist between various investigation teams working on the residual strength of soils. While Seed et al. (1984) suggests a fines adjustment for general purposes, Seed (1987) recommends another fines content correction procedure for S_r purposes only, as explained above. The correction factors evaluated by Cetin et al. (2004) fall well between the values evaluated by these two methods. In fact, Weber (2015) states that the fines correction values suggested by Idriss and Boulanger (2008) for these case histories also do not produce major differences, but they vary slightly relative to other methods mentioned. It should be noted that Olson (2001) and Olson and Stark (2002) apply no fines correction for their SPT resistances. In other words, they directly use $(N_1)_{60}$ values rather than $(N_1)_{60,cs}$ values in their residual strength

relationships. Hence, their representative penetration resistances vary slightly from the other studies for the cases with high fines content.

It is better to remark that as previously explained in Sections 3.3 and 3.4, each overall failure surface is sub-divided into smaller pieces for all case histories, and a separate SPT resistance for each of them is assigned. In the case that penetration tests are performed on the site, and their exact locations are known along the cross-section, sub-division is made based on the locations of these penetration tests, such that the overall failure plane is divided from the mid-points of the regions between these penetration tests and each test is assigned for the corresponding territory length. As a result, also separate SPT resistances are assigned for each of these sub-sections along the failure plane instead of assigning a single representative resistance value for the whole overall failure plane.

For the cases where the locations of the penetration tests were unknown along the critical cross-section, or even no penetration test data was available, the overall failure plane is sub-divided into 3-4 pieces with similar lengths. While dividing into smaller pieces, the change in effective vertical stresses and inclination of the failure plane along the soil profile is considered so that each piece represents a region with different confining stress. Nevertheless, for these cases where the locations of the penetration tests are missing, it is only possible to assign a single representative SPT resistance value for all sub-sections. Hence, it is assumed that the penetration resistance, and therefore the in-situ relative density, is almost equal along the entire failure plane, but the confining stress differs significantly at different points.

In the end, the database represented in Table 3.9 that consists of SPT resistances (N, N_{60}, $(N_1)_{60}$ and $(N_1)_{60,cs}$) of case history sub-sections is compiled.

Table 3.9 Summary of evaluated SPT-N resistances for case histories

#	Case History	Section	N	N_{60}	$(N_1)_{60}$	$(N_1)_{60,cs}$	
1	Wachusett Dam - North Dike	WND-1	11.8	8.8	6.2	6.8	6.3
		WND-2	9.8	7.3	4.3	4.8	
		WND-105	10.0	7.4	3.9	4.4	
		WND-3	25.5	19.0	8.7	9.4	
2	Fort Peck Dam	Boring 3	31.3	31.0	17.3	17.3	17.3
		Boring 7	31.3	31.0	17.3	17.3	
		Boring 6	31.3	31.0	17.3	17.3	
		Boring 7	31.3	31.0	17.3	17.3	
3	Uetsu Railway Embankment	S1	1.7	1.6	1.6	1.6	2.0
		S2	1.7	1.6	2.4	2.4	
4	Lower San Fernando Dam - U/S Slope	S103&S111	21.5	21.3	14.0	17.8	17.7
		S101&S102 &S104	21.5	21.3	14.0	17.8	
		S105	21.5	21.3	14.0	17.8	
		S105	21.5	21.3	14.0	17.7	
5	Hachiro-Gata Road Embankment	S1	2.6	2.2	4.3	5.5	5.5
		S2	2.6	2.2	4.3	5.5	
6	La Marquesa Dam - U/S Slope	B-2	3.0	2.5	3.9	5.8	5.6
		B-III	3.0	2.3	3.6	5.5	
		B-3	3.0	2.3	3.6	5.5	
7	La Marquesa Dam - D/S Slope	B-II	7.0	5.2	6.5	8.1	8.4
		B-1	7.0	5.7	7.1	8.7	
8	La Palma Dam	B-3	3.8	3.6	5.0	6.1	5.9
		B-4	3.8	3.4	4.7	5.7	
9	Lake Ackerman Highway Embankment	S1	3.9	3.6	4.4	4.4	4.4
		S2	3.9	3.6	4.4	4.4	
		S3	3.9	3.5	4.3	4.3	
10	Chonan Middle School	No.4	3.4	3.1	4.2	5.4	5.1
		No.3	3.1	2.8	3.6	4.8	
11	Soviet Tajik - May 1 Slide	S1	2.8	2.5	4.6	6.9	6.9
		S2	2.8	2.5	4.6	6.9	
12	Shibecha-Cho Embankment	B-2	3.6	3.3	4.3	5.7	5.5
		B-3	3.6	3.3	3.6	4.9	
		B-5	3.6	3.3	4.4	5.8	
		B-4	3.6	3.3	3.6	4.9	5.3
		B-5	3.6	3.3	4.4	5.8	

Table 3.9 (cont'd) Summary of evaluated SPT-N resistances for case histories

13	Route 272 at Higashiarekinai	Left	3.6	3.7	5.8	7.2	7.1
		Right	3.6	3.5	5.5	6.9	
14	Zeeland - Vlietepolder	Small-S1	16.1	15.7	14.6	15.3	15.3
		Small-S2	16.1	15.7	14.6	15.3	
		Large-S1	16.1	15.7	14.6	15.3	15.3
		Large-S2	16.1	15.7	14.6	15.3	
		Large-S3	16.1	15.7	14.6	15.3	
15	Sheffield Dam	Right	4.0	3.6	4.7	7.1	7.1
16	Helsinki Harbor	Small-S1	2.0	1.7	3.9	3.9	4.4
		Small-S2	3.0	2.6	4.9	4.9	
		Large-S1	3.5	3.3	4.7	4.7	4.6
		Large-S2	3.5	3.2	4.5	4.5	
17	Solfatara Canal Dike	S1	2.9	2.4	4.7	5.2	4.7
		S2	2.9	2.6	3.8	4.3	
18	Lake Merced Bank	Boring 2	6.7	5.8	8.3	8.3	8.3
19	El Cobre Tailings Dam	S1	1.5	1.4	1.7	3.7	3.7
		S2	1.5	1.4	1.7	3.7	
		S3	1.5	1.4	1.7	3.7	
		S4	1.5	1.4	1.7	3.7	
20	Metoki Road Embankment	S-19	0.8	0.6	3.1	4.0	4.4
		S-13	2.0	1.8	3.8	4.7	
21	Hokkaido Tailings Dam	Small-S1	0.8	0.8	1.4	3.4	3.4
		Small-S2	0.8	0.8	1.4	3.4	
		Large-S1	0.8	0.8	1.4	3.4	3.4
		Large-S2	0.8	0.8	1.4	3.4	
22	Upper San Fernando Dam - D/S Slope	A1&B1&C1	8.3	8.1	9.2	12.2	12.3
		A2&B2&C2	8.3	8.3	9.3	12.4	
		A3	8.3	8.3	9.3	12.4	
		B4&C4	8.3	8.3	9.3	12.4	
		B5&C5	8.3	8.1	9.2	12.2	
23	Tar Island Dyke	Large-S1	10.6	10.1	11.1	12.2	12.2
		Large-S2	10.6	10.1	11.1	12.2	
		Small-S1	10.6	10.1	11.1	12.2	12.2
		Small-S2	10.6	10.1	11.1	12.2	
24	Mochi-Koshi Tailings Dam 1	S1	4.3	4.2	4.0	6.4	6.4
		S2	4.3	4.2	4.0	6.4	

Table 3.9 (cont'd) Summary of evaluated SPT-N resistances for case histories

		S3	4.3	4.2	4.0	6.4	
25	Mochi-Koshi Tailings Dam 2	S1	3.1	3.0	3.0	5.2	5.2
		S2	3.1	3.0	3.0	5.2	
26	Nerlerk Embankment Slide 1	S1	6.2	8.7	13.7	14.5	14.5
		S2	6.2	8.7	13.7	14.5	
		S3	6.2	8.7	13.7	14.5	
27	Nerlerk Embankment Slide 2	S1	6.2	8.7	13.7	14.5	14.5
		S2	6.2	8.7	13.7	14.5	
		S3	6.2	8.7	13.7	14.5	
28	Nerlerk Embankment Slide 3	S1	6.2	8.7	13.7	14.5	14.5
		S2	6.2	8.7	13.7	14.5	
		S3	6.2	8.7	13.7	14.5	
29	Asele Road Embankment	S1	5.5	5.2	6.8	9.1	9.0
		S2	5.3	4.6	6.7	9.0	
30	Nalband Railway Embankment	NB-1	4.0	3.4	4.8	6.7	6.7
		Small-S2	4.0	3.4	4.8	6.7	
		NB-1	4.0	3.4	4.8	6.7	6.7
		Large-S2	4.0	3.4	4.8	6.7	
		Large-S3	4.0	3.4	4.8	6.7	
31	Sullivan Tailings	Large-S1	7.7	7.8	9.5	12.6	12.6
		CP91-29	7.7	7.8	9.5	12.6	
		CP91-31	7.7	7.8	9.5	12.6	
		Small-S1	7.7	7.8	9.5	12.6	12.6
		CP91-31	7.7	7.8	9.5	12.6	
32	Jamuna Bridge	S1	10.0	16.3	6.7	7.2	7.2
		S2	10.0	16.3	6.7	7.2	
33	Calaveras Dam	S1	14.0	13.9	14.0	17.2	17.2
		S2	14.0	13.9	14.0	17.2	
34	Koda Numa Railway Embankment	Left	1.0	0.8	2.1	2.8	2.9
		Middle	1.0	0.8	1.8	2.5	
		Right	1.1	0.9	2.5	3.3	
35	Whiskey Springs Fan	SP 1	6.0	5.3	10.8	13.7	14.9
		SP 3	16.3	16.0	12.8	16.0	
36	San Fernando Valley Juvenile Hall	Boring 2	13.0	14.5	11.4	14.8	12.6
		Boring 4	6.3	6.4	10.1	13.2	
		Boring 6	4.8	5.0	7.0	9.7	

3.6 Estimation of Limit Void Ratios and Void Ratio Ranges

Estimating the in-situ void ratio with its limits (e_{max}, e_{min}) and range (e_{max}-e_{min}) is considered to be helpful in understanding the behavior of granular soils in terms of stress-strain and permeability responses since the index properties, density, and stress states of cohesionless soils mainly control the stress-strain and permeability behavior of such soils. Referring to Tokimatsu and Seed (1984), Ishihara and Yoshimine (1992), Zhang et al. (2002), Wu and Seed (2004), Cetin et al. (2009), Cetin and Bilge (2012), Seed et al. (1975), Green et al. (2000) and many other studies on this topic, in the void ratio-effective stress domain, a soil's volumetric and shear strain or pore pressure responses are defined by its state relative to the critical state line, respectively, during drained or undrained monotonic and/or cyclic shearing. Therefore, assessment of the in-situ void ratio with its limits and range is a crucial part of the critical state concept.

When the importance of the void ratio limits and range is examined, Cubrinovski and Ishihara (2002) states that the void ratio range is indicative of the overall grain-size composition and particle characteristics of a cohesionless soil, which means it provides a general basis for evaluation of material properties over the entire range of cohesionless soils. The void ratio range can provide valuable and unique information about the material properties of cohesionless, especially sandy soils. The physical nature (grain size distribution, fines content, grain shape, and mineralogy) and the physical state of the soil (relative density, initial confining stress, fabric) are two key parameters corresponding to the stress-strain behavior of cohesionless soils.

Although the difficulties in undisturbed sampling of cohesionless soils are widely known, the densest and the loosest states of soil can be directly estimated by several standard testing procedures for the case when soil samples are available. In its most common form, the American Society for Testing and Materials suggests standard test methods for maximum and minimum index density (ASTM International D4253-00, ASTM International D4254-00). Additionally, alternative methods are also available in the literature for such estimations, such as the methods proposed by

Kolbuszewski (1948), Mulilis et al. (1977), and Vaid and Negussey (1988). All this aside, in addition to the troubles in undisturbed sampling of cohesionless soils, different values for limiting void ratios may be obtained depending on the method used during estimation such that these standards are extremely sensitive to sample preparation, equipment-used, energy-delivered, and inevitable human effects during testing. As a result, even when soil samples are available and standard laboratory tests are performed, significant variability in limiting void ratios, especially in e_{max}, is commonly possible. Even, these variabilities may lead to negative or exceeding 100% relative density values sometimes, as already discussed by ASTM Standards and as well as Cubrinovski and Ishihara (1999, 2001, 2002), Haldar and Miller (1984), Selig and Ladd (1973), Juang et al. (1996) and Igwe et al. (2012). Hence, soil sampling and laboratory testing may not be feasible for estimating limiting void ratios.

Motivated by the uncertainties of laboratory-estimated void ratio limits, a number of semi-empirical, probability-based relationships are proposed in the literature. These studies attempt to correlate the index properties of soils and their particle morphology (surface texture, roundness, sphericity) with their mechanical responses under monotonic (Yang and Wei (2012, 2014), Belkhatir et al. (2012, 2013), Cherif et al. (2016, 2018), Xiao et al. (2019) and Xie et al. (2017)) or cyclic (Yilmaz et al. (2008)) loading conditions. In addition, many of those studies also examine the effects of index properties and particle morphology of soils on minimum or maximum void ratio states. More specifically, the vast majority of these studies correlate coefficient of uniformity (C_u), mean grain size (D_{50}), fines content (FC), roundness (R), and sphericity (S), with e_{min}, e_{max} and e_{max}-e_{min} of cohesionless soils. A summary of existing predictive models for void ratio limits and their range is presented in Table 3.10.

Table 3.10 A summary of existing predictive models for void ratio limits and their range (Cetin and Ilgac, 2021)

Reference	Correlation
Shimobe and Moroto [68]	$e_{max} = 0.64 \cdot R^{-0.354}$
Cubrinovski and Ishihara [20]	$e_{max} = 0.072 + 1.53 \cdot e_{min}$
	$e_{max} = 0.25 + 1.37 \cdot e_{min}$
	$e_{max} = 0.44 + 1.21 \cdot e_{min}$
	$e_{max} = 0.44 + 1.32 \cdot e_{min}$
	$e_{max} - e_{min} = 0.43 + 0.00867 \cdot FC$
	$e_{max} - e_{min} = 0.57 + 0.004 \cdot FC$
	$e_{max} - e_{min} = 0.23 + 0.06/D_{50}$
Santamarina and Cho [70]	$e_{min} = 0.359 + 0.082 \cdot R^{-1}$
	$e_{max} = 0.554 + 0.154 \cdot R^{-1}$
Cho et al. [71]	$e_{min} = 0.80 - 0.34 \cdot R$
	$e_{max} = 1.30 - 0.62 \cdot R$
Rouse et al. [72]	$e_{min} = 0.433 + 0.051 \cdot R^{-1}$
	$e_{max} = 0.615 + 0.107 \cdot R^{-1}$
Patra et al. [75]	$e_{min} = 0.33 \cdot D_{50}^{-0.49}$
	$e_{max} = 0.60 \cdot D_{50}^{-0.30}$
Bradley and Cubrinovski [19]	$e_{max} = 0.865 \cdot D_{50}^{0.18} \cdot (FC + 1)^{0.053}$
	$e_{min} = (0.59 + 0.007 \cdot FC) \cdot e_{max} + (0.035 - 0.0133 \cdot FC)$
	$e_{min} = 0.76 \cdot e_{max} - 0.33$
Chen and Kulhawy [76]	$e_{max} - e_{min} = 0.24 + 0.34/C_u$
	$e_{max} - e_{min} = 0.25 + 0.038/D_{50}$
Zheng and Hryciw [80]	$e_{max} = R^{-0.20} \cdot S^{-0.25} \cdot {C_u}^{-0.10} \cdot e^{*}_{max}$
	$e_{min} = R^{-0.15} \cdot S^{-0.25} \cdot {C_u}^{-0.15} \cdot e^{*}_{min}$
	$\frac{e_{max}}{e_{min}} = \left(\frac{C_u}{R}\right)^{0.05} \frac{e^{*}_{max}}{e^{*}_{min}}$
Chang et al. [79]	$e_{min} = 0.50 \cdot D_{50}^{-0.11}; e_{max} = 0.79 \cdot D_{50}^{-0.13}$
	$e_{min} = 0.43 \cdot R^{-0.28}; e_{max} = 0.65 \cdot R^{-0.36}$
	$e_{min} = 0.39 + 0.006 \cdot R^{-1}; e_{max} = 0.56 + 0.13 \cdot R^{-1}$
	$e_{min} = 0.71 - 0.33 \cdot R; e_{max} = 1.24 - 0.71 \cdot R$
	$e_{min} = 0.413 \cdot R^{-0.291} \cdot D^{-0.043}; e_{max} = 0.619 \cdot R^{-0.372} \cdot D^{-0.048}$
Sarkar et al. [82]	$e_{min} = 0.69 \cdot D_{50}^{-0.029}; e_{min} = 0.5675 \cdot D_{50}^{0.038}$
	$e_{max} = (1.794 - 1.139 \cdot \rho) \cdot D_{50}^{-0.029}; e_{min} = (0.874 - 0.352 \cdot \rho) \cdot D_{50}^{0.038}$
	$e_{max} = 1.05 \cdot e^{(0.45 - 0.9\rho)}; e_{min} = e^{(0.009 - \rho)}$
	$e_{max} = 1.13 \cdot e^{(0.45 - 0.9\rho)} \cdot C_u^{-0.172}; e_{min} = 1.17 \cdot e^{(0.009 - \rho)} \cdot C_u^{-0.241}$

Among these predictive models, the semi-empirical, probability-based relationships suggested by Cetin and Ilgac (2021) are used in this study while estimating the void ratio limits and its range for several reasons:

(i) an extended and well-documented database is taken as the main source for the proposed models,

(ii) the assessment of model prediction uncertainties is being enabled with a probability-based framework,

(iii) series of jointly-regressed models are developed starting with a single input parameter but less precise models, to more precise multi-input parameter models,

(iv) a broader range of soil types extending from non-plastic silts to fine to coarse sand and gravels is allowed to be used in models,

(v) independent predictions for e_{min}, e_{max} and e_{max}-e_{min} are offered,

(vi) the estimations are presented in the form of deterministic chart solutions.

Cetin and Ilgac (2021) defines its extended and well-documented database based on Ilgac et al. (2019), which had significantly benefitted from Cubrinovski and Ishihara (2002), Zheng and Hryciw (2016) and Chen and Kulhawy (2014) studies. The database was compiled from 636 cohesionless soils with coarse-grained soils in general. In addition to unified soil classifications, R, S, FC, D_{50}, C_u, e_{min}, e_{max} and e_{max}-e_{min} data were also listed in this extended database. A complete version of the resulting database is electronically available in Ilgac et al. (2019). Due to lack of documentation, some data are not complete for every one of the 636 cohesionless soils. The database statistics are presented in Table 3.11.

Table 3.11 Ilgac et al. (2019) database statistics (Cetin and Ilgac, 2021)

	Fine Grained	Sand			Gravel	
		Fine	Medium	Coarse	Fine	Medium-Coarse
Number of Soils	19	357	153	17	44	3
	N (# of data points)	Mean	Median	Std. Dev.	Range	
C_u	419	7.38	2.00	26.86	1.1–325.3	
D_{50} (mm)	593	1.30	0.34	3.18	0.0–25.0	
FC %	93	10.10	2.50	17.75	0.0–100.0	
R	171	0.44	0.41	0.20	0.1–1.0	
S	126	0.73	0.72	0.13	0.2–1.0	
e_{min}	179[a] 92[b] 2[c] 186[d] 7[e] 9[f]	0.55	0.55	0.15	0.2–2.2	
e_{max}	202[a] 91[b] 2[c] 186[d] 6[e] 9[f]	0.92	0.91	0.26	0.4–3.0	
e_{max}-e_{min}	179[a] 221[b] 2[c] 186[d] 7[e] 9[f]	0.39	0.36	0.16	0.2–1.5	

[a] ASTM [35,36].
[b] JGS [37].
[c] Indian Standards [39].
[d] Kolbuszewski [40].
[e] Non-Standard Procedures.
[f] NA (Not Available).

The model coefficients for Cetin and Ilgac (2021) study are estimated by maximizing the likelihood functions consistent with the Maximum Likelihood methodology. The finalized forms of the resulting models are presented in Equation 3-33 through Equation 3-65 along with ± one standard deviation, which is also a function of D_{50}, C_u, or both, of the model error term.

Minimum void ratio relationships:

$$Model\ 1: ln(e_{min}) = 162.935 \cdot [ln(D_{50} + 3.336)]^{-0.005} + (-163.236) \pm (-0.357 \cdot exp(-0.376 \cdot D_{50}) + 0.466) \quad \text{Equation 3-33}$$

$$Model\ 2: ln(e_{min}) = 162.935 \cdot [ln(D_{50} + 3.336)]^{-0.005} + (0.001 \cdot (FC)^{1.1} - 163.338) \pm (-0.031 \cdot exp(0.008 \cdot D_{50}) + 0.179)$$ Equation 3-34

$$Model\ 3: ln(e_{min}) = 162.935 \cdot [ln(D_{50} + 3.336)]^{-0.005} + (-0.079 \cdot \ln(R) - 163.603) \pm (0.045 \cdot exp(-0.049 \cdot D_{50}) + 0.137)$$ Equation 3-35

$$Model\ 4: ln(e_{min}) = 162.935 \cdot [ln(D_{50} + 3.336)]^{-0.005} + (-0.079 \cdot ln(R) - 0.496 \cdot \ln(S) - 163.497) \pm (0.125 \cdot exp(-0.008 \cdot D_{50}) - 0.030)$$ Equation 3-36

$$Model\ 5: e_{min} = \frac{0.2767}{1 + 1.6302 \cdot \left(\frac{C_u}{6.3352}\right)^{2.238}} + (0.3243) \pm (-0.3158 \cdot \exp(-0.0369 \cdot C_u) + 0.4352)$$ Equation 3-37

$$Model\ 6: e_{min} = \frac{0.2767}{1 + 1.6302 \cdot \left(\frac{C_u}{6.3352}\right)^{2.238}} + (-0.0796 \cdot \ln(R) + 0.15) \pm (-0.0091 \cdot exp(-0.0088 \cdot C_u) + 0.1479)$$ Equation 3-38

$$Model\ 7: e_{min} = \frac{0.2767}{1 + 1.6302 \cdot \left(\frac{C_u}{6.3352}\right)^{2.238}} + (-0.0796 \cdot ln(R) - 0.2350 \cdot \ln(S) + 0.1864) \pm (0.0897 \cdot exp(0.0493 \cdot C_u) - 0.0219)$$ Equation 3-39

$$Model\ 8: e_{min} = 0.391 \cdot exp(162.935 \cdot [\ln(D_{50} + 3.336)]^{-0.005} - 163.2359) + 0.609 \cdot \left(\frac{0.2767}{1 + 1.6302 \cdot \left(\frac{C_u}{6.3352}\right)^{2.238}} + 0.3243 \right) + (0.0149) \pm (-0.191 \cdot \exp(-1.9676 \cdot D_{50}) + 0.5962 \cdot \exp(0.0027 \cdot C_u) - 0.333)$$ Equation 3-40

$$Model\ 9: e_{min} = 0.391 \cdot exp(162.935 \cdot [ln(D_{50} + 3.336)]^{-0.005} - 163.2359) + 0.609 \cdot \left(\frac{0.2767}{1 + 1.6302 \cdot \left(\frac{C_u}{6.3352}\right)^{2.238}} + 0.3243 \right) + (-0.0022 \cdot (FC)^{0.0002} - 0.029) \pm (0.1225 \cdot exp(-0.2376 \cdot D_{50}) + 0.0443 \cdot exp(-0.1653 \cdot C_u) - 0.0399)$$ Equation 3-41

$$Model\ 10: e_{min} = 0.391 \cdot exp(162.935 \cdot [ln(D_{50} + 3.336)]^{-0.005} - 163.2359) + 0.609 \cdot \left(\frac{0.2767}{1 + 1.6302 \cdot \left(\frac{C_u}{6.3352}\right)^{2.238}} + 0.3243 \right) + (-0.0739 \cdot \ln(R) - 0.1783) \pm (-0.4350 \cdot exp(-0.6003 \cdot D_{50}) + 0.4105 \cdot exp(-1.1725 \cdot C_u) + 0.4346)$$ Equation 3-42

$$Model\ 11: e_{min} = 0.391 \cdot exp(162.935 \cdot [ln(D_{50} + 3.336)]^{-0.005} - 163.2359) + 0.609 \cdot \left(\frac{0.2767}{1 + 1.6302 \cdot \left(\frac{C_u}{6.3352}\right)^{2.238}} + 0.3243 \right) + (-0.0739 \cdot ln(R) - 0.2152 \cdot \ln(S) - 0.1395) \pm (-0.2215 \cdot exp(-0.2314 \cdot D_{50}) - 0.1897 \cdot exp(0.0058 \cdot C_u) + 0.4645)$$ Equation 3-43

Maximum void ratio relationships:

$$Model\ 1: ln(e_{max}) = 155.237 \cdot [ln(D_{50} + 2.39)]^{-0.004} + (-155.22) \pm (-0.144 \cdot exp(-0.631 \cdot D_{50}) + 0.281)$$ Equation 3-44

$$Model\ 2: ln(e_{max}) = 155.237 \cdot [ln(D_{50} + 2.39)]^{-0.004} + (0.001 \cdot (FC)^{1.166} - 155.363) \pm (-0.030 \cdot exp(0.008 \cdot D_{50}) + 0.191)$$ Equation 3-45

$$Model\ 3: ln(e_{max}) = 155.237 \cdot [ln(D_{50} + 2.39)]^{-0.004} + (-0.077 \cdot \ln(R) - 155.606) \pm (0.038 \cdot exp(-0.046 \cdot D_{50}) + 0.095)$$ Equation 3-46

$$Model\ 4: ln(e_{max}) = 155.237 \cdot [ln(D_{50} + 2.39)]^{-0.004} + (-0.077 \cdot ln(R) - 0.408 \cdot \ln(S) - 155.539) \pm (0.114 \cdot exp(-0.006 \cdot D_{50}) - 0.028)$$ Equation 3-47

$$Model\ 5: e_{max} = \frac{0.5961}{1 + 2.2879 \cdot \left(\frac{C_u}{14.3263}\right)^{1.319}} + (0.4598) \pm (-0.0859 \cdot exp(-0.1852 \cdot C_u) + 0.2158)$$ Equation 3-48

$$Model\ 6: e_{max} = \frac{0.5961}{1 + 2.2879 \cdot \left(\frac{C_u}{14.3263}\right)^{1.319}} + (-0.1544 \cdot \ln(R) + 0.1234) \pm (-0.0108 \cdot exp(-0.0097 \cdot C_u) + 0.1493)$$ Equation 3-49

$$Model\ 7: e_{max} = \frac{0.5961}{1 + 2.2879 \cdot \left(\frac{C_u}{14.3263}\right)^{1.319}} + (-0.1544 \cdot ln(R) - 0.3213 \cdot \ln(S) + 0.1473) \pm (0.0545 \cdot exp(0.1583 \cdot C_u) - 0.0144)$$ Equation 3-50

$$Model\ 8: e_{max} = 0.232 \cdot exp(155.237 \cdot [ln(D_{50} + 2.39)]^{-0.004} - 155.22) + 0.768 \cdot \left(\frac{0.5961}{1 + 2.2879 \cdot \left(\frac{C_u}{14.3263}\right)^{2.238}} + 0.4598\right) + (0.0322) \pm (-0.1544 \cdot exp(-2.2536 \cdot D_{50}) + 0.1912 \cdot exp(0.0012 \cdot C_u) + 0.0436)$$ Equation 3-51

$$Model\ 9: e_{max} = 0.232 \cdot exp(155.237 \cdot [ln(D_{50} + 2.39)]^{-0.004} - 155.22) + 0.768 \cdot \left(\frac{0.5961}{1 + 2.2879 \cdot \left(\frac{C_u}{14.3263}\right)^{2.238}} + 0.4598 \right) + (0.1099 \cdot (FC)^{0.0011} - 0.1427) \pm (0.0805 \cdot exp(-0.2359 \cdot D_{50}) + 0.2492 \cdot exp(0.0857 \cdot C_u) - 0.2453)$$ Equation 3-52

$$Model\ 10: e_{max} = 0.232 \cdot exp(155.237 \cdot [ln(D_{50} + 2.39)]^{-0.004} - 155.22) + 0.768 \cdot \left(\frac{0.5961}{1 + 2.2879 \cdot \left(\frac{C_u}{14.3263}\right)^{2.238}} + 0.4598 \right) + (-0.1340 \cdot \ln(R) - 0.3125) \pm (-0.7796 \cdot exp(-0.2573 \cdot D_{50}) + 0.1949 \cdot exp(-0.0297 \cdot C_u) + 0.6364)$$ Equation 3-53

$$Model\ 11: e_{max} = 0.232 \cdot exp(155.237 \cdot [ln(D_{50} + 2.39)]^{-0.004} - 155.22) + 0.768 \cdot \left(\frac{0.5961}{1 + 2.2879 \cdot \left(\frac{C_u}{14.3263}\right)^{2.238}} + 0.4598 \right) + (-0.1340 \cdot ln(R) - 0.3437 \cdot \ln(S) + 0.3022) \pm (0.0828 \cdot exp(-0.1272 \cdot D_{50}) + 0.5234 \cdot exp(0.0288 \cdot C_u) - 0.5741)$$ Equation 3-54

Void ratio range relationships:

$$Model\ 1: ln(e_{max} - e_{min}) = 122.293 \cdot [ln(D_{50} + 0.989)]^{-0.002} + (-123.527) \pm (0.111 \cdot exp(-0.147 \cdot D_{50}) + 0.142)$$ Equation 3-55

$$Model\ 2: ln(e_{max} - e_{min}) = 122.293 \cdot [ln(D_{50} + 0.989)]^{-0.002} + (0.0001 \cdot (FC)^{1.1} - 123.658) \pm (-0.035 \cdot exp(0.008 \cdot D_{50}) + 0.349)$$ Equation 3-56

$$Model\ 3: ln(e_{max} - e_{min}) = 122.293 \cdot [ln(D_{50} + 0.989)]^{-0.002} + (-0.167 \cdot \ln(R) - 123.972) \pm (0.045 \cdot exp(-0.05 \cdot D_{50}) + 0.098)$$ Equation 3-57

$$Model\ 4: ln(e_{max} - e_{min}) = 122.293 \cdot [ln(D_{50} + 0.989)]^{-0.002} + (-0.167 \cdot ln(R) - 0.317 \cdot \ln(S) - 123.945) \pm (0.196 \cdot exp(-0.015 \cdot D_{50}) - 0.029)$$ Equation 3-58

$$Model\ 5: e_{max} - e_{min} = \frac{0.2048}{1 + 1.2024 \cdot \left(\frac{C_u}{10.3226}\right)^{1.875}} + (0.1993) \pm (0.26 \cdot exp(-0.016 \cdot C_u))$$ Equation 3-59

$$Model\ 6: e_{max} - e_{min} = \frac{0.2048}{1 + 1.2024 \cdot \left(\frac{C_u}{10.3226}\right)^{1.875}} + (-0.0989 \cdot \ln(R) + 0.0211) \pm (-0.009 \cdot exp(-0.009 \cdot C_u) + 0.1883)$$ Equation 3-60

$$Model\ 7: e_{max} - e_{min} = \frac{0.2048}{1 + 1.2024 \cdot \left(\frac{C_u}{10.3226}\right)^{1.875}} + (-0.0989 \cdot ln(R) - 0.0528 \cdot \ln(S) + 0.0299) \pm (0.1673 \cdot exp(0.0326 \cdot C_u) - 0.0212)$$ Equation 3-61

$$Model\ 8: e_{max} - e_{min} = 0.229 \cdot exp(122.293 \cdot [ln(D_{50} + 0.989)]^{-0.002} - 123.5274) + 0.771 \cdot \left(\frac{0.2048}{1 + 1.2024 \cdot \left(\frac{C_u}{10.3226}\right)^{1.8754}} + 0.1993\right) + (0.0058) \pm (0.3370 \cdot exp(-0.0043 \cdot D_{50}) - 0.2944 \cdot exp(0.0026 \cdot C_u) + 0.1782)$$ Equation 3-62

$$Model\ 9: e_{max} - e_{min} = 0.229 \cdot exp(122.293 \cdot [ln(D_{50} + 0.989)]^{-0.002} - 123.5274) + 0.771 \cdot \left(\frac{0.2048}{1 + 1.2024 \cdot \left(\frac{C_u}{10.3226}\right)^{1.8754}} + 0.1993 \right) + (0.1027 \cdot (FC)^{0.0005} - 0.1060) \pm (0.413 \cdot exp(-0.2347 \cdot D_{50}) + 0.4504 \cdot exp(0.0825 \cdot C_u) - 0.3270) \quad \text{Equation 3-63}$$

$$Model\ 10: e_{max} - e_{min} = 0.229 \cdot exp(122.293 \cdot [ln(D_{50} + 0.989)]^{-0.002} - 123.5274) + 0.771 \cdot \left(\frac{0.2048}{1 + 1.2024 \cdot \left(\frac{C_u}{10.3226}\right)^{1.8754}} + 0.1993 \right) + (-0.0862 \cdot \ln(R) - 0.1679) \pm (-0.4826 \cdot exp(-0.3017 \cdot D_{50}) + 0.2718 \cdot exp(-0.0213 \cdot C_u) + 0.3291) \quad \text{Equation 3-64}$$

$$Model\ 11: e_{max} - e_{min} = 0.229 \cdot exp(122.293 \cdot [ln(D_{50} + 0.989)]^{-0.002} - 123.5274) + 0.771 \cdot \left(\frac{0.2048}{1 + 1.2024 \cdot \left(\frac{C_u}{10.3226}\right)^{1.8754}} + 0.1993 \right) + (-0.0862 \cdot ln(R) - 0.0717 \cdot \ln(S) - 0.1601) \pm (-0.6017 \cdot exp(-0.086 \cdot D_{50}) + 0.2604 \cdot exp(0.0381 \cdot C_u) + 0.4288) \quad \text{Equation 3-65}$$

The limits of the model input parameters are given in Equation 3-66. For the cases when input parameters are close to these limits, it is suggested to be careful while using the proposed expressions. Furthermore, any extrapolation beyond these limits is not recommended.

$$Limits: 0.1 \leq R \leq 1.0\,;\, 0.25 \leq S \leq 1.0\,;\, 0 \leq FC(\%) \leq 100; 0.01 \leq D_{50}(mm) \leq 25; 1.0 \leq C_u \leq 300 \quad \text{Equation 3-66}$$

As discussed in the previous parts of this section, the particle grain size, distribution, shape, and fabric are fundamental parameters determining the void ratio limits and their range for cohesionless soils. To be able to develop a probability-based predictive model for post-liquefaction strength of such soils using the void ratio-effective stress domain, the initial void ratios are estimated for all case histories. While doing that, both the loosest (i.e., maximum void ratio, e_{max}) and the densest (i.e., minimum void ratio, e_{min}) states of the soils are determined using Equation 3-33 through Equation 3-65. It should be noted that there are 11 models available separately for estimating e_{min}, e_{max} and e_{max}-e_{min}, and each of these models uses a variety combination of five input parameters, R, S, FC, D_{50}, C_u. An explanation of which predictive model uses which parameter(s) is tabulated in Table 3.12.

Table 3.12 Parameters used by predictive models for void ratio limits and range

e_{min}, e_{max} and e_{max}-e_{min}	Model 1	D_{50}
	Model 2	D_{50}, FC
	Model 3	D_{50}, R
	Model 4	D_{50}, R, S
	Model 5	C_u
	Model 6	C_u, R
	Model 7	C_u, S
	Model 8	C_u, D_{50}
	Model 9	C_u, D_{50}, FC
	Model 10	C_u, D_{50}, R
	Model 11	C_u, D_{50}, R, S

For each case history, maximum void ratio (e_{max}), minimum void ratio (e_{min}) and void ratio range (e_{max}-e_{min}) are estimated by using corresponding predictive models for available parameters. As already discussed in Section 3.1, these liquefaction-triggered failures were observed several decades ago, even some of them occurred at times when the liquefaction phenomenon was not well-studied. Therefore, roundness, sphericity, fines content, mean grain size, and coefficient of uniformity data are not complete for all of them. In fact, some of these parameters are considered directly as reported in the source documents due to lack of documentation. Even, some of these parameters are missing for some case histories, as already discussed in Section 3.2. Hence, the limit void ratios and void ratio ranges are estimated by taking the arithmetic mean of specific models including available parameters.

In general, 36 case histories selected in this study are divided into two groups during the evaluation of limit void ratios and void ratio ranges. Since roundness and sphericity values are missing (only two cases have representative roundness values), and mean grain size and fines content values are available for almost all case histories, the coefficient of uniformity is selected as the separator parameter between these two groups of case histories. While the first group consists of the case histories with missing coefficient of uniformity values, the second one includes the cases with available coefficient of uniformity values. For the first group cases with missing C_u values, D_{50} and fines content are selected as the key parameters, and the arithmetic means of the limit void ratios and void ratio ranges evaluated by Model 1 and Model 2 are considered as the representative values. For the second group of case histories that consists of the cases with available C_u values, D_{50}, fines content and C_u are selected as the key parameters, and the arithmetic means of the limit void ratios and void ratio ranges evaluated by Model 8 and Model 9 are considered as the representative values. For the single specific case history, Helsinki Harbor (Case history #: 16), the fines content value was not reported in addition to the coefficient of uniformity value. Hence, the limit void ratios and void ratio range are estimated by only considering Model 1 for this special case history.

For example, both FC, D_{50} and C_u values are available for Case History #2: Fort Peck Dam as tabulated in Table 3.4; therefore, the arithmetic mean of Model 8 and Model 9 are considered while determining the limit void ratios and void ratio range for this case history. On the other hand, the coefficient of uniformity data was not reported for Case History #1: Wachusett Dam North Dike as shown in Table 3.4; thus, the arithmetic mean of Models 1 and Model 2 are taken as representative for limit void ratios and void ratio range.

It should be noted that, as already discussed in Section 3.2, there are different definitions of roundness and sphericity available in the literature, and an accurate differentiation among these available definitions could not be made due to lack of documentation in the source of references. In this study, the roundness definition proposed by Cho et al. (2006), whose details are explained in Section 3.2, is used. On the other hand, the importance of fabric was not well-understood in the years when some of these liquefaction-triggered failures occurred; therefore, the fabric information for most of the cases was not reported properly. As a result, representative roundness and sphericity values could not be assigned for most of the case histories. For exceptional 2 cases, Tar Island Dyke and Whiskey Springs Fan (Case history #: 23, 35), the liquefied zones were reported as consisting of mainly "subangular" materials in primary source references. Several research studies on surface roughness and shape of soil particles recommend common roundness ranges for subangular materials. Russell and Taylor (1937) suggests a roundness range of 0.15-0.30 for subangular materials. Similarly, Pettijohn (1949) also recommends a roundness range of 0.15-0.25 for subangular types of materials. A more popular and commonly used study, Powers (1953), provides a range of 0.25-0.35 for the roundness of subangular materials. Cho et al. (2006) also suggests a roundness range of 0.20-0.40 for subangular materials. Referring to these sources, the roundness values of these two special cases are estimated as 0.30, and the corresponding void ratio prediction models including the effect of roundness are also considered in order to award the documented roundness information.

In this study, a tiny modification is applied for the maximum void ratios of the case histories referring to Ishihara (1996). As presented in Figure 3.23, it is observed that the maximum void ratios corresponding to the loosest possible states of packing change slightly with respect to the type of the preparation method. Therefore, the case history database used in this study is also divided into four separate groups referring to these types of preparation methods, and each type of preparation method is assigned to a corresponding construction method of the case histories. As it can be seen from Figure 3.23, while larger e_{max} values are obtained for the moist placement method, lower values are observed for dry deposition and water sedimentation methods.

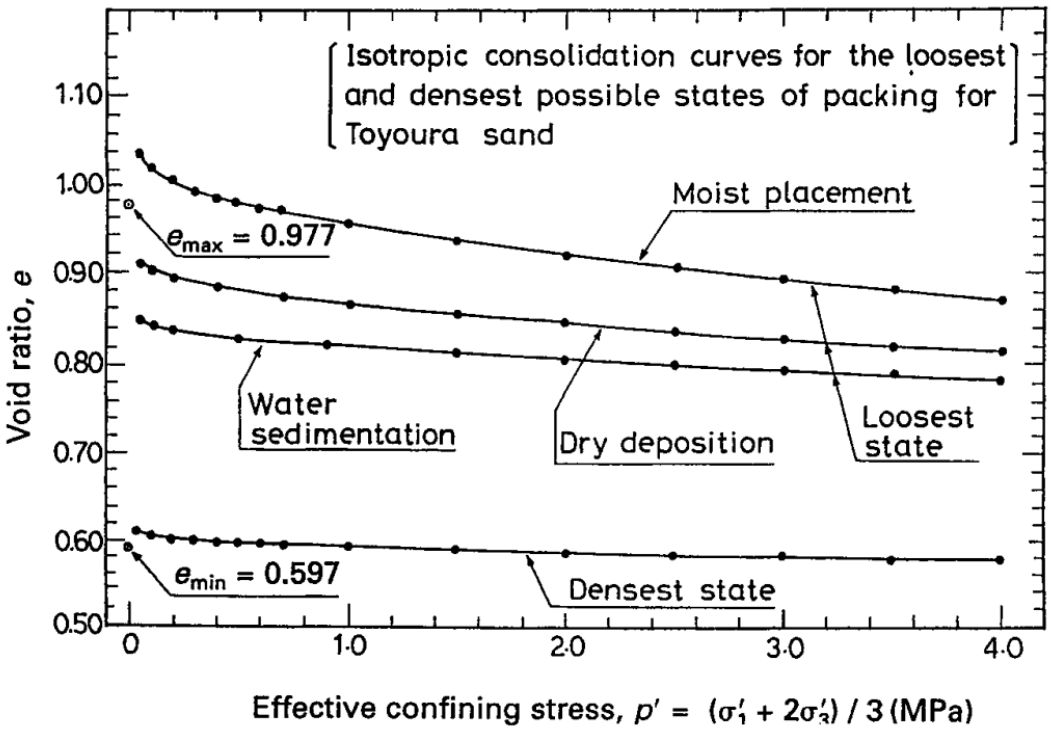

Figure 3.23. Isotropic compression curves of samples of Toyoura sand prepared by three different methods (Ishihara, 1996)

17 of the 36 case histories (Case history #: 1, 3, 5, 6, 7, 8, 10, 12, 13, 15, 18, 20, 29, 30, 34, 35, 36) were comprised of well or poorly compacted materials in the zone of liquefaction; therefore, these case histories are considered as Group 1, and matched

with the original location of the e_{max}. 14 of the 36 case histories (Case history #: 2, 4, 16, 19, 21, 22, 23, 24, 25, 26, 27, 28, 31, 33) were comprised of structures that were constructed by the hydraulic fill method; thus, these case histories are considered as Group 2, and matched with the moist placement type of preparation method. 8 of the 36 case histories (Case history #: 9, 14, 17, 21, 23, 24, 25, 32) were comprised of soil layers that formed as a result of the water sedimentation method; hence, these case histories are considered as Group 3, and matched with the water sedimentation type of preparation method. Finally, 1 of the 36 case histories (Case history #: 11) was comprised of dry deposit materials in the zone of liquefaction; therefore, it is considered as Group 4, and matched with the dry deposition type of preparation method. It should be noted that since some of the tailings type of case structures (#21, 23, 24 and 25) are both constructed with the hydraulic fill method and consist of materials that formed as a result of water sedimentation, they are both included in Group 2 and Group 3 case histories.

The maximum void ratio values evaluated by Equation 3-44 through Equation 3-54 are modified slightly by multiplying them with a constant value ranging between ~ 0.90-1.15. This constant value is evaluated with respect to the construction methods of the groups stated above, which refers to the fabric of the soils in fact. On the other hand, the fabric is not the only factor affecting the compressibility and maximum void ratio of soils. Therefore, these constant values are estimated for each group based on the probabilistic regressions by the Maximum Likelihood Method, which will be discussed in Chapter 4 in detail.

In the end, the database represented in Table 3.13, which consists of minimum and maximum void ratios and their range, is compiled by using available parameters (particle morphology (roundness and sphericity), and size and distribution (mean grain size, fines content and coefficient of uniformity)) of case histories. It should be noted that the maximum void ratios, and therefore the void ratio ranges, reported in this table are unmodified values with respect to construction methods because the modification factors differ with respect to construction method types for different

prediction models based on the probabilistic regressions by the Maximum Likelihood Method.

Table 3.13 Summary of estimated limit void ratios and void ratio ranges for case histories

#	Case History	FC (%)	D_{50} (mm)	C_u	e_{min}	e_{max}	e_{max}-e_{min}
1	Wachusett Dam - North Dike	7.5	0.420		0.563	0.935	0.372
2	Fort Peck Dam	4	0.280	2.31	0.569	0.971	0.402
3	Uetsu Railway Embankment	1	0.340	2.57	0.561	0.958	0.397
4	Lower San Fernando Dam - U/S Slope	53	0.070	31.49	0.398	0.593	0.195
5	Hachiro-Gata Road Embankment	18	0.181		0.591	0.997	0.406
6	La Marquesa Dam - U/S Slope	30	0.150		0.600	1.017	0.417
7	La Marquesa Dam - D/S Slope	20	0.150		0.595	1.007	0.412
8	La Palma Dam	15	0.200		0.588	0.990	0.402
9	Lake Ackerman Highway Embankment	1	0.390	2.50	0.561	0.958	0.397
10	Chonan Middle School	18	0.200		0.589	0.992	0.403
11	Soviet Tajik - May 1 Slide	100	0.013	6.00	0.506	0.874	0.368
12	Shibecha-Cho Embankment	20	0.200	9.71	0.461	0.790	0.329
13	Route 272 at Higashiarekinai	20	0.200		0.590	0.994	0.404
14	Zeeland - Vlietepolder	7	0.130	1.81	0.585	0.999	0.414
15	Sheffield Dam	40	0.100		0.610	1.041	0.431
16	Helsinki Harbor		0.100		0.623	1.077	0.453
17	Solfatara Canal Dike	7	0.170	2.22	0.576	0.981	0.405
18	Lake Merced Bank	3	0.210	1.92	0.580	0.990	0.410
19	El Cobre Tailings Dam	93	0.080		0.640	1.113	0.473
20	Metoki Road Embankment	15	0.120		0.597	1.011	0.414
21	Hokkaido Tailings Dam	50	0.075	1.50	0.593	1.015	0.422
22	Upper San Fernando Dam - D/S Slope	47.5	0.070	31.49	0.437	0.666	0.229
23	Tar Island Dyke	12.5	0.150		0.552	0.931	0.380
24	Mochi-Koshi Tailings Dam 1	81	0.038	16.97	0.447	0.726	0.279
25	Mochi-Koshi Tailings Dam 2	74	0.042	18.15	0.445	0.718	0.273
26	Nerlerk Embankment Slide 1	7.5	0.220	1.85	0.580	0.992	0.411
27	Nerlerk Embankment Slide 2	7.5	0.220	1.85	0.580	0.992	0.411

Table 3.13 (cont'd) Summary of estimated limit void ratios and void ratio ranges for case histories

28	Nerlerk Embankment Slide 3	7.5	0.220	1.85	0.580	0.992	0.411
29	Asele Road Embankment	30	0.276	3.51	0.543	0.929	0.386
30	Nalband Railway Embankment	28	1.629	909.10	0.387	0.546	0.160
31	Sullivan Tailings	50	0.090		0.616	1.055	0.439
32	Jamuna Bridge	6	0.150		0.590	0.995	0.406
33	Calaveras Dam	30	0.732		0.545	0.898	0.353
34	Koda Numa Railway Embankment	13	0.180	8.70	0.469	0.807	0.339
35	Whiskey Springs Fan	31.5	1.613	455.33	0.360	0.497	0.138
36	San Fernando Valley Juvenile Hall	63	0.055	17.10	0.446	0.724	0.278

Accordingly, the minimum void ratio, maximum void ratio, and void ratio range distributions of the case history database are obtained as given in Figure 3.24, Figure 3.25, and Figure 3.26, respectively.

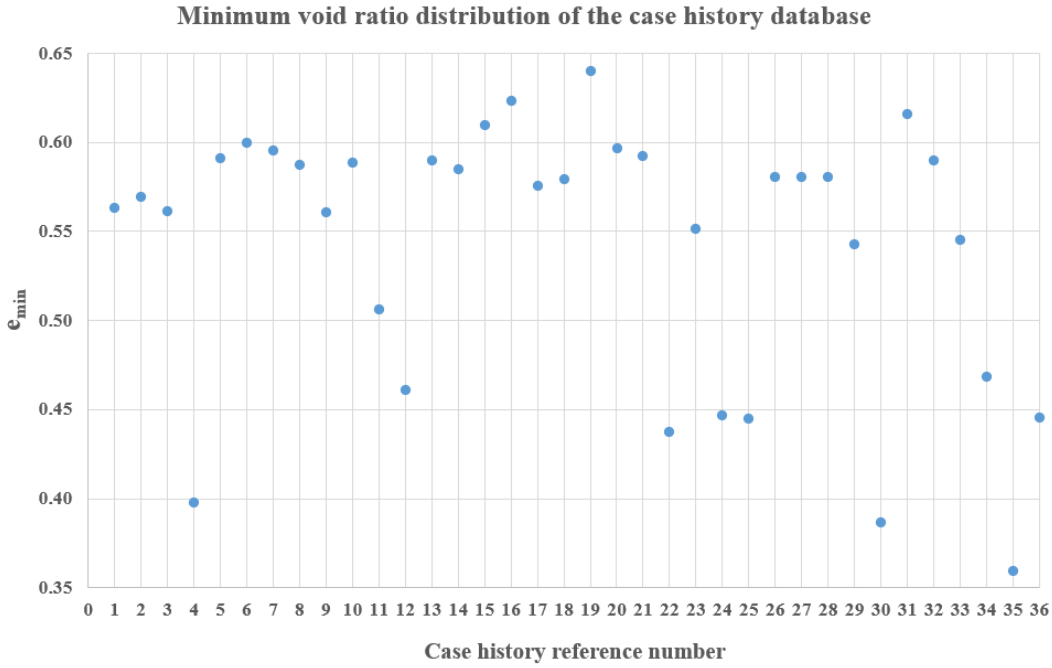

Figure 3.24. Minimum void ratio distribution of the case history database

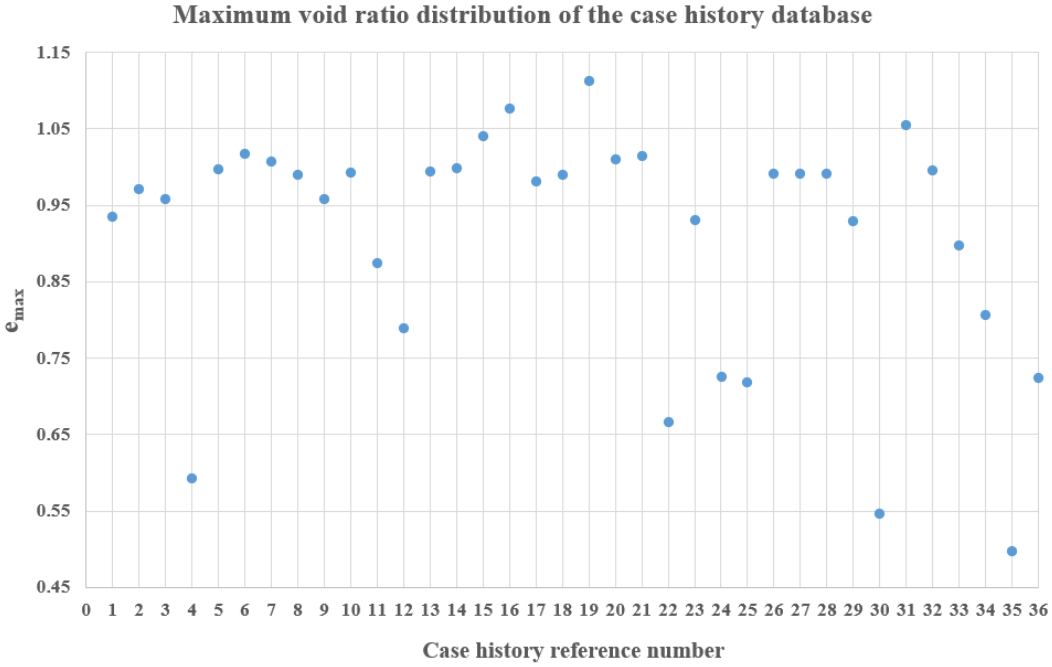

Figure 3.25. Maximum void ratio distribution of the case history database

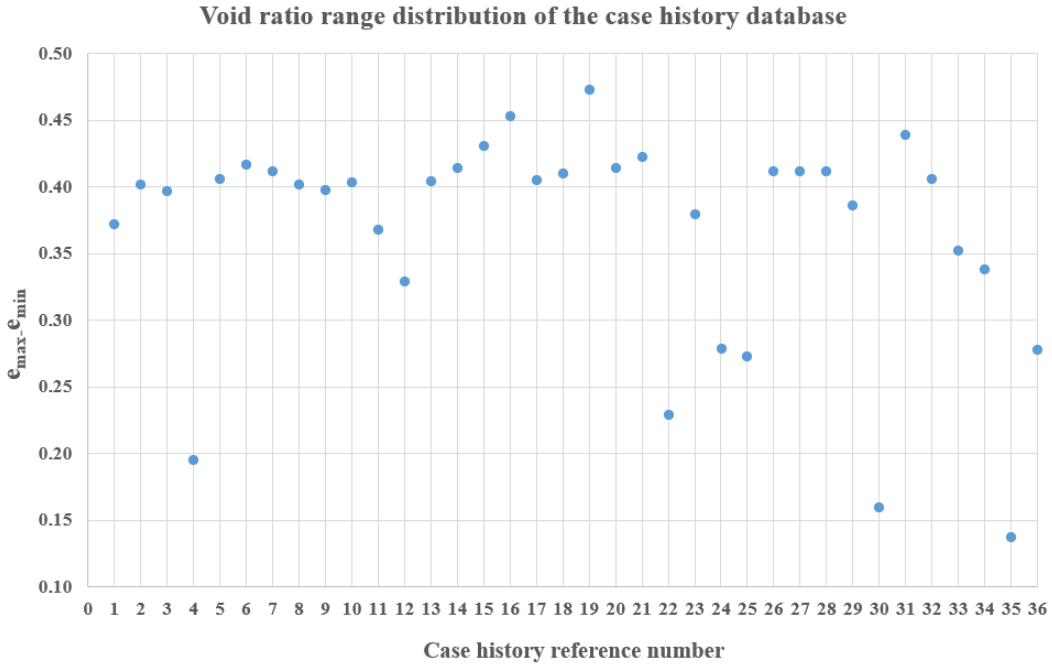

Figure 3.26. Void ratio range distribution of the case history database

3.7 Estimation of Relative Density and Initial Void Ratios

As already discussed in the previous section, the assessment of the initial void ratio is a crucial part of the critical state concept. Equation 3-67 shows that the initial void ratio of soils depends on void ratio limits, void ratio range, and relative density by definition.

$$RD(\%) = \frac{e_{max} - e}{e_{max} - e_{min}} \cdot 100 \qquad \text{Equation 3-67}$$

In this equation, while e_{max} and e_{min} represent the loosest (i.e.: maximum void ratio) and the densest (i.e.: minimum void ratio) states of soil, respectively, e symbolizes the initial void ratio of the soil. Therefore, in addition to limit void ratios e_{max} and e_{min}, relative density state is also necessary to estimate the initial void ratio. Arranging Equation 3-67, the initial void ratio (corresponding to 1 kPa confining stress approximately) of soils can be estimated as shown in Equation 3-68.

$$e = e_{max} - \left[\frac{RD(\%)}{100} \cdot (e_{max} - e_{min})\right] \qquad \text{Equation 3-68}$$

As discussed more detailly in the previous section, the difficulties in undisturbed sampling of cohesionless soils are widely known. Hence, correlations with in-situ test penetration resistances are commonly used to determine in-situ density states of cohesionless soils. Cubrinovski and Ishihara (1999, 2001), Haldar and Miller (1984), Selig and Ladd (1973), Juang et al. (1996), and Igwe et al. (2012) are some of the common studies focused on these relationships. Among in-situ penetration tests, the Standard Penetration Test (SPT) and Cone Penetration Test (CPT) are the most popular ones in engineering practice. In literature, there are several penetration resistance versus relative density relationships available such that SPT or CPT penetration resistances are used to estimate the relative density state of cohesionless soils after a series of corrections and normalizations. In general, previous studies on this topic have compromised that in-situ test penetration resistance is a good representation of relative density, and it is wise to use penetration resistance versus

relative density relationships for estimating in-situ density states of cohesionless soils as long as the relationship is well-prepared and trustworthy. Although these tests are used commonly in engineering practice, different approaches have been adopted by different researchers, and some of these differences in methodology rise from the understanding of penetration tests and factors affecting the test results. In fact, the database compiled has a significant effect on the developed relative density estimation relationships as it allows the relationship to be statistically more stable, accurate and precise. The methods using newer and larger databases are generally judged to be more credible as they include test results of more soils of different geologic origins, stress histories, and mineralogies.

Since the reported penetration test results are mostly obtained from the Standard Penetration Test for selected case histories, and there are lots of empirical and semi-empirical correlations available in the literature to convert other types of penetration resistances to SPT resistances, it is judged that relative density versus SPT penetration resistance correlations are more suitable for this study.

Although the early work performed on this topic simply correlated the SPT-N value directly with relative density, later laboratory research demonstrated that the overburden stress significantly affects the SPT-N value. Gibbs and Holtz (1957) and Holtz and Gibbs (1979) claim the effect of overburden stress and SPT-N value on relative density as shown in Figure 3.27a and Figure 3.27b, respectively.

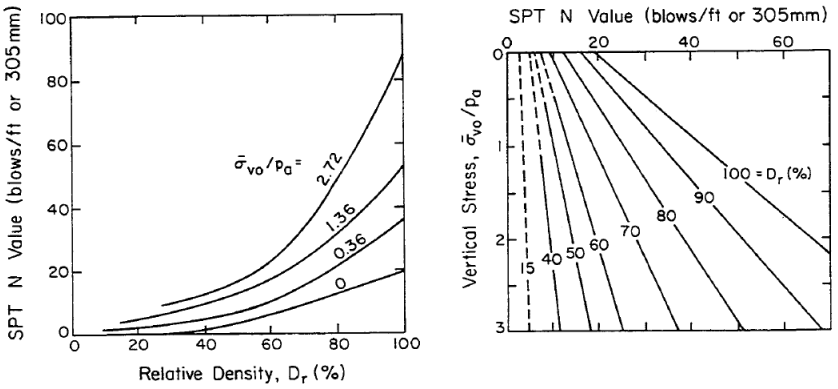

Figure 3.27. Effect of overburden stress and SPT-N value on relative density ((a) Gibbs and Holtz, 1957 and (b) Holtz and Gibbs, 1979)

Further research showed that these relationships are even more complex, and many other factors affect this relationship, such as stress history, soil type, etc. A series of studies showing some of these complexities are summarized by Marcuson and Bieganousky (1977), and represented in Figure 3.28.

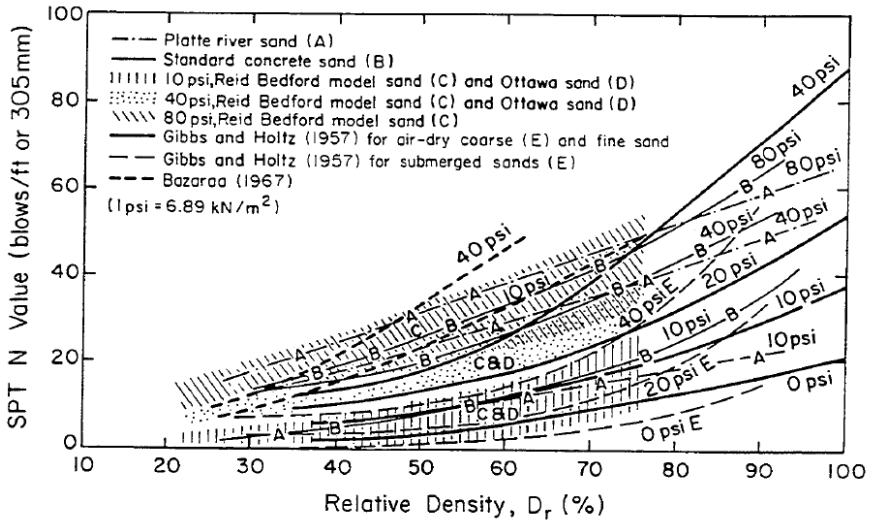

Figure 3.28. Relative density-SPT-N-stress relationships for several sands (Marcuson and Bieganousky, 1977)

The correlation for estimating relative density from SPT-N value given in Equation 3-69 is shown up referring to the studies presented in Figure 3.28. The correlation also includes the effect of overburden stress (σ_{v0}), particle size distribution (C_u), and stress history (OCR= σ_p/σ_{v0}).

$$RD(\%) = 12.2 + 0.75 \cdot \left[222 \cdot N + 2311 - 711 \cdot OCR - 779 \cdot \left(\frac{\sigma_{v0}}{p_a}\right) - 50 \cdot C_u^2\right]^{0.5} \qquad \text{Equation 3-69}$$

Following studies also showed that instead of using raw SPT-N value, a corrected value for field procedures and overburden stress should be used in these correlations for better representation and normalization. Skempton (1986) reviewed SPT calibration data from the USA, the UK, Japan, and China, and recommended some correction factors based on standard practice in these countries. These correction factors focus on the energy efficiency of the drop hammer onto the drill rods and include the effects of the type of hammer, age of the rope, size of the borehole, and

use of liners in the split spoon sampler. To eliminate the differences in SPT resistance determination standards and procedures, the hammers are corrected to a constant energy ratio (60%). Equation 3-70 gives the N_{60} value corrected for field procedures to an average energy ratio of 60%, where N represents the measured SPT-N value, and C_R, C_S, C_B and C_E represent the correction factors for rod length, sampling method, borehole diameter and energy ratio, respectively.

$$N_{60} = N \cdot C_R \cdot C_S \cdot C_B \cdot C_E \qquad \text{Equation 3-70}$$

The values suggested by Skempton (1986) for these correction factors are tabulated in Table 3.14. Alternative recommended values by other studies, the values employed in this study, and detailed explanations are already discussed in Section 3.5 during the explanation of the evaluation of SPT resistances for case histories. In this study, although these parameters are not documented well for many of the case histories, they are employed based on the values recommended by Cetin et al. (2004) and the NCEER Working Group (NCEER 1997) as given in Table 3.8.

Table 3.14 SPT correction factors for field procedures (Skempton, 1986)

Factor	*Equipment Variables*	*Correction*	
		Term	*Value*
Energy ratio	Safety hammer	C_E	0.90
	Donut hammer		0.75
Borehole diameter	65 to 115 mm (2.5 to 4.5 in)	C_B	1.00
	150 mm (6 in)		1.05
	200 mm (8 in)		1.15
Sampling method	Standard sampler	C_S	1.00
	Sampler without liner		1.20
Rod length	> 10 m (> 30 ft)	C_R	1.00
	6 to 10 m (20 to 30 ft)		0.95
	4 to 6 m (13 to 20 ft)		0.85
	3 to 4 m (10 to 13 ft)		0.75

In addition to the corrections for field procedures, overburden stress correction is also used to provide a consistent representation for SPT resistance as the SPT-N value also varies with stress level. Equation 3-71 gives the $(N_1)_{60}$ value corrected to a reference stress of one atmosphere, where N_{60} represents the value corrected for field procedures to an average energy ratio of 60%, and C_N represents the correction factor for overburden stress.

$$(N_1)_{60} = C_N \cdot N_{60} \qquad \text{Equation 3-71}$$

As already discussed detailly in Section 3.5, there are several expressions available for overburden stress correction in literature. A summary of these corrections provided by different studies is represented in Figure 3.29.

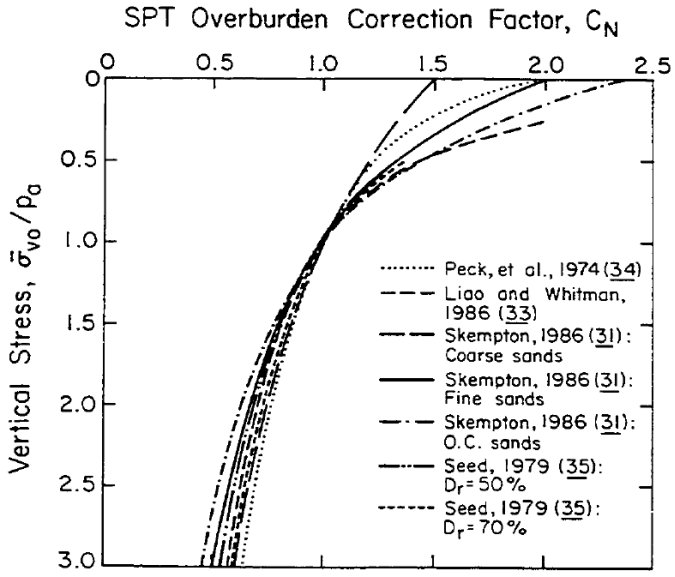

Figure 3.29. Comparison of SPT overburden corrections, C_N (Kulhawy and Mayne, 1990)

In this study, the overburden correction factor, C_N, is evaluated based on Equation 3-72, where σ'_{v0} symbolizes the effective vertical stress at penetration depth in the units of kilopascals.

$$C_N = \frac{9.78}{\sqrt{\sigma'_{v0}}} \qquad \text{Equation 3-72}$$

Once the measured SPT-N value, i.e., raw SPT-N, is corrected for field procedures and overburden effects, it can be used to estimate the relative density of soil as a function of its characteristics. It should be noted that the fines content of the soil has also an impact on the penetration resistances, and this impact should be considered during the evaluation of in-situ relative densities. On the other hand, a separate fines content correction to $(N_1)_{60}$ values is not required for relative density estimations as the effect of fines content is already included in the other parameters in relative density prediction relationships, such as mean grain size (D_{50}) and void ratio range (e_{max}-e_{min}), that will be discussed next.

Two widely known SPT-N correlations, Kulhawy and Mayne (1990) and Cubrinovski and Ishihara (1999), are used to estimate the relative density of liquefaction triggered case history failures in this study. While the relationship suggested by Kulhawy and Mayne (1990) is applicable for sands in general, the one recommended by Cubrinovski and Ishihara (1999) is useful for both sands and silts. Inspired of that, the overall representative relative density values are taken as the arithmetic mean of the values obtained by these two methods for the cases with fines content of less than 15%. For the case histories including more than 15% fine-grained soils (silty soils), the overall representative relative density values are directly taken as same to the values obtained by Cubrinovski and Ishihara (1999). These two methods are explained below in detail.

Kulhawy and Mayne (1990):

The study states that the ratio between the $(N_1)_{60}$ value and the square of the relative density, $\frac{(N_1)_{60}}{RD^2}$, is a function of soil particle size (D_{50}), i.e., mean grain size, and suggests Equation 3-73 for normally consolidated (NC), unaged sands. It compares its estimations with Skempton (1986) and claims that Skempton's interpretation underestimates the value of $\frac{(N_1)_{60}}{RD^2}$ for same D_{50} value as shown in Figure 3.30. The study re-evaluates the original data obtained from Bieganousky and Marcuson (1976, 1977) by considering both Skempton (1986)'s linearized overburden effect and Liao

and Whitman (1986)'s nonlinear overburden effect, and suggests the correlation given in Equation 3-73.

$$\frac{(N_1)_{60}}{RD^2} = 60 + 25 \cdot \log(D_{50}) \qquad \text{Equation 3-73}$$

The study declares that the laboratory data given in Figure 3.30 were obtained from studies at the Waterways Experiment Station (WES) on three sands, where most of the data were obtained from unaged, normally consolidated sands (OCR=1). However, a small series of tests were also conducted on overconsolidated sands with OCR=3. In the end, it is summarized that Equation 3-73 is applicable for NC, unaged sands, whereas OC or aged sands would give higher values.

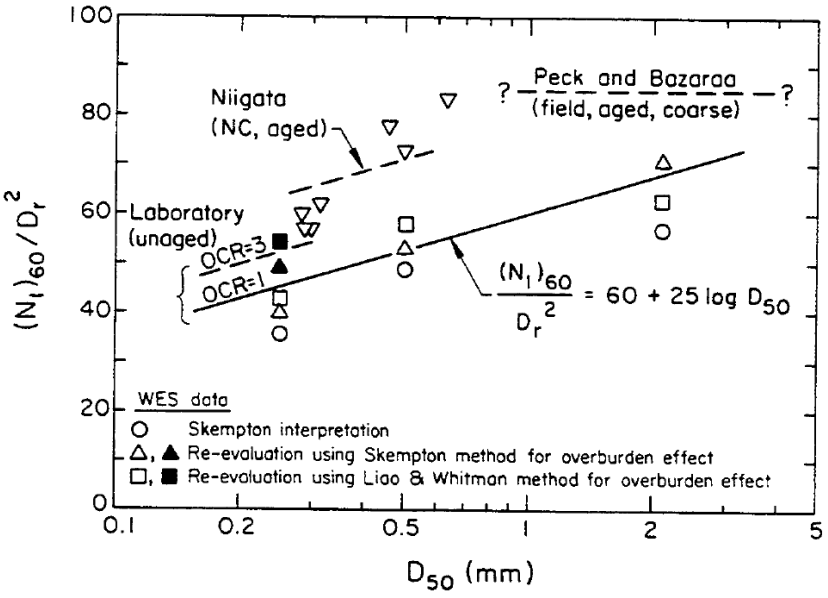

Figure 3.30. Mean grain size (D_{50}) effect on $(N_1)_{60}/RD^2$ ratio for sands (Kulhawy and Mayne, 1990)

Kulhawy and Mayne (1990) also states that aging and over consolidation have significant influences on $\frac{(N_1)_{60}}{RD^2}$ ratio, and it quantifies these effects as given in Equation 3-74.

$$RD^2 = \frac{(N_1)_{60}}{C_P \cdot C_A \cdot C_{OCR}}$$ Equation 3-74

In this equation, C_P represents particle size effects based on Figure 3.30, C_A represents aging effects based on a conservative interpretation of the imprecise data in Figure 3.31, and C_{OCR} represents over consolidation effects based on direct evaluation of the WES data. Equations for these correction factors are given in Table 3.15.

Table 3.15 SPT correction factors for sand variables such as particle size, aging and over consolidation (Kulhawy and Mayne, 1990)

Effect	*Parameter*	*Correction*	
		Term	*Value*
Particle size	D_{50} of sand (mm)	C_P	$60 + 25 \cdot \log(D_{50})$
Aging	Time (t)	C_A	$1.2 + 0.05 \cdot \log(t/100)$
Overconsolidation	$OCR = \sigma'_p/\sigma'_{v0}$	C_{OCR}	$OCR^{0.18}$

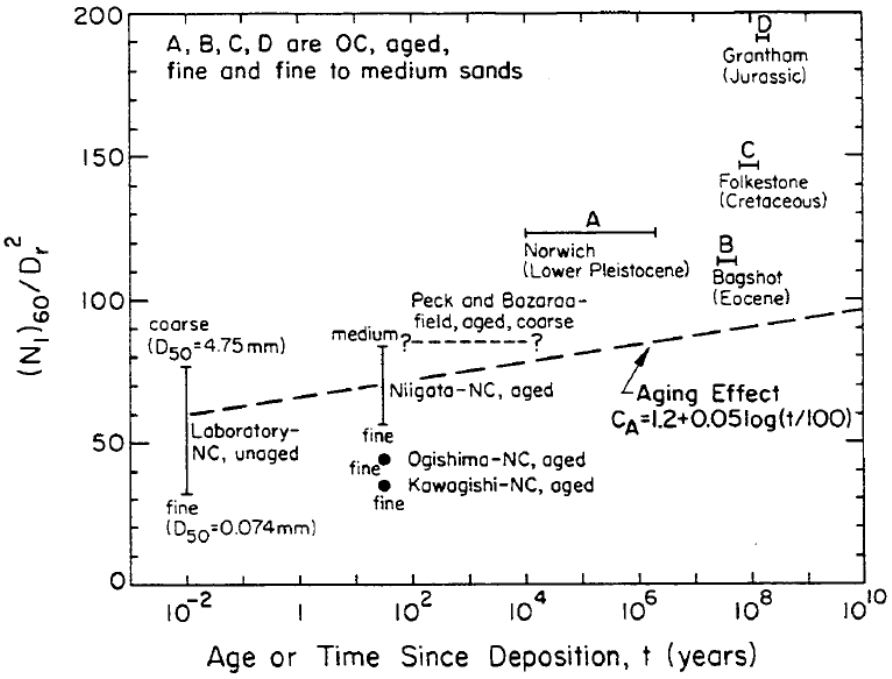

Figure 3.31. Aging effect on $(N_1)_{60}/RD^2$ ratio for sands (Kulhawy and Mayne, 1990)

Figure 3.31 illustrates the data provided in Figure 3.30 as a function of the age of the deposits. The Niigata, Ogishima and Kawagishi data represent normally consolidated fills with ages of 30-40 years approximately, and they are summarized by Skempton (1986). The age of Peck and Bazaraa data is estimated as 100-10000 years since the time is not known exactly for this overconsolidated, aged sand. The other four sites, namely A, B, C and D represent overconsolidated, aged, fine, and fine to medium sands of four geologic periods, and they are given by Barton et al. (1988).

In this study, since over consolidation and aging properties of case histories are not documented well, the effects of these factors are not considered in relative density evaluations, and Equation 3-73, which only includes the effect of particle size, is used in calculations.

Cubrinovski and Ishihara (1999):

The study states that the ratio between the normalized N-value and the square of the relative density, $\frac{N_1}{RD^2}$, is dependent on the grain size of sands, such that this dependency is also declared by the previous investigations focusing on the link between the penetration resistance and relative density. The study correlates the penetration resistance and relative density by accounting for the grain size properties of soils, and uses the void ratio range (e_{max}-e_{min}) as a measure indicative of the grain size and grain size composition. Cubrinovski and Ishihara (2002) also states that void ratio range provides a general basis for comparative evaluation of material properties, and it is well indicative of the overall grain size composition and particle characteristics of given sand.

It claims that the void ratio range has a crucial effect on $\frac{N_1}{RD^2}$ ratio, and this ratio gradually decreases with increasing e_{max}-e_{min} range. To establish this empirical correlation, the study suggests a mathematical formulation between the SPT-N value corrected to a reference stress of one atmosphere and for field procedures to an average energy ratio of 78%, and relative density as given in Equation 3-75.

$$RD(\%) = \sqrt{\frac{(N_1)_{78} \cdot (e_{max} - e_{min})^{1.7}}{9}} \cdot 100 \qquad \text{Equation 3-75}$$

The study declares that this correlation is developed by using data from high-quality undisturbed samples and SPT measurement results on natural deposits of sandy soils and gravels. Hence, it claims that this correlation is valid for various kinds of soils ranging from silty sands to gravels.

The development of this correlation mainly rises from the well-known expression of Meyerhof (1957) given in Equation 3-76, which indicates an increase in penetration resistance with the square of the relative density, and an indirect proportion to the effective overburden pressure of the sand.

$$N = \left(17 + 24 \cdot \frac{\sigma'_v}{98}\right) \cdot RD^2 \qquad \text{Equation 3-76}$$

N, σ'_v and RD represent SPT blow count number, effective overburden pressure in kPa, and relative density in ratio, not percentage, respectively. Skempton (1986) expressed this relation in a general form as given in Equation 3-77 where for σ'_v=98 kPa, the expression is reduced to the form given in Equation 3-78.

$$N = \left(a + b \cdot \frac{\sigma'_v}{98}\right) \cdot RD^2 \qquad \text{Equation 3-77}$$

$$\frac{N_1}{RD^2} = a + b \qquad \text{Equation 3-78}$$

In this simplest form, N_1 represents the normalized penetration resistance to an overburden pressure of 98 kPa, i.e., 1 kgf/cm^2. As already discussed in Kulhawy and Mayne (1990) method, Skempton (1986) claims that $\frac{N_1}{RD^2}$ ratio is influenced by the over consolidation, aging, and grain size of sands. Meyerhof (1957) claims that this ratio is almost constant over the normally encountered range of relative densities and overburden pressures, with a fixed value of $a + b = 41$. This expression has long been used in its original or modified version to estimate the in situ relative density of soils with known SPT resistances due to the absence of similar correlations for

fines-containing soils in literature. On the other hand, Tatsuoka et al. (1978), Skempton (1986), and Ishihara (1993) stated that this expression is not directly applicable to sandy soils in general as the correlation is affected by the grain size of sands. In fact, Tatsuoka et al. (1978) claims that using a fixed ratio of $a + b = 41$ tends to underestimate the relative density of fine sands and silty sands.

Although the importance of the effect of grain size on the correlation between SPT resistance and relative density was well-understood by these studies, an entirely successful correlation and appropriate parameter identifying these effects cannot be developed by them. Even though an apparent change in the value of (a + b) with mean grain size (D_{50}) is observed, the scatter of the data in the (a+b) versus D_{50} plot is somewhat too large as shown in Figure 3.32; therefore, a reasonable and accurate evaluation of the relative density based on D_{50} was challenging. Due to the fact that silty sands give smaller (a+b) values than that of clean sands, Ishihara (1993) suggests two different relations between (a+b) and D_{50} for clean sands and silty sands, as represented in Figure 3.32. This figure indicates that (a+b) values of the field data are in the range of 10-35 for silty sands and 40-80 for clean sands.

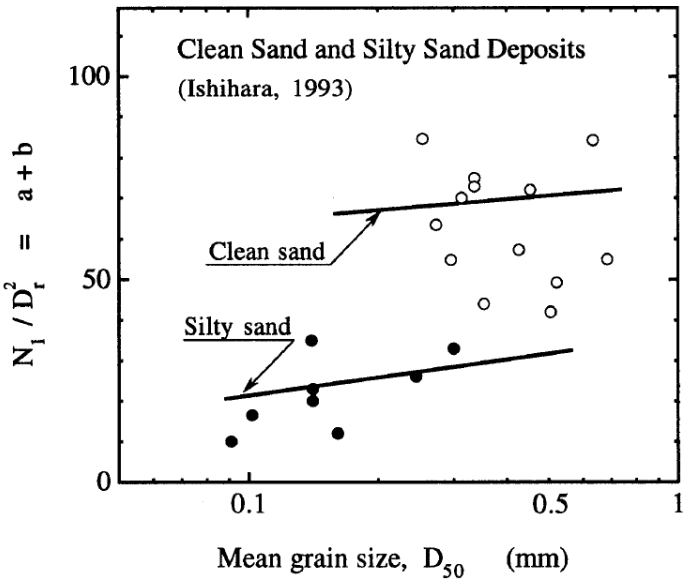

Figure 3.32. $N_1/RD^2 = a+b$ versus D_{50} plot for sandy soils obtained by conventional tube sampling (Ishihara, 1993)

It should be noted that the in-situ relative densities have been derived from laboratory measurements on undisturbed samples obtained by the conventional tube sampling method. However, the sand samples are more or less disturbed in the case of tube sampling techniques; therefore, the measured relative density may differ from the actual in-situ values. In fact, the reliability of undisturbed sampling in cohesionless soils is a separate research topic itself individually, as both the ground freezing technique and conventional tube sampling method used in the sampling of cohesionless soils may have a significant disturbance effect on saturated soil deposits. Despite the fact that Yoshimi et al. (1989) and Hatanaka et al. (1995) claim the ground freezing technique recovers higher quality sand samples as compared to the conventional technique of tube sampling, it also disturbs the soil during sampling due to the volume expansion characteristic of water under freezing temperatures.

Cubrinovski and Ishihara (1999) states that when it comes to the issue of developing a correlation between the N_1 value and relative density, it is more logical to adopt $\frac{N_1}{RD^2}$ ratio equal to a parameter called C_D, which is correlated with the grain size characteristics of soils. Hence, a newer form for the correlation is expressed as given in Equation 3-79.

$$\frac{N_1}{RD^2} = C_D \qquad \text{Equation 3-79}$$

To be able to quantify the grain size characteristics of cohesionless soils, an index parameter correlating the effects of grain size and grain size distributions is required. As already discussed in the previous section, many studies, including Cubrinovski and Ishihara (2002), declare that the void ratio range (e_{max}-e_{min}) is indicative of the overall grain-size composition and particle characteristics of a cohesionless soil, which means it provides a general basis for evaluation of material properties over the entire range of cohesionless soils. Therefore, it is judged that the void ratio range is the most appropriate parameter embodying these grading characteristics in an implicit manner.

The ability of the void ratio range to represent the overall grain-size composition and particle characteristics of a cohesionless soil is proven and well-understood in the literature with several studies. For example, the maximum and minimum void ratios tend to decrease with increasing grain size of soil, which is evidence of decreasing void ratio range with increasing D_{50}. Moreover, the soils with a greater amount of fines content for an identical D_{50} value tend to have a wider void ratio range, which proves that the void ratio range reflects not only the grain size effects but also the grain composition of the soil. The relation between (e_{max}-e_{min}) and D_{50} is shown in Figure 3.33, and an approximate expression is provided in Equation 3-80.

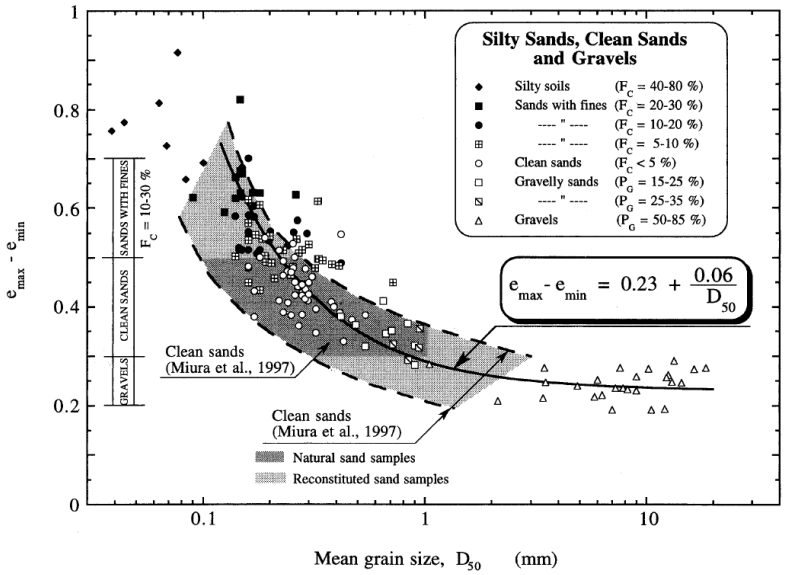

Figure 3.33. Relationship between void ratio range and mean grain size (Cubrinovski and Ishihara, 1999)

$$e_{max} - e_{min} = 0.23 + \frac{0.06}{D_{50}} \qquad \text{Equation 3-80}$$

Furthermore, Miura et al. (1997) proved that the void ratio range is also affected by the shape of the grains such that it increases with the increasing angularity of the grains, as shown in Figure 3.27. In this figure, the horizontal axis represents the two-dimensional angularity A_{2D} as a measure for quantifying the grain shape, where A_{2D}=0 for round grains, and the value of it increases with the increasing angularity of the grain.

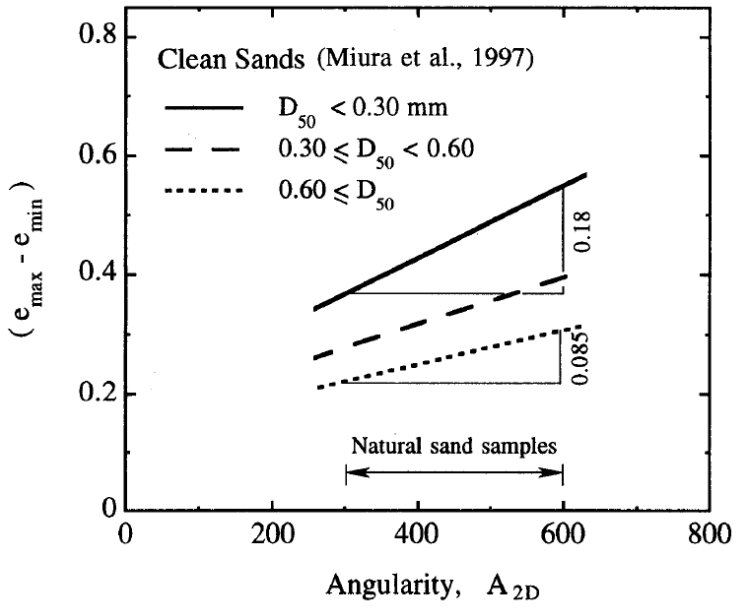

Figure 3.34. Variation of void ratio range with the angularity of grains (Cubrinovski and Ishihara, 1999)

Cubrinovski and Ishihara (1999) collected and compiled a wide data on natural silty sand, clean sand, and gravelly deposits obtained by the ground freezing technique available in Japan to correlate the ratio $\frac{N_1}{RD^2} = C_D$ and (e_{max}-e_{min}). The study found that C_D gradually decreases with increasing (e_{max}-e_{min}) as shown in Figure 3.35, and the expression represented in Equation 3-81 is summarized for the relationship between the ratio $\frac{N_1}{RD^2} = C_D$ and (e_{max}-e_{min}). It should be noted that while this equation provides a reasonable estimate for clean sands with (e_{max}-e_{min}) ≈ 0.35-0.45 with the original expression of Meyerhof (1957) for which C_D=41, it estimates greater C_D for coarser sands and lower C_D for fines-containing sands.

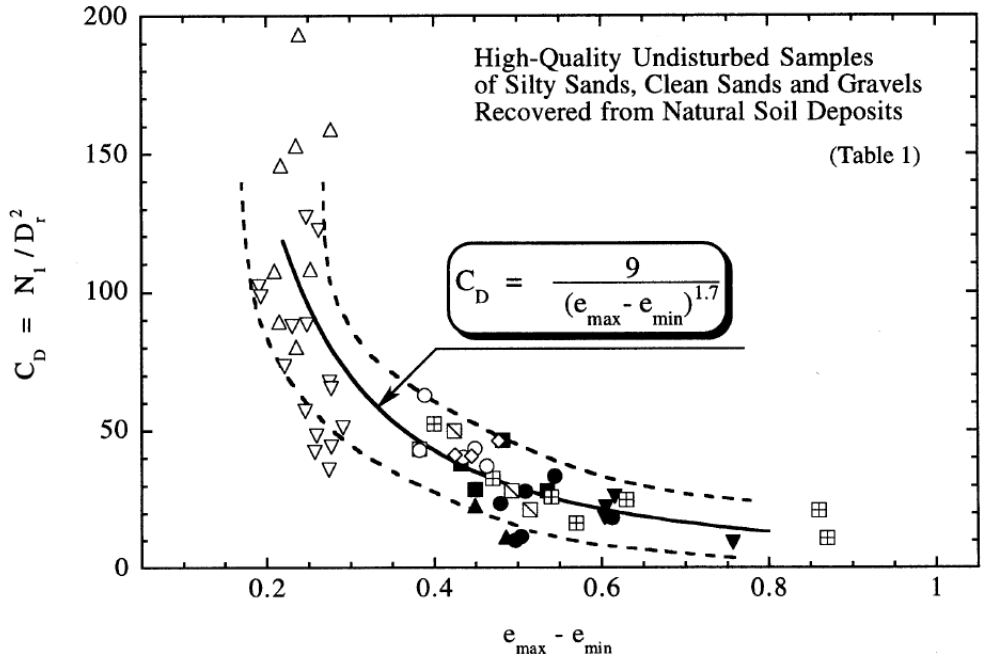

Figure 3.35. Relationship between N_1/RD^2 and void ratio range (Cubrinovski and Ishihara, 1999)

$$C_D = \frac{9}{(e_{max} - e_{min})^{1.7}} \qquad \text{Equation 3-81}$$

Putting this term in Equation 3-79 and rearranging the terms, the relative density correlation is obtained as given in Equation 3-82 in terms of the normalized penetration resistance to an overburden pressure of 98 kPa, N_1, and void ratio range, (e_{max}-e_{min}). It should be noted that Cubrinovski and Ishihara (1999) provides this expression for an SPT energy rod ratio of about 78% from the theoretical free-fall energy. In other words, the term N_1 in this equation represents $(N_1)_{78}$ value, which can be evaluated as (60/78) of the $(N_1)_{60}$ value, which is more commonly used in engineering practice.

$$RD(\%) = \sqrt{\frac{N_1 \cdot (e_{max} - e_{min})^{1.7}}{9}} \cdot 100 \qquad \text{Equation 3-82}$$

In fact, comprehensive studies on the penetration resistance by Seed (1979), Skempton (1986), Jamiolkowski et al. (1988), and Salgado et al. (1997a; 1997b)

proved that several factors such as relative density, effective overburden and lateral stresses, grain size characteristics and fabric have effects on the penetration resistance, as discussed earlier. However, this study omits the lateral stress and fabric effects for simplicity in its correlation.

Once the relative densities of the case histories are evaluated in addition to the limit void ratios, corresponding initial void ratios are estimated by using the Equation 3-68. In the end, the database represented in Table 3.16, which consists of SPT resistances for an SPT energy rod ratio of about 60% and 78% from the theoretical free-fall energy ($(N_1)_{60}$ and $(N_1)_{78}$), mean grain size (D_{50}), limit void ratios (e_{max}, e_{min}), void ratio range (e_{max}-e_{min}), relative densities estimated by Kulhawy and Mayne (1990) and Cubrinovski and Ishihara (1999) methods ($RD_{K\&M}$ and $RD_{C\&I}$), overall representative relative density ($RD_{overall}$), and initial void ratios corresponding to 1 kPa confining stress (e_0) is compiled. It should be noted that the maximum void ratios, and therefore the corresponding void ratio ranges and relative densities, reported in this table are unmodified values with respect to construction methods because the modification factors differ with respect to construction method types for different prediction models based on the probabilistic regressions by the Maximum Likelihood Method.

Table 3.16 Summary of estimated in-situ relative densities and void ratios for case histories

#	Case History	Section	$(N_1)_{60}$	$(N_1)_{78}$	D_{50} (mm)	e_{min}	e_{max}	e_{max}-e_{min}	$RD_{C\&I}$ (%)	$RD_{K\&M}$ (%)	$RD_{overall}$ (%)	e_0
1	Wachusett Dam - North Dike	WND-1	6.2	4.8	0.420	0.563	0.935	0.372	31.45	35.07	33.26	0.811
		WND-2	4.3	3.3	0.420	0.563	0.935	0.372	26.06	29.05	27.56	0.832
		WND-105	3.9	3.0	0.420	0.563	0.935	0.372	24.97	27.85	26.41	0.837
		WND-3	8.7	6.7	0.420	0.563	0.935	0.372	37.26	41.54	39.40	0.788
2	Fort Peck Dam	Boring 3	17.3	13.3	0.280	0.569	0.971	0.402	56.08	61.26	58.67	0.735
		Boring 7	17.3	13.3	0.280	0.569	0.971	0.402	56.08	61.26	58.67	0.735
		Boring 6	17.3	13.3	0.280	0.569	0.971	0.402	56.08	61.26	58.67	0.735
		Boring 7	17.3	13.3	0.280	0.569	0.971	0.402	56.08	61.26	58.67	0.735

Table 3.16 (cont'd) Summary of estimated in-situ relative densities and void ratios for case histories

3	Uetsu Railway Embankment	S1	1.6	1.2	0.340	0.561	0.958	0.397	16.98	18.33	17.66	0.888
		S2	2.4	1.8	0.340	0.561	0.958	0.397	20.47	22.11	21.29	0.874
4	Lower San Fernando Dam - U/S Slope	S103&S111	14.0	10.8	0.070	0.398	0.593	0.195	27.34	67.15	27.34	0.540
		S101&S102 &S104	14.0	10.8	0.070	0.398	0.593	0.195	27.34	67.16	27.34	0.540
		S105	14.0	10.8	0.070	0.398	0.593	0.195	27.34	67.16	27.34	0.540
		S105	14.0	10.8	0.070	0.398	0.593	0.195	27.31	67.09	27.31	0.540
5	Hachiro-Gata Road Embankment	S1	4.3	3.3	0.181	0.591	0.997	0.406	28.14	32.16	28.14	0.883
		S2	4.3	3.3	0.181	0.591	0.997	0.406	28.14	32.16	28.14	0.883
6	La Marquesa Dam - U/S Slope	B-2	3.9	3.0	0.150	0.600	1.017	0.417	27.39	31.39	27.39	0.902
		B-III	3.6	2.7	0.150	0.600	1.017	0.417	26.25	30.08	26.25	0.907
		B-3	3.6	2.8	0.150	0.600	1.017	0.417	26.40	30.26	26.40	0.907
7	La Marquesa Dam - D/S Slope	B-II	6.5	5.0	0.150	0.595	1.007	0.412	35.18	40.76	35.18	0.862
		B-1	7.1	5.5	0.150	0.595	1.007	0.412	36.73	42.55	36.73	0.856
8	La Palma Dam	B-3	5.0	3.9	0.200	0.588	0.990	0.402	30.23	34.40	30.23	0.868
		B-4	4.7	3.6	0.200	0.588	0.990	0.402	29.27	33.30	29.27	0.872
9	Lake Ackerman Highway Embankment	S1	4.4	3.4	0.390	0.561	0.958	0.397	27.96	29.71	28.84	0.844
		S2	4.4	3.4	0.390	0.561	0.958	0.397	27.96	29.71	28.84	0.844
		S3	4.3	3.3	0.390	0.561	0.958	0.397	27.65	29.38	28.51	0.845
10	Chonan Middle School	No.4	4.2	3.2	0.200	0.589	0.992	0.403	27.68	31.41	27.68	0.881
		No.3	3.6	2.8	0.200	0.589	0.992	0.403	25.76	29.23	25.76	0.889
11	Soviet Tajik - May 1 Slide	S1	4.6	3.5	0.013	0.506	0.874	0.368	26.70	59.57	26.70	0.776
		S2	4.6	3.5	0.013	0.506	0.874	0.368	26.70	59.57	26.70	0.776
12	Shibecha-Cho Embankment	B-2	4.3	3.3	0.200	0.461	0.790	0.329	23.62	31.89	23.62	0.712
		B-3	3.6	2.8	0.200	0.461	0.790	0.329	21.53	29.07	21.53	0.719
		B-5	4.4	3.4	0.200	0.461	0.790	0.329	23.93	32.31	23.93	0.711
		B-4	3.6	2.7	0.200	0.461	0.790	0.329	21.46	28.97	21.46	0.719
		B-5	4.4	3.4	0.200	0.461	0.790	0.329	23.93	32.31	23.93	0.711
13	Route 272 at Higashiareki nai	Left	5.8	4.4	0.200	0.590	0.994	0.404	32.56	36.87	32.56	0.863
		Right	5.5	4.2	0.200	0.590	0.994	0.404	31.63	35.81	31.63	0.866
14	Zeeland - Vlietepolder	Small-S1	14.6	11.2	0.130	0.585	0.999	0.414	52.72	62.04	57.38	0.762
		Small-S2	14.6	11.2	0.130	0.585	0.999	0.414	52.72	62.04	57.38	0.762
		Large-S1	14.6	11.2	0.130	0.585	0.999	0.414	52.72	62.04	57.38	0.762
		Large-S2	14.6	11.2	0.130	0.585	0.999	0.414	52.72	62.04	57.38	0.762
		Large-S3	14.6	11.2	0.130	0.585	0.999	0.414	52.72	62.04	57.38	0.762

Table 3.16 (cont'd) Summary of estimated in-situ relative densities and void ratios for case histories

15	Sheffield Dam	Right	4.7	3.6	0.100	0.610	1.041	0.431	31.04	36.72	31.04	0.907
16	Helsinki Harbor	Small-S1	3.9	3.0	0.100	0.623	1.077	0.453	29.44	33.34	31.39	0.935
		Small-S2	4.9	3.7	0.100	0.623	1.077	0.453	32.92	37.29	35.11	0.918
		Large-S1	4.7	3.6	0.100	0.623	1.077	0.453	32.34	36.63	34.48	0.921
		Large-S2	4.5	3.4	0.100	0.623	1.077	0.453	31.57	35.76	33.67	0.924
17	Solfatara Canal Dike	S1	4.7	3.6	0.170	0.576	0.981	0.405	29.41	33.94	31.68	0.853
		S2	3.8	2.9	0.170	0.576	0.981	0.405	26.50	30.59	28.55	0.865
18	Lake Merced Bank	Boring 2	8.3	6.4	0.210	0.580	0.990	0.410	39.43	43.85	41.64	0.819
19	El Cobre Tailings Dam	S1	1.7	1.3	0.080	0.640	1.113	0.473	20.00	22.65	20.00	1.018
		S2	1.7	1.3	0.080	0.640	1.113	0.473	20.00	22.65	20.00	1.018
		S3	1.7	1.3	0.080	0.640	1.113	0.473	20.00	22.65	20.00	1.018
		S4	1.7	1.3	0.080	0.640	1.113	0.473	20.00	22.65	20.00	1.018
20	Metoki Road Embankment	S-19	3.1	2.4	0.120	0.597	1.011	0.414	24.27	28.88	24.27	0.910
		S-13	3.8	2.9	0.120	0.597	1.011	0.414	26.79	31.88	26.79	0.900
21	Hokkaido Tailings Dam	Small-S1	1.4	1.1	0.075	0.593	1.015	0.422	16.85	21.25	16.85	0.943
		Small-S2	1.4	1.1	0.075	0.593	1.015	0.422	16.85	21.25	16.85	0.943
		Large-S1	1.4	1.1	0.075	0.593	1.015	0.422	16.85	21.25	16.85	0.943
		Large-S2	1.4	1.1	0.075	0.593	1.015	0.422	16.85	21.25	16.85	0.943
22	Upper San Fernando Dam - D/S Slope	A1&B1&C1	9.2	7.0	0.070	0.437	0.666	0.229	25.25	54.22	25.25	0.608
		A2&B2&C2	9.3	7.2	0.070	0.437	0.666	0.229	25.51	54.76	25.51	0.608
		A3	9.3	7.2	0.070	0.437	0.666	0.229	25.51	54.76	25.51	0.608
		B4&C4	9.3	7.2	0.070	0.437	0.666	0.229	25.51	54.77	25.51	0.608
		B5&C5	9.2	7.1	0.070	0.437	0.666	0.229	25.28	54.28	25.28	0.608
23	Tar Island Dyke	Large-S1	11.1	8.5	0.150	0.552	0.931	0.380	42.66	52.96	47.81	0.750
		Large-S2	11.1	8.5	0.150	0.552	0.931	0.380	42.66	52.96	47.81	0.750
		Small-S1	11.1	8.5	0.150	0.552	0.931	0.380	42.66	52.96	47.81	0.750
		Small-S2	11.1	8.5	0.150	0.552	0.931	0.380	42.66	52.96	47.81	0.750
24	Mochi-Koshi Tailings Dam 1	S1	4.0	3.1	0.038	0.447	0.726	0.279	19.87	40.64	19.87	0.670
		S2	4.0	3.1	0.038	0.447	0.726	0.279	19.87	40.64	19.87	0.670
		S3	4.0	3.1	0.038	0.447	0.726	0.279	19.87	40.64	19.87	0.670
25	Mochi-Koshi Tailings Dam 2	S1	3.0	2.3	0.042	0.445	0.718	0.273	16.81	34.39	16.81	0.672
		S2	3.0	2.3	0.042	0.445	0.718	0.273	16.81	34.39	16.81	0.672
26	Nerlerk Embankment Slide 1	S1	13.7	10.5	0.220	0.580	0.992	0.411	50.81	56.02	53.41	0.772
		S2	13.7	10.5	0.220	0.580	0.992	0.411	50.81	56.02	53.41	0.772
		S3	13.7	10.5	0.220	0.580	0.992	0.411	50.81	56.02	53.41	0.772

Table 3.16 (cont'd) Summary of estimated in-situ relative densities and void ratios for case histories

27	Nerlerk Embankment Slide 2	S1	13.7	10.5	0.220	0.580	0.992	0.411	50.81	56.02	53.41	0.772
		S2	13.7	10.5	0.220	0.580	0.992	0.411	50.81	56.02	53.41	0.772
		S3	13.7	10.5	0.220	0.580	0.992	0.411	50.81	56.02	53.41	0.772
28	Nerlerk Embankment Slide 3	S1	13.7	10.5	0.220	0.580	0.992	0.411	50.81	56.02	53.41	0.772
		S2	13.7	10.5	0.220	0.580	0.992	0.411	50.81	56.02	53.41	0.772
		S3	13.7	10.5	0.220	0.580	0.992	0.411	50.81	56.02	53.41	0.772
29	Asele Road Embankment	S1	6.8	5.2	0.276	0.543	0.929	0.386	33.90	38.37	33.90	0.798
		S2	6.7	5.2	0.276	0.543	0.929	0.386	33.69	38.14	33.69	0.799
30	Nalband Railway Embankment	NB-1	4.8	3.7	1.629	0.387	0.546	0.160	13.47	27.13	13.47	0.525
		Small-S2	4.8	3.7	1.629	0.387	0.546	0.160	13.47	27.13	13.47	0.525
		NB-1	4.8	3.7	1.629	0.387	0.546	0.160	13.47	27.13	13.47	0.525
		Large-S2	4.8	3.7	1.629	0.387	0.546	0.160	13.47	27.13	13.47	0.525
		Large-S3	4.8	3.7	1.629	0.387	0.546	0.160	13.47	27.13	13.47	0.525
31	Sullivan Tailings	Large-S1	9.5	7.3	0.090	0.616	1.055	0.439	44.83	53.07	44.83	0.858
		CP91-29	9.5	7.3	0.090	0.616	1.055	0.439	44.83	53.07	44.83	0.858
		CP91-31	9.5	7.3	0.090	0.616	1.055	0.439	44.83	53.07	44.83	0.858
		Small-S1	9.5	7.3	0.090	0.616	1.055	0.439	44.83	53.07	44.83	0.858
		CP91-31	9.5	7.3	0.090	0.616	1.055	0.439	44.83	53.07	44.83	0.858
32	Jamuna Bridge	S1	6.7	5.2	0.150	0.590	0.995	0.406	35.18	41.27	38.22	0.840
		S2	6.7	5.2	0.150	0.590	0.995	0.406	35.18	41.27	38.22	0.840
33	Calaveras Dam	S1	14.0	10.8	0.732	0.545	0.898	0.353	45.10	49.73	45.10	0.739
		S2	14.0	10.8	0.732	0.545	0.898	0.353	45.10	49.73	45.10	0.739
34	Koda Numa Railway Embankment	Left	2.1	1.6	0.180	0.469	0.807	0.339	16.80	22.43	19.62	0.741
		Middle	1.8	1.4	0.180	0.469	0.807	0.339	15.49	20.69	18.09	0.746
		Right	2.5	1.9	0.180	0.469	0.807	0.339	18.32	24.46	21.39	0.735
35	Whiskey Springs Fan	SP 1	10.8	8.3	1.613	0.360	0.497	0.138	17.80	40.71	17.80	0.473
		SP 3	12.8	9.9	1.613	0.360	0.497	0.138	19.38	44.33	19.38	0.471
36	San Fernando Valley Juvenile Hall	Boring 2	11.4	8.8	0.055	0.446	0.724	0.278	33.31	63.36	33.31	0.631
		Boring 4	10.1	7.8	0.055	0.446	0.724	0.278	31.27	59.48	31.27	0.637
		Boring 6	7.0	5.4	0.055	0.446	0.724	0.278	26.06	49.56	26.06	0.651

CHAPTER 4

DEVELOPMENT OF PROBABILISTIC RELATIONSHIPS FOR ENGINEERING EVALUATION OF POST-LIQUEFACTION SHEAR STRENGTH

In this chapter, the details of the development process of post-liquefaction prediction relationships are discussed. As already discussed in Chapter 1 and Chapter 3, a new critical state framework compatible methodology is introduced in this thesis to evaluate the post-liquefaction shear strength of soils on the basis of back-analyses of available case histories. The case history database used to develop these relationships is already explained in Chapter 3. Since practicing engineers are more used to performing effective stress-based stability assessments for cohesionless soils under monotonic loading conditions, corresponding volume stress models are presented in void ratio versus mean effective stress domain, which is claimed to be theoretically more correct than previous penetration resistance versus residual strength domains.

The in-situ void ratio, i.e., the in-situ relative density, is one of the critical parameters for soil to determine its susceptibility to liquefaction. Previous studies on this topic consider this effect indirectly by implementing an in-situ test index metric (e.g., $(N_1)_{60}$, q_c, V_s, etc.) in their residual strength relationships to represent the capacity of the soil. This parameter is commonly the SPT resistance due to the wide usage of this test all around the world and the abundance of conversions available in the literature to convert other types of penetration resistances to SPT resistance. On the other hand, it is always a problem to convert other types of resistances to an equivalent SPT resistance. This new framework takes this effect into account directly such that the in-situ relative densities and void ratios of the cases are presented in the void ratio versus effective stress domain immediately. Therefore, the differences in in-situ tests are automatically eliminated as the in-situ void ratio is unique for all tests, and it is possible to estimate it by using correlations developed by all types of

experiments. This convenience also explains well that the new framework sounds theoretically more correct.

In addition to SPT resistance, previous studies also developed their residual strength prediction relationships as a function of initial in-situ effective vertical stress (σ'_{v0}). This parameter represents the confining effects at the liquefied layer. On the other hand, it is already explained that other stress components including the horizontal stresses in out-of-plane and in-plane directions also have effects on confining. Thus, neglecting these impacts and imposing all confining effects to initial effective vertical stress theoretically weakens other studies. Hence, a new failure criterion including the effect of all effective principal stresses in three dimensions on residual strength is also introduced in this study.

In the literature, there is still a hot debate available about the shape of the critical state curve, whether it is a line or a curve. Since a liquefaction state curve similar to the critical state curve is defined in this domain where all data points follow this curve after the liquefaction, this debate is highly concern of this study. Steady-state and critical state curves are generally plotted in semi-logarithm space where the vertical and horizontal axes represent void ratio and logarithm of effective confining stress, respectively. In this semi-log domain, steady-state and critical state curves are approximately obtained as log-linear over the void ratio and effective stress ranges that geotechnical engineers interested in liquefiable soils. On the other hand, it is obvious that negative void ratio values can be obtained for these log-linear curves for high mean effective stresses. Therefore, some researchers claim that critical state curves should become asymptomatic to a horizontal line for higher stresses. In fact, there exist several important studies on the minimum limit void ratio that critical state curves become asymptomatic for higher stresses in the literature. Anyways, even if this is true, the stress range that these curves become asymptomatic is pretty high compared to common stress ranges of liquefiable soils. Therefore, it is not that much critical to approximate the shape of the critical state curves in high stress ranges for post-liquefaction shear strength predictions. Nevertheless, this study covers both approaches and recommends totally seven residual strength prediction

models on this purpose. While a nonlinear liquefaction state curve is defined in void ratio versus mean effective stress domain for the first two prediction models, a log-linear liquefaction state curve is defined for the rest five prediction models.

Similarly, different isotropic compression curves are also defined in these models such that the volume-stress model under isotropic states recommended by Sheng et al. (2008) is employed in the first four prediction models. For two of the rest three prediction models, a new volume-stress model is developed in this study for isotropic states, and non-linear isotropic compression curves are developed accordingly. For the last prediction model, a log-linear isotropic compression line is defined in void ratio versus mean effective stress domain. The details of these seven prediction models are discussed in this chapter.

4.1 Probabilistic Regressions by the Maximum Likelihood Method

The Maximum Likelihood Method is used to develop seven fully probabilistic prediction relationships and corresponding model parameters. No further additional weighting factors are employed for the case histories to account their quality of information and level of documentation; therefore, a subjective engineering judgment is avoided at this point.

The Maximum Likelihood Method, or the Maximum Likelihood Estimation (MLE), is the approach of estimating the unknown parameters of an assumed probability distribution by providing some actual observed data to it. A reasonable estimation is achieved by maximizing a likelihood function so that the actual observed data is the most probable under the predicted statistical model. In this study, the likelihood function is determined as the multiplication of individual probabilities of making the observation of the residual shear strengths by back-analyzed case histories. The corresponding probabilities are evaluated for a model with mean error zero and a standard deviation of model error, σ_ε. The model error term is assumed to be normally distributed for convenience. Accordingly, the model parameters (θ_1, θ_2, θ_3,

θ_4, etc.) which maximize the likelihood function are evaluated for each of the seven post-liquefaction shear strength prediction models.

It should be noted that statistical outputs of the Maximum Likelihood Method provide important clues about the statistical quality of the models such that the model with the largest sum of ln(Probability) is classified as the most accurate model. Similarly, the one with the least model error standard deviation is concluded to be the most precise model.

The details of maximum likelihood assessments are discussed in Cetin (2000), Cetin et al. (2004), and Cetin et al. (2018), and will not be repeated herein.

4.2 Comparison of Predicted Results and Modified Back-analysis Database

It is judged in this study that the approaches followed by Weber (2015) during the back-analyses of the case histories were the most reasonable and logical ones when compared to the approaches followed by other previous studies. In fact, it is the most reliable study for the "secondary" case histories that available information and documentation are inadequate for kinetics and momentum analyses. The benefits and advantages of Weber (2015)'s approaches and judgments for the back-analyses of these less well-documented case histories are already discussed in Chapter 2. As a result, the predicted post-liquefaction shear strength values in this study are compared with the back-analyses results of Weber (2015) during the probabilistic regressions by the Maximum Likelihood Method.

On the other hand, the back-analyses results of Weber (2015) are not used directly during the probabilistic regressions of this study. Even though the methods followed by Weber (2015) for less well-documented case histories were explained clearly, it is judged that there exist some partially biased approaches in these methods. As already discussed detailly in Section 2.2.6, Weber (2015) performed two different methods for the engineering evaluation of the residual strengths of Group B poorly documented case histories, and took the arithmetic average of the results of these

methods to estimate the overall residual strength value. In one of these methods, the average of the apparent pre-failure stress along the liquefied portions of the failure plane required to provide a static Factor of Safety equal to 1.0 for pre-failure geometry ($S_{r,yield}$) and the apparent residual stress required to provide a post-failure Factor of Safety equal to 1.0 for post-failure geometry ($S_{r,resid/geom}$) is multiplied by a coefficient related to the runout characteristics and overall failure mechanism of the failure (ξ). The corresponding relationship is provided in Equation 2-7.

Weber (2015) defines the value of runout characteristics and overall failure mechanism coefficient, ξ, between the range 0 and 1 with respect to the travel path ratio defined as the ratio of the travel path distance of the center of failure mass to the initial slope height. Weber (2015) claims that $S_{r,yield}$ and $S_{r,resid/geom}$ values become very close to each other, and the inertial momentum effects would be tiny for the cases in which the slide displacements are negligible or very small. Therefore, ξ can be taken as nearly 1 for these cases. Nevertheless, there would be a large difference between $S_{r,yield}$ and $S_{r,resid/geom}$ values, and the inertial momentum effects would be significant for the cases in which runout distances and slide displacements are infinitely large. In these cases, the actual post-liquefaction shear strength would be very close to zero; thus, ξ can be taken as nearly 0 for these cases. The corresponding relationship is presented in Figure 2.21.

Although the procedure for the evaluation of ξ is well explained in Weber (2015), assigning different ξ values for the case histories based on their runout characteristics and overall failure mechanisms are decided to be a biased approach. To be able to estimate ξ coefficient for the back-analysis of a case history, both pre-failure and post-failure geometries are required to be known to evaluate the runout characteristics of the failure. On the other hand, it is not possible to use this method in the forward analysis since the post-failure geometry is unknown for a designed project or stable structure. In fact, the post-liquefaction shear strength prediction relationships are developed to prevent those failures during the design process. Hence, it is decided to be a biased approach to use a method that cannot be used in forward analyses in back-analyses.

As a result, the back-analyses results of Weber (2015) are modified slightly to annihilate this inconsistency. In fact, a modification was also performed by Weber (2015) to compare its back-calculated residual strength results with Olson (2001)'s results. Olson (2001) used $S_{r,resid/geom}$ values directly as the overall post-liquefaction shear strength values of poorly documented cases. On the contrary, it is already explained that it gives the lower bound for the post-liquefaction shear strength as it under-estimates the actual value by considering the final geometry. Therefore, Weber (2015) took the arithmetic average of $S_{r,yield}$ and $S_{r,resid/geom}$ values reported by Olson (2001) for these less well-documented case histories, and multiplied the average by 0.8 referring to Figure 2.20. A similar attempt is also performed in this study for the less well-documented Group B cases such that instead of multiplying the arithmetic averages of $S_{r,yield}$ and $S_{r,resid/geom}$ values with different ξ coefficients, they are multiplied by a constant $\xi = 0.8$ value. Therefore, the method is converted to a method that is consistent with both back-analyses and forward analyses. In other words, one can also use this method in forward analysis because the runout characteristics of the failure mass are not necessary for the evaluations anymore.

Another modification is performed for the cases in which smaller initial potential failure surfaces and final overall monolithically initiated failure surfaces exist together. Weber (2015) performs initial yield stress analyses on both of these failure mechanisms, and back-calculates $S_{r,yield}$ values for each mechanism. In other words, it back-calculates separate $S_{r,yield}$ values for the smaller initial potential failure surfaces and the final overall monolithically initiated failure surfaces. In the end, it assigns weighting factors to these results based on the engineering judgment of the investigation team on failure scenarios, and develops a single overall $S_{r,yield}$ value for the case history. On the other hand, the details of the evaluation process of these weighting factors are not explained clearly in the study; thus, it is again decided to be a biased approach.

In fact, these smaller initial potential failure surfaces and final overall monolithically initiated failure surfaces are taken into account separately in this study for seven case histories as explained in Section 3.3. In other words, they are considered to be

different sub-cases as their failure planes differ from each other. Hence, the overall post-liquefaction shear strength values are predicted separately for these sub-cases in this study. Accordingly, the corresponding back-calculated residual strength values by Weber (2015) are also modified to achieve a consistent comparison with this study. While taking the average of $S_{r,yield}$ and $S_{r,resid/geom}$ values to multiply them by $\xi = 0.8$, the $S_{r,yield}$ values are directly taken equal to the values back-calculated specifically for that failure plane. In other words, the final $S_{r,yield}$ values for the case histories that obtained by taking the weighted average of the $S_{r,yield}$ values developed for the smaller initial potential failure surfaces and the final overall monolithically initiated failure surfaces are not used directly, but the individual $S_{r,yield}$ values are employed instead for smaller and larger failure planes separately. As a result, more logical and reasonable comparisons are obtained between the two methods, obviously.

Another modification for the residual strength values of Weber (2015) is employed for Mochi-Koshi Tailings Dam and Nerlerk Embankment Slides case histories. As discussed in Section 2.2.6, Weber (2015) considered Mochi-Koshi Tailings Dam and Nerlerk Embankment Slide case histories as single cases. On the other hand, some studies, including this one, divide the Mochi-Koshi Tailings Dam case history into two as Mochi-Koshi Tailings Dam 1 and Dam 2, and analyze them independently from each other. Similarly, Nerlerk Embankment Slide case history is divided into three as Nerlerk Embankment Slide 1, Slide 2, and Slide 3 since three independent slope failures occurred for that embankment. In fact, Weber (2015) also analyzed these sub-cases independently and assigned separate residual strength values for those sub-cases; however, it reported a final single value as the best estimate of post-liquefaction shear strength as the failures were quite similar to each other. Nevertheless, since separate residual strength values were already developed and documented for them by Weber (2015), they are judged to be separate case histories in this study. Accordingly, the predicted residual strength values are compared with the back-analyses results of Weber (2015) that were documented individually for the

sub-cases Mochi-Koshi Tailings Dam 1 and Dam 2, and Nerlerk Embankment Slide 1, Slide 2, and Slide 3.

A final modification for the residual strength values of Weber (2015) is employed for Wachusett Dam North Dike, Fort Peck Dam, and Hachiro-Gata Road Embankment case histories. For Wachusett Dam North Dike and Hachiro-Gata Road Embankment cases, the shear strengths of the non-saturated non-liquefied zones were modeled by taking the internal friction angle as ϕ'=30°. On the other hand, these internal friction angle values are estimated as 35° and 28° for Wachusett Dam North Dike and Hachiro-Gata Road Embankment case histories, respectively. These values are estimated by using the relationship recommended by Wolff (1989) given in Equation 4-1 based on the penetration resistances ($(N_1)_{60}$) measured in those non-liquefied regions. It should be noted that the relationship provided in Equation 4-1 is developed by Wolff (1989) based on the graphical representation reported in Peck et al. (1974) for estimating the internal friction angles of soils with respect to penetration resistances.

$$\phi' = 27.1 + 0.3 \cdot N_{60} - 0.00054 \cdot N_{60}^2 \qquad \text{Equation 4-1}$$

In this equation, while N_{60} represents the SPT resistance of the soil, ϕ' gives the corresponding internal friction angle value in degrees.

In liquefaction slope stability problems, the overall resisting force acting on the sliding surface is equal to the summation of resisting forces acting on the failure plane portions remaining in the liquefied zone and non-liquefied zone. These resisting forces coming from the liquefied zone and non-liquefied zone can be evaluated by the relationships given in Equation 4-2 and Equation 4-3, respectively.

$$F_{resisting,liq} = C_u \cdot L_{liq} \qquad \text{Equation 4-2}$$

$$F_{resisting,non-liq} = \tau \cdot L_{non-liq} \qquad \text{Equation 4-3}$$

In these equations, while L_{liq} and $L_{non\text{-}liq}$ represent the failure plane lengths remaining in the liquefied and non-liquefied portions of the soil profile, C_u and τ symbolize the

shear strength values at those portions, respectively. It should be noted that the shear strength of the non-liquefied zone can be evaluated by Equation 4-4 where σ'_N and ϕ' represent normal stress acting on the failure plane and internal friction angle of the soil, respectively.

$$\tau = \sigma'_N \cdot \tan(\phi') \qquad \text{Equation 4-4}$$

The overall resisting force acting on the sliding surface can be evaluated by adding the resisting forces obtained by Equation 4-2 and Equation 4-3. Therefore, the internal friction angle assigned for the non-liquefied zone has a crucial effect on the post-liquefaction shear strength. In fact, once the shear strength of the non-liquefied zone changes due to a change in internal friction angle, the shear strength of the liquefied zone (C_u) changes automatically. Inspired of that, the relationship provided in Equation 4-5 is used to evaluate the modified shear strength values of the liquefied zones of Wachusett Dam North Dike and Hachiro-Gata Road Embankment case histories.

$$C_{u,initial} \cdot L_{liq} + \sigma'_N \cdot \tan(\phi'_{initial}) \cdot L_{non-liq} = C_{u,modified} \cdot L_{liq} + \sigma'_N \cdot \tan(\phi'_{modified}) \cdot L_{non-liq} \qquad \text{Equation 4-5}$$

In this equation, L_{liq} and $L_{non\text{-}liq}$ represent the failure plane lengths remaining in the liquefied and non-liquefied portions of the soil profile, respectively. σ'_N represents the normal stress acting on the failure plane, which is evaluated by the linear elastic modeling of the cross-section in PLAXIS 2D Ultimate Connect Edition V22.00.00.1733 software and corresponding Mohr's circle, as discussed in Section 3.4. $\phi'_{initial}$ and $\phi'_{modified}$ symbolize the internal friction angles used by Weber (2015) and this study, respectively. Similarly, $C_{u,initial}$ and $C_{u,modified}$ represent the shear strength of the liquefied zone evaluated by Weber (2015) and this study, respectively. Once the shear strength of the liquefied zone estimated by this study is left alone in Equation 4-5, the relationship provided in Equation 4-6 is developed for the closed-form solution of $C_{u,modified}$ value.

$$C_{u,modified} = \frac{C_{u,initial} \cdot L_{liq} + \sigma'_N \cdot \tan(\phi'_{initial}) \cdot L_{non-liq} - \sigma'_N \cdot \tan(\phi'_{modified}) \cdot L_{non-liq}}{L_{liq}} \quad \text{Equation 4-6}$$

For Wachusett Dam North Dike case history, L_{liq} and $L_{non\text{-}liq}$ lengths are evaluated as 68.90 m and 20.12 m, respectively, and σ'_N value is estimated as 88.0 kPa. Weber (2015) reported the internal friction angle of the non-liquefied zone as $\phi'_{initial}$=30°, and this value is modified as $\phi'_{modified}$ =35° in this study referring to Equation 4-1. The shear strength of the liquefied zone is reported as $C_{u,initial}$=14.98 kPa by Weber (2015). Accordingly, a lower post-liquefaction shear strength value is obtained as $C_{u,modified}$=10.92 kPa for this case history referring to Equation 4-6.

For Hachiro-Gata Road Embankment case history, L_{liq} and $L_{non\text{-}liq}$ lengths are evaluated as 14.90 m and 2.68 m, respectively, and σ'_N value is estimated as 11.6 kPa. Weber (2015) reported the internal friction angle of the non-liquefied zone as $\phi'_{initial}$=30°, and this value is modified as $\phi'_{modified}$ =28° in this study referring to Equation 4-1. The shear strength of the liquefied zone is reported as $C_{u,initial}$=3.26 kPa by Weber (2015). Accordingly, a higher post-liquefaction shear strength value is obtained as $C_{u,modified}$=3.39 kPa for this case history referring to Equation 4-6.

For Fort Peck Dam case history, Weber (2015) used the critical cross-sections provided by Olson (2001) presented in Figure 4.1 during the back-analyses.

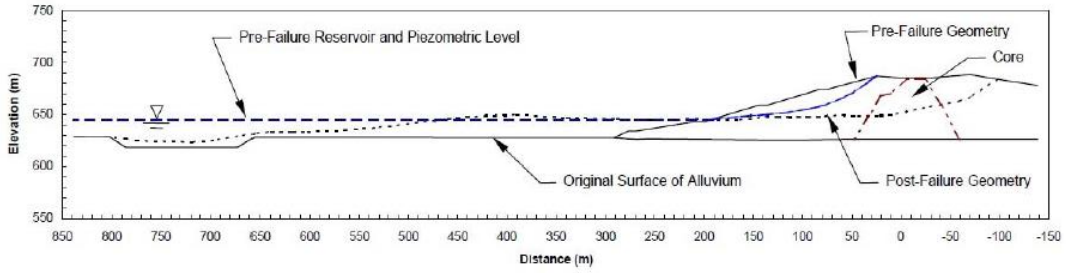

Figure 4.1. Pre-failure and post-failure cross-sections of Fort Peck Dam case history (Olson, 2001)

The pre-failure and post-failure geometries used in the back-analyses of Weber (2015), and the descriptions of the corresponding soil materials are given in Figure 4.2.

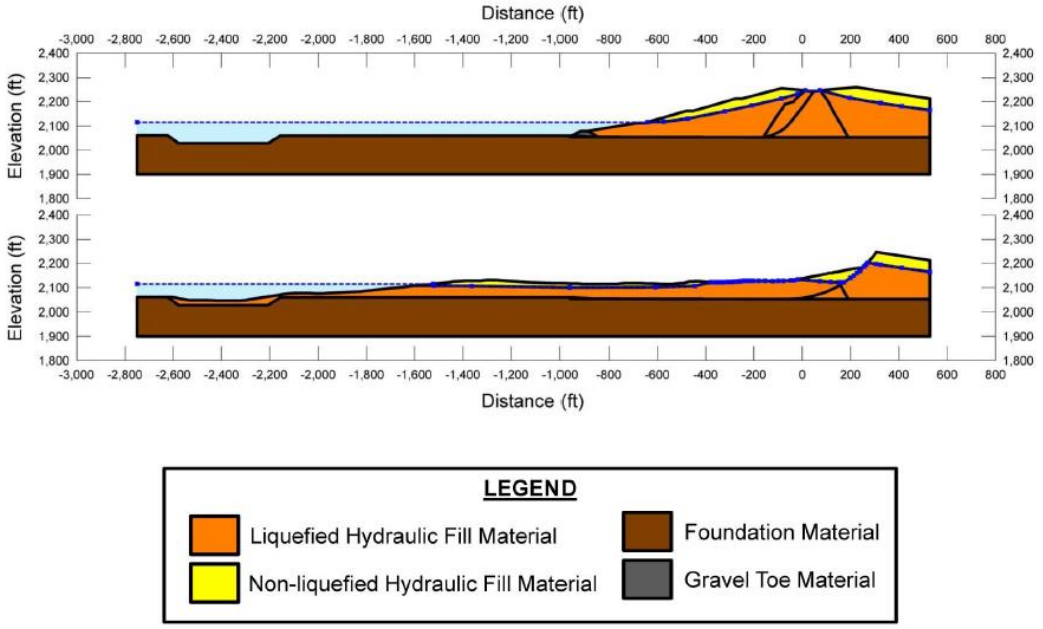

Figure 4.2. Pre-failure and post-failure cross-sections and material descriptions of Fort Peck Dam case history (Weber, 2015)

As it can be observed from Figure 4.2, Weber (2015) defined the entire zone remaining between the groundwater table and foundation material as liquefied hydraulic fill material (orange region). In other words, it kept the properties of the clay core in the middle of the dam the same as the hydraulic fill material. On the other hand, it is obvious that the material properties such as fines content, mean grain size, etc., differ significantly for the clay core and hydraulic fill materials. In fact, it is pretty questionable that whether this clay core contributed to liquefaction or not for this case history. Consequently, the portion of the failure plane that remained inside the clay core is assumed to be non-liquefied in this study. Accordingly, the overall resisting force acting on the failure plane is evaluated by Equation 4-7.

$$C_{u,initial} \cdot L_{total} = C_{u,modified} \cdot L_{liq} + C_{u,clay} \cdot L_{clay} \qquad \text{Equation 4-7}$$

In this equation, L_{liq} and L_{clay} represent the failure plane lengths remaining in the liquefied and clay core portions of the soil profile, respectively. L_{total}, on the other hand, gives the entire length of the failure plane, which is the summation of L_{liq} and L_{clay}. Again, $C_{u,initial}$ and $C_{u,modified}$ symbolize the shear strength of the liquefied zone

evaluated by Weber (2015) and this study, respectively. $C_{u,clay}$, on the other hand, represents the shear strength of the clay core zone located in the middle of the dam. Referring to the main source of references for this case history, the SPT resistance of the clay core is estimated as 20-40 blows/ft. Accordingly, the shear strength of the clay core zone is evaluated as $C_{u,clay}$=150 kPa referring to the literature.

It should be noted that the relationship provided in Equation 4-7 is employed for both pre-failure and post-failure geometries, and the shear strength of the liquefied zone is evaluated separately for both cases, namely $C_{u,modified,pre\text{-}failure}$ and $C_{u,modified,post\text{-}failure}$. Consequently, the arithmetic mean of these two shear strength values is multiplied by ξ = 0.8 as also done to other Group B case histories, and the overall post-liquefaction shear strength value is obtained as $C_{u,modified}$=12.60 kPa for this case history in the end.

An important modification is also employed for the Upper San Fernando Dam Downstream Slope case history in this study. Nevertheless, this modification is not applied to the back-calculated residual strength value of Weber (2015), but employed to the residual strength values predicted by the relationships provided by this study. In fact, the consistent modification (taking constant ξ = 0.8) applied to all Group B less well-documented cases is also employed for this case history as well, and the back-calculated post-liquefaction shear strength of the case history is modified as 27.87 kPa.

The difference of this case history from the other ones is that although it also suffered liquefaction-induced damage and displacements during the 1971 San Fernando Earthquake, it has not received as much attention from the previous studies as the Lower San Fernando Dam because the displacements were not clearly sufficient to classify this case as a post-liquefaction case history. In fact, Olson (2001), Olson and Stark (2002), Wang (2003), Kramer (2008), and Wang and Kramer (2015) did not perform back-analyses for this case history due to the same reason. Weber (2015) reported the lateral and vertical displacements of the crest of the dam towards the downstream and downwards directions as 5 feet and 3 feet, respectively.

Additionally, the toe slippage was reported as 7-9 feet towards the downstream direction. Weber (2015) decided that these displacements were adequate to include this case history in its back-analyses database. As a result, this case history is also included in this study to be able to obtain a consistent case history database with Weber (2015).

On the other hand, the predicted post-liquefaction shear strength results by the relationships recommended by this study are slightly modified for this case history due to the reasons abovementioned. As a result of these small displacements observed at the site, both of the $S_{r,yield}$ and $S_{r,resid/geom}$ values corresponding to pre-failure and post-failure geometries are evaluated very close to each other, and very high by Weber (2015). Hence, the arithmetic mean of the predicted residual strength values, and the $S_{r,yield}$ value estimated by this study is considered as the overall post-liquefaction shear strength value of this case history.

The apparent pre-failure stress along the liquefied portions of the failure plane required to provide a static Factor of Safety equal to 1.0 for pre-failure geometry, $S_{r,yield}$, value was reported as 35.62 kPa for this case history by Weber (2015). However, a different approach provided in Equation 4-26 is followed in this study to estimate the $S_{r,yield}$ value for this case. Although the details of the relationship given in Equation 4-26 will be discussed in Chapter 4 deeply, while M parameter in this equation symbolizes the slope of the stress path in q vs. p' domain, p' represents the mean effective stress of the soil. The average representative initial pre-failure mean effective stress (p'_0) is evaluated as 100 kPa for this case history by the linear elastic modeling of the cross-section in PLAXIS 2D Ultimate Connect Edition V22.00.00.1733 software. The initial slope of the stress path in q vs. p' domain, on the other hand, is evaluated as M=0.95 approximately. Consequently, the $S_{r,yield}$ value is estimated as 47.5 kPa for this case history referring to Equation 4-26. Accordingly, the average of 47.5 kPa and the predicted residual strength values obtained by the recommended relationships are reported as the overall final post-liquefaction shear strength prediction values of this case history.

It should be noted that Weber (2015) did not consider Koda Numa Railway Embankment, Whiskey Springs Fan, and San Fernando Valley Juvenile Hall case histories in the study, and did not perform residual strength back-analyses for them. In addition, even though it performs back analyses for Calaveras Dam case history, it did not use the results in the development of residual strength prediction relationships due to the unreliable penetration resistances documented for this case history. Accordingly, it develops its residual strength prediction relationships based on 32 Group A and Group B case histories (the number becomes 29 when Mochi-Koshi Tailings Dam and Nerlerk Embankment Slide case histories are taken as single cases) given in Table 2.5 and Table 2.6. Although necessary material properties (D_{50}, FC, C_u, R, and S), stress components (σ'_1, σ'_2, σ'_3, p', and q), SPT resistances ($(N_1)_{60,cs}$), limit void ratios (e_{max} and e_{min}), and relative densities (RD) were developed for Calaveras Dam, Koda Numa Railway Embankment, Whiskey Springs Fan, and San Fernando Valley Juvenile Hall case histories in this study as discussed in Chapter 3, they are also not taken into account in the development of post-liquefaction prediction relationship models to be able to achieve a consistent comparison between this study and Weber (2015) for the same 32 case histories during the probabilistic regressions by the Maximum Likelihood Method. However, the details of these case histories and their evaluated parameters are still presented in Appendix A for documentation.

In the end, the modified back-calculated post-liquefaction shear strength values of Weber (2015) are obtained as tabulated in Table 4.1 for each case history. These modified values are directly taken as the basis for the probabilistic regressions by the Maximum Likelihood Method, and the residual strength prediction models are developed accordingly.

Table 4.1 Original and modified back-calculated post-liquefaction shear strength values of Weber (2015)

#	Case History	Pre-failure $S_{r,yield}$ values of Weber (2015) (kPa)	Post-failure $S_{r,resid/geom}$ values of Weber (2015) (kPa)	Modified $S_{r,backanalyzed}$ values of Weber (2015) (kPa)	Original $S_{r,backanalyzed}$ values of Weber (2015) (kPa)
1	Wachusett Dam - North Dike	39.69	3.88	10.92	14.08
2	Fort Peck Dam	107.01	8.33	12.60	36.48
3	Uetsu Railway Embankment	17.00	0.53	1.82	1.82
4	Lower San Fernando Dam - U/S Slope	61.33	3.78	25.81	25.81
5	Hachiro-Gata Road Embankment	6.46	1.92	3.39	3.26
6	La Marquesa Dam - U/S Slope	12.11	2.35	4.36	4.93
7	La Marquesa Dam - D/S Slope	15.18	7.66	9.72	10.25
8	La Palma Dam	9.62	4.02	6.51	6.51
9	Lake Ackerman Highway Embankment	9.24	2.68	5.12	5.12
10	Chonan Middle School	9.53	4.88	6.75	6.75
11	Soviet Tajik - May 1 Slide	27.77	7.95	16.33	16.33
12-1 (L)	Shibecha-Cho Embankment	19.87	7.04	10.73	10.73
12-2 (S)		19.87	7.04	10.73	10.73
13	Route 272 at Higashiarekinai	16.33	3.30	6.61	6.61
14-1 (S)	Zeeland - Vlietepolder	17.67	5.75	10.53	7.47
14-2 (L)		17.67	5.75	7.05	7.47
15	Sheffield Dam	16.52	4.02	8.22	6.61
16-1 (S)	Helsinki Harbor	4.45	2.15	2.85	2.30
16-2 (L)		4.45	2.15	2.01	2.30
17	Solfatara Canal Dike	7.13	3.35	4.19	3.06
18	Lake Merced Bank	9.10	5.84	5.98	6.51
19	El Cobre Tailings Dam	21.55	2.39	9.58	4.55
20	Metoki Road Embankment	11.30	2.87	5.67	4.40
21-1 (S)	Hokkaido Tailings Dam	12.16	3.35	8.06	4.69
21-2 (L)		12.16	3.35	3.43	4.69
22	Upper San Fernando Dam - D/S Slope	35.62	34.04	27.87	34.76
23-1 (L)	Tar Island Dyke	35.38	21.64	15.09	24.71
23-2 (S)		35.38	21.64	26.10	24.71
24	Mochi-Koshi Tailings Dam 1	22.84	10.77	5.80	10.10
25	Mochi-Koshi Tailings Dam 2	22.84	10.77	6.97	10.10
26	Nerlerk Embankment Slide 1	7.33	2.54	4.63	3.26

Table 4.1 (cont'd) Original and modified back-calculated post-liquefaction shear strength values of Weber (2015)

27	Nerlerk Embankment Slide 2	7.33	2.54	3.54	3.26
28	Nerlerk Embankment Slide 3	7.33	2.54	2.70	3.26
29	Asele Road Embankment	14.08	6.30	6.21	6.56
30-1 (S)	Nalband Railway Embankment	10.10	6.61	7.41	8.00
30-2 (L)		10.10	6.61	5.94	8.00
31-1 (L)	Sullivan Tailings	30.02	5.94	14.08	13.26
31-2 (S)		30.02	5.94	14.69	13.26
32	Jamuna Bridge	16.76	4.31	8.43	8.38

4.3 Fundamentals of the Post-liquefaction Shear Strength Relationships

Evaluation of material properties (mean grain size (D_{50}), fines content (FC), coefficient of uniformity (C_u), roundness (R), sphericity (S), SPT resistance ($(N_1)_{60}$ and $(N_1)_{60,cs}$)) and stress components (effective principal stresses (σ'_1, σ'_2 and σ'_3), mean effective stress (p'), deviatoric stress (q)) for the case histories (and sub-cases) was the initial step of the development of the post-liquefaction shear strength relationships. These steps are already discussed in Sections 3.2, 3.4 and 3.5. Following that, the limit void ratios (e_{max} and e_{min}) and void ratio ranges (e_{max}-e_{min}) are evaluated by semi-empirical relationships mentioned in Section 3.6. Accordingly, the in situ relative densities (RD) and initial void ratios corresponding to 1 kPa confining stress approximately (e_0) are evaluated as explained in Section 3.7.

It should be reminded that the overall failure planes were sub-divided into smaller pieces as stated in Section 3.3 to be able to assign different penetration resistances (if adequate borehole data was available) and different stress components with respect to confining effects along these sub-sections. The individual failure surface lengths remaining in the liquefied portion of the soil profile were also determined for these sub-sections to be able to evaluate the final overall post-liquefaction strength along the entire failure plane.

Once these necessary model input parameters are determined for each case history, the actual in-situ void ratios (e_{ICC}) are evaluated for each of them with corresponding volume-stress models for isotropic states. It should be noted that the initial void ratios (e_0), whose evaluation process was explained in Section 3.7, are the void ratios corresponding to 1 kPa confining stress approximately. This value actually comes from the evaluation process of limit void ratios. When the limit void ratios are evaluated in the laboratory by several standard testing procedures, such as ASTM International D4253-00 and ASTM International D4254-00, the confining stress acting on the samples during the experiment is approximately 1 kPa. This value may rise up to several kilopascals more, but it is commonly assumed to be 1 kPa in general. Therefore, the initial void ratios evaluated by using these limit void ratios also correspond to 1 kPa confining stress. However, the actual confining stress values are much more higher than 1 kPa in the field for liquefaction case histories. Therefore, these initial void ratios corresponding to 1 kPa confining (mean effective) stress should be re-evaluated with respect to corresponding in-situ confining stresses, i.e., mean effective stresses in the field, and lower void ratio values should be obtained. This re-evaluation is performed with volume-stress relationships for isotropic states, i.e., isotropic compression curve relationships, for each of the seven prediction models.

The corresponding isotropic compression curves are also compared with the isotropic compression curves developed from the compression index (C_c) values reported in Mesri and Vardhanabhuti (2009). The documented data on C_c values for three groups of sands with different relative density ranges are shown in Figure 4.3.

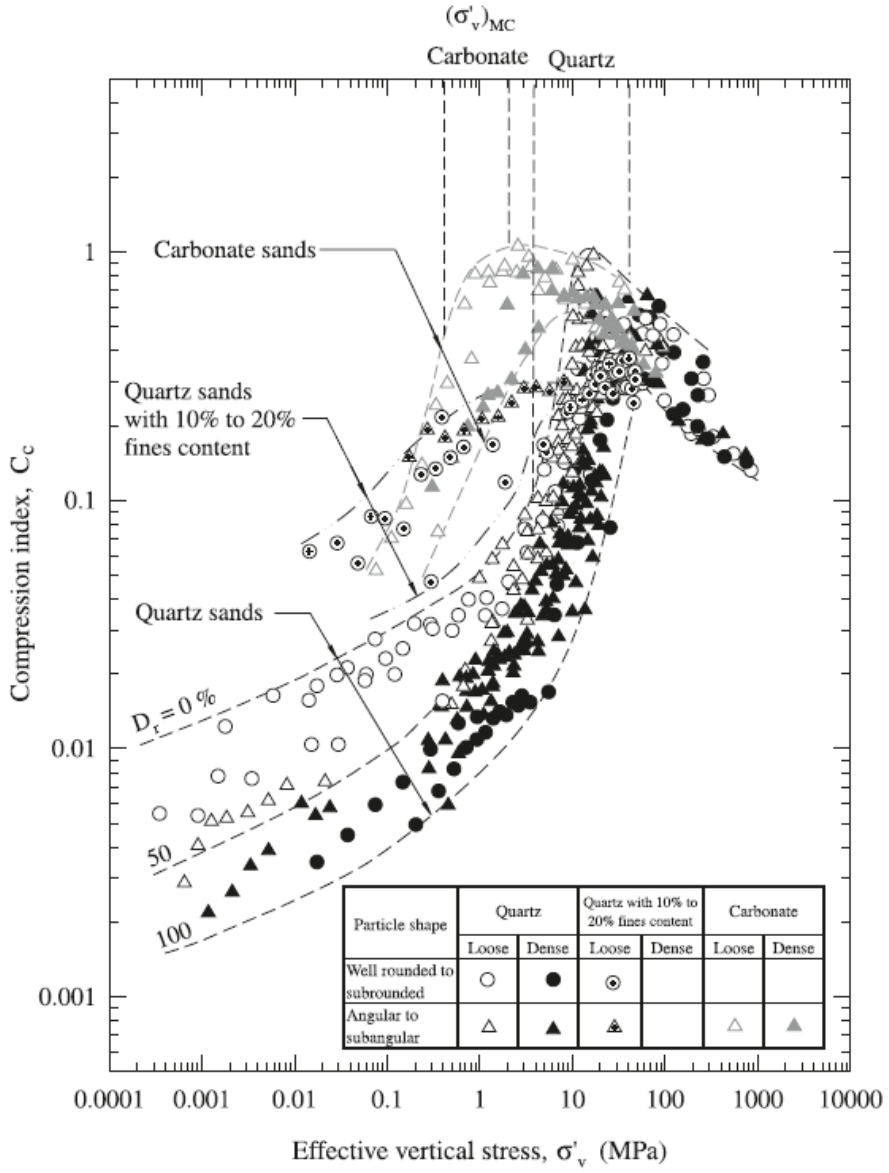

Figure 4.3. C_c values for sands as a function of effective vertical stress with respect to different relative density ranges (Mesri and Vardhanabhuti, 2009)

It is judged in this study that these C_c values can be significantly guiding in estimating the void ratio changes (Δe) of soils between their initial states (e_0 at 1 kPa confining stress) to in-situ states (e_{ICC}). Thus, the corresponding isotropic compression curves used in residual strength prediction models are encouraged to fit those curves developed by the C_c values of Mesri and Vardhanabhuti (2009).

It should be noted that the C_c values are reported as a function of relative density and effective vertical stress in Figure 4.10. Therefore, this effective vertical stress axis is converted to mean effective stress to be able to achieve consistency with e vs. p' domain. To convert σ'_{v0} values to p' values, the approximate relationship given in Equation 4-8 is employed.

$$p' = \frac{\sigma'_x + \sigma'_y + \sigma'_z}{3} = \sigma'_z \cdot \frac{\frac{\sigma'_x}{\sigma'_z} + \frac{\sigma'_y}{\sigma'_z} + \frac{\sigma'_z}{\sigma'_z}}{3} = \sigma'_z \cdot \frac{1 + 2 \cdot K_0}{3} \qquad \text{Equation 4-8}$$

In this equation, while σ'_z represents the effective vertical stress, σ'_x and σ'_y represent the effective horizontal stresses in two dimensions, respectively. K_0 represents the earth pressure coefficient at rest, which is defined as the ratio of horizontal and vertical effective stresses $\left(K_0 = \frac{\sigma'_x}{\sigma'_z} = \frac{\sigma'_y}{\sigma'_z}\right)$. For simplicity, the effective horizontal stresses in two dimensions are assumed to be equal to each other, and the relationship given in Equation 4-8 is developed.

The value of K_0 can be evaluated as a function of internal friction angle, ϕ', as presented in Equation 4-9.

$$K_0 = 1 - \sin(\phi') \qquad \text{Equation 4-9}$$

It is also known that the internal friction angle depends on the relative density of the soil. Although there are numerous relationships available in the literature between the internal friction angle and the relative density, the one recommended by Mujtaba et al. (2018) provided in Equation 4-10 is used in this study to estimate K_0 values of different relative densities. In this equation, RD represents the relative density of soil in percentage. The corresponding relationship is also presented in Figure 4.4.

$$\phi' = 0.276 \cdot RD + 18.70 \qquad \text{Equation 4-10}$$

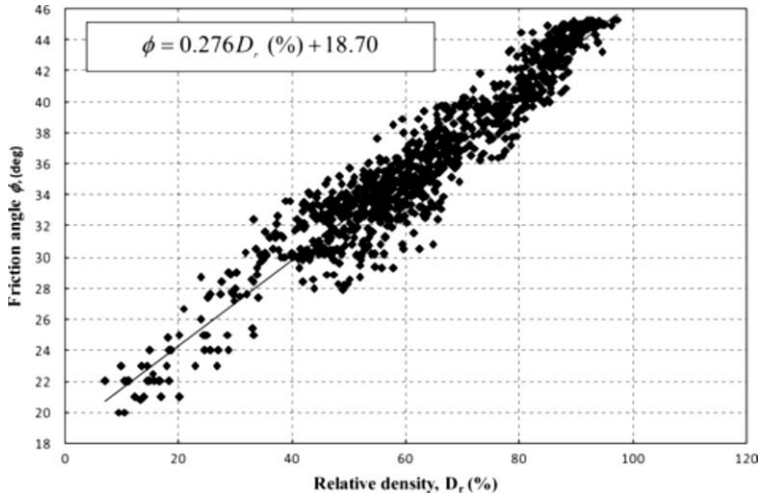

Figure 4.4. Relationship between internal friction angle (ϕ') and relative density (Mujtaba et al., 2018)

Once the initial vertical effective stress values are converted to mean effective stress values by Equation 4-8, the corresponding relationship given in Figure 4.3 between the C_c values and σ'_{v0} is converted to the relationship between the C_c values and p' as presented in Figure 4.5.

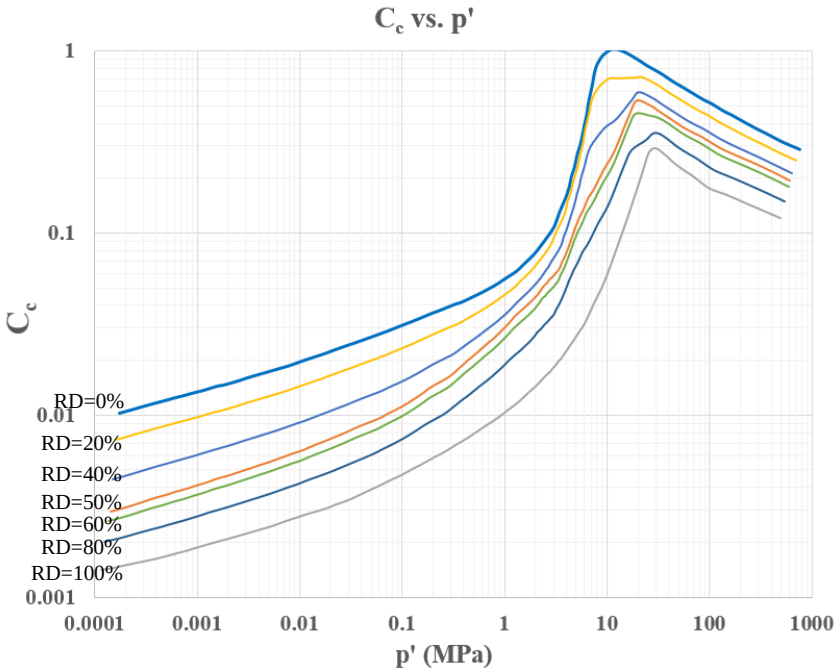

Figure 4.5. C_c values for sands as a function of mean effective stress with respect to different relative density ranges

Each curve in Figure 4.5 corresponds to the relationship between the C_c values and mean effective stresses for different relative densities. From top to bottom, they represent 0%, 20%, 40%, 50%, 60%, 80% and 100% relative density values.

To plot the corresponding isotropic compression curves at these relative densities in void ratio versus mean effective stress domain, the changes in void ratios (Δe) are evaluated at mean effective ranges by using the relevant C_c values. The formula provided in Equation 4-11 is used to calculate the void ratio changes.

$$\Delta e = C_c \cdot log\left(\frac{\sigma'_f}{\sigma'_i}\right) \qquad \text{Equation 4-11}$$

In this equation, σ'_i and σ'_f represent the initial and final mean effective stresses, respectively. The corresponding C_c values are obtained from the relationship provided in Figure 4.5, at the average mean effective stress value of σ'_i and σ'_f. Accordingly, these void ratio changes are subtracted from the initial void ratio values (e_0) of the corresponding relative densities. It should be noted that the arithmetic average of the maximum and minimum void ratios of the case histories provided in Table 3.13 are used to evaluate the initial void ratios at 0%, 20%, 40%, 60%, 80% and 100% relative densities.

As a result, the isotropic compression curves recommended by Mesri and Vardhanabhuti (2009) are developed in void ratio versus mean effective stress domain as shown in Figure 4.6 for the average limit void ratio values of the case histories. The isotropic compression curves developed during the residual strength prediction models for the same relative density values are compared with these curves, and encouraged to match them as much as possible during the probabilistic regressions.

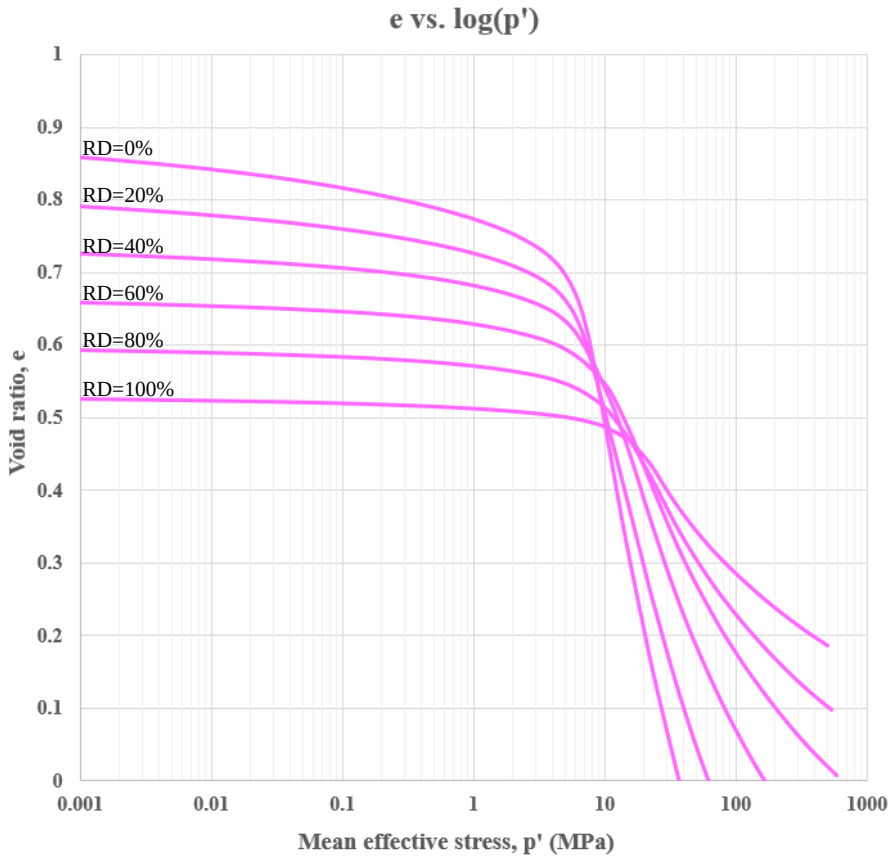

Figure 4.6. Isotropic compression curves recommended by Mesri and Vardhanabhuti (2009) for 0%, 20%, 40%, 60%, 80% and 100% relative densities

It should be noted that Mesri and Vardhanabhuti (2009) is one of the studies in the literature to suggest representative isotropic compression curves for the soils. In fact, there are also other studies available that recommend similar but different curves for isotropic states. For instance, Wei and Yang (2019) recommends the curves presented in Figure 4.7a and Figure 4.7b for the isotropic compression curves of Toyoura sand and Fujian sand, respectively. It should be noted that these sands were also mixed with some amount of crushed silica silt before the experiments.

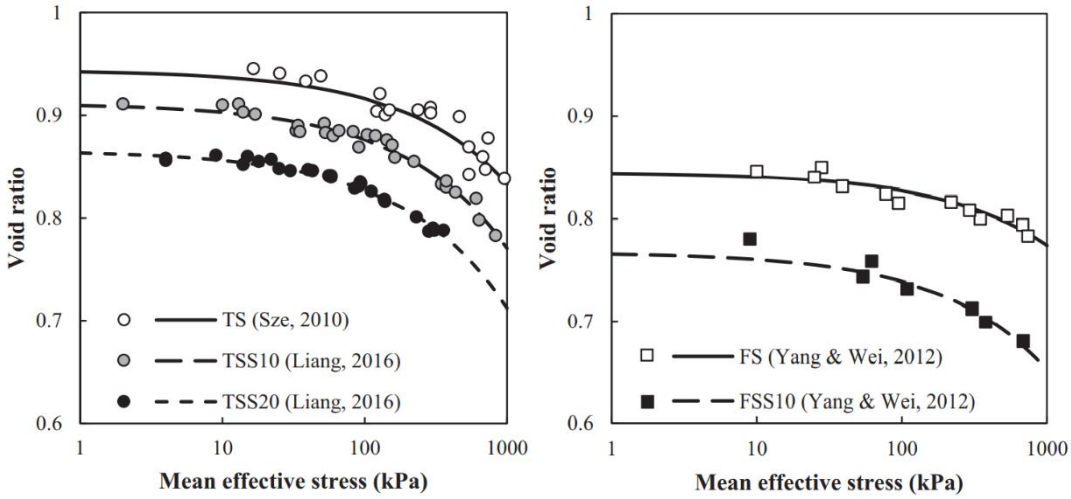

Figure 4.7. Isotropic compression curves for (a) Toyoura sand and (b) Fujian sand (Wei and Yang, 2019)

When Figure 4.6 of Mesri and Vardhanabhuti (2009) and Figure 4.7 of Wei and Yang (2019) are compared, it can be seen that while the crushing of the soil particles is observed at higher mean effective stress ranges for Mesri and Vardhanabhuti (2009) such as 2-20 MPa, this range is much lower for Wei and Yang (2019) such as 0.2-0.8 MPa. Hence, it can be concluded that the shape of the isotropic state curves is still debatable in literature in terms of larger mean effective stresses and particle crushing. In fact, the case history database developed in this study for the evaluation of post-liquefaction shear strength relationships does not contain any data for these extremely large mean effective stress ranges. Therefore, the particle crushing range of the isotropic compression curves and liquefaction state curves are out of the scope of this study. Nevertheless, the relationships provided in each of these seven residual strength prediction models for the isotropic and liquefaction state curves try to model these higher mean effective stress ranges compatible with the literature as much as possible.

Once the actual in-situ void ratios (e_{ICC}) are evaluated for each case history and sub-section, the initial data points of these cases are located in the void ratio versus mean effective stress domain with their corresponding initial mean effective stress (p'_0)

values. Since these initial mean effective stresses are evaluated for the pre-failure geometry before the event, they correspond to the initial states of the soils.

Following that, the final locations of these points are determined in the void ratio versus mean effective stress domain by using the volume-stress relationships for liquefaction states for each of the seven prediction models. For undrained conditions, the initial state of soils follows a horizontal path in this domain (towards the right and left for dense and loose soils, respectively) as no volume change occurs and the void ratio remains the same. Therefore, the mean effective stresses, i.e., the final location of the data points, corresponding to the liquefaction state for each sub-section are evaluated by using the same in-situ void ratio (e_{ICC}) in liquefaction state curve relationships.

Once the initial and final locations of the data points are determined in the void ratio versus mean effective stress domain, other parameters used in the evaluation of failure criterion, such as the liquefaction state friction angle (ϕ'_{ls}), Lode angle (θ), slope of the stress paths in q vs. p' domain for triaxial compression tests (M_{tc}) and in general (M), are calculated. These parameters are selected with certain care and attention to be able to include all effective principal stress components in three dimensions in confining effect. Accordingly, the residual strength values are predicted based on this criterion for each sub-section.

Finally, these residual strength values are multiplied by the individual failure plane lengths of the sub-sections (L_i), and corresponding sub-section results are summed for each case history. Then, this summation is divided by the total length of the failure plane (L_t) in order to evaluate the representative overall post-liquefaction shear strength value for the corresponding case history.

4.4 Post-liquefaction Shear Strength Prediction Relationships

Seven different post-liquefaction shear strength prediction relationships are developed in the scope of this thesis based on the Maximum Likelihood Method, and

they are compared with each other to determine the best model producing the most accurate and precise results when compared to back analyses of the same case histories. The differences between these models rise from the relationships used for the liquefaction states and isotropic states. The details of these models are explained in this section.

4.4.1 Model 1

The first residual strength prediction model utilizes a double logarithmic void ratio versus mean effective stress domain (ln(e) vs. ln(p')) for both the liquefaction and isotropic compression responses. In other words, the liquefaction and isotropic state curves become asymptomatic to a horizontal line at higher stresses, and negative void ratio values at these higher stress ranges are avoided as a result of this asymptote and the log-nature of the relationships.

The basic mathematical relationship recommended by Sheng et al. (2008) given in Equation 4-12 is implemented for the isotropic compression curves.

$$ICC: \quad \ln(e - e_{lim}) = \ln(N) - \lambda \cdot \ln\,(p' + p'_r) \qquad \text{Equation 4-12}$$

In this equation, while p' represents the in-situ mean effective stress measured at the field, e represents the corresponding void ratio at this mean effective stress value. λ and N are defined as the slope of the isotropic compression curves, and the void ratio on these curves when $p' + p'_r = 1$ (unit stress), respectively.

Although a constant value of λ was suggested by Sheng et al. (2008) as a fitting parameter to this relationship, it is defined as a function of void ratio range (e_{max}-e_{min}) and relative density (RD in decimals) in this study referring to the literature. The relationship given in Equation 4-13 is used to evaluate the slope of the isotropic compression curves (ICC).

$$\lambda = \frac{\theta_3 \cdot exp\big(\theta_4 \cdot (e_{max} - e_{min})\big)}{1 + \theta_5 \cdot RD} \qquad \text{Equation 4-13}$$

The relative density should be written in decimals, not in percentage, in Equation 4-13. As it can be seen from this equation, the slope of the isotropic compression curves decreases as relative density of the soil increases.

Jefferies and Been (2006) presents Figure 4.8 given below for the relationship between the slope of the critical state line and the fines content of the uniformly graded soils. Although this figure is provided for the slope of the CSLs, the same λ value is employed for the slope of the isotropic compression lines for Model 1 as it will be discussed. Therefore, Figure 4.8 can also be a guide for the λ values of the isotropic compression curves.

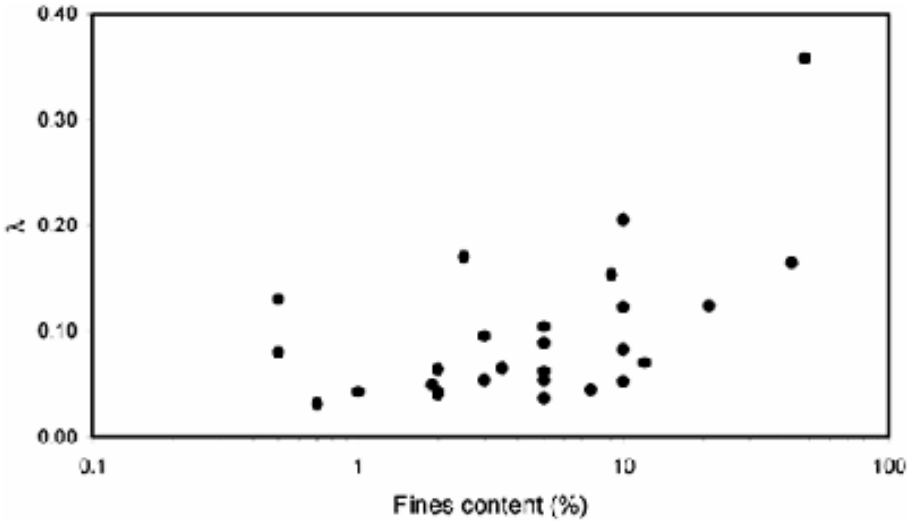

Figure 4.8. Relationship between the slope of the critical state line and fines content of the uniformly graded soils (Jefferies and Been, 2006)

As it can be seen from this figure, a relationship exists between the fines content and λ value of soil. Hence, the relationship provided for λ in Equation 4-13 is also developed in the light of that. In fact, the void ratio range term in Equation 4-13 does the same job with fines content as e_{max}-e_{min} value changes significantly with respect to fines content as discussed in Section 3.2.

In Equation 4-12, e_{lim} gives the minimum limit void ratio that the curves become asymptomatic at very high stresses. This value is directly taken as zero in Model 1

to avoid any negative void ratios, and updated as 0.35 in Model 2 due to some reasons that will be discussed in the next section.

p'_r represents the shifting stress controlling the curvature of the isotropic compression curves, and is defined as the form given in Equation 4-14.

$$p'_r = \left(\frac{N}{e_0 - e_{lim}}\right)^{1/\lambda} - p'_0 \qquad \text{Equation 4-14}$$

In this equation, e_0 represents the void ratio at a known mean stress p'_0 on the ICCs. In our case, these values are regarded as the initial state of the soil. In other words, p'_0 is taken as 1 kPa = 0.001 MPa referring to the confining stress acting on samples during limit void ratio determination experiments, and e_0 is taken as the corresponding initial void ratio at this confining stress evaluated by Equation 3-68. In the current case that $e_{lim} = 0$, the ratio of $\frac{N}{e_0}$ automatically reflects the curvature of the ICCs.

The corresponding void ratio on the isotropic compression curves when $p' + p'_r = 1$ (unit stress) in Equation 4-12 and Equation 4-14 is symbolized with the capital letter N, and defined as a function of void ratio range similar to λ compatible to the literature. Again, Jefferies and Been (2006) presents Figure 4.9 given below for the relationship between the void ratio value on the critical state line for p'=1 kPa (Γ_1) and the maximum void ratio (e_{max}) of the uniformly graded soils.

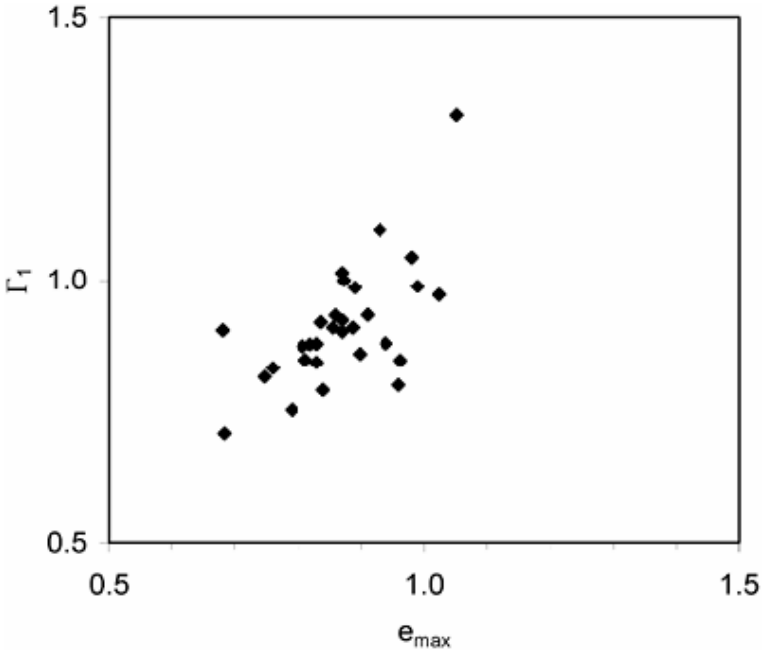

Figure 4.9. Relationship between the void ratio value on the critical state line for p'=1 kPa and the maximum void ratio of the uniformly graded soils (Jefferies and Been, 2006)

A similar relationship can also be applied to the isotropic compression curves because the void ratio value on the isotropic compression curve for p'=1 (unit stress) is unique for each soil and depends on the characteristics of the material. Once the possible trends are evaluated between the value of N and e_{max}, e_{min} or e_{max}-e_{min}, the relationship between N and e_{max}-e_{min} is decided to be employed in this study. Inspired of that, the relationship provided in Equation 4-15 is used to evaluate N values.

$$N = \theta_1 \cdot (e_{max} - e_{min}) \qquad \text{Equation 4-15}$$

In the end, the void ratios (e) evaluated by Equation 4-12 are defined as the actual in-situ void ratios (e_{ICC}), and they are directly located in the void ratio versus mean effective stress domain as the initial state points of the corresponding case histories (green dots in Figure 4.11).

The liquefaction state curve is also defined in a similar manner such that again the basic mathematical relationship recommended by Sheng et al. (2008) given in Equation 4-16 is implemented for the liquefaction state curves (LSC).

$$LSC: \quad \ln(e - e_{lim}) = \ln(\Gamma) - \lambda \cdot \ln\left(p'_{ls} + p'_{cr}\right) \qquad \text{Equation 4-16}$$

In this equation, p'_{ls} represents the final mean effective stress after the event at the liquefaction state. In other words, it is the reduced mean effective stress due to the increasing excess pore pressures during the liquefaction. In fact, the difference between p' in Equation 4-12 and p'_{ls} in Equation 4-16 estimates the excess pore pressures developed during the liquefaction. Therefore, other parameters in Equation 4-16 are evaluated first to be able to estimate p'_{ls} in the end.

The void ratio (e) in Equation 4-16 is already the same as the void ratio evaluated by Equation 4-12, e_{ICC}, because the void ratio remains the same under undrained conditions.

In Equation 4-16, λ and Γ are defined as the slope of the liquefaction state curves, and the void ratio on these curves when $p'_{ls} + p'_{cr} = 1$ (unit stress), respectively. The same slope with isotropic compression curves is assigned to liquefaction state curves to achieve parallelism between them; thus, Equation 4-13 can be used to evaluate λ values with respect to void ratio range and relative density of the cases.

e_{lim} coefficient again represents the minimum limit void ratio that the curves become asymptomatic at very high stresses, and it is equal to the one defined in Equation 4-12, which is equal to zero for Model 1.

p'_{cr} represents the shifting stress controlling the curvature of the liquefaction state curves, and is defined as the form given in Equation 4-17.

$$p'_{cr} = \left(\frac{\Gamma}{e_{c0}}\right)^{1/\lambda} - p'_{c0} \qquad \text{Equation 4-17}$$

In this equation, e_{c0} represents the void ratio at a known mean effective stress p'_{c0} on the LSCs. This reference stress value of p'_{c0} is again taken as 1 kPa = 0.001 MPa

similar to p'_0 in this study. The void ratios located on the LSCs corresponding to 1 kPa = 0.001 MPa mean effective stress are estimated as a function of the maximum void ratio (e_{max}) and limit void ratio (e_{lim}) as given in Equation 4-18 referring to the literature.

$$e_{c0} = \theta_6 \cdot e_{max} - e_{lim} \qquad \text{Equation 4-18}$$

A similar relationship between the limit void ratios (e_{max} or e_{min}) and e_{c0} is also suggested by Cho et al. (2006) as shown in Figure 4.10. In this figure, the vertical axis labeled as Intercept (Γ) corresponds to the e_{c0} in Equation 4-18 as both of them represent the interception of Critical State Curves (or Liquefaction State Curves in our case) with the vertical axis in semi-logarithmic void ratio versus mean effective stress domain. In other words, they give the corresponding void ratio value when mean effective stress is equal to unit stress.

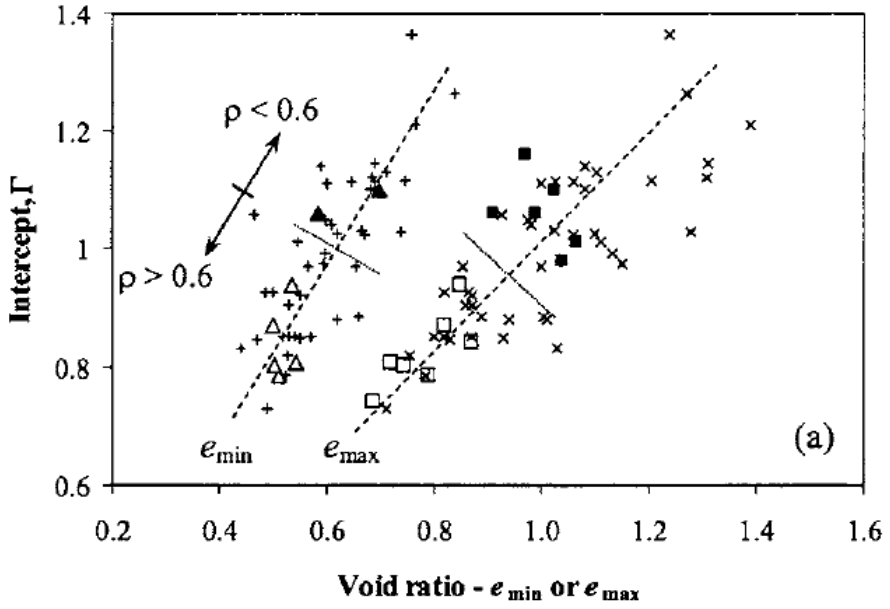

Figure 4.10. Relationship between the limit void ratios and the void ratio on Critical State Curves when mean effective stress is equal to unity (Cho et al., 2006)

The corresponding void ratio on the liquefaction state curves when $p'_{ls} + p'_{cr} = 1$ (unit stress) in Equation 4-16 and Equation 4-17 is symbolized with Γ, and again defined as a function of void ratio range similar to λ and N compatible to the

literature. Figure 4.9 provided by Jefferies and Been (2006) shows the relationship between the void ratio value on the critical state line for p'=1 kPa (Γ_1) and the maximum void ratio (e_{max}) of the uniformly graded soils. Once the possible trends are evaluated between the value of Γ and e_{max}, e_{min} or e_{max}-e_{min}, the relationship between Γ and e_{max}-e_{min} is decided to be employed in this study. Inspired of that, the relationship provided in Equation 4-20 is used to evaluate Γ values.

$$\Gamma = \theta_2 \cdot (e_{max} - e_{min}) \qquad \text{Equation 4-19}$$

In the end, the final mean effective stress values after the liquefaction are evaluated by solving p'_{ls} in Equation 4-16 for each sub-section of the case histories. The closed-form solution of the relationship is provided in Equation 4-20.

$$p'_{ls} = exp\left(\frac{\ln(\Gamma) - \ln(e_{ICC} - e_{lim})}{\lambda}\right) - \left(\frac{\Gamma}{\theta_6 \cdot e_{max} - e_{lim}}\right)^{\frac{1}{\lambda}} + p'_{c0} \qquad \text{Equation 4-20}$$

In this equation, e_{ICC} and λ can be evaluated by using Equation 4-12 and Equation 4-13, respectively.

Once the final mean effective stress values after the liquefaction (p'_{ls}) are evaluated by Equation 4-20, the corresponding data points are located in the void ratio versus mean effective stress domain as the liquefaction state points of the corresponding case histories (red squares in Figure 4.11).

Accordingly, the other parameters used in the evaluation of failure criterion, such as the liquefaction state friction angle (ϕ'_{ls}), Lode angle (θ), slope of the stress paths in q vs. p' domain for triaxial compression tests (M_{tc}) and in general (M), are computed. Taking the triaxial compression test as a reference, and M_{tc} as the reference soil property, M values are evaluated as a function of Lode angle (θ) and M_{tc} as given in Equation 4-21.

$$M = \frac{3\sqrt{3}}{cos\theta \cdot \left(1 + \frac{6}{M_{tc}}\right) - \sqrt{3} \cdot sin\theta} \qquad \text{Equation 4-21}$$

M_{tc} values are evaluated by Equation 4-22 referring to the fundamentals of the critical state theory in literature.

$$M_{tc} = \frac{6 \cdot \sin(\phi'_{ls})}{3 - \sin(\phi'_{ls})} \qquad \text{Equation 4-22}$$

In the literature, various studies such as Cho et al. (2006) declare that the critical state friction angle, which is similar to the liquefaction state angle in this study, depends on the angularity of the soil particles, and ranges between 26°-38° for sands and silty sands. In fact, it is stated that its value also depends on the fines content of the soil such that its value decreases with increasing fines content. Furthermore, it is also declared that the uniformity of soils has an impact on the critical state friction angle such that for well-graded soils having a coefficient of uniformity greater than 4-6, the critical state friction angles are expected to be greater than that of poorly-graded or uniformly graded soils. Inspired of that, the liquefaction state angle is defined as a function of roundness (R), sphericity (S), fines content (FC) and coefficient of uniformity (C_u) in this study. The relationship provided in Equation 4-23 is employed for the evaluation of liquefaction state friction angle values in degrees.

$$\phi'_{ls} = \left(\frac{\theta_{10}}{\theta_{12} + \theta_{13} \cdot \left(\frac{FC - \theta_{14}}{\theta_{15}} \right)} \right) \cdot \left(1 + (\theta_{11} \cdot R \cdot S) \right) + \theta_{16} \qquad \text{Equation 4-23}$$

In this equation, fines content (FC) is given in terms of percentage, and its value is limited with an upper bound of 50%. In other words, for larger fines content values than 50%, FC=50% should be used in this relationship.

In Equation 4-23, θ_{16} represents the additional friction angle value added for well-graded soils. Therefore, its value is adjusted with respect to the coefficient of uniformity value. If the coefficient of uniformity value is greater than a constant value of θ_{17}, then θ_{16} is added to the liquefaction state friction angles. On the contrary, for uniformly graded soils having coefficient of uniformity values less than θ_{17}, no additional angle is added to the liquefaction state friction angles; i.e., $\theta_{16} = 0$ is

considered. The value of θ_{17} should vary between 4 and 6 as it is the boundary for the coefficient of uniformity between uniformly graded and well-graded soils, and it is adjusted as 4 in this study inspired from the literature. On the other hand, the value of θ_{16}, which is the additional friction angle value added for well-graded soils, is evaluated based on probabilistic regressions by the Maximum Likelihood Method for each prediction model.

For the Lode angle (θ), the well-known definition in the literature represented in Equation 4-24 is used. It should be noted that the resulting θ value obtained by Equation 4-24 is in the units of radians, and there are different representations are available for Lode angle as a function of stress invariants I_1, I_2, I_3 or J_1, J_2, J_3.

$$\theta = \frac{1}{3} \cdot arcsin\left[\frac{1}{q^3} \cdot \frac{-27}{2} \cdot \left(\frac{2 \cdot \sigma'_1 - \sigma'_2 - \sigma'_3}{3}\right) \cdot \left(\frac{2 \cdot \sigma'_2 - \sigma'_1 - \sigma'_3}{3}\right) \cdot \left(\frac{2 \cdot \sigma'_3 - \sigma'_1 - \sigma'_2}{3}\right)\right] \quad \text{Equation 4-24}$$

In this equation, σ'_1, σ'_2, σ'_3 and q represent major, intermediate and minor effective principal stresses, and deviatoric stress, respectively. Although there are different definitions of deviatoric stress is available in the literature based on the type of the tests and failure criterion, the definition shown in Equation 4-25 is used in this study to include the effects of all effective principal stresses in three dimensions.

$$q = \sqrt{\frac{(\sigma'_1 - \sigma'_2)^2}{2} + \frac{(\sigma'_2 - \sigma'_3)^2}{2} + \frac{(\sigma'_3 - \sigma'_1)^2}{2}} \quad \text{Equation 4-25}$$

Finally, the post-liquefaction shear strength values for each sub-section is predicted by using the relationship provided in Equation 4-26 as a function M and liquefaction state mean effective stress (p'_{ls}) values.

$$\tau_{liq,i} = \frac{q_{ls,i}}{2} = \frac{M_i \cdot p'_{ls,i}}{2} \quad \text{Equation 4-26}$$

It should be noted that these τ_{liq} values represent the post-liquefaction shear strength values of the sub-sections of the case histories. To be able to evaluate the overall

representative post-liquefaction shear strength value of the entire case history, these values are multiplied by the individual failure plane lengths of the sub-sections (L_i) and summed together. Then, this summation is divided by the total length of the failure plane (L_t) in order to evaluate the representative overall post-liquefaction shear strength value for the corresponding case history as given in Equation 4-27.

$$\tau_{liq,overall} = \frac{\sum_{i=1}^{n} \tau_{liq,i} \cdot L_i}{L_t} \qquad \text{Equation 4-27}$$

In this equation, n represents the total number of the sub-sections in the corresponding case history. In other words, it is the number of the failure plane slices that individual stress measurements and penetration resistance evaluations are performed, as discussed in Sections 3.3, 3.4 and 3.5.

Once the residual strength predictions evaluated by Equation 4-27 are compared with the modified back-analyses results of Weber (2015) given in Table 4.1 for the same case histories, the overall best-fit model parameters are developed as given in Table 4.2 for Model 1 as a result of probabilistic regressions by the Maximum Likelihood Method.

Table 4.2 Best-fit model parameters for Model 1

θ_1	1.191
θ_2	0.361
θ_3	1.168
θ_4	-1.257
θ_5	0.995
θ_6	0.996
θ_{10}	31.105
θ_{11}	-0.071
θ_{12}	0.881
θ_{13}	-0.080
θ_{14}	18.917

Table 4.2 (cont'd) Best-fit model parameters for Model 1

θ_{15}	31.083
θ_{16}	3.500
θ_{17}	4

Consequently, the equations of isotropic compression curves and liquefaction state curves are obtained as given in Equation 4-28 and Equation 4-29, respectively.

$$ICC: \quad \ln(e) = \ln\left(1.191 \cdot (e_{max} - e_{min})\right) - \left(\frac{1.168 \cdot exp\left(-1.257 \cdot (e_{max} - e_{min})\right)}{1 + 0.995 \cdot RD}\right) \cdot \ln\left[p' + \left(\frac{1.191 \cdot (e_{max} - e_{min})}{e_0}\right)^{\frac{1+0.995 \cdot RD}{1.168 \cdot exp\left(-1.257 \cdot (e_{max} - e_{min})\right)}} - 0.001\right] \quad \text{Equation 4-28}$$

$$LSC: \quad ln(e) = \ln\left(0.361 \cdot (e_{max} - e_{min})\right) - \left(\frac{1.168 \cdot exp\left(-1.257 \cdot (e_{max} - e_{min})\right)}{1 + 0.995 \cdot RD}\right) \cdot \ln\left(p'_{ls} + \left(\frac{0.361 \cdot (e_{max} - e_{min})}{0.996 \cdot e_{max}}\right)^{\frac{1+0.995 \cdot RD}{1.168 \cdot exp\left(-1.257 \cdot (e_{max} - e_{min})\right)}} - 0.001\right) \quad \text{Equation 4-29}$$

Using these equations, the case history data points with respect to their initial states and liquefaction states are located in the void ratio versus mean effective stress domain as presented in Figure 4.11.

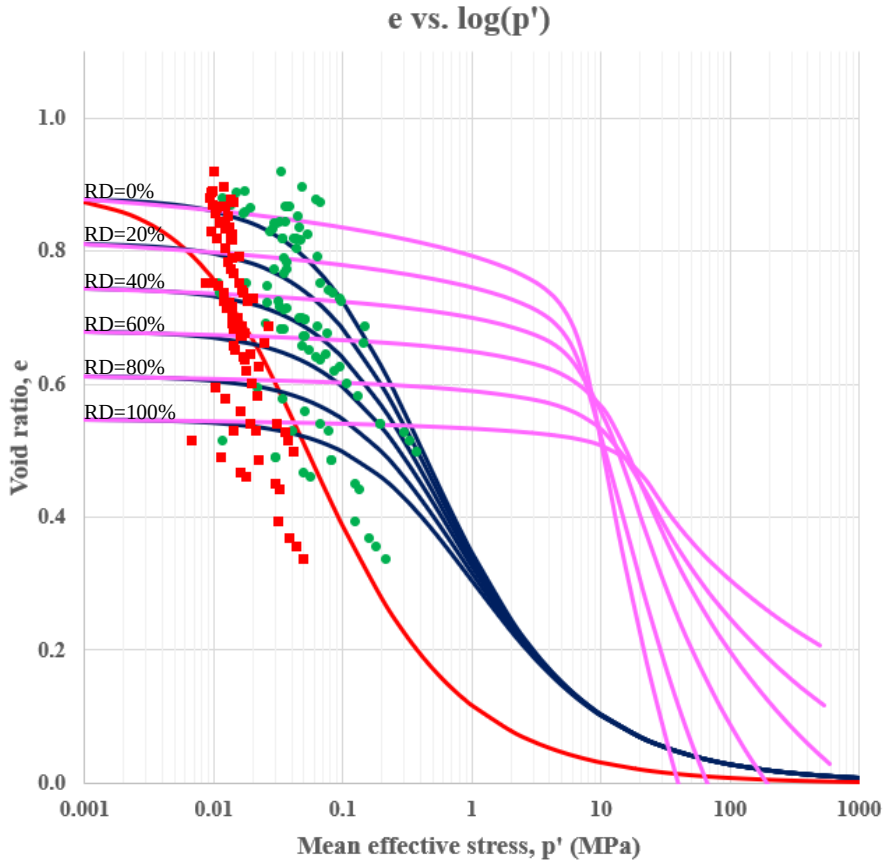

Figure 4.11. Void ratio versus mean effective stress domain for Model 1

In Figure 4.11, while the green dots and red squares represent the initial and liquefaction states of the case history data points, the purple and blue curves represent the isotropic compression curves recommended by Mesri and Vardhanabhuti (2009), and developed for Model 1 by Equation 4-12, respectively, for 0%, 20%, 40%, 60%, 80%, and 100% relative densities. The red curve presents the liquefaction state curve evaluated by Equation 4-16 by using the average λ, Γ, e_{c0} and p'_{cr} values of the case histories. It should be noted that the stress differences between the initial and liquefaction states, i.e., between the green dots and red squares, give the generated excess pore pressures during the liquefaction.

A summary of the evaluated parameters for Model 1 is tabulated in Table 4.3 for each sub-section of the case histories.

Table 4.3 Summary of the evaluated parameters for Model 1

#	Case History	Section	e_{c0}	N	Γ	p'_r (MPa)	λ	p'_{cr} (MPa)	p'_{ls} (MPa)	e_{ICC}
1	Wachusett Dam - North Dike	WND-1	0.941	0.454	0.138	0.338	0.543	0.028	0.014	0.774
		WND-2	0.941	0.454	0.138	0.338	0.568	0.033	0.020	0.730
		WND-105	0.941	0.454	0.138	0.338	0.573	0.034	0.026	0.688
		WND-3	0.941	0.454	0.138	0.340	0.520	0.024	0.025	0.663
2	Fort Peck Dam	Boring 3	0.919	0.421	0.128	0.325	0.473	0.014	0.035	0.528
		Boring 7	0.919	0.421	0.128	0.325	0.473	0.014	0.042	0.499
		Boring 6	0.919	0.421	0.128	0.325	0.473	0.014	0.038	0.515
		Boring 7	0.919	0.421	0.128	0.325	0.473	0.014	0.014	0.692
3	Uetsu Railway Embankment	S1	0.964	0.484	0.147	0.355	0.596	0.042	0.014	0.825
		S2	0.964	0.484	0.147	0.354	0.578	0.038	0.011	0.843
4	Lower San Fernando Dam - U/S Slope	S103&S111	0.561	0.197	0.060	0.273	0.746	0.049	0.031	0.394
		S101&S102&S104	0.561	0.197	0.060	0.273	0.746	0.049	0.043	0.355
		S105	0.561	0.197	0.060	0.273	0.746	0.049	0.050	0.337
		S105	0.561	0.197	0.060	0.273	0.746	0.049	0.039	0.369
5	Hachiro-Gata Road Embankment	S1	1.004	0.496	0.150	0.338	0.541	0.029	0.010	0.865
		S2	1.004	0.496	0.150	0.338	0.541	0.029	0.012	0.844
6	La Marquesa Dam - U/S Slope	B-2	1.023	0.509	0.154	0.337	0.536	0.028	0.013	0.853
		B-III	1.023	0.509	0.154	0.337	0.541	0.029	0.012	0.868
		B-3	1.023	0.509	0.154	0.337	0.541	0.029	0.010	0.891
7	La Marquesa Dam - D/S Slope	B-II	1.013	0.503	0.152	0.340	0.509	0.023	0.012	0.835
		B-1	1.013	0.503	0.152	0.341	0.503	0.022	0.016	0.792
8	La Palma Dam	B-3	0.996	0.491	0.149	0.338	0.535	0.028	0.014	0.818
		B-4	0.996	0.491	0.149	0.338	0.539	0.028	0.010	0.858
9	Lake Ackerman Highway Embankment	S1	0.850	0.348	0.105	0.282	0.629	0.035	0.014	0.701
		S2	0.850	0.348	0.105	0.282	0.629	0.035	0.013	0.714
		S3	0.850	0.348	0.105	0.283	0.630	0.036	0.009	0.753
10	Chonan Middle School	No.4	0.999	0.492	0.149	0.338	0.545	0.030	0.010	0.870
		No.3	0.999	0.492	0.149	0.338	0.553	0.031	0.013	0.837
11	Soviet Tajik - May 1 Slide	S1	0.810	0.366	0.111	0.330	0.627	0.041	0.019	0.646
		S2	0.810	0.366	0.111	0.330	0.627	0.041	0.022	0.627
12	Shibecha-Cho Embankment	B-2	0.795	0.401	0.122	0.389	0.619	0.047	0.014	0.682
		B-3	0.795	0.401	0.122	0.390	0.630	0.050	0.016	0.672
		B-5	0.795	0.401	0.122	0.389	0.618	0.047	0.014	0.682
		B-4	0.795	0.401	0.122	0.390	0.630	0.050	0.016	0.673
		B-5	0.795	0.401	0.122	0.389	0.618	0.047	0.014	0.682

Table 4.3 (cont'd) Summary of the evaluated parameters for Model 1

13	Route 272 at Higashiarekinai	Left	1.001	0.494	0.150	0.339	0.524	0.026	0.013	0.819
		Right	1.001	0.494	0.150	0.338	0.528	0.026	0.014	0.820
14	Zeeland - Vlietepolder	Small-S1	0.886	0.362	0.110	0.261	0.507	0.015	0.015	0.651
		Small-S2	0.886	0.362	0.110	0.261	0.507	0.015	0.018	0.620
		Large-S1	0.886	0.362	0.110	0.261	0.507	0.015	0.014	0.657
		Large-S2	0.886	0.362	0.110	0.261	0.507	0.015	0.022	0.583
		Large-S3	0.886	0.362	0.110	0.261	0.507	0.015	0.020	0.602
15	Sheffield Dam	Right	1.047	0.526	0.159	0.338	0.512	0.024	0.012	0.867
16	Helsinki Harbor	Small-S1	1.019	0.476	0.144	0.307	0.539	0.026	0.009	0.881
		Small-S2	1.019	0.476	0.144	0.306	0.524	0.023	0.010	0.859
		Large-S1	1.019	0.476	0.144	0.306	0.526	0.023	0.012	0.843
		Large-S2	1.019	0.476	0.144	0.306	0.529	0.024	0.012	0.844
17	Solfatara Canal Dike	S1	0.870	0.354	0.107	0.274	0.611	0.032	0.010	0.751
		S2	0.870	0.354	0.107	0.278	0.626	0.034	0.011	0.747
18	Lake Merced Bank	Boring 2	0.996	0.500	0.152	0.357	0.487	0.020	0.014	0.790
19	El Cobre Tailings Dam	S1	1.053	0.497	0.151	0.310	0.576	0.033	0.014	0.873
		S2	1.053	0.497	0.151	0.310	0.576	0.033	0.014	0.879
		S3	1.053	0.497	0.151	0.310	0.576	0.033	0.012	0.898
		S4	1.053	0.497	0.151	0.310	0.576	0.033	0.010	0.920
20	Metoki Road Embankment	S-19	1.017	0.505	0.153	0.338	0.552	0.031	0.012	0.868
		S-13	1.017	0.505	0.153	0.338	0.541	0.029	0.010	0.888
21	Hokkaido Tailings Dam	Small-S1	0.930	0.406	0.123	0.306	0.652	0.044	0.011	0.820
		Small-S2	0.930	0.406	0.123	0.306	0.652	0.044	0.012	0.805
		Large-S1	0.930	0.406	0.123	0.306	0.652	0.044	0.011	0.820
		Large-S2	0.930	0.406	0.123	0.306	0.652	0.044	0.010	0.831
22	Upper San Fernando Dam - D/S Slope	A1&B1&C1	0.631	0.233	0.071	0.283	0.730	0.049	0.014	0.530
		A2&B2&C2	0.631	0.233	0.071	0.283	0.728	0.049	0.022	0.486
		A3	0.631	0.233	0.071	0.283	0.728	0.049	0.030	0.449
		B4&C4	0.631	0.233	0.071	0.283	0.728	0.049	0.032	0.441
		B5&C5	0.631	0.233	0.071	0.283	0.730	0.049	0.022	0.487
23	Tar Island Dyke	Large-S1	0.854	0.363	0.110	0.287	0.539	0.021	0.017	0.637
		Large-S2	0.854	0.363	0.110	0.287	0.539	0.021	0.031	0.540
		Small-S1	0.854	0.363	0.110	0.287	0.539	0.021	0.017	0.640
		Small-S2	0.854	0.363	0.110	0.287	0.539	0.021	0.031	0.540
24	Mochi-Koshi Tailings Dam 1	S1	0.665	0.263	0.080	0.310	0.739	0.056	0.010	0.594
		S2	0.665	0.263	0.080	0.310	0.739	0.056	0.016	0.559

Table 4.3 (cont'd) Summary of the evaluated parameters for Model 1

		S3	0.665	0.263	0.080	0.310	0.739	0.056	0.021	0.530
25	Mochi-Koshi Tailings Dam 2	S1	0.658	0.257	0.078	0.311	0.763	0.060	0.019	0.540
		S2	0.658	0.257	0.078	0.311	0.763	0.060	0.012	0.578
26	Nerlerk Embankment Slide 1	S1	0.939	0.431	0.131	0.318	0.484	0.016	0.014	0.716
		S2	0.939	0.431	0.131	0.318	0.484	0.016	0.015	0.699
		S3	0.939	0.431	0.131	0.318	0.484	0.016	0.013	0.722
27	Nerlerk Embankment Slide 2	S1	0.939	0.431	0.131	0.318	0.484	0.016	0.014	0.713
		S2	0.939	0.431	0.131	0.318	0.484	0.016	0.016	0.687
		S3	0.939	0.431	0.131	0.318	0.484	0.016	0.012	0.738
28	Nerlerk Embankment Slide 3	S1	0.939	0.431	0.131	0.318	0.484	0.016	0.018	0.676
		S2	0.939	0.431	0.131	0.318	0.484	0.016	0.015	0.700
		S3	0.939	0.431	0.131	0.318	0.484	0.016	0.012	0.737
29	Asele Road Embankment	S1	0.935	0.471	0.143	0.364	0.531	0.028	0.014	0.767
		S2	0.935	0.471	0.143	0.364	0.532	0.028	0.013	0.774
30	Nalband Railway Embankment	NB-1	0.550	0.197	0.060	0.305	0.837	0.069	0.011	0.490
		Small-S2	0.550	0.197	0.060	0.305	0.837	0.069	0.016	0.468
		NB-1	0.550	0.197	0.060	0.305	0.837	0.069	0.011	0.490
		Large-S2	0.550	0.197	0.060	0.305	0.837	0.069	0.018	0.460
		Large-S3	0.550	0.197	0.060	0.305	0.837	0.069	0.007	0.514
31	Sullivan Tailings	Large-S1	0.998	0.460	0.140	0.305	0.497	0.018	0.013	0.785
		CP91-29	0.998	0.460	0.140	0.305	0.497	0.018	0.018	0.724
		CP91-31	0.998	0.460	0.140	0.305	0.497	0.018	0.016	0.753
		Small-S1	0.998	0.460	0.140	0.305	0.497	0.018	0.017	0.742
		CP91-31	0.998	0.460	0.140	0.305	0.497	0.018	0.017	0.737
32	Jamuna Bridge	S1	0.883	0.353	0.107	0.260	0.583	0.026	0.014	0.698
		S2	0.883	0.353	0.107	0.260	0.583	0.026	0.012	0.724

In the end, the post-liquefaction shear strength values are predicted by Model 1 as tabulated in Table 4.4 for each sub-section of the case histories.

Table 4.4 Summary of the predicted post-liquefaction shear strength values for Model 1

#	Case History	Section	L_i (m)	L_t (m)	ϕ'_{ls} (deg)	M_{tc}	θ (deg)	M	$\tau_{liq,i}$ (kPa)	$\sum \tau_{liq,i} \cdot L_i / L_t$ (kPa)
1	Wachusett Dam - North Dike	WND-1	19.3	68.9	33.43	1.350	-20.16	0.910	6.20	9.5
		WND-2	20.9		33.43	1.350	-23.99	0.915	9.20	
		WND-105	18.4		33.43	1.350	-25.03	0.917	12.11	
		WND-3	10.2		33.43	1.350	-23.86	0.915	11.38	
2	Fort Peck Dam	Boring 3	200.3	389.3	33.10	1.335	-24.40	0.909	16.07	15.8
		Boring 7	67.9		33.10	1.335	-25.23	0.910	18.94	
		Boring 6	79.4		33.10	1.335	-24.05	0.908	17.25	
		Boring 7	41.7		33.10	1.335	-3.45	0.930	6.38	
3	Uetsu Railway Embankment	S1	9.4	20.3	32.83	1.323	-22.54	0.900	6.17	5.5
		S2	10.9		32.83	1.323	-23.15	0.901	5.00	
4	Lower San Fernando Dam - U/S Slope	S103&S111	54.8	103.8	41.49	1.701	-26.24	1.076	16.86	20.1
		S101&S102&S104	16.9		41.49	1.701	-23.82	1.073	23.21	
		S105	16.8		41.49	1.701	-22.48	1.072	26.68	
		S105	15.3		41.49	1.701	-24.04	1.073	20.76	
5	Hachiro-Gata Road Embankment	S1	10.9	14.9	34.45	1.394	-23.20	0.935	4.88	5.1
		S2	4.0		34.45	1.394	-26.01	0.940	5.78	
6	La Marquesa Dam - U/S Slope	B-2	6.6	21.8	35.70	1.449	-22.31	0.960	6.20	5.5
		B-III	7.2		35.70	1.449	-26.21	0.966	5.69	
		B-3	8.0		35.70	1.449	-25.83	0.965	4.73	
7	La Marquesa Dam - D/S Slope	B-II	10.1	15.8	34.65	1.403	-19.75	0.936	5.72	6.3
		B-1	5.7		34.65	1.403	-26.25	0.945	7.38	
8	La Palma Dam	B-3	6.1	15.9	34.15	1.381	-24.28	0.931	6.39	5.4
		B-4	9.8		34.15	1.381	-18.45	0.925	4.81	
9	Lake Ackerman Highway Embankment	S1	5.9	29.6	32.83	1.323	-24.32	0.903	6.33	6.1
		S2	12.5		32.83	1.323	27.11	1.256	7.91	
		S3	11.2		32.83	1.323	-24.27	0.903	3.93	
10	Chonan Middle School	No.4	6.7	15.4	34.45	1.394	-22.12	0.934	4.56	5.5
		No.3	8.7		34.45	1.394	-23.51	0.936	6.16	
11	Soviet Tajik - May 1 Slide	S1	44.9	68.8	41.49	1.701	-19.75	1.072	10.37	10.9
		S2	24.0		41.49	1.701	-16.90	1.074	11.97	
12	Shibecha-Cho Embankment	B-2	8.3	47.3	38.15	1.556	-25.53	1.013	7.34	7.9
		B-3	25.9		38.15	1.556	-26.59	1.015	8.37	
		B-5	13.1		38.15	1.556	-19.06	1.008	7.25	

Table 4.4 (cont'd) Summary of the predicted post-liquefaction shear strength values for Model 1

		B-4	10.9	24.0	38.15	1.556	-23.50	1.010	8.23	7.7
		B-5	13.1		38.15	1.556	-19.06	1.008	7.25	
13	Route 272 at Higashiarekinai	Left	6.7	22.9	34.65	1.403	-25.82	0.944	6.32	6.3
		Right	16.2		34.65	1.403	-21.61	0.937	6.35	
14	Zeeland - Vlietepolder	Small-S1	31.3	75.7	33.38	1.348	-25.02	0.916	6.71	7.5
		Small-S2	44.4		33.38	1.348	-25.38	0.917	8.08	
		Large-S1	100.2	318.6	33.38	1.348	-28.70	0.926	6.53	8.7
		Large-S2	107.4		33.38	1.348	-29.98	0.930	10.20	
		Large-S3	111.0		33.38	1.348	-28.30	0.924	9.07	
15	Sheffield Dam	Right	14.9	14.9	36.81	1.497	-23.36	0.984	6.07	6.1
16	Helsinki Harbor	Small-S1	6.7	16.0	32.74	1.319	-26.65	0.906	4.18	4.4
		Small-S2	9.2		32.74	1.319	-25.29	0.903	4.63	
		Large-S1	35.5	71.3	32.74	1.319	-28.98	0.913	5.28	5.3
		Large-S2	35.8		32.74	1.319	-29.10	0.913	5.33	
17	Solfatara Canal Dike	S1	4.6	9.4	33.38	1.348	-29.86	0.929	4.58	4.7
		S2	4.8		33.38	1.348	-21.71	0.911	4.88	
18	Lake Merced Bank	Boring 2	30.3	30.3	33.01	1.331	-21.91	0.903	6.25	6.2
19	El Cobre Tailings Dam	S1	83.7	348.1	37.99	1.549	-20.17	1.005	7.14	6.1
		S2	43.8		37.99	1.549	-27.09	1.013	6.92	
		S3	85.8		37.99	1.549	-28.94	1.018	6.08	
		S4	134.8		37.99	1.549	-29.71	1.021	5.16	
20	Metoki Road Embankment	S-19	6.8	14.0	34.15	1.381	-22.39	0.928	5.47	5.0
		S-13	7.2		34.15	1.381	-21.85	0.927	4.47	
21	Hokkaido Tailings Dam	Small-S1	18.3	23.2	37.99	1.549	-29.20	1.019	5.40	5.6
		Small-S2	5.0		37.99	1.549	-22.74	1.006	6.12	
		Large-S1	18.3	48.6	37.99	1.549	-29.20	1.019	5.40	5.0
		Large-S2	30.4		37.99	1.549	-27.21	1.014	4.82	
22	Upper San Fernando Dam - D/S Slope	A1&B1&C1	14.3	111.1	41.19	1.688	-16.83	1.069	7.69	13.9
		A2&B2&C2	10.0		41.19	1.688	-18.92	1.067	11.86	
		A3	23.2		41.19	1.688	-29.14	1.078	16.35	
		B4&C4	33.4		41.19	1.688	-26.36	1.071	17.34	
		B5&C5	30.2		41.19	1.688	-24.32	1.068	11.89	
23	Tar Island Dyke	Large-S1	260.2	308.6	34.20	1.384	-29.41	0.945	8.14	9.1
		Large-S2	48.4		34.20	1.384	-22.71	0.929	14.43	
		Small-S1	27.6	76.0	34.20	1.384	-20.91	0.927	7.81	12.0

Table 4.4 (cont'd) Summary of the predicted post-liquefaction shear strength values for Model 1

		Small-S2	48.4		34.20	1.384	-22.71	0.929	14.43	
24	Mochi-Koshi Tailings Dam 1	S1	61.2	183.7	41.49	1.701	-25.71	1.076	5.56	8.6
		S2	61.0		41.49	1.701	-24.13	1.073	8.67	
		S3	61.6		41.49	1.701	-21.33	1.072	11.49	
25	Mochi-Koshi Tailings Dam 2	S1	34.8	70.9	41.49	1.701	-23.32	1.073	10.20	8.4
		S2	36.1		41.49	1.701	-19.35	1.072	6.63	
26	Nerlerk Embankment Slide 1	S1	23.5	166.7	33.43	1.350	-26.51	0.920	6.35	6.6
		S2	71.7		33.43	1.350	-27.33	0.922	7.06	
		S3	71.4		33.43	1.350	-27.98	0.924	6.12	
27	Nerlerk Embankment Slide 2	S1	18.9	155.5	33.43	1.350	-26.72	0.921	6.47	6.5
		S2	68.5		33.43	1.350	-28.11	0.925	7.59	
		S3	68.1		33.43	1.350	-16.52	0.910	5.45	
28	Nerlerk Embankment Slide 3	S1	80.5	361.9	33.43	1.350	-28.69	0.927	8.11	6.7
		S2	140.5		33.43	1.350	-28.52	0.926	7.03	
		S3	140.9		33.43	1.350	-29.72	0.930	5.60	
29	Asele Road Embankment	S1	20.1	26.5	35.70	1.449	-19.47	0.958	6.76	6.7
		S2	6.4		35.70	1.449	-22.90	0.961	6.48	
30	Nalband Railway Embankment	NB-1	25.3	32.5	38.99	1.592	-28.58	1.036	5.85	6.4
		Small-S2	7.2		38.99	1.592	-24.82	1.028	8.23	
		NB-1	25.3	57.2	38.99	1.592	-28.58	1.036	5.85	7.1
		Large-S2	25.8		38.99	1.592	-28.25	1.035	9.11	
		Large-S3	6.1		38.99	1.592	-21.44	1.025	3.50	
31	Sullivan Tailings	Large-S1	13.8	38.6	37.99	1.549	-10.45	1.017	6.56	7.8
		CP91-29	10.7		37.99	1.549	-20.69	1.005	9.21	
		CP91-31	14.2		37.99	1.549	-25.19	1.010	7.86	
		Small-S1	6.5	23.5	37.99	1.549	-23.15	1.007	8.34	8.5
		CP91-31	17.1		37.99	1.549	-25.32	1.010	8.62	
32	Jamuna Bridge	S1	44.9	88.3	33.29	1.344	-26.99	0.919	6.59	6.0
		S2	43.4		33.29	1.344	-14.97	0.907	5.38	

4.4.2 Model 2

The second residual strength prediction model again utilizes a double logarithmic void ratio versus mean effective stress domain (ln(e) vs. ln(p')) for both the

liquefaction and isotropic compression responses. In other words, the liquefaction and isotropic state curves become asymptomatic to a horizontal line at higher stresses, and negative void ratio values at these higher stress ranges are avoided as a result of this asymptote and the log-nature of the relationships.

There is only a very tiny difference exists between Model 1 and Model 2. In fact, the same relationships employed for Model 1 are also used for this model. The basic mathematical relationships recommended by Sheng et al. (2008) given in Equation 4-12 and Equation 4-16 are implemented for the isotropic compression curves and liquefaction state curves, respectively. The required parameters used in these relationships, i.e., N, Γ, λ, p'_r, p'_{cr}, and e_{c0}, are again evaluated by Equation 4-15, Equation 4-19, Equation 4-13, Equation 4-14, Equation 4-17, and Equation 4-18, respectively. In the end, the final mean effective stress values after the liquefaction are evaluated by solving p'_{ls} in Equation 4-16 for each sub-section of the case histories, and the closed-form solution of the relationship is obtained as given in Equation 4-20.

The only difference between Model 1 and Model 2 is that the minimum limit void ratio that the isotropic and liquefaction state curves become asymptomatic at very high stresses, e_{lim} value, is selected as 0.35 instead of zero in Model 2. This value of 0.35 is not randomly determined, but defined referring to Cubrinovski and Ishihara (2002). In that study, the loosest and densest possible packing of single-sized sphere shape of soil particles are presented as shown in Figure 4.12a and Figure 4.12b, respectively.

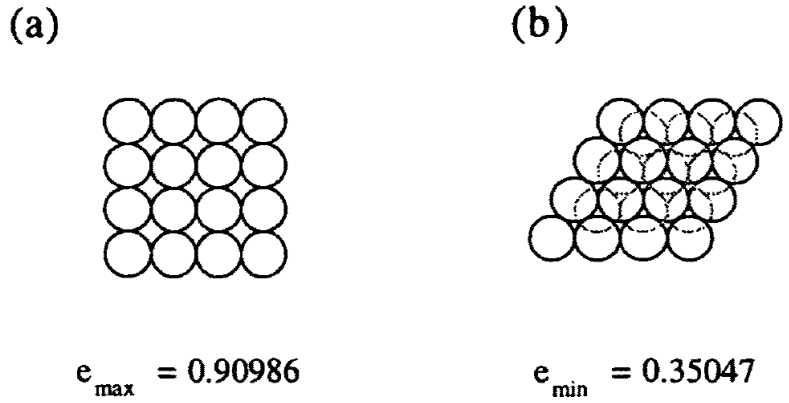

Figure 4.12. Schematic illustration of (a) the loosest and (b) the densest possible packing of single-sized sphere shape of soil particles

As presented in Figure 4.12b, the void ratio of the densest possible packing of single-sized sphere shape of soil particles is given as 0.35. This value directly comes from the geometry, and the corresponding relationship is provided in Equation 4-30. As it can be observed from this relationship, the minimum limit void ratio is independent of the size of the spheres.

$$e_{min} = \frac{3\sqrt{2} - \pi}{\pi} = 0.35047 \qquad \text{Equation 4-30}$$

The single-sized sphere shape of the soil particles can be matched with the shape of the soil particles at very high stress ranges because significant level of particle crushing occurs at those extreme stress levels. As a result of these particle crushings, the angularity of the soil particles disappears automatically, and a smooth sphere shape is obtained for them. Hence, defining the minimum limit void ratio that the isotropic and liquefaction state curves become asymptomatic at very high stresses as e_{lim} = 0.35 is pretty reasonable for Model 2.

Once the e_{lim} value is arranged as 0.35 for Model 2, the remaining procedure is exactly the same as Model 1 such that the other parameters used in the evaluation of failure criterion, such as the liquefaction state friction angle (ϕ'_{ls}), Lode angle (θ), slope of the stress paths in q vs. p' domain for triaxial compression tests (M_{tc}) and in

general (M), can be evaluated by using Equation 4-23, Equation 4-24, Equation 4-22 and Equation 4-21, respectively.

Finally, the post-liquefaction shear strength values for each sub-section can be predicted by using the relationship provided in Equation 4-26 as a function M and liquefaction state mean effective stress (p'_{ls}) values. Accordingly, the overall representative post-liquefaction shear strength values of all case histories can be predicted by using Equation 4-27.

Once the residual strength predictions evaluated by Equation 4-27 are compared with the modified back-analyses results of Weber (2015) given in Table 4.1 for the same case histories, the overall best-fit model parameters are developed as given in Table 4.5 for Model 2 as a result of probabilistic regressions by the Maximum Likelihood Method.

Table 4.5 Best-fit model parameters for Model 2

θ_1	0.839
θ_2	0.461
θ_3	0.372
θ_4	-0.370
θ_5	0.788
θ_6	0.984
θ_{10}	31.318
θ_{11}	-0.075
θ_{12}	1.088
θ_{13}	-0.250
θ_{14}	23.275
θ_{15}	27.725
θ_{16}	0.819
θ_{17}	4

Consequently, the equations of isotropic compression curves and liquefaction state curves are obtained as given in Equation 4-31 and Equation 4-32, respectively.

$$ICC: \quad \ln(e-0.35) = \ln\left(0.839\cdot(e_{max}-e_{min})\right) - \left(\frac{0.372\cdot exp\left(-0.37\cdot(e_{max}-e_{min})\right)}{1+0.788\cdot RD}\right) \cdot \ln\left[p' + \left(\frac{0.839\cdot(e_{max}-e_{min})}{e_0-0.35}\right)^{\frac{1+0.788\cdot RD}{0.372\cdot exp\left(-0.37\cdot(e_{max}-e_{min})\right)}} - 0.001\right] \qquad \text{Equation 4-31}$$

$$LSC: \quad ln(e-0.35) = \ln\left(0.461\cdot(e_{max}-e_{min})\right) - \left(\frac{0.372\cdot exp\left(-0.37\cdot(e_{max}-e_{min})\right)}{1+0.788\cdot RD}\right) \cdot \ln\left(p'_{ls} + \left(\frac{0.461\cdot(e_{max}-e_{min})}{0.984\cdot e_{max}-0.35}\right)^{\frac{1+0.788\cdot RD}{0.372\cdot exp\left(-0.37\cdot(e_{max}-e_{min})\right)}} - 0.001\right) \qquad \text{Equation 4-32}$$

Using these equations, the case history data points with respect to their initial states and liquefaction states are located in the void ratio versus mean effective stress domain as presented in Figure 4.13.

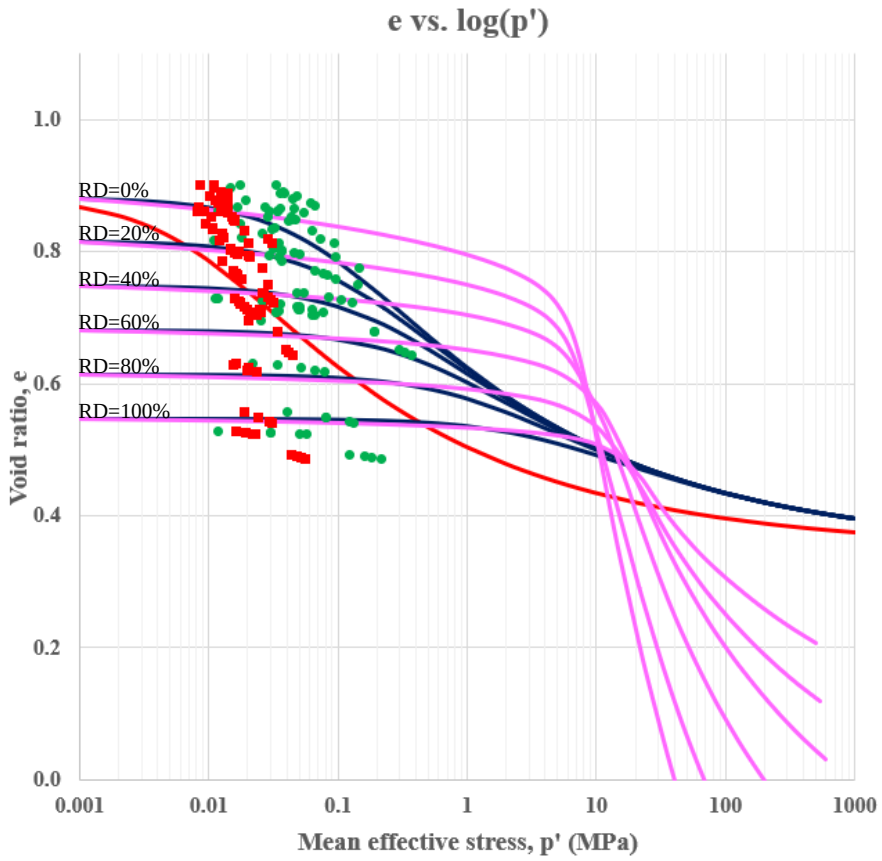

Figure 4.13. Void ratio versus mean effective stress domain for Model 2

In Figure 4.13, while the green dots and red squares represent the initial and liquefaction states of the case history data points, the purple and blue curves represent the isotropic compression curves recommended by Mesri and Vardhanabhuti (2009), and developed for Model 2 by Equation 4-12, respectively, for 0%, 20%, 40%, 60%, 80%, and 100% relative densities. The red curve presents the liquefaction state curve evaluated by Equation 4-16 by using the average λ, Γ, e_{c0} and p'_{cr} values of the case histories. It should be noted that the stress differences between the initial and liquefaction states, i.e., between the green dots and red squares, give the generated excess pore pressures during the liquefaction.

When Figure 4.11 of Model 1 and Figure 4.13 of Model 2 are compared with each other, it can be observed that while the isotropic compression and liquefaction state curves become asymptomatic to zero void ratio at very high stress ranges for Model 1, they become asymptomatic to a void ratio value of 0.35 for Model 2, which is pretty reasonable as discussed in Equation 4-30.

A summary of the evaluated parameters for Model 2 is tabulated in Table 4.6 for each sub-section of the case histories.

Table 4.6 Summary of the evaluated parameters for Model 2

#	Case History	Section	e_{c0}	N	Γ	p'_r (MPa)	λ	p'_{cr} (MPa)	p'_{ls} (MPa)	e_{ICC}
1	Wachusett Dam - North Dike	WND-1	0.579	0.320	0.176	0.227	0.256	0.009	0.017	0.800
		WND-2	0.579	0.320	0.176	0.201	0.265	0.010	0.021	0.792
		WND-105	0.579	0.320	0.176	0.197	0.267	0.011	0.026	0.776
		WND-3	0.579	0.320	0.176	0.264	0.247	0.007	0.029	0.749
2	Fort Peck Dam	Boring 3	0.524	0.268	0.147	0.302	0.226	0.003	0.040	0.651
		Boring 7	0.524	0.268	0.147	0.302	0.226	0.003	0.045	0.643
		Boring 6	0.524	0.268	0.147	0.302	0.226	0.003	0.042	0.648
		Boring 7	0.524	0.268	0.147	0.302	0.226	0.003	0.020	0.695
3	Uetsu Railway Embankment	S1	0.602	0.341	0.187	0.187	0.281	0.015	0.014	0.859
		S2	0.602	0.341	0.187	0.198	0.274	0.013	0.012	0.862
4	Lower San Fernando Dam - U/S Slope	S103&S111	0.184	0.122	0.067	0.452	0.290	0.029	0.044	0.493
		S101&S102&S104	0.184	0.122	0.067	0.452	0.290	0.029	0.051	0.489
		S105	0.184	0.122	0.067	0.452	0.290	0.029	0.055	0.487
		S105	0.184	0.122	0.067	0.452	0.290	0.030	0.048	0.490

Table 4.6 (cont'd) Summary of the evaluated parameters for Model 2

5	Hachiro-Gata Road Embankment	S1	0.641	0.349	0.192	0.187	0.261	0.009	0.012	0.877
		S2	0.641	0.349	0.192	0.187	0.261	0.009	0.014	0.867
6	La Marquesa Dam - U/S Slope	B-2	0.661	0.359	0.197	0.181	0.261	0.009	0.014	0.879
		B-III	0.661	0.359	0.197	0.177	0.263	0.009	0.013	0.889
		B-3	0.661	0.359	0.197	0.178	0.263	0.009	0.011	0.901
7	La Marquesa Dam - D/S Slope	B-II	0.651	0.354	0.195	0.215	0.249	0.007	0.015	0.853
		B-1	0.651	0.354	0.195	0.223	0.247	0.007	0.019	0.832
8	La Palma Dam	B-3	0.634	0.346	0.190	0.197	0.258	0.008	0.016	0.848
		B-4	0.634	0.346	0.190	0.193	0.260	0.009	0.012	0.869
9	Lake Ackerman Highway Embankment	S1	0.565	0.309	0.170	0.200	0.265	0.010	0.016	0.798
		S2	0.565	0.309	0.170	0.200	0.265	0.010	0.015	0.803
		S3	0.565	0.309	0.170	0.198	0.265	0.010	0.012	0.818
10	Chonan Middle School	No.4	0.636	0.347	0.191	0.187	0.262	0.009	0.011	0.879
		No.3	0.636	0.347	0.191	0.180	0.265	0.010	0.014	0.865
11	Soviet Tajik - May 1 Slide	S1	0.597	0.382	0.210	0.383	0.260	0.017	0.029	0.819
		S2	0.597	0.382	0.210	0.383	0.260	0.017	0.031	0.814
12	Shibecha-Cho Embankment	B-2	0.435	0.283	0.155	0.385	0.277	0.023	0.025	0.710
		B-3	0.435	0.283	0.155	0.364	0.281	0.025	0.025	0.712
		B-5	0.435	0.283	0.155	0.388	0.276	0.023	0.025	0.709
		B-4	0.435	0.283	0.155	0.364	0.281	0.025	0.024	0.712
		B-5	0.435	0.283	0.155	0.388	0.276	0.023	0.025	0.709
13	Route 272 at Higashiarekinai	Left	0.638	0.348	0.191	0.205	0.254	0.008	0.016	0.846
		Right	0.638	0.348	0.191	0.201	0.255	0.008	0.016	0.848
14	Zeeland - Vlietepolder	Small-S1	0.604	0.322	0.177	0.383	0.222	0.003	0.027	0.737
		Small-S2	0.604	0.322	0.177	0.383	0.222	0.003	0.029	0.732
		Large-S1	0.604	0.322	0.177	0.383	0.222	0.003	0.026	0.739
		Large-S2	0.604	0.322	0.177	0.383	0.222	0.003	0.032	0.724
		Large-S3	0.604	0.322	0.177	0.383	0.222	0.003	0.030	0.728
15	Sheffield Dam	Right	0.685	0.370	0.204	0.189	0.254	0.007	0.014	0.889
16	Helsinki Harbor	Small-S1	0.620	0.304	0.167	0.125	0.261	0.006	0.008	0.861
		Small-S2	0.620	0.304	0.167	0.132	0.255	0.005	0.009	0.843
		Large-S1	0.620	0.304	0.167	0.130	0.256	0.005	0.011	0.835
		Large-S2	0.620	0.304	0.167	0.129	0.257	0.005	0.011	0.836
17	Solfatara Canal Dike	S1	0.587	0.316	0.173	0.193	0.259	0.008	0.013	0.822
		S2	0.587	0.316	0.173	0.182	0.264	0.009	0.013	0.828
18	Lake Merced Bank	Boring 2	0.634	0.353	0.194	0.288	0.240	0.006	0.020	0.812

Table 4.6 (cont'd) Summary of the evaluated parameters for Model 2

19	El Cobre Tailings Dam	S1	0.652	0.318	0.175	0.106	0.279	0.008	0.012	0.869
		S2	0.652	0.318	0.175	0.106	0.279	0.008	0.012	0.873
		S3	0.652	0.318	0.175	0.106	0.279	0.008	0.010	0.885
		S4	0.652	0.318	0.175	0.106	0.279	0.008	0.008	0.900
20	Metoki Road Embankment	S-19	0.655	0.356	0.196	0.173	0.267	0.010	0.012	0.890
		S-13	0.655	0.356	0.196	0.181	0.263	0.009	0.011	0.897
21	Hokkaido Tailings Dam	Small-S1	0.591	0.305	0.168	0.132	0.287	0.011	0.009	0.861
		Small-S2	0.591	0.305	0.168	0.132	0.287	0.011	0.010	0.853
		Large-S1	0.591	0.305	0.168	0.132	0.287	0.011	0.009	0.861
		Large-S2	0.591	0.305	0.168	0.132	0.287	0.011	0.008	0.868
22	Upper San Fernando Dam - D/S Slope	A1&B1&C1	0.250	0.145	0.079	0.250	0.291	0.019	0.019	0.557
		A2&B2&C2	0.250	0.145	0.079	0.252	0.291	0.018	0.024	0.549
		A3	0.250	0.145	0.079	0.252	0.291	0.018	0.029	0.542
		B4&C4	0.250	0.145	0.079	0.252	0.291	0.018	0.031	0.541
		B5&C5	0.250	0.145	0.079	0.251	0.291	0.019	0.024	0.549
23	Tar Island Dyke	Large-S1	0.514	0.274	0.150	0.277	0.240	0.005	0.023	0.703
		Large-S2	0.514	0.274	0.150	0.277	0.240	0.005	0.034	0.678
		Small-S1	0.514	0.274	0.150	0.277	0.240	0.005	0.023	0.704
		Small-S2	0.514	0.274	0.150	0.277	0.240	0.005	0.034	0.678
24	Mochi-Koshi Tailings Dam 1	S1	0.323	0.199	0.109	0.289	0.295	0.024	0.016	0.631
		S2	0.323	0.199	0.109	0.289	0.295	0.024	0.020	0.624
		S3	0.323	0.199	0.109	0.289	0.295	0.024	0.024	0.618
25	Mochi-Koshi Tailings Dam 2	S1	0.316	0.194	0.107	0.271	0.302	0.026	0.020	0.620
		S2	0.316	0.194	0.107	0.271	0.302	0.026	0.016	0.628
26	Nerlerk Embankment Slide 1	S1	0.543	0.275	0.151	0.238	0.232	0.003	0.017	0.722
		S2	0.543	0.275	0.151	0.238	0.232	0.003	0.019	0.717
		S3	0.543	0.275	0.151	0.238	0.232	0.003	0.017	0.724
27	Nerlerk Embankment Slide 2	S1	0.543	0.275	0.151	0.238	0.232	0.003	0.018	0.721
		S2	0.543	0.275	0.151	0.238	0.232	0.003	0.020	0.713
		S3	0.543	0.275	0.151	0.238	0.232	0.003	0.016	0.729
28	Nerlerk Embankment Slide 3	S1	0.543	0.275	0.151	0.238	0.232	0.003	0.021	0.709
		S2	0.543	0.275	0.151	0.238	0.232	0.003	0.019	0.717
		S3	0.543	0.275	0.151	0.238	0.232	0.003	0.016	0.729
29	Asele Road Embankment	S1	0.573	0.332	0.182	0.290	0.254	0.010	0.021	0.792
		S2	0.573	0.332	0.182	0.288	0.254	0.010	0.020	0.794

Table 4.6 (cont'd) Summary of the evaluated parameters for Model 2

30	Nalband Railway Embankment	NB-1	0.193	0.139	0.076	0.441	0.316	0.052	0.019	0.526
		Small-S2	0.193	0.139	0.076	0.441	0.316	0.052	0.022	0.524
		NB-1	0.193	0.139	0.076	0.441	0.316	0.052	0.019	0.526
		Large-S2	0.193	0.139	0.076	0.441	0.316	0.052	0.023	0.523
		Large-S3	0.193	0.139	0.076	0.441	0.316	0.052	0.016	0.528
31	Sullivan Tailings	Large-S1	0.600	0.293	0.161	0.156	0.242	0.003	0.013	0.786
		CP91-29	0.600	0.293	0.161	0.156	0.242	0.003	0.018	0.759
		CP91-31	0.600	0.293	0.161	0.156	0.242	0.003	0.015	0.772
		Small-S1	0.600	0.293	0.161	0.156	0.242	0.003	0.016	0.767
		CP91-31	0.600	0.293	0.161	0.156	0.242	0.003	0.017	0.764
32	Jamuna Bridge	S1	0.600	0.316	0.173	0.197	0.249	0.006	0.017	0.796
		S2	0.600	0.316	0.173	0.197	0.249	0.006	0.015	0.805

In the end, the post-liquefaction shear strength values are predicted by Model 2 as tabulated in Table 4.7 for each sub-section of the case histories.

Table 4.7 Summary of the predicted post-liquefaction shear strength values for Model 2

#	Case History	Section	L_i (m)	L_t (m)	ϕ'_{ls} (deg)	M_{tc}	θ (deg)	M	$\tau_{liq,i}$ (kPa)	$\sum \tau_{liq,i} \cdot L_i / L_t$ (kPa)
1	Wachusett Dam - North Dike	WND-1	19.3	68.9	24.88	0.979	-20.16	0.713	6.03	8.0
		WND-2	20.9		24.88	0.979	-23.99	0.720	7.52	
		WND-105	18.4		24.88	0.979	-25.03	0.722	9.38	
		WND-3	10.2		24.88	0.979	-23.86	0.719	10.41	
2	Fort Peck Dam	Boring 3	200.3	389.3	24.26	0.952	-24.40	0.705	13.96	13.7
		Boring 7	67.9		24.26	0.952	-25.23	0.708	15.94	
		Boring 6	79.4		24.26	0.952	-24.05	0.705	14.76	
		Boring 7	41.7		24.26	0.952	-3.45	0.703	7.20	
3	Uetsu Railway Embankment	S1	9.4	20.3	23.75	0.930	-22.54	0.689	4.77	4.5
		S2	10.9		23.75	0.930	-23.15	0.690	4.29	
4	Lower San Fernando Dam - U/S Slope	S103&S111	54.8	103.8	36.95	1.504	-26.24	0.991	21.61	23.4
		S101&S102&S104	16.9		36.95	1.504	-23.82	0.987	25.22	
		S105	16.8		36.95	1.504	-22.48	0.985	27.20	
		S105	15.3		36.95	1.504	-24.04	0.987	23.79	

Table 4.7 (cont'd) Summary of the predicted post-liquefaction shear strength values for Model 2

5	Hachiro-Gata Road Embankment	S1	10.9	14.9	26.95	1.068	-23.20	0.768	4.61	4.8
		S2	4.0		26.95	1.068	-26.01	0.775	5.31	
6	La Marquesa Dam - U/S Slope	B-2	6.6	21.8	29.79	1.191	-22.31	0.832	5.84	5.2
		B-III	7.2		29.79	1.191	-26.21	0.840	5.36	
		B-3	8.0		29.79	1.191	-25.83	0.839	4.59	
7	La Marquesa Dam - D/S Slope	B-II	10.1	15.8	27.39	1.087	-19.75	0.773	5.88	6.4
		B-1	5.7		27.39	1.087	-26.25	0.785	7.40	
8	La Palma Dam	B-3	6.1	15.9	26.33	1.041	-24.28	0.755	5.87	5.1
		B-4	9.8		26.33	1.041	-18.45	0.746	4.58	
9	Lake Ackerman Highway Embankment	S1	5.9	29.6	23.75	0.930	-24.32	0.693	5.49	5.5
		S2	12.5		23.75	0.930	27.11	0.889	6.61	
		S3	11.2		23.75	0.930	-24.27	0.693	4.18	
10	Chonan Middle School	No.4	6.7	15.4	26.95	1.068	-22.12	0.766	4.34	4.9
		No.3	8.7		26.95	1.068	-23.51	0.769	5.39	
11	Soviet Tajik - May 1 Slide	S1	44.9	68.8	36.95	1.504	-19.75	0.984	14.06	14.4
		S2	24.0		36.95	1.504	-16.90	0.984	15.04	
12	Shibecha-Cho Embankment	B-2	8.3	47.3	28.21	1.122	-25.53	0.803	10.02	10.0
		B-3	25.9		28.21	1.122	-26.59	0.805	9.94	
		B-5	13.1		28.21	1.122	-19.06	0.792	9.96	
		B-4	10.9	24.0	28.21	1.122	-23.50	0.798	9.76	9.9
		B-5	13.1		28.21	1.122	-19.06	0.792	9.96	
13	Route 272 at Higashiarekinai	Left	6.7	22.9	27.39	1.087	-25.82	0.784	6.17	6.1
		Right	16.2		27.39	1.087	-21.61	0.775	6.06	
14	Zeeland - Vlietepolder	Small-S1	31.3	75.7	24.79	0.975	-25.02	0.720	9.55	10.0
		Small-S2	44.4		24.79	0.975	-25.38	0.721	10.32	
		Large-S1	100.2	318.6	24.79	0.975	-28.70	0.731	9.55	10.8
		Large-S2	107.4		24.79	0.975	-29.98	0.736	11.66	
		Large-S3	111.0		24.79	0.975	-28.30	0.730	10.96	
15	Sheffield Dam	Right	14.9	14.9	32.66	1.316	-23.36	0.897	6.33	6.3
16	Helsinki Harbor	Small-S1	6.7	16.0	23.58	0.923	-26.65	0.695	2.85	3.1
		Small-S2	9.2		23.58	0.923	-25.29	0.691	3.25	
		Large-S1	35.5	71.3	23.58	0.923	-28.98	0.702	3.71	3.7
		Large-S2	35.8		23.58	0.923	-29.10	0.703	3.73	
17	Solfatara Canal Dike	S1	4.6	9.4	24.79	0.975	-29.86	0.735	4.72	4.6
		S2	4.8		24.79	0.975	-21.71	0.713	4.50	

Table 4.7 (cont'd) Summary of the predicted post-liquefaction shear strength values for Model 2

18	Lake Merced Bank	Boring 2	30.3	30.3	24.08	0.945	-21.91	0.696	7.11	7.1
19	El Cobre Tailings Dam	S1	83.7	348.1	36.13	1.468	-20.17	0.967	5.94	5.0
		S2	43.8		36.13	1.468	-27.09	0.977	5.74	
		S3	85.8		36.13	1.468	-28.94	0.982	4.99	
		S4	134.8		36.13	1.468	-29.71	0.985	4.17	
20	Metoki Road Embankment	S-19	6.8	14.0	26.33	1.041	-22.39	0.751	4.69	4.4
		S-13	7.2		26.33	1.041	-21.85	0.751	4.11	
21	Hokkaido Tailings Dam	Small-S1	18.3	23.2	36.13	1.468	-29.20	0.983	4.50	4.6
		Small-S2	5.0		36.13	1.468	-22.74	0.969	5.02	
		Large-S1	18.3	48.6	36.13	1.468	-29.20	0.983	4.50	4.2
		Large-S2	30.4		36.13	1.468	-27.21	0.977	4.06	
22	Upper San Fernando Dam - D/S Slope	A1&B1&C1	14.3	111.1	36.01	1.463	-16.83	0.965	9.04	12.9
		A2&B2&C2	10.0		36.01	1.463	-18.92	0.964	11.59	
		A3	23.2		36.01	1.463	-29.14	0.980	14.39	
		B4&C4	33.4		36.01	1.463	-26.36	0.973	14.92	
		B5&C5	30.2		36.01	1.463	-24.32	0.969	11.59	
23	Tar Island Dyke	Large-S1	260.2	308.6	26.06	1.029	-29.41	0.764	8.90	9.5
		Large-S2	48.4		26.06	1.029	-22.71	0.746	12.55	
		Small-S1	27.6	76.0	26.06	1.029	-20.91	0.743	8.53	11.1
		Small-S2	48.4		26.06	1.029	-22.71	0.746	12.55	
24	Mochi-Koshi Tailings Dam 1	S1	61.2	183.7	36.95	1.504	-25.71	0.990	8.11	9.9
		S2	61.0		36.95	1.504	-24.13	0.987	9.98	
		S3	61.6		36.95	1.504	-21.33	0.984	11.66	
25	Mochi-Koshi Tailings Dam 2	S1	34.8	70.9	36.95	1.504	-23.32	0.986	9.81	8.7
		S2	36.1		36.95	1.504	-19.35	0.984	7.64	
26	Nerlerk Embankment Slide 1	S1	23.5	166.7	24.88	0.979	-26.51	0.726	6.34	6.5
		S2	71.7		24.88	0.979	-27.33	0.729	6.85	
		S3	71.4		24.88	0.979	-27.98	0.731	6.19	
27	Nerlerk Embankment Slide 2	S1	18.9	155.5	24.88	0.979	-26.72	0.727	6.42	6.4
		S2	68.5		24.88	0.979	-28.11	0.731	7.23	
		S3	68.1		24.88	0.979	-16.52	0.709	5.62	
28	Nerlerk Embankment Slide 3	S1	80.5	361.9	24.88	0.979	-28.69	0.733	7.61	6.6
		S2	140.5		24.88	0.979	-28.52	0.733	6.84	
		S3	140.9		24.88	0.979	-29.72	0.737	5.86	

Table 4.7 (cont'd) Summary of the predicted post-liquefaction shear strength values for Model 2

29	Asele Road Embankment	S1	20.1	26.5	29.79	1.191	-19.47	0.829	8.56	8.5
		S2	6.4		29.79	1.191	-22.90	0.833	8.34	
30	Nalband Railway Embankment	NB-1	25.3	32.5	30.10	1.204	-28.58	0.854	8.15	8.4
		Small-S2	7.2		30.10	1.204	-24.82	0.844	9.30	
		NB-1	25.3	57.2	30.10	1.204	-28.58	0.854	8.15	8.8
		Large-S2	25.8		30.10	1.204	-28.25	0.853	9.82	
		Large-S3	6.1		30.10	1.204	-21.44	0.838	6.82	
31	Sullivan Tailings	Large-S1	13.8	38.6	36.13	1.468	-10.45	0.977	6.26	7.3
		CP91-29	10.7		36.13	1.468	-20.69	0.967	8.62	
		CP91-31	14.2		36.13	1.468	-25.19	0.973	7.43	
		Small-S1	6.5	23.5	36.13	1.468	-23.15	0.970	7.85	8.0
		CP91-31	17.1		36.13	1.468	-25.32	0.973	8.11	
32	Jamuna Bridge	S1	44.9	88.3	24.61	0.967	-26.99	0.721	5.98	5.6
		S2	43.4		24.61	0.967	-14.97	0.701	5.21	

4.4.3 Model 3

The third residual strength prediction model utilizes a double logarithmic void ratio versus mean effective stress domain (ln(e) vs. ln(p')) for isotropic compression responses, but a semi-logarithmic void ratio versus mean effective stress domain (e vs. ln(p')) for liquefaction states. In other words, while the isotropic state curves become asymptomatic to a horizontal line at higher stresses, the liquefaction state curves are defined as log-linear over the void ratio versus mean effective stress domain. Since ICCs are defined in the double logarithmic ln(e) vs. ln(p') domain, they converge to a horizontal line passing from the minimum limit void ratio (e_{lim}) asymptomatically, and therefore the negative void ratio values at these higher stress ranges are still avoided as a result of this asymptote and the log-nature of the relationship.

Similar to Model 1 and Model 2, Model 3 also employs the same mathematical relationships recommended by Sheng et al. (2008) given in Equation 4-12, Equation

4-13, Equation 4-14 and Equation 4-15 for the isotropic compression states, and the minimum limit void ratio that the isotropic compression curves become asymptomatic at very high stresses (e_{lim}) is defined as zero similar to Model 1. Accordingly, the void ratios (e) evaluated by Equation 4-12 are defined as the actual in-situ void ratios (e_{ICC}), and they are directly located in the void ratio versus mean effective stress domain as the initial state points of the corresponding case histories (green dots in Figure 4.14).

On the other hand, different relationships are used for the liquefaction state curves in Model 3. In fact, these liquefaction state curves can be defined as liquefaction state lines for Model 3, 4, 5, 6 and 7 because they are defined as log-linear over the void ratio versus mean effective stress domain.

The simple mathematical relationship provided in Equation 4-33 is implemented for the liquefaction state lines (LSL).

$$LSL: \quad e = \Gamma - \lambda_{ls} \cdot \ln\left(p'_{ls}\right) \qquad \text{Equation 4-33}$$

In this equation, p'_{ls} represents the final mean effective stress after the event at the liquefaction state. In other words, it is the reduced mean effective stress due to the increasing excess pore pressures during the liquefaction. In fact, the difference between p' in Equation 4-12 and p'_{ls} in Equation 4-33 estimates the excess pore pressures developed during the liquefaction. Therefore, other parameters in Equation 4-33 are evaluated first to be able to estimate p'_{ls} in the end.

The void ratio (e) in Equation 4-33 is already the same as the void ratio evaluated by Equation 4-12, e_{ICC}, because the void ratio remains the same under undrained conditions.

In Equation 4-33, λ_{ls} and Γ are defined as the slope of the liquefaction state lines, and the void ratio on these curves when $p'_{ls} = 1$ (unit stress), respectively. It should be noted that the same slope with isotropic compression curves was assigned to liquefaction state curves to achieve parallelism between them in Model 1 and Model 2; however, parallelism between these curves is not aimed for Model 3 because while

a double logarithmic void ratio versus mean effective stress domain (ln(e) vs. ln(p')) is defined for isotropic states, a semi-logarithmic void ratio versus mean effective stress domain (e vs. ln(p')) is employed for liquefaction states. Therefore, the slopes of these two curves are separated from each other by defining different λ and λ_{ls} values. On the other hand, the mathematical form to be used in the evaluation of λ_{ls} values is selected very similar to the mathematical form of λ provided in Equation 4-13. In fact, only a minor change is applied in the relationship of λ_{ls} such that its dependency on the relative density of the soil is eliminated. In other words, it is defined as a function of void ratio range only. This minor change is pretty reasonable such that the critical state phenomenon is not a function of the relative density of the soil; therefore, it should also not be a factor affecting the liquefaction state. Inspired of that, the relationship given in Equation 4-34 is used to evaluate the slope of the liquefaction state lines (LSL).

$$\lambda_{ls} = \theta_7 \cdot exp\big(\theta_8 + \theta_9 \cdot (e_{max} - e_{min})\big) \qquad \text{Equation 4-34}$$

Γ values in Equation 4-33 are evaluated as a function of the maximum void ratio (e_{max}) as given in Equation 4-35 since it represents the void ratio at a known mean stress p'_{cs} = 1 kPa = 0.001 MPa on the LSLs. In fact, this relationship is quite similar to the one provided in Equation 4-18 where Γ employed in Equation 4-35 meant for e_{c0} in Equation 4-18. Therefore, it is again reasonable here to use a similar relationship suggested by Cho et al. (2006) given in Figure 4.10 between the limit void ratios (e_{max} or e_{min}) and Γ. Moreover, a similar relationship was also provided by Jefferies and Been (2006) shown in Figure 4.9 such that Γ values were defined as a function of maximum void ratio, e_{max}.

$$\Gamma = \theta_6 \cdot e_{max} \qquad \text{Equation 4-35}$$

In the end, the final mean effective stress values after the liquefaction are evaluated by solving p'_{ls} in Equation 4-33 for each sub-section of the case histories. The closed-form solution of the relationship is provided in Equation 4-36.

$$p'_{ls} = exp\left(\frac{\Gamma - exp\left(ln(N) - \lambda \cdot ln\left(p' + \left(\frac{N}{e_0 - e_{lim}}\right)^{\frac{1+\theta_5 \cdot RD}{\theta_3 \cdot exp(\theta_4 \cdot (e_{max} - e_{min}))}} - p'_0\right)\right) - e_{lim}}{\theta_7 \cdot exp(\theta_8 + \theta_9 \cdot (e_{max} - e_{min}))}\right) \quad \text{Equation 4-36}$$

Once the final mean effective stress values after the liquefaction (p'_{ls}) are evaluated by Equation 4-36, the corresponding data points are located in the void ratio versus mean effective stress domain as the liquefaction state points of the corresponding case histories (red squares in Figure 4.14).

Accordingly, the other parameters used in the evaluation of the failure criterion, such as the liquefaction friction angle (ϕ'_{ls}), Lode angle (θ), slope of the stress paths in q vs. p' domain for triaxial compression tests (M_{tc}) and in general (M), are evaluated with the same procedure followed in Model 1 and Model 2 by using Equation 4-23, Equation 4-24, Equation 4-22 and Equation 4-21, respectively.

Finally, the post-liquefaction shear strength values for each sub-section are predicted by using the relationship provided in Equation 4-26 as a function M and liquefaction state mean effective stress (p'_{ls}) values. Accordingly, the overall representative post-liquefaction shear strength values of all case histories are predicted by using Equation 4-27.

Once the residual strength predictions evaluated by Equation 4-27 are compared with the modified back-analyses results of Weber (2015) given in Table 4.1 for the same case histories, the overall best-fit model parameters are developed as given in Table 4.8 for Model 3 as a result of probabilistic regressions by the Maximum Likelihood Method.

Table 4.8 Best-fit model parameters for Model 3

θ_1	1.571
θ_3	0.919
θ_4	4.491
θ_5	10.936

Table 4.8 (cont'd) Best-fit model parameters for Model 3

θ_6	0.174
θ_7	0.063
θ_8	0.157
θ_9	1.720
θ_{10}	28.528
θ_{11}	-0.140
θ_{12}	0.850
θ_{13}	-0.080
θ_{14}	18.917
θ_{15}	31.083
θ_{16}	2.814
θ_{17}	4

Consequently, the equations of isotropic compression curves and liquefaction state lines are obtained as given in Equation 4-37 and Equation 4-38, respectively.

$$ICC: \quad \ln(e) = \ln\left(1.571 \cdot (e_{max} - e_{min})\right) - \left(\frac{0.919 \cdot exp\left(4.491 \cdot (e_{max} - e_{min})\right)}{1 + 10.936 \cdot RD}\right) \cdot \ln\,(p' + \left(\frac{1.571 \cdot (e_{max} - e_{min})}{e_0}\right)^{\frac{1+10.936 \cdot RD}{0.919 \cdot exp\left(4.491 \cdot (e_{max} - e_{min})\right)}} - 0.001) \qquad \text{Equation 4-37}$$

$$LSL: \quad e = (0.174 \cdot e_{max}) - 0.063 \cdot exp\left(0.157 + 1.72 \cdot (e_{max} - e_{min})\right) \cdot \ln\,(p'_{ls}) \qquad \text{Equation 4-38}$$

Using these equations, the case history data points with respect to their initial states and liquefaction states are located in the void ratio versus mean effective stress domain as presented in Figure 4.14.

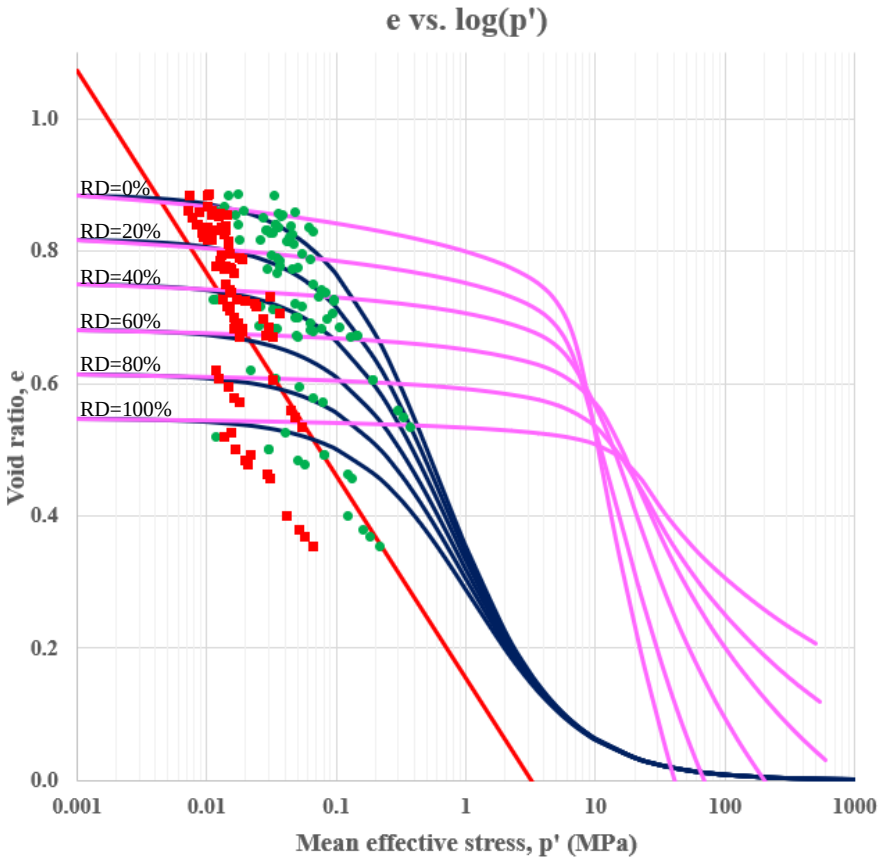

Figure 4.14. Void ratio versus mean effective stress domain for Model 3

In Figure 4.14, while the green dots and red squares represent the initial and liquefaction states of the case history data points, the purple and blue curves represent the isotropic compression curves recommended by Mesri and Vardhanabhuti (2009), and developed for Model 3 by Equation 4-12, respectively, for 0%, 20%, 40%, 60%, 80%, and 100% relative densities. The red curve presents the liquefaction state curve evaluated by Equation 4-33 by using the average λ_{ls} and Γ values of the case histories. It should be noted that the stress differences between the initial and liquefaction states, i.e., between the green dots and red squares, give the generated excess pore pressures during the liquefaction.

A summary of the evaluated parameters for Model 3 is tabulated in Table 4.9 for each sub-section of the case histories.

Table 4.9 Summary of the evaluated parameters for Model 3

#	Case History	Section	Γ	N	p'_r (MPa)	λ	λ_{ds}	p'_{ls} (MPa)	e_{ICC}
1	Wachusett Dam - North Dike	WND-1	0.165	0.599	0.752	1.097	0.143	0.014	0.777
		WND-2	0.165	0.599	0.765	1.268	0.143	0.020	0.724
		WND-105	0.165	0.599	0.769	1.309	0.143	0.029	0.673
		WND-3	0.165	0.599	0.744	0.958	0.143	0.029	0.672
2	Fort Peck Dam	Boring 3	0.156	0.509	0.544	0.531	0.130	0.044	0.559
		Boring 7	0.156	0.509	0.544	0.531	0.130	0.054	0.534
		Boring 6	0.156	0.509	0.544	0.531	0.130	0.049	0.548
		Boring 7	0.156	0.509	0.544	0.531	0.130	0.017	0.687
3	Uetsu Railway Embankment	S1	0.169	0.639	0.839	1.944	0.149	0.015	0.796
		S2	0.169	0.639	0.828	1.712	0.149	0.012	0.832
4	Lower San Fernando Dam - U/S Slope	S103&S111	0.095	0.232	0.175	0.447	0.096	0.042	0.399
		S101&S102&S104	0.095	0.232	0.175	0.447	0.096	0.058	0.368
		S105	0.095	0.232	0.175	0.447	0.096	0.067	0.354
		S105	0.095	0.232	0.175	0.448	0.096	0.051	0.379
5	Hachiro-Gata Road Embankment	S1	0.176	0.654	0.809	1.460	0.152	0.011	0.862
		S2	0.176	0.654	0.809	1.460	0.152	0.013	0.837
6	La Marquesa Dam - U/S Slope	B-2	0.179	0.671	0.822	1.566	0.155	0.014	0.839
		B-III	0.179	0.671	0.825	1.616	0.155	0.013	0.856
		B-3	0.179	0.671	0.824	1.609	0.155	0.010	0.886
7	La Marquesa Dam - D/S Slope	B-II	0.177	0.663	0.806	1.260	0.153	0.014	0.832
		B-1	0.177	0.663	0.805	1.217	0.153	0.019	0.787
8	La Palma Dam	B-3	0.174	0.647	0.800	1.357	0.151	0.015	0.812
		B-4	0.174	0.647	0.801	1.391	0.151	0.011	0.856
9	Lake Ackerman Highway Embankment	S1	0.164	0.594	0.757	1.208	0.142	0.014	0.774
		S2	0.164	0.594	0.757	1.208	0.142	0.013	0.785
		S3	0.164	0.594	0.758	1.218	0.142	0.010	0.818
10	Chonan Middle School	No.4	0.175	0.650	0.806	1.460	0.151	0.010	0.868
		No.3	0.175	0.650	0.811	1.540	0.151	0.014	0.825
11	Soviet Tajik - May 1 Slide	S1	0.168	0.716	0.914	1.813	0.163	0.031	0.731
		S2	0.168	0.716	0.914	1.813	0.163	0.037	0.706
12	Shibecha-Cho Embankment	B-2	0.139	0.529	0.768	1.163	0.132	0.016	0.683
		B-3	0.139	0.529	0.775	1.242	0.132	0.018	0.671
		B-5	0.139	0.529	0.767	1.152	0.132	0.016	0.684
		B-4	0.139	0.529	0.775	1.245	0.132	0.018	0.672
		B-5	0.139	0.529	0.767	1.152	0.132	0.016	0.684

Table 4.9 (cont'd) Summary of the evaluated parameters for Model 3

13	Route 272 at Higashiarekinai	Left	0.175	0.651	0.799	1.295	0.151	0.015	0.815
		Right	0.175	0.651	0.800	1.324	0.151	0.015	0.815
14	Zeeland - Vlietepolder	Small-S1	0.171	0.619	0.766	0.741	0.146	0.024	0.717
		Small-S2	0.171	0.619	0.766	0.741	0.146	0.027	0.697
		Large-S1	0.171	0.619	0.766	0.741	0.146	0.023	0.720
		Large-S2	0.171	0.619	0.766	0.741	0.146	0.033	0.671
		Large-S3	0.171	0.619	0.766	0.741	0.146	0.030	0.685
15	Sheffield Dam	Right	0.183	0.693	0.832	1.516	0.159	0.014	0.856
16	Helsinki Harbor	Small-S1	0.173	0.577	0.678	1.078	0.140	0.007	0.861
		Small-S2	0.173	0.577	0.665	0.987	0.140	0.008	0.841
		Large-S1	0.173	0.577	0.667	1.001	0.140	0.009	0.827
		Large-S2	0.173	0.577	0.670	1.020	0.140	0.009	0.828
17	Solfatara Canal Dike	S1	0.168	0.606	0.755	1.163	0.144	0.011	0.818
		S2	0.168	0.606	0.763	1.260	0.144	0.011	0.818
18	Lake Merced Bank	Boring 2	0.174	0.660	0.814	1.091	0.153	0.018	0.789
19	El Cobre Tailings Dam	S1	0.179	0.603	0.755	1.616	0.144	0.011	0.829
		S2	0.179	0.603	0.755	1.616	0.144	0.010	0.836
		S3	0.179	0.603	0.755	1.616	0.144	0.009	0.859
		S4	0.179	0.603	0.755	1.616	0.144	0.007	0.885
20	Metoki Road Embankment	S-19	0.178	0.667	0.826	1.689	0.154	0.012	0.854
		S-13	0.178	0.667	0.821	1.571	0.154	0.010	0.884
21	Hokkaido Tailings Dam	Small-S1	0.168	0.583	0.775	1.712	0.141	0.008	0.839
		Small-S2	0.168	0.583	0.775	1.712	0.141	0.010	0.822
		Large-S1	0.168	0.583	0.775	1.712	0.141	0.008	0.839
		Large-S2	0.168	0.583	0.775	1.712	0.141	0.008	0.852
22	Upper San Fernando Dam - D/S Slope	A1&B1&C1	0.107	0.276	0.259	0.537	0.100	0.015	0.527
		A2&B2&C2	0.107	0.276	0.257	0.533	0.100	0.022	0.492
		A3	0.107	0.276	0.257	0.533	0.100	0.029	0.462
		B4&C4	0.107	0.276	0.257	0.533	0.100	0.031	0.456
		B5&C5	0.107	0.276	0.259	0.537	0.100	0.022	0.492
23	Tar Island Dyke	Large-S1	0.154	0.523	0.607	0.658	0.132	0.019	0.678
		Large-S2	0.154	0.523	0.607	0.658	0.132	0.032	0.606
		Small-S1	0.154	0.523	0.607	0.658	0.132	0.018	0.681
		Small-S2	0.154	0.523	0.607	0.658	0.132	0.032	0.606
24	Mochi-Koshi Tailings Dam 1	S1	0.120	0.381	0.546	0.861	0.113	0.012	0.621
		S2	0.120	0.381	0.546	0.861	0.113	0.015	0.595

Table 4.9 (cont'd) Summary of the evaluated parameters for Model 3

		S3	0.120	0.381	0.546	0.861	0.113	0.018	0.573
25	Mochi-Koshi Tailings Dam 2	S1	0.119	0.372	0.558	0.938	0.112	0.016	0.579
		S2	0.119	0.372	0.558	0.938	0.112	0.012	0.608
26	Nerlerk Embankment Slide 1	S1	0.159	0.522	0.562	0.596	0.131	0.015	0.712
		S2	0.159	0.522	0.562	0.596	0.131	0.016	0.699
		S3	0.159	0.522	0.562	0.596	0.131	0.014	0.716
27	Nerlerk Embankment Slide 2	S1	0.159	0.522	0.562	0.596	0.131	0.015	0.710
		S2	0.159	0.522	0.562	0.596	0.131	0.018	0.691
		S3	0.159	0.522	0.562	0.596	0.131	0.013	0.727
28	Nerlerk Embankment Slide 3	S1	0.159	0.522	0.562	0.596	0.131	0.019	0.682
		S2	0.159	0.522	0.562	0.596	0.131	0.016	0.700
		S3	0.159	0.522	0.562	0.596	0.131	0.013	0.727
29	Asele Road Embankment	S1	0.164	0.621	0.798	1.152	0.147	0.016	0.767
		S2	0.164	0.621	0.799	1.158	0.147	0.016	0.773
30	Nalband Railway Embankment	NB-1	0.096	0.259	0.399	0.779	0.099	0.017	0.501
		Small-S2	0.096	0.259	0.399	0.779	0.099	0.020	0.484
		NB-1	0.096	0.259	0.399	0.779	0.099	0.017	0.501
		Large-S2	0.096	0.259	0.399	0.779	0.099	0.021	0.478
		Large-S3	0.096	0.259	0.399	0.779	0.099	0.014	0.518
31	Sullivan Tailings	Large-S1	0.169	0.557	0.610	0.764	0.137	0.012	0.777
		CP91-29	0.169	0.557	0.610	0.764	0.137	0.017	0.726
		CP91-31	0.169	0.557	0.610	0.764	0.137	0.014	0.751
		Small-S1	0.169	0.557	0.610	0.764	0.137	0.015	0.742
		CP91-31	0.169	0.557	0.610	0.764	0.137	0.016	0.737
32	Jamuna Bridge	S1	0.170	0.606	0.732	1.003	0.144	0.015	0.775
		S2	0.170	0.606	0.732	1.003	0.144	0.013	0.795

In the end, the post-liquefaction shear strength values are predicted by Model 3 as tabulated in Table 4.10 for each sub-section of the case histories.

Table 4.10 Summary of the predicted post-liquefaction shear strength values for Model 3

#	Case History	Section	L_i (m)	L_t (m)	ϕ'_{ls} (deg)	M_{tc}	θ (deg)	M	$\tau_{liq,i}$ (kPa)	$\sum \tau_{liq,i} \cdot L_i / L_t$ (kPa)
1	Wachusett Dam - North Dike	WND-1	19.3	68.9	31.07	1.247	-20.16	0.858	5.95	9.5
		WND-2	20.9		31.07	1.247	-23.99	0.864	8.64	
		WND-105	18.4		31.07	1.247	-25.03	0.866	12.39	
		WND-3	10.2		31.07	1.247	-23.86	0.864	12.46	
2	Fort Peck Dam	Boring 3	200.3	389.3	30.75	1.233	-24.40	0.858	19.08	18.9
		Boring 7	67.9		30.75	1.233	-25.23	0.859	23.31	
		Boring 6	79.4		30.75	1.233	-24.05	0.857	20.80	
		Boring 7	41.7		30.75	1.233	-3.45	0.872	7.23	
3	Uetsu Railway Embankment	S1	9.4	20.3	30.49	1.221	-22.54	0.848	6.38	5.6
		S2	10.9		30.49	1.221	-23.15	0.849	5.01	
4	Lower San Fernando Dam - U/S Slope	S103&S111	54.8	103.8	38.29	1.562	-26.24	1.017	21.25	25.3
		S101&S102&S104	16.9		38.29	1.562	-23.82	1.013	29.26	
		S105	16.8		38.29	1.562	-22.48	1.012	33.80	
		S105	15.3		38.29	1.562	-24.04	1.014	26.09	
5	Hachiro-Gata Road Embankment	S1	10.9	14.9	32.05	1.290	-23.20	0.884	4.83	5.1
		S2	4.0		32.05	1.290	-26.01	0.890	5.73	
6	La Marquesa Dam - U/S Slope	B-2	6.6	21.8	33.26	1.342	-22.31	0.909	6.38	5.6
		B-III	7.2		33.26	1.342	-26.21	0.916	5.76	
		B-3	8.0		33.26	1.342	-25.83	0.915	4.76	
7	La Marquesa Dam - D/S Slope	B-II	10.1	15.8	32.25	1.298	-19.75	0.884	6.18	7.0
		B-1	5.7		32.25	1.298	-26.25	0.895	8.38	
8	La Palma Dam	B-3	6.1	15.9	31.76	1.277	-24.28	0.880	6.41	5.4
		B-4	9.8		31.76	1.277	-18.45	0.873	4.76	
9	Lake Ackerman Highway Embankment	S1	5.9	29.6	30.49	1.221	-24.32	0.852	5.83	5.9
		S2	12.5		30.49	1.221	27.11	1.161	7.35	
		S3	11.2		30.49	1.221	-24.27	0.852	4.28	
10	Chonan Middle School	No.4	6.7	15.4	32.05	1.290	-22.12	0.882	4.49	5.3
		No.3	8.7		32.05	1.290	-23.51	0.885	6.00	
11	Soviet Tajik - May 1 Slide	S1	44.9	68.8	38.29	1.562	-19.75	1.011	15.75	16.7
		S2	24.0		38.29	1.562	-16.90	1.012	18.47	
12	Shibecha-Cho Embankment	B-2	8.3	47.3	35.06	1.421	-25.53	0.952	7.83	8.2
		B-3	25.9		35.06	1.421	-26.59	0.954	8.61	
		B-5	13.1		35.06	1.421	-19.06	0.944	7.74	

Table 4.10 (cont'd) Summary of the predicted post-liquefaction shear strength values for Model 3

		B-4	10.9	24.0	35.06	1.421	-23.50	0.948	8.47	8.1
		B-5	13.1		35.06	1.421	-19.06	0.944	7.74	
13	Route 272 at Higashiarekinai	Left	6.7	22.9	32.25	1.298	-25.82	0.893	6.52	6.5
		Right	16.2		32.25	1.298	-21.61	0.886	6.48	
14	Zeeland - Vlietepolder	Small-S1	31.3	75.7	31.02	1.245	-25.02	0.865	10.33	11.2
		Small-S2	44.4		31.02	1.245	-25.38	0.866	11.82	
		Large-S1	100.2	318.6	31.02	1.245	-28.70	0.875	10.18	12.6
		Large-S2	107.4		31.02	1.245	-29.98	0.880	14.35	
		Large-S3	111.0		31.02	1.245	-28.30	0.874	12.98	
15	Sheffield Dam	Right	14.9	14.9	34.33	1.389	-23.36	0.933	6.71	6.7
16	Helsinki Harbor	Small-S1	6.7	16.0	30.40	1.217	-26.65	0.855	3.10	3.4
		Small-S2	9.2		30.40	1.217	-25.29	0.852	3.54	
		Large-S1	35.5	71.3	30.40	1.217	-28.98	0.862	3.97	4.0
		Large-S2	35.8		30.40	1.217	-29.10	0.863	3.96	
17	Solfatara Canal Dike	S1	4.6	9.4	31.02	1.245	-29.86	0.879	4.82	4.8
		S2	4.8		31.02	1.245	-21.71	0.859	4.72	
18	Lake Merced Bank	Boring 2	30.3	30.3	30.66	1.229	-21.91	0.851	7.62	7.6
19	El Cobre Tailings Dam	S1	83.7	348.1	35.48	1.439	-20.17	0.954	5.15	4.3
		S2	43.8		35.48	1.439	-27.09	0.964	4.95	
		S3	85.8		35.48	1.439	-28.94	0.969	4.24	
		S4	134.8		35.48	1.439	-29.71	0.972	3.56	
20	Metoki Road Embankment	S-19	6.8	14.0	31.76	1.277	-22.39	0.876	5.44	4.9
		S-13	7.2		31.76	1.277	-21.85	0.876	4.48	
21	Hokkaido Tailings Dam	Small-S1	18.3	23.2	35.48	1.439	-29.20	0.970	4.09	4.2
		Small-S2	5.0		35.48	1.439	-22.74	0.956	4.55	
		Large-S1	18.3	48.6	35.48	1.439	-29.20	0.970	4.09	3.9
		Large-S2	30.4		35.48	1.439	-27.21	0.964	3.73	
22	Upper San Fernando Dam - D/S Slope	A1&B1&C1	14.3	111.1	38.00	1.549	-16.83	1.006	7.69	12.7
		A2&B2&C2	10.0		38.00	1.549	-18.92	1.005	10.87	
		A3	23.2		38.00	1.549	-29.14	1.019	14.80	
		B4&C4	33.4		38.00	1.549	-26.36	1.012	15.70	
		B5&C5	30.2		38.00	1.549	-24.32	1.008	10.88	
23	Tar Island Dyke	Large-S1	260.2	308.6	32.08	1.291	-29.41	0.900	8.40	9.3
		Large-S2	48.4		32.08	1.291	-22.71	0.884	14.29	

Table 4.10 (cont'd) Summary of the predicted post-liquefaction shear strength values for Model 3

		Small-S1	27.6	76.0	32.08	1.291	-20.91	0.882	8.07	12.0
		Small-S2	48.4		32.08	1.291	-22.71	0.884	14.29	
24	Mochi-Koshi Tailings Dam 1	S1	61.2	183.7	38.29	1.562	-25.71	1.016	5.99	7.6
		S2	61.0		38.29	1.562	-24.13	1.014	7.54	
		S3	61.6		38.29	1.562	-21.33	1.011	9.13	
25	Mochi-Koshi Tailings Dam 2	S1	34.8	70.9	38.29	1.562	-23.32	1.013	8.19	7.2
		S2	36.1		38.29	1.562	-19.35	1.011	6.30	
26	Nerlerk Embankment Slide 1	S1	23.5	166.7	31.07	1.247	-26.51	0.870	6.49	6.7
		S2	71.7		31.07	1.247	-27.33	0.872	7.15	
		S3	71.4		31.07	1.247	-27.98	0.874	6.29	
27	Nerlerk Embankment Slide 2	S1	18.9	155.5	31.07	1.247	-26.72	0.870	6.60	6.7
		S2	68.5		31.07	1.247	-28.11	0.874	7.66	
		S3	68.1		31.07	1.247	-16.52	0.857	5.68	
28	Nerlerk Embankment Slide 3	S1	80.5	361.9	31.07	1.247	-28.69	0.876	8.18	6.9
		S2	140.5		31.07	1.247	-28.52	0.876	7.12	
		S3	140.9		31.07	1.247	-29.72	0.880	5.85	
29	Asele Road Embankment	S1	20.1	26.5	33.26	1.342	-19.47	0.906	7.39	7.3
		S2	6.4		33.26	1.342	-22.90	0.909	7.09	
30	Nalband Railway Embankment	NB-1	25.3	32.5	35.86	1.456	-28.58	0.976	8.05	8.4
		Small-S2	7.2		35.86	1.456	-24.82	0.967	9.49	
		NB-1	25.3	57.2	35.86	1.456	-28.58	0.976	8.05	8.8
		Large-S2	25.8		35.86	1.456	-28.25	0.975	10.12	
		Large-S3	6.1		35.86	1.456	-21.44	0.962	6.65	
31	Sullivan Tailings	Large-S1	13.8	38.6	35.48	1.439	-10.45	0.963	5.61	6.7
		CP91-29	10.7		35.48	1.439	-20.69	0.954	8.07	
		CP91-31	14.2		35.48	1.439	-25.19	0.960	6.77	
		Small-S1	6.5	23.5	35.48	1.439	-23.15	0.956	7.21	7.4
		CP91-31	17.1		35.48	1.439	-25.32	0.960	7.49	
32	Jamuna Bridge	S1	44.9	88.3	30.93	1.241	-26.99	0.868	6.53	6.1
		S2	43.4		30.93	1.241	-14.97	0.854	5.61	

4.4.4 Model 4

The fourth residual strength prediction model again utilizes a double logarithmic void ratio versus mean effective stress domain (ln(e) vs. ln(p')) for isotropic compression responses, but a semi-logarithmic void ratio versus mean effective stress domain (e vs. ln(p')) for liquefaction states similar to Model 3. In other words, while the isotropic state curves become asymptomatic to a horizontal line at higher stresses, the liquefaction state curves are defined as log-linear over the void ratio versus mean effective stress domain. Since ICCs are defined in the double logarithmic ln(e) vs. ln(p') domain, they converge to a horizontal line passing from the minimum limit void ratio (e_{lim}) asymptomatically, and therefore the negative void ratio values at these higher stress ranges are still avoided as a result of this asymptote and the log-nature of the relationship.

There is only a very tiny difference exists between Model 3 and Model 4, which is the same difference between Model 1 and Model 2. For Model 4, the minimum limit void ratio that the isotropic state curves become asymptomatic at very high stresses, e_{lim} value, is selected as 0.35 instead of zero similar to Model 2. As already discussed in Section 4.4.2 during the explanation of residual strength prediction Model 2, this value of 0.35 is not randomly determined, but defined referring to Cubrinovski and Ishihara (2002) such that the void ratio of the densest possible packing of single-sized sphere shape of soil particles is given as 0.35 geometrically as presented in Figure 4.12b and Equation 4-30.

The single-sized sphere shape of the soil particles can be matched with the shape of the soil particles at very high stress ranges because significant level of particle crushing occurs at those extreme stress levels, and the angularity of the soil particles disappears automatically. Accordingly, a smooth sphere shape is obtained for them naturally. Hence, defining the minimum limit void ratio that the isotropic state curves become asymptomatic at very high stresses as $e_{lim} = 0.35$ is pretty reasonable for Model 4.

Other than this little e_{lim} difference, the same relationships employed for Model 3 is also used for Model 4. The basic mathematical relationship recommended by Sheng et al. (2008) given in Equation 4-12 is implemented for the isotropic compression curves. The required parameters used in this relationship, i.e., N, λ and p'_r, are again evaluated by Equation 4-15, Equation 4-13 and Equation 4-14, respectively. For the liquefaction state lines, the relationship provided in Equation 4-33 is employed, and the required parameters used in this relationship, i.e., λ_{ls} and Γ, are evaluated by Equation 4-34 and Equation 4-35, respectively. In the end, the final mean effective stress values after the liquefaction are evaluated by solving p'_{ls} in Equation 4-33 for each sub-section of the case histories, and the closed-form solution of the relationship is obtained as given in Equation 4-36.

The other parameters used in the evaluation of failure criterion, such as the liquefaction state friction angle (ϕ'_{ls}), Lode angle (θ), slope of the stress paths in q vs. p' domain for triaxial compression tests (M_{tc}) and in general (M), are also evaluated by using Equation 4-23, Equation 4-24, Equation 4-22 and Equation 4-21, respectively.

Finally, the post-liquefaction shear strength values for each sub-section can be predicted by using the relationship provided in Equation 4-26 as a function M and liquefaction state mean effective stress (p'_{ls}) values. Accordingly, the overall representative post-liquefaction shear strength values of all case histories can be predicted by using Equation 4-27.

Once the residual strength predictions evaluated by Equation 4-27 are compared with the modified back-analyses results of Weber (2015) given in Table 4.1 for the same case histories, the overall best-fit model parameters are developed as given in Table 4.11 for Model 4 as a result of probabilistic regressions by the Maximum Likelihood Method.

Table 4.11 Best-fit model parameters for Model 4

θ_1	0.749
θ_3	0.113
θ_4	11.682
θ_5	33.312
θ_6	0.255
θ_7	0.062
θ_8	0.153
θ_9	1.529
θ_{10}	28.25
θ_{11}	-0.209
θ_{12}	0.818
θ_{13}	-0.080
θ_{14}	18.917
θ_{15}	31.083
θ_{16}	2.814
θ_{17}	4

Consequently, the equations of isotropic compression curves and liquefaction state lines are obtained as given in Equation 4-39 and Equation 4-40, respectively.

$$ICC: \quad \ln(e-0.35) = \ln\left(0.749\cdot(e_{max}-e_{min})\right) - \left(\frac{0.113\cdot exp\left(11.682\cdot(e_{max}-e_{min})\right)}{1+33.312\cdot RD}\right) \cdot \ln\left(p' + \left(\frac{0.749\cdot(e_{max}-e_{min})}{e_0-0.35}\right)^{\frac{1+33.312\cdot RD}{0.113\cdot exp\left(11.682\cdot(e_{max}-e_{min})\right)}} - 0.001\right) \qquad \text{Equation 4-39}$$

$$LSL: \quad e = (0.255\cdot e_{max}) - 0.062\cdot exp\left(0.153+1.529\cdot(e_{max}-e_{min})\right)\cdot \ln\left(p'_{ls}\right) \qquad \text{Equation 4-40}$$

Using these equations, the case history data points with respect to their initial states and liquefaction states are located in the void ratio versus mean effective stress domain as presented in Figure 4.15.

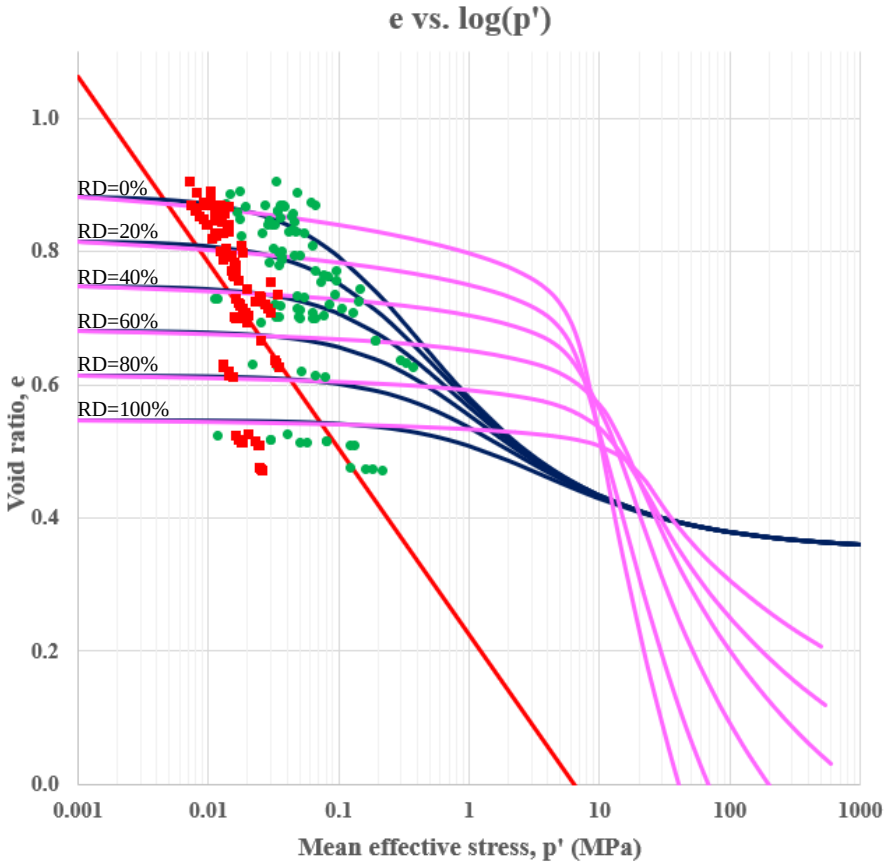

Figure 4.15. Void ratio versus mean effective stress domain for Model 4

In Figure 4.15, while the green dots and red squares represent the initial and liquefaction states of the case history data points, the purple and blue curves represent the isotropic compression curves recommended by Mesri and Vardhanabhuti (2009), and developed for Model 4 by Equation 4-12, respectively, for 0%, 20%, 40%, 60%, 80%, and 100% relative densities. The red curve presents the liquefaction state curve evaluated by Equation 4-33 by using the average λ_{ls} and Γ values of the case histories. It should be noted that the stress differences between the initial and liquefaction states, i.e., between the green dots and red squares, give the generated excess pore pressures during the liquefaction.

A summary of the evaluated parameters for Model 4 is tabulated in Table 4.12 for each sub-section of the case histories.

Table 4.12 Summary of the evaluated parameters for Model 4

#	Case History	Section	Γ	N	p'_r (MPa)	λ	λ_{ds}	p'_{ls} (MPa)	e_{ICC}
1	Wachusett Dam - North Dike	WND-1	0.240	0.282	0.517	0.759	0.129	0.014	0.791
		WND-2	0.240	0.282	0.545	0.900	0.129	0.016	0.771
		WND-105	0.240	0.282	0.553	0.935	0.129	0.020	0.744
		WND-3	0.240	0.282	0.500	0.649	0.129	0.023	0.725
2	Fort Peck Dam	Boring 3	0.228	0.243	0.211	0.242	0.119	0.032	0.636
		Boring 7	0.228	0.243	0.211	0.242	0.119	0.035	0.627
		Boring 6	0.228	0.243	0.211	0.242	0.119	0.034	0.632
		Boring 7	0.228	0.243	0.211	0.242	0.119	0.020	0.694
3	Uetsu Railway Embankment	S1	0.246	0.301	0.718	1.786	0.134	0.013	0.828
		S2	0.246	0.301	0.690	1.519	0.134	0.011	0.846
4	Lower San Fernando Dam - U/S Slope	S103&S111	0.139	0.111	0.004	0.063	0.091	0.025	0.476
		S101&S102&S104	0.139	0.111	0.004	0.063	0.091	0.025	0.473
		S105	0.139	0.111	0.004	0.063	0.091	0.026	0.472
		S105	0.139	0.111	0.004	0.063	0.091	0.025	0.474
5	Hachiro-Gata Road Embankment	S1	0.256	0.308	0.656	1.324	0.136	0.011	0.867
		S2	0.256	0.308	0.656	1.324	0.136	0.013	0.851
6	La Marquesa Dam - U/S Slope	B-2	0.261	0.316	0.692	1.541	0.138	0.013	0.856
		B-III	0.261	0.316	0.698	1.601	0.138	0.012	0.869
		B-3	0.261	0.316	0.697	1.593	0.138	0.011	0.890
7	La Marquesa Dam - D/S Slope	B-II	0.258	0.312	0.646	1.154	0.137	0.014	0.841
		B-1	0.258	0.312	0.642	1.109	0.137	0.018	0.809
8	La Palma Dam	B-3	0.254	0.305	0.634	1.183	0.135	0.014	0.831
		B-4	0.254	0.305	0.638	1.218	0.135	0.011	0.860
9	Lake Ackerman Highway Embankment	S1	0.238	0.279	0.526	0.832	0.128	0.013	0.795
		S2	0.238	0.279	0.526	0.832	0.128	0.012	0.801
		S3	0.238	0.279	0.527	0.841	0.128	0.011	0.820
10	Chonan Middle School	No.4	0.254	0.306	0.650	1.302	0.135	0.010	0.871
		No.3	0.254	0.306	0.661	1.389	0.135	0.013	0.845
11	Soviet Tajik - May 1 Slide	S1	0.245	0.341	0.855	2.332	0.145	0.030	0.755
		S2	0.245	0.341	0.855	2.332	0.145	0.034	0.736
12	Shibecha-Cho Embankment	B-2	0.202	0.249	0.539	0.619	0.121	0.016	0.702
		B-3	0.202	0.249	0.550	0.672	0.121	0.016	0.701
		B-5	0.202	0.249	0.537	0.612	0.121	0.016	0.701
		B-4	0.202	0.249	0.550	0.674	0.121	0.016	0.701
		B-5	0.202	0.249	0.537	0.612	0.121	0.016	0.701

Table 4.12 (cont'd) Summary of the evaluated parameters for Model 4

13	Route 272 at Higashiarekinai	Left	0.255	0.306	0.631	1.136	0.136	0.014	0.831
		Right	0.255	0.306	0.635	1.166	0.136	0.014	0.832
14	Zeeland - Vlietepolder	Small-S1	0.248	0.291	0.544	0.527	0.131	0.025	0.732
		Small-S2	0.248	0.291	0.544	0.527	0.131	0.027	0.722
		Large-S1	0.248	0.291	0.544	0.527	0.131	0.025	0.734
		Large-S2	0.248	0.291	0.544	0.527	0.131	0.030	0.708
		Large-S3	0.248	0.291	0.544	0.527	0.131	0.029	0.715
15	Sheffield Dam	Right	0.267	0.326	0.715	1.619	0.141	0.014	0.867
16	Helsinki Harbor	Small-S1	0.253	0.275	0.404	0.717	0.127	0.008	0.866
		Small-S2	0.253	0.275	0.382	0.647	0.127	0.009	0.848
		Large-S1	0.253	0.275	0.385	0.658	0.127	0.010	0.840
		Large-S2	0.253	0.275	0.390	0.673	0.127	0.010	0.841
17	Solfatara Canal Dike	S1	0.244	0.285	0.527	0.834	0.130	0.012	0.823
		S2	0.244	0.285	0.543	0.917	0.130	0.011	0.828
18	Lake Merced Bank	Boring 2	0.254	0.311	0.648	0.967	0.137	0.018	0.799
19	El Cobre Tailings Dam	S1	0.261	0.287	0.570	1.303	0.130	0.009	0.869
		S2	0.261	0.287	0.570	1.303	0.130	0.009	0.874
		S3	0.261	0.287	0.570	1.303	0.130	0.008	0.889
		S4	0.261	0.287	0.570	1.303	0.130	0.007	0.906
20	Metoki Road Embankment	S-19	0.259	0.314	0.701	1.660	0.138	0.012	0.869
		S-13	0.259	0.314	0.687	1.520	0.138	0.010	0.887
21	Hokkaido Tailings Dam	Small-S1	0.245	0.276	0.580	1.266	0.127	0.008	0.862
		Small-S2	0.245	0.276	0.580	1.266	0.127	0.009	0.852
		Large-S1	0.245	0.276	0.580	1.266	0.127	0.008	0.862
		Large-S2	0.245	0.276	0.580	1.266	0.127	0.007	0.869
22	Upper San Fernando Dam - D/S Slope	A1&B1&C1	0.156	0.131	0.003	0.093	0.095	0.020	0.526
		A2&B2&C2	0.156	0.131	0.003	0.092	0.095	0.023	0.515
		A3	0.156	0.131	0.003	0.092	0.095	0.024	0.509
		B4&C4	0.156	0.131	0.003	0.092	0.095	0.025	0.508
		B5&C5	0.156	0.131	0.003	0.093	0.095	0.023	0.515
23	Tar Island Dyke	Large-S1	0.225	0.248	0.270	0.317	0.120	0.019	0.699
		Large-S2	0.225	0.248	0.270	0.317	0.120	0.026	0.666
		Small-S1	0.225	0.248	0.270	0.317	0.120	0.019	0.701
		Small-S2	0.225	0.248	0.270	0.317	0.120	0.026	0.666
24	Mochi-Koshi Tailings Dam 1	S1	0.175	0.180	0.145	0.247	0.105	0.013	0.630
		S2	0.175	0.180	0.145	0.247	0.105	0.014	0.620

Table 4.12 (cont'd) Summary of the evaluated parameters for Model 4

		S3	0.175	0.180	0.145	0.247	0.105	0.016	0.611
25	Mochi-Koshi Tailings Dam 2	S1	0.173	0.176	0.150	0.266	0.104	0.014	0.614
		S2	0.173	0.176	0.150	0.266	0.104	0.013	0.626
26	Nerlerk Embankment Slide 1	S1	0.233	0.249	0.220	0.290	0.120	0.017	0.721
		S2	0.233	0.249	0.220	0.290	0.120	0.018	0.713
		S3	0.233	0.249	0.220	0.290	0.120	0.017	0.723
27	Nerlerk Embankment Slide 2	S1	0.233	0.249	0.220	0.290	0.120	0.018	0.719
		S2	0.233	0.249	0.220	0.290	0.120	0.019	0.708
		S3	0.233	0.249	0.220	0.290	0.120	0.016	0.730
28	Nerlerk Embankment Slide 3	S1	0.233	0.249	0.220	0.290	0.120	0.020	0.704
		S2	0.233	0.249	0.220	0.290	0.120	0.018	0.714
		S3	0.233	0.249	0.220	0.290	0.120	0.016	0.730
29	Asele Road Embankment	S1	0.238	0.293	0.611	0.881	0.132	0.016	0.780
		S2	0.238	0.293	0.611	0.886	0.132	0.016	0.784
30	Nalband Railway Embankment	NB-1	0.140	0.122	0.063	0.137	0.093	0.017	0.518
		Small-S2	0.140	0.122	0.063	0.137	0.093	0.018	0.514
		NB-1	0.140	0.122	0.063	0.137	0.093	0.017	0.518
		Large-S2	0.140	0.122	0.063	0.137	0.093	0.018	0.512
		Large-S3	0.140	0.122	0.063	0.137	0.093	0.016	0.523
31	Sullivan Tailings	Large-S1	0.247	0.265	0.286	0.444	0.125	0.013	0.788
		CP91-29	0.247	0.265	0.286	0.444	0.125	0.017	0.756
		CP91-31	0.247	0.265	0.286	0.444	0.125	0.015	0.772
		Small-S1	0.247	0.265	0.286	0.444	0.125	0.016	0.766
		CP91-31	0.247	0.265	0.286	0.444	0.125	0.016	0.763
32	Jamuna Bridge	S1	0.247	0.285	0.482	0.702	0.130	0.015	0.793
		S2	0.247	0.285	0.482	0.702	0.130	0.014	0.805

In the end, the post-liquefaction shear strength values are predicted by Model 4 as tabulated in Table 4.13 for each sub-section of the case histories.

Table 4.13 Summary of the predicted post-liquefaction shear strength values for Model 4

#	Case History	Section	L_i (m)	L_t (m)	ϕ'_{ls} (deg)	M_{tc}	θ (deg)	M	$\tau_{liq,i}$ (kPa)	$\sum \tau_{liq,i} \cdot L_i / L_t$ (kPa)
1	Wachusett Dam - North Dike	WND-1	19.3	68.9	31.26	1.255	-20.16	0.863	5.98	7.6
		WND-2	20.9		31.26	1.255	-23.99	0.868	7.05	
		WND-105	18.4		31.26	1.255	-25.03	0.870	8.69	
		WND-3	10.2		31.26	1.255	-23.86	0.868	10.04	
2	Fort Peck Dam	Boring 3	200.3	389.3	30.93	1.241	-24.40	0.862	13.93	13.7
		Boring 7	67.9		30.93	1.241	-25.23	0.864	15.15	
		Boring 6	79.4		30.93	1.241	-24.05	0.861	14.44	
		Boring 7	41.7		30.93	1.241	-3.45	0.876	8.71	
3	Uetsu Railway Embankment	S1	9.4	20.3	30.66	1.229	-22.54	0.852	5.53	5.1
		S2	10.9		30.66	1.229	-23.15	0.853	4.82	
4	Lower San Fernando Dam - U/S Slope	S103&S111	54.8	103.8	38.71	1.580	-26.24	1.025	12.60	12.8
		S101&S102&S104	16.9		38.71	1.580	-23.82	1.021	12.97	
		S105	16.8		38.71	1.580	-22.48	1.020	13.13	
		S105	15.3		38.71	1.580	-24.04	1.022	12.83	
5	Hachiro-Gata Road Embankment	S1	10.9	14.9	32.29	1.300	-23.20	0.889	4.94	5.1
		S2	4.0		32.29	1.300	-26.01	0.895	5.61	
6	La Marquesa Dam - U/S Slope	B-2	6.6	21.8	33.56	1.355	-22.31	0.915	6.15	5.5
		B-III	7.2		33.56	1.355	-26.21	0.922	5.63	
		B-3	8.0		33.56	1.355	-25.83	0.921	4.85	
7	La Marquesa Dam - D/S Slope	B-II	10.1	15.8	32.50	1.309	-19.75	0.890	6.34	7.0
		B-1	5.7		32.50	1.309	-26.25	0.900	8.08	
8	La Palma Dam	B-3	6.1	15.9	31.99	1.287	-24.28	0.885	6.17	5.4
		B-4	9.8		31.99	1.287	-18.45	0.878	4.92	
9	Lake Ackerman Highway Embankment	S1	5.9	29.6	30.66	1.229	-24.32	0.855	5.57	5.9
		S2	12.5		30.66	1.229	27.11	1.168	7.25	
		S3	11.2		30.66	1.229	-24.27	0.855	4.58	
10	Chonan Middle School	No.4	6.7	15.4	32.29	1.300	-22.12	0.888	4.66	5.2
		No.3	8.7		32.29	1.300	-23.51	0.890	5.66	
11	Soviet Tajik - May 1 Slide	S1	44.9	68.8	38.71	1.580	-19.75	1.019	15.30	16.1
		S2	24.0		38.71	1.580	-16.90	1.020	17.50	
12	Shibecha-Cho Embankment	B-2	8.3	47.3	35.31	1.432	-25.53	0.957	7.62	7.6
		B-3	25.9		35.31	1.432	-26.59	0.959	7.69	
		B-5	13.1		35.31	1.432	-19.06	0.950	7.59	

Table 4.13 (cont'd) Summary of the predicted post-liquefaction shear strength values for Model 4

		B-4	10.9	24.0	35.31	1.432	-23.50	0.953	7.60	7.6
		B-5	13.1		35.31	1.432	-19.06	0.950	7.59	
13	Route 272 at Higashiarekinai	Left	6.7	22.9	32.50	1.309	-25.82	0.899	6.43	6.4
		Right	16.2		32.50	1.309	-21.61	0.891	6.33	
14	Zeeland - Vlietepolder	Small-S1	31.3	75.7	31.22	1.253	-25.02	0.869	10.98	11.5
		Small-S2	44.4		31.22	1.253	-25.38	0.870	11.87	
		Large-S1	100.2	318.6	31.22	1.253	-28.70	0.879	10.94	12.3
		Large-S2	107.4		31.22	1.253	-29.98	0.884	13.34	
		Large-S3	111.0		31.22	1.253	-28.30	0.878	12.57	
15	Sheffield Dam	Right	14.9	14.9	34.69	1.405	-23.36	0.940	6.72	6.7
16	Helsinki Harbor	Small-S1	6.7	16.0	30.57	1.225	-26.65	0.859	3.45	3.7
		Small-S2	9.2		30.57	1.225	-25.29	0.856	3.95	
		Large-S1	35.5	71.3	30.57	1.225	-28.98	0.866	4.27	4.3
		Large-S2	35.8		30.57	1.225	-29.10	0.866	4.23	
17	Solfatara Canal Dike	S1	4.6	9.4	31.22	1.253	-29.86	0.883	5.08	4.9
		S2	4.8		31.22	1.253	-21.71	0.863	4.79	
18	Lake Merced Bank	Boring 2	30.3	30.3	30.84	1.237	-21.91	0.855	7.90	7.9
19	El Cobre Tailings Dam	S1	83.7	348.1	35.90	1.458	-20.17	0.962	4.55	4.0
		S2	43.8		35.90	1.458	-27.09	0.972	4.43	
		S3	85.8		35.90	1.458	-28.94	0.978	3.97	
		S4	134.8		35.90	1.458	-29.71	0.980	3.50	
20	Metoki Road Embankment	S-19	6.8	14.0	31.99	1.287	-22.39	0.881	5.24	4.9
		S-13	7.2		31.99	1.287	-21.85	0.881	4.59	
21	Hokkaido Tailings Dam	Small-S1	18.3	23.2	35.90	1.458	-29.20	0.978	3.86	3.9
		Small-S2	5.0		35.90	1.458	-22.74	0.964	4.11	
		Large-S1	18.3	48.6	35.90	1.458	-29.20	0.978	3.86	3.7
		Large-S2	30.4		35.90	1.458	-27.21	0.973	3.62	
22	Upper San Fernando Dam - D/S Slope	A1&B1&C1	14.3	111.1	38.40	1.567	-16.83	1.014	10.31	11.8
		A2&B2&C2	10.0		38.40	1.567	-18.92	1.013	11.51	
		A3	23.2		38.40	1.567	-29.14	1.027	12.43	
		B4&C4	33.4		38.40	1.567	-26.36	1.020	12.50	
		B5&C5	30.2		38.40	1.567	-24.32	1.016	11.52	
23	Tar Island Dyke	Large-S1	260.2	308.6	32.59	1.313	-29.41	0.911	8.79	9.2
		Large-S2	48.4		32.59	1.313	-22.71	0.895	11.41	

Table 4.13 (cont'd) Summary of the predicted post-liquefaction shear strength values for Model 4

		Small-S1	27.6	76.0	32.59	1.313	-20.91	0.893	8.53	10.4
		Small-S2	48.4		32.59	1.313	-22.71	0.895	11.41	
24	Mochi-Koshi Tailings Dam 1	S1	61.2	183.7	38.71	1.580	-25.71	1.024	6.66	7.3
		S2	61.0		38.71	1.580	-24.13	1.022	7.37	
		S3	61.6		38.71	1.580	-21.33	1.019	7.96	
25	Mochi-Koshi Tailings Dam 2	S1	34.8	70.9	38.71	1.580	-23.32	1.021	7.32	6.9
		S2	36.1		38.71	1.580	-19.35	1.019	6.54	
26	Nerlerk Embankment Slide 1	S1	23.5	166.7	31.26	1.255	-26.51	0.874	7.61	7.8
		S2	71.7		31.26	1.255	-27.33	0.876	8.10	
		S3	71.4		31.26	1.255	-27.98	0.878	7.47	
27	Nerlerk Embankment Slide 2	S1	18.9	155.5	31.26	1.255	-26.72	0.874	7.69	7.7
		S2	68.5		31.26	1.255	-28.11	0.878	8.46	
		S3	68.1		31.26	1.255	-16.52	0.861	6.93	
28	Nerlerk Embankment Slide 3	S1	80.5	361.9	31.26	1.255	-28.69	0.880	8.81	7.9
		S2	140.5		31.26	1.255	-28.52	0.880	8.10	
		S3	140.9		31.26	1.255	-29.72	0.884	7.13	
29	Asele Road Embankment	S1	20.1	26.5	33.56	1.355	-19.47	0.913	7.45	7.4
		S2	6.4		33.56	1.355	-22.90	0.916	7.25	
30	Nalband Railway Embankment	NB-1	25.3	32.5	36.15	1.469	-28.58	0.981	8.39	8.5
		Small-S2	7.2		36.15	1.469	-24.82	0.973	8.71	
		NB-1	25.3	57.2	36.15	1.469	-28.58	0.981	8.39	8.6
		Large-S2	25.8		36.15	1.469	-28.25	0.981	8.90	
		Large-S3	6.1		36.15	1.469	-21.44	0.968	7.83	
31	Sullivan Tailings	Large-S1	13.8	38.6	35.90	1.458	-10.45	0.972	6.35	7.2
		CP91-29	10.7		35.90	1.458	-20.69	0.963	8.11	
		CP91-31	14.2		35.90	1.458	-25.19	0.968	7.22	
		Small-S1	6.5	23.5	35.90	1.458	-23.15	0.965	7.54	7.7
		CP91-31	17.1		35.90	1.458	-25.32	0.968	7.74	
32	Jamuna Bridge	S1	44.9	88.3	31.12	1.249	-26.99	0.872	6.51	6.2
		S2	43.4		31.12	1.249	-14.97	0.858	5.86	

4.4.5 Model 5

The fifth residual strength prediction model utilizes a totally different mathematical form than the previous four models for isotropic compression responses, but a semi-logarithmic void ratio versus mean effective stress domain (e vs. ln(p')) for liquefaction states similar to Model 3 and Model 4. The new mathematical form for the isotropic compression responses is defined in this study for the first time, and it is again arranged such that the isotropic compression curves become asymptomatic to a horizontal line passing from the minimum limit void ratio (e_{lim}) at higher stresses. Thus, the negative void ratio values at these higher stress ranges are still avoided for this new mathematical form due to the log-nature of the relationship. The liquefaction state lines, on the other hand, are defined as log-linear over the void ratio versus mean effective stress domain similar to Model 3 and Model 4.

The mathematical relationship given in Equation 4-41 is implemented for the isotropic compression curves.

$$ICC: \quad e = e_{lim} + \frac{\theta_1}{\theta_2} - \frac{\theta_1}{\theta_2 + \theta_3 \cdot exp\left(-\theta_4 \cdot \left(p' - p'_r\right)\right)} \qquad \text{Equation 4-41}$$

In this equation, while p' represents the in-situ mean effective stress measured at the field, e represents the corresponding void ratio at this mean effective stress value. Similar to previous residual strength prediction models, e_{lim} defined in this equation gives the minimum limit void ratio that the isotropic compression curves become asymptomatic at very high stresses. This value is directly taken as zero in Model 5 Similar to Model 1 and Model 3 to avoid any negative void ratios.

The parameter p'_r in Equation 4-41 is defined as the form given in Equation 4-42.

$$p'_r = p'_0 + \frac{ln\left(\frac{\frac{\theta_1}{e_{lim} + \frac{\theta_1}{\theta_2} - e_0} - \theta_2}{\theta_3}\right)}{\theta_4} \qquad \text{Equation 4-42}$$

In this equation, e_0 represents the void ratio at a known mean stress p'_0 on the ICCs. In our case, these values are regarded as the initial state of the soil. In other words, p'_0 is taken as 1 kPa = 0.001 MPa referring to the confining stress acting on samples during limit void ratio determination experiments, and e_0 is taken as the corresponding initial void ratio at this confining stress evaluated by Equation 3-68.

In the end, the void ratios (e) evaluated by Equation 4-41 are defined as the actual in-situ void ratios (e_{ICC}), and they are directly located in the void ratio versus mean effective stress domain as the initial state points of the corresponding case histories (green dots in Figure 4.16).

For the liquefaction state curves, the relationship employed for Model 3 and Model 4 given in Equation 4-33 is also used for Model 5. In other words, log-linear lines are defined over the void ratio versus mean effective stress domain; therefore, they are called liquefaction state lines also for this model. Same procedures are followed during the evaluation of required parameters for the development of LSLs such that Equation 4-34 and Equation 4-35 are employed for the evaluation of λ_{cs} and Γ values, respectively.

The void ratio (e) in Equation 4-33 is already the same as the void ratio evaluated by Equation 4-41, e_{ICC}, because the void ratio remains the same under undrained conditions.

In the end, the final mean effective stress values after the liquefaction are evaluated by solving p'_{ls} in Equation 4-33 for each sub-section of the case histories, and the closed-form solution of the relationship is obtained as given in Equation 4-43. In this equation, p'_r values can be evaluated by using Equation 4-42.

$$p'_{ls} = exp\left(\frac{(\theta_6 \cdot e_{max}) - \left(e_{lim} + \frac{\theta_1}{\theta_2} - \frac{\theta_1}{\theta_2 + \theta_3 \cdot exp\left(-\theta_4 \cdot \left(p' - p'_r\right)\right)}\right)}{\theta_7 \cdot exp\left(\theta_8 + \theta_9 \cdot (e_{max} - e_{min})\right)}\right) \quad \text{Equation 4-43}$$

Once the final mean effective stress values after the liquefaction (p'_{ls}) are evaluated by Equation 4-43, the corresponding data points are located in the void ratio versus mean effective stress domain as the liquefaction state points of the corresponding case histories (red squares in Figure 4.16).

Accordingly, the other parameters used in the evaluation of the failure criterion, such as the liquefaction/critical state friction angle (ϕ'_{ls}), Lode angle (θ), slope of the stress paths in q vs. p' domain for triaxial compression tests (M_{tc}) and in general (M), are evaluated with the same procedure followed in previous models by using Equation 4-23, Equation 4-24, Equation 4-22 and Equation 4-21, respectively.

Finally, the post-liquefaction shear strength values for each sub-section are predicted by using the relationship provided in Equation 4-26 as a function M and liquefaction state mean effective stress (p'_{ls}) values. Accordingly, the overall representative post-liquefaction shear strength values of all case histories are predicted by using Equation 4-27.

Once the residual strength predictions evaluated by Equation 4-27 are compared with the modified back-analyses results of Weber (2015) given in Table 4.1 for the same case histories, the overall best-fit model parameters are developed as given in Table 4.14 for Model 5 as a result of probabilistic regressions by the Maximum Likelihood Method.

Table 4.14 Best-fit model parameters for Model 5

θ_1	0.194
θ_2	-0.068
θ_3	0.001
θ_4	0.618

Table 4.14 (cont'd) Best-fit model parameters for Model 5

θ_6	0.073
θ_7	0.085
θ_8	0.030
θ_9	1.760
θ_{10}	28.02
θ_{11}	-0.273
θ_{12}	0.786
θ_{13}	-0.100
θ_{14}	18.979
θ_{15}	31.021
θ_{16}	5.187
θ_{17}	4

Consequently, the equations of isotropic compression curves and liquefaction state lines are obtained as given in Equation 4-44 and Equation 4-45, respectively.

$$ICC:\ e = -2.853 - \frac{0.194}{-0.068 + 0.001 \cdot exp\left(-0.618 \cdot \left(p' - 0.001 - \frac{ln\left(\frac{\frac{0.194}{-2.853 - e_0} + 0.068}{0.001}\right)}{0.618}\right)\right)} \quad \text{Equation 4-44}$$

$$LSL:\quad e = (0.073 \cdot e_{max}) - 0.085 \cdot exp\big(0.03 + 1.76 \cdot (e_{max} - e_{min})\big) \cdot \ln\left(p'_{ls}\right) \quad \text{Equation 4-45}$$

Using these equations, the case history data points with respect to their initial states and liquefaction states are located in the void ratio versus mean effective stress domain as presented in Figure 4.16.

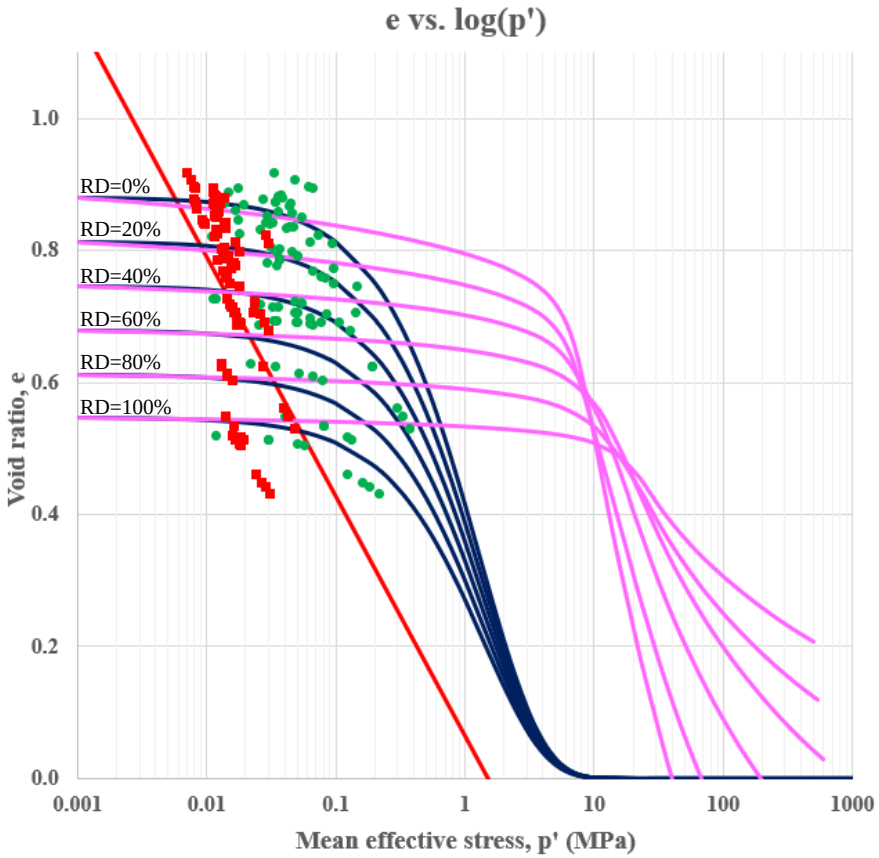

Figure 4.16. Void ratio versus mean effective stress domain for Model 5

In Figure 4.16, while the green dots and red squares represent the initial and liquefaction states of the case history data points, the purple and blue curves represent the isotropic compression curves recommended by Mesri and Vardhanabhuti (2009), and developed for Model 5 by Equation 4-41, respectively, for 0%, 20%, 40%, 60%, 80%, and 100% relative densities. The red curve presents the liquefaction state curve evaluated by Equation 4-33 by using the average λ_{ls} and Γ values of the case histories. It should be noted that the stress differences between the initial and liquefaction states, i.e., between the green dots and red squares, give the generated excess pore pressures during the liquefaction.

A summary of the evaluated parameters for Model 5 is tabulated in Table 4.15Table 4.12 for each sub-section of the case histories.

Table 4.15 Summary of the evaluated parameters for Model 5

#	Case History	Section	Γ	p'_r (MPa)	λ_{ls}	p'_{ls} (MPa)	e_{ICC}
1	Wachusett Dam - North Dike	WND-1	0.068	4.411	0.168	0.014	0.788
		WND-2	0.068	4.443	0.168	0.015	0.772
		WND-105	0.068	4.450	0.168	0.018	0.746
		WND-3	0.068	4.375	0.168	0.023	0.706
2	Fort Peck Dam	Boring 3	0.065	4.224	0.154	0.039	0.562
		Boring 7	0.065	4.224	0.154	0.048	0.531
		Boring 6	0.065	4.224	0.154	0.043	0.548
		Boring 7	0.065	4.224	0.154	0.017	0.688
3	Uetsu Railway Embankment	S1	0.070	4.524	0.176	0.012	0.851
		S2	0.070	4.503	0.176	0.012	0.854
4	Lower San Fernando Dam - U/S Slope	S103&S111	0.040	3.780	0.113	0.024	0.461
		S101&S102&S104	0.040	3.780	0.113	0.029	0.441
		S105	0.040	3.780	0.113	0.031	0.431
		S105	0.040	3.780	0.113	0.027	0.449
5	Hachiro-Gata Road Embankment	S1	0.073	4.516	0.179	0.012	0.870
		S2	0.073	4.516	0.179	0.012	0.858
6	La Marquesa Dam - U/S Slope	B-2	0.074	4.543	0.182	0.013	0.871
		B-III	0.074	4.550	0.182	0.012	0.882
		B-3	0.074	4.549	0.182	0.011	0.895
7	La Marquesa Dam - D/S Slope	B-II	0.073	4.487	0.181	0.014	0.843
		B-1	0.073	4.478	0.181	0.017	0.814
8	La Palma Dam	B-3	0.072	4.496	0.178	0.013	0.837
		B-4	0.072	4.501	0.178	0.012	0.861
9	Lake Ackerman Highway Embankment	S1	0.068	4.434	0.169	0.013	0.798
		S2	0.068	4.434	0.169	0.013	0.804
		S3	0.068	4.436	0.169	0.012	0.821
10	Chonan Middle School	No.4	0.072	4.513	0.178	0.011	0.872
		No.3	0.072	4.524	0.178	0.012	0.857
11	Soviet Tajik - May 1 Slide	S1	0.073	4.501	0.211	0.029	0.823
		S2	0.073	4.501	0.211	0.030	0.810
12	Shibecha-Cho Embankment	B-2	0.057	4.244	0.156	0.017	0.694
		B-3	0.057	4.256	0.156	0.017	0.692
		B-5	0.057	4.242	0.156	0.017	0.693
		B-4	0.057	4.257	0.156	0.017	0.692
		B-5	0.057	4.242	0.156	0.017	0.693

Table 4.15 (cont'd) Summary of the evaluated parameters for Model 5

13	Route 272 at Higashiarekinai	Left	0.072	4.487	0.178	0.014	0.835
		Right	0.072	4.493	0.178	0.014	0.837
14	Zeeland - Vlietepolder	Small-S1	0.071	4.313	0.174	0.024	0.721
		Small-S2	0.071	4.313	0.174	0.026	0.703
		Large-S1	0.071	4.313	0.174	0.023	0.724
		Large-S2	0.071	4.313	0.174	0.030	0.679
		Large-S3	0.071	4.313	0.174	0.028	0.692
15	Sheffield Dam	Right	0.076	4.550	0.187	0.014	0.880
16	Helsinki Harbor	Small-S1	0.072	4.501	0.166	0.008	0.864
		Small-S2	0.072	4.481	0.166	0.009	0.847
		Large-S1	0.072	4.485	0.166	0.010	0.840
		Large-S2	0.072	4.489	0.166	0.010	0.842
17	Solfatara Canal Dike	S1	0.070	4.448	0.171	0.012	0.825
		S2	0.070	4.466	0.171	0.012	0.831
18	Lake Merced Bank	Boring 2	0.072	4.423	0.180	0.018	0.798
19	El Cobre Tailings Dam	S1	0.074	4.597	0.170	0.008	0.894
		S2	0.074	4.597	0.170	0.008	0.897
		S3	0.074	4.597	0.170	0.008	0.907
		S4	0.074	4.597	0.170	0.007	0.918
20	Metoki Road Embankment	S-19	0.074	4.554	0.181	0.012	0.884
		S-13	0.074	4.540	0.181	0.011	0.890
21	Hokkaido Tailings Dam	Small-S1	0.070	4.536	0.167	0.008	0.873
		Small-S2	0.070	4.536	0.167	0.008	0.867
		Large-S1	0.070	4.536	0.167	0.008	0.873
		Large-S2	0.070	4.536	0.167	0.008	0.878
22	Upper San Fernando Dam - D/S Slope	A1&B1&C1	0.044	3.941	0.119	0.014	0.550
		A2&B2&C2	0.044	3.940	0.119	0.016	0.533
		A3	0.044	3.940	0.119	0.019	0.517
		B4&C4	0.044	3.940	0.119	0.019	0.513
		B5&C5	0.044	3.941	0.119	0.016	0.534
23	Tar Island Dyke	Large-S1	0.064	4.264	0.156	0.018	0.687
		Large-S2	0.064	4.264	0.156	0.028	0.625
		Small-S1	0.064	4.264	0.156	0.018	0.689
		Small-S2	0.064	4.264	0.156	0.028	0.625
24	Mochi-Koshi Tailings Dam 1	S1	0.050	4.102	0.133	0.013	0.628
		S2	0.050	4.102	0.133	0.014	0.615

Table 4.15 (cont'd) Summary of the evaluated parameters for Model 5

		S3	0.050	4.102	0.133	0.016	0.603
25	Mochi-Koshi Tailings Dam 2	S1	0.049	4.103	0.132	0.014	0.609
		S2	0.049	4.103	0.132	0.013	0.623
26	Nerlerk Embankment Slide 1	S1	0.066	4.281	0.156	0.015	0.715
		S2	0.066	4.281	0.156	0.016	0.705
		S3	0.066	4.281	0.156	0.015	0.719
27	Nerlerk Embankment Slide 2	S1	0.066	4.281	0.156	0.016	0.714
		S2	0.066	4.281	0.156	0.017	0.698
		S3	0.066	4.281	0.156	0.014	0.727
28	Nerlerk Embankment Slide 3	S1	0.066	4.281	0.156	0.018	0.692
		S2	0.066	4.281	0.156	0.016	0.706
		S3	0.066	4.281	0.156	0.014	0.727
29	Asele Road Embankment	S1	0.068	4.390	0.173	0.016	0.777
		S2	0.068	4.391	0.173	0.016	0.781
30	Nalband Railway Embankment	NB-1	0.040	3.838	0.116	0.017	0.513
		Small-S2	0.040	3.838	0.116	0.018	0.506
		NB-1	0.040	3.838	0.116	0.017	0.513
		Large-S2	0.040	3.838	0.116	0.018	0.504
		Large-S3	0.040	3.838	0.116	0.016	0.521
31	Sullivan Tailings	Large-S1	0.070	4.407	0.162	0.012	0.786
		CP91-29	0.070	4.407	0.162	0.015	0.750
		CP91-31	0.070	4.407	0.162	0.013	0.768
		Small-S1	0.070	4.407	0.162	0.014	0.762
		CP91-31	0.070	4.407	0.162	0.014	0.758
32	Jamuna Bridge	S1	0.071	4.432	0.171	0.015	0.793
		S2	0.071	4.432	0.171	0.014	0.805

In the end, the post-liquefaction shear strength values are predicted by Model 5 as tabulated in Table 4.16 for each sub-section of the case histories.

Table 4.16 Summary of the predicted post-liquefaction shear strength values for Model 5

#	Case History	Section	L_i (m)	L_t (m)	ϕ'_{ls} (deg)	M_{tc}	θ (deg)	M	$\tau_{liq,i}$ (kPa)	$\sum \tau_{liq,i} \cdot L_i / L_t$ (kPa)
1	Wachusett Dam - North Dike	WND-1	19.3	68.9	31.26	1.255	-20.16	0.863	6.00	7.2
		WND-2	20.9		31.26	1.255	-23.99	0.868	6.64	
		WND-105	18.4		31.26	1.255	-25.03	0.870	7.78	
		WND-3	10.2		31.26	1.255	-23.86	0.868	9.86	
2	Fort Peck Dam	Boring 3	200.3	389.3	30.84	1.237	-24.40	0.860	16.89	16.9
		Boring 7	67.9		30.84	1.237	-25.23	0.861	20.74	
		Boring 6	79.4		30.84	1.237	-24.05	0.859	18.42	
		Boring 7	41.7		30.84	1.237	-3.45	0.874	7.54	
3	Uetsu Railway Embankment	S1	9.4	20.3	30.49	1.221	-22.54	0.848	5.02	5.0
		S2	10.9		30.49	1.221	-23.15	0.849	4.94	
4	Lower San Fernando Dam - U/S Slope	S103&S111	54.8	103.8	42.70	1.752	-26.24	1.098	13.23	14.4
		S101&S102&S104	16.9		42.70	1.752	-23.82	1.095	15.62	
		S105	16.8		42.70	1.752	-22.48	1.094	17.05	
		S105	15.3		42.70	1.752	-24.04	1.095	14.65	
5	Hachiro-Gata Road Embankment	S1	10.9	14.9	32.61	1.314	-23.20	0.896	5.20	5.3
		S2	4.0		32.61	1.314	-26.01	0.902	5.59	
6	La Marquesa Dam - U/S Slope	B-2	6.6	21.8	34.29	1.387	-22.31	0.930	5.88	5.5
		B-III	7.2		34.29	1.387	-26.21	0.937	5.58	
		B-3	8.0		34.29	1.387	-25.83	0.937	5.21	
7	La Marquesa Dam - D/S Slope	B-II	10.1	15.8	32.87	1.325	-19.75	0.898	6.34	6.8
		B-1	5.7		32.87	1.325	-26.25	0.908	7.53	
8	La Palma Dam	B-3	6.1	15.9	32.21	1.296	-24.28	0.889	6.00	5.5
		B-4	9.8		32.21	1.296	-18.45	0.883	5.20	
9	Lake Ackerman Highway Embankment	S1	5.9	29.6	30.49	1.221	-24.32	0.852	5.67	6.1
		S2	12.5		30.49	1.221	27.11	1.161	7.46	
		S3	11.2		30.49	1.221	-24.27	0.851	4.93	
10	Chonan Middle School	No.4	6.7	15.4	32.61	1.314	-22.12	0.894	5.02	5.3
		No.3	8.7		32.61	1.314	-23.51	0.896	5.47	
11	Soviet Tajik - May 1 Slide	S1	44.9	68.8	42.70	1.752	-19.75	1.094	15.62	16.0
		S2	24.0		42.70	1.752	-16.90	1.097	16.65	
12	Shibecha-Cho Embankment	B-2	8.3	47.3	38.06	1.552	-25.53	1.011	8.60	8.7
		B-3	25.9		38.06	1.552	-26.59	1.014	8.74	
		B-5	13.1		38.06	1.552	-19.06	1.006	8.58	

Table 4.16 (cont'd) Summary of the predicted post-liquefaction shear strength values for Model 5

		B-4	10.9	24.0	38.06	1.552	-23.50	1.008	8.65	8.6
		B-5	13.1		38.06	1.552	-19.06	1.006	8.58	
13	Route 272 at Higashiarekinai	Left	6.7	22.9	32.87	1.325	-25.82	0.907	6.32	6.2
		Right	16.2		32.87	1.325	-21.61	0.900	6.19	
14	Zeeland - Vlietepolder	Small-S1	31.3	75.7	31.20	1.252	-25.02	0.869	10.30	10.9
		Small-S2	44.4		31.20	1.252	-25.38	0.870	11.38	
		Large-S1	100.2	318.6	31.20	1.252	-28.70	0.879	10.23	12.0
		Large-S2	107.4		31.20	1.252	-29.98	0.883	13.27	
		Large-S3	111.0		31.20	1.252	-28.30	0.878	12.26	
15	Sheffield Dam	Right	14.9	14.9	35.82	1.454	-23.36	0.964	6.51	6.5
16	Helsinki Harbor	Small-S1	6.7	16.0	30.37	1.216	-26.65	0.855	3.56	3.8
		Small-S2	9.2		30.37	1.216	-25.29	0.851	3.93	
		Large-S1	35.5	71.3	30.37	1.216	-28.98	0.862	4.15	4.1
		Large-S2	35.8		30.37	1.216	-29.10	0.862	4.10	
17	Solfatara Canal Dike	S1	4.6	9.4	31.20	1.252	-29.86	0.883	5.36	5.2
		S2	4.8		31.20	1.252	-21.71	0.863	5.04	
18	Lake Merced Bank	Boring 2	30.3	30.3	30.72	1.231	-21.91	0.853	7.61	7.6
19	El Cobre Tailings Dam	S1	83.7	348.1	37.51	1.528	-20.17	0.995	4.05	3.8
		S2	43.8		37.51	1.528	-27.09	1.004	4.01	
		S3	85.8		37.51	1.528	-28.94	1.009	3.80	
		S4	134.8		37.51	1.528	-29.71	1.011	3.58	
20	Metoki Road Embankment	S-19	6.8	14.0	32.21	1.296	-22.39	0.886	5.10	5.0
		S-13	7.2		32.21	1.296	-21.85	0.885	4.93	
21	Hokkaido Tailings Dam	Small-S1	18.3	23.2	37.51	1.528	-29.20	1.010	4.08	4.1
		Small-S2	5.0		37.51	1.528	-22.74	0.997	4.20	
		Large-S1	18.3	48.6	37.51	1.528	-29.20	1.010	4.08	4.0
		Large-S2	30.4		37.51	1.528	-27.21	1.004	3.94	
22	Upper San Fernando Dam - D/S Slope	A1&B1&C1	14.3	111.1	42.26	1.734	-16.83	1.089	7.68	9.4
		A2&B2&C2	10.0		42.26	1.734	-18.92	1.087	8.81	
		A3	23.2		42.26	1.734	-29.14	1.096	10.17	
		B4&C4	33.4		42.26	1.734	-26.36	1.090	10.45	
		B5&C5	30.2		42.26	1.734	-24.32	1.087	8.79	
23	Tar Island Dyke	Large-S1	260.2	308.6	33.03	1.332	-29.41	0.920	8.47	9.1
		Large-S2	48.4		33.03	1.332	-22.71	0.904	12.45	
		Small-S1	27.6	76.0	33.03	1.332	-20.91	0.902	8.20	10.9

Table 4.16 (cont'd) Summary of the predicted post-liquefaction shear strength values for Model 5

		Small-S2	48.4		33.03	1.332	-22.71	0.904	12.45	
24	Mochi-Koshi Tailings Dam 1	S1	61.2	183.7	42.70	1.752	-25.71	1.097	7.18	7.9
		S2	61.0		42.70	1.752	-24.13	1.095	7.94	
		S3	61.6		42.70	1.752	-21.33	1.094	8.68	
25	Mochi-Koshi Tailings Dam 2	S1	34.8	70.9	42.70	1.752	-23.32	1.094	7.92	7.5
		S2	36.1		42.70	1.752	-19.35	1.094	7.08	
26	Nerlerk Embankment Slide 1	S1	23.5	166.7	31.26	1.255	-26.51	0.874	6.76	6.9
		S2	71.7		31.26	1.255	-27.33	0.876	7.22	
		S3	71.4		31.26	1.255	-27.98	0.878	6.64	
27	Nerlerk Embankment Slide 2	S1	18.9	155.5	31.26	1.255	-26.72	0.874	6.84	6.9
		S2	68.5		31.26	1.255	-28.11	0.878	7.57	
		S3	68.1		31.26	1.255	-16.52	0.861	6.17	
28	Nerlerk Embankment Slide 3	S1	80.5	361.9	31.26	1.255	-28.69	0.880	7.93	7.0
		S2	140.5		31.26	1.255	-28.52	0.880	7.21	
		S3	140.9		31.26	1.255	-29.72	0.884	6.35	
29	Asele Road Embankment	S1	20.1	26.5	34.29	1.387	-19.47	0.928	7.64	7.6
		S2	6.4		34.29	1.387	-22.90	0.931	7.48	
30	Nalband Railway Embankment	NB-1	25.3	32.5	39.18	1.601	-28.58	1.040	8.75	8.9
		Small-S2	7.2		39.18	1.601	-24.82	1.032	9.24	
		NB-1	25.3	57.2	39.18	1.601	-28.58	1.040	8.75	9.0
		Large-S2	25.8		39.18	1.601	-28.25	1.039	9.50	
		Large-S3	6.1		39.18	1.601	-21.44	1.028	8.14	
31	Sullivan Tailings	Large-S1	13.8	38.6	37.51	1.528	-10.45	1.007	6.04	6.7
		CP91-29	10.7		37.51	1.528	-20.69	0.995	7.46	
		CP91-31	14.2		37.51	1.528	-25.19	1.000	6.71	
		Small-S1	6.5	23.5	37.51	1.528	-23.15	0.997	6.96	7.1
		CP91-31	17.1		37.51	1.528	-25.32	1.000	7.13	
32	Jamuna Bridge	S1	44.9	88.3	31.08	1.247	-26.99	0.871	6.41	6.1
		S2	43.4		31.08	1.247	-14.97	0.857	5.87	

4.4.6 Model 6

The sixth residual strength prediction model again utilizes the same new mathematical form employed for Model 5 for isotropic compression responses, and

a semi-logarithmic void ratio versus mean effective stress domain (e vs. ln(p')) for liquefaction states similar to Model 3, Model 4 and Model 5. In other words, the liquefaction state lines are defined as log-linear over the void ratio versus mean effective stress domain.

There is only a very tiny difference exists between Model 5 and Model 6, which is the same difference between Model 1 and Model 2, and Model 3 and Model 4. For Model 6, the minimum limit void ratio that the isotropic state curves become asymptomatic at very high stresses, e_{lim} value, is selected as 0.35 instead of zero similar to Model 2 and Model 4.

As already discussed in Section 4.4.2 during the explanation of residual strength prediction Model 2, this value of 0.35 is not randomly determined, but defined referring to Cubrinovski and Ishihara (2002) such that the void ratio of the densest possible packing of single-sized sphere shape of soil particles is given as 0.35 geometrically as presented in Figure 4.12b and Equation 4-30.

The single-sized sphere shape of the soil particles can be matched with the shape of the soil particles at very high stress ranges because significant level of particle crushing occurs at those extreme stress levels, and the angularity of the soil particles disappears automatically. Accordingly, a smooth sphere shape is obtained for them naturally. Hence, defining the minimum limit void ratio that the isotropic state curves become asymptomatic at very high stresses as $e_{lim} = 0.35$ is pretty reasonable for Model 6.

Other than this little e_{lim} difference, the same relationships employed for Model 5 is also used for Model 6. The mathematical relationship developed in this study given in Equation 4-41 is implemented for the isotropic compression curves. The p'_r values used in this relationship are again evaluated by Equation 4-42. For the liquefaction state lines, the relationship provided in Equation 4-33 is employed, and the required parameters used in this relationship, i.e., λ_{ls} and Γ, are evaluated by Equation 4-34 and Equation 4-35, respectively. In the end, the final mean effective stress values after the liquefaction are evaluated by solving p'_{ls} in Equation 4-33 for each sub-

section of the case histories, and the closed-form solution of the relationship is obtained as given in Equation 4-43.

The other parameters used in the evaluation of failure criterion, such as the liquefaction state friction angle (ϕ'_{ls}), Lode angle (θ), slope of the stress paths in q vs. p' domain for triaxial compression tests (M_{tc}) and in general (M), are also evaluated by using Equation 4-23, Equation 4-24, Equation 4-22 and Equation 4-21, respectively.

Finally, the post-liquefaction shear strength values for each sub-section can be predicted by using the relationship provided in Equation 4-26 as a function M and liquefaction state mean effective stress (p'_{ls}) values. Accordingly, the overall representative post-liquefaction shear strength values of all case histories can be predicted by using Equation 4-27.

Once the residual strength predictions evaluated by Equation 4-27 are compared with the modified back-analyses results of Weber (2015) given in Table 4.1 for the same case histories, the overall best-fit model parameters are developed as given in Table 4.17 for Model 6 as a result of probabilistic regressions by the Maximum Likelihood Method.

Table 4.17 Best-fit model parameters for Model 6

θ_1	0.597
θ_2	-0.015
θ_3	0.425
θ_4	1.600
θ_6	0.155
θ_7	0.077
θ_8	0.030
θ_9	1.750
θ_{10}	23.85
θ_{11}	-0.472

Table 4.17 (cont'd) Best-fit model parameters for Model 6

θ_{12}	0.712
θ_{13}	-0.13
θ_{14}	6.000
θ_{15}	44.000
θ_{16}	5.050
θ_{17}	4

Consequently, the equations of isotropic compression curves and liquefaction state lines are obtained as given in Equation 4-46 and Equation 4-47, respectively.

$$ICC: e = -39.45 - \frac{0.597}{-0.015 + 0.425 \cdot exp\left(-1.6 \cdot \left(p' - 0.001 - \frac{ln\left(\frac{\frac{0.597}{-39.45 - e_0} + 0.015}{0.425}\right)}{1.6}\right)\right)} \quad \text{Equation 4-46}$$

$$LSL: \quad e = (0.155 \cdot e_{max}) - 0.077 \cdot exp\big(0.03 + 1.75 \cdot (e_{max} - e_{min})\big) \cdot \ln\left(p'_{ls}\right) \quad \text{Equation 4-47}$$

Using these equations, the case history data points with respect to their initial states and liquefaction states are located in the void ratio versus mean effective stress domain as presented in Figure 4.17.

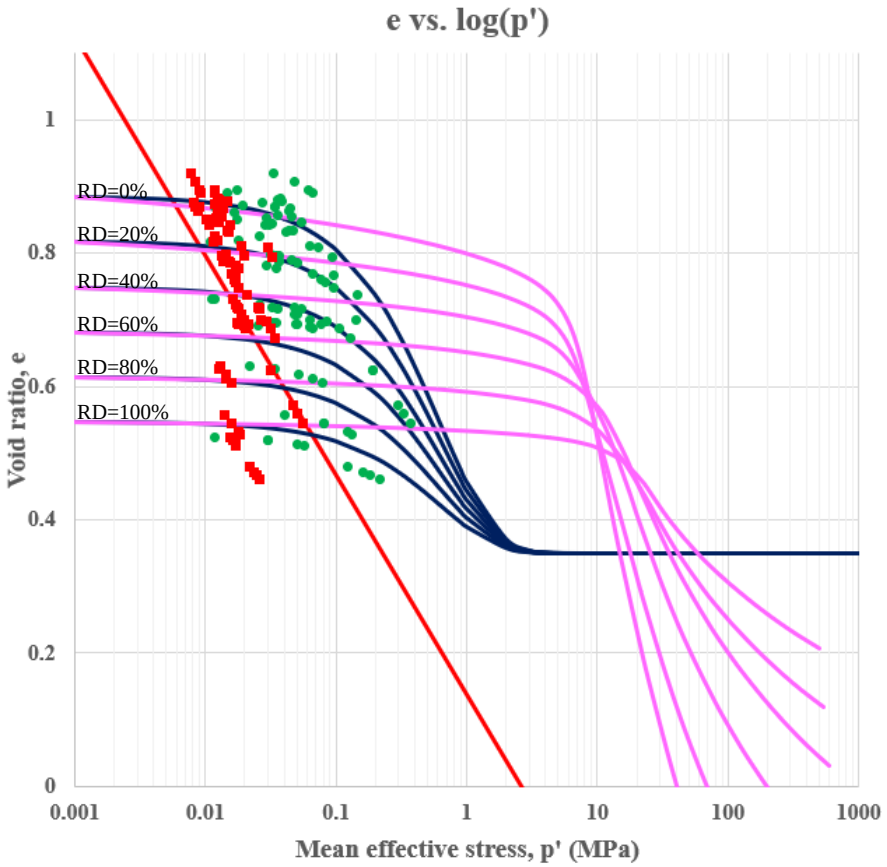

Figure 4.17. Void ratio versus mean effective stress domain for Model 6

In Figure 4.17, while the green dots and red squares represent the initial and liquefaction states of the case history data points, the purple and blue curves represent the isotropic compression curves recommended by Mesri and Vardhanabhuti (2009), and developed for Model 6 by Equation 4-41, respectively, for 0%, 20%, 40%, 60%, 80%, and 100% relative densities. The red curve presents the liquefaction state curve evaluated by Equation 4-33 by using the average λ_{ls} and Γ values of the case histories. It should be noted that the stress differences between the initial and liquefaction states, i.e., between the green dots and red squares, give the generated excess pore pressures during the liquefaction.

A summary of the evaluated parameters for Model 6 is tabulated in Table 4.18Table 4.12 for each sub-section of the case histories.

Table 4.18 Summary of the evaluated parameters for Model 6

#	Case History	Section	Γ	p'_r (MPa)	λ_{ls}	p'_{ls} (MPa)	e_{ICC}
1	Wachusett Dam - North Dike	WND-1	0.146	-4.873	0.153	0.015	0.788
		WND-2	0.146	-4.845	0.153	0.017	0.767
		WND-105	0.146	-4.839	0.153	0.021	0.738
		WND-3	0.146	-4.904	0.153	0.027	0.701
2	Fort Peck Dam	Boring 3	0.139	-5.038	0.141	0.046	0.571
		Boring 7	0.139	-5.038	0.141	0.056	0.545
		Boring 6	0.139	-5.038	0.141	0.050	0.560
		Boring 7	0.139	-5.038	0.141	0.020	0.692
3	Uetsu Railway Embankment	S1	0.149	-4.777	0.160	0.013	0.848
		S2	0.149	-4.794	0.160	0.012	0.854
4	Lower San Fernando Dam - U/S Slope	S103&S111	0.085	-5.544	0.103	0.022	0.479
		S101&S102&S104	0.085	-5.544	0.103	0.024	0.468
		S105	0.085	-5.544	0.103	0.026	0.462
		S105	0.085	-5.544	0.103	0.023	0.472
5	Hachiro-Gata Road Embankment	S1	0.155	-4.784	0.162	0.012	0.871
		S2	0.155	-4.784	0.162	0.013	0.857
6	La Marquesa Dam - U/S Slope	B-2	0.158	-4.761	0.166	0.014	0.868
		B-III	0.158	-4.756	0.166	0.013	0.881
		B-3	0.158	-4.757	0.166	0.012	0.896
7	La Marquesa Dam - D/S Slope	B-II	0.157	-4.808	0.164	0.015	0.843
		B-1	0.157	-4.816	0.164	0.019	0.810
8	La Palma Dam	B-3	0.154	-4.801	0.161	0.015	0.835
		B-4	0.154	-4.796	0.161	0.012	0.862
9	Lake Ackerman Highway Embankment	S1	0.144	-4.861	0.151	0.014	0.790
		S2	0.144	-4.861	0.151	0.013	0.797
		S3	0.144	-4.860	0.151	0.012	0.817
10	Chonan Middle School	No.4	0.155	-4.786	0.162	0.012	0.874
		No.3	0.155	-4.777	0.162	0.013	0.854
11	Soviet Tajik - May 1 Slide	S1	0.155	-4.808	0.187	0.030	0.809
		S2	0.155	-4.808	0.187	0.033	0.794
12	Shibecha-Cho Embankment	B-2	0.123	-5.022	0.142	0.018	0.696
		B-3	0.123	-5.010	0.142	0.018	0.693
		B-5	0.123	-5.024	0.142	0.018	0.695
		B-4	0.123	-5.010	0.142	0.018	0.694
		B-5	0.123	-5.024	0.142	0.018	0.695

Table 4.18 (cont'd) Summary of the evaluated parameters for Model 6

13	Route 272 at Higashiarekinai	Left	0.155	-4.808	0.162	0.015	0.833
		Right	0.155	-4.803	0.162	0.015	0.835
14	Zeeland - Vlietepolder	Small-S1	0.150	-4.967	0.155	0.026	0.716
		Small-S2	0.150	-4.967	0.155	0.029	0.698
		Large-S1	0.150	-4.967	0.155	0.025	0.719
		Large-S2	0.150	-4.967	0.155	0.034	0.674
		Large-S3	0.150	-4.967	0.155	0.031	0.687
15	Sheffield Dam	Right	0.162	-4.756	0.170	0.015	0.878
16	Helsinki Harbor	Small-S1	0.154	-4.792	0.152	0.009	0.870
		Small-S2	0.154	-4.808	0.152	0.010	0.852
		Large-S1	0.154	-4.806	0.152	0.011	0.843
		Large-S2	0.154	-4.802	0.152	0.011	0.845
17	Solfatara Canal Dike	S1	0.148	-4.849	0.153	0.012	0.820
		S2	0.148	-4.834	0.153	0.012	0.825
18	Lake Merced Bank	Boring 2	0.154	-4.863	0.164	0.020	0.797
19	El Cobre Tailings Dam	S1	0.160	-4.713	0.156	0.009	0.891
		S2	0.160	-4.713	0.156	0.009	0.895
		S3	0.160	-4.713	0.156	0.008	0.907
		S4	0.160	-4.713	0.156	0.008	0.921
20	Metoki Road Embankment	S-19	0.157	-4.753	0.165	0.012	0.882
		S-13	0.157	-4.764	0.165	0.012	0.891
21	Hokkaido Tailings Dam	Small-S1	0.149	-4.769	0.151	0.008	0.871
		Small-S2	0.149	-4.769	0.151	0.009	0.863
		Large-S1	0.149	-4.769	0.151	0.008	0.871
		Large-S2	0.149	-4.769	0.151	0.008	0.876
22	Upper San Fernando Dam - D/S Slope	A1&B1&C1	0.096	-5.333	0.108	0.014	0.557
		A2&B2&C2	0.096	-5.334	0.108	0.016	0.544
		A3	0.096	-5.334	0.108	0.018	0.531
		B4&C4	0.096	-5.334	0.108	0.018	0.528
		B5&C5	0.096	-5.333	0.108	0.016	0.544
23	Tar Island Dyke	Large-S1	0.137	-5.006	0.141	0.020	0.687
		Large-S2	0.137	-5.006	0.141	0.031	0.625
		Small-S1	0.137	-5.006	0.141	0.020	0.689
		Small-S2	0.137	-5.006	0.141	0.031	0.625
24	Mochi-Koshi Tailings Dam 1	S1	0.107	-5.164	0.121	0.013	0.630
		S2	0.107	-5.164	0.121	0.014	0.617

Table 4.18 (cont'd) Summary of the evaluated parameters for Model 6

		S3	0.107	-5.164	0.121	0.016	0.606
25	Mochi-Koshi Tailings Dam 2	S1	0.105	-5.163	0.119	0.014	0.612
		S2	0.105	-5.163	0.119	0.013	0.626
26	Nerlerk Embankment Slide 1	S1	0.142	-4.985	0.143	0.018	0.718
		S2	0.142	-4.985	0.143	0.019	0.708
		S3	0.142	-4.985	0.143	0.017	0.722
27	Nerlerk Embankment Slide 2	S1	0.142	-4.985	0.143	0.018	0.717
		S2	0.142	-4.985	0.143	0.020	0.700
		S3	0.142	-4.985	0.143	0.016	0.731
28	Nerlerk Embankment Slide 3	S1	0.142	-4.985	0.143	0.021	0.693
		S2	0.142	-4.985	0.143	0.019	0.709
		S3	0.142	-4.985	0.143	0.016	0.731
29	Asele Road Embankment	S1	0.145	-4.891	0.157	0.018	0.777
		S2	0.145	-4.890	0.157	0.017	0.782
30	Nalband Railway Embankment	NB-1	0.085	-5.471	0.105	0.016	0.519
		Small-S2	0.085	-5.471	0.105	0.017	0.514
		NB-1	0.085	-5.471	0.105	0.016	0.519
		Large-S2	0.085	-5.471	0.105	0.017	0.512
		Large-S3	0.085	-5.471	0.105	0.015	0.524
31	Sullivan Tailings	Large-S1	0.151	-4.873	0.148	0.014	0.788
		CP91-29	0.151	-4.873	0.148	0.018	0.748
		CP91-31	0.151	-4.873	0.148	0.016	0.768
		Small-S1	0.151	-4.873	0.148	0.016	0.761
		CP91-31	0.151	-4.873	0.148	0.017	0.757
32	Jamuna Bridge	S1	0.150	-4.863	0.153	0.016	0.785
		S2	0.150	-4.863	0.153	0.014	0.799

In the end, the post-liquefaction shear strength values are predicted by Model 6 as tabulated in Table 4.19 for each sub-section of the case histories.

Table 4.19 Summary of the predicted post-liquefaction shear strength values for Model 6

#	Case History	Section	L_i (m)	L_t (m)	ϕ'_{ls} (deg)	M_{tc}	θ (deg)	M	$\tau_{liq,i}$ (kPa)	$\sum \tau_{liq,i} \cdot L_i / L_t$ (kPa)
1	Wachusett Dam - North Dike	WND-1	19.3	68.9	28.93	1.154	-20.16	0.810	6.06	7.7
		WND-2	20.9		28.93	1.154	-23.99	0.816	7.02	
		WND-105	18.4		28.93	1.154	-25.03	0.818	8.52	
		WND-3	10.2		28.93	1.154	-23.86	0.815	10.82	
2	Fort Peck Dam	Boring 3	200.3	389.3	28.51	1.135	-24.40	0.807	18.72	18.6
		Boring 7	67.9		28.51	1.135	-25.23	0.809	22.58	
		Boring 6	79.4		28.51	1.135	-24.05	0.806	20.29	
		Boring 7	41.7		28.51	1.135	-3.45	0.815	8.04	
3	Uetsu Railway Embankment	S1	9.4	20.3	28.17	1.120	-22.54	0.795	5.03	4.9
		S2	10.9		28.17	1.120	-23.15	0.796	4.84	
4	Lower San Fernando Dam - U/S Slope	S103&S111	54.8	103.8	40.22	1.646	-26.24	1.053	11.47	12.1
		S101&S102&S104	16.9		40.22	1.646	-23.82	1.050	12.81	
		S105	16.8		40.22	1.646	-22.48	1.049	13.55	
		S105	15.3		40.22	1.646	-24.04	1.050	12.28	
5	Hachiro-Gata Road Embankment	S1	10.9	14.9	30.26	1.211	-23.20	0.844	5.16	5.3
		S2	4.0		30.26	1.211	-26.01	0.850	5.67	
6	La Marquesa Dam - U/S Slope	B-2	6.6	21.8	31.93	1.284	-22.31	0.880	6.05	5.6
		B-III	7.2		31.93	1.284	-26.21	0.888	5.67	
		B-3	8.0		31.93	1.284	-25.83	0.887	5.17	
7	La Marquesa Dam - D/S Slope	B-II	10.1	15.8	30.52	1.223	-19.75	0.846	6.47	7.0
		B-1	5.7		30.52	1.223	-26.25	0.857	8.00	
8	La Palma Dam	B-3	6.1	15.9	29.87	1.194	-24.28	0.838	6.17	5.5
		B-4	9.8		29.87	1.194	-18.45	0.830	5.14	
9	Lake Ackerman Highway Embankment	S1	5.9	29.6	28.17	1.120	-24.32	0.799	5.51	5.8
		S2	12.5		28.17	1.120	27.11	1.067	7.04	
		S3	11.2		28.17	1.120	-24.27	0.799	4.61	
10	Chonan Middle School	No.4	6.7	15.4	30.26	1.211	-22.12	0.842	4.94	5.3
		No.3	8.7		30.26	1.211	-23.51	0.845	5.58	
11	Soviet Tajik - May 1 Slide	S1	44.9	68.8	40.22	1.646	-19.75	1.048	15.78	16.2
		S2	24.0		40.22	1.646	-16.90	1.050	17.07	
12	Shibecha-Cho Embankment	B-2	8.3	47.3	35.58	1.444	-25.53	0.962	8.44	8.5
		B-3	25.9		35.58	1.444	-26.59	0.965	8.62	
		B-5	13.1		35.58	1.444	-19.06	0.955	8.40	

Table 4.19 (cont'd) Summary of the predicted post-liquefaction shear strength values for Model 6

		B-4	10.9	24.0	35.58	1.444	-23.50	0.959	8.51	8.4
		B-5	13.1		35.58	1.444	-19.06	0.955	8.40	
13	Route 272 at Higashiarekinai	Left	6.7	22.9	30.52	1.223	-25.82	0.856	6.50	6.4
		Right	16.2		30.52	1.223	-21.61	0.848	6.37	
14	Zeeland - Vlietepolder	Small-S1	31.3	75.7	28.87	1.151	-25.02	0.817	10.59	11.4
		Small-S2	44.4		28.87	1.151	-25.38	0.818	11.90	
		Large-S1	100.2	318.6	28.87	1.151	-28.70	0.827	10.49	12.6
		Large-S2	107.4		28.87	1.151	-29.98	0.832	14.18	
		Large-S3	111.0		28.87	1.151	-28.30	0.826	12.96	
15	Sheffield Dam	Right	14.9	14.9	33.47	1.352	-23.36	0.915	6.74	6.7
16	Helsinki Harbor	Small-S1	6.7	16.0	28.05	1.115	-26.65	0.802	3.60	3.9
		Small-S2	9.2		28.05	1.115	-25.29	0.798	4.05	
		Large-S1	35.5	71.3	28.05	1.115	-28.98	0.809	4.33	4.3
		Large-S2	35.8		28.05	1.115	-29.10	0.810	4.29	
17	Solfatara Canal Dike	S1	4.6	9.4	28.87	1.151	-29.86	0.831	5.10	4.9
		S2	4.8		28.87	1.151	-21.71	0.810	4.80	
18	Lake Merced Bank	Boring 2	30.3	30.3	28.40	1.130	-21.91	0.800	7.86	7.9
19	El Cobre Tailings Dam	S1	83.7	348.1	35.17	1.426	-20.17	0.947	4.40	4.0
		S2	43.8		35.17	1.426	-27.09	0.958	4.34	
		S3	85.8		35.17	1.426	-28.94	0.963	4.04	
		S4	134.8		35.17	1.426	-29.71	0.965	3.72	
20	Metoki Road Embankment	S-19	6.8	14.0	29.87	1.194	-22.39	0.834	5.14	5.0
		S-13	7.2		29.87	1.194	-21.85	0.833	4.85	
21	Hokkaido Tailings Dam	Small-S1	18.3	23.2	35.17	1.426	-29.20	0.964	4.03	4.1
		Small-S2	5.0		35.17	1.426	-22.74	0.949	4.19	
		Large-S1	18.3	48.6	35.17	1.426	-29.20	0.964	4.03	3.9
		Large-S2	30.4		35.17	1.426	-27.21	0.958	3.86	
22	Upper San Fernando Dam - D/S Slope	A1&B1&C1	14.3	111.1	39.78	1.627	-16.83	1.041	7.30	8.8
		A2&B2&C2	10.0		39.78	1.627	-18.92	1.040	8.25	
		A3	23.2		39.78	1.627	-29.14	1.052	9.37	
		B4&C4	33.4		39.78	1.627	-26.36	1.045	9.58	
		B5&C5	30.2		39.78	1.627	-24.32	1.042	8.24	
23	Tar Island Dyke	Large-S1	260.2	308.6	31.50	1.265	-29.41	0.888	9.01	9.7
		Large-S2	48.4		31.50	1.265	-22.71	0.871	13.71	

Table 4.19 (cont'd) Summary of the predicted post-liquefaction shear strength values for Model 6

		Small-S1	27.6	76.0	31.50	1.265	-20.91	0.869	8.69	11.9
		Small-S2	48.4		31.50	1.265	-22.71	0.871	13.71	
24	Mochi-Koshi Tailings Dam 1	S1	61.2	183.7	40.22	1.646	-25.71	1.052	6.86	7.6
		S2	61.0		40.22	1.646	-24.13	1.050	7.61	
		S3	61.6		40.22	1.646	-21.33	1.048	8.34	
25	Mochi-Koshi Tailings Dam 2	S1	34.8	70.9	40.22	1.646	-23.32	1.049	7.55	7.1
		S2	36.1		40.22	1.646	-19.35	1.048	6.72	
26	Nerlerk Embankment Slide 1	S1	23.5	166.7	28.93	1.154	-26.51	0.822	7.26	7.4
		S2	71.7		28.93	1.154	-27.33	0.824	7.83	
		S3	71.4		28.93	1.154	-27.98	0.826	7.09	
27	Nerlerk Embankment Slide 2	S1	18.9	155.5	28.93	1.154	-26.72	0.822	7.35	7.4
		S2	68.5		28.93	1.154	-28.11	0.827	8.27	
		S3	68.1		28.93	1.154	-16.52	0.807	6.51	
28	Nerlerk Embankment Slide 3	S1	80.5	361.9	28.93	1.154	-28.69	0.829	8.72	7.6
		S2	140.5		28.93	1.154	-28.52	0.828	7.81	
		S3	140.9		28.93	1.154	-29.72	0.832	6.73	
29	Asele Road Embankment	S1	20.1	26.5	31.93	1.284	-19.47	0.877	7.76	7.7
		S2	6.4		31.93	1.284	-22.90	0.881	7.57	
30	Nalband Railway Embankment	NB-1	25.3	32.5	36.69	1.492	-28.58	0.992	8.01	8.1
		Small-S2	7.2		36.69	1.492	-24.82	0.983	8.34	
		NB-1	25.3	57.2	36.69	1.492	-28.58	0.992	8.01	8.2
		Large-S2	25.8		36.69	1.492	-28.25	0.991	8.55	
		Large-S3	6.1		36.69	1.492	-21.44	0.979	7.53	
31	Sullivan Tailings	Large-S1	13.8	38.6	35.17	1.426	-10.45	0.956	6.54	7.4
		CP91-29	10.7		35.17	1.426	-20.69	0.947	8.51	
		CP91-31	14.2		35.17	1.426	-25.19	0.953	7.48	
		Small-S1	6.5	23.5	35.17	1.426	-23.15	0.950	7.83	8.0
		CP91-31	17.1		35.17	1.426	-25.32	0.954	8.06	
32	Jamuna Bridge	S1	44.9	88.3	28.75	1.146	-26.99	0.819	6.39	6.1
		S2	43.4		28.75	1.146	-14.97	0.803	5.72	

4.4.7 Model 7

The seventh and final residual strength prediction model utilizes a semi-logarithmic void ratio versus mean effective stress domain (e vs. ln(p')) for both the liquefaction and isotropic compression responses. In other words, both isotropic compression and liquefaction state curves are defined as log-linear over the void ratio versus mean effective stress domain.

The basic mathematical relationship given in Equation 4-48 is implemented for the isotropic compression lines.

$$ICL: \quad e = e_0 \ - \lambda \cdot \ln\left(\frac{p'}{p'_0}\right) \qquad \text{Equation 4-48}$$

In this equation, while p' represents the in-situ mean effective stress measured at the field, e represents the corresponding void ratio at this mean effective stress value. Similar to the previous models, while λ is defined as the slope of the isotropic compression curves, e_0 is defined as the void ratio at a known mean stress p'_0 on the ICCs. In our case, these values are regarded as the initial state of the soil. In other words, p'_0 is taken as 1 kPa = 0.001 MPa referring to the confining stress acting on samples during limit void ratio determination experiments, and e_0 is taken as the corresponding initial void ratio at this confining stress evaluated by Equation 3-68.

The slope of the isotropic compression curves, λ, is again defined as a function of void ratio range and relative density of the soil by the same relationship employed for Model 1, Model 2, Model 3 and Model 4 given in Equation 4-13.

In the end, the void ratios (e) evaluated by Equation 4-48 are defined as the actual in-situ void ratios (e_{ICC}), and they are directly located in void ratio versus mean effective stress domain as the initial state points of the corresponding case histories (green dots in Figure 4.18).

For the liquefaction state lines, the simple mathematical relationship provided in Equation 4-49 is implemented.

$$LSL: \quad e = \Gamma - \lambda_{ls} \cdot \ln\left(\frac{p'_{ls}}{p'_{c0}}\right) \qquad \text{Equation 4-49}$$

In this equation, p'_{ls} represents the final mean effective stress after the event at the liquefaction state. In other words, it is the reduced mean effective stress due to the increasing excess pore pressures during the liquefaction. In fact, the difference between p' in Equation 4-48 and p'_{ls} in Equation 4-49 estimates the excess pore pressures developed during the liquefaction. Therefore, other parameters in Equation 4-49 are evaluated first to be able to estimate p'_{ls} in the end.

The void ratio (e) in Equation 4-49Equation 4-33 is already the same as the void ratio evaluated by Equation 4-48, e_{ICC}, because the void ratio remains the same under undrained conditions.

In Equation 4-49, λ_{ls} and Γ are defined as the slope of the liquefaction state lines, and the void ratio on these curves when $p'_{ls} = p'_{c0}$, respectively. The value of the reference stress, p'_{c0}, is again taken as 1 kPa = 0.001 MPa in this study similar to Model 1 and Model 2.

The relationship given in Equation 4-34 is used to evaluate the slope of the liquefaction state lines as a function of the void ratio range. Γ values are also evaluated as a function of the maximum void ratio (e_{max}) as shown in Equation 4-35.

In the end, the final mean effective stress values after the liquefaction are evaluated by solving p'_{ls} in Equation 4-49 for each sub-section of the case histories. The closed-form solution of the relationship is provided in Equation 4-50.

$$p'_{ls} = p'_{c0} \cdot exp\left(\frac{\theta_6 \cdot e_{max} - e_0 + \frac{\theta_3 \cdot exp\left(\theta_4 \cdot (e_{max} - e_{min})\right)}{1 + \theta_5 \cdot RD} \cdot \ln\left(\frac{p'}{p'_0}\right)}{\theta_7 \cdot exp\left(\theta_8 + \theta_9 \cdot (e_{max} - e_{min})\right)}\right) \qquad \text{Equation 4-50}$$

Once the final mean effective stress values after the liquefaction (p'_{ls}) are evaluated by Equation 4-50, the corresponding data points are located in the void ratio versus mean effective stress domain as the liquefaction state points of the corresponding case histories (red squares in Figure 4.18).

Accordingly, the other parameters used in the evaluation of the failure criterion, such as the liquefaction friction angle (ϕ'_{ls}), Lode angle (θ), slope of the stress paths in q vs. p' domain for triaxial compression tests (M_{tc}) and in general (M), are evaluated with the same procedure followed in previous models by using Equation 4-23, Equation 4-24, Equation 4-22 and Equation 4-21, respectively.

Finally, the post-liquefaction shear strength values for each sub-section can be predicted by using the relationship provided in Equation 4-26 as a function M and liquefaction state mean effective stress (p'_{ls}) values. Accordingly, the overall representative post-liquefaction shear strength values of all case histories can be predicted by using Equation 4-27.

Once the residual strength predictions evaluated by Equation 4-27 are compared with the modified back-analyses results of Weber (2015) given in Table 4.1 for the same case histories, the overall best-fit model parameters are developed as given in Table 4.20 for Model 7 as a result of probabilistic regressions by the Maximum Likelihood Method.

Table 4.20 Best-fit model parameters for Model 7

θ_3	0.012
θ_4	0.366
θ_5	0.309
θ_6	1.333
θ_7	0.046
θ_8	0.064
θ_9	3.314
θ_{10}	22.61
θ_{11}	-0.692
θ_{12}	0.684
θ_{13}	-0.178
θ_{14}	5.000

Table 4.20 (cont'd) Best-fit model parameters for Model 7

θ_{15}	45.000
θ_{16}	5.050
θ_{17}	4

Consequently, the equations of isotropic compression lines and liquefaction state lines are obtained as given in Equation 4-51 and Equation 4-52, respectively.

$$ICL: \quad e = e_0 - \frac{0.012 \cdot exp\left(0.366 \cdot (e_{max} - e_{min})\right)}{1 + 0.309 \cdot RD} \cdot \ln\left(\frac{p'}{0.001}\right) \qquad \text{Equation 4-51}$$

$$LSL: \quad e = 1.333 \cdot e_{max} - \left(0.046 \cdot exp\left(0.064 + 3.314 \cdot (e_{max} - e_{min})\right)\right) \cdot \ln\left(\frac{p'_{ls}}{0.001}\right) \qquad \text{Equation 4-52}$$

Using these equations, the case history data points with respect to their initial states and liquefaction states are located in the void ratio versus mean effective stress domain as presented in Figure 4.18.

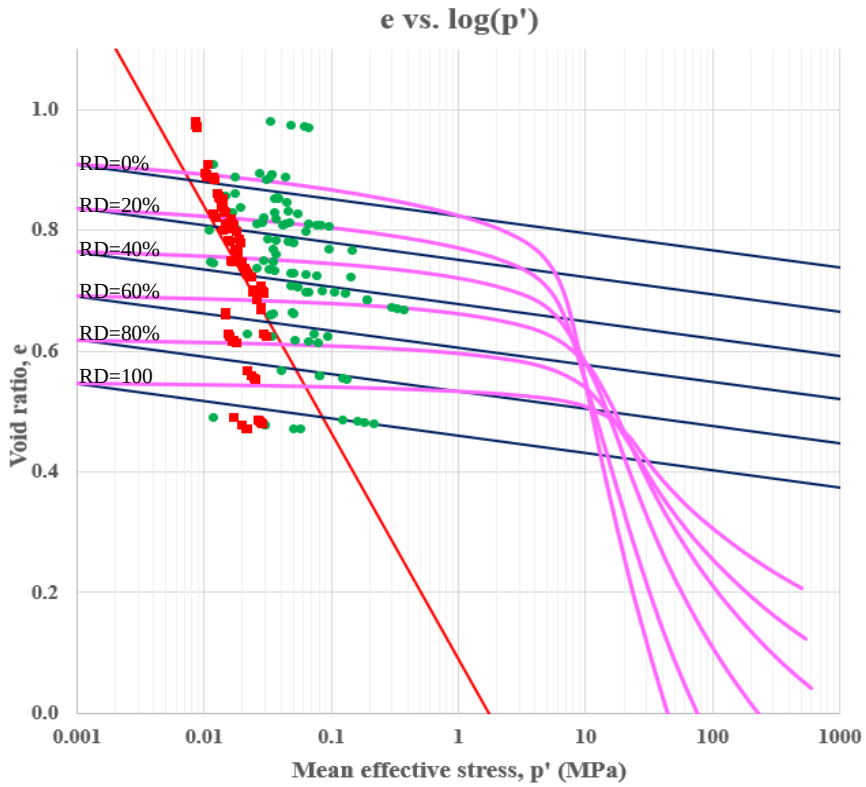

Figure 4.18. Void ratio versus mean effective stress domain for Model 7

In Figure 4.18, while the green dots and red squares represent the initial and liquefaction states of the case history data points, the purple and blue curves represent the isotropic compression curves recommended by Mesri and Vardhanabhuti (2009), and developed for Model 7 by Equation 4-48, respectively, for 0%, 20%, 40%, 60%, 80%, and 100% relative densities. The red curve presents the liquefaction state curve evaluated by Equation 4-49 by using the average λ_{ls} and Γ values of the case histories. It should be noted that the stress differences between the initial and liquefaction states, i.e., between the green dots and red squares, give the generated excess pore pressures during the liquefaction.

A summary of the evaluated parameters for Model 7 is tabulated in Table 4.21Table 4.12 for each sub-section of the case histories.

Table 4.21 Summary of the evaluated parameters for Model 7

#	Case History	Section	Γ	λ	λ_{ls}	p'_{ls} (MPa)	e_{ICC}
1	Wachusett Dam - North Dike	WND-1	1.234	0.012	0.162	0.019	0.760
		WND-2	1.234	0.013	0.162	0.018	0.768
		WND-105	1.234	0.013	0.162	0.018	0.767
		WND-3	1.234	0.012	0.162	0.023	0.722
2	Fort Peck Dam	Boring 3	1.307	0.012	0.191	0.028	0.672
		Boring 7	1.307	0.012	0.191	0.028	0.669
		Boring 6	1.307	0.012	0.191	0.028	0.671
		Boring 7	1.307	0.012	0.191	0.024	0.701
3	Uetsu Railway Embankment	S1	1.264	0.013	0.176	0.012	0.828
		S2	1.264	0.013	0.176	0.012	0.822
4	Lower San Fernando Dam - U/S Slope	S103&S111	0.798	0.012	0.095	0.027	0.487
		S101&S102&S104	0.798	0.012	0.095	0.028	0.482
		S105	0.798	0.012	0.095	0.028	0.480
		S105	0.798	0.012	0.095	0.027	0.484
5	Hachiro-Gata Road Embankment	S1	1.316	0.013	0.181	0.014	0.838
		S2	1.316	0.013	0.181	0.015	0.830
6	La Marquesa Dam - U/S Slope	B-2	1.341	0.013	0.188	0.014	0.846
		B-III	1.341	0.013	0.188	0.013	0.854
		B-3	1.341	0.013	0.188	0.013	0.862

Table 4.21 (cont'd) Summary of the evaluated parameters for Model 7

7	La Marquesa Dam - D/S Slope	B-II	1.329	0.013	0.185	0.016	0.814
		B-1	1.329	0.012	0.185	0.018	0.798
8	La Palma Dam	B-3	1.306	0.013	0.179	0.016	0.813
		B-4	1.306	0.013	0.179	0.014	0.829
9	Lake Ackerman Highway Embankment	S1	1.251	0.013	0.171	0.016	0.782
		S2	1.251	0.013	0.171	0.015	0.784
		S3	1.251	0.013	0.171	0.014	0.801
10	Chonan Middle School	No.4	1.309	0.013	0.180	0.014	0.840
		No.3	1.309	0.013	0.180	0.014	0.832
11	Soviet Tajik - May 1 Slide	S1	0.991	0.012	0.107	0.030	0.628
		S2	0.991	0.012	0.107	0.030	0.625
12	Shibecha-Cho Embankment	B-2	1.042	0.013	0.141	0.015	0.661
		B-3	1.042	0.013	0.141	0.015	0.663
		B-5	1.042	0.013	0.141	0.015	0.661
		B-4	1.042	0.013	0.141	0.015	0.663
		B-5	1.042	0.013	0.141	0.015	0.661
13	Route 272 at Higashiarekinai	Left	1.312	0.013	0.180	0.016	0.809
		Right	1.312	0.013	0.180	0.016	0.812
14	Zeeland - Vlietepolder	Small-S1	1.305	0.012	0.180	0.028	0.706
		Small-S2	1.305	0.012	0.180	0.029	0.701
		Large-S1	1.305	0.012	0.180	0.028	0.707
		Large-S2	1.305	0.012	0.180	0.029	0.696
		Large-S3	1.305	0.012	0.180	0.029	0.698
15	Sheffield Dam	Right	1.373	0.013	0.197	0.014	0.853
16	Helsinki Harbor	Small-S1	1.449	0.013	0.227	0.011	0.910
		Small-S2	1.449	0.013	0.227	0.012	0.888
		Large-S1	1.449	0.013	0.227	0.012	0.884
		Large-S2	1.449	0.013	0.227	0.012	0.887
17	Solfatara Canal Dike	S1	1.281	0.013	0.175	0.015	0.803
		S2	1.281	0.013	0.175	0.015	0.810
18	Lake Merced Bank	Boring 2	1.306	0.012	0.184	0.018	0.770
19	El Cobre Tailings Dam	S1	1.498	0.013	0.243	0.009	0.971
		S2	1.498	0.013	0.243	0.009	0.972
		S3	1.498	0.013	0.243	0.009	0.975
		S4	1.498	0.013	0.243	0.008	0.980

Table 4.21 (cont'd) Summary of the evaluated parameters for Model 7

20	Metoki Road Embankment	S-19	1.334	0.013	0.186	0.013	0.856
		S-13	1.334	0.013	0.186	0.013	0.858
21	Hokkaido Tailings Dam	Small-S1	1.345	0.013	0.194	0.010	0.892
		Small-S2	1.345	0.013	0.194	0.010	0.889
		Large-S1	1.345	0.013	0.194	0.010	0.892
		Large-S2	1.345	0.013	0.194	0.010	0.895
22	Upper San Fernando Dam - D/S Slope	A1&B1&C1	0.897	0.012	0.107	0.022	0.568
		A2&B2&C2	0.897	0.012	0.107	0.024	0.560
		A3	0.897	0.012	0.107	0.025	0.555
		B4&C4	0.897	0.012	0.107	0.025	0.554
		B5&C5	0.897	0.012	0.107	0.024	0.560
23	Tar Island Dyke	Large-S1	1.235	0.012	0.169	0.024	0.697
		Large-S2	1.235	0.012	0.169	0.026	0.684
		Small-S1	1.235	0.012	0.169	0.024	0.698
		Small-S2	1.235	0.012	0.169	0.026	0.684
24	Mochi-Koshi Tailings Dam 1	S1	0.963	0.013	0.122	0.016	0.629
		S2	0.963	0.013	0.122	0.017	0.618
		S3	0.963	0.013	0.122	0.018	0.613
25	Mochi-Koshi Tailings Dam 2	S1	0.952	0.013	0.119	0.017	0.616
		S2	0.952	0.013	0.119	0.016	0.625
26	Nerlerk Embankment Slide 1	S1	1.335	0.012	0.197	0.021	0.735
		S2	1.335	0.012	0.197	0.022	0.730
		S3	1.335	0.012	0.197	0.021	0.738
27	Nerlerk Embankment Slide 2	S1	1.335	0.012	0.197	0.021	0.734
		S2	1.335	0.012	0.197	0.022	0.727
		S3	1.335	0.012	0.197	0.020	0.748
28	Nerlerk Embankment Slide 3	S1	1.335	0.012	0.197	0.022	0.725
		S2	1.335	0.012	0.197	0.022	0.730
		S3	1.335	0.012	0.197	0.020	0.747
29	Asele Road Embankment	S1	1.226	0.012	0.170	0.017	0.748
		S2	1.226	0.012	0.170	0.016	0.751
30	Nalband Railway Embankment	NB-1	0.721	0.012	0.081	0.020	0.478
		Small-S2	0.721	0.012	0.081	0.021	0.472
		NB-1	0.721	0.012	0.081	0.020	0.478
		Large-S2	0.721	0.012	0.081	0.022	0.471
		Large-S3	0.721	0.012	0.081	0.017	0.490

Table 4.21 (cont'd) Summary of the evaluated parameters for Model 7

31	Sullivan Tailings	Large-S1	1.420	0.012	0.216	0.016	0.819
		CP91-29	1.420	0.012	0.216	0.017	0.807
		CP91-31	1.420	0.012	0.216	0.017	0.812
		Small-S1	1.420	0.012	0.216	0.017	0.810
		CP91-31	1.420	0.012	0.216	0.017	0.809
32	Jamuna Bridge	S1	1.300	0.012	0.175	0.020	0.779
		S2	1.300	0.012	0.175	0.019	0.785

In the end, the post-liquefaction shear strength values are predicted by Model 7 as tabulated in Table 4.22 for each sub-section of the case histories.

Table 4.22 Summary of the predicted post-liquefaction shear strength values for Model 7

#	Case History	Section	L_i (m)	L_t (m)	ϕ'_{ls} (deg)	M_{tc}	θ (deg)	M	$\tau_{liq,i}$ (kPa)	$\sum \tau_{liq,i} \cdot L_i / L_t$ (kPa)
1	Wachusett Dam - North Dike	WND-1	19.3	68.9	26.56	1.051	-20.16	0.754	6.97	7.1
		WND-2	20.9		26.56	1.051	-23.99	0.760	6.70	
		WND-105	18.4		26.56	1.051	-25.03	0.763	6.78	
		WND-3	10.2		26.56	1.051	-23.86	0.760	8.89	
2	Fort Peck Dam	Boring 3	200.3	389.3	26.02	1.028	-24.40	0.748	10.42	10.3
		Boring 7	67.9		26.02	1.028	-25.23	0.751	10.60	
		Boring 6	79.4		26.02	1.028	-24.05	0.748	10.48	
		Boring 7	41.7		26.02	1.028	-3.45	0.750	8.96	
3	Uetsu Railway Embankment	S1	9.4	20.3	25.58	1.009	-22.54	0.734	4.37	4.5
		S2	10.9		25.58	1.009	-23.15	0.735	4.52	
4	Lower San Fernando Dam - U/S Slope	S103&S111	54.8	103.8	40.43	1.655	-26.24	1.057	14.03	14.3
		S101&S102&S104	16.9		40.43	1.655	-23.82	1.054	14.68	
		S105	16.8		40.43	1.655	-22.48	1.053	14.97	
		S105	15.3		40.43	1.655	-24.04	1.054	14.44	
5	Hachiro-Gata Road Embankment	S1	10.9	14.9	28.30	1.126	-23.20	0.800	5.57	5.6
		S2	4.0		28.30	1.126	-26.01	0.806	5.87	
6	La Marquesa Dam - U/S Slope	B-2	6.6	21.8	30.60	1.226	-22.31	0.850	5.93	5.7
		B-III	7.2		30.60	1.226	-26.21	0.858	5.75	
		B-3	8.0		30.60	1.226	-25.83	0.857	5.49	

Table 4.22 (cont'd) Summary of the predicted post-liquefaction shear strength values for Model 7

7	La Marquesa Dam - D/S Slope	B-II	10.1	15.8	28.66	1.142	-19.75	0.803	6.53	6.8
		B-1	5.7		28.66	1.142	-26.25	0.815	7.22	
8	La Palma Dam	B-3	6.1	15.9	27.78	1.104	-24.28	0.790	6.21	5.8
		B-4	9.8		27.78	1.104	-18.45	0.781	5.60	
9	Lake Ackerman Highway Embankment	S1	5.9	29.6	25.58	1.009	-24.32	0.738	5.78	6.2
		S2	12.5		25.58	1.009	27.11	0.963	7.41	
		S3	11.2		25.58	1.009	-24.27	0.738	5.15	
10	Chonan Middle School	No.4	6.7	15.4	28.30	1.126	-22.12	0.798	5.42	5.6
		No.3	8.7		28.30	1.126	-23.51	0.800	5.69	
11	Soviet Tajik - May 1 Slide	S1	44.9	68.8	40.43	1.655	-19.75	1.052	15.58	15.7
		S2	24.0		40.43	1.655	-16.90	1.054	16.04	
12	Shibecha-Cho Embankment	B-2	8.3	47.3	33.71	1.362	-25.53	0.924	6.82	6.8
		B-3	25.9		33.71	1.362	-26.59	0.926	6.77	
		B-5	13.1		33.71	1.362	-19.06	0.916	6.79	
		B-4	10.9	24.0	33.71	1.362	-23.50	0.920	6.70	6.7
		B-5	13.1		33.71	1.362	-19.06	0.916	6.79	
13	Route 272 at Higashiarekinai	Left	6.7	22.9	28.66	1.142	-25.82	0.814	6.62	6.5
		Right	16.2		28.66	1.142	-21.61	0.805	6.44	
14	Zeeland - Vlietepolder	Small-S1	31.3	75.7	26.48	1.047	-25.02	0.761	10.59	10.8
		Small-S2	44.4		26.48	1.047	-25.38	0.762	10.92	
		Large-S1	100.2	318.6	26.48	1.047	-28.70	0.772	10.66	11.1
		Large-S2	107.4		26.48	1.047	-29.98	0.776	11.44	
		Large-S3	111.0		26.48	1.047	-28.30	0.770	11.20	
15	Sheffield Dam	Right	14.9	14.9	32.81	1.323	-23.36	0.901	6.34	6.3
16	Helsinki Harbor	Small-S1	6.7	16.0	25.44	1.003	-26.65	0.740	3.98	4.2
		Small-S2	9.2		25.44	1.003	-25.29	0.737	4.36	
		Large-S1	35.5	71.3	25.44	1.003	-28.98	0.748	4.51	4.5
		Large-S2	35.8		25.44	1.003	-29.10	0.748	4.46	
17	Solfatara Canal Dike	S1	4.6	9.4	26.48	1.047	-29.86	0.776	5.95	5.7
		S2	4.8		26.48	1.047	-21.71	0.754	5.55	
18	Lake Merced Bank	Boring 2	30.3	30.3	25.88	1.021	-21.91	0.740	6.84	6.8
19	El Cobre Tailings Dam	S1	83.7	348.1	35.38	1.435	-20.17	0.951	4.18	4.2
		S2	43.8		35.38	1.435	-27.09	0.962	4.21	
		S3	85.8		35.38	1.435	-28.94	0.967	4.17	
		S4	134.8		35.38	1.435	-29.71	0.970	4.10	

Table 4.22 (cont'd) Summary of the predicted post-liquefaction shear strength values for Model 7

20	Metoki Road Embankment	S-19	6.8	14.0	27.78	1.104	-22.39	0.786	5.12	5.1
		S-13	7.2		27.78	1.104	-21.85	0.785	5.06	
21	Hokkaido Tailings Dam	Small-S1	18.3	23.2	35.38	1.435	-29.20	0.968	4.98	5.0
		Small-S2	5.0		35.38	1.435	-22.74	0.954	4.99	
		Large-S1	18.3	48.6	35.38	1.435	-29.20	0.968	4.98	4.9
		Large-S2	30.4		35.38	1.435	-27.21	0.962	4.88	
22	Upper San Fernando Dam - D/S Slope	A1&B1&C1	14.3	111.1	39.75	1.625	-16.83	1.041	11.37	12.6
		A2&B2&C2	10.0		39.75	1.625	-18.92	1.039	12.34	
		A3	23.2		39.75	1.625	-29.14	1.052	13.08	
		B4&C4	33.4		39.75	1.625	-26.36	1.045	13.12	
		B5&C5	30.2		39.75	1.625	-24.32	1.042	12.31	
23	Tar Island Dyke	Large-S1	260.2	308.6	30.23	1.210	-29.41	0.860	10.37	10.5
		Large-S2	48.4		30.23	1.210	-22.71	0.843	10.96	
		Small-S1	27.6	76.0	30.23	1.210	-20.91	0.840	10.09	10.6
		Small-S2	48.4		30.23	1.210	-22.71	0.843	10.96	
24	Mochi-Koshi Tailings Dam 1	S1	61.2	183.7	40.43	1.655	-25.71	1.056	8.22	8.8
		S2	61.0		40.43	1.655	-24.13	1.054	8.95	
		S3	61.6		40.43	1.655	-21.33	1.052	9.32	
25	Mochi-Koshi Tailings Dam 2	S1	34.8	70.9	40.43	1.655	-23.32	1.053	8.83	8.5
		S2	36.1		40.43	1.655	-19.35	1.052	8.23	
26	Nerlerk Embankment Slide 1	S1	23.5	166.7	26.56	1.051	-26.51	0.767	8.05	8.1
		S2	71.7		26.56	1.051	-27.33	0.769	8.29	
		S3	71.4		26.56	1.051	-27.98	0.771	7.98	
27	Nerlerk Embankment Slide 2	S1	18.9	155.5	26.56	1.051	-26.72	0.767	8.10	7.9
		S2	68.5		26.56	1.051	-28.11	0.772	8.44	
		S3	68.1		26.56	1.051	-16.52	0.750	7.38	
28	Nerlerk Embankment Slide 3	S1	80.5	361.9	26.56	1.051	-28.69	0.774	8.56	8.1
		S2	140.5		26.56	1.051	-28.52	0.773	8.32	
		S3	140.9		26.56	1.051	-29.72	0.777	7.68	
29	Asele Road Embankment	S1	20.1	26.5	30.60	1.226	-19.47	0.847	7.03	7.0
		S2	6.4		30.60	1.226	-22.90	0.851	6.95	
30	Nalband Railway Embankment	NB-1	25.3	32.5	35.24	1.429	-28.58	0.963	9.48	9.6
		Small-S2	7.2		35.24	1.429	-24.82	0.954	10.11	
		NB-1	25.3	57.2	35.24	1.429	-28.58	0.963	9.48	9.7
		Large-S2	25.8		35.24	1.429	-28.25	0.962	10.39	

Table 4.22 (cont'd) Summary of the predicted post-liquefaction shear strength values for Model 7

		Large-S3	6.1		35.24	1.429	-21.44	0.949	8.11	
31	Sullivan Tailings	Large-S1	13.8	38.6	35.38	1.435	-10.45	0.960	7.72	7.9
		CP91-29	10.7		35.38	1.435	-20.69	0.952	8.08	
		CP91-31	14.2		35.38	1.435	-25.19	0.958	7.96	
		Small-S1	6.5	23.5	35.38	1.435	-23.15	0.954	8.00	8.0
		CP91-31	17.1		35.38	1.435	-25.32	0.958	8.06	
32	Jamuna Bridge	S1	44.9	88.3	26.33	1.041	-26.99	0.763	7.44	7.2
		S2	43.4		26.33	1.041	-14.97	0.744	7.02	

CHAPTER 5

DISCUSSION OF RESULTS

In this chapter, developed post-liquefaction shear strength prediction models presented in Chapter 4 are compared with each other in order to determine the most accurate and precise model among them from both statistical and engineering points of view. In addition, corresponding models are also compared with the residual strength prediction model of Weber (2015).

5.1 Discussion of Post-liquefaction Shear Strength Prediction Models

As already discussed in previous chapters, a new critical state framework compatible methodology is introduced in this thesis to evaluate the post-liquefaction shear strength of soils on the basis of back-analyses of available case histories. Since practicing engineers are more used to performing effective stress-based stability assessments for cohesionless soils under monotonic loading conditions, corresponding volume stress models are presented in void ratio versus mean effective stress domain, which is claimed to be theoretically more preferable than previous penetration resistance versus undrained residual strength domains.

Due to the fact that there exists a hot debate about the shape of the critical state curve, or liquefaction state curve in our case, whether it is a line or a curve in void ratio versus mean effective strain domain, this study covers both approaches and recommends totally seven residual strength prediction models on this purpose. While a nonlinear liquefaction state curve is defined in void ratio versus mean effective stress domain for the first two prediction models, a log-linear liquefaction state curve is defined for the rest five prediction models.

The Maximum Likelihood Method is used to develop these seven fully probabilistic prediction relationships and corresponding model parameters. As discussed in Chapter 4, due to its well-documented and transparent nature, Weber (2015) is chosen as the reference study for comparison purposes. Therefore, the predicted post-liquefaction shear strength values in this study are compared with the back-analyses results of Weber (2015) for the same case histories during the probabilistic regressions by the Maximum Likelihood Method.

On the other hand, the back-analyses results of Weber (2015) are modified when necessary for the same case histories as discussed in Chapter 4. Accordingly, the modified back-calculated post-liquefaction shear strength values of Weber (2015) are obtained as tabulated in Table 5.1. These modified values are directly used for the probabilistic regressions by the Maximum Likelihood Method, and the residual strength prediction models are developed accordingly.

Table 5.1 Original and modified back-calculated post-liquefaction shear strength values of Weber (2015)

#	Case History	Pre-failure $S_{r,yield}$ values of Weber (2015) (kPa)	Post-failure $S_{r,resid/geom}$ values of Weber (2015) (kPa)	Modified $S_{r,backanalyzed}$ values of Weber (2015) (kPa)	Original $S_{r,backanalyzed}$ values of Weber (2015) (kPa)
1	Wachusett Dam - North Dike	39.69	3.88	10.92	14.08
2	Fort Peck Dam	107.01	8.33	12.60	36.48
3	Uetsu Railway Embankment	17.00	0.53	1.82	1.82
4	Lower San Fernando Dam - U/S Slope	61.33	3.78	25.81	25.81
5	Hachiro-Gata Road Embankment	6.46	1.92	3.39	3.26
6	La Marquesa Dam - U/S Slope	12.11	2.35	4.36	4.93
7	La Marquesa Dam - D/S Slope	15.18	7.66	9.72	10.25
8	La Palma Dam	9.62	4.02	6.51	6.51
9	Lake Ackerman Highway Embankment	9.24	2.68	5.12	5.12
10	Chonan Middle School	9.53	4.88	6.75	6.75
11	Soviet Tajik - May 1 Slide	27.77	7.95	16.33	16.33
12-1 (L)	Shibecha-Cho Embankment	19.87	7.04	10.73	10.73
12-2 (S)		19.87	7.04	10.73	10.73
13	Route 272 at Higashiarekinai	16.33	3.30	6.61	6.61

Table 5.1 (cont'd) Original and modified back-calculated post-liquefaction shear strength values of Weber (2015)

14-1 (S)	Zeeland - Vlietepolder	17.67	5.75	10.53	7.47
14-2 (L)		17.67	5.75	7.05	7.47
15	Sheffield Dam	16.52	4.02	8.22	6.61
16-1 (S)	Helsinki Harbor	4.45	2.15	2.85	2.30
16-2 (L)		4.45	2.15	2.01	2.30
17	Solfatara Canal Dike	7.13	3.35	4.19	3.06
18	Lake Merced Bank	9.10	5.84	5.98	6.51
19	El Cobre Tailings Dam	21.55	2.39	9.58	4.55
20	Metoki Road Embankment	11.30	2.87	5.67	4.40
21-1 (S)	Hokkaido Tailings Dam	12.16	3.35	8.06	4.69
21-2 (L)		12.16	3.35	3.43	4.69
22	Upper San Fernando Dam - D/S Slope	35.62	34.04	27.87	34.76
23-1 (L)	Tar Island Dyke	35.38	21.64	15.09	24.71
23-2 (S)		35.38	21.64	26.10	24.71
24	Mochi-Koshi Tailings Dam 1	22.84	10.77	5.80	10.10
25	Mochi-Koshi Tailings Dam 2	22.84	10.77	6.97	10.10
26	Nerlerk Embankment Slide 1	7.33	2.54	4.63	3.26
27	Nerlerk Embankment Slide 2	7.33	2.54	3.54	3.26
28	Nerlerk Embankment Slide 3	7.33	2.54	2.70	3.26
29	Asele Road Embankment	14.08	6.30	6.21	6.56
30-1 (S)	Nalband Railway Embankment	10.10	6.61	7.41	8.00
30-2 (L)		10.10	6.61	5.94	8.00
31-1 (L)	Sullivan Tailings	30.02	5.94	14.08	13.26
31-2 (S)		30.02	5.94	14.69	13.26
32	Jamuna Bridge	16.76	4.31	8.43	8.38

The residual strength values obtained from the post-liquefaction shear strength prediction relationship developed by Weber (2015) (as given in Equation 5-1) are also compared with the modified back-calculated post-liquefaction shear strength values tabulated in Table 5.1 for consistency purposes.

$$S_{r,predicted}\ (33^{rd} precentile) = \exp\left(0.1407 \cdot (N_1)_{60,cs} + 4.2399 \cdot \sigma'^{0.120}_{v0}\right) - 0.43991 \cdot \left((N_1)^{1.45}_{60,cs} + 0.2 \cdot (N_1)_{60,cs} \cdot \sigma'^{2.48}_{v0} + 41.13\right) \quad \text{Equation 5-1}$$

The predicted residual strength values of Weber (2015) with its own input parameters, and the comparison of the results are presented in Table 5.2 and Figure 5.1, respectively.

Table 5.2 Input parameters and predicted residual strength values of Weber (2015)

#	Case History	σ'_{v0} (atm)	$(N_1)_{60,cs}$	$S_{r,backanalyzed}$ (kPa)	$S_{r,predicted}$ (kPa)
1	Wachusett Dam - North Dike	1.485	7.5	10.92	10.39
2	Fort Peck Dam	3.430	12.5	12.60	35.11
3	Uetsu Railway Embankment	0.684	3	1.82	3.22
4	Lower San Fernando Dam - U/S Slope	1.500	13.5	25.81	25.49
5	Hachiro-Gata Road Embankment	0.318	7	3.39	3.94
6	La Marquesa Dam - U/S Slope	0.464	6.5	4.36	4.52
7	La Marquesa Dam - D/S Slope	0.574	10.5	9.72	9.56
8	La Palma Dam	0.362	5	6.51	3.04
9	Lake Ackerman Highway Embankment	0.430	3.5	5.12	2.61
10	Chonan Middle School	0.488	6.5	6.75	4.65
11	Soviet Tajik - May 1 Slide	0.901	10.5	16.33	12.27
12-1	Shibecha-Cho Embankment	0.669	7.5	10.73	6.55
12-2		0.669	7.5	10.73	6.55
13	Route 272 at Higashiarekinai	0.607	8	6.61	6.70
14-1	Zeeland - Vlietepolder	1.176	8	10.53	9.78
14-2		1.176	8	7.05	9.78
15	Sheffield Dam	0.618	7	8.22	5.78
16-1	Helsinki Harbor	0.400	6	2.85	3.82
16-2		0.400	6	2.01	3.82
17	Solfatara Canal Dike	0.316	4.5	4.19	2.57
18	Lake Merced Bank	0.394	8.5	5.98	5.68
19	El Cobre Tailings Dam	0.981	2	9.58	3.43
20	Metoki Road Embankment	0.412	2.5	5.67	2.13

Table 5.2 (cont'd) Input parameters and predicted residual strength values of Weber (2015)

21-1	Hokkaido Tailings Dam	0.568	4	8.06	3.39
21-2		0.568	4	3.43	3.39
22	Upper San Fernando Dam - D/S Slope	1.483	15	27.87	31.57
23-1	Tar Island Dyke	1.983	11	15.09	20.66
23-2		1.983	11	26.10	20.66
24	Mochi-Koshi Tailings Dam 1	0.724	6	5.80	5.42
25	Mochi-Koshi Tailings Dam 2	0.724	6	6.97	5.42
26	Nerlerk Embankment Slide 1	0.553	7.5	4.63	5.87
27	Nerlerk Embankment Slide 2	0.553	7.5	3.54	5.87
28	Nerlerk Embankment Slide 3	0.553	7.5	2.70	5.87
29	Asele Road Embankment	0.490	9.5	6.21	7.51
30-1	Nalband Railway Embankment	0.571	7.5	7.41	5.98
30-2		0.571	7.5	5.94	5.98
31-1	Sullivan Tailings	1.144	9.5	14.08	12.08
31-2		1.144	9.5	14.69	12.08
32	Jamuna Bridge	0.663	10.5	8.43	10.36

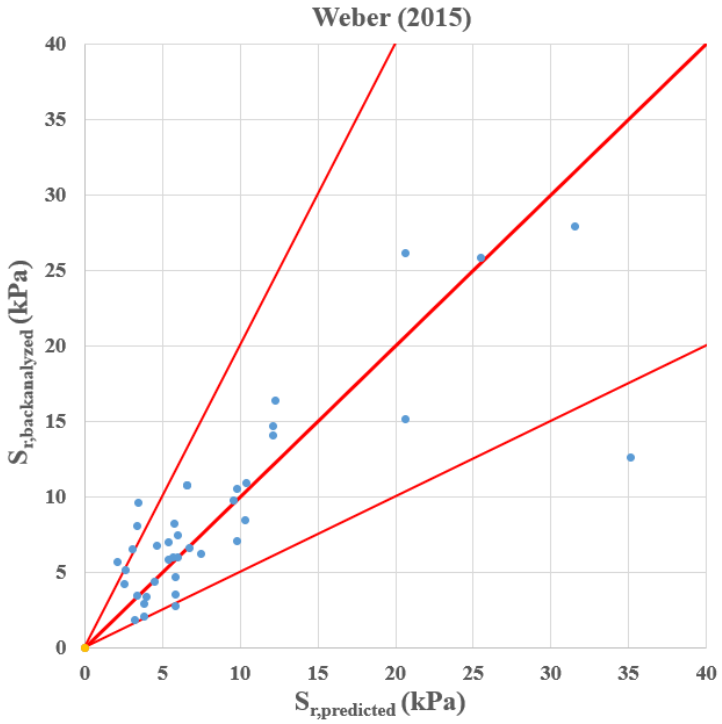

Figure 5.1. Comparison of the residual strength results of Weber (2015)

In Figure 5.1, while each blue dot represents the data point of a case history, the red lines represent 1 vs 1, 1 vs 2, and 2 vs 1 lines for the ease of comparison of the accuracy and precision of the predicted and back-calculated residual strength values.

During the probabilistic regressions by the Maximum Likelihood Method, the corresponding probabilities are evaluated for a model with mean error zero and a standard deviation of model error, σ_ε. The model error term is assumed to be normally distributed for convenience. The details of maximum likelihood assessments are discussed in Cetin (2000), Cetin et al. (2004), and Cetin et al. (2018), and will not be repeated herein.

Accordingly, the model parameters (θ_1, θ_2, θ_3, θ_4, etc.) which maximize the likelihood function (i.e., multiplication of individual probabilities of making the observation of the residual shear strengths by back-analyzed case histories) are then evaluated for each of the seven post-liquefaction shear strength prediction models.

Note that the model with the largest sum of ln(Probability) is concluded to be the most accurate model. Similarly, the one with the least model error standard deviation is concluded to be the most precise model.

To be able to measure the quality of models subjectively and investigate the effect of input parameters on the predicted post-liquefaction shear strength results, the residual plots for each of the seven prediction models are also prepared and documented in this chapter for SPT resistance ($(N_1)_{60}$), mean grain size (D_{50}), fines content (FC) and coefficient of uniformity (C_u) values of the case history database. These plots are prepared such that the values of the input parameters for each case history are plotted against the error between the modified back-analysis residual strength values of Weber (2015) provided in Table 5.1 and the predicted residual strength values by the corresponding model of this study.

The discussion of each residual strength prediction model in terms of statistics and engineering, and their comparisons with Weber (2015) are explained below.

5.1.1 Discussion of Model 1

The first residual strength prediction model utilizes a double logarithmic void ratio versus mean effective stress domain (ln(e) vs. ln(p')) for both the liquefaction and isotropic compression responses. In other words, the liquefaction and isotropic state curves become asymptomatic to a horizontal line at higher stresses, and negative void ratio values at these higher stress ranges are avoided as a result of this asymptote and the log-nature of the relationships.

The best-fit model parameters are developed as given in Table 4.2 for Model 1 as a result of probabilistic regressions by the Maximum Likelihood Method. Based on these model parameters, the mathematical relationships given in Equation 5-2 and Equation 5-3 are obtained for the isotropic compression and liquefaction state curves, respectively.

$$ICC: \quad \ln(e) = \ln\left(1.191 \cdot (e_{max} - e_{min})\right) - \left(\frac{1.168 \cdot exp\left(-1.257 \cdot (e_{max} - e_{min})\right)}{1 + 0.995 \cdot RD}\right) \cdot \ln\left[p' + \left(\frac{1.191 \cdot (e_{max} - e_{min})}{e_0}\right)^{\frac{1+0.995 \cdot RD}{1.168 \cdot exp\left(-1.257 \cdot (e_{max} - e_{min})\right)}} - 0.001\right] \quad \text{Equation 5-2}$$

$$LSC: \quad ln(e) = \ln\left(0.361 \cdot (e_{max} - e_{min})\right) - \left(\frac{1.168 \cdot exp\left(-1.257 \cdot (e_{max} - e_{min})\right)}{1 + 0.995 \cdot RD}\right) \cdot \ln\left(p'_{ls} + \left(\frac{0.361 \cdot (e_{max} - e_{min})}{0.996 \cdot e_{max}}\right)^{\frac{1+0.995 \cdot RD}{1.168 \cdot exp\left(-1.257 \cdot (e_{max} - e_{min})\right)}} - 0.001\right) \quad \text{Equation 5-3}$$

Based on these relationships, the case history data points with respect to their initial states and liquefaction states are located in the void ratio versus mean effective stress domain as presented in Figure 5.2.

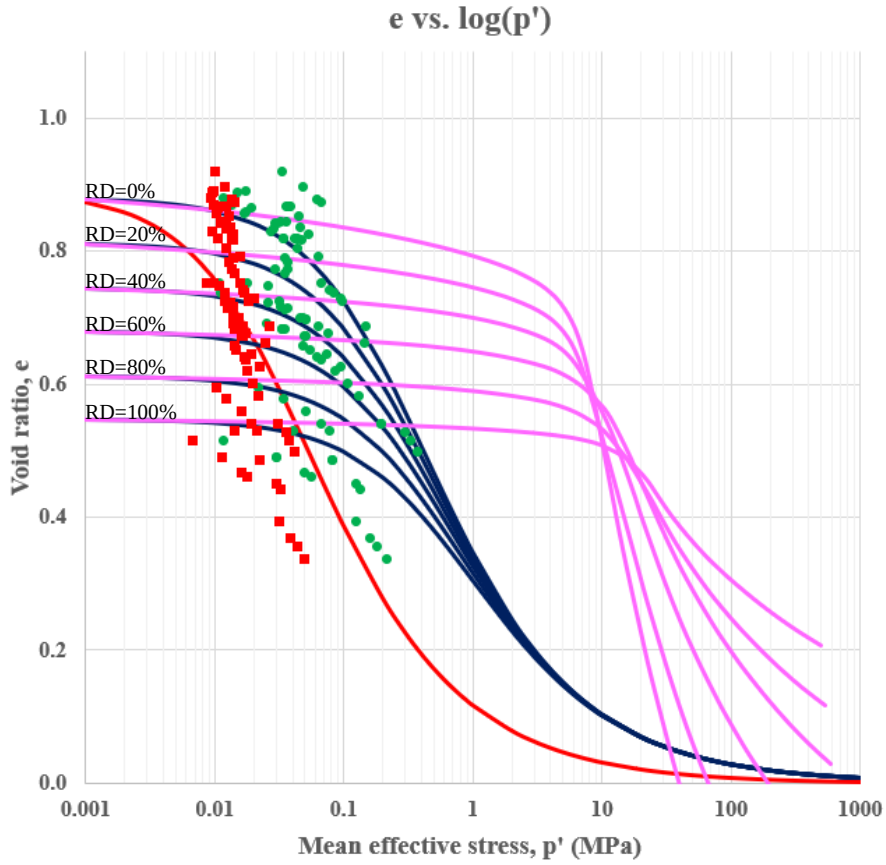

Figure 5.2. Void ratio versus mean effective stress domain for Model 1

Consequently, the post-liquefaction shear strength values and the corresponding probabilities with their natural logarithms are obtained for the first prediction model as tabulated in Table 5.3. The summation of ln(Probability) values, and the corresponding standard deviation of the model are evaluated as -22.87 and 0.45, respectively, for Model 1.

Table 5.3 Predicted post-liquefaction shear strength values and corresponding probabilities for Model 1

#	Case History	$S_{r,backanalyzed}$ (kPa)	$\tau_{liq,predicted}$ (kPa)	P( )	Ln(P)
1	Wachusett Dam - North Dike	10.92	9.46	0.847	-0.166
2	Fort Peck Dam	12.60	15.77	0.786	-0.241

Table 5.3 (cont'd) Predicted post-liquefaction shear strength values and corresponding probabilities for Model 1

3	Uetsu Railway Embankment	1.82	5.54	0.040	-3.213
4	Lower San Fernando Dam - U/S Slope	25.81	20.05	0.760	-0.274
5	Hachiro-Gata Road Embankment	3.39	5.12	0.583	-0.539
6	La Marquesa Dam - U/S Slope	4.36	5.49	0.779	-0.249
7	La Marquesa Dam - D/S Slope	9.72	6.33	0.562	-0.575
8	La Palma Dam	6.51	5.41	0.818	-0.201
9	Lake Ackerman Highway Embankment	5.12	6.09	0.827	-0.190
10	Chonan Middle School	6.75	5.47	0.798	-0.226
11	Soviet Tajik - May 1 Slide	16.33	10.93	0.596	-0.518
12-1	Shibecha-Cho Embankment	10.73	7.88	0.703	-0.352
12-2		10.73	7.69	0.677	-0.390
13	Route 272 at Higashiarekinai	6.61	6.34	0.887	-0.119
14-1	Zeeland - Vlietepolder	10.53	7.52	0.671	-0.399
14-2		7.05	8.65	0.803	-0.220
15	Sheffield Dam	8.22	6.07	0.708	-0.345
16-1	Helsinki Harbor	2.85	4.44	0.547	-0.604
16-2		2.01	5.30	0.085	-2.461
17	Solfatara Canal Dike	4.19	4.73	0.859	-0.152
18	Lake Merced Bank	5.98	6.25	0.887	-0.120
19	El Cobre Tailings Dam	9.58	6.09	0.534	-0.627
20	Metoki Road Embankment	5.67	4.96	0.852	-0.160
21-1	Hokkaido Tailings Dam	8.06	5.55	0.630	-0.462
21-2		3.43	5.04	0.616	-0.485
22	Upper San Fernando Dam - D/S Slope	27.87	30.71	0.871	-0.139
23-1	Tar Island Dyke	15.09	9.13	0.474	-0.746
23-2		26.10	12.02	0.199	-1.615
24	Mochi-Koshi Tailings Dam 1	5.80	8.58	0.609	-0.496
25	Mochi-Koshi Tailings Dam 2	6.97	8.38	0.819	-0.200

Table 5.3 (cont'd) Predicted post-liquefaction shear strength values and corresponding probabilities for Model 1

26	Nerlerk Embankment Slide 1	4.63	6.56	0.660	-0.415
27	Nerlerk Embankment Slide 2	3.54	6.52	0.353	-1.042
28	Nerlerk Embankment Slide 3	2.70	6.71	0.112	-2.185
29	Asele Road Embankment	6.21	6.69	0.879	-0.129
30-1	Nalband Railway Embankment	7.41	6.38	0.842	-0.172
30-2		5.94	7.07	0.826	-0.191
31-1	Sullivan Tailings	14.08	7.77	0.369	-0.998
31-2		14.69	8.54	0.428	-0.849
32	Jamuna Bridge	8.43	6.00	0.668	-0.404

The comparison of the predicted residual strength values with the modified back-calculated post-liquefaction shear strength values of Weber (2015) for Model 1 is presented in Figure 5.3.

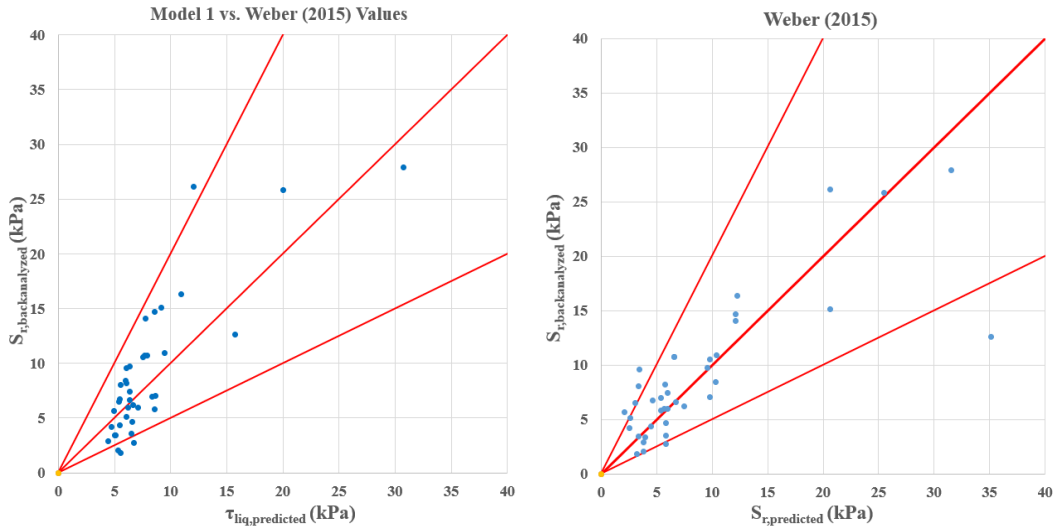

Figure 5.3. Residual strength comparison of Model 1 and Weber (2015)

In addition, the residual plots for SPT resistance ($(N_1)_{60}$), mean grain size (D_{50}), fines content (FC), and coefficient of uniformity (C_u) are obtained as shown in Figure 5.4 for Model 1.

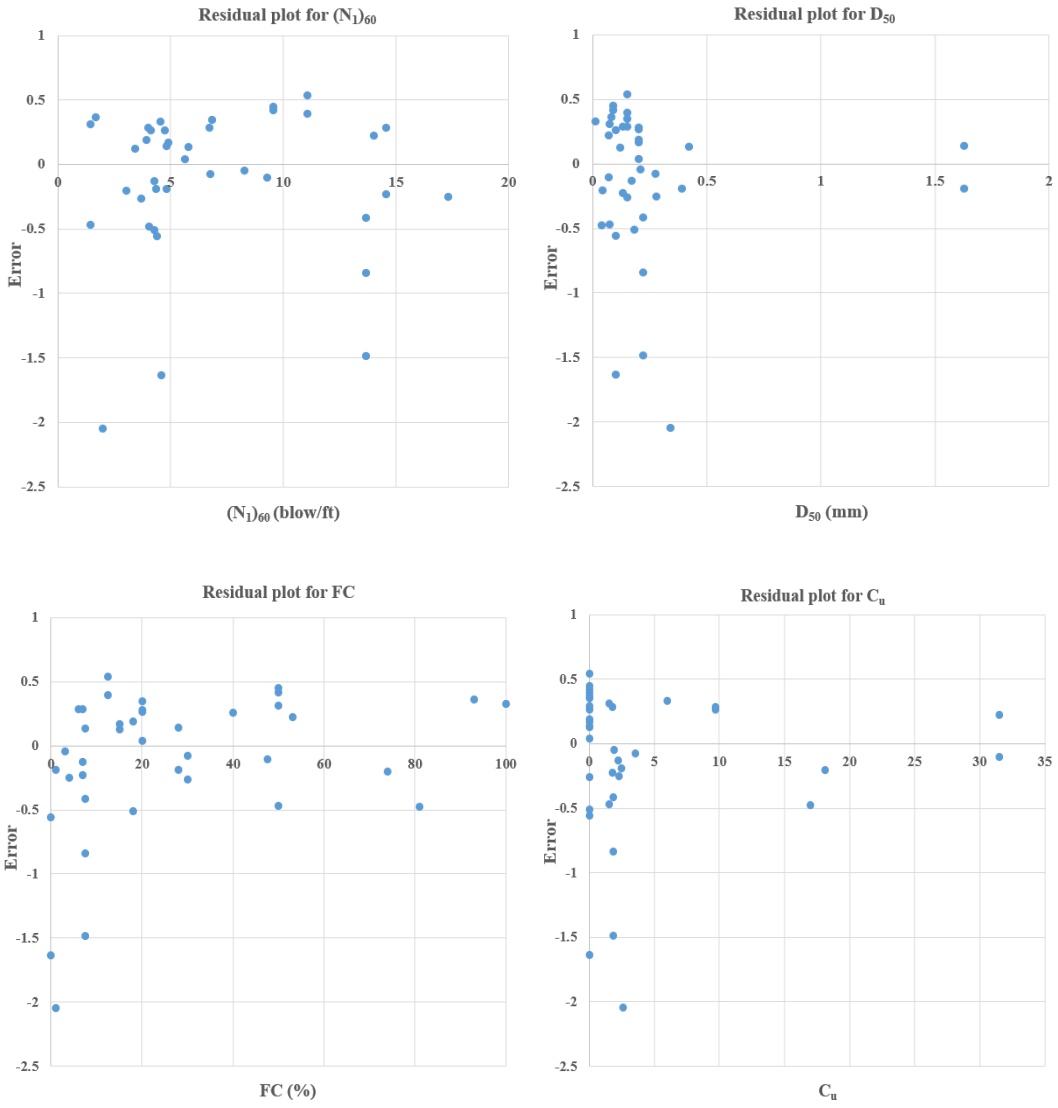

Figure 5.4. Residual plots of input parameters for Model 1

As it can be seen from Figure 5.3, the predicted post-liquefaction shear strength values imply that Model 1 is a viable alternative to the prediction model of Weber (2015). In fact, the predicted post-liquefaction shear strength results fit well to the modified back-analyses residual strength values of Weber (2015) for smaller strength ranges such as 0-20 kPa. For higher stress ranges, on the other hand, the prediction model of Weber (2015) provides comparable predictions.

When the residual plots shown in Figure 5.4 are examined, it can be judged that a significant trend does not exist for any of the presented input parameters. This means that none of these parameters has a misleading or exaggerated effect on the model. For most of the cases, the data points distribute around the zero line, which implies an unbiased fit to the back-analyses residual strength values. On the other hand, some scatter data points exist for all input parameters suggesting an imperfect model.

Referring to Figure 5.2, it is also possible to say that isotropic compression curves given in blue color exhibit nonlinearity earlier than 1-10 MPa (typical crushing values reported in the literature) for Model 1. In fact, it is already discussed in Chapter 4 that while the ICCs recommended by Mesri and Vardhanabhuti (2009) given in purple color crush at higher mean effective stress ranges such as 2-20 MPa, this range is much lower for the data presented by Wei and Yang (2019) such as 0.2-0.8 MPa as presented in Figure 4.7. Therefore, there is no consensus in the literature regarding where nonlinearity starts for cohesionless soils. Also, it should be noted that these curves are plotted by using the average values of the case history database; therefore, they may vary with respect to individual case points once their parameters are employed instead of average values.

These mean effective stress values beyond which nonlinearity is more pronounced are governed by the mathematical relationships used for isotropic compression and liquefaction state curves given in Equation 4-12 and Equation 4-16, respectively. As it can be understood from these two equations, the slope of the ICCs and LSCs are directed to be equal by assigning the same λ value to them to achieve the parallelism between them at high stresses. Therefore, any change employed in λ affects both of these curves. In fact, the slope of the liquefaction state curve should not be a function of the initial relative density as the liquefaction state, or critical state, is independent of the initial relative density. Hence, it is quite challenging for this model to fit the crushing points of the isotropic compression curves with the literature, and residual strength predictions with the ones of Weber (2015) at the same time.

5.1.2 Discussion of Model 2

The second residual strength prediction model again utilizes a double logarithmic void ratio versus mean effective stress domain (ln(e) vs. ln(p')) for both the liquefaction and isotropic compression responses. In other words, the liquefaction and isotropic state curves become asymptomatic to a horizontal line at higher stresses, and negative void ratio values at these higher stress ranges are avoided as a result of this asymptote and log-nature of the relationships.

The only difference between Model 1 and Model 2 is that the minimum limit void ratio that the isotropic and liquefaction state curves become asymptomatic at very high stresses, e_{lim} value, is selected as 0.35 instead of zero in Model 2. This value of 0.35 is not randomly determined, but defined referring to Cubrinovski and Ishihara (2002) as discussed in Section 4.4.2.

The best-fit model parameters are developed as given in Table 4.5 for Model 2 as a result of probabilistic regressions by the Maximum Likelihood Method. Based on these model parameters, the mathematical relationships given in Equation 5-4 and Equation 5-5 are obtained for the isotropic compression and liquefaction state curves, respectively.

$$ICC: \quad \ln(e-0.35) = \ln\left(0.839\cdot(e_{max}-e_{min})\right) - \left(\frac{0.372\cdot exp\left(-0.37\cdot(e_{max}-e_{min})\right)}{1+0.788\cdot RD}\right) \cdot \ln\left[p' + \left(\frac{0.839\cdot(e_{max}-e_{min})}{e_0-0.35}\right)^{\frac{1+0.788\cdot RD}{0.372\cdot exp\left(-0.37\cdot(e_{max}-e_{min})\right)}} - 0.001\right] \quad \text{Equation 5-4}$$

$$LSC: \quad ln(e-0.35) = \ln\left(0.461\cdot(e_{max}-e_{min})\right) - \left(\frac{0.372\cdot exp\left(-0.37\cdot(e_{max}-e_{min})\right)}{1+0.788\cdot RD}\right) \cdot \ln\left(p'_{ls} + \left(\frac{0.461\cdot(e_{max}-e_{min})}{0.984\cdot e_{max}-0.35}\right)^{\frac{1+0.788\cdot RD}{0.372\cdot exp\left(-0.37\cdot(e_{max}-e_{min})\right)}} - 0.001\right) \quad \text{Equation 5-5}$$

Based on these relationships, the case history data points with respect to their initial states and liquefaction states are located in the void ratio versus mean effective stress domain as presented in Figure 5.5.

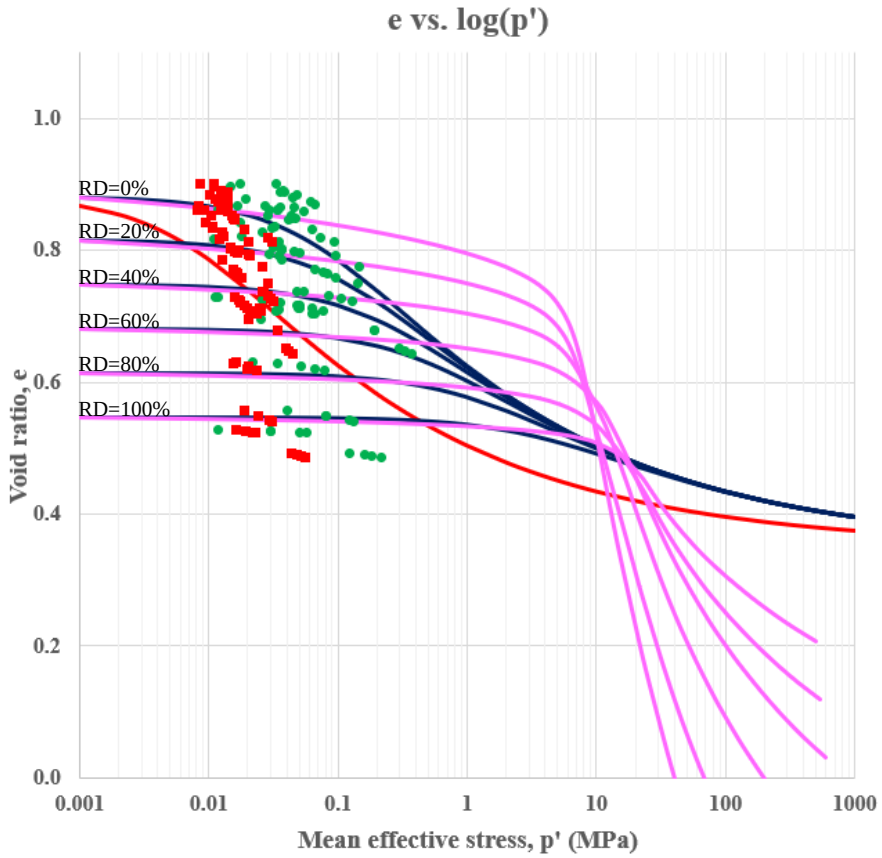

Figure 5.5. Void ratio versus mean effective stress domain for Model 2

Consequently, the post-liquefaction shear strength values and the corresponding probabilities with their natural logarithms are obtained for the second prediction model as tabulated in Table 5.4. The summation of ln(Probability) values, and the corresponding standard deviation of the model are evaluated as -21.28 and 0.44, respectively, for Model 2.

Table 5.4 Predicted post-liquefaction shear strength values and corresponding probabilities for Model 2

#	Case History	$S_{r,backanalyzed}$ (kPa)	$\tau_{liq,predicted}$ (kPa)	P( )	Ln(P)
1	Wachusett Dam - North Dike	10.92	8.03	0.712	-0.340
2	Fort Peck Dam	12.60	13.74	0.893	-0.113

Table 5.4 (cont'd) Predicted post-liquefaction shear strength values and corresponding probabilities for Model 2

3	Uetsu Railway Embankment	1.82	4.51	0.106	-2.243
4	Lower San Fernando Dam - U/S Slope	25.81	23.42	0.889	-0.118
5	Hachiro-Gata Road Embankment	3.39	4.80	0.665	-0.408
6	La Marquesa Dam - U/S Slope	4.36	5.22	0.836	-0.179
7	La Marquesa Dam - D/S Slope	9.72	6.43	0.584	-0.537
8	La Palma Dam	6.51	5.07	0.774	-0.257
9	Lake Ackerman Highway Embankment	5.12	5.47	0.901	-0.105
10	Chonan Middle School	6.75	4.94	0.706	-0.348
11	Soviet Tajik - May 1 Slide	16.33	14.40	0.874	-0.134
12-1	Shibecha-Cho Embankment	10.73	9.96	0.898	-0.108
12-2		10.73	9.87	0.895	-0.111
13	Route 272 at Higashiarekinai	6.61	6.09	0.895	-0.110
14-1	Zeeland - Vlietepolder	10.53	10.00	0.905	-0.100
14-2		7.05	10.75	0.572	-0.559
15	Sheffield Dam	8.22	6.33	0.763	-0.270
16-1	Helsinki Harbor	2.85	3.08	0.897	-0.109
16-2		2.01	3.72	0.340	-1.079
17	Solfatara Canal Dike	4.19	4.61	0.890	-0.116
18	Lake Merced Bank	5.98	7.11	0.842	-0.173
19	El Cobre Tailings Dam	9.58	4.99	0.301	-1.199
20	Metoki Road Embankment	5.67	4.39	0.768	-0.264
21-1	Hokkaido Tailings Dam	8.06	4.61	0.404	-0.907
21-2		3.43	4.23	0.813	-0.208
22	Upper San Fernando Dam - D/S Slope	27.87	30.18	0.896	-0.110
23-1	Tar Island Dyke	15.09	9.47	0.517	-0.660
23-2		26.10	11.09	0.135	-2.005
24	Mochi-Koshi Tailings Dam 1	5.80	9.92	0.430	-0.843
25	Mochi-Koshi Tailings Dam 2	6.97	8.71	0.801	-0.222

Table 5.4 (cont'd) Predicted post-liquefaction shear strength values and corresponding probabilities for Model 2

26	Nerlerk Embankment Slide 1	4.63	6.50	0.677	-0.391
27	Nerlerk Embankment Slide 2	3.54	6.43	0.362	-1.017
28	Nerlerk Embankment Slide 3	2.70	6.63	0.111	-2.196
29	Asele Road Embankment	6.21	8.51	0.705	-0.350
30-1	Nalband Railway Embankment	7.41	8.40	0.874	-0.134
30-2		5.94	8.76	0.614	-0.488
31-1	Sullivan Tailings	14.08	7.34	0.302	-1.199
31-2		14.69	8.04	0.353	-1.041
32	Jamuna Bridge	8.43	5.60	0.590	-0.527

The comparison of the predicted residual strength values with the modified back-calculated post-liquefaction shear strength values of Weber (2015) for Model 2 is presented in Figure 5.6.

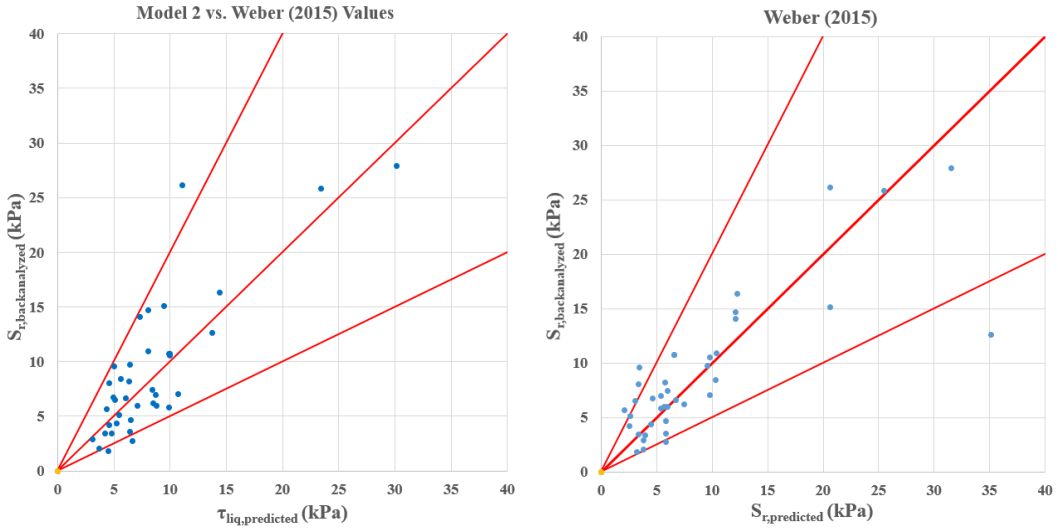

Figure 5.6. Residual strength comparison of Model 2 and Weber (2015)

In addition, the residual plots for SPT resistance ($(N_1)_{60}$), mean grain size (D_{50}), fines content (FC), and coefficient of uniformity (C_u) are obtained as shown in Figure 5.7 for Model 2.

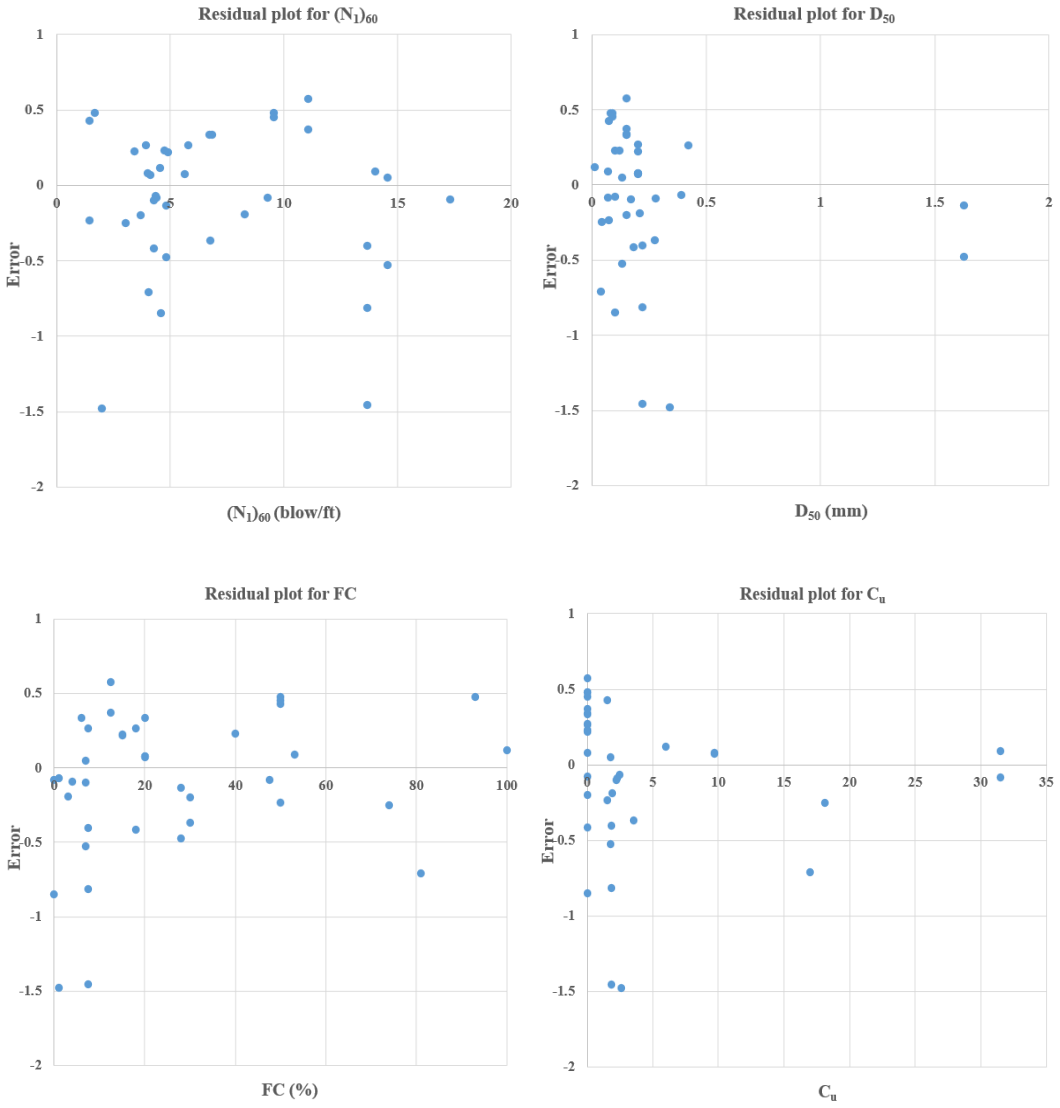

Figure 5.7. Residual plots of input parameters for Model 2

As it can be seen from Figure 5.6, the predicted post-liquefaction shear strength values imply that Model 2 is a viable alternative to the prediction model of Weber (2015). In fact, the predicted post-liquefaction shear strength results fit well to the modified back-analyses residual strength values of Weber (2015) for both smaller and larger strength ranges. For higher stress ranges, only one scatter case data point exists beyond the 1 vs. 2 line.

When the residual plots shown in Figure 5.7 are examined, it can be judged that a significant trend does not exist for any of the presented input parameters. This means that none of these parameters has a misleading or exaggerated effect on the model. For most of the cases, the data points distribute around the zero line, which implies an unbiased fit to the back-analyses residual strength values. On the other hand, some scatter data points exist for all input parameters suggesting an imperfect model.

Referring to Figure 5.5, it is also possible to say that isotropic compression curves given in blue color exhibit nonlinearity earlier than typical crushing values reported in the literature for Model 2 for lower relative density ranges. In fact, it is already discussed in Chapter 4 that while the ICCs recommended by Mesri and Vardhanabhuti (2009) given in purple color crush at higher mean effective stress ranges such as 2-20 MPa, this range is much lower for the data presented by Wei and Yang (2019) such as 0.2-0.8 MPa as presented in Figure 4.7. Therefore, there is no consensus in the literature regarding where nonlinearity starts for cohesionless soils. Besides, the mean effective stress values that the nonlinearity starts for higher relative densities fit well to the ones recommended by Wei and Yang (2019) shown in Figure 4.7. Also, it should be noted that these curves are plotted by using the average values of the case history database; therefore, they may vary with respect to individual case points once their parameters are employed instead of average values.

These mean effective stress values beyond which nonlinearity is more pronounced are governed by the mathematical relationships used for isotropic compression and liquefaction state curves given in Equation 4-12 and Equation 4-16, respectively. As it can be understood from these two equations, the slope of the ICCs and LSCs are directed to be equal by assigning the same λ value to them to achieve the parallelism between them at high stresses. Therefore, any change employed in λ affects both of these curves. In fact, the slope of the liquefaction state curve should not be a function of the initial relative density as the liquefaction state, or critical state, is independent of the initial relative density. Hence, it is quite challenging for this model to fit the crushing points of the isotropic compression curves for lower relative densities with

the literature, and residual strength predictions with the ones of Weber (2015) at the same time. On the other hand, the ICCs developed for Model 2 for higher relative density ranges fit well with the ones in literature due to the assigned minimum limit void ratio value (e_{lim}) that the isotropic and liquefaction state curves become asymptomatic at very high stresses. Arranging the e_{lim} value as 0.35 refferring to Cubrinovski and Ishihara (2002) as discussed in Section 4.4.2 increases the mean effective stress values for particle crushing at high relative density ranges, and provides better fits with the literature. Thus, it can be concluded that Model 2 provides better results than Model 1 in terms of both statistical and engineering points of view.

5.1.3 Discussion of Model 3

The third residual strength prediction model utilizes a double logarithmic void ratio versus mean effective stress domain (ln(e) vs. ln(p')) for isotropic compression responses, but a semi-logarithmic void ratio versus mean effective stress domain (e vs. ln(p')) for liquefaction states. In other words, while the isotropic state curves become asymptomatic to a horizontal line at higher stresses, the liquefaction state curves are defined as log-linear over the void ratio versus mean effective stress domain. Since ICCs are defined in the double logarithmic ln(e) vs. ln(p') domain, they converge to a horizontal line passing from the minimum limit void ratio (e_{lim}) asymptomatically, and therefore the negative void ratio values at these higher stress ranges are still avoided as a result of this asymptote and the log-nature of the relationship.

The best-fit model parameters are developed as given in Table 4.8 for Model 3 as a result of probabilistic regressions by the Maximum Likelihood Method. Based on these model parameters, the mathematical relationships given in Equation 5-6 and Equation 5-7 are obtained for the isotropic compression curves and liquefaction state lines, respectively.

$$ICC: \quad \ln(e) = \ln\left(1.571 \cdot (e_{max} - e_{min})\right) - \left(\frac{0.919 \cdot exp\left(4.491 \cdot (e_{max} - e_{min})\right)}{1 + 10.936 \cdot RD}\right) \cdot \ln\left(p' + \left(\frac{1.571 \cdot (e_{max} - e_{min})}{e_0}\right)^{\frac{1+10.936 \cdot RD}{0.919 \cdot exp\left(4.491 \cdot (e_{max} - e_{min})\right)}} - 0.001\right) \quad \text{Equation 5-6}$$

$$LSL: \quad e = (0.174 \cdot e_{max}) - 0.063 \cdot exp\left(0.157 + 1.72 \cdot (e_{max} - e_{min})\right) \cdot \ln\left(p'_{ls}\right) \quad \text{Equation 5-7}$$

Based on these relationships, the case history data points with respect to their initial states and liquefaction states are located in the void ratio versus mean effective stress domain as presented in Figure 5.8.

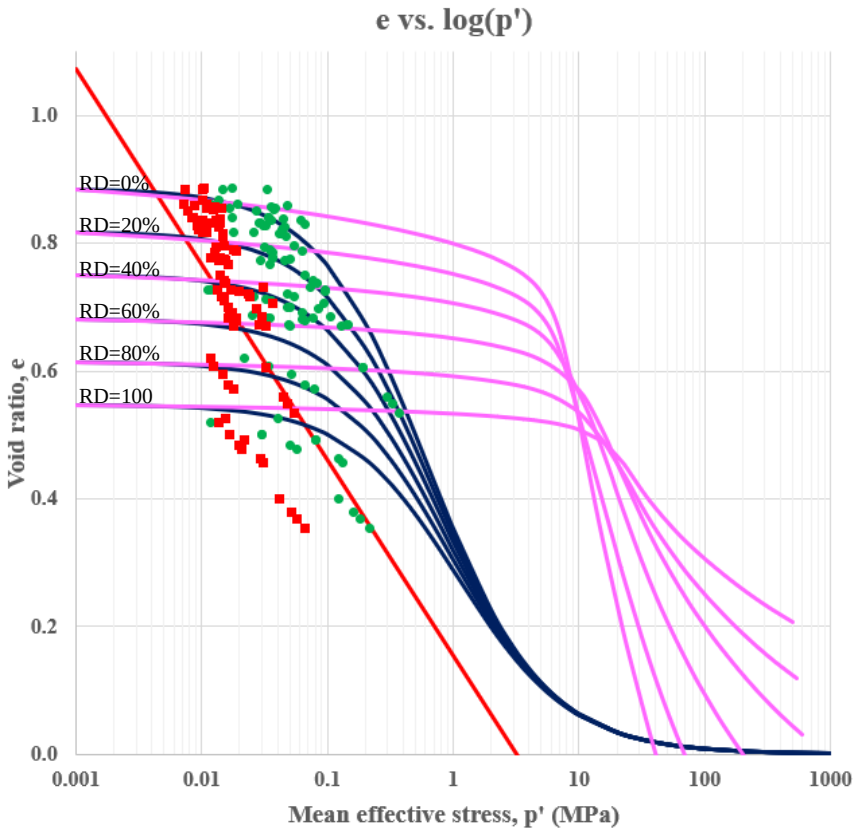

Figure 5.8. Void ratio versus mean effective stress domain for Model 3

Consequently, the post-liquefaction shear strength values and the corresponding probabilities with their natural logarithms are obtained for the third prediction model as tabulated in Table 5.5. The summation of ln(Probability) values, and the corresponding standard deviation of the model are evaluated as -23.82 and 0.45, respectively, for Model 3.

Table 5.5 Predicted post-liquefaction shear strength values and corresponding probabilities for Model 3

#	Case History	$S_{r,backanalyzed}$ (kPa)	$\tau_{liq,predicted}$ (kPa)	P( )	Ln(P)
1	Wachusett Dam - North Dike	10.92	9.45	0.836	-0.179
2	Fort Peck Dam	12.60	18.90	0.590	-0.528
3	Uetsu Railway Embankment	1.82	5.64	0.039	-3.240
4	Lower San Fernando Dam - U/S Slope	25.81	25.30	0.879	-0.129
5	Hachiro-Gata Road Embankment	3.39	5.07	0.593	-0.522
6	La Marquesa Dam - U/S Slope	4.36	5.58	0.758	-0.277
7	La Marquesa Dam - D/S Slope	9.72	6.98	0.673	-0.395
8	La Palma Dam	6.51	5.39	0.806	-0.215
9	Lake Ackerman Highway Embankment	5.12	5.89	0.839	-0.175
10	Chonan Middle School	6.75	5.35	0.771	-0.260
11	Soviet Tajik - May 1 Slide	16.33	16.70	0.878	-0.130
12-1	Shibecha-Cho Embankment	10.73	8.23	0.742	-0.298
12-2		10.73	8.07	0.723	-0.324
13	Route 272 at Higashiarekinai	6.61	6.49	0.879	-0.129
14-1	Zeeland - Vlietepolder	10.53	11.20	0.872	-0.138
14-2		7.05	12.56	0.390	-0.940
15	Sheffield Dam	8.22	6.71	0.796	-0.228
16-1	Helsinki Harbor	2.85	3.36	0.825	-0.192
16-2		2.01	3.96	0.288	-1.246
17	Solfatara Canal Dike	4.19	4.77	0.845	-0.168
18	Lake Merced Bank	5.98	7.62	0.761	-0.272
19	El Cobre Tailings Dam	9.58	4.29	0.183	-1.699
20	Metoki Road Embankment	5.67	4.95	0.841	-0.174
21-1	Hokkaido Tailings Dam	8.06	4.19	0.311	-1.169
21-2		3.43	3.87	0.849	-0.164

Table 5.5 (cont'd) Predicted post-liquefaction shear strength values and corresponding probabilities for Model 3

22	Upper San Fernando Dam - D/S Slope	27.87	30.12	0.867	-0.143
23-1	Tar Island Dyke	15.09	9.32	0.500	-0.693
23-2		26.10	12.03	0.204	-1.588
24	Mochi-Koshi Tailings Dam 1	5.80	7.55	0.743	-0.297
25	Mochi-Koshi Tailings Dam 2	6.97	7.23	0.877	-0.131
26	Nerlerk Embankment Slide 1	4.63	6.69	0.634	-0.456
27	Nerlerk Embankment Slide 2	3.54	6.66	0.334	-1.098
28	Nerlerk Embankment Slide 3	2.70	6.86	0.106	-2.244
29	Asele Road Embankment	6.21	7.31	0.825	-0.193
30-1	Nalband Railway Embankment	7.41	8.37	0.848	-0.164
30-2		5.94	8.83	0.599	-0.512
31-1	Sullivan Tailings	14.08	6.72	0.232	-1.460
31-2		14.69	7.41	0.282	-1.265
32	Jamuna Bridge	8.43	6.08	0.679	-0.387

The comparison of the predicted residual strength values with the modified back-calculated post-liquefaction shear strength values of Weber (2015) for Model 3 is presented in Figure 5.9.

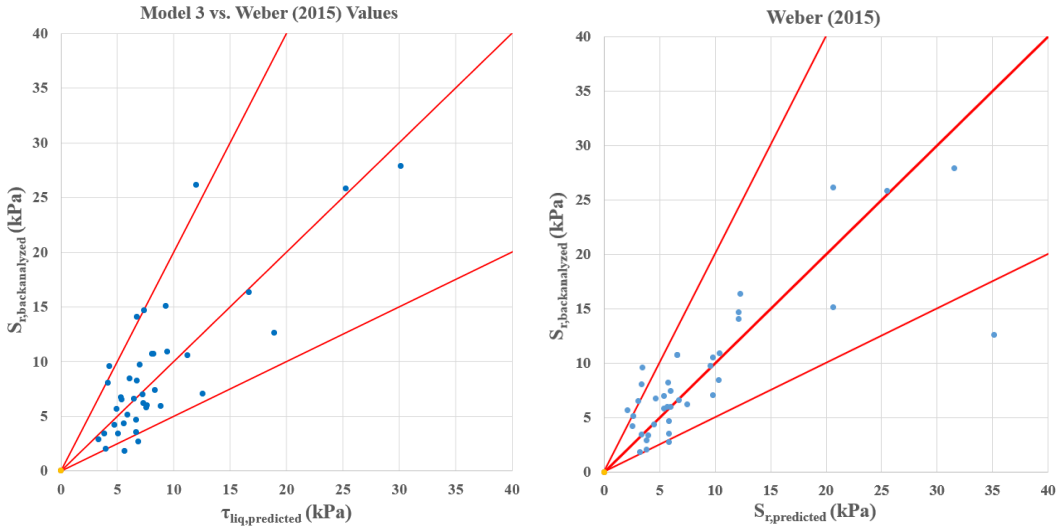

Figure 5.9. Residual strength comparison of Model 3 and Weber (2015)

In addition, the residual plots for SPT resistance ($(N_1)_{60}$), mean grain size (D_{50}), fines content (FC), and coefficient of uniformity (C_u) are obtained as shown in Figure 5.10 for Model 3.

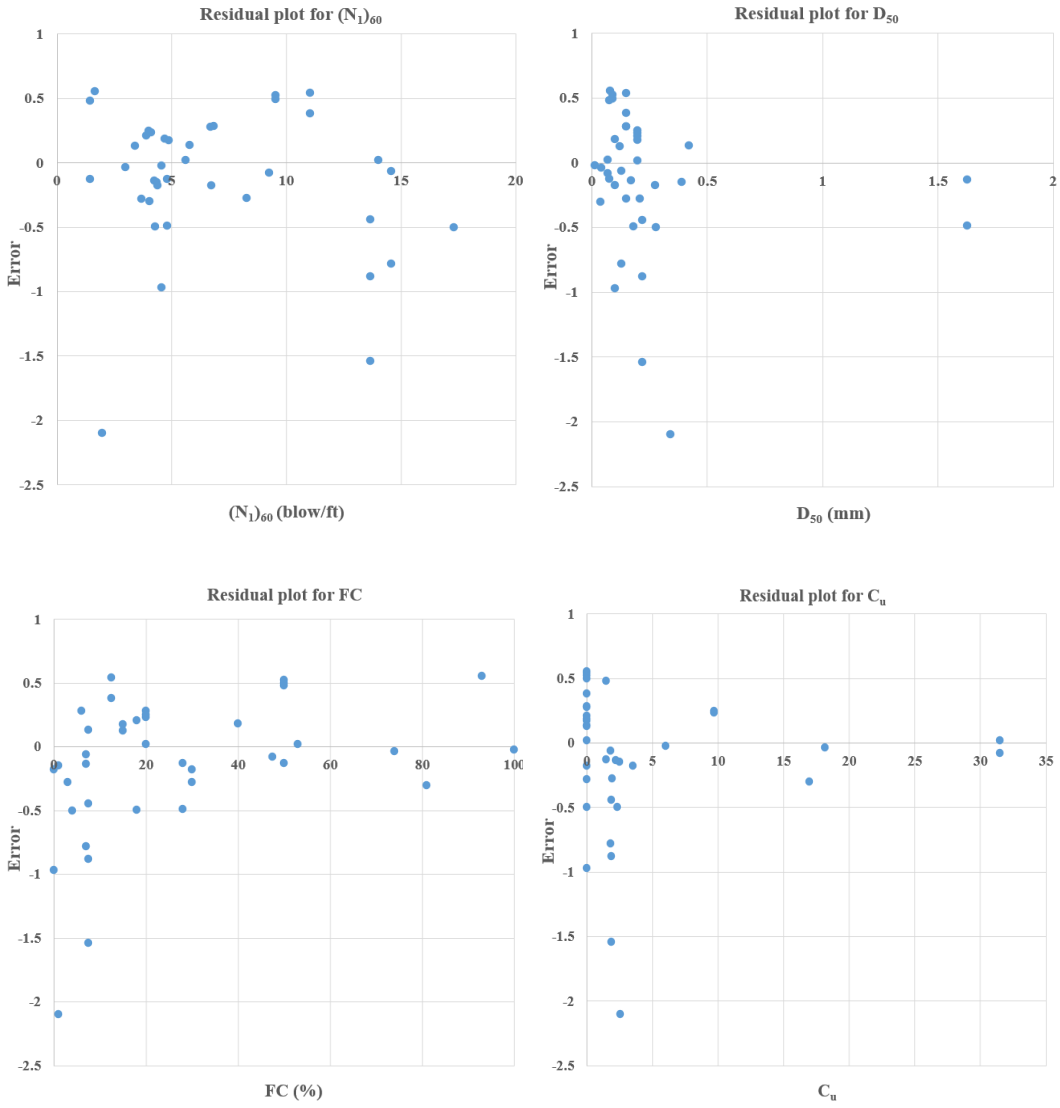

Figure 5.10. Residual plots of input parameters for Model 3

As it can be seen from Figure 5.9, the predicted post-liquefaction shear strength values imply that Model 3 is a viable alternative to the prediction model of Weber (2015). In fact, the predicted post-liquefaction shear strength results fit well to the

modified back-analyses residual strength values of Weber (2015) for both smaller and larger strength ranges. For higher stress ranges, only one scatter case data point exists beyond the 1 vs. 2 line.

When the residual plots shown in Figure 5.10 are examined, it can be judged that a significant trend does not exist for any of the presented input parameters. This means that none of these parameters has a misleading or exaggerated effect on the model. For most of the cases, the data points distribute around the zero line, which implies an unbiased fit to the back-analyses residual strength values. On the other hand, some scatter data points exist for all input parameters suggesting an imperfect model.

Referring to Figure 5.8, it is also possible to say that isotropic compression curves given in blue color exhibit nonlinearity earlier than 1-10 MPa (typical crushing values reported in the literature) for Model 3. In fact, it is already discussed in Chapter 4 that while the ICCs recommended by Mesri and Vardhanabhuti (2009) given in purple color crush at higher mean effective stress ranges such as 2-20 MPa, this range is much lower for the data presented by Wei and Yang (2019) such as 0.2-0.8 MPa as presented in Figure 4.7. Therefore, there is no consensus in the literature regarding where nonlinearity starts for cohesionless soils. Also, it should be noted that these curves are plotted by using the average values of the case history database; therefore, they may vary with respect to individual case points once their parameters are employed instead of average values.

The difference between the mean effective stress values beyond which nonlinearity is more pronounced is governed by the nature of the post-liquefaction case history data points such that the database consists of soils with high compressibility. Hence, they tend to yield and crush earlier at low mean effective stress ranges. In fact, since we do not have data points in those higher mean effective stress ranges, it is difficult to model those regions mathematically. Hence, it is quite challenging for this model to fit the crushing points of the isotropic compression curves with the literature, and residual strength predictions with the ones of Weber (2015) at the same time.

5.1.4 Discussion of Model 4

The fourth residual strength prediction model again utilizes a double logarithmic void ratio versus mean effective stress domain (ln(e) vs. ln(p')) for isotropic compression responses, but a semi-logarithmic void ratio versus mean effective stress domain (e vs. ln(p')) for liquefaction states similar to Model 3. In other words, while the isotropic state curves become asymptomatic to a horizontal line at higher stresses, the liquefaction state curves are defined as log-linear over the void ratio versus mean effective stress domain. Since ICCs are defined in the double logarithmic ln(e) vs. ln(p') domain, they converge to a horizontal line passing from the minimum limit void ratio (e_{lim}) asymptomatically, and therefore the negative void ratio values at these higher stress ranges are still avoided as a result of this asymptote and the log-nature of the relationship.

The only difference between Model 3 and Model 4 is that the minimum limit void ratio that the isotropic state curves become asymptomatic at very high stresses, e_{lim} value, is selected as 0.35 instead of zero in Model 4. This value of 0.35 is not randomly determined, but defined referring to Cubrinovski and Ishihara (2002) as discussed in Section 4.4.2.

The best-fit model parameters are developed as given in Table 4.11 for Model 4 as a result of probabilistic regressions by the Maximum Likelihood Method. Based on these model parameters, the mathematical relationships given in Equation 5-8 and Equation 5-9 are obtained for the isotropic compression curves and liquefaction state lines, respectively.

$$ICC: \quad \ln(e-0.35) = \ln\left(0.749\cdot(e_{max}-e_{min})\right) - \left(\frac{0.113\cdot exp\left(11.682\cdot(e_{max}-e_{min})\right)}{1+33.312\cdot RD}\right) \cdot \ln\left(p' + \left(\frac{0.749\cdot(e_{max}-e_{min})}{e_0-0.35}\right)^{\frac{1+33.312\cdot RD}{0.113\cdot exp\left(11.682\cdot(e_{max}-e_{min})\right)}} - 0.001\right) \qquad \text{Equation 5-8}$$

$$LSL: \quad e = (0.255\cdot e_{max}) - 0.062\cdot exp\left(0.153+1.529\cdot(e_{max}-e_{min})\right)\cdot \ln\left(p'_{ls}\right) \qquad \text{Equation 5-9}$$

Based on these relationships, the case history data points with respect to their initial states and liquefaction states are located in the void ratio versus mean effective stress domain as presented in Figure 5.11.

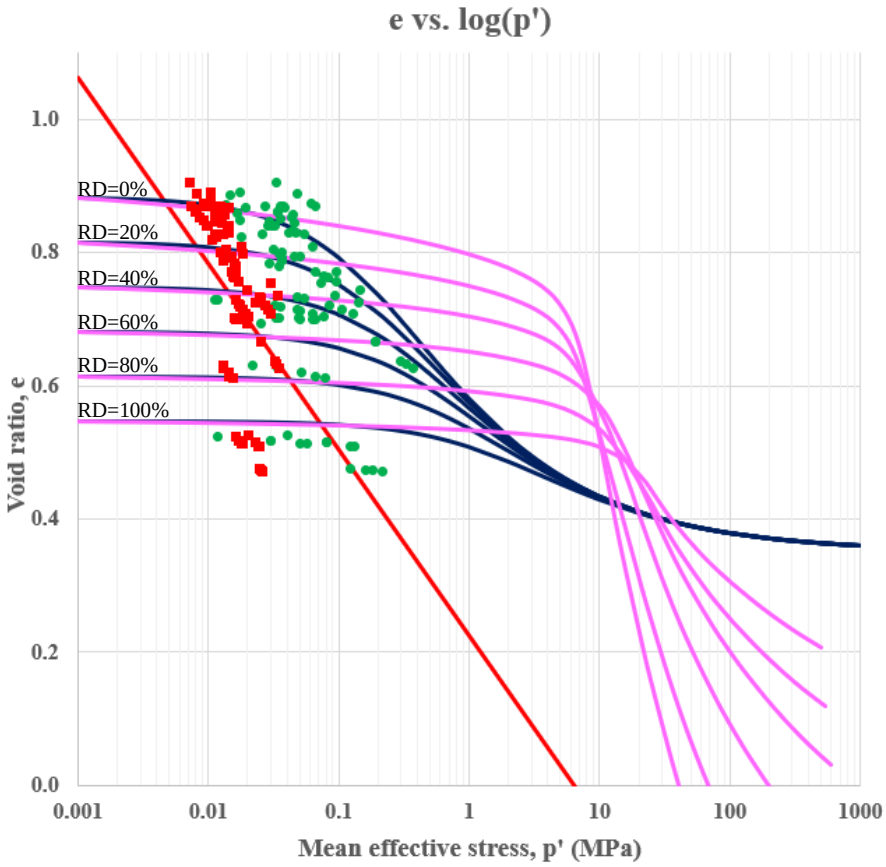

Figure 5.11. Void ratio versus mean effective stress domain for Model 4

Consequently, the post-liquefaction shear strength values and the corresponding probabilities with their natural logarithms are obtained for the second prediction model as tabulated in Table 5.6. The summation of ln(Probability) values, and the corresponding standard deviation of the model are evaluated as -27.06 and 0.49, respectively, for Model 4.

Table 5.6 Predicted post-liquefaction shear strength values and corresponding probabilities for Model 4

#	Case History	$S_{r,backanalyzed}$ (kPa)	$\tau_{liq,predicted}$ (kPa)	P( )	Ln(P)
1	Wachusett Dam - North Dike	10.92	7.63	0.625	-0.470
2	Fort Peck Dam	12.60	13.69	0.807	-0.214
3	Uetsu Railway Embankment	1.82	5.15	0.084	-2.480
4	Lower San Fernando Dam - U/S Slope	25.81	12.78	0.289	-1.241
5	Hachiro-Gata Road Embankment	3.39	5.12	0.573	-0.557
6	La Marquesa Dam - U/S Slope	4.36	5.50	0.730	-0.314
7	La Marquesa Dam - D/S Slope	9.72	6.97	0.649	-0.433
8	La Palma Dam	6.51	5.40	0.761	-0.274
9	Lake Ackerman Highway Embankment	5.12	5.91	0.785	-0.242
10	Chonan Middle School	6.75	5.23	0.713	-0.338
11	Soviet Tajik - May 1 Slide	16.33	16.07	0.818	-0.200
12-1	Shibecha-Cho Embankment	10.73	7.65	0.643	-0.441
12-2		10.73	7.59	0.637	-0.451
13	Route 272 at Higashiarekinai	6.61	6.36	0.816	-0.203
14-1	Zeeland - Vlietepolder	10.53	11.50	0.806	-0.216
14-2		7.05	12.32	0.425	-0.856
15	Sheffield Dam	8.22	6.72	0.752	-0.286
16-1	Helsinki Harbor	2.85	3.74	0.702	-0.354
16-2		2.01	4.25	0.252	-1.380
17	Solfatara Canal Dike	4.19	4.93	0.775	-0.255
18	Lake Merced Bank	5.98	7.90	0.695	-0.364
19	El Cobre Tailings Dam	9.58	3.98	0.162	-1.819
20	Metoki Road Embankment	5.67	4.91	0.784	-0.244
21-1	Hokkaido Tailings Dam	8.06	3.91	0.272	-1.302
21-2		3.43	3.71	0.808	-0.213

Table 5.6 (cont'd) Predicted post-liquefaction shear strength values and corresponding probabilities for Model 4

22	Upper San Fernando Dam - D/S Slope	27.87	29.67	0.812	-0.208
23-1	Tar Island Dyke	15.09	9.20	0.489	-0.715
23-2		26.10	10.36	0.136	-1.998
24	Mochi-Koshi Tailings Dam 1	5.80	7.33	0.729	-0.315
25	Mochi-Koshi Tailings Dam 2	6.97	6.92	0.819	-0.200
26	Nerlerk Embankment Slide 1	4.63	7.76	0.468	-0.760
27	Nerlerk Embankment Slide 2	3.54	7.70	0.231	-1.467
28	Nerlerk Embankment Slide 3	2.70	7.88	0.073	-2.615
29	Asele Road Embankment	6.21	7.40	0.768	-0.264
30-1	Nalband Railway Embankment	7.41	8.46	0.789	-0.237
30-2		5.94	8.56	0.617	-0.482
31-1	Sullivan Tailings	14.08	7.16	0.312	-1.164
31-2		14.69	7.68	0.338	-1.086
32	Jamuna Bridge	8.43	6.19	0.670	-0.401

The comparison of the predicted residual strength values with the modified back-calculated post-liquefaction shear strength values of Weber (2015) for Model 4 is presented in Figure 5.12.

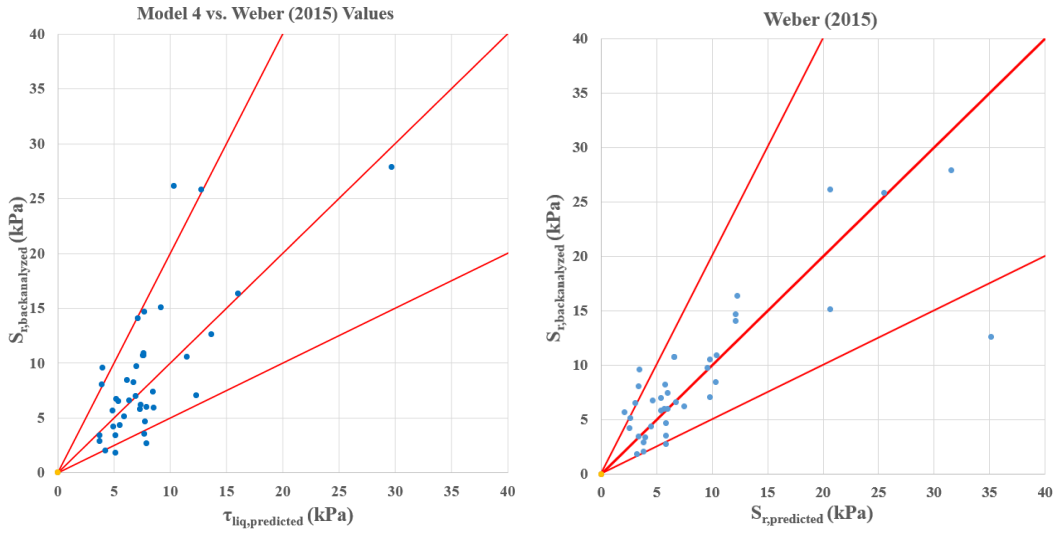

Figure 5.12. Residual strength comparison of Model 4 and Weber (2015)

In addition, the residual plots for SPT resistance ($(N_1)_{60}$), mean grain size (D_{50}), fines content (FC), and coefficient of uniformity (C_u) are obtained as shown in Figure 5.13 for Model 4.

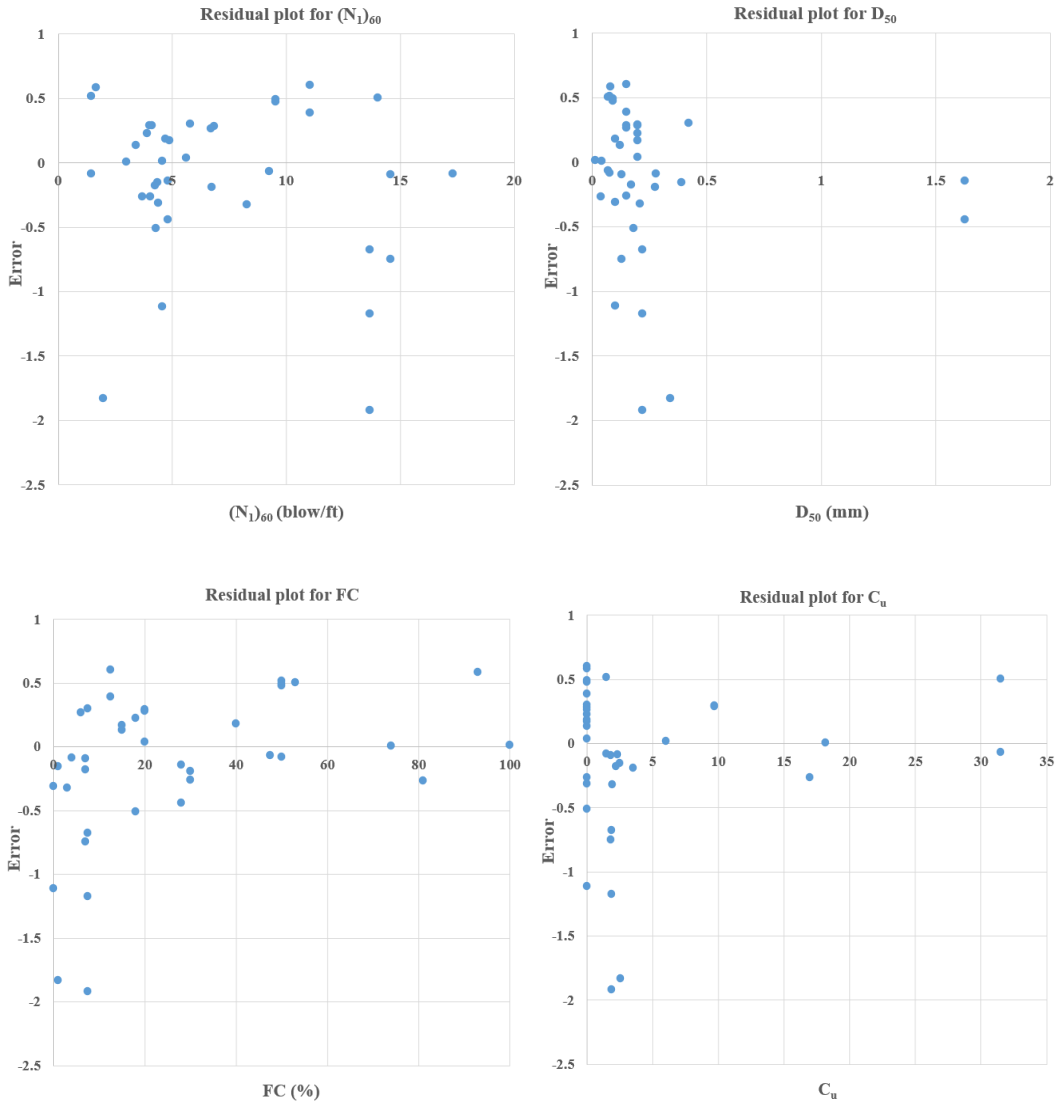

Figure 5.13. Residual plots of input parameters for Model 4

As it can be seen from Figure 5.12, the predicted post-liquefaction shear strength values imply that Model 4 is a viable alternative to the prediction model of Weber (2015). In fact, the predicted post-liquefaction shear strength results fit well to the

modified back-analyses residual strength values of Weber (2015) for smaller strength ranges such as 0-20 kPa. For higher stress ranges, on the other hand, the prediction model of Weber (2015) provides comparable predictions.

When the residual plots shown in Figure 5.13 are examined, it can be judged that a significant trend does not exist for any of the presented input parameters. This means that none of these parameters has a misleading or exaggerated effect on the model. Nevertheless, it is possible to see some minor trends for FC and C_u parameters, which imply that the model provides slightly unsteady results than the usual for some ranges of these parameters. However, the data points distribute around the zero line for most of the cases in general, which implies an unbiased fit to the back-analyses residual strength values. It should also be noted that some scatter data points exist for all input parameters suggesting an imperfect model.

Referring to Figure 5.11, it is also possible to say that isotropic compression curves given in blue color exhibit nonlinearity earlier than typical crushing values reported in the literature for Model 4 for lower relative density ranges. In fact, it is already discussed in Chapter 4 that while the ICCs recommended by Mesri and Vardhanabhuti (2009) given in purple color crush at higher mean effective stress ranges such as 2-20 MPa, this range is much lower for the data presented by Wei and Yang (2019) such as 0.2-0.8 MPa as presented in Figure 4.7. Therefore, there is no consensus in the literature regarding where nonlinearity starts for cohesionless soils. Besides, the mean effective stress values that the nonlinearity starts for higher relative densities fit well to the ones recommended by Wei and Yang (2019) shown in Figure 4.7. Also, it should be noted that these curves are plotted by using the average values of the case history database; therefore, they may vary with respect to individual case points once their parameters are employed instead of average values.

The difference between the mean effective stress values beyond which nonlinearity is more pronounced is governed by the nature of the post-liquefaction case history data points such that the database consists of soils with high compressibility. Hence, they tend to yield and crush earlier at low mean effective stress ranges. In fact, since

we do not have data points in those higher mean effective stress ranges, it is difficult to model those regions mathematically. Hence, it is quite challenging for this model to fit the crushing points of the isotropic compression curves for lower relative densities with the literature, and residual strength predictions with the ones of Weber (2015) at the same time. On the other hand, the ICCs developed for Model 4 for higher relative density ranges fit well with the ones in literature due to the assigned minimum limit void ratio value (e_{lim}) that the isotropic and liquefaction state curves become asymptomatic at very high stresses. Arranging the e_{lim} value as 0.35 refferring to Cubrinovski and Ishihara (2002) as discussed in Section 4.4.2 increases the mean effective stress values for particle crushing at high relative density ranges, and provides better fits with the literature.

5.1.5 Discussion of Model 5

The fifth residual strength prediction model utilizes a different mathematical form than the previous four models for isotropic compression responses, but a semi-logarithmic void ratio versus mean effective stress domain (e vs. ln(p')) for liquefaction states similar to Model 3 and Model 4. The new mathematical form for the isotropic compression responses is again arranged such that the isotropic compression curves become asymptomatic to a horizontal line passing from the minimum limit void ratio (e_{lim}) at higher stresses. Thus, the negative void ratio values at these higher stress ranges are still avoided for this new mathematical form due to the log-nature of the relationship. The liquefaction state lines, on the other hand, are defined as log-linear over the void ratio versus mean effective stress domain similar to Model 3 and Model 4.

The best-fit model parameters are developed as given in Table 4.14 for Model 5 as a result of probabilistic regressions by the Maximum Likelihood Method. Based on these model parameters, the mathematical relationships given in Equation 5-10 and Equation 5-11 are obtained for the isotropic compression curves and liquefaction state lines, respectively.

$$ICC:\ e = -2.853 - \frac{0.194}{-0.068 + 0.001 \cdot exp\left(-0.618 \cdot \left(p' - 0.001 - \frac{ln\left(\frac{\frac{0.194}{-2.853 - e_0} + 0.068}{0.001}\right)}{0.618}\right)\right)} \quad \text{Equation 5-10}$$

$$LSL:\quad e = (0.073 \cdot e_{max}) - 0.085 \cdot exp\left(0.03 + 1.76 \cdot (e_{max} - e_{min})\right) \cdot \ln\left(p'_{ls}\right) \quad \text{Equation 5-11}$$

Based on these relationships, the case history data points with respect to their initial states and liquefaction states are located in the void ratio versus mean effective stress domain as presented in Figure 5.14.

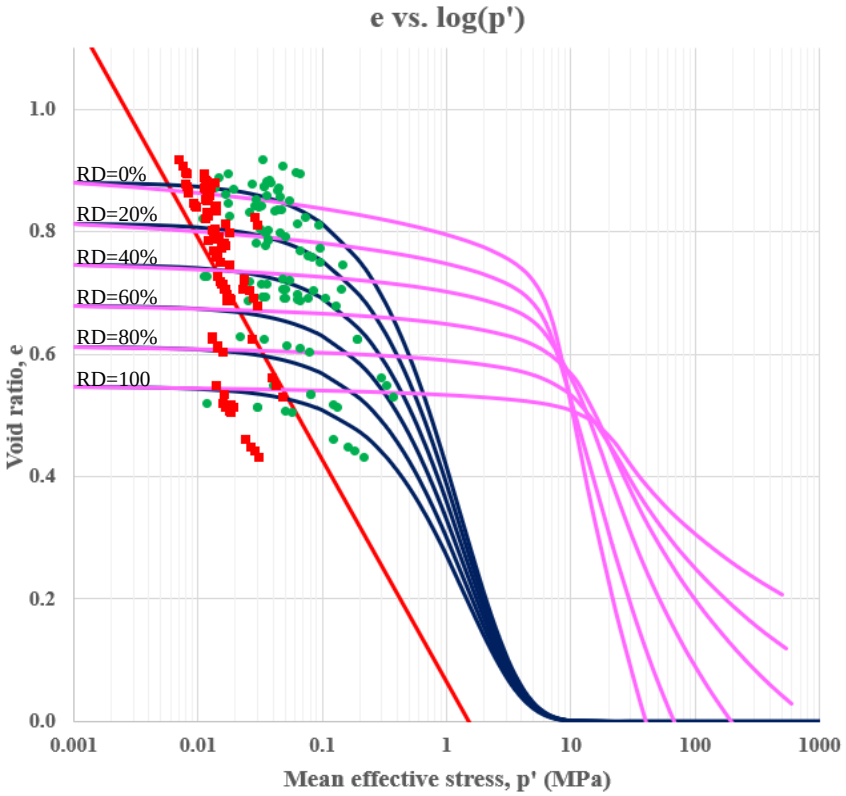

Figure 5.14. Void ratio versus mean effective stress domain for Model 5

Consequently, the post-liquefaction shear strength values and the corresponding probabilities with their natural logarithms are obtained for the third prediction model as tabulated in Table 5.7. The summation of ln(Probability) values, and the

corresponding standard deviation of the model are evaluated as -26.00 and 0.47, respectively, for Model 5.

Table 5.7 Predicted post-liquefaction shear strength values and corresponding probabilities for Model 5

#	Case History	$S_{r,backanalyzed}$ (kPa)	$\tau_{liq,predicted}$ (kPa)	P( )	Ln(P)
1	Wachusett Dam - North Dike	10.92	7.24	0.578	-0.548
2	Fort Peck Dam	12.60	16.87	0.696	-0.363
3	Uetsu Railway Embankment	1.82	4.97	0.089	-2.417
4	Lower San Fernando Dam - U/S Slope	25.81	14.45	0.398	-0.921
5	Hachiro-Gata Road Embankment	3.39	5.31	0.538	-0.620
6	La Marquesa Dam - U/S Slope	4.36	5.54	0.740	-0.301
7	La Marquesa Dam - D/S Slope	9.72	6.78	0.630	-0.463
8	La Palma Dam	6.51	5.50	0.789	-0.236
9	Lake Ackerman Highway Embankment	5.12	6.15	0.781	-0.247
10	Chonan Middle School	6.75	5.28	0.734	-0.309
11	Soviet Tajik - May 1 Slide	16.33	15.98	0.840	-0.175
12-1	Shibecha-Cho Embankment	10.73	8.67	0.760	-0.274
12-2		10.73	8.61	0.755	-0.281
13	Route 272 at Higashiarekinai	6.61	6.23	0.834	-0.182
14-1	Zeeland - Vlietepolder	10.53	10.94	0.838	-0.177
14-2		7.05	11.96	0.452	-0.795
15	Sheffield Dam	8.22	6.51	0.745	-0.294
16-1	Helsinki Harbor	2.85	3.78	0.706	-0.348
16-2		2.01	4.13	0.267	-1.320
17	Solfatara Canal Dike	4.19	5.19	0.759	-0.275
18	Lake Merced Bank	5.98	7.61	0.738	-0.304
19	El Cobre Tailings Dam	9.58	3.80	0.126	-2.070
20	Metoki Road Embankment	5.67	5.01	0.813	-0.207
21-1	Hokkaido Tailings Dam	8.06	4.11	0.306	-1.184

Table 5.7 (cont'd) Predicted post-liquefaction shear strength values and corresponding probabilities for Model 5

21-2		3.43	4.00	0.798	-0.226
22	Upper San Fernando Dam - D/S Slope	27.87	28.47	0.840	-0.175
23-1	Tar Island Dyke	15.09	9.09	0.476	-0.743
23-2		26.10	10.90	0.155	-1.865
24	Mochi-Koshi Tailings Dam 1	5.80	7.93	0.677	-0.391
25	Mochi-Koshi Tailings Dam 2	6.97	7.49	0.831	-0.185
26	Nerlerk Embankment Slide 1	4.63	6.90	0.591	-0.526
27	Nerlerk Embankment Slide 2	3.54	6.87	0.318	-1.146
28	Nerlerk Embankment Slide 3	2.70	7.04	0.110	-2.209
29	Asele Road Embankment	6.21	7.60	0.768	-0.264
30-1	Nalband Railway Embankment	7.41	8.85	0.783	-0.244
30-2		5.94	9.02	0.570	-0.562
31-1	Sullivan Tailings	14.08	6.68	0.245	-1.408
31-2		14.69	7.09	0.258	-1.353
32	Jamuna Bridge	8.43	6.15	0.674	-0.395

The comparison of the predicted residual strength values with the modified back-calculated post-liquefaction shear strength values of Weber (2015) for Model 5 is presented in Figure 5.15.

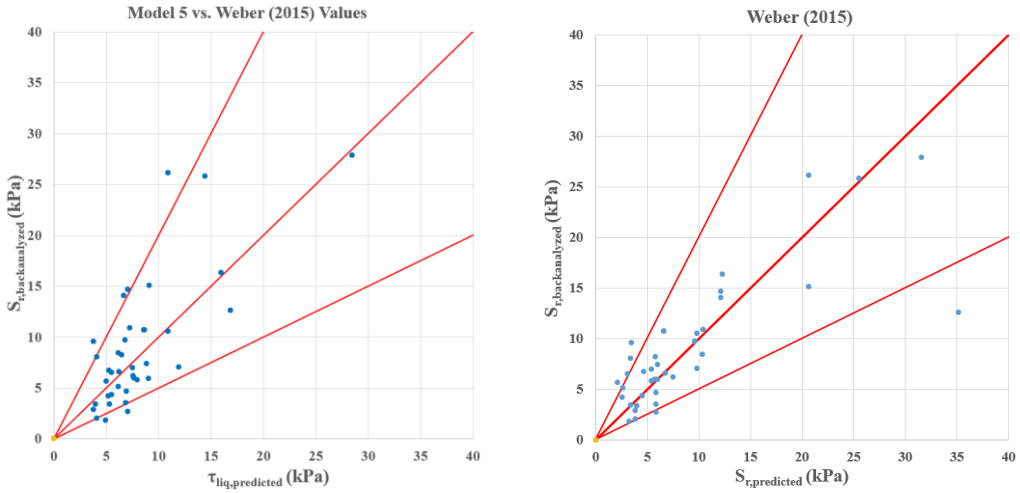

Figure 5.15. Residual strength comparison of Model 5 and Weber (2015)

In addition, the residual plots for SPT resistance ($(N_1)_{60}$), mean grain size (D_{50}), fines content (FC), and coefficient of uniformity (C_u) are obtained as shown in Figure 5.16 for Model 5.

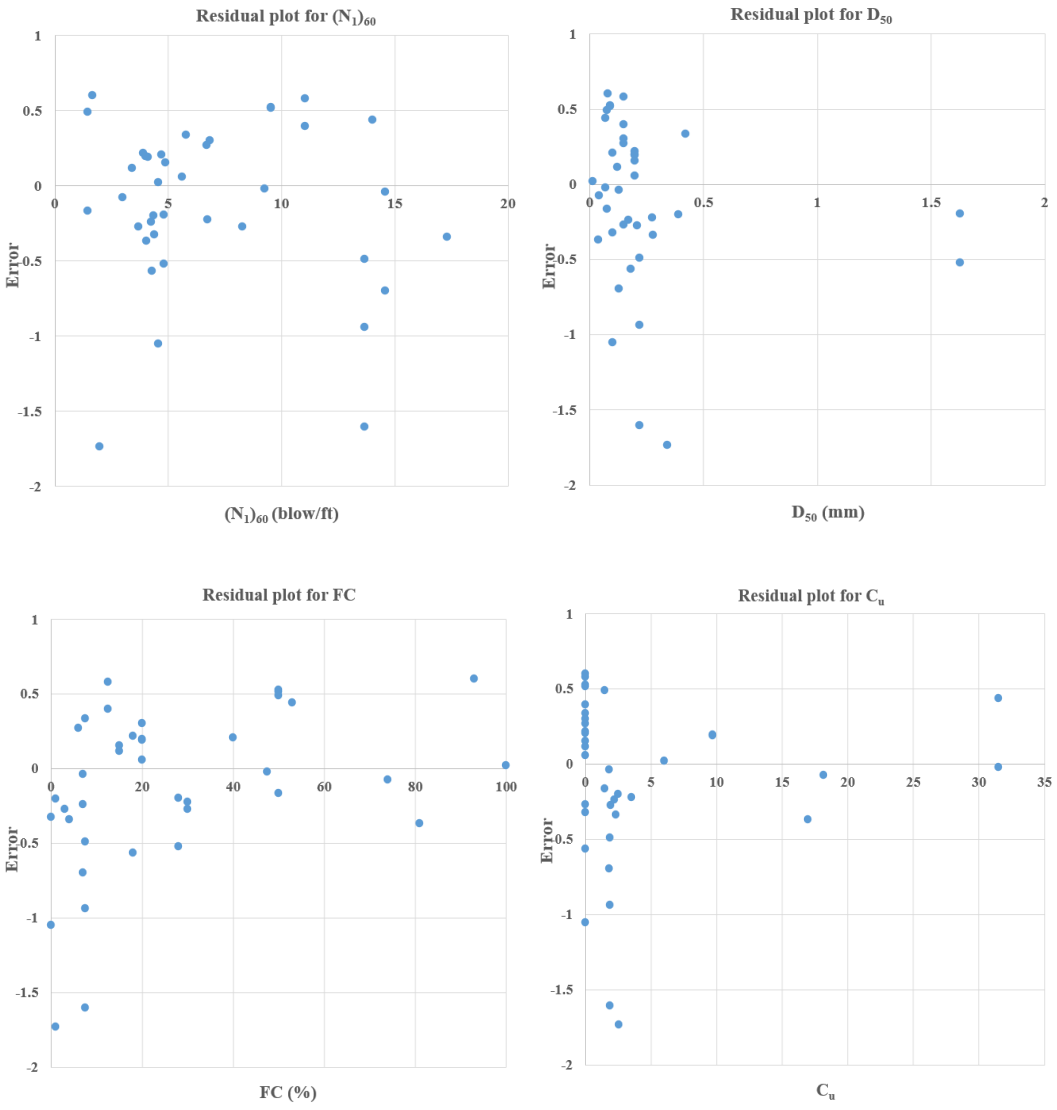

Figure 5.16. Residual plots of input parameters for Model 5

As it can be seen from Figure 5.15, the predicted post-liquefaction shear strength values imply that Model 5 is a viable alternative to the prediction model of Weber (2015). In fact, the predicted post-liquefaction shear strength results fit well to the

modified back-analyses residual strength values of Weber (2015) for smaller strength ranges such as 0-20 kPa. For higher stress ranges, on the other hand, the prediction model of Weber (2015) provides comparable predictions.

When the residual plots shown in Figure 5.16 are examined, it can be judged that a significant trend does not exist for any of the presented input parameters. This means that none of these parameters has a misleading or exaggerated effect on the model. Nevertheless, it is possible to see some minor trends for $(N_1)_{60}$, FC and C_u parameters, which imply that the model provides slightly unsteady results than the usual for some ranges of these parameters. However, the data points distribute around the zero line for most of the cases in general, which implies an unbiased fit to the back-analyses residual strength values. It should also be noted that some scatter data points exist for all input parameters suggesting an imperfect model.

Referring to Figure 5.14, it is also possible to say that isotropic compression curves given in blue color exhibit nonlinearity earlier than 1-10 MPa (typical crushing values reported in the literature) for Model 5. In fact, it is already discussed in Chapter 4 that while the ICCs recommended by Mesri and Vardhanabhuti (2009) given in purple color crush at higher mean effective stress ranges such as 2-20 MPa, this range is much lower for the data presented by Wei and Yang (2019) such as 0.2-0.8 MPa as presented in Figure 4.7. Therefore, there is no consensus in the literature regarding where nonlinearity starts for cohesionless soils. In fact, the difference between the mean effective stress values beyond which the nonlinearity is more pronounced is not significant such that the crushing points of the ICCs shown in Figure 5.14 are similar to the ones reported in Wei and Yang (2019). Also, it should be noted that these curves are plotted by using the average values of the case history database; therefore, they may vary with respect to individual case points once their parameters are employed instead of average values.

The difference between the mean effective stress values beyond which nonlinearity is more pronounced is governed by the nature of the post-liquefaction case history data points such that the database consists of soils with high compressibility. Hence,

they tend to yield and crush earlier at low mean effective stress ranges. In fact, since we do not have data points in those higher mean effective stress ranges, it is difficult to model those regions mathematically. Hence, it is quite challenging for this model to fit the crushing points of the isotropic compression curves with the literature, and residual strength predictions with the ones of Weber (2015) at the same time.

5.1.6 Discussion of Model 6

The sixth residual strength prediction model again utilizes the mathematical form employed for Model 5 for isotropic compression responses, and a semi-logarithmic void ratio versus mean effective stress domain (e vs. ln(p')) for liquefaction states similar to Model 3, Model 4 and Model 5. In other words, the liquefaction state lines are defined as log-linear over the void ratio versus mean effective stress domain.

The only difference between Model 5 and Model 6 is that the minimum limit void ratio that the isotropic state curves become asymptomatic at very high stresses, e_{lim} value, is selected as 0.35 instead of zero in Model 6. This value of 0.35 is not randomly determined, but defined referring to Cubrinovski and Ishihara (2002) as discussed in Section 4.4.2.

The best-fit model parameters are developed as given in Table 4.17 for Model 6 as a result of probabilistic regressions by the Maximum Likelihood Method. Based on these model parameters, the mathematical relationships given in Equation 5-12 and Equation 5-13 are obtained for the isotropic compression curves and liquefaction state lines, respectively.

$$ICC: e = -39.45 - \frac{0.597}{-0.015 + 0.425 \cdot exp\left(-1.6 \cdot \left(p' - 0.001 - \frac{ln\left(\frac{\frac{0.597}{-39.45 - e_0} + 0.015}{0.425}\right)}{1.6}\right)\right)} \quad \text{Equation 5-12}$$

$$LSL: \quad e = (0.155 \cdot e_{max}) - 0.077 \cdot exp\big(0.03 + 1.75 \cdot (e_{max} - e_{min})\big) \cdot \ln\left(p'_{ls}\right) \quad \text{Equation 5-13}$$

Based on these relationships, the case history data points with respect to their initial states and liquefaction states are located in the void ratio versus mean effective stress domain as presented in Figure 5.17.

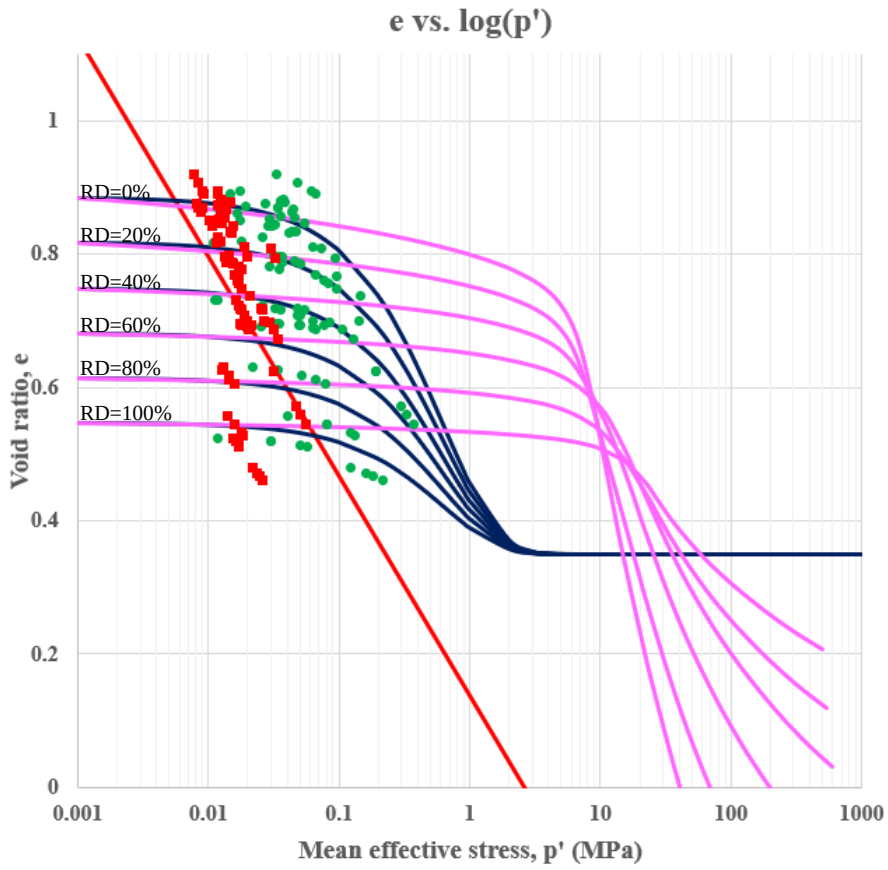

Figure 5.17. Void ratio versus mean effective stress domain for Model 6

Consequently, the post-liquefaction shear strength values and the corresponding probabilities with their natural logarithms are obtained for the second prediction model as tabulated in Table 5.8. The summation of ln(Probability) values, and the corresponding standard deviation of the model are evaluated as -25.84 and 0.46, respectively, for Model 6.

Table 5.8 Predicted post-liquefaction shear strength values and corresponding probabilities for Model 6

#	Case History	$S_{r,backanalyzed}$ (kPa)	$\tau_{liq,predicted}$ (kPa)	P( )	Ln(P)
1	Wachusett Dam - North Dike	10.92	7.72	0.653	-0.426
2	Fort Peck Dam	12.60	18.57	0.608	-0.497
3	Uetsu Railway Embankment	1.82	4.93	0.082	-2.504
4	Lower San Fernando Dam - U/S Slope	25.81	12.14	0.225	-1.491
5	Hachiro-Gata Road Embankment	3.39	5.30	0.541	-0.614
6	La Marquesa Dam - U/S Slope	4.36	5.60	0.749	-0.289
7	La Marquesa Dam - D/S Slope	9.72	7.03	0.678	-0.389
8	La Palma Dam	6.51	5.53	0.817	-0.202
9	Lake Ackerman Highway Embankment	5.12	5.82	0.837	-0.178
10	Chonan Middle School	6.75	5.30	0.757	-0.278
11	Soviet Tajik - May 1 Slide	16.33	16.23	0.870	-0.139
12-1	Shibecha-Cho Embankment	10.73	8.53	0.768	-0.264
12-2		10.73	8.45	0.760	-0.274
13	Route 272 at Higashiarekinai	6.61	6.41	0.868	-0.141
14-1	Zeeland - Vlietepolder	10.53	11.36	0.859	-0.153
14-2		7.05	12.59	0.391	-0.940
15	Sheffield Dam	8.22	6.74	0.792	-0.233
16-1	Helsinki Harbor	2.85	3.86	0.700	-0.356
16-2		2.01	4.31	0.218	-1.524
17	Solfatara Canal Dike	4.19	4.95	0.815	-0.204
18	Lake Merced Bank	5.98	7.86	0.728	-0.318
19	El Cobre Tailings Dam	9.58	4.04	0.148	-1.911
20	Metoki Road Embankment	5.67	4.99	0.837	-0.178
21-1	Hokkaido Tailings Dam	8.06	4.07	0.285	-1.255
21-2		3.43	3.92	0.834	-0.182
22	Upper San Fernando Dam - D/S Slope	27.87	28.13	0.870	-0.139

Table 5.8 (cont'd) Predicted post-liquefaction shear strength values and corresponding probabilities for Model 6

23-1	Tar Island Dyke	15.09	9.74	0.552	-0.594
23-2		26.10	11.88	0.199	-1.612
24	Mochi-Koshi Tailings Dam 1	5.80	7.60	0.732	-0.312
25	Mochi-Koshi Tailings Dam 2	6.97	7.13	0.869	-0.140
26	Nerlerk Embankment Slide 1	4.63	7.43	0.512	-0.670
27	Nerlerk Embankment Slide 2	3.54	7.39	0.241	-1.423
28	Nerlerk Embankment Slide 3	2.70	7.59	0.068	-2.683
29	Asele Road Embankment	6.21	7.71	0.779	-0.250
30-1	Nalband Railway Embankment	7.41	8.08	0.855	-0.157
30-2		5.94	8.20	0.679	-0.387
31-1	Sullivan Tailings	14.08	7.43	0.329	-1.111
31-2		14.69	8.00	0.361	-1.018
32	Jamuna Bridge	8.43	6.06	0.672	-0.397

The comparison of the predicted residual strength values with the modified back-calculated post-liquefaction shear strength values of Weber (2015) for Model 6 is presented in Figure 5.18.

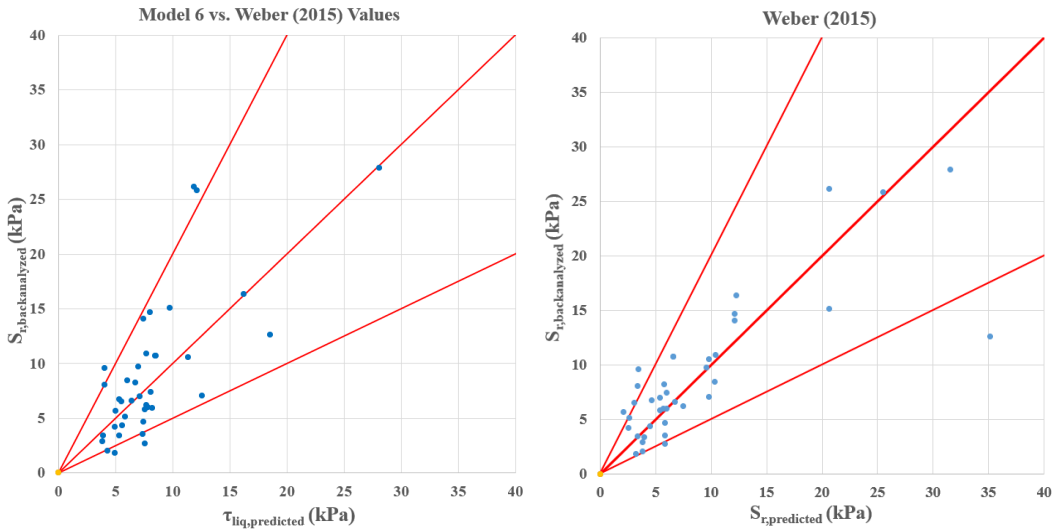

Figure 5.18. Residual strength comparison of Model 6 and Weber (2015)

In addition, the residual plots for SPT resistance ($(N_1)_{60}$), mean grain size (D_{50}), fines content (FC), and coefficient of uniformity (C_u) are obtained as shown in Figure 5.19 for Model 6.

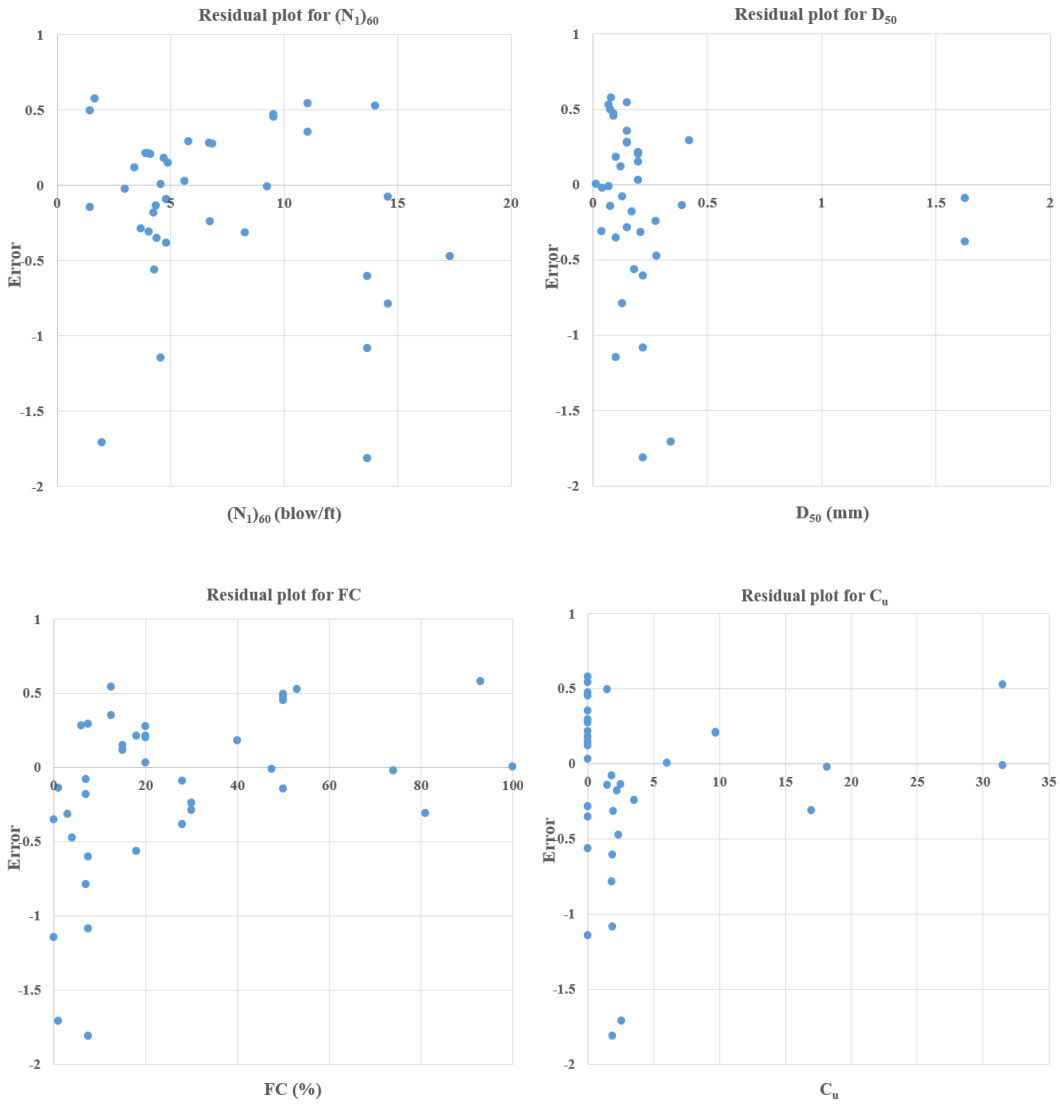

Figure 5.19. Residual plots of input parameters for Model 6

As it can be seen from Figure 5.18, the predicted post-liquefaction shear strength values imply that Model 6 is a viable alternative to the prediction model of Weber (2015). In fact, the predicted post-liquefaction shear strength results fit well to the

modified back-analyses residual strength values of Weber (2015) for smaller strength ranges such as 0-20 kPa. For higher stress ranges, on the other hand, the prediction model of Weber (2015) provides comparable predictions.

When the residual plots shown in Figure 5.19 are examined, it can be judged that a significant trend does not exist for any of the presented input parameters. This means that none of these parameters has a misleading or exaggerated effect on the model. Nevertheless, it is possible to see some minor trends for FC and C_u parameters, which imply that the model provides slightly unsteady results than the usual for some ranges of these parameters. However, the data points distribute around the zero line for most of the cases in general, which implies an unbiased fit to the back-analyses residual strength values. It should also be noted that some scatter data points exist for all input parameters suggesting an imperfect model.

Referring to Figure 5.17, it is also possible to say that isotropic compression curves given in blue color exhibit nonlinearity earlier than typical crushing values reported in the literature for Model 6 for lower relative density ranges. In fact, it is already discussed in Chapter 4 that while the ICCs recommended by Mesri and Vardhanabhuti (2009) given in purple color crush at higher mean effective stress ranges such as 2-20 MPa, this range is much lower for the data presented by Wei and Yang (2019) such as 0.2-0.8 MPa as presented in Figure 4.7. Therefore, there is no consensus in the literature regarding where nonlinearity starts for cohesionless soils. Besides, the mean effective stress values that the nonlinearity starts for higher relative densities fit well to the ones recommended by Wei and Yang (2019) shown in Figure 4.7. Also, it should be noted that these curves are plotted by using the average values of the case history database; therefore, they may vary with respect to individual case points once their parameters are employed instead of average values.

The difference between the mean effective stress values beyond which nonlinearity is more pronounced is governed by the nature of the post-liquefaction case history data points such that the database consists of soils with high compressibility. Hence, they tend to yield and crush earlier at low mean effective stress ranges. In fact, since

we do not have data points in those higher mean effective stress ranges, it is difficult to model those regions mathematically. Hence, it is quite challenging for this model to fit the crushing points of the isotropic compression curves for lower relative densities with the literature, and residual strength predictions with the ones of Weber (2015) at the same time. On the other hand, the ICCs developed for Model 6 for higher relative density ranges fit well with the ones in the literature due to the assigned minimum limit void ratio value (e_{lim}) that the isotropic and liquefaction state curves become asymptomatic at very high stresses. Arranging the e_{lim} value as 0.35 refferring to Cubrinovski and Ishihara (2002) as discussed in Section 4.4.2 increases the mean effective stress values for particle crushing at high relative density ranges, and provides better fits with the literature.

5.1.7 Discussion of Model 7

The seventh residual strength prediction model utilizes a semi-logarithmic void ratio versus mean effective stress domain (e vs. ln(p')) for both the liquefaction and isotropic compression responses. In other words, both isotropic compression and liquefaction state curves are defined as log-linear over the void ratio versus mean effective stress domain.

The best-fit model parameters are developed as given in Table 4.20 for Model 7 as a result of probabilistic regressions by the Maximum Likelihood Method. Based on these model parameters, the mathematical relationships given in Equation 5-14 and Equation 5-15 are obtained for the isotropic compression and liquefaction state lines, respectively.

$$ICL: \quad e = e_0 - \frac{0.012 \cdot exp\big(0.366 \cdot (e_{max} - e_{min})\big)}{1 + 0.309 \cdot RD} \cdot \ln\left(\frac{p'}{0.001}\right) \qquad \text{Equation 5-14}$$

$$LSL: \quad e = 1.333 \cdot e_{max} - \Big(0.046 \cdot exp\big(0.064 + 3.314 \cdot (e_{max} - e_{min})\big)\Big) \cdot \ln\left(\frac{p'_{ls}}{0.001}\right) \qquad \text{Equation 5-15}$$

Based on these relationships, the case history data points with respect to their initial states and liquefaction states are located in the void ratio versus mean effective stress domain as presented in Figure 5.20.

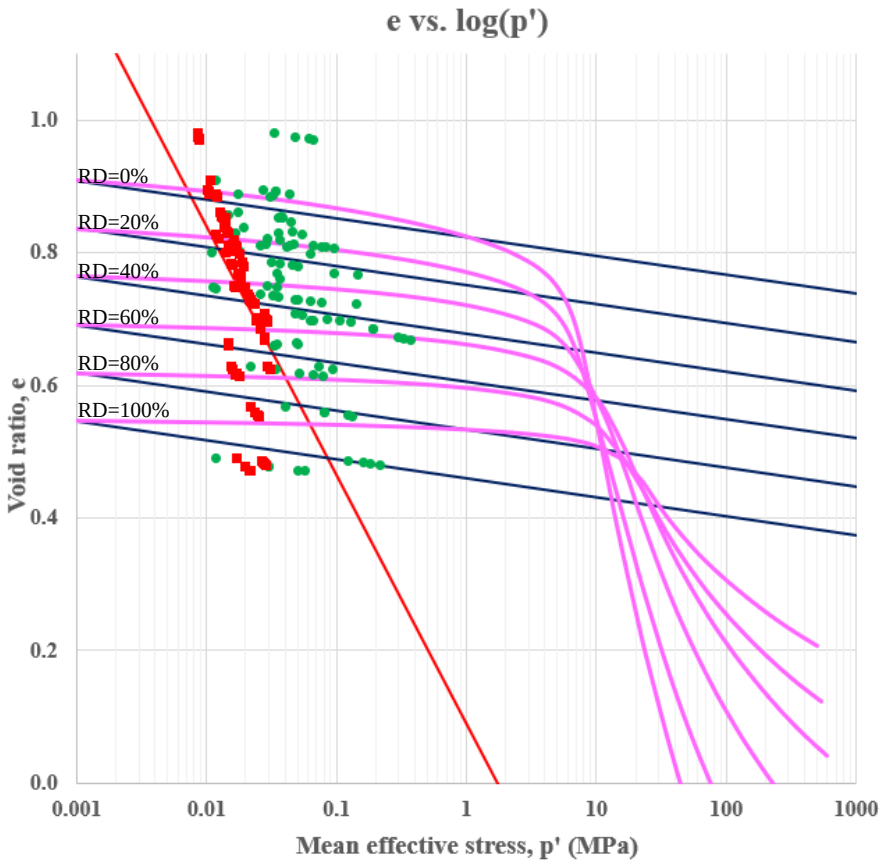

Figure 5.20. Void ratio versus mean effective stress domain for Model 7

Consequently, the post-liquefaction shear strength values and the corresponding probabilities with their natural logarithms are obtained for the third prediction model as tabulated in Table 5.9. The summation of ln(Probability) values, and the corresponding standard deviation of the model are evaluated as -26.72 and 0.48, respectively, for Model 7.

Table 5.9 Predicted post-liquefaction shear strength values and corresponding probabilities for Model 7

#	Case History	$S_{r,backanalyzed}$ (kPa)	$\tau_{liq,predicted}$ (kPa)	P( )	Ln(P)
1	Wachusett Dam - North Dike	10.92	7.12	0.559	-0.582
2	Fort Peck Dam	12.60	10.31	0.758	-0.277
3	Uetsu Railway Embankment	1.82	4.45	0.148	-1.909
4	Lower San Fernando Dam - U/S Slope	25.81	14.35	0.394	-0.931
5	Hachiro-Gata Road Embankment	3.39	5.65	0.473	-0.749
6	La Marquesa Dam - U/S Slope	4.36	5.71	0.707	-0.347
7	La Marquesa Dam - D/S Slope	9.72	6.78	0.626	-0.469
8	La Palma Dam	6.51	5.83	0.805	-0.216
9	Lake Ackerman Highway Embankment	5.12	6.23	0.761	-0.273
10	Chonan Middle School	6.75	5.58	0.764	-0.269
11	Soviet Tajik - May 1 Slide	16.33	15.74	0.824	-0.193
12-1	Shibecha-Cho Embankment	10.73	6.78	0.527	-0.641
12-2		10.73	6.75	0.521	-0.652
13	Route 272 at Higashiarekinai	6.61	6.49	0.826	-0.191
14-1	Zeeland - Vlietepolder	10.53	10.78	0.826	-0.192
14-2		7.05	11.11	0.530	-0.636
15	Sheffield Dam	8.22	6.34	0.716	-0.334
16-1	Helsinki Harbor	2.85	4.20	0.600	-0.511
16-2		2.01	4.49	0.208	-1.572
17	Solfatara Canal Dike	4.19	5.75	0.668	-0.403
18	Lake Merced Bank	5.98	6.84	0.795	-0.230
19	El Cobre Tailings Dam	9.58	4.15	0.185	-1.690
20	Metoki Road Embankment	5.67	5.09	0.806	-0.216
21-1	Hokkaido Tailings Dam	8.06	4.98	0.503	-0.687
21-2		3.43	4.92	0.625	-0.469
22	Upper San Fernando Dam - D/S Slope	27.87	30.05	0.817	-0.203

Table 5.9 (cont'd) Predicted post-liquefaction shear strength values and corresponding probabilities for Model 7

23-1	Tar Island Dyke	15.09	10.46	0.619	-0.479
23-2		26.10	10.64	0.147	-1.920
24	Mochi-Koshi Tailings Dam 1	5.80	8.83	0.566	-0.569
25	Mochi-Koshi Tailings Dam 2	6.97	8.53	0.758	-0.278
26	Nerlerk Embankment Slide 1	4.63	8.13	0.420	-0.867
27	Nerlerk Embankment Slide 2	3.54	7.93	0.205	-1.586
28	Nerlerk Embankment Slide 3	2.70	8.12	0.061	-2.792
29	Asele Road Embankment	6.21	7.01	0.801	-0.222
30-1	Nalband Railway Embankment	7.41	9.62	0.714	-0.336
30-2		5.94	9.74	0.488	-0.717
31-1	Sullivan Tailings	14.08	7.91	0.405	-0.904
31-2		14.69	8.05	0.380	-0.968
32	Jamuna Bridge	8.43	7.23	0.786	-0.241

The comparison of the predicted residual strength values with the modified back-calculated post-liquefaction shear strength values of Weber (2015) for Model 7 is presented in Figure 5.21.

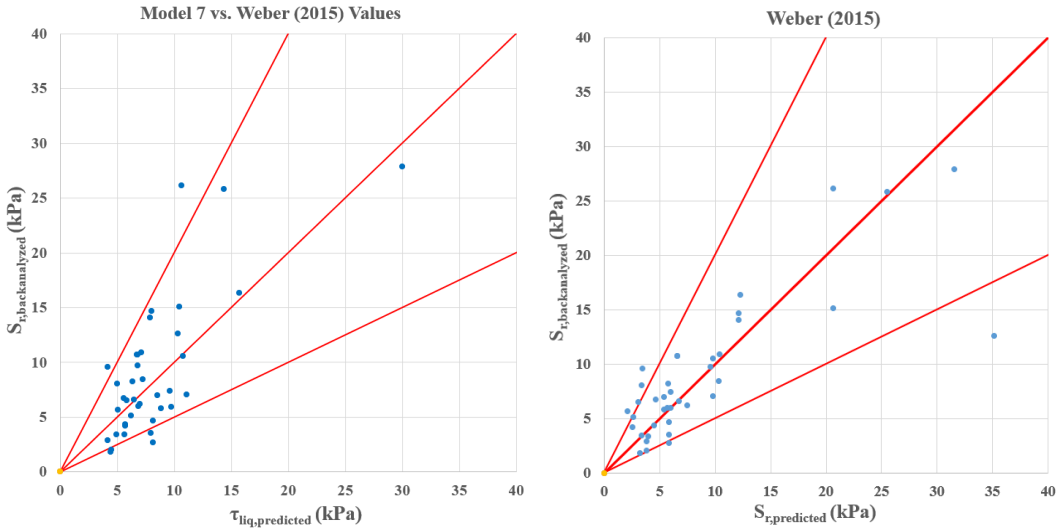

Figure 5.21. Residual strength comparison of Model 7 and Weber (2015)

In addition, the residual plots for SPT resistance ($(N_1)_{60}$), mean grain size (D_{50}), fines content (FC), and coefficient of uniformity (C_u) are obtained as shown in Figure 5.22 for Model 7.

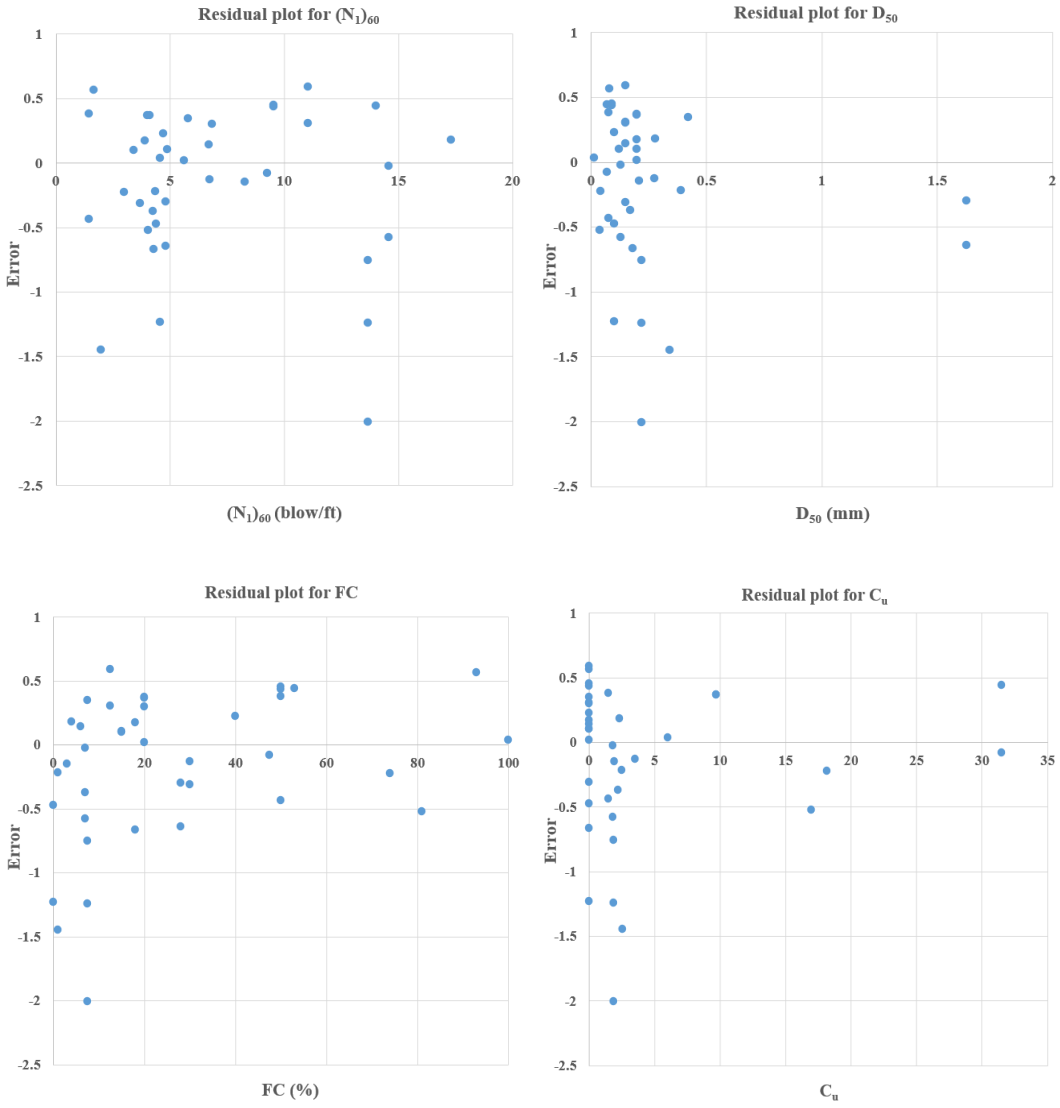

Figure 5.22. Residual plots of input parameters for Model 7

As it can be seen from Figure 5.21, the predicted post-liquefaction shear strength values imply that Model 7 is a viable alternative to the prediction model of Weber (2015). In fact, the predicted post-liquefaction shear strength results fit well to the modified back-analyses residual strength values of Weber (2015) for smaller

strength ranges such as 0-20 kPa. For higher stress ranges, on the other hand, the prediction model of Weber (2015) provides comparable predictions.

When the residual plots shown in Figure 5.22 are examined, it can be judged that a significant trend does not exist for any of the presented input parameters. This means that none of these parameters has a misleading or exaggerated effect on the model. For most of the cases, the data points distribute around the zero line, which implies an unbiased fit to the back-analyses residual strength values. On the other hand, some scatter data points exist for all input parameters suggesting an imperfect model.

Referring to Figure 5.20, it is possible to say that while the isotropic compression lines given in blue color fit well with the ones recommended by Mesri and Vardhanabhuti (2009) given in purple color for lower relative densities, they do not match with each other well for higher relative densities. In fact, the ICLs developed in Model 7 have larger slopes (steeper) than the ICCs suggested by Mesri and Vardhanabhuti (2009). Furthermore, since a semi-logarithmic void ratio versus mean effective stress domain (e vs. ln(p')) is employed for the isotropic compression responses, log-linear lines with no curvature or non-linearity are observed in this domain. It should be noted that these curves are plotted by using the average values of the case history database; therefore, they may vary with respect to individual case points once their parameters are employed instead of average values.

The difference between the slopes of the isotropic compression lines and curves again mainly rises from the nature of the post-liquefaction case history data points such that the database consists of soils with high compressibility. Hence, it is also challenging for this model to fit the isotropic compression lines with the ones in the literature, and residual strength predictions with the ones of Weber (2015) at the same time.

5.2 Comparison of Residual Strength Prediction Models

In the scope of this thesis, totally seven post-liquefaction shear strength prediction models are developed based on the probabilistic regressions by the Maximum Likelihood Method. These prediction models are compared with each other and literature to determine the best of them that produces the most accurate and precise results when compared to back analyses of the same case histories. As discussed in the previous section, the differences between these models rise from the relationships used for the isotropic and liquefaction states. The resulting summation of the maximum likelihood values along with the standard deviations of the model error terms are given in Table 5.10 for each prediction model.

Table 5.10 Summation of the maximum likelihood values and the standard deviations of the model error terms for each prediction model

Prediction Model	Sum ln(Probability)	Model Error Standard Deviation
Model 1	-22.87	0.45
Model 2	-21.28	0.44
Model 3	-23.82	0.45
Model 4	-27.06	0.49
Model 5	-26.00	0.47
Model 6	-25.84	0.46
Model 7	-26.72	0.48

Once the predicted residual strength results are compared with the predictions of Weber (2015) for the same case histories, it is observed that all models provide good results in overall. In fact, each of them can be categorized as a viable and superior alternative to existing post-liquefaction shear strength prediction models available in the literature.

Although each model provides reasonable and compatible results with the literature, there are minor differences exist between them in terms of engineering approaches and statistics. In fact, the statistical differences between these models can be measured by comparing the summation of ln(Probability) values and the corresponding standard deviations of the models. While larger summation of ln(Probability) value and lower model standard deviation imply a better model in terms of statistics, smaller summation of ln(Probability) value and higher model standard deviation imply a worse model. Therefore, it is quite possible to compare the models quantitatively based on their statistical outputs.

On the other hand, the statistical output is not the only factor that determines whether a model is better than the others or not. In fact, it is possible to obtain extremely perfect models in terms of statistics with very large summation of ln(Probability) values and very low model standard deviations. However, these models may not represent the correct engineering behavior.

In this study, the best model is evaluated based on both engineering and statistical point of view. The statistical outputs, i.e., summation of ln(Probability) values and model standard deviations, are compared with each other by considering the engineering behaviors of the models at the same time. The soil responses in each model are evaluated, and the models are listed in order accordingly with respect to their correct behaviors. Consequently, the second prediction model is evaluated as the best model among the developed seven residual strength prediction models in terms of engineering and statistics.

In fact, Model 2 is the model with the largest summation of ln(Probability) and lowest model error standard deviation referring to Table 5.11. Therefore, it is the most accurate and precise model at the same time, and obviously the best model in terms of statistical point of view. Besides, the predicted post-liquefaction shear strength results fit well to the modified back-analyses residual strength values of Weber (2015) for both smaller and larger strength ranges. Therefore, it is applicable for all stress ranges. Moreover, no trend is observed for the case history data points

in any of the residual plots of the input parameters. Hence, none of the input parameters has a misleading or exaggerative effect on the model.

On the contrary, it was pretty challenging to evaluate the best model in terms of engineering scale. The shape and slope of the isotropic compression and liquefaction state curves, the void ratio values, the crushing strengths, etc., are some of the crucial factors that determine the quality of models in terms of engineering behavior and soil responses. Once the prediction models are compared based on these factors, Model 2 and Model 5 are judged to be the best models. When these two models are compared with each other specifically, Model 2 is decided to be better due to the difference of it for the value of the minimum limit void ratio that the isotropic state curves become asymptomatic at very high stresses, e_{lim}. It is concluded that assigning $e_{lim} = 0.35$ instead of zero referring to Cubrinovski and Ishihara (2002) as discussed in Section 4.4.2 is theoretically sounder in terms of liquefaction state because the single-sized sphere shape of the soil particles can be matched with the shape of the soil particles at very high stress ranges as significant level of particle crushing occurs at those extreme stress levels.

For ease of understanding, a step-by-step flow chart for the post-liquefaction shear strength evaluation process by the new liquefaction state-like framework, and a forward analysis example for Model 2 is explained in the next section.

5.3 Flow Chart and Forward Analysis for Liquefaction State Framework

The step-by-step flow chart given below can be taken as the guide for the post-liquefaction shear strength evaluation process by the new liquefaction state-like framework.

Table 5.11 Step-by-step flow chart for the post-liquefaction shear strength evaluation process by the new liquefaction state-like framework

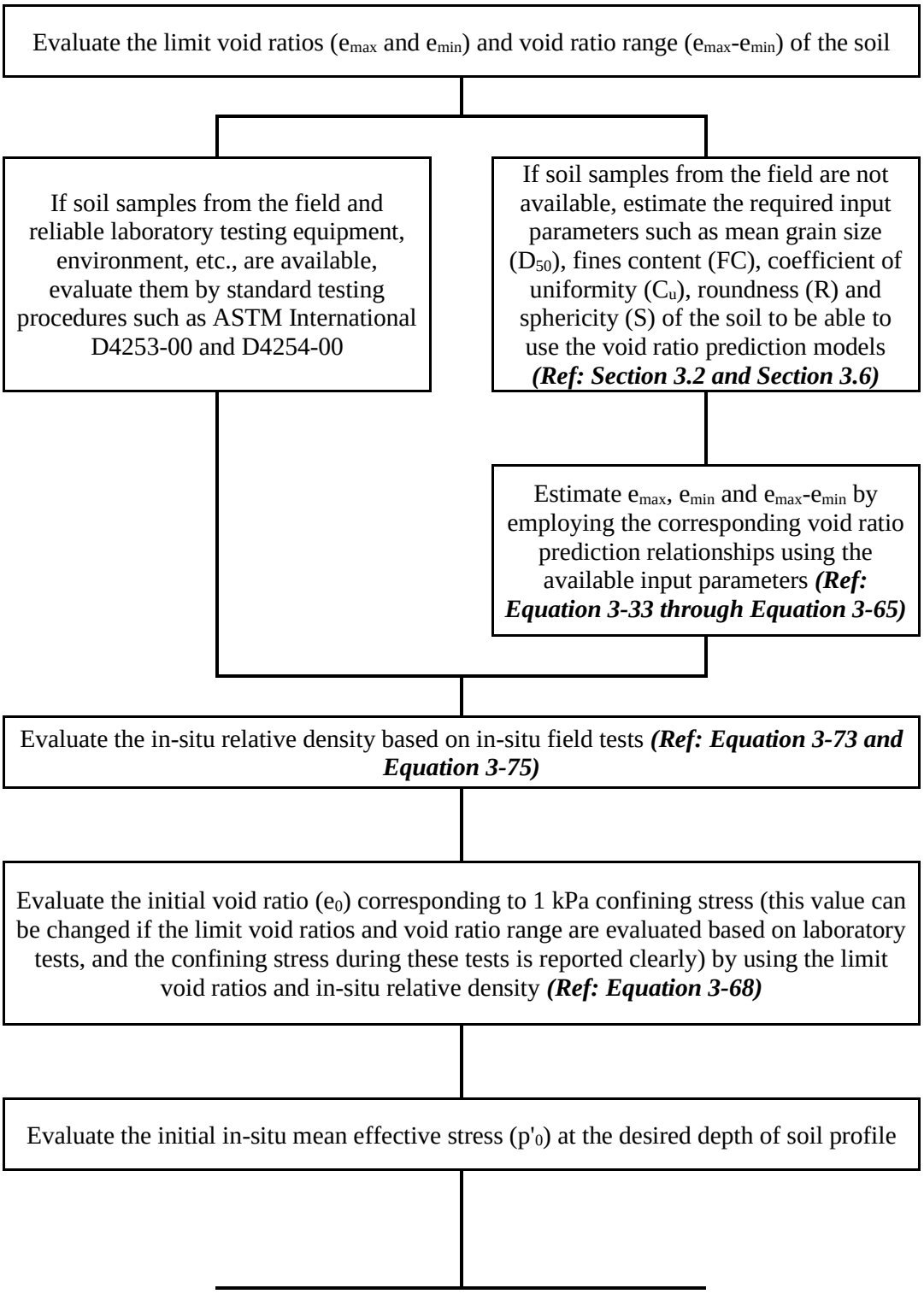

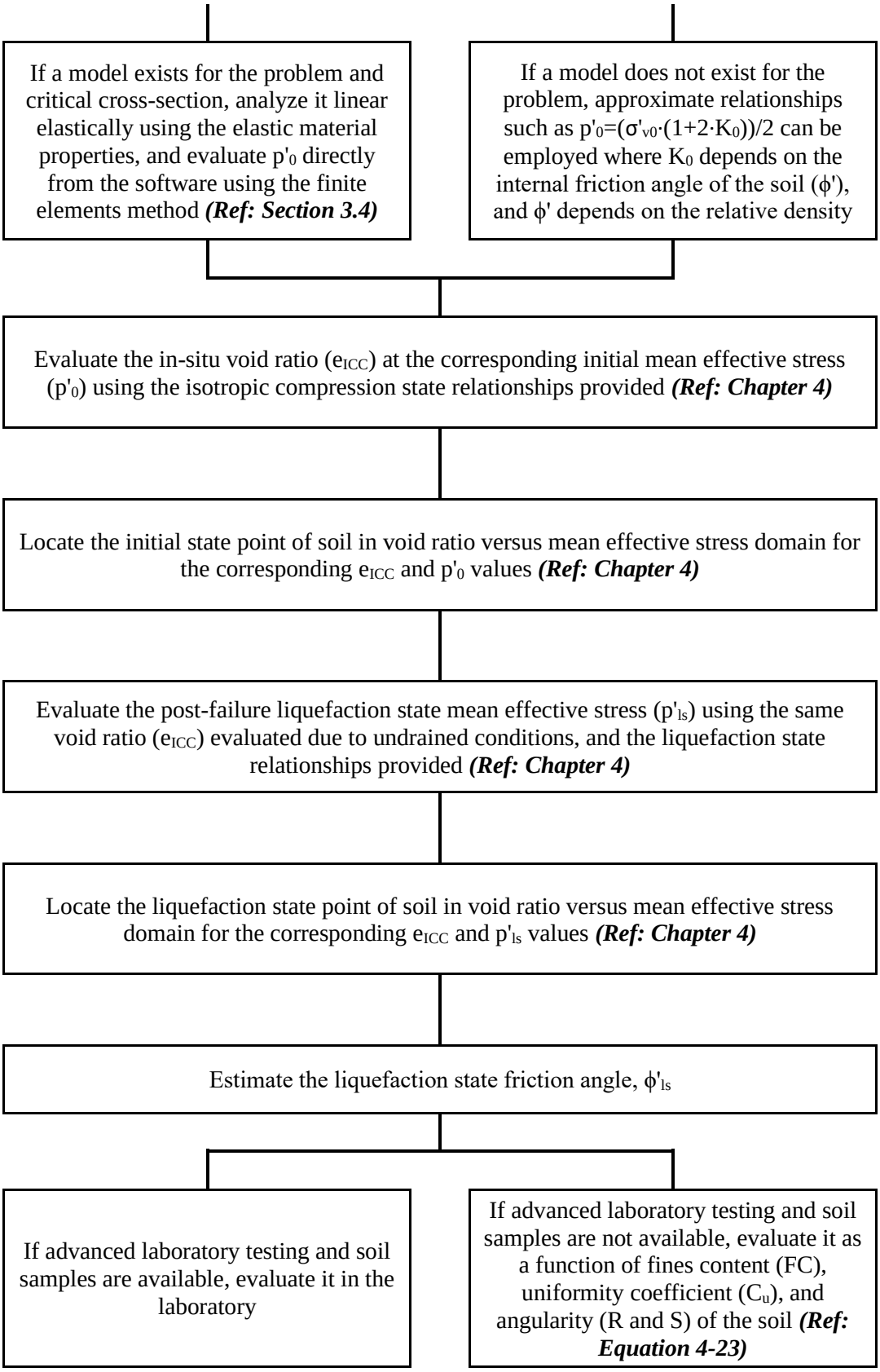
If a model exists for the problem and critical cross-section, analyze it linear elastically using the elastic material properties, and evaluate p'_0 directly from the software using the finite elements method ***(Ref: Section 3.4)***
If a model does not exist for the problem, approximate relationships such as $p'_0=(\sigma'_{v0}\cdot(1+2\cdot K_0))/2$ can be employed where K_0 depends on the internal friction angle of the soil (ϕ'), and ϕ' depends on the relative density
Evaluate the in-situ void ratio (e_{ICC}) at the corresponding initial mean effective stress (p'_0) using the isotropic compression state relationships provided ***(Ref: Chapter 4)***
Locate the initial state point of soil in void ratio versus mean effective stress domain for the corresponding e_{ICC} and p'_0 values ***(Ref: Chapter 4)***
Evaluate the post-failure liquefaction state mean effective stress (p'_{ls}) using the same void ratio (e_{ICC}) evaluated due to undrained conditions, and the liquefaction state relationships provided ***(Ref: Chapter 4)***
Locate the liquefaction state point of soil in void ratio versus mean effective stress domain for the corresponding e_{ICC} and p'_{ls} values ***(Ref: Chapter 4)***
Estimate the liquefaction state friction angle, ϕ'_{ls}
If advanced laboratory testing and soil samples are available, evaluate it in the laboratory
If advanced laboratory testing and soil samples are not available, evaluate it as a function of fines content (FC), uniformity coefficient (C_u), and angularity (R and S) of the soil ***(Ref: Equation 4-23)***

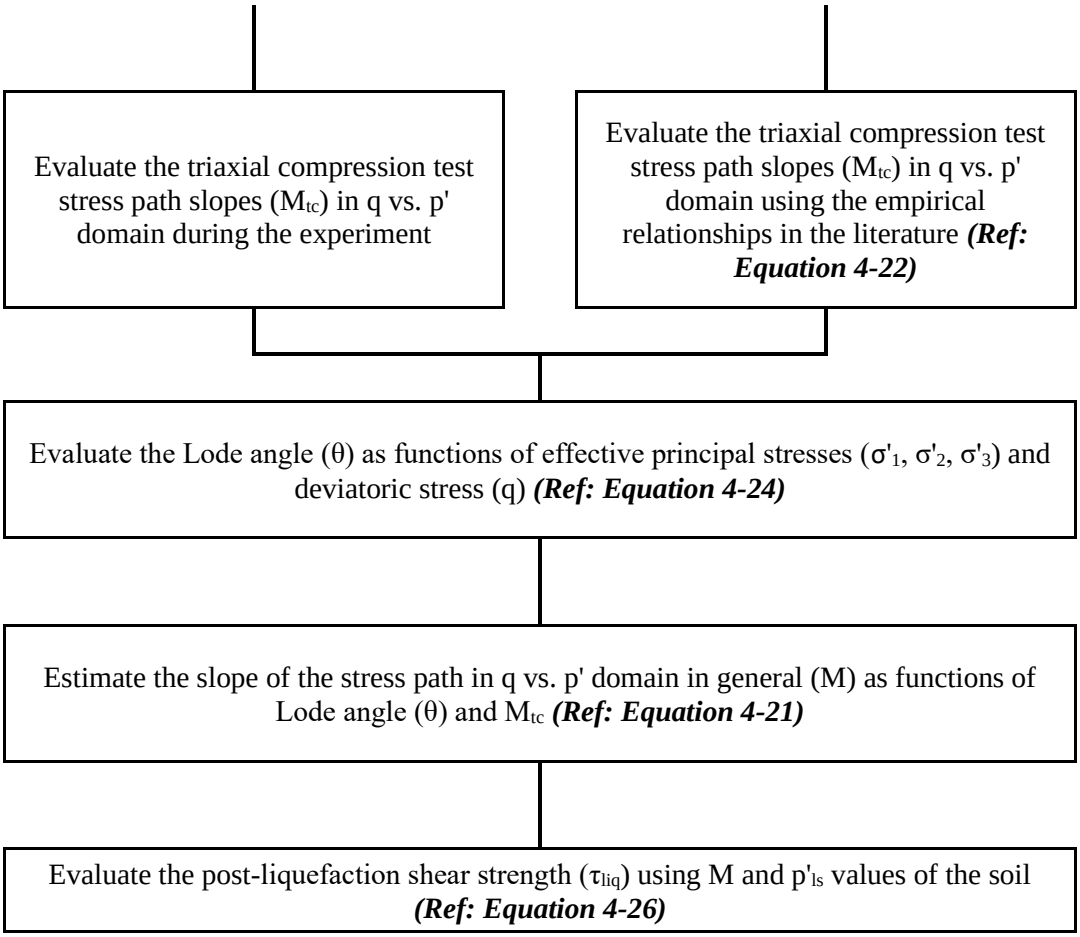

Referring to this step-by-step flow chart, an example forward analysis for the evaluation of post-liquefaction shear strength is explained below for Case History #9 Lake Ackerman Highway Embankment using the relationships recommended for Model 2. It is assumed that the embankment has not failed, and the residual strength is aimed to be evaluated during the design process.

Considering that soil samples are not available from the field, the limit void ratios (e_{max} and e_{min}) and void ratio range (e_{max}-e_{min}) are evaluated by using the void ratio prediction relationships discussed in Section 3.6. To be able to use these relationships, required input parameters are tried to be estimated as much as possible. Since the grain size distribution curve was available for the soil to be analyzed (see Appendix A.9), the mean grain size (D_{50}), fines content (FC), and uniformity coefficient (C_u) values are directly evaluated from the curve as 0.390 mm, 1%, and

2.50, respectively. On the other hand, any information regarding the angularity, i.e., roundness and sphericity, of the soil particles cannot be evaluated. Accordingly, 8th and 9th void ratio prediction models summarized in Table 3.12 are employed for the estimation of limit void ratios and void ratio range.

For the minimum void ratio corresponding to the densest state of the soil, the relationships provided in Equation 3-40 and Equation 3-41 are employed as follows with the corresponding input parameters:

$$Model\ 8{:}\ e_{min} = 0.391 \cdot exp(162.935 \cdot [\ln(0.390 + 3.336)]^{-0.005} - 163.2359) + 0.609 \cdot \left(\frac{0.2767}{1 + 1.6302 \cdot \left(\frac{2.50}{6.3352}\right)^{2.238}} + 0.3243 \right) + (0.0149) = 0.584 \qquad \text{Equation 5-16}$$

$$Model\ 9{:}\ e_{min} = 0.391 \cdot exp(162.935 \cdot [ln(0.390 + 3.336)]^{-0.005} - 163.2359) + 0.609 \cdot \left(\frac{0.2767}{1 + 1.6302 \cdot \left(\frac{2.50}{6.3352}\right)^{2.238}} + 0.3243 \right) + (-0.0022 \cdot (1)^{0.0002} - 0.029) = 0.538 \qquad \text{Equation 5-17}$$

Then, the arithmetic mean of these two predictions are considered as the overall e_{min} value.

$$e_{min} = \frac{0.584 + 0.538}{2} = 0.561 \qquad \text{Equation 5-18}$$

For the maximum void ratio corresponding to the loosest state of the soil, the relationships provided in Equation 3-51 and Equation 3-52 are employed as follows with the corresponding input parameters:

$$Model\ 8{:}\ e_{max} = 0.232 \cdot exp(155.237 \cdot [ln(0.390 + 2.39)]^{-0.004} - 155.22) + 0.768 \cdot \left(\frac{0.5961}{1 + 2.2879 \cdot \left(\frac{2.50}{14.3263}\right)^{2.238}} + 0.4598 \right) + (0.0322) = 0.991 \qquad \text{Equation 5-19}$$

$$Model\ 9: e_{max} = 0.232 \cdot exp(155.237 \cdot [ln(0.390 + 2.39)]^{-0.004} - 155.22) + 0.768 \cdot \left(\frac{0.5961}{1 + 2.2879 \cdot \left(\frac{2.50}{14.3263}\right)^{2.238}} + 0.4598 \right) + (0.1099 \cdot (1)^{0.0011} - 0.1427) = 0.926 \quad \text{Equation 5-20}$$

Then, the arithmetic mean of these two predictions is considered as the overall e_{max} value.

$$e_{max} = \frac{0.991 + 0.926}{2} = 0.958 \quad \text{Equation 5-21}$$

It should be noted that the e_{max} value evaluated based on the prediction relationships given in Equation 5-21 is slightly modified with respect to the performed construction method at the field as discussed in Section 3.6. Since the embankment fill sand was end-dumped into the lake during the construction, it is judged that the soil layer of interest was formed as a result of water sedimentation. Therefore, a slightly lower e_{max} value is assigned for this case referring to Figure 3.23. The modification factor is determined as 0.97 based on the probabilistic regressions by the Maximum Likelihood Method for Model 2 for the cases constructed by the water sedimentation method. Accordingly, the final value of the maximum void ratio corresponding to the loosest state of the soil is evaluated as 0.929 as shown in Equation 5-22.

$$e_{max} = 0.97 \cdot 0.958 = 0.929 \quad \text{Equation 5-22}$$

Then, the void ratio range is evaluated as 0.369 referring to Equation 5-23.

$$e_{max} - e_{min} = 0.929 - 0.561 = 0.369 \quad \text{Equation 5-23}$$

Once the limit void ratios and void ratio range are evaluated for the soil of interest, the in-situ relative density is estimated based on the in-situ test results. Since

Standard Penetration Tests were conducted at the site, the relative density correlations including the SPT resistance as an input parameter are utilized.

Considering that we are dealing with the second sub-section of the cross-section (S2), the energy, equipment, procedure, and overburden stress corrected SPT resistances are evaluated as $(N_1)_{60}$ = 4.39 blow/ft and $(N_1)_{78}$ = (60/78)·4.39 = 3.38 blow/ft referring to the main source of references (see Appendix A.9). Since the fines content value is evaluated as 1%, which is less than 15%, it is judged that the soil of interest consists of sand-type of soils rather than silty soils, and therefore the arithmetic mean of the relative densities evaluated from the relationships recommended by Kulhawy and Mayne (1990) and Cubrinovski and Ishihara (1999) is taken as the overall relative density of the soil. The corresponding relative densities are evaluated as follows by these two methods referring to Equation 3-73 and Equation 3-75, respectively:

$$K\&M\ (1990):\ \frac{4.39}{RD^2} = 60 + 25 \cdot \log(0.390) \rightarrow RD = 0.2971 = 29.71\% \qquad \text{Equation 5-24}$$

$$C\&I\ (1999):\ RD = \sqrt{\frac{3.38 \cdot (0.369)^{1.7}}{9}} = 0.2796 = 27.96\% \qquad \text{Equation 5-25}$$

Then, the arithmetic mean of these two predictions is considered as the overall in-situ relative density value.

$$RD\ (\%) = \frac{29.71 + 27.96}{2} = 28.84\% \qquad \text{Equation 5-26}$$

Accordingly, the initial void ratio (e_0) is estimated referring to Equation 3-68. The corresponding confining stress at that void ratio is approximated as 1 kPa since no laboratory tests were performed for the estimation of limit void ratios.

$$e_0 = 0.929 - \left[\frac{28.84}{100} \cdot 0.369\right] = 0.823 \qquad \text{Equation 5-27}$$

For the second sub-section of the cross-section (S2), the initial in-situ mean effective stress (p'_0) is evaluated as 36.5 kPa for the desired depth of the soil from the PLAXIS

2D Ultimate Connect Edition V22.00.00.1733 software based on linear elastic modeling of the pre-failure cross-section with finite elements method.

Then, the in-situ void ratio (e_{ICC}) at this mean effective stress value is evaluated by using the isotropic state relationship given in Equation 4-12 for Model 2. The slope of the isotropic compression curve is evaluated as $\lambda = 0.265$ referring to Equation 4-13 as shown below:

$$\lambda = \frac{0.372 \cdot exp(-0.37 \cdot 0.369)}{1 + (0.788 \cdot 0.2884)} = 0.265 \qquad \text{Equation 5-28}$$

Then, the void ratio on the isotropic compression curve corresponding to $p' + p'_r = 1$ (unit stress) is evaluated as $N = 0.309$ referring to Equation 4-15 as follows:

$$N = 0.839 \cdot 0.369 = 0.309 \qquad \text{Equation 5-29}$$

Accordingly, the shifting stress controlling the curvature of the isotropic compression curve is estimated as $p'_r = 0.2$ MPa using the relationship provided in Equation 4-14 as follows:

$$p'_r = \left(\frac{0.309}{0.823 - 0.35}\right)^{1/0.265} - 0.001 = 0.200\ MPa \qquad \text{Equation 5-30}$$

Based on these parameters, the in-situ void ratio at $p'_0 = 36.5$ kPa = 0.037 MPa mean effective stress is evaluated as $e_{ICC} = 0.803$ by using the isotropic state relationship given in Equation 4-12 for Model 2.

$$\ln(e - 0.35) = \ln(0.309) - 0.265 \cdot \ln(0.037 + 0.2) \quad \rightarrow \quad e_{ICC} = 0.803 \qquad \text{Equation 5-31}$$

Then, the post-failure liquefaction state mean effective stress (p'_{ls}) is evaluated using the relationship provided in Equation 4-16. The void ratio (e) in Equation 4-16 is already the same as the void ratio evaluated by Equation 4-12, $e_{ICC} = 0.803$, because the void ratio remains the same under undrained conditions. In addition, the slope of the liquefaction state curve is also equal to the slope of the isotropic compression curve due to parallelism between them as discussed in Sections 4.2.1 and 4.2.2.

The void ratio on the liquefaction state curve corresponding to p' + p'_{cr} = 1 (unit stress) is evaluated as Γ = 0.170 referring to Equation 4-19 as follows:

$$\Gamma = 0.461 \cdot 0.369 = 0.170 \quad \text{Equation 5-32}$$

Additionally, e_{c0} = 0.565 is evaluated as a function of maximum void ratio referring to Equation 4-18 as shown below. Therefore, the void ratio located on the liquefaction state curve corresponding to 1 kPa = 0.001 MPa mean effective stress is obtained as 0.565 + 0.35 = 0.915.

$$e_{c0} = (0.984 \cdot 0.929) - 0.35 = 0.565 \quad \text{Equation 5-33}$$

Accordingly, the shifting stress controlling the curvature of the liquefaction state curve is estimated as p'_{cr} = 0.010 MPa using the relationship provided in Equation 4-17 as follows:

$$p'_{cr} = \left(\frac{0.170}{0.565}\right)^{1/0.265} - 0.001 = 0.010\ MPa \quad \text{Equation 5-34}$$

Based on these parameters, the post-failure liquefaction state mean effective stress is evaluated as p'_{ls} = 0.015 MPa = 15 kPa using the relationship provided in Equation 4-16.

$$\ln(0.803 - 0.35) = \ln(0.170) - 0.265 \cdot \ln(p'_{ls} + 0.010) \rightarrow p'_{ls} = 0.015\ MPa \quad \text{Equation 5-35}$$

Accordingly, the initial and liquefaction states of the soil is located in the void ratio versus mean effective stress domain as shown in Figure 5.23.

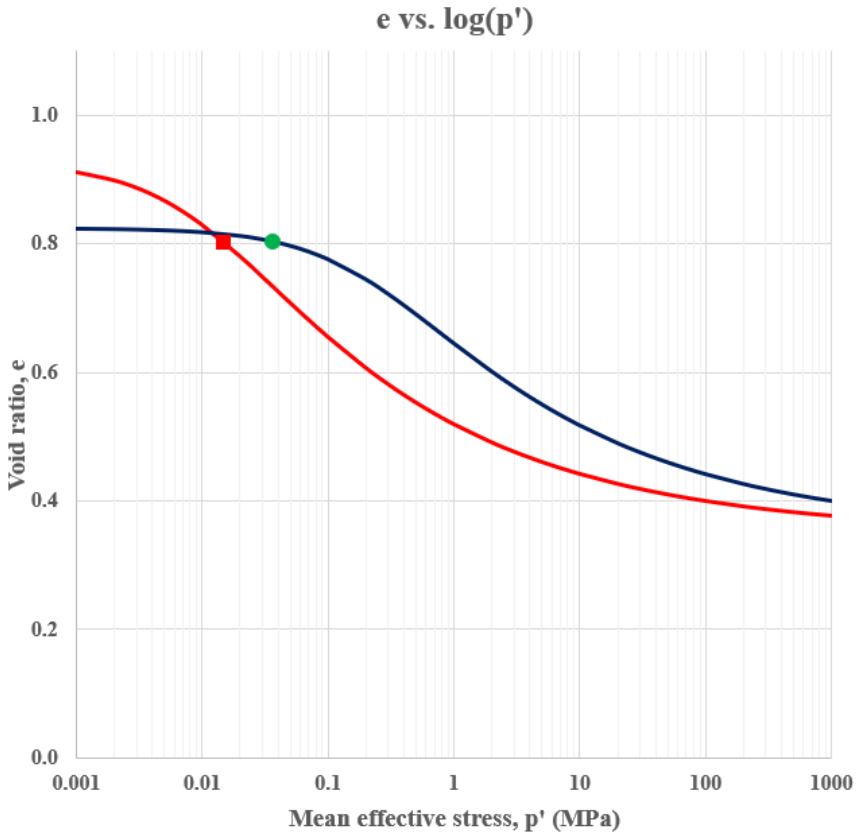

Figure 5.23. Void ratio versus mean effective stress domain for forward analysis example of the second sub-section of Lake Ackerman Highway Embankment case history

In Figure 5.23, while the green dot represents the initial state of the soil with e = 0.803 and p'_0 = 0.037 MPa, the red square symbolizes its liquefaction state with e = 0.803 and p'_{ls} = 0.015 MPa. The blue curve represents the isotropic compression curve evaluated by Equation 4-12 for Model 2 for 28.84% in-situ relative density, and the red curve gives the liquefaction state curve evaluated by Equation 4-16 for the same model.

Then, the liquefaction state friction angle (ϕ'_{ls}) is evaluated as a function of fines content (FC), uniformity coefficient (C_u), and angularity (R and S) of the soil as no laboratory testing data was available regarding the critical state friction angle of the soil. Thus, Equation 4-23 is employed for the estimation of the liquefaction state friction angle, and the value is obtained as ϕ'_{ls} = 23.8° as shown below:

$$\phi'_{ls} = \left(\frac{31.318}{1.088 - 0.25 \cdot \left(\frac{1 - 23.275}{27.725}\right)}\right) \cdot \left(1 + (-0.075 \cdot 0.5 \cdot 0.6)\right) = 23.8° \qquad \text{Equation 5-36}$$

It should be noted that although no information was available about the angularity of the soil particles for this case, roundness and sphericity values are assumed to be 0.50 and 0.60, respectively, to be used in the liquefaction state friction angle estimations. These values are selected carefully such that they fall in the middle of the limits determined by Cho et al. (2006) well given in Equation 3-66. For the cases that these values are evaluated exactly and reliably, more accurate liquefaction state friction angles would be obtained. It should also be noted that since the coefficient of uniformity is estimated as 2.50, which is less than 4, for this case, it is judged that the soil of interest is uniformly graded. Therefore, no additional friction angle is added, i.e., θ_{16} in Equation 4-23 is taken as zero.

Based on this liquefaction state friction angle value, the slope of the stress path corresponding to triaxial compression test is estimated as M_{tc} = 0.930 referring to Equation 4-22 as given below:

$$M_{tc} = \frac{6 \cdot \sin(23.8)}{3 - \sin(23.8)} = 0.930 \qquad \text{Equation 5-37}$$

In addition to that, the Lode angle (θ) is evaluated by using the relationship provided in Equation 4-24. The major, intermediate, and minor effective principal stresses are obtained as 60.2 kPa, 58.0 kPa, and 22.2 kPa, respectively, to be used in the evaluation of the Lode angle based on the linear elastic modeling of the pre-failure cross-section with finite elements method in PLAXIS 2D Ultimate Connect Edition V22.00.00.1733 software. By using these effective principal stress values, the deviatoric stress is evaluated as q = 37 kPa referring to Equation 4-25 as shown below:

$$q = \sqrt{\frac{(60.2 - 58.0)^2}{2} + \frac{(58.0 - 22.2)^2}{2} + \frac{(22.2 - 60.2)^2}{2}} = 37.0\ kPa \qquad \text{Equation 5-38}$$

Accordingly, the Lode angle is determined as θ = 27.11° by using these stress values referring to Equation 4-24 as given below:

$$\theta = \frac{1}{3} \cdot arcsin\left[\frac{1}{37.0^3} \cdot \frac{-27}{2} \cdot \left(\frac{2 \cdot 60.2 - 58.0 - 22.2}{3}\right) \cdot \left(\frac{2 \cdot 58.0 - 60.2 - 22.2}{3}\right) \cdot \left(\frac{2 \cdot 22.2 - 60.2 - 58.0}{3}\right)\right] = 27.11° \quad \text{Equation 5-39}$$

Then, the slope of the stress path in general is estimated as M = 0.889 as function of Lode angle (θ) and the slope of the stress path corresponding to the triaxial compression test (M_{tc}). The corresponding relationship is given below referring to Equation 4-21:

$$M = \frac{3\sqrt{3}}{\cos(27.11) \cdot \left(1 + \frac{6}{0.930}\right) - \sqrt{3} \cdot \sin(27.11)} = 0.889 \quad \text{Equation 5-40}$$

Finally, the post-liquefaction shear strength is evaluated as τ_{liq} = 6.61 kPa for the second sub-section of this case history (S2) referring to Equation 4-26 as shown below:

$$\tau_{liq,i} = \frac{M_i \cdot p'_{ls,i}}{2} = \frac{0.889 \cdot 15}{2} = 6.61\ kPa \quad \text{Equation 5-41}$$

It should be noted that this τ_{liq} value represents the post-liquefaction shear strength value of the second sub-section of the corresponding case history. To be able to evaluate the overall representative post-liquefaction shear strength value of the entire case history, τ_{liq} values of all sub-sections should be multiplied by the individual failure plane lengths of the sub-sections (L_i), and then summed together. After that, this summation is needed to be divided by the total length of the failure plane (L_t) in order to evaluate the representative overall post-liquefaction shear strength value for the corresponding case history, as explained in Equation 4-27. If the cross-section is not divided into smaller pieces, and the material and stress parameters are evaluated for the entire profile completely during the design, then the obtained result automatically gives the overall post-liquefaction shear strength of the soil.

Considering the sub-sectioning case instead, the failure plane lengths of the first, second, and third sub-sections (S1, S2, and S3) remaining in the potential liquefied zone are evaluated as 5.9 m, 12.5 m, and 11.2 m, respectively, based on the pre-failure geometry of the soil profile. In addition, the post-liquefaction shear strength values of the first and third sub-sections are estimated as 5.49 kPa and 4.18 kPa, respectively, with respect to the same procedure followed for the second sub-section. Accordingly, the overall post-liquefaction shear strength of the case history is evaluated as 5.47 kPa referring to Equation 4-27 as shown below:

$$\tau_{liq,overall} = \frac{(5.49 \cdot 5.9) + (6.61 \cdot 12.5) + (4.18 \cdot 11.2)}{5.9 + 12.5 + 11.2} = 5.47\ kPa \qquad \text{Equation 5-42}$$

It should be noted that Weber (2015) reports 5.12 kPa post-liquefaction shear strength for Lake Ackerman Highway Embankment case history based on the back-analysis with the incremental momentum method explained in Section 2.2.6. In fact, it is one of the Group A high-qualified cases of Weber (2015) that the incremental momentum method is applied; therefore, the back-analysis result is also considered to be reliable in this study, and the value is directly used as 5.12 kPa without any change.

When the predicted post-liquefaction shear strength value (5.47 kPa) of Model 2 is compared with the back-calculated post-liquefaction shear strength value of Weber (2015) (5.12 kPa), only 6.84% absolute error is obtained as shown in Equation 5-43. This error is judged to be pretty low, and it is decided that the predicted residual strength value fits well with the target back-analysis result.

$$Error\ (\%) = \left|\frac{S_{r,backanalyzed} - \tau_{liq,predicted}}{S_{r,backanalyzed}}\right| \cdot 100 = \left|\frac{5.12 - 5.47}{5.12}\right| \cdot 100 = 6.84\% \qquad \text{Equation 5-43}$$

CHAPTER 6

SUMMARY AND CONCLUSIONS

6.1 Summary

Although the term “soil liquefaction” was used earlier, major advances in the field have started after the 1964 Great Alaskan Earthquake (M_W = 9.2) and the 1964 Niigata Earthquake (M_W = 7.7). At the early stages, the evaluation of initiation and triggering were the only concerns about soil liquefaction assessments. Numerous well-established methods including empirical methods based on laboratory and in-situ tests, and advanced fully nonlinear constitutive models using finite elements or finite difference computer analysis frameworks have advanced since then.

As the decades passed, liquefaction risk and mitigation techniques began to develop. These developments also initiated the investigation of the resulting performances; in other words, the consequences of liquefaction triggering in terms of deformations, displacements, and damages. While the post-liquefaction strengths and stiffnesses were commonly assumed to be rather small and erroneously assumed to be zero, it was soon realized that this approach was totally over-conservative with the further understanding of the mechanics of soil liquefaction and critical state soil mechanics and the development of advanced laboratory techniques covering large strain ranges. Accordingly, more accurate and hence realistic post-liquefaction strength and performance assessment methods are proposed, and continuing development of these assessments has been ongoing over the past decades.

Due to the difficulties and challenges in large strain cyclic laboratory testing, empirical and semi-empirical relationships founded on back-analyses of full-scale field liquefaction failure case histories have become the preferred approach in engineering practice for the evaluation of residual strengths. Therefore, developing relationships for the post-liquefaction shear strength requires the compilation of

high-quality case histories from liquefaction-induced failure sites. Previous studies exhibited perfect examples of these efforts, and contributed to the completion of the entire puzzle. They developed new methods including the contribution of momentum effects to perform more accurate and reliable back-analyses, and these efforts resulted in a high-qualified case history database at the end. Accordingly, new predictive relationships for engineering evaluation of post-liquefaction strength were developed by probabilistic regressions including the uncertainties in the case history database.

Although very detailed and transparently documented studies were performed on this topic in the literature, the back-analysis of the case histories were not totally perfect at all. In fact, the differences between the back-analysis results of various studies source from the engineering approach followed. Various engineering judgments had to be made in this study, and the case history database is believed to be improved along many paths. The back-analysis post-liquefaction shear strength results are arranged in a sounder way, and the biased approaches followed by previous studies are discussed as much as possible. Consequently, a clear and reliable case history back-analysis database is prepared to be used in the development of post-liquefaction shear strength prediction relationships.

Commonly, previous studies on post-liquefaction shear strength recommend undrained residual strength relationships as a function of equipment, energy, and procedure corrected (also some include fines content correction) SPT resistance, and initial in-situ effective vertical stress. On the other hand, the use of the term “undrained” without any reference to the induced excess pore pressures can be misleading for practicing engineers, who are much familiar with performing effective stress-based stability assessments for cohesionless soils.

Hence, a critical state-like liquefaction state framework is introduced in this thesis to assess the post-liquefaction shear strength of soils on the basis of back-analyses of available case histories. The void ratio versus mean effective stress domain, which is a well-known domain in geotechnical engineering in performing effective stress-

based stability assessments for cohesionless soils, is defined instead of the strength versus penetration resistance domain suggested by previous studies. Therefore, the mean effective stresses, void ratios, and relative densities are selected as the key factors of the new framework. Accordingly, new material properties regarding the physical nature and physical state of the soil such as mean grain size (D_{50}), fines content (FC), coefficient of uniformity (C_u), roundness (R) and sphericity (S) are defined as the new descriptive key parameters of the problem in addition to SPT resistances.

Once the limit void ratios, void ratio ranges, in-situ relative densities, and initial void ratios are estimated by using the new descriptive key parameters abovementioned, the corresponding initial states of the soils are defined in e vs. p' domain by employing isotropic state relationships. Required parameters to evaluate these isotropic compression curves are discussed detailly, and defined as functions of various material properties. Accordingly, the liquefaction states of the soils are defined in the same domain that each soil particle follows after the liquefaction. This state is defined such that the initial location of the soils shifts horizontally in the void ratio versus the mean effective stress domain as a result of changing pore water pressures and mean effective stresses during seismic earthquake shaking or vibration. Again, the required parameters to evaluate liquefaction state curves are discussed detailly, and defined as functions of various material properties.

It should be noted that previous studies also consider the effect of in-situ relative densities indirectly by implementing an in-situ test index metric (e.g., $(N_1)_{60}$, q_c, V_s, etc.) in their residual strength relationships to represent the capacity of the soil. This parameter is commonly the SPT resistance due to the wide usage of this test all around the world and the abundance of conversions available in the literature to convert other types of penetration resistances to SPT resistance. On the other hand, it is always a problem to convert other types of resistances to an equivalent SPT resistance. However, the in-situ relative densities and void ratios of the cases are presented in the correct domain immediately as a result of the void ratio versus mean effective stress domain. Therefore, the differences in in-situ tests are automatically

eliminated as the in-situ void ratio is unique for all tests, and it is possible to estimate it by using correlations developed by all types of experiments.

It is also important that in-situ effective vertical stress (σ'_{v0}) is the only stress component in previous studies to represent the confining effects. On the other hand, other stress components including the horizontal stresses in out-of-plane and in-plane directions also have effects on confining. Neglecting these impacts and imposing all confining effects to initial effective vertical stress theoretically weakens other studies. Hence, the confining effect of the liquefied soil is well better implemented in this study by considering three-dimensional (3D) stress components together. The effects of major, intermediate, and minor effective principal stresses, mean effective stresses and deviatoric stresses are all included in the evaluation of residual strengths.

The Maximum Likelihood Method is used to develop fully probabilistic prediction relationships and corresponding model parameters. No further additional weighting factors are employed for the case histories to account their quality of information and level of documentation; therefore, a subjective engineering judgment is avoided at this point. Although totally different approaches from head to toe are followed in this study, the predictions have shown a good agreement with previous studies. Significant advantages of the new framework are observed, and the void ratio versus mean effective stress domain is judged to be more correct for representing the post-liquefaction shear strengths. In fact, this study provides relatively more accurate and precise models thanks to its strong theoretical background. As a result, it is quite advantageous to use recommended relationships in the design of routine and high-level projects.

6.2 Conclusions

Based on the new liquefaction state framework compatible methodology to evaluate post-liquefaction strength of soils on the basis of back-analyses of available case

histories, totally seven prediction models are developed in this study including different approaches for isotropic and liquefaction states. While a nonlinear liquefaction state curve is defined in void ratio versus mean effective stress domain for the first two prediction models, a log-linear liquefaction state curve is defined for the rest five prediction models. Similarly, different isotropic compression curves are also defined in these models such that while the volume-stress model under isotropic states recommended by Sheng et al. (2008) is employed in the first four prediction models, a new volume-stress model is developed in this study for isotropic states, and non-linear isotropic compression curves are developed accordingly for two of the rest three prediction models. For the last prediction model, a log-linear isotropic compression line is defined in void ratio versus mean effective stress domain.

It is judged in this study that the approaches followed by Weber (2015) during the back-analyses of the case histories were the most reasonable and logical ones when compared to the approaches followed by other previous studies. Therefore, the predicted post-liquefaction shear strength values in this study are compared with the back-analyses results of Weber (2015) during the probabilistic regressions by the Maximum Likelihood Method. On the other hand, the back-analyses results of Weber (2015) are not used directly during the probabilistic regressions, but modified slightly for some cases due to the reasons explained in Chapter 4.

Once the seven prediction models are compared with each other and the literature in terms of both statistical and engineering points of view, the second prediction model is evaluated as the best model among them. Therefore, Model 2 is recommended in this study in the end for the most accurate and precise evaluations of post-liquefaction shear strengths of soils.

Referring to Model 2, Equation 6-1 and Equation 6-2 are recommended for the evaluation of isotropic compression and liquefaction state curves, respectively.

$$ICC: \quad \ln(e-0.35) = \ln\left(0.839 \cdot (e_{max}-e_{min})\right) - \left(\frac{0.372 \cdot exp\left(-0.37 \cdot (e_{max}-e_{min})\right)}{1+0.788 \cdot RD}\right) \cdot \ln\left[p' + \left(\frac{0.839 \cdot (e_{max}-e_{min})}{e_0 - 0.35}\right)^{\frac{1+0.788 \cdot RD}{0.372 \cdot exp\left(-0.37 \cdot (e_{max}-e_{min})\right)}} - 0.001\right] \quad \text{Equation 6-1}$$

$$LSC: \quad ln(e-0.35) = \ln\left(0.461 \cdot (e_{max}-e_{min})\right) - \left(\frac{0.372 \cdot exp\left(-0.37 \cdot (e_{max}-e_{min})\right)}{1+0.788 \cdot RD}\right) \cdot \ln\left(p'_{ls} + \left(\frac{0.461 \cdot (e_{max}-e_{min})}{0.984 \cdot e_{max} - 0.35}\right)^{\frac{1+0.788 \cdot RD}{0.372 \cdot exp\left(-0.37 \cdot (e_{max}-e_{min})\right)}} - 0.001\right) \quad \text{Equation 6-2}$$

The final mean effective stress values after the liquefaction are evaluated by solving p'_{ls} in Equation 6-2. The closed-form solution of the relationship is provided in Equation 6-3.

$$p'_{ls} = exp\left(\frac{\ln\left(0.461 \cdot (e_{max}-e_{min})\right) - \ln(e_{ICC}-0.35)}{\frac{0.372 \cdot exp\left(-0.37 \cdot (e_{max}-e_{min})\right)}{1+(0.788 \cdot RD)}}\right) - \left(\frac{0.461 \cdot (e_{max}-e_{min})}{(0.984 \cdot e_{max}) - 0.35}\right)^{\frac{1+(0.788 \cdot RD)}{0.372 \cdot exp\left(-0.37 \cdot (e_{max}-e_{min})\right)}} + 0.001 \quad \text{Equation 6-3}$$

In this equation, e_{ICC} can be evaluated by using Equation 6-1 since the void ratio remains the same under undrained conditions.

Then, the post-liquefaction shear strength can be evaluated by using the relationship provided in Equation 6-4.

$$\tau_{liq} = \frac{M \cdot p'_{ls}}{2} \quad \text{Equation 6-4}$$

In this relationship, while p'_{ls} represents the final mean effective stress of soil after the liquefaction evaluated by Equation 6-3, M symbolizes the slope of the stress path in q vs. p' domain in general, which can be estimated by Equation 6-5 as functions of the slope of the stress path in q vs. p' domain for triaxial compression tests (M_{tc}) and Lode angle (θ).

$$M = \frac{3\sqrt{3}}{cos\theta \cdot \left(1 + \frac{6}{M_{tc}}\right) - \sqrt{3} \cdot sin\theta} \quad \text{Equation 6-5}$$

M_{tc} values can be evaluated by Equation 6-6 referring to the fundamentals of the critical state theory in literature.

$$M_{tc} = \frac{6 \cdot \sin(\phi'_{ls})}{3 - \sin(\phi'_{ls})} \qquad \text{Equation 6-6}$$

Here, ϕ'_{ls} symbolizes the liquefaction state friction angle of the soil which can be estimated as functions of fines content (FC), coefficient of uniformity (C_u), and angularity (R and S) of soil as shown in Equation 6-7. In this equation, the constant 0.819 represents the additional friction angle value added for well-graded soils (C_u > 4). It should be noted that fines content is given in terms of percentage in this relationship, and its value is limited with an upper bound of 50%.

$$\phi'_{ls} = \left(\frac{31.318}{1.088 - 0.25 \cdot \left(\frac{FC - 23.275}{27.725} \right)} \right) \cdot \left(1 - (0.075 \cdot R \cdot S) \right) + 0.819 \qquad \text{Equation 6-7}$$

The Lode angle (θ) used in Equation 6-5 can be evaluated as functions of effective principal stresses and deviatoric stress as shown in Equation 6-8.

$$\theta = \frac{1}{3} \cdot arcsin \left[\frac{1}{q^3} \cdot \frac{-27}{2} \cdot \left(\frac{2 \cdot \sigma'_1 - \sigma'_2 - \sigma'_3}{3} \right) \cdot \left(\frac{2 \cdot \sigma'_2 - \sigma'_1 - \sigma'_3}{3} \right) \cdot \left(\frac{2 \cdot \sigma'_3 - \sigma'_1 - \sigma'_2}{3} \right) \right] \qquad \text{Equation 6-8}$$

For the definition of deviatoric stress, the mathematical form provided in Equation 6-9 can be employed.

$$q = \sqrt{\frac{(\sigma'_1 - \sigma'_2)^2}{2} + \frac{(\sigma'_2 - \sigma'_3)^2}{2} + \frac{(\sigma'_3 - \sigma'_1)^2}{2}} \qquad \text{Equation 6-9}$$

For ease of understanding, a step-by-step flow chart for the post-liquefaction shear strength evaluation process by the new liquefaction state-like framework, and a forward analysis example for Model 2 is explained in Section 5.3.

It should be noted that Model 2 is the one with the highest summation of ln(Probability) and lowest model standard deviation among the seven prediction models as shown in Table 5.10. Therefore, it is the most accurate and precise model at the same time. Besides, the predicted post-liquefaction shear strength results fit well to the modified back-analyses residual strength values of Weber (2015) for both smaller and larger strength ranges as shown in Figure 5.6. Moreover, no trend is observed for the case history data points in any of the residual plots of the input parameters as shown in Figure 5.7, which means none of the input parameters has a misleading or exaggerative effect on the model. Hence, it is quite possible to say that it offers potentially significant advantages over previously available recommendations, and provides a viable alternative to the residual strength prediction models existing in the literature. In fact, the new liquefaction-state framework and corresponding void ratio versus mean effective stress domain are theoretically sounder than the frameworks of the previous studies.

6.3 Future Works

Developing relationships for the post-liquefaction shear strength predictions requires the compilation of high-quality case histories from liquefaction-induced failure sites. On the other hand, most of these cases suffered from liquefaction many years ago. Even, some of them occurred at times when the liquefaction phenomenon was not well-studied. Therefore, documentation is not sufficient for most of the post-liquefaction case histories available in the literature. In fact, poor documentation is the main source of uncertainties and variances in many of the cases. Hence, it is quite challenging to evaluate the descriptive parameters of the problem such as soil properties (mean grain size, fines content, uniformity coefficient, roundness, sphericity, unit weight, etc.), site conditions (pre-failure and post-failure geometries, location of the water table level at the time of failure, soil stratigraphy, construction method, penetration resistance, etc.) and so on. Therefore, further investigations to these failure sites such as soil sampling, in-situ field testing, etc., may provide

additional information corresponding to these missing points, and increase the quality of available data. Once more information is learned for the case histories, the quality of the residual strength back-analyses and the accuracy of the prediction relationships may increase.

In fact, individual back-analyses for the post-liquefaction case histories have not been performed in this study for the evaluation of residual strengths due to the mentioned poor documentation issue. It is obvious that a significant effort is required to back-calculate the residual strengths of these case histories, and still many points will remain unclear in terms of engineering. Thus, the back-analyses results of Weber (2015) are used in this study with minor modifications instead. At this point, it is my debt and responsibility to thank Joseph Patrick Weber and UC Berkeley GeoSystems Engineering community for putting this extraordinary effort into doing such a detailed study. In fact, thanks are for all studies focused on this topic and shed light on the future studies such as Seed and Harder (1990), Olson and Stark (2002), Wang (2003), Kramer (2008), and so on. Nevertheless, individual back-analyses for the post-liquefaction case histories may be performed in the future for this study in order to develop more accurate and fully independent prediction relationships in terms of back-calculated case history database.

Last but not least, an uncertainty analysis for the input parameters of the problem may be performed for the post-liquefaction shear strength prediction relationships in the future to be able to include the effect of variances of material properties, site conditions, construction methods, etc., in the prediction models.

REFERENCES

Alarcon-Guzman, A., Leonards, G. A., & Chameau, J. L. (1988). Undrained monotonic and cyclic strength of sands. Journal of Geotechnical Engineering, 114(10), 1089-1109.

Andresen, A., & Bjerrum, L. (1968). Slides in subaqueous slopes in loose sand and silt. Norwegian Geotechnical Institute Publication No. 81, 1-9.

Andrus, R. D., & Youd, T. L. (1987). Subsurface investigation of a liquefaction-induced lateral spread, Thousand Springs Valley, Idaho.

ASTM International (2000). D4253-00 Standard test methods for maximum index density and unit weight of soils using a vibratory table. ASTM Standards.

ASTM International (2000). D4254−00 Standard test methods for minimum index density and unit weight of soils and calculation of relative density. ASTM Standards.

ASTM International (2017). D2487-17e1 Standard practice for classification of soils for engineering purposes (Unified Soil Classification System). ASTM Standards.

ASTM International (2017). D6913-D6913M-17 Standard test methods for particle-size distribution (gradation) of soils using sieve analysis. ASTM Standards.

Barrett, P. J. (1980). The shape of rock particles, a critical review. Sedimentology, 27(3), 291-303.

Barton, M. E, Palmer, S. N. (1988). The relative density of geologically aged British fine and fine-medium sands. Quarterly Journal Engineering Geology, London, UK, 22:49–59.

Been, K., Conlin, B. H., Crooks, J. H. A., Fitzpatrick, S. W., Jefferies, M. G., Rogers, B. T., & Shinde, S. (1987). Back analysis of the Nerlerk berm liquefaction slides: Discussion. Canadian Geotechnical Journal, 24(1), 170-179.

Belkhatir, M., Arab, A., Della, N., & Schanz, T. (2012). Experimental study of undrained shear strength of silty sand: effect of fines and gradation. Geotechnical and Geological Engineering, 30(5), 1103-1118.

Belkhatir, M., Schanz, T., & Arab, A. (2013). Effect of fines content and void ratio on the saturated hydraulic conductivity and undrained shear strength of sand–silt mixtures. Environmental Earth Sciences, 70(6), 2469-2479.

Bennett, M. J. (1989). Liquefaction analysis of the 1971 ground failure at the San Fernando Valley Juvenile Hall, California. Bulletin of Association of Engineering Geologists, 26(2), 209-226.

Bensoula, M., Missoum, H., & Bendani, K. (2018). Liquefaction potential sand-silt mixtures under static loading. Revista de la Construcción. Journal of Construction, 17(2), 196-208.

Bieganousky, W. A., & Marcuson III, W. F. (1976). Uniform placement of sand. Journal of the Geotechnical Engineering Division, 102(3), 229-233.

Bieganousky, W. A., & Marcuson, W. F. (1977). Liquefaction potential of dams and foundations: Report 2, laboratory standard penetration tests on platte river sand and standard concrete sands. Department of Defense, Department of the Army, Corps of Engineers, Waterways Experiment Station, Soils and Pavements Laboratory.

Blaker, Ø., Lunne, T., Vestgården, T., Krogh, L., Thomsen, N. V., Powell, J. J. M., & Wallace, C. F. (2015). Method dependency for determining maximum and minimum dry unit weights of sands. In Meyer, Vaughan (Herausgeber): Frontiers in offshore geotechnics III, Proceedings of the third International Symposium on Frontiers in Offshore Geotechnics (ISFOG 2015), Osla, Norway, 1159-1166.

Castro, G., Keller, T.O., and Boynton, S.S. (1989). Re-evaluation of the Lower San Fernando Dam: Report 1, an investigation of the February 9, 1971 slide. U.S. Army Corps of Engineers Contract Report GL-89-2, Vols. 1 and 2, U.S. Army Corps of Engineers Waterways Experiment Station, Vicksburg, Mississippi.

Castro, G. & Poulos, S. J. (1977). Factors affecting liquefaction and cyclic mobility. Journal of Geotechnical Engineering Division, 103(6), 501-516.

Castro, G., Seed, R. B., Keller, T. O., & Seed, H. B. (1992). Steady-state strength analysis of lower San Fernando Dam slide. Journal of Geotechnical Engineering, 118(3), 406-427.

Cetin, K. O. (2000). Reliability-based assessment of seismic soil liquefaction initiation hazard. (Doctoral Dissertation) University of California, Berkeley.

Cetin, K. O., & Bilge, H. T. (2012). Cyclic large strain and induced pore pressure models for saturated clean sands. Journal of Geotechnical and Geoenvironmental Engineering, 138(3), 309-323.

Cetin, K. O., Bilge, H. T., Wu, J., Kammerer, A. M., & Seed, R. B. (2009). Probabilistic model for the assessment of cyclically induced reconsolidation (volumetric) settlements. Journal of Geotechnical and Geoenvironmental Engineering, 135(3), 387-398.

Cetin, K. O., & Ilgac, M. (2021). Probabilistic assessments of void ratio limits and their range for cohesionless soils. Soil Dynamics and Earthquake Engineering, 142, 106481.

Cetin, K. O., Seed, R. B., Der Kiureghian, A., Tokimatsu, K., Harder Jr, L. F., Kayen, R. E., & Moss, R. E. (2004). Standard penetration test-based probabilistic and deterministic assessment of seismic soil liquefaction potential. Journal of Geotechnical and Geoenvironmental Engineering, 130(12), 1314.

Cetin, K. O., Seed, R. B., Kayen, R. E., Moss, R. E., Bilge, H. T., Ilgac, M., & Chowdhury, K. (2018). SPT-based probabilistic and deterministic assessment of seismic soil liquefaction triggering hazard. Soil Dynamics and Earthquake Engineering, 115, 698-709.

Chen, J. R., & Kulhawy, F. H. (2014). Characteristics and intercorrelations of index properties for cohesionless gravelly soils. In Geo-Congress 2014: Geo-characterization and Modeling for Sustainability, 1-13.

Cherif Taiba, A., Belkhatir, M., Kadri, A., Mahmoudi, Y., & Schanz, T. (2016). Insight into the effect of granulometric characteristics on the static liquefaction susceptibility of silty sand soils. Geotechnical and Geological Engineering, 34(1), 367-382.

Cherif Taiba, A., Mahmoudi, Y., Belkhatir, M., Kadri, A., & Schanz, T. (2018). Experimental characterization of the undrained instability and steady state of silty sand soils under monotonic loading conditions. International Journal of Geotechnical Engineering, 12(5), 513-529.

Chillarige, A. V., Morgenstern, N. R., Robertson, P. K., & Christian, H. A. (1997). Seabed instability due to flow liquefaction in the Fraser River delta. Canadian Geotechnical Journal, 34(4), 520-533.

Cho, G. C., Dodds, J., & Santamarina, J. C. (2006). Particle shape effects on packing density, stiffness, and strength: natural and crushed sands. Journal of Geotechnical and Geoenvironmental engineering, 132(5), 591-602.

Cubrinovski, M., & Ishihara, K. (1999). Empirical correlation between SPT N-value and relative density for sandy soils. Soils and Foundations, 39(5), 61-71.

Cubrinovski, M., & Ishihara, K. (2001). Correlation between penetration resistance and relative density of sandy soils. In 15th International Conference on Soil Mechanics and Geotechnical Engineering, Istanbul, Turkey, 393-6.

Cubrinovski, M., & Ishihara, K. (2002). Maximum and minimum void ratio characteristics of sands. Soils and Foundations, 42(6), 65-78.

Davies, M. P., & Campanella, R. G. (1994). Selecting design values of undrained strength for cohesionless soils. In Proceedings of the 47th Canadian Geotechnical Conference, Halifax, Nova Scotia, 176-186.

Davies, M. P., Chin, B. G., & Dawson, B. G. (1998, October). Static liquefaction slump of mine tailings–a case history. In Proceedings, 51st Canadian Geotechnical Conference.

Davis Jr, A. P., Poulos, S. J., & Castro, G. (1988). Strengths backfigured from liquefaction case histories. In Second International Conference on Case Histories in Geotechnical Engineering, June 1-5, St. Louis, Missouri, 1693-1701.

De Alba, P. A., Seed, H. B., Retamal, E., & Seed, R. B. (1987). Residual strength of sand from dam failures in the Chilean earthquake of March 3, 1985. Earthquake Engineering Research Center Report No. UCB/EERC-87-11, University of California, Berkeley, CA.

De Alba, P. A., Seed, H. B., Retamal, E., & Seed, R. B. (1988). Analyses of dam failures in 1985 Chilean earthquake. Journal of Geotechnical Engineering, 114(12), 1414-1434.

Deger, T. T. (2014). Overburden stress normalization and rod length corrections for the standard penetration test (SPT). (Doctoral Dissertation) University of California.

Dobry, R., & Alvarez, L. (1967). Seismic failures of Chilean tailings dams. Journal of the Soil Mechanics and Foundations Division, 93(6), 237-260.

Ekstrom, A., & Olofsson, T. (1985). Water and frost-stability risks for embankments of fine-grained soils. In Symposium on failures in earthworks (pp. 155-170).

Engineering News Record (1925). What happened to municipal utilities at Santa Barbara. Engineering News Record, 95(4), 146-149.

Gibbs, H. J., & Holtz, W. G. (1957). Research on determining the density of sands by spoon penetration testing. In 4th International Conference on Soil Mechanics and Foundation Engineering, London, England, 1, 35–39.

Green, R. A., Mitchell, J. K., & Polito, C. P. (2000). An energy-based excess pore pressure generation model for cohesionless soils. In Proceedings of the John Booker Memorial Symposium, Sidney Australia, AA Balkema Publishers, Rotterdam, Netherlands.

Gutierrez, M., Eddy, M., & Lumbatoruan, P. M. H. (2006). Probabilistic residual shear strength criteria for post-liquefaction evaluation of cohesionless soil deposits (No. 04HQGR0076). Final Technical Report to the US Geological Survey, Department of the Interior, USGS Award.

GZA GeoEnvironmental, Inc. (1991). Wachusett Dam – Clinton, Massachusetts – North Dike Stability. Stage I Report, Volume II, Report to the Commonwealth of Massachusetts, Metropolitan District Commission, Boston, Massachusetts.

Haldar, A., & Miller, F. J. (1984). Statistical evaluation of cyclic strength of sand. Journal of Geotechnical Engineering, 110(12), 1785-1802.

Harder, L. F. J. (1988). Use of penetration tests to determine the cyclic loading resistance of gravelly soils during earthquake shaking. (Doctoral Dissertation) University of California, Berkeley.

Hatanaka, M., Uchida, A., & Oh-oka, H. (1995). Correlation between the liquefaction strengths of saturated sands obtained by in-situ freezing method and rotary-type triple tube method. Soils and Foundations, 35(2), 67-75.

Hazen, A. (1918). A study of the slip in the Calaveras Dam. Engineering News Record, 81(26), 1158-1164.

Hazen, A. (1920). Hydraulic-fill dams. Transactions of the American Society of Civil Engineers, Paper No. 1458, 1713-1821 (including discussions).

Holtz, W. G., & Gibbs, H. J. (1979). Spt and relative density in course sand. Journal of Geotechnical and Geoenvironmental Engineering, 105.

Hryciw, R. D., Vitton, S., & Thomann, T. G. (1990). Liquefaction and flow failure during seismic exploration. Journal of Geotechnical Engineering, 116(12), 1881-1899.

Idriss, I. M. & Boulanger, R.W. (2008). Soil liquefaction during earthquakes. EERI Monograph 12, Earthquake Engineering Research Institute, Oakland, California, 262.

Igwe, O., Fukuoka, H., & Sassa, K. (2012). The effect of relative density and confining stress on shear properties of sands with varying grading. Geotechnical and Geological Engineering, 30(5), 1207-1229.

Ilgac, M., Can, G., & Cetin, K. O. (2019). A dataset on void ratio limits and their range for cohesionless soils. Data in brief, 27, 104696.

Inada (1982). Methods of in situ soil investigations. Japanese Society of Soil Mechanics and Foundation Engineering, 217.

Ishihara, K. (1984). Post-earthquake failure of a tailings dam due to liquefaction of pond deposit.

Ishihara, K. (1993). Liquefaction and flow failure during earthquakes. Geotechnique, 43(3), 351-451.

Ishihara, K. (1996). Soil behaviour in earthquake geotechnics. Oxford Science Publications.

Ishihara, K., Yasuda, S., & Yoshida, Y. (1990). Liquefaction-induced flow failure of embankments and residual strength of silty sands. Soils and Foundations, 30(3), 69-80.

Ishihara, K., & Yoshimine, M. (1992). Evaluation of settlements in sand deposits following liquefaction during earthquakes. Soils and Foundations, 32(1), 173-188.

Jamiolkowski, M., Ghionna, V. N., Lancelotta, R., & Pasqualini, E. (1988). New correlations of penetration tests for design practice, Proceedings of the First International Symposium on Penetration Testing, Orlando, USA.

Jefferies, M., & Been, K. (2006). Soil liquefaction. Abingdon, UK: Taylor & Francis.

Jefferies, M. G., Been, K., & Hachey, J. E. (1990). Influence of scale on the constitutive behavior of sand. In Proceedings of the 43rd Canadian Geotechnical Engineering Conference, Laval University, Quebec, 1, 263-273.

Juang, C. H., Huang, X. H., Holtz, R. D., & Chen, J. W. (1996). Determining relative density of sands from CPT using fuzzy sets. Journal of Geotechnical Engineering, 122(1), 1-6.

Kolbuszewski, J. J. (1948). An experimental study of the maximum and minimum porosities of sands. In Proceedings of the Second International Conference on Soil Mechanics and Foundation Engineering, 158-165.

Konrad, J. M. (1991). The Nerlerk berm case history: some considerations for the design of hydraulic sand fills. Canadian Geotechnical Journal, 28(4), 601-612.

Konrad, J. M., & Watts, B. D. (1995). Undrained shear strength for liquefaction flow failure analysis. Canadian Geotechnical Journal, 32(5), 783-794.

Koppejan, A. W., Van Wamelen, B. M., & Weinberg, L. J. H. (1948). Coastal flow slides in the Dutch province of Zeeland.

Kramer, S. L. (2008). Evaluation of liquefaction hazards in Washington State (No. WA-RD 668.1). Washington State Department of Transportation, Office of Research and Library Services.

Kramer, S. L., & Wang, C. H. (2015). Empirical model for estimation of the residual strength of liquefied soil. Journal of Geotechnical and Geoenvironmental Engineering, 141(9), 04015038.

Krumbein, W. C. (1941). Measurement and geological significance of shape and roundness of sedimentary particles. Journal of Sedimentary Research, 11(2), 64-72.

Krumbein, W. C., & Sloss, L. L. (1963). Stratigraphy and sedimentation. San Francisco: H Freeman and Company.

Kulhawy, F. H., & Mayne, P. W. (1990). Manual on estimating soil properties for foundation design. Electric Power Research Institute (No. EPRI-EL-6800), Palo Alto, CA (USA); Cornell Univ., Ithaca, NY (USA). Geotechnical Engineering Group.

Lee, K. L., Seed, H. B., Idriss, I. M., & Makdisi, F. I. (1975). Properties of soil in the San Fernando hydraulic fill dams. Journal of the Geotechnical Engineering division, 101(8), 801-821.

Liao, S. S., & Whitman, R. V. (1986). Overburden correction factors for SPT in sand. Journal of Geotechnical Engineering, 112(3), 373-377.

Marcuson III, W. F., & Bieganousky, W. A. (1977). SPT and relative density in coarse sands. Journal of the Geotechnical Engineering Division, 103(11), 1295-1309.

Marcuson, W. F., & Krinitzsky, E. L. (1976). Dynamic analysis of Fort Peck dam. US Department of Defense, Department of the Army, Corps of Engineers, Waterways Experiment Station, Soils and Pavements Laboratory.

Mesri, G., & Vardhanabhuti, B. (2009). Compression of granular materials. Canadian Geotechnical Journal, 46(4), 369-392.

Meyerhof, G. G. (1957). Discussion on soil properties and their measurement, Discussion 2. In IVth International, Conference of Soil Mechanics and Foundation Engineering, 110.

Mishima, S. and Kimura, H. (1970). Characteristics of landslides and embankment failures during the Tokachioki earthquake. Soils and Foundations, 10(2), 39-51.

Mitchell, D. E. (1984). Liquefaction slides in hydraulically placed sands. In Proceedings of 4th International Symposium on Landslides, Toronto, Ont.

Mittal, H. K., & Hardy, R. M. (1977). Geotechnical aspects of a tar sand tailings dyke. In Geotechnical Practice for Disposal of Solid Waste Materials (pp. 327-347). ASCE.

Miura, K., Maeda, K., Furukawa, M., & Toki, S. (1997). Physical characteristics of sands with different primary properties. Soils and Foundations, 37(3), 53-64.

Miura, K., Yoshida, N., & Wakamatsu, K. (1995). Damage to fill embankment during the 1993 Kushiro-oki earthquake. In Earthquake Geotechnical Engineering (pp. 1057-1062).

Miura, K., Yoshida, N., Nishimura, M., & Wakamatsu, K. (1998). Stability analysis of the fill embankment damaged by recent two major earthquakes in Hokkaido, Japan. In Geotechnical Earthquake Engineering and Soil Dynamics III (pp. 926-937). ASCE.

Mori, S. (1993). Reconnaissance report on the liquefaction aspects of the Kushiro-oki earthquake, January 15, 1993. In Proc., 28th Japan National Conf. on Soil Mechanics and Foundation Engineering (pp. 1091-1094).

Mujtaba, H., Farooq, K., Sivakugan, N., & Das, B. M. (2018). Evaluation of relative density and friction angle based on SPT-N values. KSCE Journal of Civil Engineering, 22(2), 572-581.

Mulilis, J. P., Seed, H. B., Chan, C. K., Mitchell, J. K., & Arulanandan, K. (1977). Effects of sample preparation on sand liquefaction. Journal of the Geotechnical Engineering Division, 103(2), 91-108.

National Center for Earthquake Engineering Research, (NCEER). (1997). Proceedings of the NCEER workshop on evaluation of liquefaction resistance of soils. Technical Rep. No. NCEER-97-0022, T. L Youd and I. M. Idriss, eds., SUNY, Buffalo, N.Y.

National Research Council. (1985). Liquefaction of soils during earthquakes. Report No. CETS-EE-001, Committee on Earthquake Engineering, National Academy Press, Washington, D.C.

Ohya, S., Iwasaki, T., & Wakamatsu, M. (1985). Comparative study of various penetration tests in ground that underwent liquefaction during the 1983 Nihon-Kai-Chubu and 1964 Niigata earthquakes. In Proceedings of the Workshop on In-Situ Testing Methods for Evaluation of Soil Liquefaction Susceptibility, San Francisco, California (Vol. 1, pp. 56-88).

Okusa, S., & Anma, S. (1980). Slope failures and tailings dam damage in the 1978 Izu-Ohshima-Kinkai earthquake. Engineering Geology, 16(3-4), 195-224.

Olivia Chen Consultants, Inc. (2003). Report on the Seismic Stability of Calaveras Dam. Report prepared for the San Francisco Public Utilities Commission. Utilities Engineering Bureau.

Olson, S. M. (2001). Liquefaction analysis of level and sloping ground using field case histories and penetration resistance. (Doctoral Dissertation) University of Illinois at Urbana-Champaign.

Olson, S. M., & Stark, T. D. (2002). Liquefied strength ratio from liquefaction flow failure case histories. Canadian Geotechnical Journal, 39(3), 629-647.

Peck, R. B., Hanson, W. E., and Thornburn, T. H. (1974). Foundation engineering, 2nd Ed., Wiley, New York.

Pettijohn, F. J. (1949). Sedimentary rocks. Harper and Brothers, New York.

PLAXIS 2D Ultimate Connect Edition V22.00.00.1733 software

Plewes, H. D., O'Neil, G. D., McRoberts, E. C., & Chan, W. K. (1989, September). Liquefaction considerations for Suncor tailings pond. In Proceedings of the Dam Safety Seminar, Edmonton, Alberta, Sept (Vol. 1, pp. 61-89).

Poulos, S. J. (1981). The steady state of deformation. Journal of the Geotechnical Engineering Division, 107(5), 553-562.

Poulos, S. J., Castro, G. & France, W. (1985). Liquefaction evaluation procedure. Journal of Geotechnical Engineering, 111(6), 772-792.

Powers, M. C. (1953). A new roundness scale for sedimentary particles. Journal of Sedimentary Research, 23(2), 117-119.

Riemer, M. F., & Seed, R. B. (1997). Factors affecting apparent position of steady-state line. Journal of Geotechnical and Geoenvironmental Engineering, 123(3), 281-288.

Robertson, P. K., & Campanella, R. G. (1983). Interpretation of cone penetration tests. Part I: Sand. Canadian geotechnical journal, 20(4), 718-733.

Rogers, B. T., Been, K., Hardy, M. D., Johnson, G. J., & Hachey, J. E. (1990). Re-analysis of Nerlerk B-67 berm failures. In Proceedings of the 43rd Canadian Geotechnical Conference-Prediction of Performance in GCotechnique, Quebec, Canada (Vol. 1, pp. 227-237).

Ross, G. A. (1968). Case studies of soil stability problems resulting from earthquakes. University of California, Berkeley.

Russell, R. D., & Taylor, R. E. (1937). Roundness and shape of Mississippi River sands. The Journal of Geology, 45(3), 225-267.

Saito, K. and Ine, N. (1993). Private communication to K. Miura, reported in Miura et al. (1998).

Salgado, R., Boulanger, R. W., & Mitchell, J. K. (1997b). Lateral stress effects on CPT liquefaction resistance correlations. Journal of geotechnical and geoenvironmental engineering, 123(8), 726-735.

Salgado, R., Mitchell, J. K., & Jamiolkowski, M. (1997a). Cavity expansion and penetration resistance in sand. Journal of Geotechnical and Geoenvironmental Engineering, 123(4), 344-354.

Sasaki, Y. (1994). Embankment failure caused by the Kushiro-Oki earthquake of January 15, 1993. In Performance of Ground and Soil Structures during Earthquakes, 13th Int. Conf. on SMFE (pp. 61-68).

Seed, H. B. (1979). Considerations in the earthquake-resistant design of earth and rockfill dams. Geotechnique, 29(3), 215-263.

Seed, H. B. (1987). Design problems in soil liquefaction. Journal of Geotechnical Engineering, 113(8), 827-845.

Seed, B. H., Lee, K. L., & Idriss, I. M. (1969). Analysis of Sheffield dam failure. Journal of the Soil Mechanics and Foundations Division, 95(6), 1453-1490.

Seed, H. B., Lee, K. L., Idriss, I. M., & Makdisi, F. (1973). “Analysis of the slides in the San Fernando Dams during the earthquake of Feb. 9, 1971.” Earthquake Engineering Research Center 73-2, University of California, Berkeley, California.

Seed, H. B., Lee, K. L., Idriss, I. M., & Makdisi, F. I. (1975). The slides in the San Fernando dams during the earthquake of February 9, 1971. Journal of the Geotechnical Engineering Division, 101(7), 651-688.

Seed, H. B., Tokimatsu, K., Harder, L. F., & Chung, R. (1984). The influence of SPT procedures on soil liquefaction resistance evaluations. Report No. UCB/EERC-84/15, Earthquake Engineering Research Center, Univ. of California, Berkeley, CA, October.

Seed, H. B., Seed, R. B., Harder, L. F., & Jong, H. L. (1989). Re-Evaluation of the Lower San Fernando Dam. Report 2. Examination of the Post-Earthquake Slide of February 9, 1971. SEED (H BOLTON) INC ORINDA CA.

Seed, R. B., & Harder, L. F. (1990). SPT-based analysis of cyclic pore pressure generation and undrained residual strength. H. Bolton Seed memorial symposium proceedings.

Selig, E. T., & Ladd, R. S. (1973). Evaluation of relative density measurements and applications. In: Evaluation of relative density and its role in Geotechnical projects involving cohesionless soils, 487-504.

Sheng, D., Yao, Y., & Carter, J. P. (2008). A volume–stress model for sands under isotropic and critical stress states. Canadian Geotechnical Journal, 45(11), 1639-1645.

Silvis, F., & Groot, M. D. (1995). Flow slides in the Netherlands: experience and engineering practice. Canadian geotechnical journal, 32(6), 1086-1092.

Skempton, A. W. (1986). Standard penetration test procedures and the effects in sands of overburden pressure, relative density, particle size, ageing and overconsolidation. Geotechnique, 36(3), 425-447.

Sladen, J. A., D'hollander, R. D., & Krahn, J. (1985). The liquefaction of sands, a collapse surface approach. Canadian geotechnical journal, 22(4), 564-578.

Sladen, J. A., D'hollander, R. D., Krahn, J., & Mitchell, D. E. (1985). Back analysis of the Nerlerk berm liquefaction slides. Canadian geotechnical journal, 22(4), 579-588.

Sladen, J. A., D'Hollander, R. D., Krahn, J., & Mitchell, D. E. (1987). Back analysis of the Nerlerk berm liquefaction slides: Reply. Canadian Geotechnical Journal, 24(1), 179-185.

Sladen, J. A., & Hewitt, K. J. (1989). Influence of placement method on the in situ density of hydraulic sand fills. Canadian Geotechnical Journal, 26(3), 453-466.

Srbulov, M. (2008). Geotechnical earthquake engineering: simplified analyses with case studies and examples (Vol. 9). Springer Science & Business Media.

Stark, T. D., & Mesri, G. (1992). Undrained shear strength of liquefied sands for stability analysis. Journal of Geotechnical Engineering, 118(11), 1727-1747.

Stark, T. D., & Olson, S. M. (1995). Liquefaction resistance using CPT and field case histories. Journal of Geotechnical Engineering, 121(12), 856-869.

Tatsuoka, F., Iwasaki, T., Tokida, K. I., Yasuda, S., Hirose, M., Imai, T., & KoN-No, M. (1978). A method for estimating undrained cyclic strength of sandy soils using standard penetration resistances. Soils and Foundations, 18(3), 43-58.

Tavenas, F. A., Ladd, R. S., & La Rochelle, P. (1973). Accuracy of relative density measurements: results of a comparative test program. In: Evaluation of relative density and its role in geotechnical projects involving cohesionless soils, 523, 18-60.

Tokimatsu, K., & Seed, H. B. (1984). Simplified procedures for the evaluation of settlements in clean sands. College of Engineering, University of California.

TS 1900-1 (2006). Methods of testing soils for civil engineering purposes in the laboratory - Part 1: Determination of physical properties. Turkish Standard.

U.S. Army Corps of Engineers. (1939). Report on the slide of a portion of the upstream face of the Fort Peck Dam, Fort Peck, Montana. United States Government Printing Office, Washington, D.C.

U.S. Army Corps of Engineers. (1949). "Report on investigation of failure of Sheffield Dam, Santa Barbara, California." Office of the District Engineer, Los Angeles, California, June.

Vaid, Y. P., & Negussey, D. (1988). Preparation of reconstituted sand specimens. Advanced Triaxial Testing of Soil and Rock, ASTM STP, 977, 405-417.

Vásárhelyi, B. (2009). A possible method for estimating the Poisson's rate values of the rock masses. Acta Geodaetica et Geophysica Hungarica, 44(3), 313-322.

Von Thun, J. L. (1979). Analysis of dynamic compaction foundation treatment requirements, Stage 1, Jackson Lake Dam. Technical memorandum No. TM-JL-230-26, Bureau of Reclamation, Engineering and Research Center, Division of Dam and Waterway Design, Embankment Dams Branch.

Wadell, H. (1932). Volume, shape, and roundness of rock particles. The Journal of Geology, 40(5), 443-451.

Wang, C. H. (2003). Prediction of the residual strength of liquefied soils. (Doctoral Dissertation) University of Washington.

Weber, J. P. (2015). Engineering evaluation of post-liquefaction strength. (Doctoral Dissertation) University of California, Berkeley.

Wei, X., & Yang, J. (2019). Characterizing the effects of fines on the liquefaction resistance of silty sands. Soils and Foundations, 59(6), 1800-1812.

Wolff, T. F. (1989). Pile capacity prediction using parameter functions. In Predicted and observed axial behavior of piles: results of a pile prediction symposium, 96-106.

Wride, C. E., McRoberts, E. C., & Robertson, P. K. (1999). Reconsideration of case histories for estimating undrained shear strength in sandy soils. Canadian geotechnical journal, 36(5), 907-933.

Wu, J., & Seed, R. B. (2004). Estimation of liquefaction-induced ground settlement (case studies).

Xiao, Y., Yuan, Z., Lin, J., Ran, J., Dai, B., Chu, J., & Liu, H. (2019). Effect of particle shape of glass beads on the strength and deformation of cemented sands. Acta Geotechnica, 14(6), 2123-2131.

Xie, Y. H., Yang, Z. X., Barreto, D., & Jiang, M. D. (2017). The influence of particle geometry and the intermediate stress ratio on the shear behavior of granular materials. Granular Matter, 19(2), 1-13.

Yamada, G. (1966). Damage to Earth Structures and Foundations by the Niigata Earthquake June 16, 1964, in JNR. Soils and foundations, 6(1), 1-13.

Yamamuro, J. A., & Covert, K. M. (2001). Monotonic and cyclic liquefaction of very loose sands with high silt content. Journal of Geotechnical and Geoenvironmental Engineering, 127(4), 314-324.

Yang, J., & Wei, L. M. (2012). Collapse of loose sand with the addition of fines: the role of particle shape. Géotechnique, 62(12), 1111-1125.

Yang, J., & Wei, L. M. (2014). Static liquefaction of granular soils: The Role of Grain Shape and Size. In International Workshop on Bifurcation and Degradation in Geomaterials, Springer, Cham, 199-205.

Yasuda, S. (1993). Mechanical properties of soil where ground failure occurred during the Kushiro-oki earthquake. In Proc., 22nd JSCE Earthquake Engineering Symposium (pp. 395-398).

Yegian, M. K., Ghahraman, V. G., & Harutiunyan, R. N. (1994). Liquefaction and embankment failure case histories, 1988 Armenia earthquake. Journal of geotechnical engineering, 120(3), 581-596.

Yilmaz, Y., Mollamahmutoglu, M., Ozaydin, V., & Kayabali, K. (2008). Experimental investigation of the effect of grading characteristics on the liquefaction resistance of various graded sands. Engineering Geology, 100(3-4), 91-100.

Yoshimi, Y., Tokimatsu, K., & Hosaka, Y. (1989). Evaluation of liquefaction resistance of clean sands based on high-quality undisturbed samples. Soils and Foundations, 29(1), 93-104.

Yoshimine, M., & Ishihara, K. (1998). Flow potential of sand during liquefaction. Soils and Foundations, 38(3), 189-198.

Yoshimine, M., Robertson, P. K., & Wride, C. E. (1999). Undrained shear strength of clean sands to trigger flow liquefaction. Canadian Geotechnical Journal, 36(5), 891-906.

Zhang, G., Robertson, P. K., & Brachman, R. W. (2002). Estimating liquefaction-induced ground settlements from CPT for level ground. Canadian Geotechnical Journal, 39(5), 1168-1180.

Zheng, J., & Hryciw, R. D. (2016). Index void ratios of sands from their intrinsic properties. Journal of Geotechnical and Geoenvironmental Engineering, 142(12), 06016019.

APPENDIX

A EVALUATION OF CASE HISTORIES

The details of the liquefaction failure case histories studied in this thesis are discussed in Appendix A.

#	Case History	Failure Date
A.1	Wachusett Dam - North Dike	1907 Reservoir Filling
A.2	Fort Peck Dam	1938 Construction
A.3	Uetsu Railway Embankment	1964 Niigata Eq (M=7.5)
A.4	Lower San Fernando Dam - U/S Slope	1971 San Fernando Eq (M_w=6.6)
A.5	Hachiro-Gata Road Embankment	1983 Nihon-Kai-Chubu Eq (M=7.7)
A.6	La Marquesa Dam - U/S Slope	1985 Chilean Eq (M_s=7.8)
A.7	La Marquesa Dam - D/S Slope	1985 Chilean Eq (M_s=7.8)
A.8	La Palma Dam	1985 Chilean Eq (M_s=7.8)
A.9	Lake Ackerman Highway Embankment	1987 Seismic Survey
A.10	Chonan Middle School	1987 Chiba-Toho-Oki Eq (M=6.7)
A.11	Soviet Tajik - May 1 Slide	1989 Tajik, Soviet Union Eq (M_L=5.5)
A.12	Shibecha-Cho Embankment	1993 Kushiro-Oki Eq (M_L=7.8)
A.13	Route 272 at Higashiarekinai	1993 Kushiro-Oki Eq (M_L=7.8)
A.14	Zeeland - Vlietepolder	1889 High Tide
A.15	Sheffield Dam	1925 Santa Barbara Eq (M_L=6.3)
A.16	Helsinki Harbor	1936 Construction
A.17	Solfatara Canal Dike	1940 El Centro Eq (M=7.2)
A.18	Lake Merced Bank	1957 San Francisco Eq (M=5.7)
A.19	El Cobre Tailings Dam	1965 Chilean Eq (M_L=7 to 7.25)
A.20	Metoki Road Embankment	1968 Tokachi-Oki Eq (M=7.9)
A.21	Hokkaido Tailings Dam	1968 Tokachi-Oki Eq (M=7.9)
A.22	Upper San Fernando Dam - D/S Slope	1971 San Fernando Eq (M_w=6.6)
A.23	Tar Island Dyke	1974 Construction
A.24	Mochi-Koshi Tailings Dam 1	1978 Izu-Oshima Eq (M=7.0)
A.25	Mochi-Koshi Tailings Dam 2	1978 Izu-Oshima Eq (M=7.0)
A.26	Nerlerk Embankment Slide 1	1983 Construction

A.27	Nerlerk Embankment Slide 2	1983 Construction
A.28	Nerlerk Embankment Slide 3	1983 Construction
A.29	Asele Road Embankment	1983 Pavement Repairs
A.30	Nalband Railway Embankment	1988 Armenian Eq (M_s=6.8)
A.31	Sullivan Tailings	1991 Dyke Rising, British Columbia
A.32	Jamuna Bridge	1994 Construction, Bangladesh
A.33	Calaveras Dam	1918 Construction
A.34	Koda Numa Railway Embankment	1968 Tokachi-Oki Eq (M=7.9)
A.35	Whiskey Springs Fan	1983 Borah Peak Eq (M=7.3)
A.36	San Fernando Valley Juvenile Hall	1971 San Fernando Eq (M_w=6.6)

A.1 Wachusett Dam – North Dike (1907 Reservoir Filling)

A.1.1 Brief Summary of the Case History

Wachusett Dam – North Dike was located in Massachusetts, USA, and the exact date of the failure was reported as April 11, 1907. The fundamental reason behind the failure was reported as the initial filling of the reservoir. The type of the structure can be classified as a poorly constructed earthen dam, and the maximum slope height is reported as ~ 27 m. GZA GeoEnvironmental (1991) is taken into account as the main source of reference. Olson (2001), Wang (2003) and Weber (2015) also studied this case history during their back-analyses of liquefaction failure case histories.

A.1.2 Site Geology and Critical Cross-section

Figure A.1.1 and Figure A.1.2 show the pre-failure and post-failure cross-sections of the case structure, respectively. It is decided that the idealized soil profile consists of three soil layers namely non-liquefied zone, liquefied zone, and foundation. The parts of the poorly constructed earthen dam remaining above and below the water table level at the time of failure are classified as non-liquefied zone and liquefied zone, respectively. The layer underlying the earthen dam is defined as the foundation.

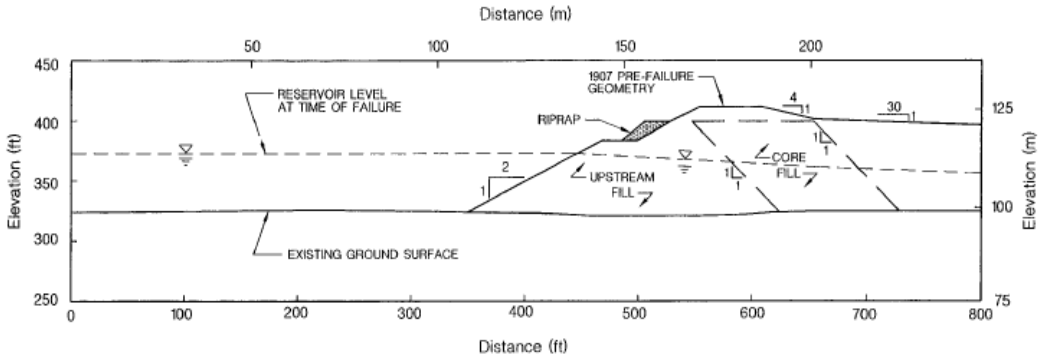

Figure A.1.1. Pre-failure cross-section of the Wachusett Dam-North Dike (Olson et al., 2000)

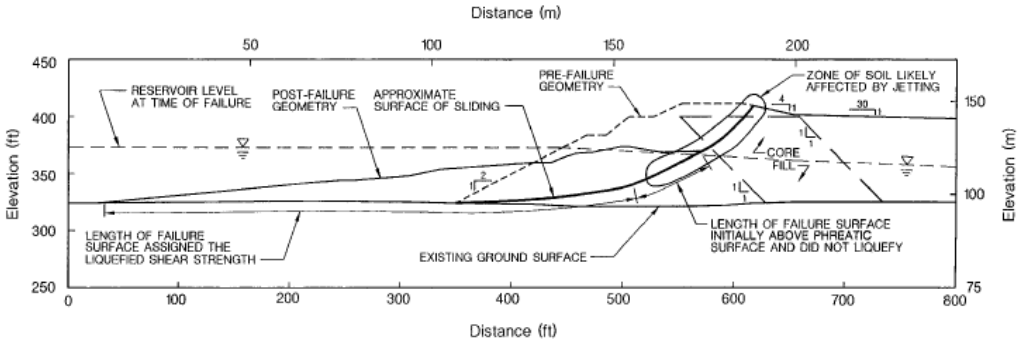

Figure A.1.2. Post-failure cross-section of the Wachusett Dam-North Dike (Olson et al., 2000)

A.1.3 Evaluation of Material Properties

Since the grain size distribution curve of the case history was not reported by the main sources of references or other residual strength-related studies, mean grain size (D_{50}), fines content (FC) and coefficient of uniformity (C_u) values are estimated based on the documented representative values in those references, if available.

Mean grain size (D_{50}): The exact value of the mean grain size was reported as D_{50} = 0.420 mm in GZA GeoEnvironmental (1991) and Olson (2001). Hence, the representative D_{50} value is also taken as 0.420 mm in this study.

Fines content (FC): A range of 5-10% was reported for fines content by GZA GeoEnvironmental (1991), Olson (2001) and Weber (2015). Therefore, the average value of this range, FC = 7.5%, is taken as the representative fines content value in this study.

Coefficient of uniformity (C_u): Since no coefficient of uniformity value was reported by the main sources of references or other relative studies, no value has been set for this parameter.

Roundness (R): Since no roundness value was reported by the main sources of references or other studies, no value has been set for this parameter for the evaluation

of limit void ratios and void ratio ranges. However, R = 0.50 is taken approximately as a representative value for the evaluation of liquefaction state friction angle.

Sphericity (S): Since no sphericity value was reported by the main sources of references or other studies, no value has been set for this parameter for the evaluation of limit void ratios and void ratio ranges. However, S = 0.60 is taken approximately as a representative value for the evaluation of liquefaction state friction angle.

Unit weight (γ_{dry} and γ_{sat}): As the results are not sensitive to unit weight, the dry and saturated unit weights of all soil layers are assigned as 17.4 kN/m^3 and 19.3 kN/m^3, respectively, to be compatible with Olson (2001) and Weber (2015).

A.1.4 Sub-sectioning of the Cross-section and Failure Plane

The exact locations of the SPT boreholes were known for this case history. Therefore, the sub-sectioning is made based on the locations of these penetration tests as presented in Figure A.1.3. Each test is assigned (names of the logs are directly assigned as the name of the sub-section) for the corresponding territory length.

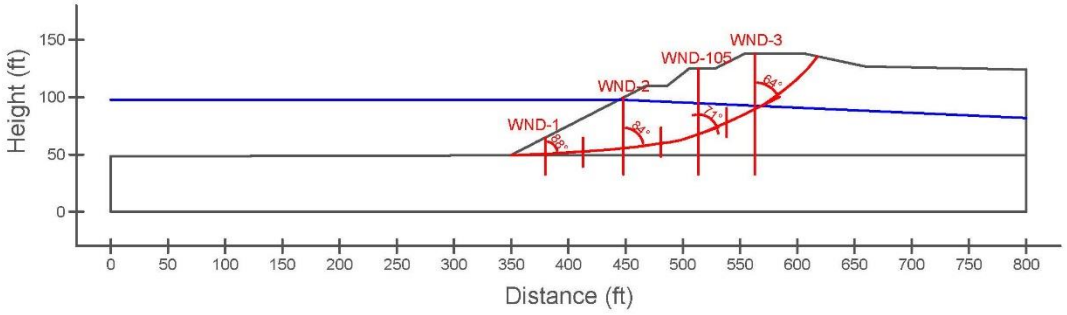

Figure A.1.3. Sub-sectioning of the cross-section and failure plane for Wachusett Dam - North Dike

The territory lengths (L_i) and inclinations (α_i) (positive sign for CCW direction) of the failure plane are evaluated as given in Table A.1.1 for each sub-section.

Table A.1.1 Sub-sections with their corresponding failure plane lengths and inclinations for Wachusett Dam - North Dike

Case History	Section	Failure plane length, L_i (m)	Total failure plane length, L_t (m)	Failure plane inclination, α_i (degrees)
Wachusett Dam - North Dike	WND-1	19.29	68.87	2
	WND-2	20.92		6
	WND-105	18.45		19
	WND-3	10.20		26

A.1.5 Elastic Modeling and Stress Rotation

All stress components are evaluated linear elastically at the points where boreholes and failure plane intersect in Figure A.1.3. The initial and deformed shape of the cross-section are presented in Figure A.1.4 and Figure A.1.5, respectively. All lengths are given in meters.

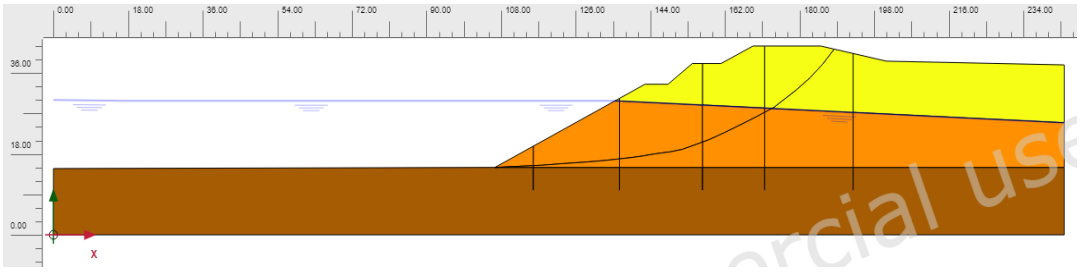

Figure A.1.4. Initial cross-section used in linear elastic modeling of Wachusett Dam - North Dike

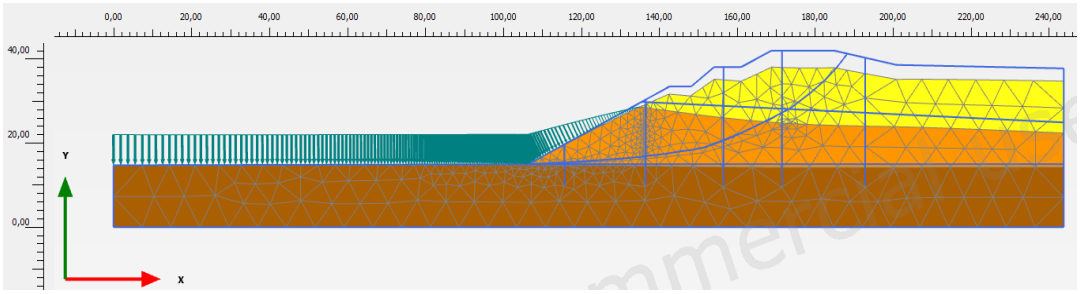

Figure A.1.5. Deformed cross-section obtained after linear elastic modeling of Wachusett Dam - North Dike

During the elastic modeling process in PLAXIS 2D Ultimate Connect Edition V22.00.00.1733 software, the Poisson's ratio values of the non-liquefied zone, liquefied zone, and foundation are defined as 0.30, 0.33, and 0.30, respectively. The elastic modulus values of the same layers, on the other hand, are estimated as 10 MPa, 5 MPa, and 30 MPa, respectively.

The effective normal (σ'_N) and shear (τ_{static}) stresses acting on the inclined failure plane are evaluated with corresponding Mohr's circles. The corresponding Mohr's circles and the effective stress components of the sub-sections are presented in Figure A.1.6 and Table A.1.2, respectively. All stresses are given in kilopascals.

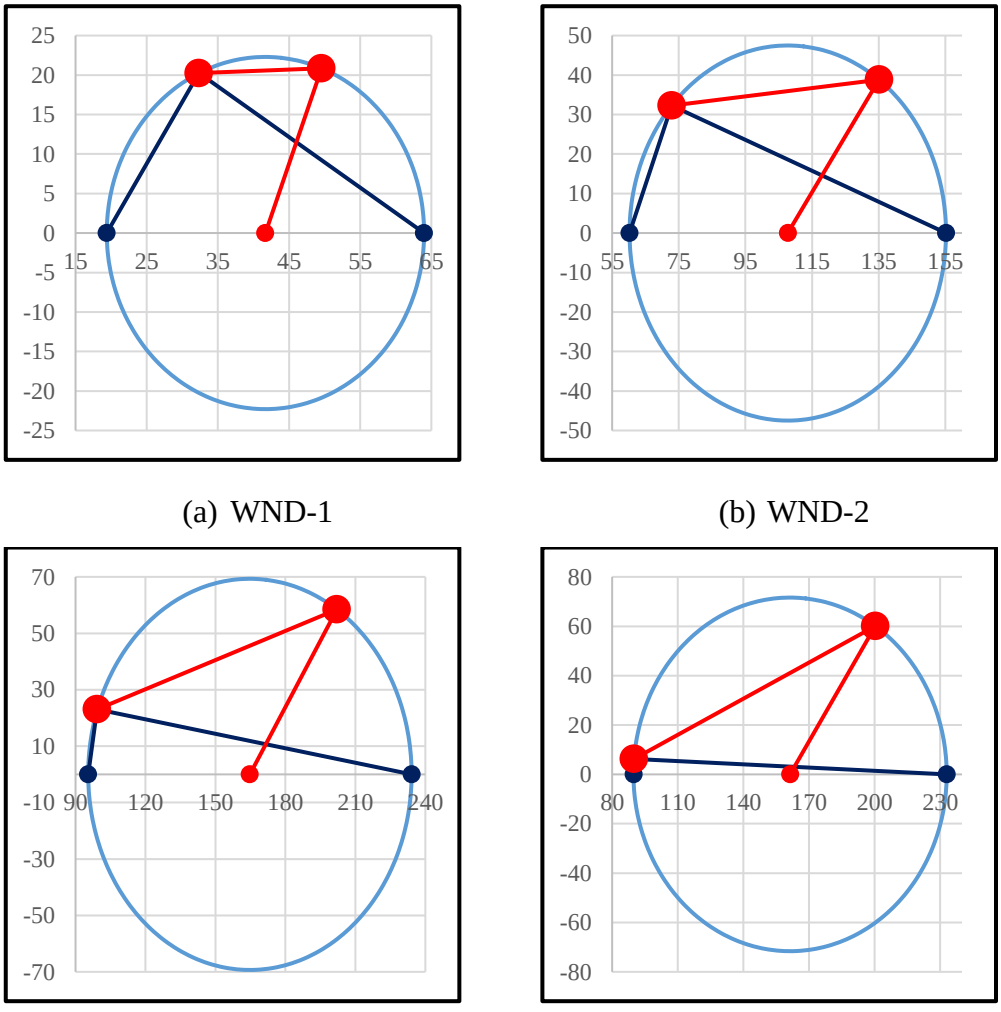

(a) WND-1 (b) WND-2

(c) WND-105 (d) WND-3

Figure A.1.6. Mohr's circles for Wachusett Dam - North Dike

Table A.1.2 Evaluated stress components for Wachusett Dam - North Dike

Case History	Section	σ'_1 (kPa)	σ'_2 (kPa)	σ'_3 (kPa)	p_0' (kPa)	q (kPa)	σ'_N (kPa)	τ_{static} (kPa)	$\lvert\tau_{static}\rvert$ (kPa)
Wachusett Dam - North Dike	WND-1	64.0	27.5	19.4	37.0	41.1	49.6	20.9	20.9
	WND-2	155.2	71.1	60.2	95.5	90.0	135.1	38.8	38.8
	WND-105	234.1	108.7	95.4	146.1	132.5	202.1	58.4	58.4
	WND-3	233.0	106.5	89.8	143.1	135.7	200.4	60.1	60.1

A.1.6 Evaluation of SPT Resistance

The exact locations of the SPT boreholes were documented by Olson et al. (2000) as given in Figure A.1.7.

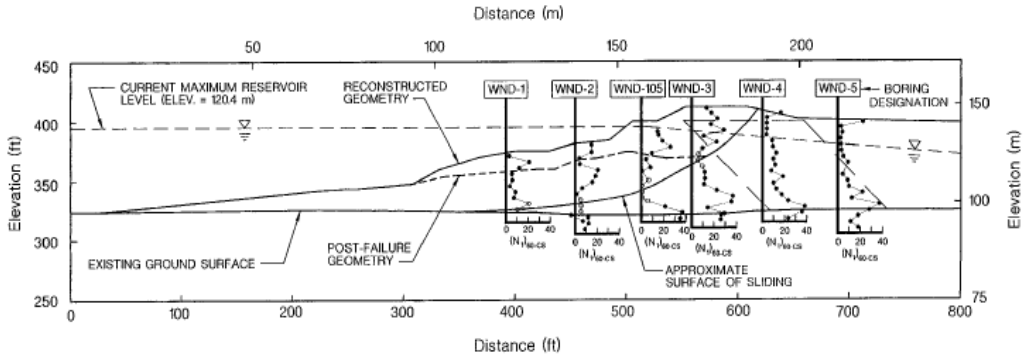

Figure A.1.7. SPT data for Wachusett Dam - North Dike (Olson et al., 2000)

Since $(N_1)_{60,cs}$ values were reported instead of raw SPT-N values, they are converted into the raw SPT-N values initially, and then corrected for equipment, overburden stress, and fines content with the same procedures to achieve consistency. The raw SPT-N values are evaluated by back-analyzing the corrected $(N_1)_{60,cs}$ values with the same correction methods used by the reporting teams.

Once the raw SPT-N values are estimated, the correction factors for nonstandardized sampler configuration (C_S) and borehole diameter (C_B) are taken as 1.0 since no reliable information related to these coefficients was reported in any of the sources. The energy ratio was reported as 45% in GZA GeoEnvironmental (1991) and Olson

(2001); therefore, the energy efficiency correction factor (C_E) is taken as 45/60 = 0.75. The short rod length (C_R) and fines content correction factors (C_{fines}) are evaluated with the methods and relationships explained in Section 3.5. The overburden stress correction factors (C_N) are evaluated based on the effective vertical stresses estimated at the point of penetration for each recording, and average values are documented for simplicity. Accordingly, the correction factors and SPT resistances are estimated as given in Table A.1.3.

Table A.1.3 Evaluated SPT-N resistances for Wachusett Dam - North Dike

Case History	Section	C_N	C_B	C_R	C_S	C_E	C_{fines}	N	N_{60}	$(N_1)_{60}$	$(N_1)_{60,cs}$	
Wachusett Dam - North Dike	WND-1	0.69	1.0	0.99	1.0	0.75	1.09	11.84	8.81	6.22	6.78	6.33
	WND-2	0.51	1.0	0.99	1.0	0.75	1.12	9.81	7.30	4.27	4.77	
	WND-105	0.49	1.0	0.99	1.0	0.75	1.13	9.95	7.41	3.92	4.42	
	WND-3	0.44	1.0	0.99	1.0	0.75	1.07	25.49	18.99	8.73	9.37	

A.1.7 Evaluation of Limit Void Ratios, Void Ratio Ranges, Relative Densities and Initial Void Ratios

Since mean grain size (D_{50}) and fines content (FC) information were available among the required material properties for the void ratio prediction models, the arithmetic means of the limit void ratios (e_{min} and e_{max}) evaluated by Model 1 and Model 2 are considered as the representative values. The e_{max} value is slightly modified then with respect to the construction method of the case history for each prediction model.

Since the fines content value is evaluated as 7.5%, which is less than 15%, it is judged that the soil of interest consists of sand type of soils. Therefore, the arithmetic mean of the relative densities evaluated by the correlations recommended by Kulhawy and Mayne (1990) and Cubrinovski and Ishihara (1999) is taken as the overall relative density of the soil. Based on these relative densities and limit void ratios, the initial void ratios (e_0) corresponding to approximately 1 kPa confining stress are estimated referring to Equation 3-68. Accordingly, the limit void ratios, void ratio ranges

(without any modification for the construction method), in-situ relative densities, and initial void ratios are estimated as given in Table A.1.4.

Table A.1.4 Evaluated limit void ratios, void ratio ranges, in-situ relative densities, and initial void ratios for Wachusett Dam - North Dike

Case History	Section	e_{min}	e_{max}	e_{max}-e_{min}	$RD_{C\&I}$ (%)	$RD_{K\&M}$ (%)	$RD_{overall}$ (%)	e_0
Wachusett Dam - North Dike	WND-1	0.563	0.935	0.372	31.45	35.07	33.26	0.811
	WND-2	0.563	0.935	0.372	26.06	29.05	27.56	0.832
	WND-105	0.563	0.935	0.372	24.97	27.85	26.41	0.837
	WND-3	0.563	0.935	0.372	37.26	41.54	39.40	0.788

A.2 Fort Peck Dam (1938 Construction)

A.2.1 Brief Summary of the Case History

Fort Peck Dam was located in Montana, USA, and the exact date of the failure was reported as September 22, 1938. The fundamental reason behind the failure was reported as the construction. The type of the structure can be classified as a hydraulic fill dam, and the maximum slope height is reported as ~ 60 m. U.S Army Corps of Engineers (1939) and Marcuson and Krinitsky (1976) are considered as the main sources of references. Olson (2001), Wang (2003) and Weber (2015) also studied this case history during their back-analyses of liquefaction failure case histories.

A.2.2 Site Geology and Critical Cross-section

Figure A.2.1 presents the soil stratigraphy of the dam cross-section, and Figure A.2.2 shows the pre-failure and post-failure cross-sections of the case structure. It is decided that the idealized soil profile consists of four soil layers namely clay core, non-liquefied zone, liquefied zone, and foundation. The parts of the hydraulic fill dam remaining above and below the water table level at the time of failure are

classified as non-liquefied zone and liquefied zone, respectively. The layer underlying the dam is defined as the foundation, and the middle part of the dam body is classified as clay core.

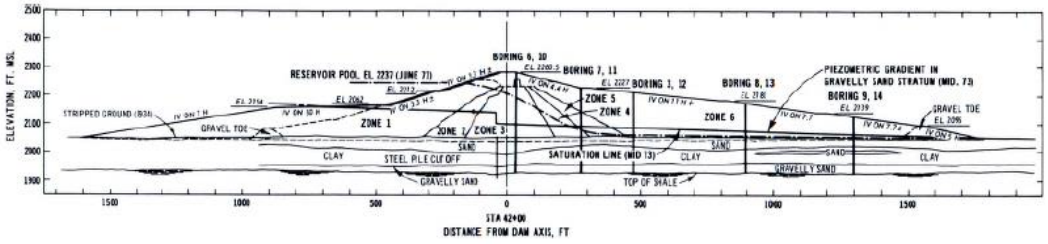

Figure A.2.1. Soil stratigraphy of the Fort Peck Dam (Marcuson and Krinitzsky, 1976)

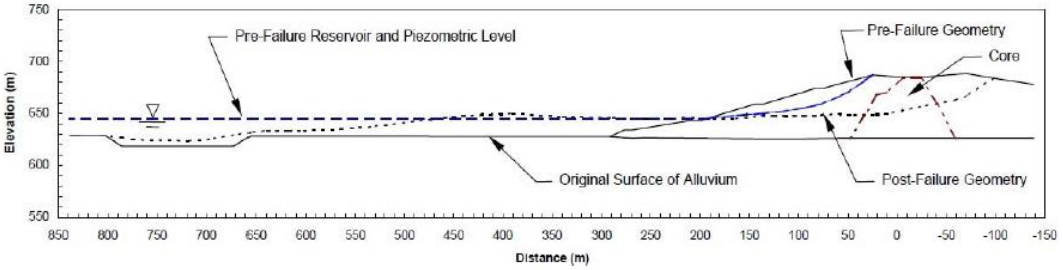

Figure A.2.2. Pre-failure and post-failure cross-sections of the Fort Peck Dam (Olson, 2001)

A.2.3 Evaluation of Material Properties

Since the grain size distribution curve of the case history was reported by the main sources of references as given in Figure A.2.3, mean grain size (D_{50}), fines content (FC) and coefficient of uniformity (C_u) values are evaluated based on this curve.

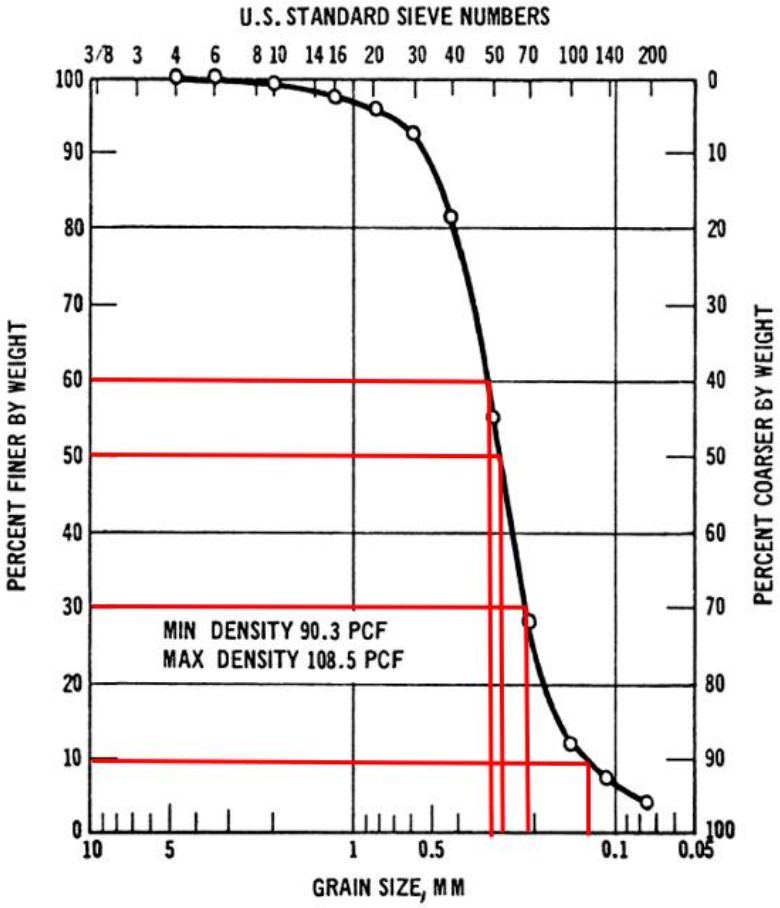

Figure A.2.3. Grain size distribution curve of the shell material of the Fort Peck Dam (Marcuson and Krinitzsky, 1976)

Mean grain size (D_{50}): D_{50} = 0.280 mm is evaluated representatively based on the grain size distribution curve of the case history. Olson (2001) also suggests a range of 0.06-0.2 mm for D_{50} value of this case history considering the clayey core zone.

Fines content (FC): FC = 4% is evaluated representatively for the liquefied shell zone based on the grain size distribution curve of the case history. It should be noted that some other studies such as Gutierrez et al. (2016) suggests larger fines content values for this case considering the clayey core zone.

Coefficient of uniformity (C_u): D_{10} and D_{60} values are evaluated as 0.13 mm and 0.30 mm, respectively, based on the grain size distribution curve of the case history. Therefore, the uniformity coefficient is estimated as $C_u = D_{60}/D_{10} = 0.30/0.13 = 2.31$.

Roundness (R): Since no roundness value was reported by the main sources of references or other studies, no value has been set for this parameter for the evaluation of limit void ratios and void ratio ranges. However, R = 0.50 is taken approximately as a representative value for the evaluation of liquefaction state friction angle.

Sphericity (S): Since no sphericity value was reported by the main sources of references or other studies, no value has been set for this parameter for the evaluation of limit void ratios and void ratio ranges. However, S = 0.60 is taken approximately as a representative value for the evaluation of liquefaction state friction angle.

Unit weight (γ_{dry} and γ_{sat}): As the results are not sensitive to unit weight, the dry and saturated unit weights of the clay core, non-liquefied fill and liquefied fill layers are assigned as 18.1 kN/m^3 and 19.2 kN/m^3, respectively. The unit weight of the foundation, on the other hand, is defined as 19.7 kN/m^3. These values are selected to be compatible with Olson (2001) and Weber (2015).

A.2.4 Sub-sectioning of the Cross-section and Failure Plane

The exact locations of the SPT boreholes were known for the downstream part of the dam. By considering the similarities between the upstream and downstream parts, these boreholes are also considered for the upstream symmetrically. Therefore, the sub-sectioning is made based on the locations of these penetration tests as presented in Figure A.2.1. Each test is assigned (names of the logs are directly assigned as the name of the sub-section) for the corresponding territory length.

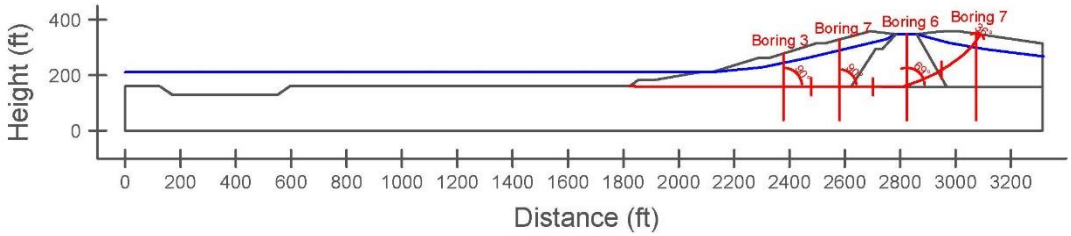

Figure A.2.4. Sub-sectioning of the cross-section and failure plane for Fort Peck Dam

The territory lengths (L_i) and inclinations (α_i) (positive sign for CCW direction) of the failure plane are evaluated as given in Table A.2.1 for each sub-section.

Table A.2.1 Sub-sections with their corresponding failure plane lengths and inclinations for Fort Peck Dam

Case History	Section	Failure plane length, L_i (m)	Total failure plane length, L_t (m)	Failure plane inclination, α_i (degrees)
Fort Peck Dam	Boring 3	200.25	389.30	0
	Boring 7	67.93		0
	Boring 6	79.37		21
	Boring 7	41.75		54

A.2.5 Elastic Modeling and Stress Rotation

All stress components are evaluated linear elastically at the points where boreholes and failure plane intersect in Figure A.2.4. The initial and deformed shape of the cross-section are presented in Figure A.2.5 and Figure A.2.6, respectively. All lengths are given in meters.

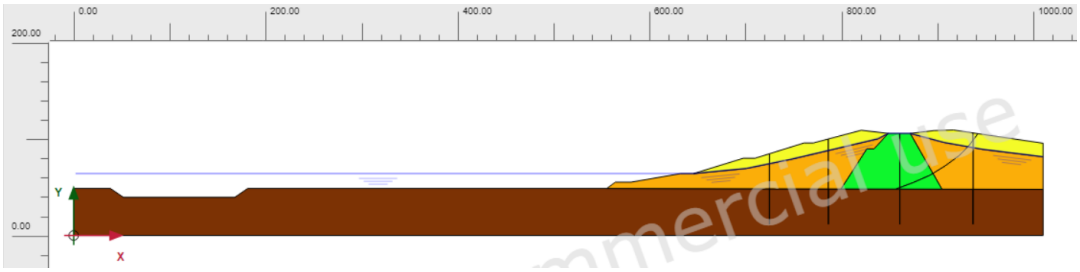

Figure A.2.5. Initial cross-section used in linear elastic modeling of Fort Peck Dam

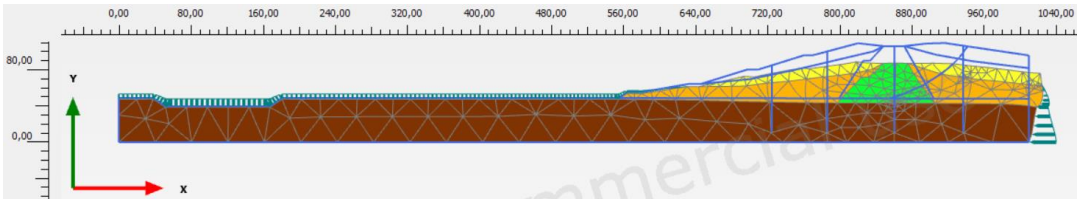

Figure A.2.6. Deformed cross-section obtained after linear elastic modeling of Fort Peck Dam

During the elastic modeling process in PLAXIS 2D Ultimate Connect Edition V22.00.00.1733 software, the Poisson's ratio values of the clay core, non-liquefied zone, liquefied zone, and foundation are defined as 0.33, 0.30, 0.33, and 0.30, respectively. The elastic modulus values of the same layers, on the other hand, are estimated as 5 MPa, 10 MPa, 5 MPa, and 30 MPa, respectively.

The effective normal (σ'_N) and shear (τ_{static}) stresses acting on the inclined failure plane are evaluated with corresponding Mohr's circles. The corresponding Mohr's circles and the effective stress components of the sub-sections are presented in Figure A.2.7 and Table A.2.2, respectively. All stresses are given in kilopascals.

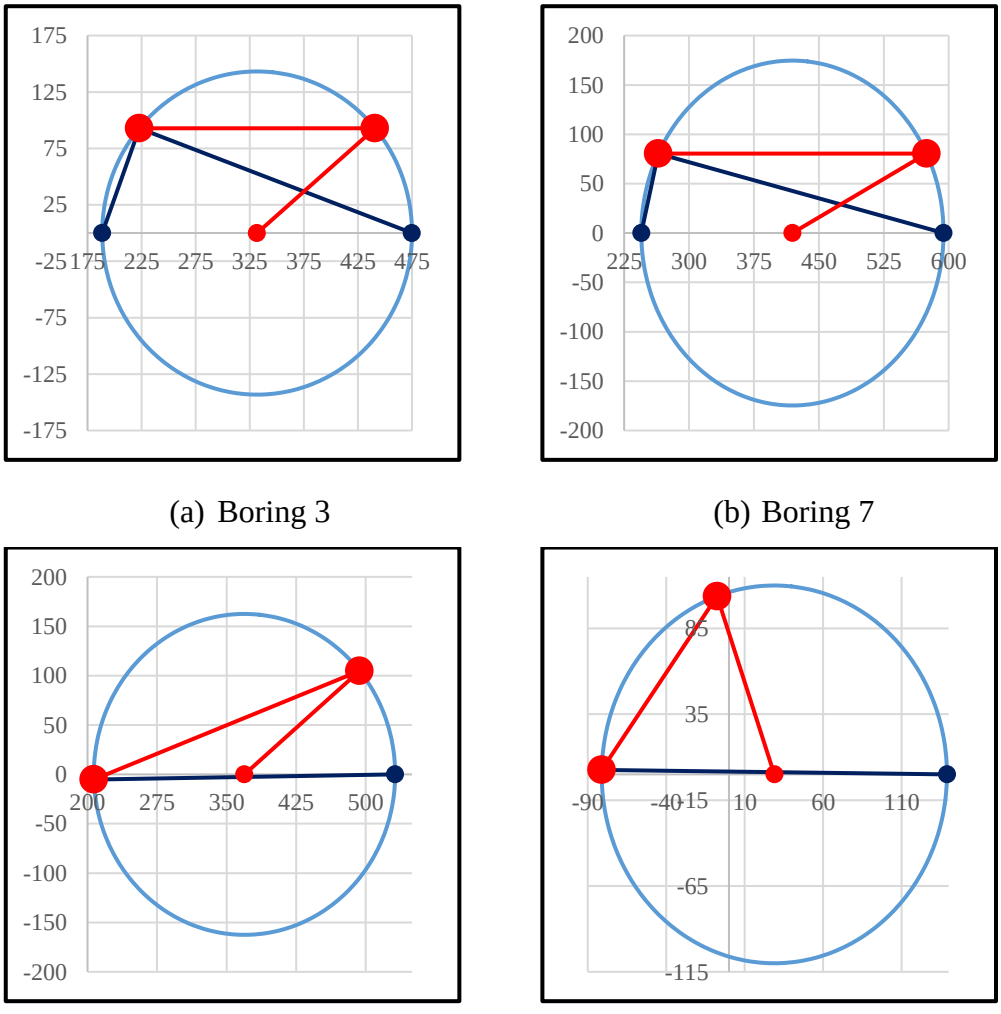

(a) Boring 3 (b) Boring 7

(c) Boring 6 (d) Boring 7

Figure A.2.7. Mohr's circles for Fort Peck Dam

Table A.2.2 Evaluated stress components for Fort Peck Dam

Case History	Section	σ'_1 (kPa)	σ'_2 (kPa)	σ'_3 (kPa)	p_0' (kPa)	q (kPa)	σ'_N (kPa)	τ_{static} (kPa)	$\lvert\tau_{static}\rvert$ (kPa)
Fort Peck Dam	Boring 3	475.0	219.3	188.6	294.5	272.4	440.8	92.8	92.8
	Boring 7	594.1	276.9	244.8	372.2	334.4	574.5	80.5	80.5
	Boring 6	531.8	243.7	206.8	327.4	308.2	493.5	104.8	104.8
	Boring 7	138.9	17.4	-81.1	25.1	190.9	-7.6	103.8	103.8

A.2.6 Evaluation of SPT Resistance

The exact locations of the SPT boreholes were documented by Marcuson and Krinitzsky (1976) for the downstream of the dam as given in Figure A.2.1. By considering the similarities between the upstream and downstream parts, these boreholes are also considered for the upstream symmetrically. SPT boreholes are presented in Figure A.2.8 for Boring 3, Boring 6, and Boring 7, respectively.

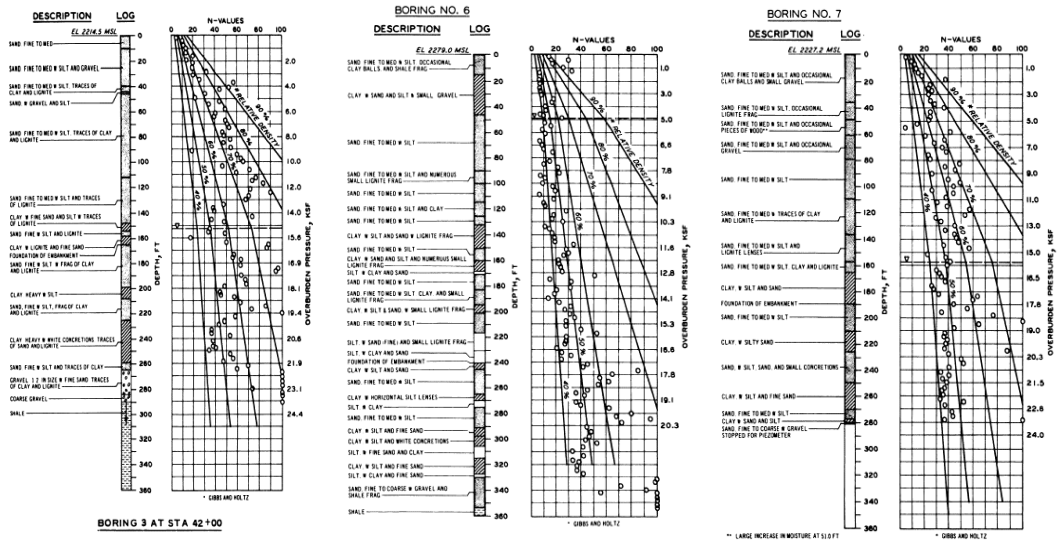

(a) Boring 3 (b) Boring 6 (c) Boring 7

Figure A.2.8. SPT boreholes for Fort Peck Dam (Marcuson and Krinitzsky, 1976)

The correction factors for nonstandardized sampler configuration (C_S), borehole diameter (C_B), and energy efficiency (C_E) are taken as 1.0 since no reliable information related to these coefficients was reported in any of the sources. The short

rod length (C_R) and fines content correction factors (C_{fines}) are evaluated with the methods and relationships explained in Section 3.5. The overburden stress correction factors (C_N) are evaluated based on the effective vertical stresses estimated at the point of penetration for each recording, and average values are documented for simplicity. Accordingly, the correction factors and SPT resistances are estimated as given in Table A.2.3.

Table A.2.3 Evaluated SPT-N resistances for Fort Peck Dam

Case History	Section	C_N	C_B	C_R	C_S	C_E	C_{fines}	N	N_{60}	$(N_1)_{60}$	$(N_1)_{60,cs}$	
Fort Peck Dam	Boring 3	0.56	1.0	0.99	1.0	1.00	1.00	31.25	31.03	17.33	17.33	17.33
	Boring 7	0.55	1.0	0.99	1.0	1.00	1.00	31.25	31.03	17.33	17.33	
	Boring 6	0.53	1.0	0.99	1.0	1.00	1.00	31.25	31.03	17.33	17.33	
	Boring 7	1.71	1.0	0.99	1.0	1.00	1.00	31.25	30.99	17.33	17.33	

A.2.7 Evaluation of Limit Void Ratios, Void Ratio Ranges, Relative Densities and Initial Void Ratios

Since mean grain size (D_{50}), fines content (FC), and coefficient of uniformity (C_u) information were available among the required material properties for the void ratio prediction models, the arithmetic means of the limit void ratios (e_{min} and e_{max}) evaluated by Model 8 and Model 9 are considered as the representative values. The e_{max} value is slightly modified then with respect to the construction method of the case history for each prediction model.

Since the fines content value is evaluated as 4%, which is less than 15%, it is judged that the soil of interest consists of sand type of soils. Therefore, the arithmetic mean of the relative densities evaluated by the correlations recommended by Kulhawy and Mayne (1990) and Cubrinovski and Ishihara (1999) is taken as the overall relative density of the soil. Based on these relative densities and limit void ratios, the initial void ratios (e_0) corresponding to approximately 1 kPa confining stress are estimated referring to Equation 3-68. Accordingly, the limit void ratios, void ratio ranges

(without any modification for the construction method), in-situ relative densities, and initial void ratios are estimated as given in Table A.2.4.

Table A.2.4 Evaluated limit void ratios, void ratio ranges, in-situ relative densities, and initial void ratios for Fort Peck Dam

Case History	Section	e_{min}	e_{max}	e_{max}-e_{min}	$RD_{C\&I}$ (%)	$RD_{K\&M}$ (%)	$RD_{overall}$ (%)	e_0
Fort Peck Dam	Boring 3	0.569	0.971	0.402	56.08	61.26	58.67	0.735
	Boring 7	0.569	0.971	0.402	56.08	61.26	58.67	0.735
	Boring 6	0.569	0.971	0.402	56.08	61.26	58.67	0.735
	Boring 7	0.569	0.971	0.402	56.08	61.26	58.67	0.735

A.3 Uetsu Railway Embankment (1964 Niigata Earthquake, M_w=7.5)

A.3.1 Brief Summary of the Case History

Uetsu Railway Embankment was located in Niigata, Japan, and the exact date of the failure was reported as June 16, 1964. The fundamental reason behind the failure was reported as the 1964 Niigata Earthquake (M_w=7.5). The type of the structure can be classified as a poorly compacted embankment, and the maximum slope height is reported as ~ 10 m. Yamada (1966) is considered as the main source of reference. Olson (2001), Wang (2003) and Weber (2015) also studied this case history during their back-analyses of liquefaction failure case histories.

A.3.2 Site Geology and Critical Cross-section

Figure A.3.1 shows the soil stratigraphy and pre-failure and post-failure cross-sections of the case structure. It is decided that the idealized soil profile consists of three soil layers namely non-liquefied zone, liquefied zone, and foundation. The parts of the embankment remaining above and below the water table level at the time

of failure are classified as non-liquefied zone and liquefied zone, respectively. The layer underlying the embankment is defined as the foundation.

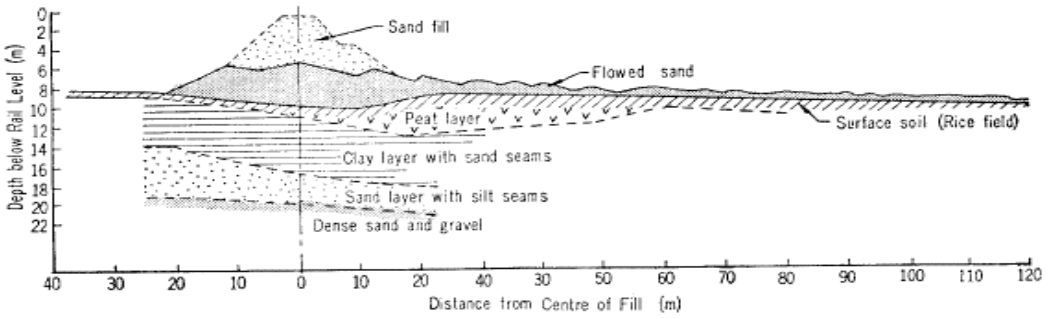

Figure A.3.1. Soil stratigraphy and pre-failure and post-failure cross-sections of the Uetsu Railway Embankment (Yamada, 1966)

A.3.3 Evaluation of Material Properties

Since the grain size distribution curve of the case history was reported by the main sources of references as given in Figure A.3.2, mean grain size (D_{50}), fines content (FC) and coefficient of uniformity (C_u) values are evaluated based on this curve.

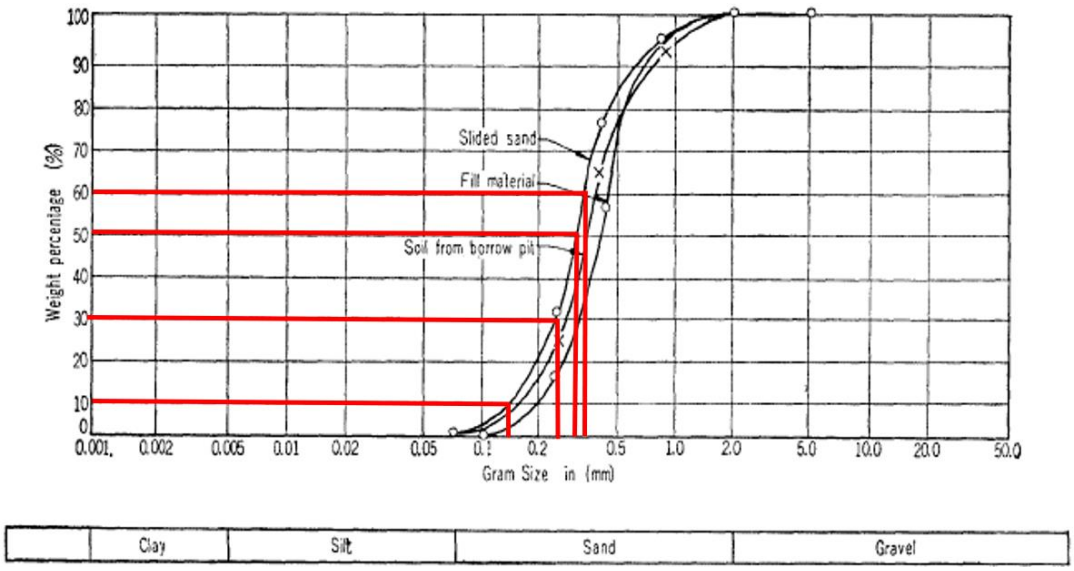

Figure A.3.2. Grain size distribution curve of the slided sand of the Uetsu Railway Embankment (Yamada, 1966)

Mean grain size (D_{50}): D_{50} = 0.340 mm, which is compatible with the value reported by Srbulov (2008), is evaluated representatively based on the grain size distribution curve. Olson (2001) also suggests a range of 0.3-0.4 mm for D_{50} value.

Fines content (FC): FC = 1% is evaluated representatively for the slided sand material based on the grain size distribution curve of the case history. This value is also compatible with the values reported by Srbulov (2008) and Gutierrez et al. (2016). Weber (2015) also suggests FC ≤ 5% for this case history.

Coefficient of uniformity (C_u): D_{10} and D_{60} values are evaluated as 0.14 mm and 0.36 mm, respectively, based on the grain size distribution curve of the case history. Therefore, the uniformity coefficient is estimated as $C_u = D_{60}/D_{10} = 0.36/0.14 = 2.57$.

Roundness (R): Since no roundness value was reported by the main sources of references or other studies, no value has been set for this parameter for the evaluation of limit void ratios and void ratio ranges. However, R = 0.50 is taken approximately as a representative value for the evaluation of liquefaction state friction angle.

Sphericity (S): Since no sphericity value was reported by the main sources of references or other studies, no value has been set for this parameter for the evaluation of limit void ratios and void ratio ranges. However, S = 0.60 is taken approximately as a representative value for the evaluation of liquefaction state friction angle.

Unit weight (γ_{dry} and γ_{sat}): As the results are not sensitive to unit weight, the dry and saturated unit weights of all soil layers are assigned as 17.9 kN/m^3 and 18.5 kN/m^3, respectively, to be compatible with Olson (2001) and Weber (2015).

A.3.4 Sub-sectioning of the Cross-section and Failure Plane

The exact locations of the SPT boreholes were not known for this case history. Therefore, the sub-sectioning is made based on imaginary boreholes assigned on the cross-section. These imaginary boreholes are defined with respect to changes in effective vertical stresses and inclination angles of the failure plane. Accordingly, two sub-sections are assigned for the liquefied zone as presented in Figure A.3.3.

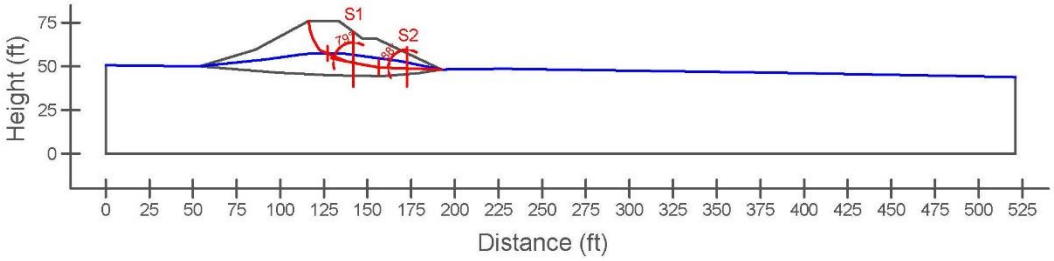

Figure A.3.3. Sub-sectioning of the cross-section and failure plane for Uetsu Railway Embankment

The territory lengths (L_i) and inclinations (α_i) (positive sign for CCW direction) of the failure plane are evaluated as given in Table A.3.1 for each sub-section.

Table A.3.1 Sub-sections with their corresponding failure plane lengths and inclinations for Uetsu Railway Embankment

Case History	Section	Failure plane length, L_i (m)	Total failure plane length, L_t (m)	Failure plane inclination, α_i (degrees)
Uetsu Railway Embankment	S1	9.39	20.27	-11
	S2	10.88		-2

A.3.5 Elastic Modeling and Stress Rotation

All stress components are evaluated linear elastically at the points where boreholes and failure plane intersect in Figure A.3.3. The initial and deformed shape of the cross-section are presented in Figure A.3.4 and Figure A.3.5, respectively. All lengths are given in meters.

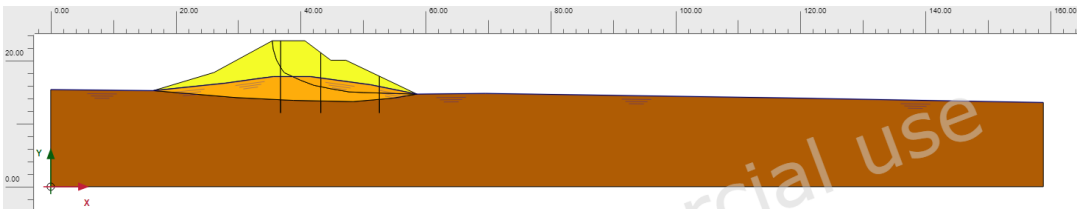

Figure A.3.4. Initial cross-section used in linear elastic modeling of Uetsu Railway Embankment

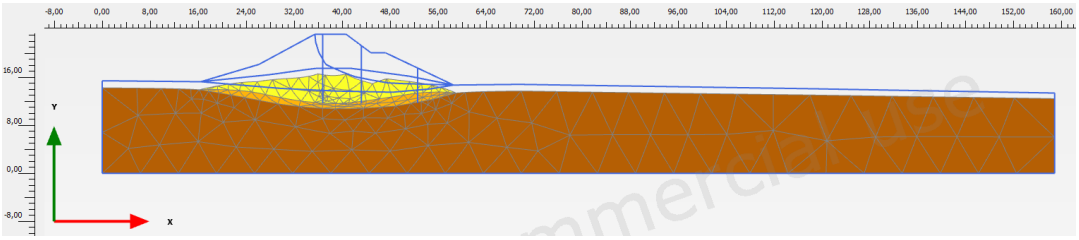

Figure A.3.5. Deformed cross-section obtained after linear elastic modeling of Uetsu Railway Embankment

During the elastic modeling process in PLAXIS 2D Ultimate Connect Edition V22.00.00.1733 software, the Poisson's ratio values of the non-liquefied zone, liquefied zone, and foundation are defined as 0.30, 0.33, and 0.30, respectively. The elastic modulus values of the same layers, on the other hand, are estimated as 10 MPa, 5 MPa, and 30 MPa, respectively.

The effective normal (σ'_N) and shear (τ_{static}) stresses acting on the inclined failure plane are evaluated with corresponding Mohr's circles. The corresponding Mohr's circles and the effective stress components of the sub-sections are presented in Figure A.3.6 and Table A.3.2, respectively. All stresses are given in kilopascals.

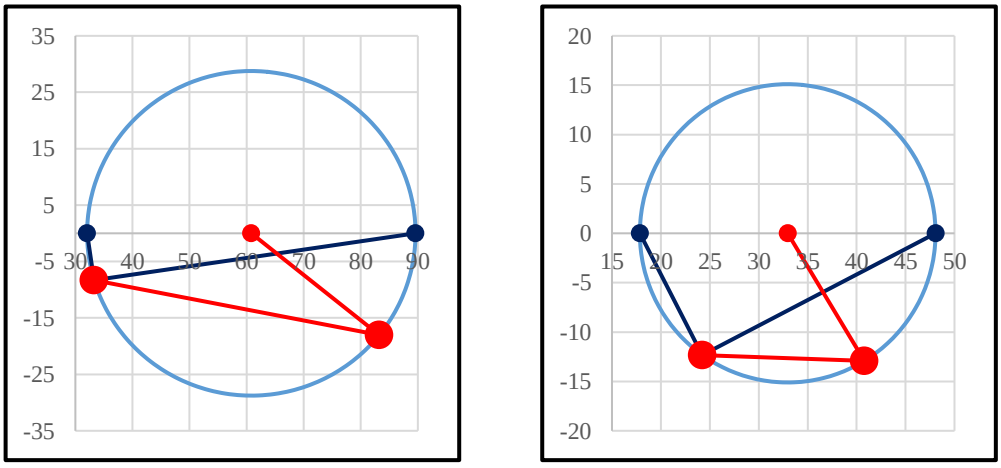

(a) S1 (b) S2

Figure A.3.6. Mohr's circles for Uetsu Railway Embankment

Table A.3.2 Evaluated stress components for Uetsu Railway Embankment

Case History	Section	σ'_1 (kPa)	σ'_2 (kPa)	σ'_3 (kPa)	p_0' (kPa)	q (kPa)	σ'_N (kPa)	τ_{static} (kPa)	$\lvert\tau_{static}\rvert$ (kPa)
Uetsu Railway Embankment	S1	89.6	40.2	32.1	53.9	53.9	83.2	-18.0	18.0
	S2	48.1	21.8	17.9	29.3	28.5	40.8	-12.9	12.9

A.3.6 Evaluation of SPT Resistance

The exact locations of the SPT boreholes were not documented for this case history. Therefore, imaginary boreholes are assigned along the cross-section as shown in Figure A.3.3. SPT data used for this case history is presented in Figure A.3.7.

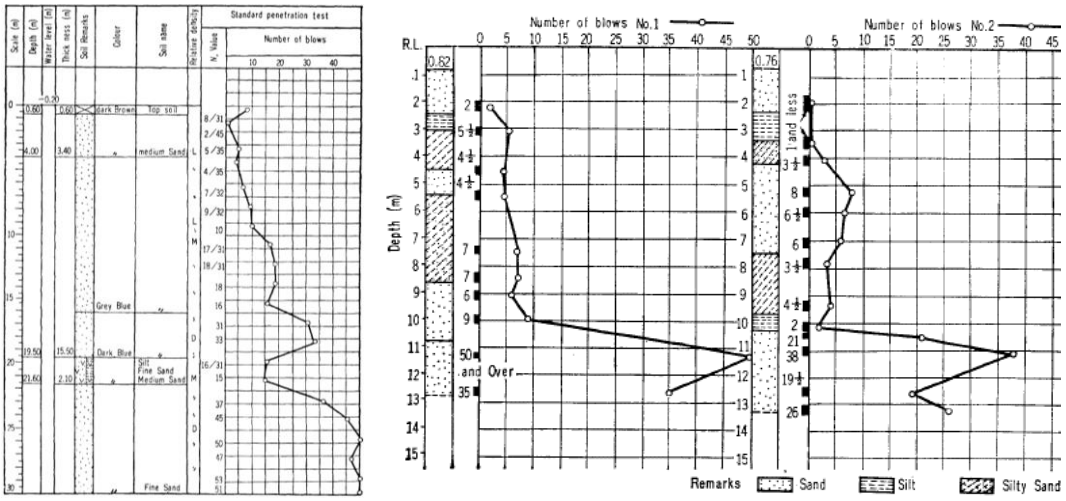

Figure A.3.7. SPT boreholes for Uetsu Railway Embankment (Yamada, 1966)

The correction factors for nonstandardized sampler configuration (C_S), borehole diameter (C_B), and energy efficiency (C_E) are taken as 1.0 since no reliable information related to these coefficients was reported in any of the sources. The short rod length (C_R) and fines content correction factors (C_{fines}) are evaluated with the methods and relationships explained in Section 3.5. The overburden stress correction factors (C_N) are evaluated based on the effective vertical stresses estimated at the point of penetration for each recording, and average values are documented for simplicity. Accordingly, the correction factors and SPT resistances are estimated as given in Table A.3.3.

Table A.3.3 Evaluated SPT-N resistances for Uetsu Railway Embankment

Case History	Section	C_N	C_B	C_R	C_S	C_E	C_{fines}	N	N_{60}	$(N_1)_{60}$	$(N_1)_{60,cs}$	
Uetsu Railway Embankment	S1	1.04	1.0	0.93	1.0	1.00	1.00	1.67	1.56	1.62	1.62	1.99
	S2	1.51	1.0	0.93	1.0	1.00	1.00	1.67	1.56	2.36	2.36	

A.3.7 Evaluation of Limit Void Ratios, Void Ratio Ranges, Relative Densities and Initial Void Ratios

Since mean grain size (D_{50}), fines content (FC), and coefficient of uniformity (C_u) information were available among the required material properties for the void ratio prediction models, the arithmetic means of the limit void ratios (e_{min} and e_{max}) evaluated by Model 8 and Model 9 are considered as the representative values. The e_{max} value is slightly modified then with respect to the construction method of the case history for each prediction model.

Since the fines content value is evaluated as 1%, which is less than 15%, it is judged that the soil of interest consists of sand type of soils. Therefore, the arithmetic mean of the relative densities evaluated by the correlations recommended by Kulhawy and Mayne (1990) and Cubrinovski and Ishihara (1999) is taken as the overall relative density of the soil. Based on these relative densities and limit void ratios, the initial void ratios (e_0) corresponding to approximately 1 kPa confining stress are estimated referring to Equation 3-68. Accordingly, the limit void ratios, void ratio ranges (without any modification for the construction method), in-situ relative densities, and initial void ratios are estimated as given in Table A.3.4.

Table A.3.4 Evaluated limit void ratios, void ratio ranges, in-situ relative densities, and initial void ratios for Uetsu Railway Embankment

Case History	Section	e_{min}	e_{max}	e_{max}-e_{min}	$RD_{C\&I}$ (%)	$RD_{K\&M}$ (%)	$RD_{overall}$ (%)	e_0
Uetsu Railway Embankment	S1	0.561	0.958	0.397	16.98	18.33	17.66	0.888
	S2	0.561	0.958	0.397	20.47	22.11	21.29	0.874

A.4 Lower San Fernando Dam – U/S Slope (1971 San Fernando Earthquake, M_w=6.6)

A.4.1 Brief Summary of the Case History

Lower San Fernando Dam was located in California, USA, and the exact date of the failure was reported as February 9, 1971. The fundamental reason behind the failure was reported as the 1971 San Fernando Earthquake (M_w=6.6). The type of the structure can be classified as a hydraulic fill dam, and the maximum slope height is reported as ~ 43 m. Seed et al. (1989) and Castro et al. (1989, 1992) are considered as the main sources of references. Olson (2001), Wang (2003) and Weber (2015) also studied this case during their back-analyses of liquefaction failure case histories.

A.4.2 Site Geology and Critical Cross-section

Figure A.4.1 presents the soil stratigraphy and pre-failure and post-failure cross-sections of the case structure, Figure A.4.2 shows the reconstructed cross-section of the dam. Referring to Figure A.4.1, it is decided that the idealized soil profile consists of many soil layers with various thickness. Basically, the layer underlying the dam is defined as the foundation, and the middle part of the dam body is classified as clay core. The upper portion of the clay core and downstream slope are defined as rolled fill and rock fill, respectively. The hydraulic fill materials at the upstream and downstream parts of the dam are classified as liquefied hydraulic fill, and moist or saturated hydraulic fill, respectively, based on the location of the groundwater surface at the time of failure.

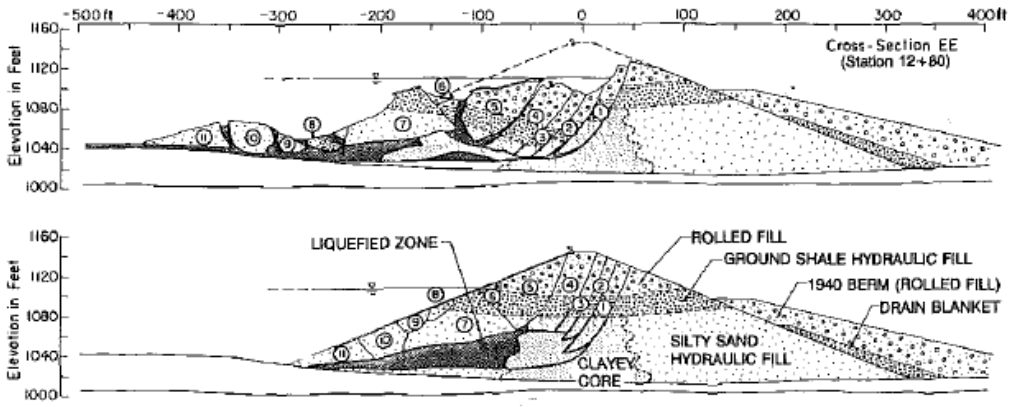

Figure A.4.1. Soil stratigraphy and pre-failure and post-failure cross-sections of the Lower San Fernando Dam (Castro et al., 1992)

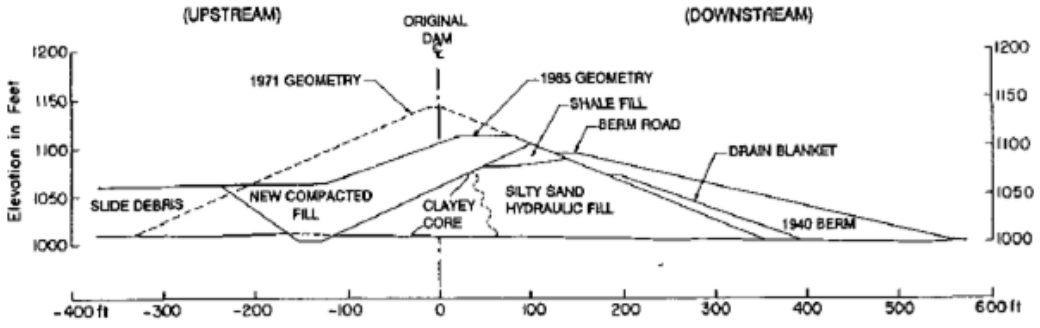

Figure A.4.2. Reconstructed cross-sections of the Lower San Fernando Dam (Castro et al., 1992)

A.4.3 Evaluation of Material Properties

Since the grain size distribution curves of the case history were reported by the main sources of references as given in Figure A.4.3 and Figure A.4.4, mean grain size (D_{50}), fines content (FC) and coefficient of uniformity (C_u) values are evaluated based on these curves. Two different but similar GSD curves were documented in Castro et al. (1989) and Castro et al. (1992); thus, the arithmetic mean of the values obtained from these two graphs are taken as the representative values.

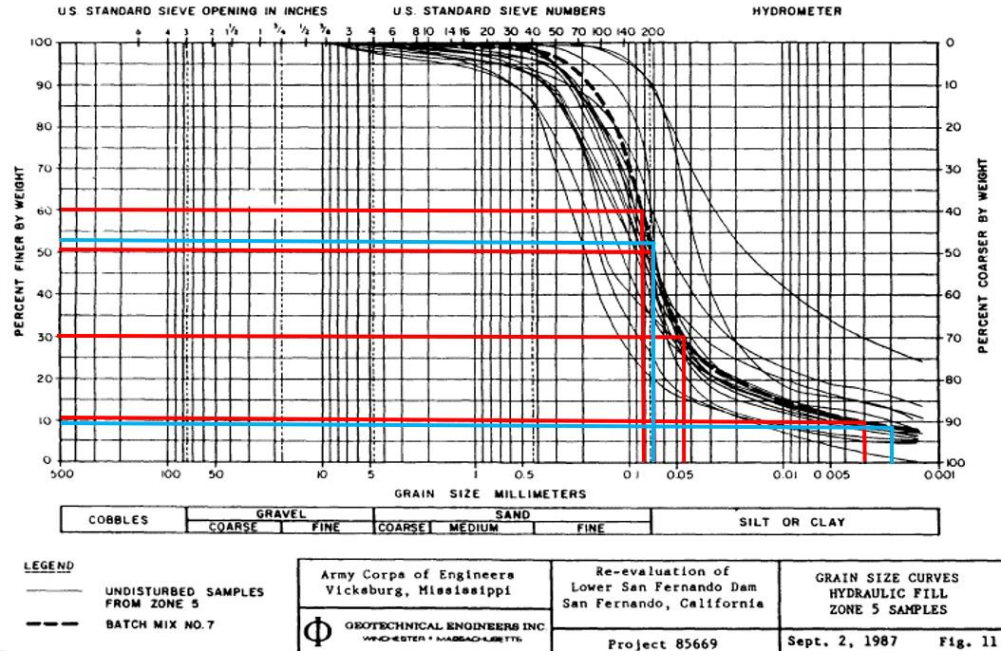

Figure A.4.3. Grain size distribution curve of the liquefied zone of the Lower San Fernando Dam (Castro et al., 1989)

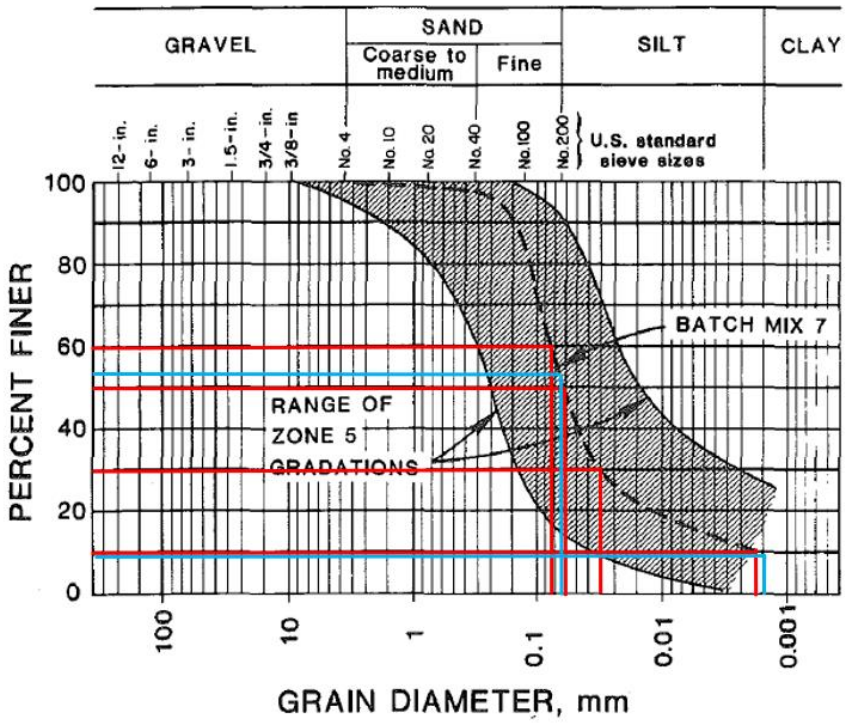

Figure A.4.4. Grain size distribution curve of the liquefied zone of the Lower San Fernando Dam (Castro et al., 1992)

Mean grain size (D_{50}): D_{50} = 0.070 mm is evaluated representatively based on the grain size distribution curves of the case history. Olson (2001) also suggests 0.075 mm for D_{50} value.

Fines content (FC): FC = 53% is evaluated representatively for the liquefied zone based on the grain size distribution curves of the case history. Olson (2001) also suggests FC = 50%.

Coefficient of uniformity (C_u): D_{10} and D_{60} values are evaluated as 0.0027 mm and 0.082 mm, respectively, based on the grain size distribution curves of the case history. Therefore, the uniformity coefficient is estimated as $C_u = D_{60}/D_{10}$ = 0.082/0.0027 = 31.49, which indicates well-graded soil.

Roundness (R): Since no roundness value was reported by the main sources of references or other studies, no value has been set for this parameter for the evaluation of limit void ratios and void ratio ranges. However, R = 0.50 is taken approximately as a representative value for the evaluation of liquefaction state friction angle.

Sphericity (S): Since no sphericity value was reported by the main sources of references or other studies, no value has been set for this parameter for the evaluation of limit void ratios and void ratio ranges. However, S = 0.60 is taken approximately as a representative value for the evaluation of liquefaction state friction angle.

Unit weight (γ_{dry} and γ_{sat}): As the results are not sensitive to unit weight, the dry and saturated unit weights of hydraulic fill materials are assigned as 18.9 kN/m^3 and 19.3 kN/m^3, respectively. For foundation, rolled fill, and rock fill layers, the unit weights are defined as 19.6 kN/m^3. For the clay core materials, the unit weights are estimated as 18.9 kN/m^3. All these values are evaluated accordingly to be compatible with Olson (2001) and Weber (2015).

A.4.4 Sub-sectioning of the Cross-section and Failure Plane

The exact locations of the SPT boreholes were known for the downstream part of the dam as shown in Figure A.4.5 as an example. By considering the similarities between the upstream and downstream parts, these boreholes are also considered for the upstream symmetrically. Therefore, the sub-sectioning is made based on the locations of these penetration tests as presented in Figure A.4.6. Each test is assigned (names of the logs are directly assigned as the name of the sub-section) for the corresponding territory length.

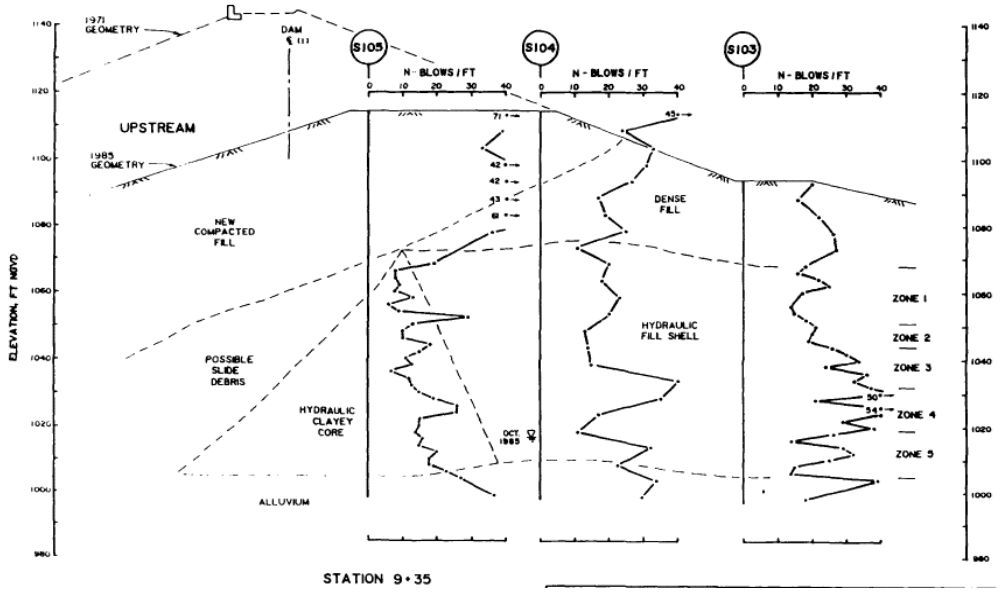

Figure A.4.5. Location of SPT boreholes for Lower San Fernando Dam (Castro et al., 1989)

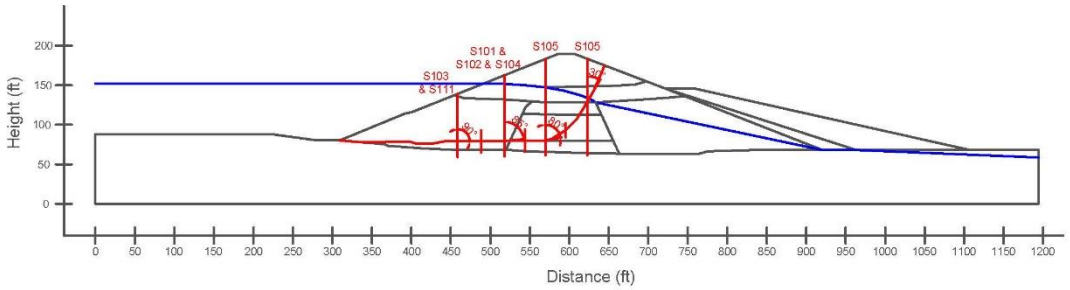

Figure A.4.6. Sub-sectioning of the cross-section and failure plane for Lower San Fernando Dam

The territory lengths (L_i) and inclinations (α_i) (positive sign for CCW direction) of the failure plane are evaluated as given in Table A.4.1 for each sub-section.

Table A.4.1 Sub-sections with their corresponding failure plane lengths and inclinations for Lower San Fernando Dam

Case History	Section	Failure plane length, L_i (m)	Total failure plane length, L_t (m)	Failure plane inclination, α_i (degrees)
Lower San Fernando Dam	S103&S111	54.84	103.82	0
	S101&S102&S104	16.94		5
	S105	16.77		10
	S105	15.28		60

A.4.5 Elastic Modeling and Stress Rotation

All stress components are evaluated linear elastically at the points where boreholes and failure plane intersect in Figure A.4.6. The initial and deformed shape of the cross-section are presented in Figure A.4.7 and Figure A.4.8, respectively. All lengths are given in meters.

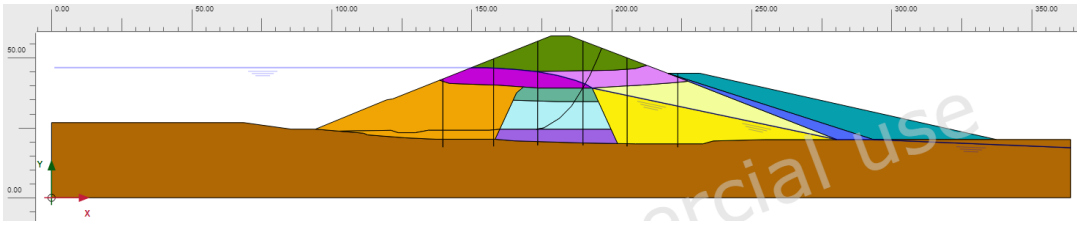

Figure A.4.7. Initial cross-section used in linear elastic modeling of Lower San Fernando Dam

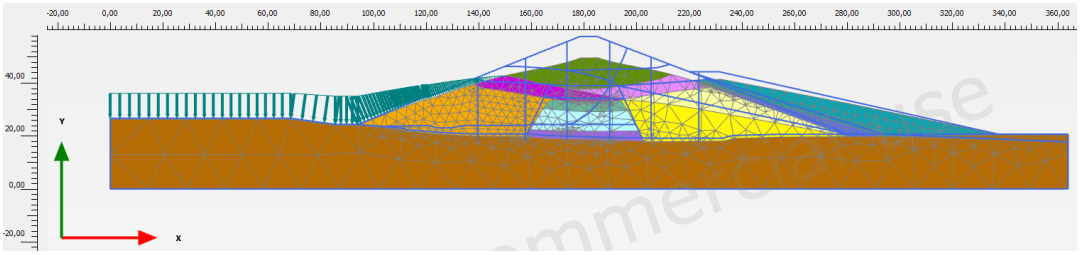

Figure A.4.8. Deformed cross-section obtained after linear elastic modeling of Lower San Fernando Dam

During the elastic modeling process in PLAXIS 2D Ultimate Connect Edition V22.00.00.1733 software, the Poisson's ratio values of the clay core, rolled fill and liquefied hydraulic fill materials are defined as 0.33. For these materials, the elastic modulus values are estimated as 5 MPa. For non-liquefied hydraulic fill, rock fill and foundation, the Poisson's ratio values are defined as 0.30. The elastic modulus values of these layers are estimated as 10 MPa, 20 MPa, and 30 MPa, respectively.

The effective normal (σ'_N) and shear (τ_{static}) stresses acting on the inclined failure plane are evaluated with corresponding Mohr's circles. The corresponding Mohr's circles and the effective stress components of the sub-sections are presented in Figure A.4.9 and Table A.4.2, respectively. All stresses are given in kilopascals.

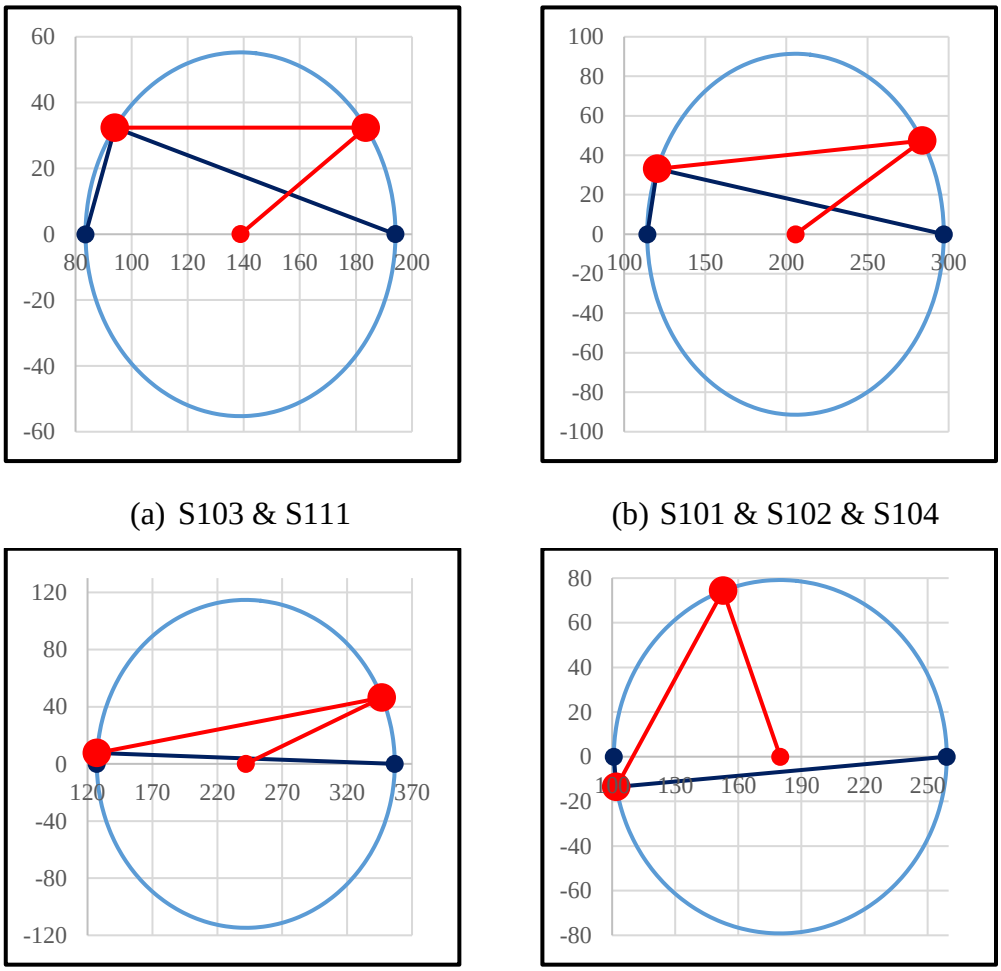

(a) S103 & S111 (b) S101 & S102 & S104

(c) S105 (d) S105

Figure A.4.9. Mohr's circles for Lower San Fernando Dam

Table A.4.2 Evaluated stress components for Lower San Fernando Dam

Case History	Section	σ'_1 (kPa)	σ'_2 (kPa)	σ'_3 (kPa)	p_0' (kPa)	q (kPa)	σ'_N (kPa)	τ_{static} (kPa)	$\lvert\tau_{static}\rvert$ (kPa)
Lower San Fernando Dam	S103&S111	194.1	91.7	83.6	123.2	106.7	183.6	32.4	32.4
	S101,102,104	297.0	135.7	114.2	182.3	173.1	283.8	47.4	47.4
	S105	356.7	159.7	127.2	214.5	215.1	346.9	46.3	46.3
	S105	259.1	118.8	100.8	159.6	150.1	152.7	74.3	74.3

A.4.6 Evaluation of SPT Resistance

The exact locations of the SPT boreholes were documented by Castro et al. (1989) for the downstream of the dam as given in Figure A.4.5. By considering the similarities between the upstream and downstream parts, these boreholes are also considered for the upstream symmetrically.

The correction factors for nonstandardized sampler configuration (C_S), borehole diameter (C_B), and energy efficiency (C_E) are taken as 1.0 since no reliable information related to these coefficients was reported in any of the sources. The short rod length (C_R) and fines content correction factors (C_{fines}) are evaluated with the methods and relationships explained in Section 3.5. The overburden stress correction factors (C_N) are evaluated based on the effective vertical stresses estimated at the point of penetration for each recording, and average values are documented for simplicity. Accordingly, the correction factors and SPT resistances are estimated as given in Table A.4.3.

Table A.4.3 Evaluated SPT-N resistances for Lower San Fernando Dam

Case History	Section	C_N	C_B	C_R	C_S	C_E	C_{fines}	N	N_{60}	$(N_1)_{60}$	$(N_1)_{60,cs}$	
Lower San Fernando Dam	S103&S111	0.71	1.0	0.99	1.0	1.00	1.26	21.45	21.29	14.04	17.75	17.75
	S101,102,104	0.66	1.0	0.99	1.0	1.00	1.26	21.45	21.30	14.04	17.76	
	S105	0.61	1.0	0.99	1.0	1.00	1.26	21.45	21.30	14.04	17.76	
	S105	0.61	1.0	0.99	1.0	1.00	1.26	21.45	21.25	14.01	17.72	

A.4.7 Evaluation of Limit Void Ratios, Void Ratio Ranges, Relative Densities and Initial Void Ratios

Since mean grain size (D_{50}), fines content (FC), and coefficient of uniformity (C_u) information were available among the required material properties for the void ratio prediction models, the arithmetic means of the limit void ratios (e_{min} and e_{max}) evaluated by Model 8 and Model 9 are considered as the representative values. The e_{max} value is slightly modified then with respect to the construction method of the case history for each prediction model.

Since the fines content value is evaluated as 53%, which is greater than 15%, it is judged that the soil of interest consists of silty soils. Therefore, the relative densities evaluated by the correlation recommended by Cubrinovski and Ishihara (1999) are directly taken as the representative relative densities of the soils. Based on these relative densities and limit void ratios, the initial void ratios (e_0) corresponding to approximately 1 kPa confining stress are estimated referring to Equation 3-68. Accordingly, the limit void ratios, void ratio ranges (without any modification for the construction method), in-situ relative densities, and initial void ratios are estimated as given in Table A.4.4.

Table A.4.4 Evaluated limit void ratios, void ratio ranges, in-situ relative densities, and initial void ratios for Fort Peck Dam

Case History	Section	e_{min}	e_{max}	e_{max}-e_{min}	$RD_{C\&I}$ (%)	$RD_{K\&M}$ (%)	$RD_{overall}$ (%)	e_0
Lower San Fernando Dam	S103&S111	0.398	0.593	0.195	27.34	67.15	27.34	0.540
	S101&S102&S104	0.398	0.593	0.195	27.34	67.16	27.34	0.540
	S105	0.398	0.593	0.195	27.34	67.16	27.34	0.540
	S105	0.398	0.593	0.195	27.31	67.09	27.31	0.540

A.5 Hachiro-Gata Road Embankment (1983 Nihon-Kai-Chubu Earthquake, M_w=7.7)

A.5.1 Brief Summary of the Case History

Hachiro-Gata Road Embankment was located in Akita, Japan, and the exact date of the failure was reported as May 26, 1983. The fundamental reason behind the failure was reported as the 1983 Nihon-Kai-Chubu Earthquake (M_L=7.7). The type of the structure can be classified as a poorly compacted embankment, and the maximum slope height is reported as ~ 4 m. Ohya et al. (1985) is considered as the main source of reference. Olson (2001), Wang (2003) and Weber (2015) also studied this case history during their back-analyses of liquefaction failure case histories.

A.5.2 Site Geology and Critical Cross-section

Figure A.5.1 shows the soil stratigraphy and pre-failure and post-failure cross-sections of the case structure. It is decided that the idealized soil profile consists of four soil layers namely non-liquefied zone, liquefied zone, medium-dense sand, and dense sand. The parts of the embankment remaining above and below the water table level at the time of failure are classified as non-liquefied zone and liquefied zone, respectively. The layers underlying the embankment are defined as the medium-dense sand and dense sand, from top to bottom respectively.

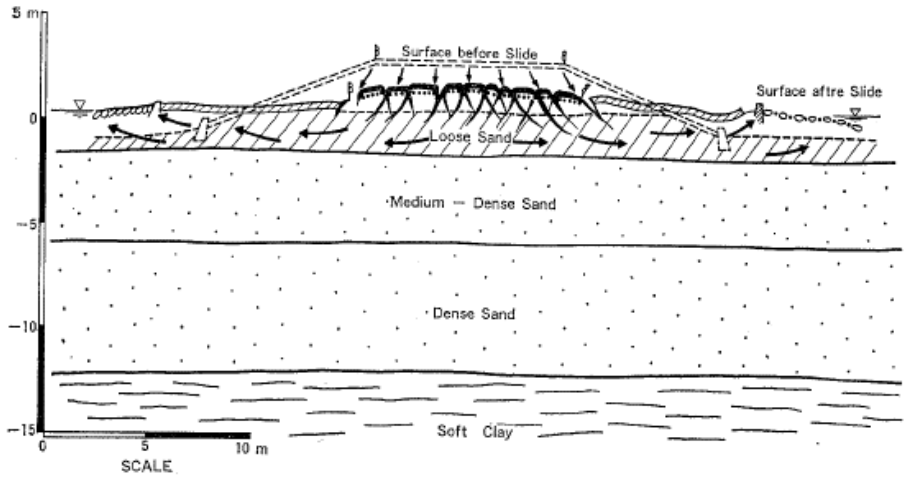

Figure A.5.1. Soil stratigraphy and pre-failure and post-failure cross-sections of the Hachiro-Gata Road Embankment (Ohya et al., 1985)

A.5.3 Evaluation of Material Properties

Since the grain size distribution curve of the case history was not reported by the main sources of references or other residual strength-related studies, mean grain size (D_{50}), fines content (FC) and coefficient of uniformity (C_u) values are estimated based on the documented representative values in those references, if available. In fact, the distribution of the soil types and grain sizes with depth were reported in Ohya et al. (1985) with a sketch presented in Figure A.5.2. Therefore, available material properties are estimated according to this plot.

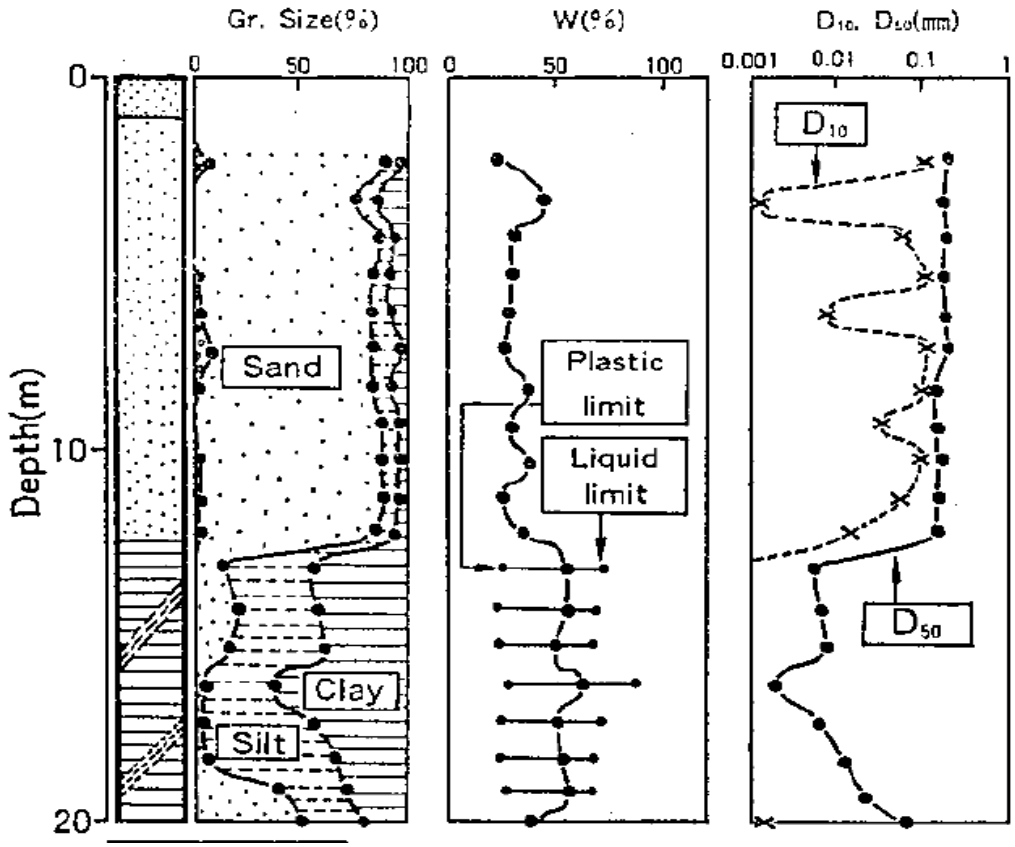

Figure A.5.2. The distribution of soil types and grain sizes with depth for the Hachiro-Gata Road Embankment (Ohya et al., 1985)

Mean grain size (D_{50}): D_{50} = 0.181 mm is evaluated representatively for the liquefied zone based on the grain size distribution with depth plot. Olson (2001) also suggests 0.2 mm for D_{50} value.

Fines content (FC): FC = 18% is evaluated representatively for the liquefied zone based on the soil type distribution with depth plot of the case history. This value is also compatible with the value reported by Srbulov (2008), which is 15%. Olson (2001) also suggests a range of 10%-20% for fines content of this case history.

Coefficient of uniformity (C_u): Since only D_{10} and D_{50} values were reported in the grain size distribution with depth plot, and no information were reported for D_{60} values, a value could not be set for this parameter.

Roundness (R): Since no roundness value was reported by the main sources of references or other studies, no value has been set for this parameter for the evaluation of limit void ratios and void ratio ranges. However, R = 0.50 is taken approximately as a representative value for the evaluation of liquefaction state friction angle.

Sphericity (S): Since no sphericity value was reported by the main sources of references or other studies, no value has been set for this parameter for the evaluation of limit void ratios and void ratio ranges. However, S = 0.60 is taken approximately as a representative value for the evaluation of liquefaction state friction angle.

Unit weight (γ_{dry} and γ_{sat}): As the results are not sensitive to unit weight, the dry and saturated unit weights of all soil layers are assigned as 18.1 kN/m^3 and 19.2 kN/m^3, respectively, to be compatible with Olson (2001) and Weber (2015).

A.5.4 Sub-sectioning of the Cross-section and Failure Plane

The exact locations of the SPT boreholes were not known for this case history. Therefore, the sub-sectioning is made based on imaginary boreholes assigned on the cross-section. These imaginary boreholes are defined with respect to changes in effective vertical stresses and inclination angles of the failure plane. Accordingly, two sub-sections are assigned for the liquefied zone as presented in Figure A.5.3.

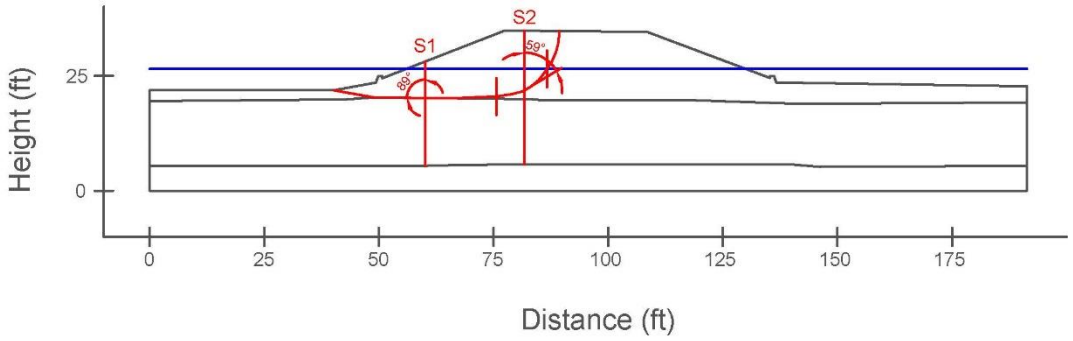

Figure A.5.3. Sub-sectioning of the cross-section and failure plane for Hachiro-Gata Road Embankment

The territory lengths (L_i) and inclinations (α_i) (positive sign for CCW direction) of the failure plane are evaluated as given in Table A.5.1 for each sub-section.

Table A.5.1 Sub-sections with their corresponding failure plane lengths and inclinations for Hachiro-Gata Road Embankment

Case History	Section	Failure plane length, L_i (m)	Total failure plane length, L_t (m)	Failure plane inclination, α_i (degrees)
Hachiro-Gata Embankment	S1	10.85	14.86	-1
	S2	4.01		31

A.5.5 Elastic Modeling and Stress Rotation

All stress components are evaluated linear elastically at the points where boreholes and failure plane intersect in Figure A.5.3. The initial and deformed shape of the cross-section are presented in Figure A.5.4 and Figure A.5.5, respectively. All lengths are given in meters.

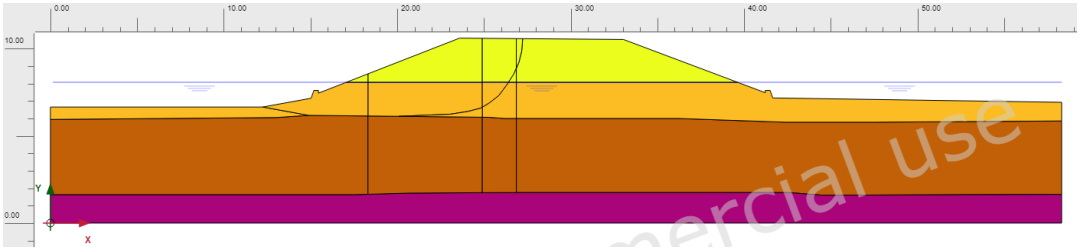

Figure A.5.4. Initial cross-section used in linear elastic modeling of Hachiro-Gata Road Embankment

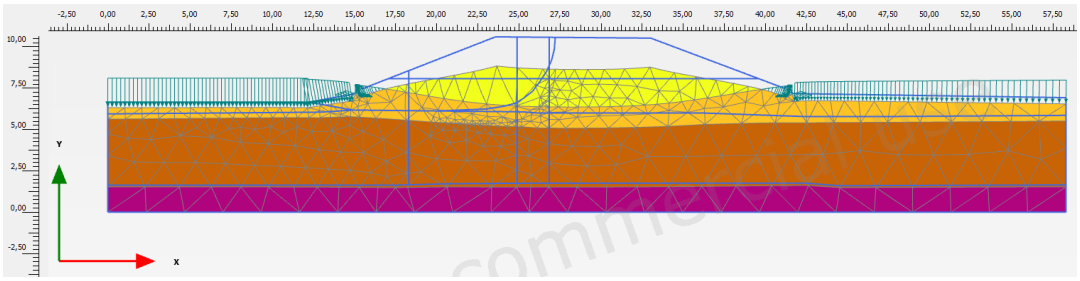

Figure A.5.5. Deformed cross-section obtained after linear elastic modeling of Hachiro-Gata Road Embankment

During the elastic modeling process in PLAXIS 2D Ultimate Connect Edition V22.00.00.1733 software, the Poisson's ratio values of the non-liquefied zone, liquefied zone, medium-dense sand, and dense sand are defined as 0.30, 0.33, 0.30, and 0.30, respectively. The elastic modulus values of the same layers, on the other hand, are estimated as 10 MPa, 5 MPa, 20 MPa, and 30 MPa, respectively.

The effective normal (σ'_N) and shear (τ_{static}) stresses acting on the inclined failure plane are evaluated with corresponding Mohr's circles. The corresponding Mohr's circles and the effective stress components of the sub-sections are presented in Figure A.5.6 and Table A.5.2, respectively. All stresses are given in kilopascals.

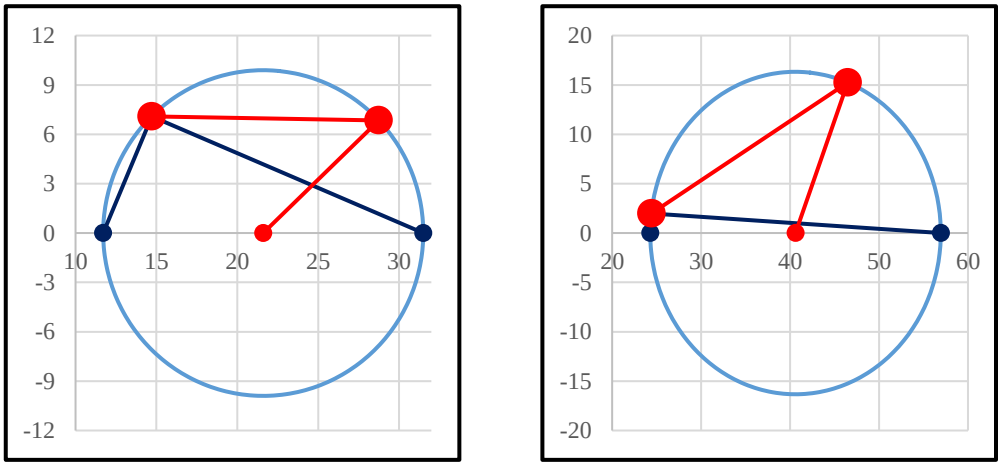

(a) S1 (b) S2

Figure A.5.6. Mohr's circles for Hachiro-Gata Road Embankment

Table A.5.2 Evaluated stress components for Hachiro-Gata Road Embankment

Case History	Section	σ'_1 (kPa)	σ'_2 (kPa)	σ'_3 (kPa)	p_0' (kPa)	q (kPa)	σ'_N (kPa)	τ_{static} (kPa)	$\lvert\tau_{static}\rvert$ (kPa)
Hachiro-Gata Road Embankment	S1	31.5	14.3	11.7	19.2	18.6	28.8	6.8	6.8
	S2	56.9	26.8	24.3	36.0	31.5	46.5	15.2	15.2

A.5.6 Evaluation of SPT Resistance

The exact locations of the SPT boreholes were not documented for this case history. Therefore, imaginary boreholes are assigned along the cross-section as shown in Figure A.5.3. SPT data used for this case history is presented in Figure A.5.7.

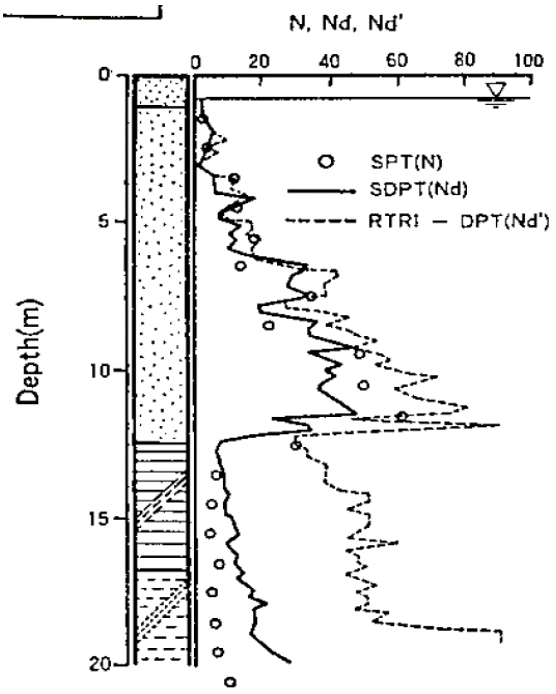

Figure A.5.7. SPT boreholes for Hachiro-Gata Road Embankment (Ohya et al., 1985)

The correction factors for nonstandardized sampler configuration (C_S) and energy efficiency (C_E) are taken as 1.0 since no reliable information related to these coefficients was reported in any of the sources. The borehole diameter was reported as 66-86 mm for this Standard Penetration Test; thus, the correction factor for borehole diameter (C_B) is also taken as 1.0. The short rod length (C_R) and fines content correction factors (C_{fines}) are evaluated with the methods and relationships explained in Section 3.5. The overburden stress correction factors (C_N) are evaluated based on the effective vertical stresses estimated at the point of penetration for each recording, and average values are documented for simplicity. Accordingly, the correction factors and SPT resistances are estimated as given in Table A.5.3.

Table A.5.3 Evaluated SPT-N resistances for Hachiro-Gata Road Embankment

Case History	Section	C_N	C_B	C_R	C_S	C_E	C_{fines}	N	N_{60}	$(N_1)_{60}$	$(N_1)_{60,cs}$	
Hachiro-Gata Road Embankment	S1	1.92	1.0	0.86	1.0	1.00	1.28	2.60	2.23	4.29	5.49	5.49
	S2	1.92	1.0	0.86	1.0	1.00	1.28	2.60	2.23	4.29	5.49	

A.5.7 Evaluation of Limit Void Ratios, Void Ratio Ranges, Relative Densities and Initial Void Ratios

Since mean grain size (D_{50}) and fines content (FC) information were available among the required material properties for the void ratio prediction models, the arithmetic means of the limit void ratios (e_{min} and e_{max}) evaluated by Model 1 and Model 2 are considered as the representative values. The e_{max} value is slightly modified then with respect to the construction method of the case history for each prediction model.

Since the fines content value is evaluated as 18%, which is greater than 15%, it is judged that the soil of interest consists of silty soils. Therefore, the relative densities evaluated by the correlation recommended by Cubrinovski and Ishihara (1999) are directly taken as the representative relative densities of the soils. Based on these relative densities and limit void ratios, the initial void ratios (e_0) corresponding to approximately 1 kPa confining stress are estimated referring to Equation 3-68. Accordingly, the limit void ratios, void ratio ranges (without any modification for the construction method), in-situ relative densities, and initial void ratios are estimated as given in Table A.5.4.

Table A.5.4 Evaluated limit void ratios, void ratio ranges, in-situ relative densities, and initial void ratios for Hachiro-Gata Road Embankment

Case History	Section	e_{min}	e_{max}	e_{max}-e_{min}	$RD_{C\&I}$ (%)	$RD_{K\&M}$ (%)	$RD_{overall}$ (%)	e_0
Hachiro-Gata Road Embankment	S1	0.591	0.997	0.406	28.14	32.16	28.14	0.883
	S2	0.591	0.997	0.406	28.14	32.16	28.14	0.883

A.6 La Marquesa Dam – U/S Slope (1985 Chilean Earthquake, M_s=7.8)

A.6.1 Brief Summary of the Case History

La Marquesa Dam was located in Chile, and the exact date of the failure was reported as March 3, 1985. The fundamental reason behind the failure was reported as the 1985 Central Chilean Earthquake (M_s=7.8). The type of the structure can be classified as a poorly compacted zoned earthen dam, and the maximum slope height is reported as ~ 9 m. De Alba et al. (1987, 1988) are taken into account as the main sources of references. Olson (2001), Wang (2003) and Weber (2015) also studied this case history during their back-analyses of liquefaction failure case histories.

A.6.2 Site Geology and Critical Cross-section

Figure A.6.1 presents the soil stratigraphy and pre-failure and post-failure cross-sections of the case structure. It is decided that the idealized soil profile consists of six soil layers namely moist silty and clayey sand shell, saturated silty and clayey sand shell, liquefied zone, sandy clay core, sandy clay, and outside toe material. The parts of the earthen dam remaining above and below the water table level at the time of failure are classified as moist silty and clayey sand shell and saturated silty and clayey sand shell, respectively. The lower portion of the saturated silty and clayey sand shell is evaluated as the liquefied zone. The layer underlying the earthen dam is defined as the sandy clay zone. The middle part of the dam body is classified as sandy clay core, and the zone existing at the outside portion of the toe is defined as outside toe material.

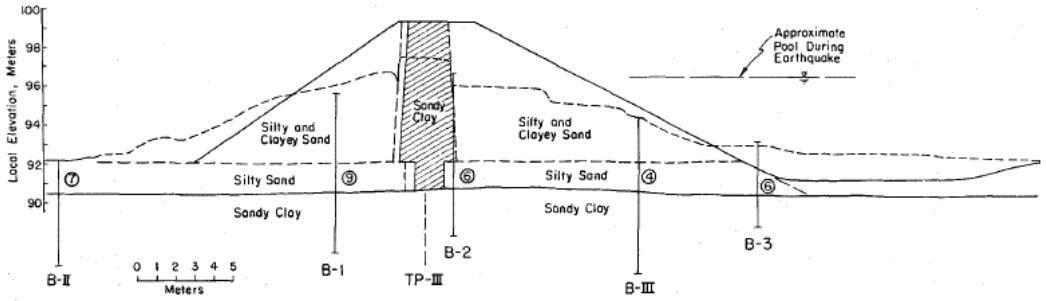

Figure A.6.1. Soil stratigraphy and pre-failure and post-failure cross-sections of the La Marquesa Dam (Alba et al., 1987)

A.6.3 Evaluation of Material Properties

Since the grain size distribution curve of the case history was not reported by the main sources of references or other residual strength-related studies, mean grain size (D_{50}), fines content (FC) and coefficient of uniformity (C_u) values are estimated based on the documented representative values in those references, if available.

Mean grain size (D_{50}): The exact value of the mean grain size was reported as D_{50} = 0.150 mm in Olson (2001) and Srbulov (2008). Hence, the representative D_{50} value is also taken as 0.150 mm in this study.

Fines content (FC): The exact value of the fines content was reported as FC = 30% in Alba et al. (1987,1988), Olson (2001), Srbulov (2008) and Weber (2015) for the upstream portion of the dam. Hence, the representative FC value is also taken as 30% in this study.

Coefficient of uniformity (C_u): Since no coefficient of uniformity value was reported by the main sources of references or other relative studies, no value has been set for this parameter.

Roundness (R): Since no roundness value was reported by the main sources of references or other studies, no value has been set for this parameter for the evaluation of limit void ratios and void ratio ranges. However, R = 0.50 is taken approximately as a representative value for the evaluation of liquefaction state friction angle.

Sphericity (S): Since no sphericity value was reported by the main sources of references or other studies, no value has been set for this parameter for the evaluation of limit void ratios and void ratio ranges. However, S = 0.60 is taken approximately as a representative value for the evaluation of liquefaction state friction angle.

Unit weight (γ_{dry} and γ_{sat}): As the results are not sensitive to unit weight, the dry and saturated unit weights of all soil layers are assigned as 18.9 kN/m^3 and 19.6 kN/m^3, respectively, to be compatible with Olson (2001) and Weber (2015).

A.6.4 Sub-sectioning of the Cross-section and Failure Plane

The exact locations of the SPT boreholes were known for this case history. Therefore, the sub-sectioning is made based on the locations of these penetration tests as presented in Figure A.6.2. Each test is assigned (names of the logs are directly assigned as the name of the sub-section) for the corresponding territory length.

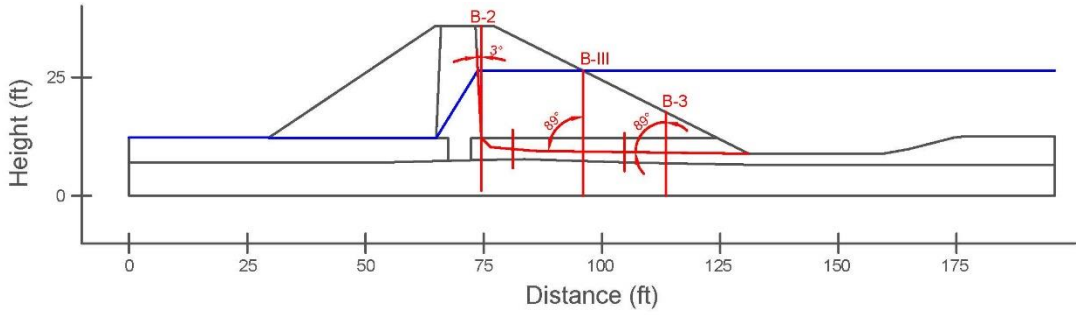

Figure A.6.2. Sub-sectioning of the cross-section and failure plane for La Marquesa Dam – U/S Slope

The territory lengths (L_i) and inclinations (α_i) (positive sign for CCW direction) of the failure plane are evaluated as given in Table A.6.1 for each sub-section.

Table A.6.1 Sub-sections with their corresponding failure plane lengths and inclinations for La Marquesa Dam – U/S Slope

Case History	Section	Failure plane length, L_i (m)	Total failure plane length, L_t (m)	Failure plane inclination, α_i (degrees)
La Marquesa Dam – U/S Slope	B-2	6.61	21.81	-87
	B-III	7.20		-1
	B-3	8.00		-1

A.6.5 Elastic Modeling and Stress Rotation

All stress components are evaluated linear elastically at the points where boreholes and failure plane intersect in Figure A.6.2. The initial and deformed shape of the cross-section are presented in Figure A.6.3 and Figure A.6.4, respectively. All lengths are given in meters.

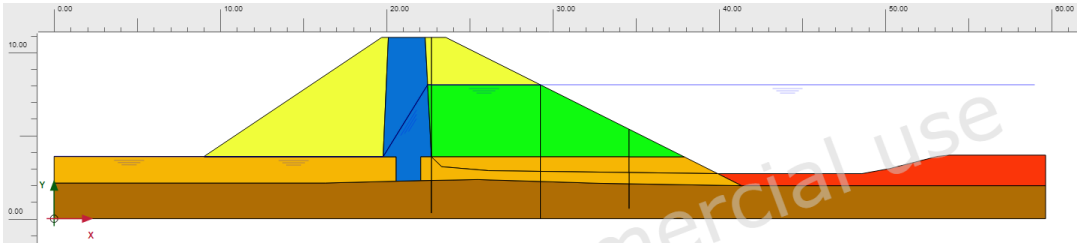

Figure A.6.3. Initial cross-section used in linear elastic modeling of La Marquesa Dam – U/S Slope

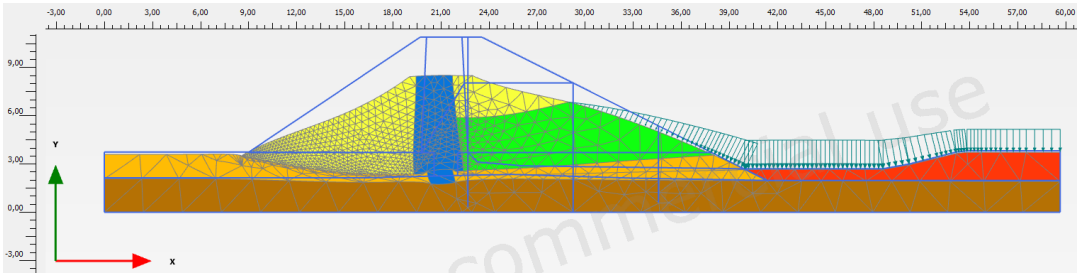

Figure A.6.4. Deformed cross-section obtained after linear elastic modeling of La Marquesa Dam – U/S Slope

During the elastic modeling process in PLAXIS 2D Ultimate Connect Edition V22.00.00.1733 software, while the Poisson's ratio values of all materials other than liquefied zone are defined as 0.30, it is estimated as 0.33 for the liquefied zone. For moist silty and clayey sand shell, saturated silty and clayey sand shell, liquefied zone, sandy clay core, sandy clay, and outside toe material, the elastic modulus values are evaluated as 10 MPa, 10 MPa, 5 MPa, 20 MPa, 30 MPa, and 20 MPa, respectively.

The effective normal (σ'_N) and shear (τ_{static}) stresses acting on the inclined failure plane are evaluated with corresponding Mohr's circles. The corresponding Mohr's circles and the effective stress components of the sub-sections are presented in Figure A.6.5 and Table A.6.2, respectively. All stresses are given in kilopascals.

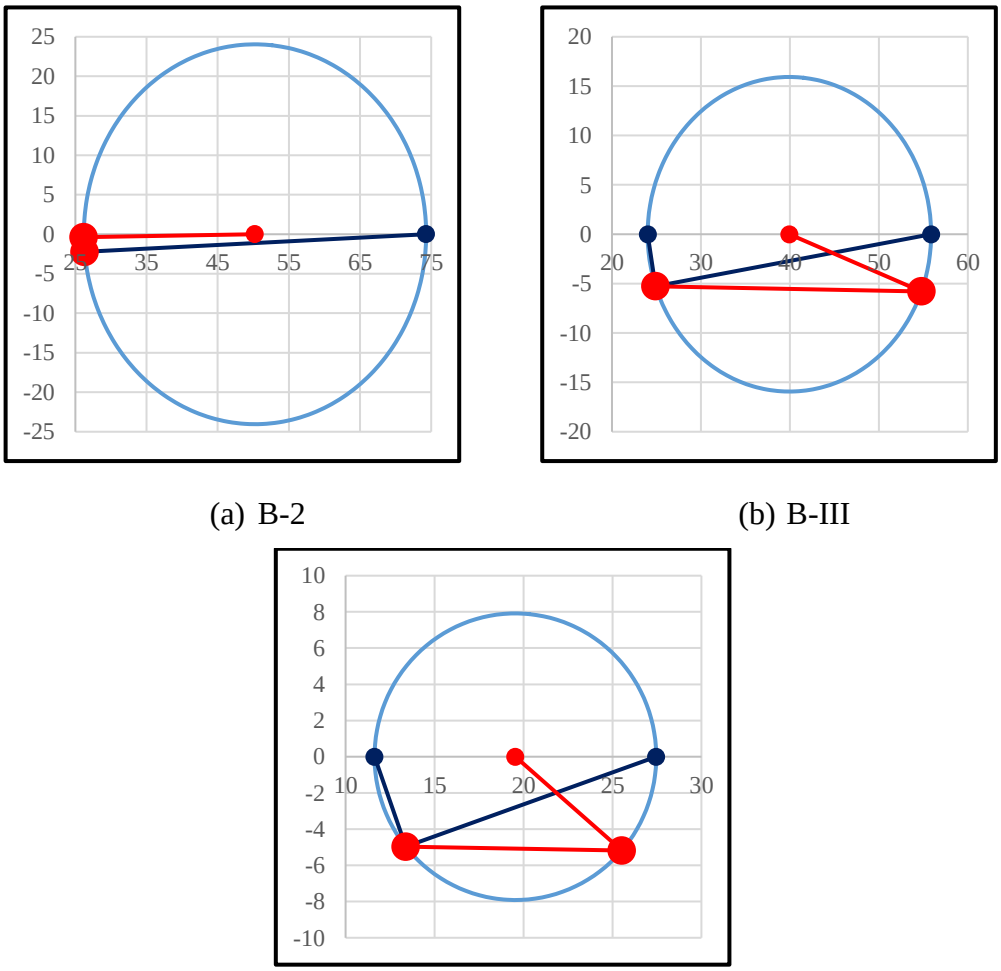

(a) B-2 (b) B-III

(c) B-3

Figure A.6.5. Mohr's circles for La Marquesa Dam – U/S Slope

Table A.6.2 Evaluated stress components for La Marquesa Dam – U/S Slope

Case History	Section	σ'_1 (kPa)	σ'_2 (kPa)	σ'_3 (kPa)	p_0' (kPa)	q (kPa)	σ'_N (kPa)	τ_{static} (kPa)	$\lvert\tau_{static}\rvert$ (kPa)
La Marquesa Dam – U/S Slope	B-2	74.3	33.2	26.2	44.6	45.0	26.2	-0.4	0.4
	B-III	55.9	26.4	24.0	35.4	30.8	54.8	-5.8	5.8
	B-3	27.5	12.9	11.6	17.3	15.2	25.5	-5.2	5.2

A.6.6 Evaluation of SPT Resistance

The exact locations of the SPT boreholes were documented by Alba et al. (1987) as given in Figure A.6.6.

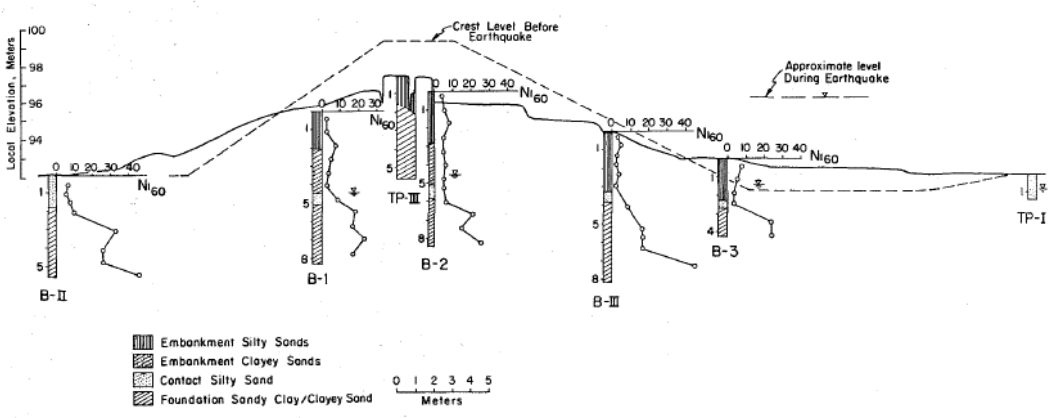

Figure A.6.6. SPT data for La Marquesa Dam (Alba et al., 1987)

SPT boreholes are presented in Figure A.6.7 for B-2, B-III, and B-3 of the upstream slope, respectively.

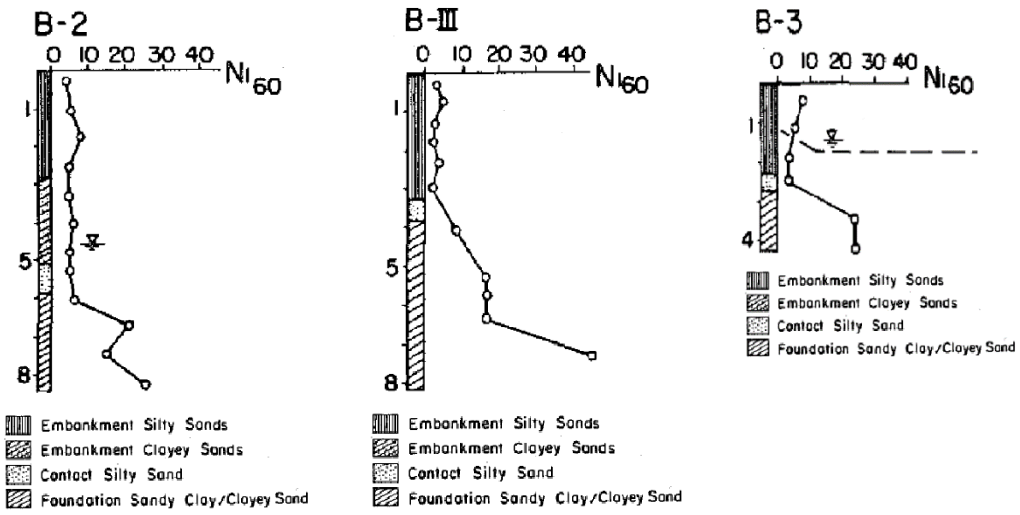

(a) B-2 (b) B-III (c) B-3

Figure A.6.7. SPT boreholes for La Marquesa Dam – U/S Slope (Alba et al., 1987)

Since $(N_1)_{60}$ values were reported instead of raw SPT-N values, they are converted into the raw SPT-N values initially, and then corrected for equipment, overburden stress, and fines content with the same procedures to achieve consistency. The raw SPT-N values are evaluated by back-analyzing the corrected $(N_1)_{60}$ values with the same correction methods used by the reporting teams.

Once the raw SPT-N values are estimated, the correction factors for nonstandardized sampler configuration (C_S) and borehole diameter (C_B) are taken as 1.0 since no reliable information related to these coefficients was reported in any of the sources. The energy ratio was reported as 56% in Alba et al. (1987, 1988); therefore, the energy efficiency correction factor (C_E) is taken as 56/60 = 0.93. The short rod length (C_R) and fines content correction factors (C_{fines}) are evaluated with the methods and relationships explained in Section 3.5. The overburden stress correction factors (C_N) are evaluated based on the effective vertical stresses estimated at the point of penetration for each recording, and average values are documented for simplicity. Accordingly, the correction factors and SPT resistances are estimated as given in Table A.6.3.

Table A.6.3 Evaluated SPT-N resistances for La Marquesa Dam – U/S Slope

Case History	Section	C_N	C_B	C_R	C_S	C_E	C_{fines}	N	N_{60}	$(N_1)_{60}$	$(N_1)_{60,cs}$	
La Marquesa Dam – U/S Slope	B-2	2.39	1.0	0.89	1.0	0.93	1.51	3.02	2.51	3.88	5.85	5.63
	B-III	3.02	1.0	0.82	1.0	0.93	1.54	3.02	2.30	3.57	5.49	
	B-3	2.40	1.0	0.83	1.0	0.93	1.54	3.02	2.33	3.61	5.54	

A.6.7 Evaluation of Limit Void Ratios, Void Ratio Ranges, Relative Densities and Initial Void Ratios

Since mean grain size (D_{50}) and fines content (FC) information were available among the required material properties for the void ratio prediction models, the arithmetic means of the limit void ratios (e_{min} and e_{max}) evaluated by Model 1 and Model 2 are considered as the representative values. The e_{max} value is slightly modified then with respect to the construction method of the case history for each prediction model.

Since the fines content value is evaluated as 30%, which is greater than 15%, it is judged that the soil of interest consists of silty soils. Therefore, the relative densities evaluated by the correlation recommended by Cubrinovski and Ishihara (1999) are directly taken as the representative relative densities of the soils. Based on these relative densities and limit void ratios, the initial void ratios (e_0) corresponding to approximately 1 kPa confining stress are estimated referring to Equation 3-68. Accordingly, the limit void ratios, void ratio ranges (without any modification for the construction method), in-situ relative densities, and initial void ratios are estimated as given in Table A.6.4.

Table A.6.4 Evaluated limit void ratios, void ratio ranges, in-situ relative densities, and initial void ratios for La Marquesa Dam – U/S Slope

Case History	Section	e_{min}	e_{max}	e_{max}-e_{min}	$RD_{C\&I}$ (%)	$RD_{K\&M}$ (%)	$RD_{overall}$ (%)	e_0
La Marquesa Dam – U/S Slope	B-2	0.600	1.017	0.417	27.39	31.39	27.39	0.902
	B-III	0.600	1.017	0.417	26.25	30.08	26.25	0.907
	B-3	0.600	1.017	0.417	26.40	30.26	26.40	0.907

A.7 La Marquesa Dam – D/S Slope (1985 Chilean Earthquake, M_s=7.8)

A.7.1 Brief Summary of the Case History

La Marquesa Dam was located in Chile, and the exact date of the failure was reported as March 3, 1985. The fundamental reason behind the failure was reported as the 1985 Central Chilean Earthquake (M_s=7.8). The type of the structure can be classified as a poorly compacted zoned earthen dam, and the maximum slope height is reported as ~ 9 m. De Alba et al. (1987, 1988) are taken into account as the main sources of references. Olson (2001), Wang (2003) and Weber (2015) also studied this case history during their back-analyses of liquefaction failure case histories.

A.7.2 Site Geology and Critical Cross-section

Figure A.7.1 presents the soil stratigraphy and pre-failure and post-failure cross-sections of the case structure. It is decided that the idealized soil profile consists of six soil layers namely moist silty and clayey sand shell, saturated silty and clayey sand shell, liquefied zone, sandy clay core, sandy clay, and outside toe material. The parts of the earthen dam remaining above and below the water table level at the time of failure are classified as moist silty and clayey sand shell and saturated silty and clayey sand shell, respectively. The lower portion of the saturated silty and clayey sand shell is evaluated as the liquefied zone. The layer underlying the earthen dam is defined as the sandy clay zone. The middle part of the dam body is classified as sandy clay core, and the zone existing at the outside portion of the toe is defined as outside toe material.

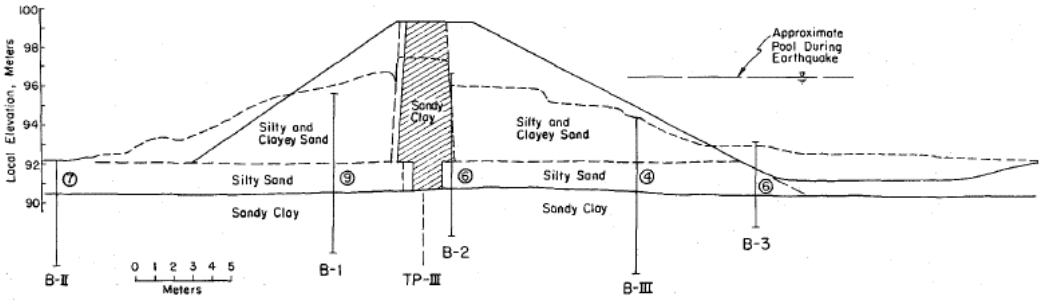

Figure A.7.1. Soil stratigraphy and pre-failure and post-failure cross-sections of the La Marquesa Dam (Alba et al., 1987)

A.7.3 Evaluation of Material Properties

Since the grain size distribution curve of the case history was not reported by the main sources of references or other residual strength-related studies, mean grain size (D_{50}), fines content (FC) and coefficient of uniformity (C_u) values are estimated based on the documented representative values in those references, if available.

Mean grain size (D_{50}): The exact value of the mean grain size was reported as D_{50} = 0.150 mm in Olson (2001) and Srbulov (2008). Hence, the representative D_{50} value is also taken as 0.150 mm in this study.

Fines content (FC): The exact value of the fines content was reported as FC = 20% in Alba et al. (1987,1988), Olson (2001), and Weber (2015) for the downstream part of the dam. Hence, the representative FC value is also taken as 20% in this study.

Coefficient of uniformity (C_u): Since no coefficient of uniformity value was reported by the main sources of references or other relative studies, no value has been set for this parameter.

Roundness (R): Since no roundness value was reported by the main sources of references or other studies, no value has been set for this parameter for the evaluation of limit void ratios and void ratio ranges. However, R = 0.50 is taken approximately as a representative value for the evaluation of liquefaction state friction angle.

Sphericity (S): Since no sphericity value was reported by the main sources of references or other studies, no value has been set for this parameter for the evaluation of limit void ratios and void ratio ranges. However, S = 0.60 is taken approximately as a representative value for the evaluation of liquefaction state friction angle.

Unit weight (γ_{dry} and γ_{sat}): As the results are not sensitive to unit weight, the dry and saturated unit weights of all soil layers are assigned as 18.9 kN/m^3 and 19.6 kN/m^3, respectively, to be compatible with Olson (2001) and Weber (2015).

A.7.4 Sub-sectioning of the Cross-section and Failure Plane

The exact locations of the SPT boreholes were known for this case history. Therefore, the sub-sectioning is made based on the locations of these penetration tests as presented in Figure A.7.2. Each test is assigned (names of the logs are directly assigned as the name of the sub-section) for the corresponding territory length.

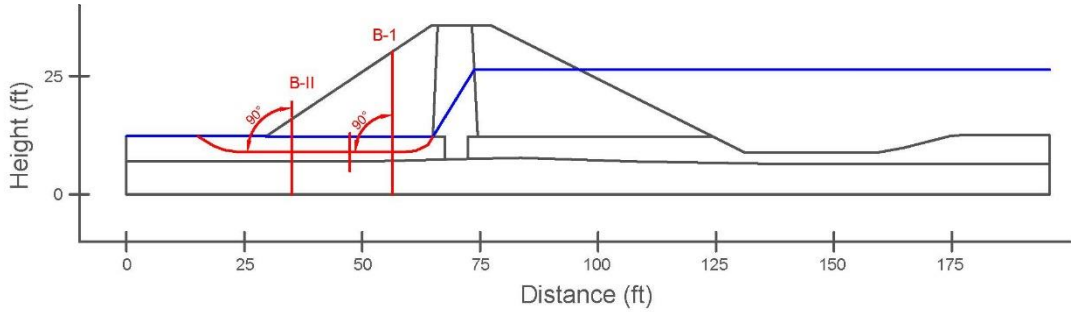

Figure A.7.2. Sub-sectioning of the cross-section and failure plane for La Marquesa Dam – D/S Slope

The territory lengths (L_i) and inclinations (α_i) (positive sign for CCW direction) of the failure plane are evaluated as given in Table A.7.1 for each sub-section.

Table A.7.1 Sub-sections with their corresponding failure plane lengths and inclinations for La Marquesa Dam – D/S Slope

Case History	Section	Failure plane length, L_i (m)	Total failure plane length, L_t (m)	Failure plane inclination, α_i (degrees)
La Marquesa Dam – D/S Slope	B-II	10.07	15.81	0
	B-1	5.75		0

A.7.5 Elastic Modeling and Stress Rotation

All stress components are evaluated linear elastically at the points where boreholes and failure plane intersect in Figure A.7.2. The initial and deformed shape of the cross-section are presented in Figure A.7.3 and Figure A.7.4, respectively. All lengths are given in meters.

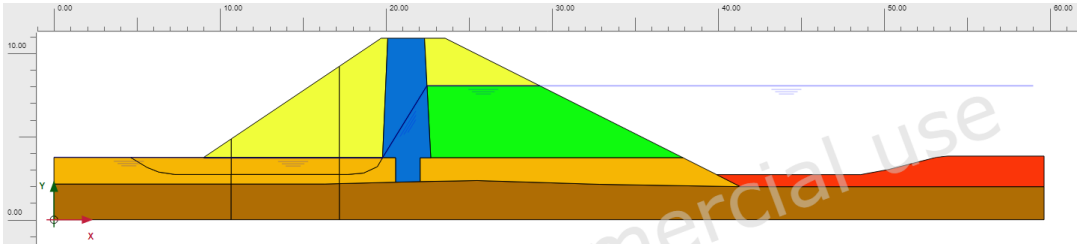

Figure A.7.3. Initial cross-section used in linear elastic modeling of La Marquesa Dam – D/S Slope

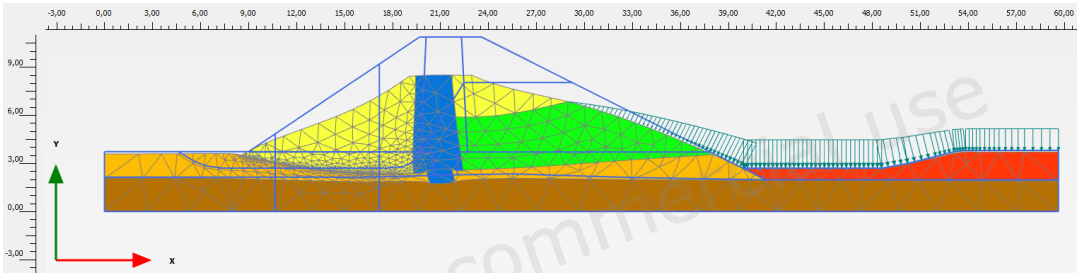

Figure A.7.4. Deformed cross-section obtained after linear elastic modeling of La Marquesa Dam – D/S Slope

During the elastic modeling process in PLAXIS 2D Ultimate Connect Edition V22.00.00.1733 software, while the Poisson's ratio values of all materials other than

liquefied zone are defined as 0.30, it is estimated as 0.33 for the liquefied zone. For moist silty and clayey sand shell, saturated silty and clayey sand shell, liquefied zone, sandy clay core, sandy clay, and outside toe material, the elastic modulus values are evaluated as 10 MPa, 10 MPa, 5 MPa, 20 MPa, 30 MPa, and 20 MPa, respectively.

The effective normal (σ'_N) and shear (τ_{static}) stresses acting on the inclined failure plane are evaluated with corresponding Mohr's circles. The corresponding Mohr's circles and the effective stress components of the sub-sections are presented in Figure A.7.5 and Table A.7.2, respectively. All stresses are given in kilopascals.

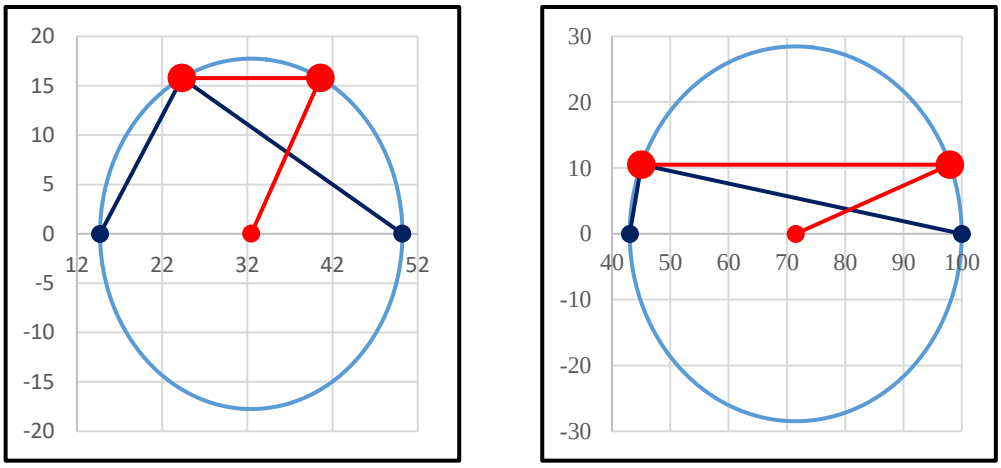

(a) B-II (b) B-1

Figure A.7.5. Mohr's circles for La Marquesa Dam – D/S Slope

Table A.7.2 Evaluated stress components for La Marquesa Dam – D/S Slope

Case History	Section	σ'_1 (kPa)	σ'_2 (kPa)	σ'_3 (kPa)	p_0' (kPa)	q (kPa)	σ'_N (kPa)	τ_{static} (kPa)	$\lvert\tau_{static}\rvert$ (kPa)
La Marquesa Dam – D/S Slope	B-II	50.2	21.4	14.7	28.8	32.7	40.6	15.8	15.8
	B-1	100.0	47.2	43.0	63.4	55.0	98.0	10.5	10.5

A.7.6 Evaluation of SPT Resistance

The exact locations of the SPT boreholes were documented by Alba et al. (1987) as given in Figure A.7.6.

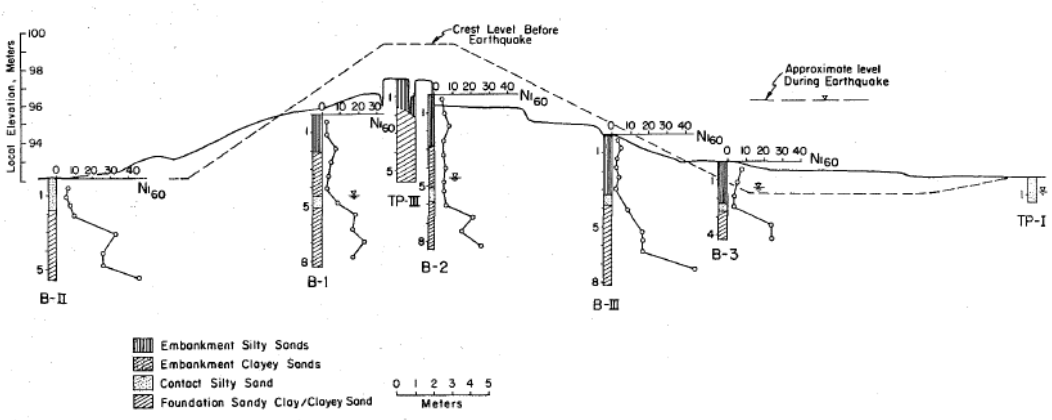

Figure A.7.6. SPT data for La Marquesa Dam (Alba et al., 1987)

SPT boreholes are presented in Figure A.7.7 for B-II and B-1 of the downstream slope, respectively.

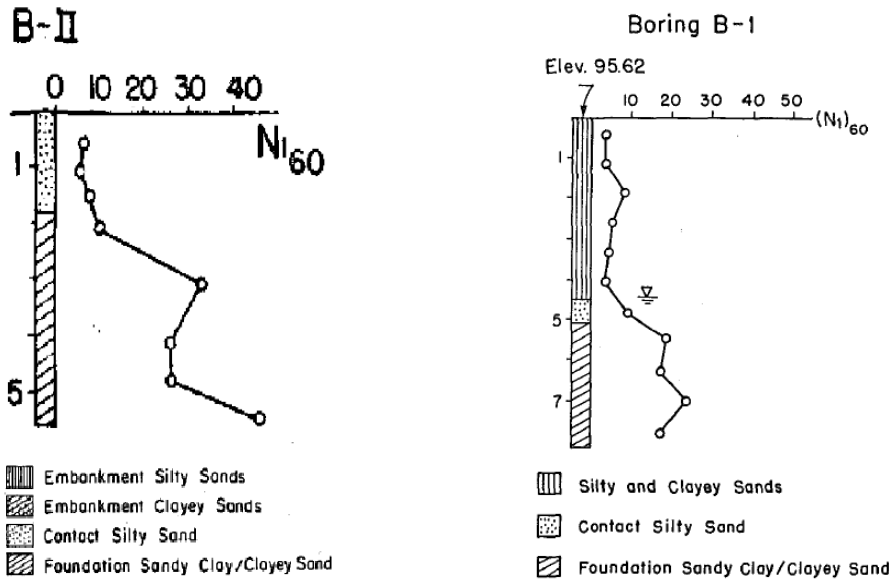

(a) B-II (b) B-1

Figure A.7.7. SPT boreholes for La Marquesa Dam – D/S Slope (Alba et al., 1987)

Since $(N_1)_{60}$ values were reported instead of raw SPT-N values, they are converted into the raw SPT-N values initially, and then corrected for equipment, overburden stress, and fines content with the same procedures to achieve consistency. The raw

SPT-N values are evaluated by back-analyzing the corrected $(N_1)_{60}$ values with the same correction methods used by the reporting teams.

Once the raw SPT-N values are estimated, the correction factors for nonstandardized sampler configuration (C_S) and borehole diameter (C_B) are taken as 1.0 since no reliable information related to these coefficients was reported in any of the sources. The energy ratio was reported as 56% in Alba et al. (1987, 1988); therefore, the energy efficiency correction factor (C_E) is taken as 56/60 = 0.93. The short rod length (C_R) and fines content correction factors (C_{fines}) are evaluated with the methods and relationships explained in Section 3.5. The overburden stress correction factors (C_N) are evaluated based on the effective vertical stresses estimated at the point of penetration for each recording, and average values are documented for simplicity. Accordingly, the correction factors and SPT resistances are estimated as given in Table A.7.3.

Table A.7.3 Evaluated SPT-N resistances for La Marquesa Dam – D/S Slope

Case History	Section	C_N	C_B	C_R	C_S	C_E	C_{fines}	N	N_{60}	$(N_1)_{60}$	$(N_1)_{60,cs}$	
La Marquesa Dam – D/S Slope	B-II	2.99	1.0	0.80	1.0	0.93	1.23	7.01	5.21	6.54	8.07	8.39
	B-1	1.70	1.0	0.87	1.0	0.93	1.22	7.01	5.68	7.13	8.70	

A.7.7 Evaluation of Limit Void Ratios, Void Ratio Ranges, Relative Densities and Initial Void Ratios

Since mean grain size (D_{50}) and fines content (FC) information were available among the required material properties for the void ratio prediction models, the arithmetic means of the limit void ratios (e_{min} and e_{max}) evaluated by Model 1 and Model 2 are considered as the representative values. The e_{max} value is slightly modified then with respect to the construction method of the case history for each prediction model.

Since the fines content value is evaluated as 20%, which is greater than 15%, it is judged that the soil of interest consists of silty soils. Therefore, the relative densities

evaluated by the correlation recommended by Cubrinovski and Ishihara (1999) are directly taken as the representative relative densities of the soils. Based on these relative densities and limit void ratios, the initial void ratios (e_0) corresponding to approximately 1 kPa confining stress are estimated referring to Equation 3-68. Accordingly, the limit void ratios, void ratio ranges (without any modification for the construction method), in-situ relative densities, and initial void ratios are estimated as given in Table A.7.4.

Table A.7.4 Evaluated limit void ratios, void ratio ranges, in-situ relative densities, and initial void ratios for La Marquesa Dam – D/S Slope

Case History	Section	e_{min}	e_{max}	e_{max}-e_{min}	$RD_{C\&I}$ (%)	$RD_{K\&M}$ (%)	$RD_{overall}$ (%)	e_0
La Marquesa Dam – D/S Slope	B-II	0.595	1.007	0.412	35.18	40.76	35.18	0.862
	B-1	0.595	1.007	0.412	36.73	42.55	36.73	0.856

A.8 La Palma Dam (1985 Chilean Earthquake, M_s=7.8)

A.8.1 Brief Summary of the Case History

La Palma Dam was located in Chile, and the exact date of the failure was reported as March 3, 1985. The fundamental reason behind the failure was reported as the 1985 Central Chilean Earthquake (M_s=7.8). The type of the structure can be classified as a poorly compacted zoned earthen dam, and the maximum slope height is reported as ~ 8 m. De Alba et al. (1987, 1988) are taken into account as the main sources of references. Olson (2001), Wang (2003) and Weber (2015) also studied this case history during their back-analyses of liquefaction failure case histories.

A.8.2 Site Geology and Critical Cross-section

Figure A.8.1 presents the soil stratigraphy and pre-failure and post-failure cross-sections of the case structure. It is decided that the idealized soil profile consists of

seven soil layers namely moist silty and clayey sand shell, saturated silty and clayey sand shell, liquefied zone, sandy clay core, sandy clay, silty sand, and downstream silty sand. The parts of the earthen dam remaining above and below the water table level at the time of failure are classified as moist silty and clayey sand shell and saturated silty and clayey sand shell, respectively. The lower portion of the saturated silty and clayey sand shell is evaluated as the liquefied zone. Below the liquefied zone, silty sand layer is defined. The layer underlying the earthen dam is defined as the sandy clay zone. The middle part of the dam body is classified as sandy clay core, and the zone existing below the moist silty and clayey sand shell in the downstream is defined as downstream silty sand layer.

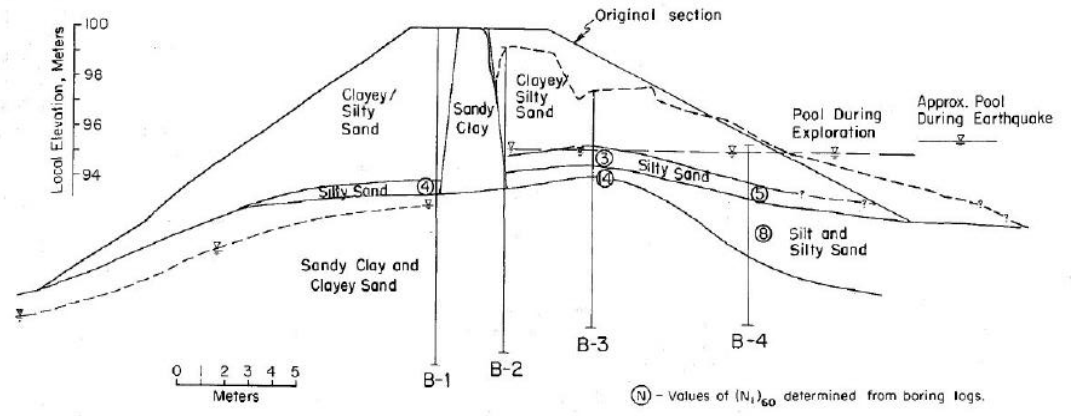

Figure A.8.1. Soil stratigraphy and pre-failure and post-failure cross-sections of the La Palma Dam (Alba et al., 1987)

A.8.3 Evaluation of Material Properties

Since the grain size distribution curve of the case history was not reported by the main sources of references or other residual strength-related studies, mean grain size (D_{50}), fines content (FC) and coefficient of uniformity (C_u) values are estimated based on the documented representative values in those references, if available.

Mean grain size (D_{50}): The exact value of the mean grain size was reported as D_{50} = 0.200 mm in Olson (2001) and Srbulov (2008). Hence, the representative D_{50} value is also taken as 0.200 mm in this study.

Fines content (FC): The exact value of the fines content was reported as FC = 15% in Alba et al. (1987,1988), Olson (2001), Srbulov (2008), and Weber (2015) for this case history. Hence, the representative FC value is also taken as 15% in this study.

Coefficient of uniformity (C_u): Since no coefficient of uniformity value was reported by the main sources of references or other relative studies, no value has been set for this parameter.

Roundness (R): Since no roundness value was reported by the main sources of references or other studies, no value has been set for this parameter for the evaluation of limit void ratios and void ratio ranges. However, R = 0.50 is taken approximately as a representative value for the evaluation of liquefaction state friction angle.

Sphericity (S): Since no sphericity value was reported by the main sources of references or other studies, no value has been set for this parameter for the evaluation of limit void ratios and void ratio ranges. However, S = 0.60 is taken approximately as a representative value for the evaluation of liquefaction state friction angle.

Unit weight (γ_{dry} and γ_{sat}): As the results are not sensitive to unit weight, the dry and saturated unit weights of all soil layers are assigned as 18.9 kN/m^3 and 19.6 kN/m^3, respectively, to be compatible with Olson (2001) and Weber (2015).

A.8.4 Sub-sectioning of the Cross-section and Failure Plane

The exact locations of the SPT boreholes were known for this case history. Therefore, the sub-sectioning is made based on the locations of these penetration tests as presented in Figure A.8.2. Each test is assigned (names of the logs are directly assigned as the name of the sub-section) for the corresponding territory length.

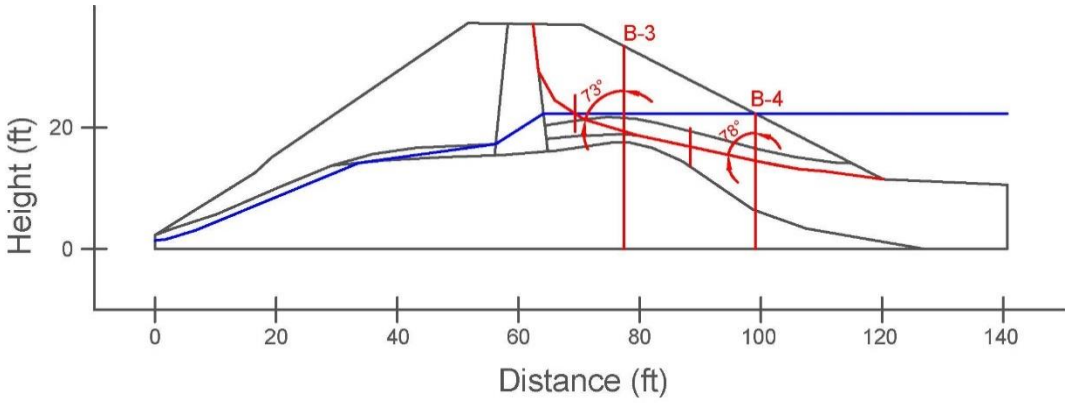

Figure A.8.2. Sub-sectioning of the cross-section and failure plane for La Palma Dam

The territory lengths (L_i) and inclinations (α_i) (positive sign for CCW direction) of the failure plane are evaluated as given in Table A.8.1 for each sub-section.

Table A.8.1 Sub-sections with their corresponding failure plane lengths and inclinations for La Palma Dam

Case History	Section	Failure plane length, L_i (m)	Total failure plane length, L_t (m)	Failure plane inclination, α_i (degrees)
La Palma Dam	B-3	6.06	15.91	-17
	B-4	9.85		-12

A.8.5 Elastic Modeling and Stress Rotation

All stress components are evaluated linear elastically at the points where boreholes and failure plane intersect in Figure A.8.2. The initial and deformed shape of the cross-section are presented in Figure A.8.3 and Figure A.8.4, respectively. All lengths are given in meters.

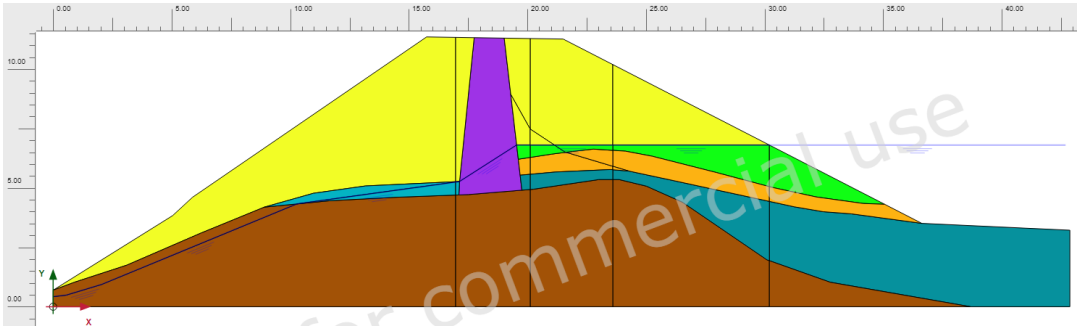

Figure A.8.3. Initial cross-section used in linear elastic modeling of La Palma Dam

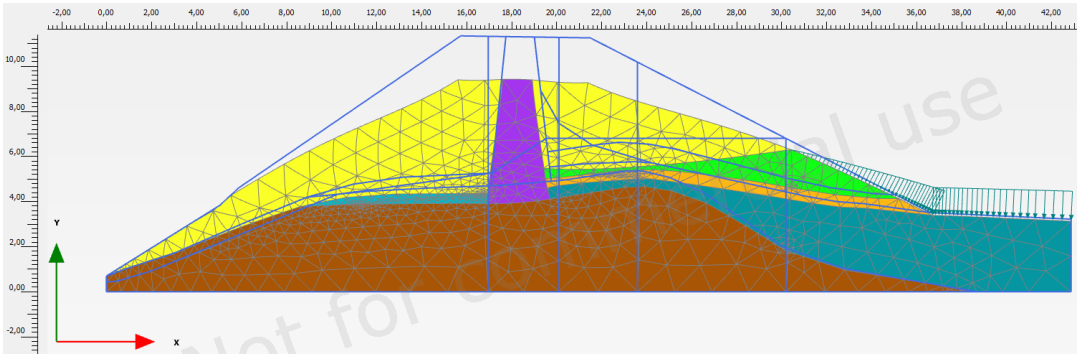

Figure A.8.4. Deformed cross-section obtained after linear elastic modeling of La Palma Dam

During the elastic modeling process in PLAXIS 2D Ultimate Connect Edition V22.00.00.1733 software, while the Poisson's ratio values of all materials other than liquefied zone are defined as 0.30, it is estimated as 0.33 for the liquefied zone. For moist silty and clayey sand shell, saturated silty and clayey sand shell, liquefied zone, sandy clay core, sandy clay, silty sand, and downstream silty sand, the elastic modulus values are evaluated as 10 MPa, 10 MPa, 5 MPa, 20 MPa, 30 MPa, 20 MPa, and 20 MPa, respectively.

The effective normal (σ'_N) and shear (τ_{static}) stresses acting on the inclined failure plane are evaluated with corresponding Mohr's circles. The corresponding Mohr's circles and the effective stress components of the sub-sections are presented in Figure A.8.5 and Table A.8.2, respectively. All stresses are given in kilopascals.

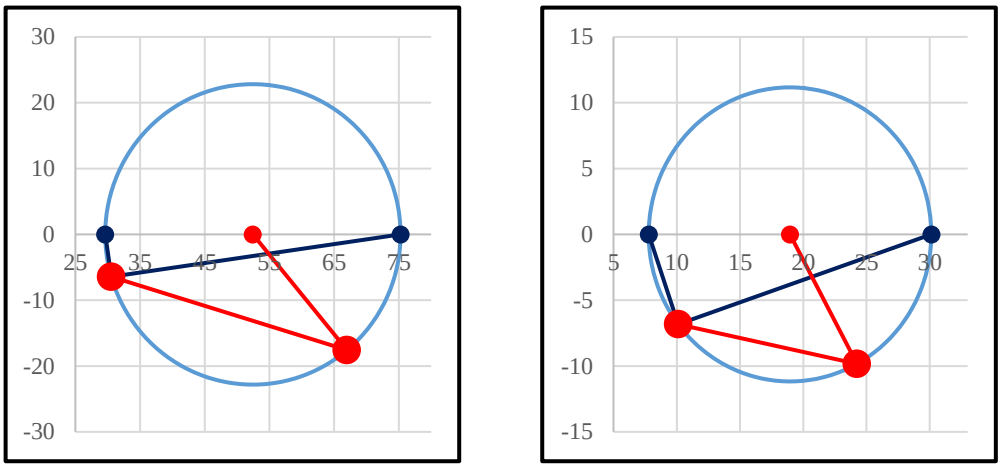

(a) B-3 (b) B-4

Figure A.8.5. Mohr's circles for La Palma Dam

Table A.8.2 Evaluated stress components for La Palma Dam

Case History	Section	σ'_1 (kPa)	σ'_2 (kPa)	σ'_3 (kPa)	p_0' (kPa)	q (kPa)	σ'_N (kPa)	τ_{static} (kPa)	$\lvert\tau_{static}\rvert$ (kPa)
La Palma Dam	B-3	75.3	34.6	29.6	46.5	43.4	67.0	-17.6	17.6
	B-4	30.1	12.5	7.8	16.8	20.4	24.2	-9.8	9.8

A.8.6 Evaluation of SPT Resistance

The exact locations of the SPT boreholes were documented by Alba et al. (1987) as given in Figure A.8.6.

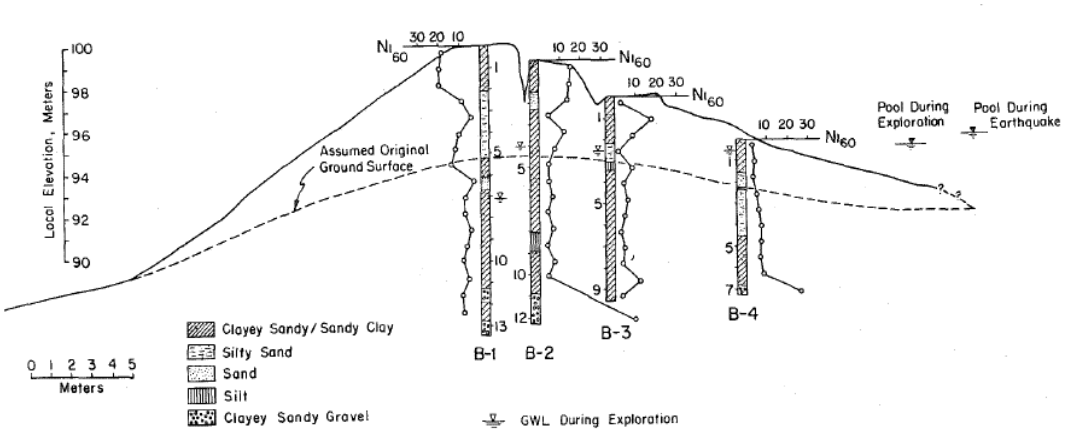

Figure A.8.6. SPT data for La Palma Dam (Alba et al., 1987)

SPT boreholes are presented in Figure A.8.7 for B-3 and B-4 of the downstream slope, respectively.

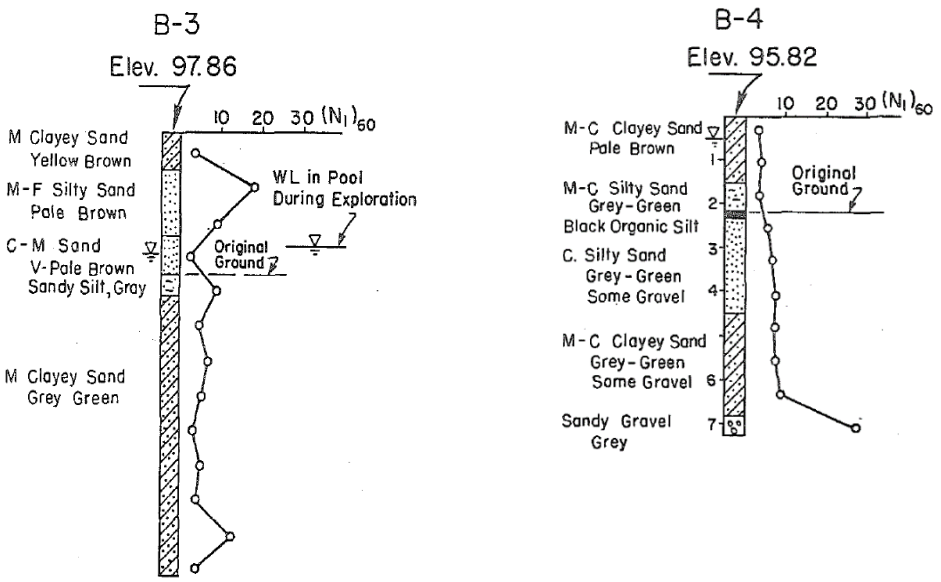

(a) B-3 (b) B-4

Figure A.8.7. SPT boreholes for La Palma Dam (Alba et al., 1987)

Since $(N_1)_{60}$ values were reported instead of raw SPT-N values, they are converted into the raw SPT-N values initially, and then corrected for equipment, overburden stress, and fines content with the same procedures to achieve consistency. The raw SPT-N values are evaluated by back-analyzing the corrected $(N_1)_{60}$ values with the same correction methods used by the reporting teams.

The correction factors for nonstandardized sampler configuration (C_S), borehole diameter (C_B), and energy efficiency (C_E) are taken as 1.0 since no reliable information related to these coefficients was reported in any of the sources. The short rod length (C_R) and fines content correction factors (C_{fines}) are evaluated with the methods and relationships explained in Section 3.5. The overburden stress correction factors (C_N) are evaluated based on the effective vertical stresses estimated at the point of penetration for each recording, and average values are documented for simplicity. Accordingly, the correction factors and SPT resistances are estimated as given in Table A.8.3.

Table A.8.3 Evaluated SPT-N resistances for La Palma Dam

Case History	Section	C_N	C_B	C_R	C_S	C_E	C_{fines}	N	N_{60}	$(N_1)_{60}$	$(N_1)_{60,cs}$	
La Palma Dam	B-3	1.06	1.0	0.95	1.0	1.00	1.21	3.77	3.60	5.03	6.08	5.92
	B-4	1.74	1.0	0.89	1.0	1.00	1.22	3.77	3.37	4.72	5.75	

A.8.7 Evaluation of Limit Void Ratios, Void Ratio Ranges, Relative Densities and Initial Void Ratios

Since mean grain size (D_{50}) and fines content (FC) information were available among the required material properties for the void ratio prediction models, the arithmetic means of the limit void ratios (e_{min} and e_{max}) evaluated by Model 1 and Model 2 are considered as the representative values. The e_{max} value is slightly modified then with respect to the construction method of the case history for each prediction model.

Since the fines content value is evaluated as 15%, it is judged that the soil of interest consists of silty soils. Therefore, the relative densities evaluated by the correlation recommended by Cubrinovski and Ishihara (1999) are directly taken as the representative relative densities of the soils. Based on these relative densities and limit void ratios, the initial void ratios (e_0) corresponding to approximately 1 kPa confining stress are estimated referring to Equation 3-68. Accordingly, the limit void ratios, void ratio ranges (without any modification for the construction method), in-situ relative densities, and initial void ratios are estimated as given in Table A.8.4.

Table A.8.4 Evaluated limit void ratios, void ratio ranges, in-situ relative densities, and initial void ratios for La Palma Dam

Case History	Section	e_{min}	e_{max}	e_{max}-e_{min}	$RD_{C\&I}$ (%)	$RD_{K\&M}$ (%)	$RD_{overall}$ (%)	e_0
La Palma Dam	B-3	0.588	0.990	0.402	30.23	34.40	30.23	0.868
	B-4	0.588	0.990	0.402	29.27	33.30	29.27	0.872

A.9 Lake Ackerman Highway Embankment (1987 Seismic Survey)

A.9.1 Brief Summary of the Case History

Lake Ackerman Highway Embankment was located in Michigan, USA, and the exact date of the failure was reported as July 24, 1987. The fundamental reason behind the failure was reported as the excitation by large geophysical exploration shakers. The type of the structure can be classified as an embankment constructed by water sedimentation method, and the maximum slope height is reported as ~ 8 m. Hryciw et al. (1990) is considered as the main source of reference. Olson (2001), Wang (2003) and Weber (2015) also studied this case history during their back-analyses of liquefaction failure case histories.

A.9.2 Site Geology and Critical Cross-section

Figure A.9.1 presents the soil stratigraphy of the embankment cross-section, and Figure A.9.2 shows the pre-failure and post-failure cross-sections of the case structure. It is decided that the idealized soil profile consists of three soil layers namely non-liquefied zone, liquefied zone, and dense sand. The parts of the embankment remaining above and below the water table level at the time of failure are classified as non-liquefied zone and liquefied zone, respectively. The layer underlying the embankment is defined as dense sand.

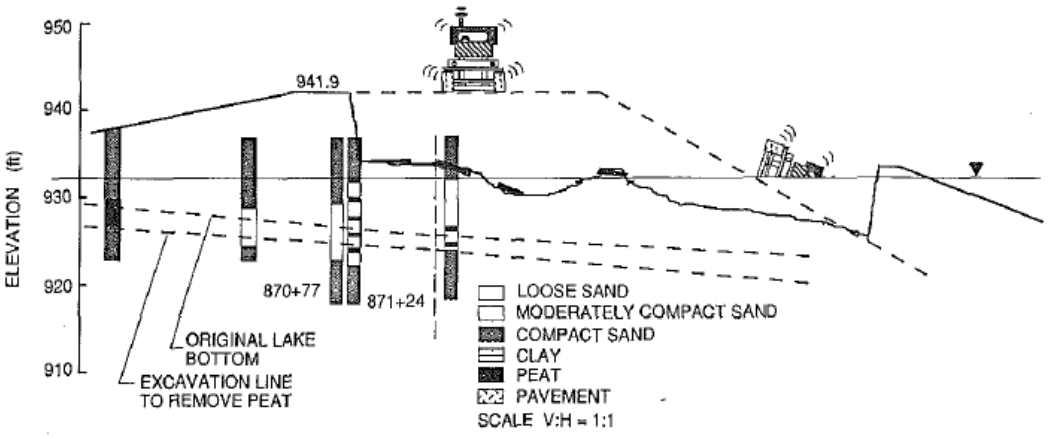

Figure A.9.1. Soil stratigraphy of the Lake Ackerman Highway Embankment (Hryciw et al., 1990)

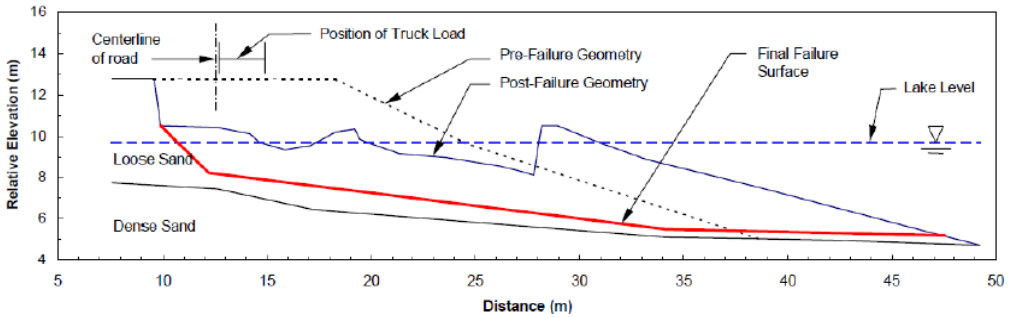

Figure A.9.2. Pre-failure and post-failure cross-sections of the Lake Ackerman Highway Embankment (Olson, 2001)

A.9.3 Evaluation of Material Properties

Since the grain size distribution curve of the case history was reported by the main sources of references as given in Figure A.9.3, mean grain size (D_{50}), fines content (FC) and coefficient of uniformity (C_u) values are evaluated based on this curve.

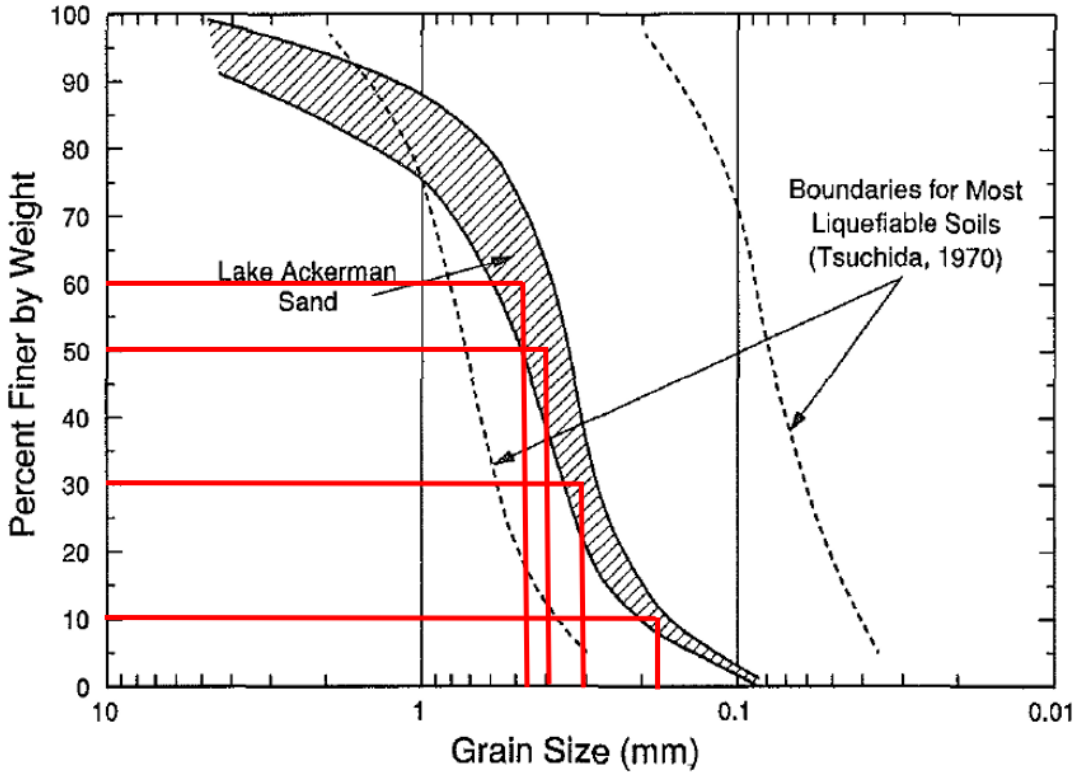

Figure A.9.3. Grain size distribution curve of the Lake Ackerman Highway Embankment (Hryciw et al., 1990)

Mean grain size (D_{50}): D_{50} = 0.390 mm is evaluated representatively based on the grain size distribution curve of the case history. Olson (2001) also suggests 0.400 mm for D_{50} value of this case history.

Fines content (FC): FC = 1% is evaluated representatively based on the grain size distribution curve of the case history. Olson (2001) also suggests FC = 0%.

Coefficient of uniformity (C_u): D_{10} and D_{60} values are evaluated as 0.18 mm and 0.45 mm, respectively, based on the grain size distribution curve of the case history. Therefore, the uniformity coefficient is estimated as $C_u = D_{60}/D_{10} = 0.45/0.18 = 2.50$.

Roundness (R): Since no roundness value was reported by the main sources of references or other studies, no value has been set for this parameter for the evaluation of limit void ratios and void ratio ranges. However, R = 0.50 is taken approximately as a representative value for the evaluation of liquefaction state friction angle.

Sphericity (S): Since no sphericity value was reported by the main sources of references or other studies, no value has been set for this parameter for the evaluation of limit void ratios and void ratio ranges. However, S = 0.60 is taken approximately as a representative value for the evaluation of liquefaction state friction angle.

Unit weight (γ_{dry} and γ_{sat}): As the results are not sensitive to unit weight, the dry and saturated unit weights of all soil layers are assigned as 18.1 kN/m^3 and 19.3 kN/m^3, respectively, to be compatible with Olson (2001) and Weber (2015).

A.9.4 Sub-sectioning of the Cross-section and Failure Plane

The exact locations of the SPT boreholes were not known for this case history. Therefore, the sub-sectioning is made based on imaginary boreholes assigned on the cross-section. These imaginary boreholes are defined with respect to changes in effective vertical stresses and inclination angles of the failure plane. Accordingly, three sub-sections are assigned for the liquefied zone as presented in Figure A.9.4.

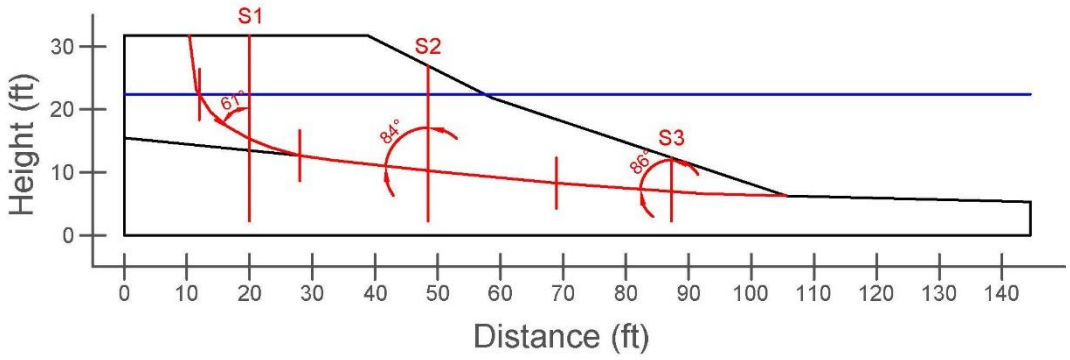

Figure A.9.4. Sub-sectioning of the cross-section and failure plane for Lake Ackerman Highway Embankment

The territory lengths (L_i) and inclinations (α_i) (positive sign for CCW direction) of the failure plane are evaluated as given in Table A.9.1 for each sub-section.

Table A.9.1 Sub-sections with their corresponding failure plane lengths and inclinations for Lake Ackerman Highway Embankment

Case History	Section	Failure plane length, L_i (m)	Total failure plane length, L_t (m)	Failure plane inclination, α_i (degrees)
Lake Ackerman Highway Embankment	S1	5.90	29.65	-29
	S2	12.55		-6
	S3	11.20		-4

A.9.5 Elastic Modeling and Stress Rotation

All stress components are evaluated linear elastically at the points where boreholes and failure plane intersect in Figure A.9.4. The initial and deformed shape of the cross-section are presented in Figure A.9.5 and Figure A.9.6, respectively. All lengths are given in meters.

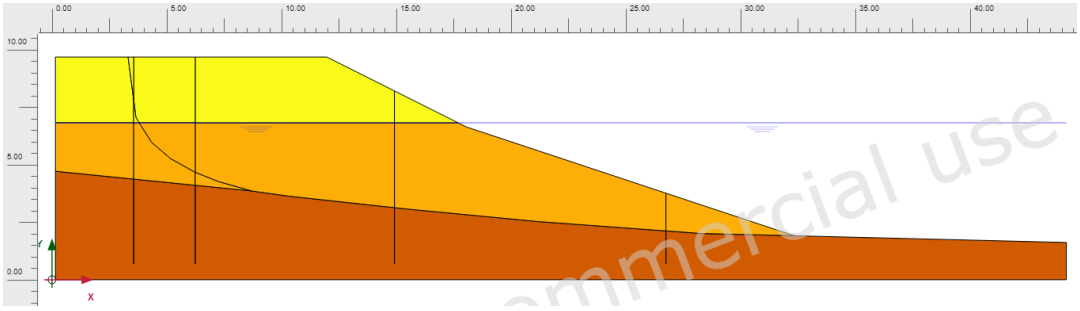

Figure A.9.5. Initial cross-section used in linear elastic modeling of Lake Ackerman Highway Embankment

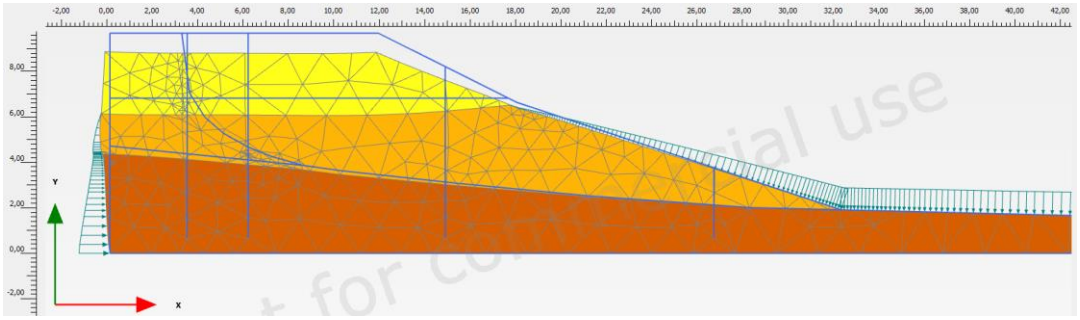

Figure A.9.6. Deformed cross-section obtained after linear elastic modeling of Lake Ackerman Highway Embankment

During the elastic modeling process in PLAXIS 2D Ultimate Connect Edition V22.00.00.1733 software, the Poisson's ratio values of the non-liquefied zone, liquefied zone, and dense sand are defined as 0.30, 0.33, and 0.30, respectively. The elastic modulus values of the same layers, on the other hand, are estimated as 10 MPa, 5 MPa, and 30 MPa, respectively.

The effective normal (σ'_N) and shear (τ_{static}) stresses acting on the inclined failure plane are evaluated with corresponding Mohr's circles. The corresponding Mohr's circles and the effective stress components of the sub-sections are presented in Figure A.9.7 and Table A.9.2, respectively. All stresses are given in kilopascals.

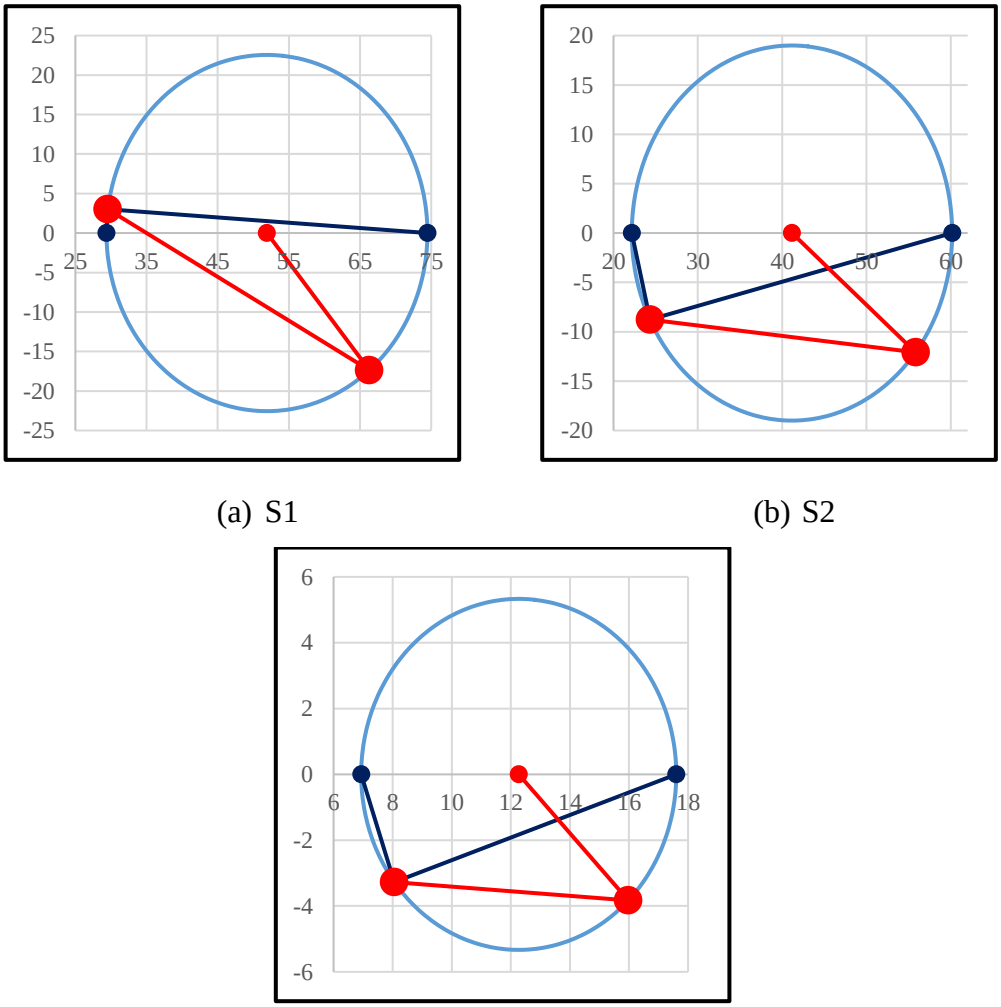

(a) S1 (b) S2

(c) S3

Figure A.9.7. Mohr's circles for Lake Ackerman Highway Embankment

Table A.9.2 Evaluated stress components for Lake Ackerman Highway Embankment

Case History	Section	σ'_1 (kPa)	σ'_2 (kPa)	σ'_3 (kPa)	p_0' (kPa)	q (kPa)	σ'_N (kPa)	τ_{static} (kPa)	$\lvert\tau_{static}\rvert$ (kPa)
Lake Ackerman Highway Embankment	S1	74.5	34.3	29.4	46.0	42.9	66.3	-17.4	17.4
	S2	60.2	58.0	22.2	36.5	37.0	55.8	-12.1	12.1
	S3	17.6	8.1	6.9	10.9	10.1	16.0	-3.8	3.8

A.9.6 Evaluation of SPT Resistance

The exact locations of the SPT boreholes were not documented for this case history. Therefore, imaginary boreholes are assigned along the cross-section as shown in Figure A.9.4. SPT data used for this case history is presented in Figure A.9.8.

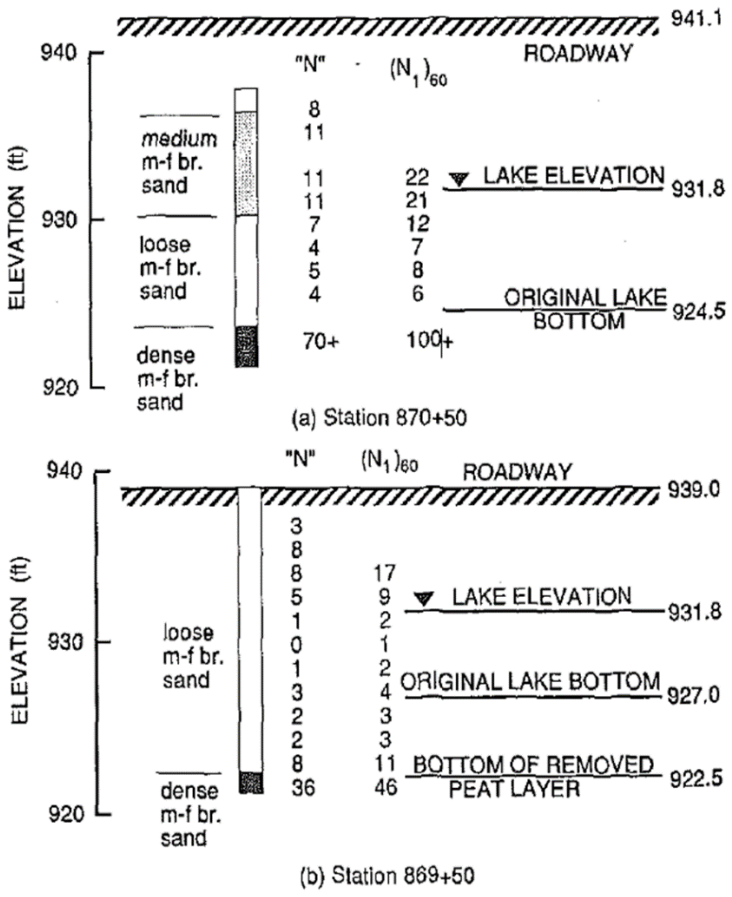

Figure A.9.8. SPT boreholes for Lake Ackerman Highway Embankment (Hryciw et al., 1990)

The correction factors for nonstandardized sampler configuration (C_S), borehole diameter (C_B), and energy efficiency (C_E) are taken as 1.0 since no reliable information related to these coefficients was reported in any of the sources. The short rod length (C_R) and fines content correction factors (C_{fines}) are evaluated with the methods and relationships explained in Section 3.5. The overburden stress correction factors (C_N) are evaluated based on the effective vertical stresses estimated at the point of penetration for each recording, and average values are documented for simplicity. Accordingly, the correction factors and SPT resistances are estimated as given in Table A.9.3.

Table A.9.3 Evaluated SPT-N resistances for Lake Ackerman Highway Embankment

Case History	Section	C_N	C_B	C_R	C_S	C_E	C_{fines}	N	N_{60}	$(N_1)_{60}$	$(N_1)_{60,cs}$	
Lake Ackerman Highway Embankment	S1	1.22	1.0	0.92	1.0	1.00	1.00	3.92	3.61	4.39	4.39	4.36
	S2	1.22	1.0	0.92	1.0	1.00	1.00	3.92	3.61	4.39	4.39	
	S3	1.23	1.0	0.90	1.0	1.00	1.00	3.92	3.53	4.30	4.30	

A.9.7 Evaluation of Limit Void Ratios, Void Ratio Ranges, Relative Densities and Initial Void Ratios

Since mean grain size (D_{50}), fines content (FC), and coefficient of uniformity (C_u) information were available among the required material properties for the void ratio prediction models, the arithmetic means of the limit void ratios (e_{min} and e_{max}) evaluated by Model 8 and Model 9 are considered as the representative values. The e_{max} value is slightly modified then with respect to the construction method of the case history for each prediction model.

Since the fines content value is evaluated as 1%, which is less than 15%, it is judged that the soil of interest consists of sand type of soils. Therefore, the arithmetic mean of the relative densities evaluated by the correlations recommended by Kulhawy and Mayne (1990) and Cubrinovski and Ishihara (1999) is taken as the overall relative

density of the soil. Based on these relative densities and limit void ratios, the initial void ratios (e_0) corresponding to approximately 1 kPa confining stress are estimated referring to Equation 3-68. Accordingly, the limit void ratios, void ratio ranges (without any modification for the construction method), in-situ relative densities, and initial void ratios are estimated as given in Table A.9.4.

Table A.9.4 Evaluated limit void ratios, void ratio ranges, in-situ relative densities, and initial void ratios for Lake Ackerman Highway Embankment

Case History	Section	e_{min}	e_{max}	e_{max}-e_{min}	$RD_{C\&I}$ (%)	$RD_{K\&M}$ (%)	$RD_{overall}$ (%)	e_0
Lake Ackerman Highway Embankment	S1	0.561	0.958	0.397	27.96	29.71	28.84	0.844
	S2	0.561	0.958	0.397	27.96	29.71	28.84	0.844
	S3	0.561	0.958	0.397	27.65	29.38	28.51	0.845

A.10 Chonan Middle School (1987 Chiba-Toho-Oki Earthquake, M=6.7)

A.10.1 Brief Summary of the Case History

Chonan Middle School was located in Chiba, Japan, and the exact date of the failure was reported as December 17, 1987. The fundamental reason behind the failure was reported as the 1987 Chiba-Toho-Oki Earthquake (M=6.7). The type of the case structure can be classified as a poorly compacted embankment fill, and the maximum slope height is reported as ~ 6 m. Ishihara et al. (1990) and Ishihara (1993) are considered as the main sources of references. Olson (2001), Wang (2003) and Weber (2015) also studied this case history during their back-analyses of liquefaction failure case histories.

A.10.2 Site Geology and Critical Cross-section

Figure A.10.1 shows the soil stratigraphy and pre-failure and post-failure cross-sections of the case structure. It is decided that the idealized soil profile consists of

three soil layers namely non-liquefied zone, liquefied zone, and original ground. The parts of the poorly compacted embankment fill remaining above and below the water table level at the time of failure are classified as non-liquefied zone and liquefied zone, respectively. The layer underlying the embankment is defined as the original ground.

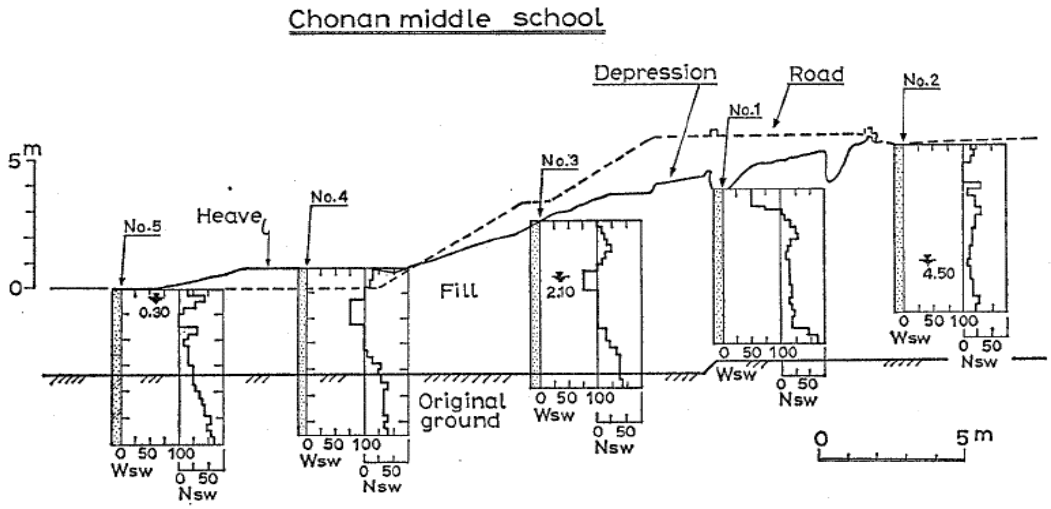

Figure A.10.1. Soil stratigraphy and pre-failure and post-failure cross-sections of the Chonan Middle School Embankment (Ishihara et al., 1990)

A.10.3 Evaluation of Material Properties

Since the grain size distribution curve of the case history was not reported by the main sources of references or other residual strength-related studies, mean grain size (D_{50}), fines content (FC) and coefficient of uniformity (C_u) values are estimated based on the documented representative values in those references, if available.

Mean grain size (D_{50}): The exact value of the mean grain size was reported as D_{50} = 0.200 mm in Olson (2001) and Srbulov (2008). Hence, the representative D_{50} value is also taken as 0.200 mm in this study.

Fines content (FC): The exact value of the fines content was reported as FC = 18% in Ishihara (1993), Olson (2001) and Srbulov (2008). Hence, the representative FC value is also taken as 18% in this study.

Coefficient of uniformity (C_u): Since no coefficient of uniformity value was reported by the main sources of references or other relative studies, no value has been set for this parameter.

Roundness (R): Since no roundness value was reported by the main sources of references or other studies, no value has been set for this parameter for the evaluation of limit void ratios and void ratio ranges. However, R = 0.50 is taken approximately as a representative value for the evaluation of liquefaction state friction angle.

Sphericity (S): Since no sphericity value was reported by the main sources of references or other studies, no value has been set for this parameter for the evaluation of limit void ratios and void ratio ranges. However, S = 0.60 is taken approximately as a representative value for the evaluation of liquefaction state friction angle.

Unit weight (γ_{dry} and γ_{sat}): As the results are not sensitive to unit weight, the dry and saturated unit weights of all soil layers are assigned as 18.1 kN/m^3 and 18.9 kN/m^3, respectively, to be compatible with Olson (2001) and Weber (2015).

A.10.4 Sub-sectioning of the Cross-section and Failure Plane

The exact locations of the Swedish CPT boreholes were known for this case history as presented in Figure A.10.1. Therefore, the sub-sectioning is made based on the locations of these penetration tests as presented in Figure A.10.2. Each test is assigned (names of the logs are directly assigned as the name of the sub-section) for the corresponding territory length.

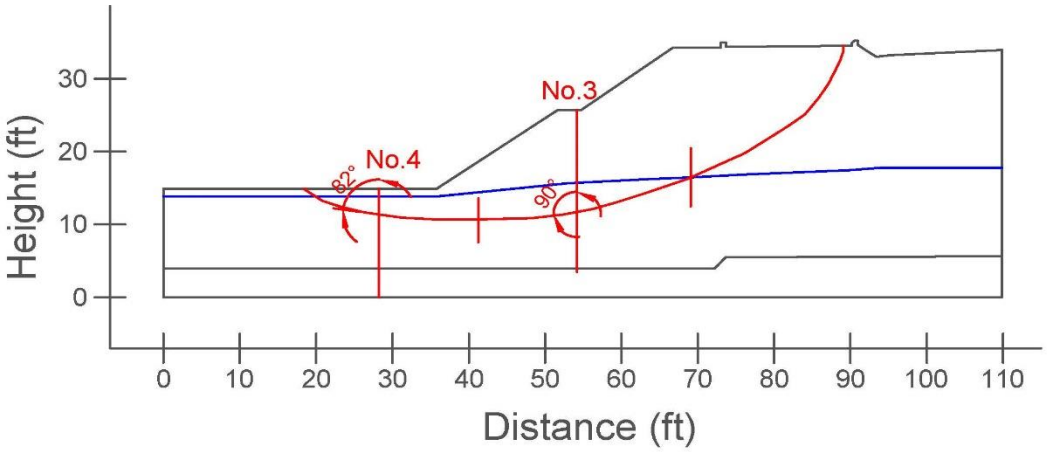

Figure A.10.2. Sub-sectioning of the cross-section and failure plane for Chonan Middle School Embankment

The territory lengths (L_i) and inclinations (α_i) (positive sign for CCW direction) of the failure plane are evaluated as given in Table A.10.1 for each sub-section.

Table A.10.1 Sub-sections with their corresponding failure plane lengths and inclinations for Chonan Middle School Embankment

Case History	Section	Failure plane length, L_i (m)	Total failure plane length, L_t (m)	Failure plane inclination, α_i (degrees)
Chonan Middle School	No.4	6.65	15.40	-8
	No.3	8.75		0

A.10.5 Elastic Modeling and Stress Rotation

All stress components are evaluated linear elastically at the points where boreholes and failure plane intersect in Figure A.10.2. The initial and deformed shape of the cross-section are presented in Figure A.10.3 and Figure A.10.4, respectively. All lengths are given in meters.

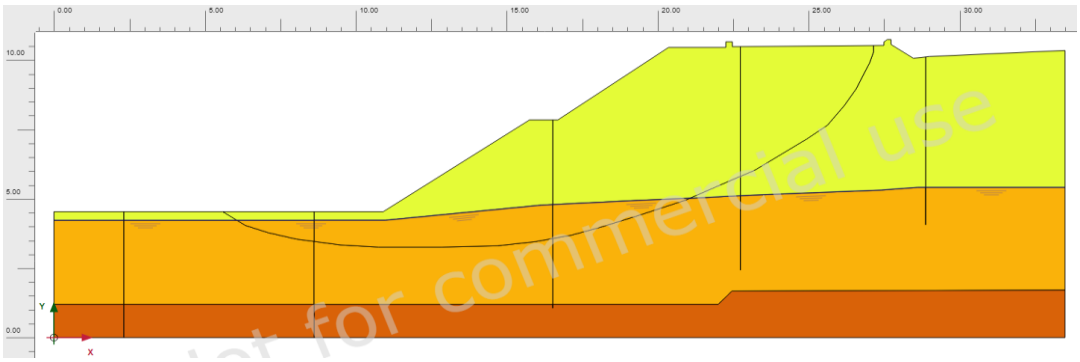

Figure A.10.3. Initial cross-section used in linear elastic modeling of Chonan Middle School Embankment

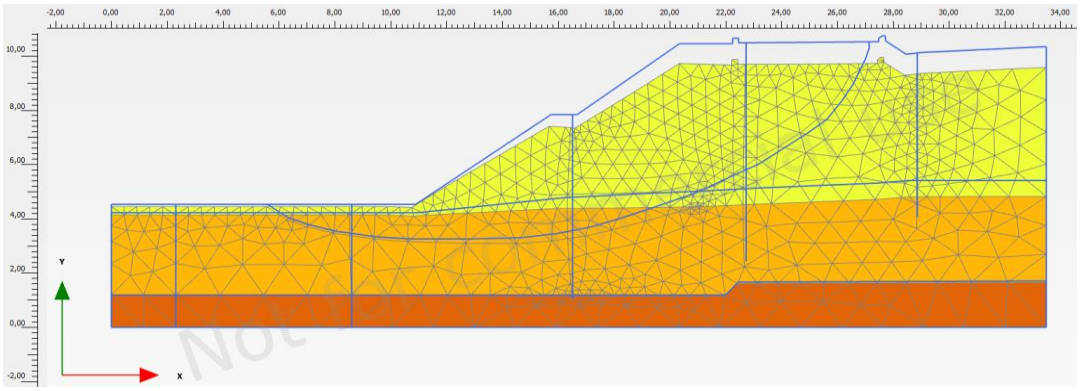

Figure A.10.4. Deformed cross-section obtained after linear elastic modeling of Chonan Middle School Embankment

During the elastic modeling process in PLAXIS 2D Ultimate Connect Edition V22.00.00.1733 software, the Poisson's ratio values of the non-liquefied zone, liquefied zone, and original ground are defined as 0.30, 0.33, and 0.30, respectively. The elastic modulus values of the same layers, on the other hand, are estimated as 10 MPa, 5 MPa, and 30 MPa, respectively.

The effective normal (σ'_N) and shear (τ_{static}) stresses acting on the inclined failure plane are evaluated with corresponding Mohr's circles. The corresponding Mohr's circles and the effective stress components of the sub-sections are presented in Figure A.10.5 and Table A.10.2, respectively. All stresses are given in kilopascals.

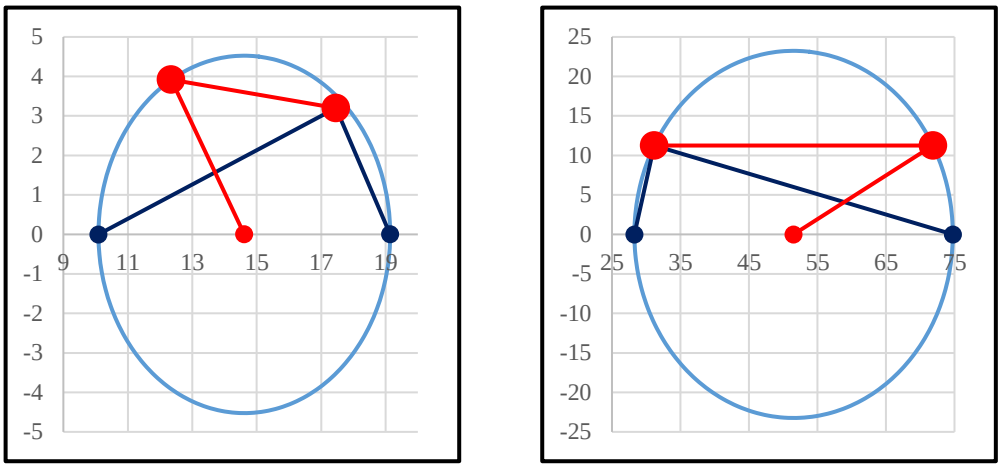

(a) No.4 (b) No.3

Figure A.10.5. Mohr's circles for Chonan Middle School Embankment

Table A.10.2 Evaluated stress components for Chonan Middle School Embankment

Case History	Section	σ'_1 (kPa)	σ'_2 (kPa)	σ'_3 (kPa)	p_0' (kPa)	q (kPa)	σ'_N (kPa)	τ_{static} (kPa)	$\lvert\tau_{static}\rvert$ (kPa)
Chonan Middle School	No.4	19.1	11.4	10.1	13.6	8.5	12.3	3.9	3.9
	No.3	74.8	34.0	28.3	45.7	43.9	71.8	11.3	11.3

A.10.6 Evaluation of SPT Resistance

The exact locations of the Swedish CPT boreholes were documented by Ishihara et al. (1990) as given in Figure A.10.1. Corresponding SCPT boreholes are presented in Figure A.10.6 for No.4 and No.3 logs, respectively.

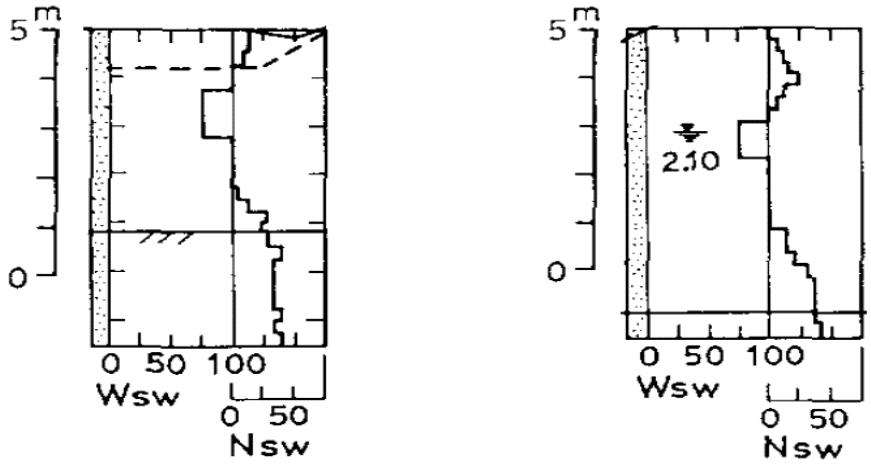

(a) No.4 (b) No.3

Figure A.10.6. SCPT boreholes for Chonan Middle School Embankment (Ishihara et al., 1990)

The SCPT resistances are converted to raw SPT-N values by using the correlation proposed by Inada (1982) explained in Section 3.5. These SPT-N values are assumed to be almost equal to N_{60} values as equipment, energy, and procedure corrections are not applicable for SCPT. However, the short rod length correction factors (C_R) are still evaluated with the methods and relationships explained in Section 3.5. Similarly, the overburden stress correction factors (C_N) are again evaluated based on the effective vertical stresses estimated at the point of penetration for each recording, and average values are documented for simplicity. The fines content correction factors (C_{fines}) are also evaluated with the methods and relationships explained in Section 3.5. Accordingly, the correction factors and SPT resistances are estimated as given in Table A.10.3.

Table A.10.3 Evaluated SPT-N resistances for Chonan Middle School Embankment

Case History	Section	C_N	C_B	C_R	C_S	C_E	C_{fines}	N	N_{60}	$(N_1)_{60}$	$(N_1)_{60,cs}$	
Chonan Middle School	No.4	1.45	-	0.91	-	-	1.29	3.36	3.05	4.19	5.40	5.10
	No.3	1.36	-	0.91	-	-	1.32	3.08	2.81	3.63	4.79	

A.10.7 Evaluation of Limit Void Ratios, Void Ratio Ranges, Relative Densities and Initial Void Ratios

Since mean grain size (D_{50}) and fines content (FC) information were available among the required material properties for the void ratio prediction models, the arithmetic means of the limit void ratios (e_{min} and e_{max}) evaluated by Model 1 and Model 2 are considered as the representative values. The e_{max} value is slightly modified then with respect to the construction method of the case history for each prediction model.

Since the fines content value is evaluated as 18%, which is greater than 15%, it is judged that the soil of interest consists of silty soils. Therefore, the relative densities evaluated by the correlation recommended by Cubrinovski and Ishihara (1999) are directly taken as the representative relative densities of the soils. Based on these relative densities and limit void ratios, the initial void ratios (e_0) corresponding to approximately 1 kPa confining stress are estimated referring to Equation 3-68. Accordingly, the limit void ratios, void ratio ranges (without any modification for the construction method), in-situ relative densities, and initial void ratios are estimated as given in Table A.10.4.

Table A.10.4 Evaluated limit void ratios, void ratio ranges, in-situ relative densities, and initial void ratios for Chonan Middle School Embankment

Case History	Section	e_{min}	e_{max}	e_{max}-e_{min}	$RD_{C\&I}$ (%)	$RD_{K\&M}$ (%)	$RD_{overall}$ (%)	e_0
Chonan Middle School	No.4	0.589	0.992	0.403	27.68	31.41	27.68	0.881
	No.3	0.589	0.992	0.403	25.76	29.23	25.76	0.889

A.11 Soviet Tajik – May 1 Slide (1989 Tajik, Soviet Union Earthquake, M_L=5.5)

A.11.1 Brief Summary of the Case History

Soviet Tajikistan Slope was located in Tajikistan Republic, and the exact date of the failure was reported as January 23, 1989. The fundamental reason behind the failure was reported as the 1989 Soviet Tajik Earthquake (M_L=5.5). The type of the structure can be classified as a loess dry deposit, and the maximum slope height is reported as ~ 30 m. Ishihara et al. (1990) is considered as the main source of reference. Olson (2001), Wang (2003) and Weber (2015) also studied this case during their back-analyses of liquefaction failure case histories.

A.11.2 Site Geology and Critical Cross-section

Figure A.11.1 and Figure A.11.2 show the pre-failure and post-failure cross-sections of the case structure. It is decided that the idealized soil profile consists of three soil layers namely non-liquefied zone, liquefied zone, and stable loess. The parts of the loess slope remaining above and below the water table level at the time of failure are classified as non-liquefied zone and liquefied zone, respectively. The layer underlying the liquefied zone is defined as the stable loess.

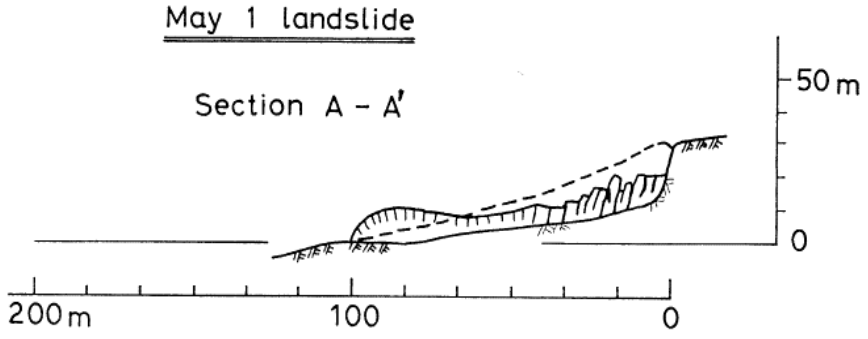

Figure A.11.1. Pre-failure and post-failure cross-sections of the Soviet Tajik – May 1 Slide (Ishihara et al., 1990)

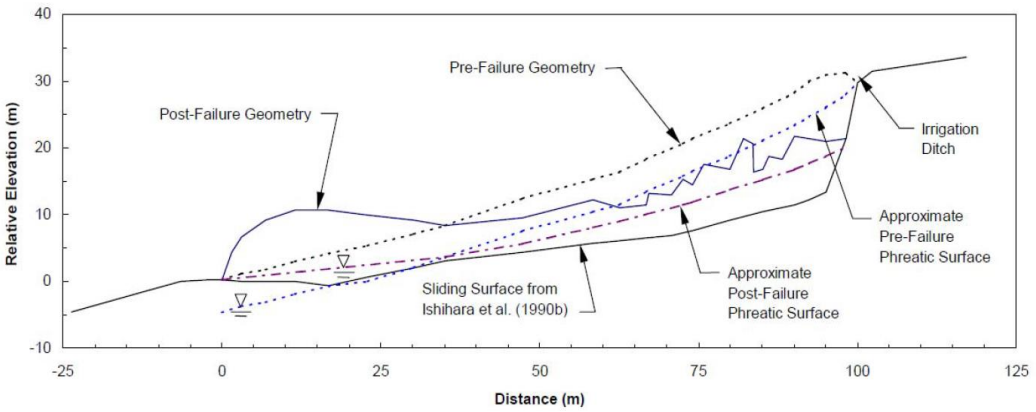

Figure A.11.2. Pre-failure and post-failure cross-sections of the Soviet Tajik – May 1 Slide (Olson, 2001)

A.11.3 Evaluation of Material Properties

Since the grain size distribution curve of the case history was reported by the main sources of references as given in Figure A.11.3, mean grain size (D_{50}), fines content (FC) and coefficient of uniformity (C_u) values are evaluated based on this curve.

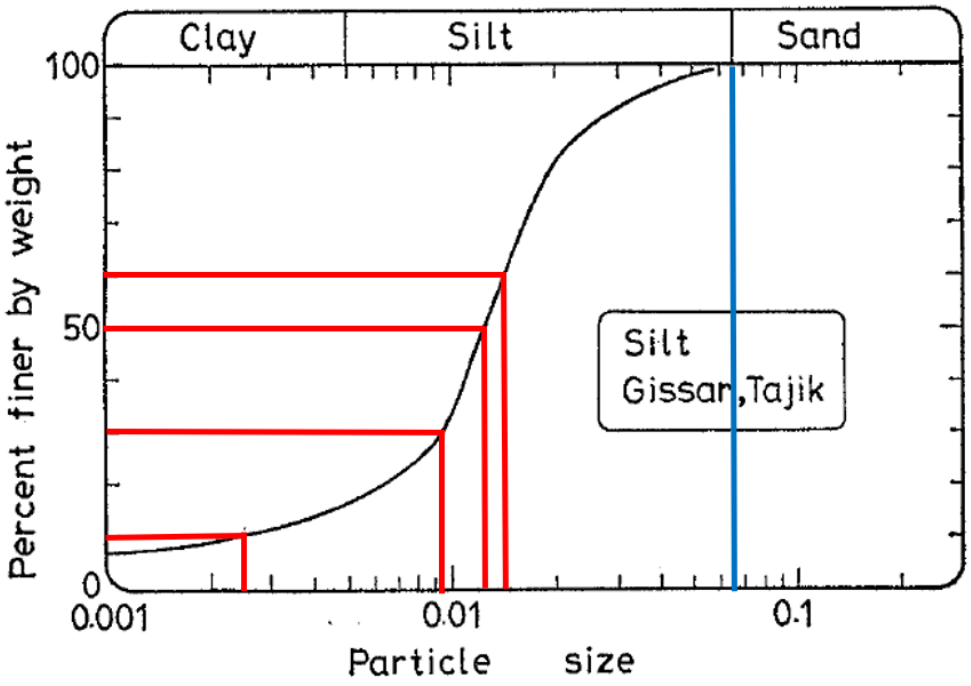

Figure A.11.3. Grain size distribution curve of the Soviet Tajik – May 1 Slide (Ishihara et al., 1990)

Mean grain size (D_{50}): D_{50} = 0.013 mm is evaluated representatively based on the grain size distribution curve of the case history. Olson (2001) also suggests 0.012 mm for D_{50} value of this case history.

Fines content (FC): FC = 100% is evaluated representatively based on the grain size distribution curve of the case history. Olson (2001) also suggests FC = 100%.

Coefficient of uniformity (C_u): D_{10} and D_{60} values are evaluated as 0.0025 mm and 0.015 mm, respectively, based on the grain size distribution curve of the case history. Therefore, the uniformity coefficient is estimated as $C_u = D_{60}/D_{10} = 0.015/0.0025 = 6.00$, which indicates well-graded soil.

Roundness (R): Since no roundness value was reported by the main sources of references or other studies, no value has been set for this parameter for the evaluation of limit void ratios and void ratio ranges. However, R = 0.50 is taken approximately as a representative value for the evaluation of liquefaction state friction angle.

Sphericity (S): Since no sphericity value was reported by the main sources of references or other studies, no value has been set for this parameter for the evaluation of limit void ratios and void ratio ranges. However, S = 0.60 is taken approximately as a representative value for the evaluation of liquefaction state friction angle.

Unit weight (γ_{dry} and γ_{sat}): As the results are not sensitive to unit weight, the dry and saturated unit weights of all soil layers are assigned as 16.5 kN/m^3 and 18.5 kN/m^3, respectively, to be compatible with Olson (2001) and Weber (2015).

A.11.4 Sub-sectioning of the Cross-section and Failure Plane

The exact locations of the CPT boreholes were not known for this case history. Therefore, the sub-sectioning is made based on imaginary boreholes assigned on the cross-section. These imaginary boreholes are defined with respect to changes in effective vertical stresses and inclination angles of the failure plane. Accordingly, two sub-sections are assigned for the liquefied zone as presented in Figure A.11.4.

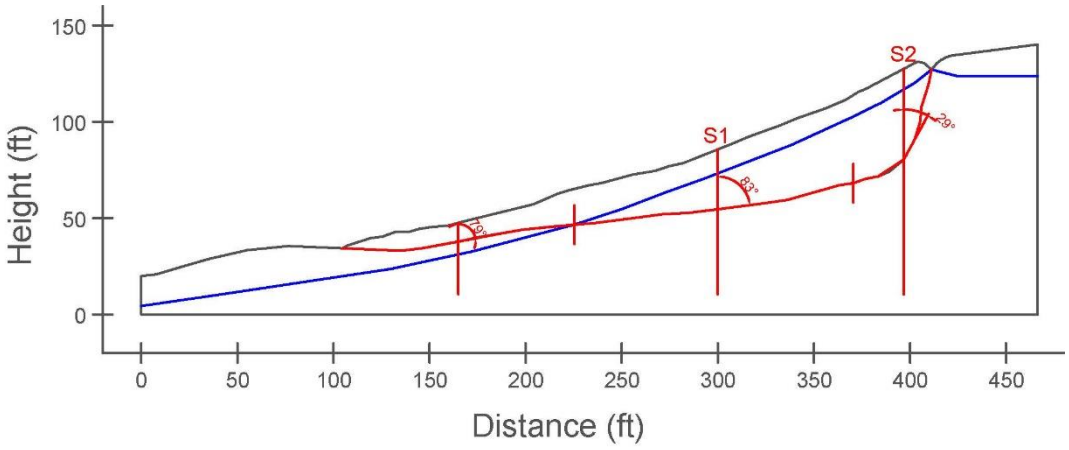

Figure A.11.4. Sub-sectioning of the cross-section and failure plane for Soviet Tajik – May 1 Slide

The territory lengths (L_i) and inclinations (α_i) (positive sign for CCW direction) of the failure plane are evaluated as given in Table A.11.1 for each sub-section.

Table A.11.1 Sub-sections with their corresponding failure plane lengths and inclinations for Soviet Tajik – May 1 Slide

Case History	Section	Failure plane length, L_i (m)	Total failure plane length, L_t (m)	Failure plane inclination, α_i (degrees)
Soviet Tajik – May 1 Slide	S1	44.85	68.84	7
	S2	23.99		61

A.11.5 Elastic Modeling and Stress Rotation

All stress components are evaluated linear elastically at the points where boreholes and failure plane intersect in Figure A.11.4. The initial and deformed shape of the cross-section are presented in Figure A.11.5 and Figure A.11.6, respectively. All lengths are given in meters.

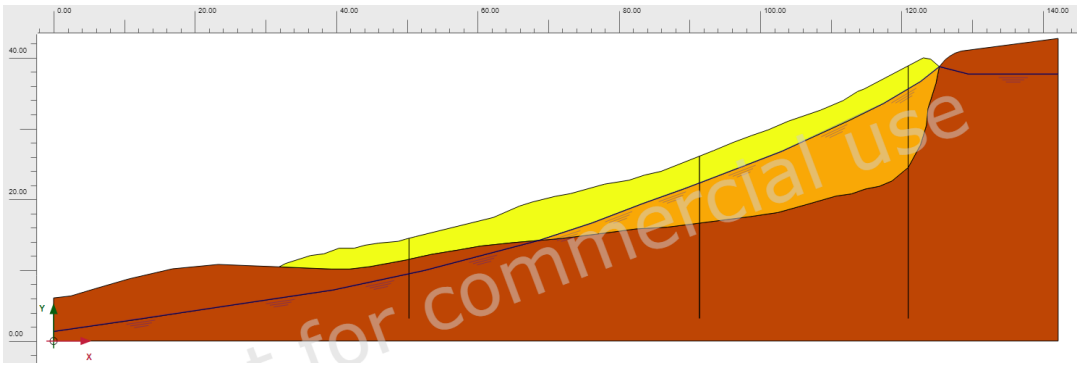

Figure A.11.5. Initial cross-section used in linear elastic modeling of Soviet Tajik – May 1 Slide

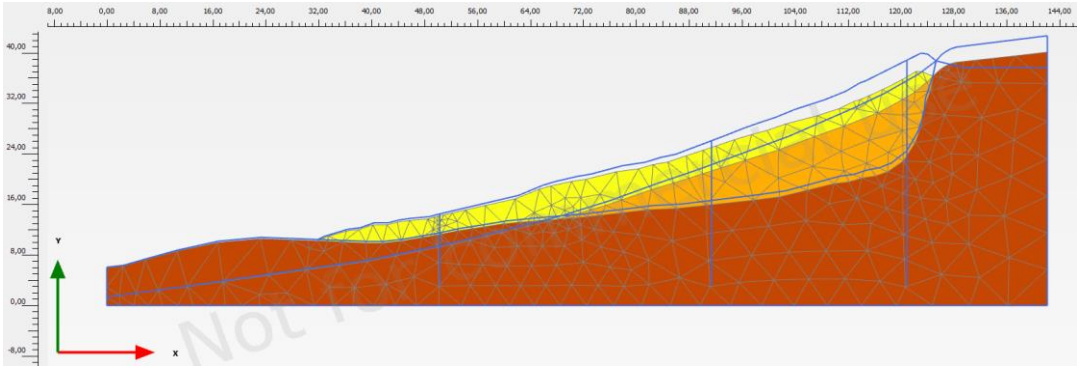

Figure A.11.6. Deformed cross-section obtained after linear elastic modeling of Soviet Tajik – May 1 Slide

During the elastic modeling process in PLAXIS 2D Ultimate Connect Edition V22.00.00.1733 software, the Poisson's ratio values of the non-liquefied zone, liquefied zone, and stable loess are defined as 0.30, 0.33, and 0.30, respectively. The elastic modulus values of the same layers, on the other hand, are estimated as 10 MPa, 5 MPa, and 30 MPa, respectively.

The effective normal (σ'_N) and shear (τ_{static}) stresses acting on the inclined failure plane are evaluated with corresponding Mohr's circles. The corresponding Mohr's circles and the effective stress components of the sub-sections are presented in Figure A.11.7 and Table A.11.2, respectively. All stresses are given in kilopascals.

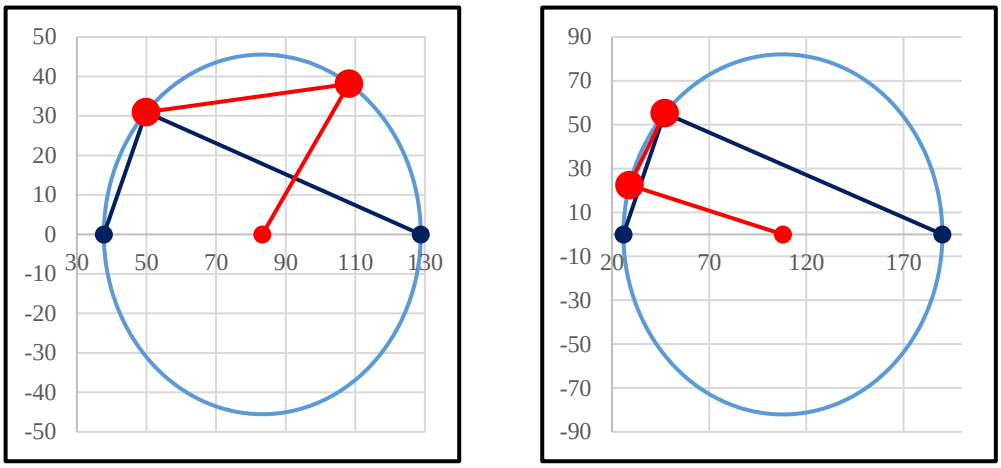

(a) S1 (b) S2

Figure A.11.7. Mohr's circles for Soviet Tajik – May 1 Slide

Table A.11.2 Evaluated stress components for Soviet Tajik – May 1 Slide

Case History	Section	σ'_1 (kPa)	σ'_2 (kPa)	σ'_3 (kPa)	p_0' (kPa)	q (kPa)	σ'_N (kPa)	τ_{static} (kPa)	$\lvert\tau_{static}\rvert$ (kPa)
Soviet Tajik – May 1 Slide	S1	128.8	55.0	37.7	73.8	83.8	108.2	38.1	38.1
	S2	190.0	64.8	25.9	93.5	148.6	29.0	22.5	22.5

A.11.6 Evaluation of SPT Resistance

The exact locations of the CPT boreholes were not documented for this case history. Therefore, imaginary boreholes are assigned along the cross-section as shown in Figure A.11.4. CPT data used for this case history is presented in Figure A.11.8.

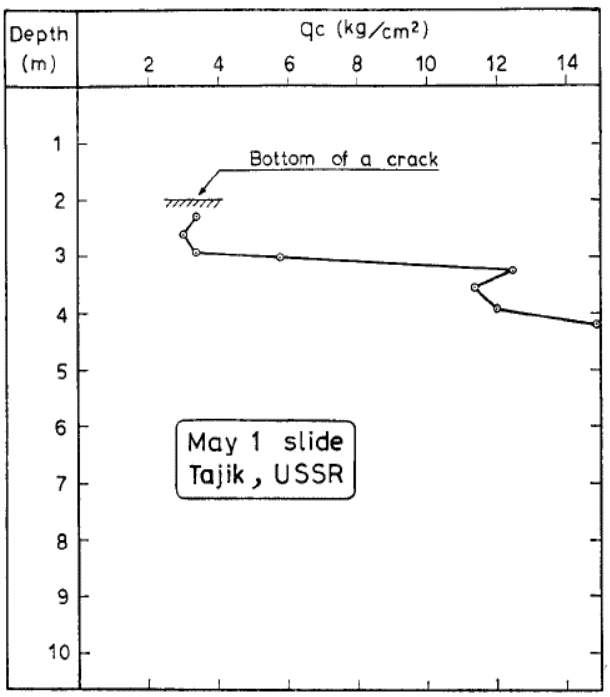

Figure A.11.8. CPT data for Soviet Tajik – May 1 Slide (Ishihara et al., 1990)

The CPT cone tip resistances are converted to raw SPT-N and N_{60} values by using the correlations proposed by Ishihara et al. (1990) and Kulhawy and Mayne (1990), respectively, as explained in Section 3.5. Then, the overburden stress correction factors (C_N) are again evaluated to be able to estimate $(N_1)_{60}$ values based on the effective vertical stresses estimated at the point of penetration for each recording, and average values are documented for simplicity. The fines content correction factors (C_{fines}) are also evaluated with the methods and relationships explained in Section 3.5. Accordingly, the correction factors and SPT resistances are estimated as given in Table A.11.3.

Table A.11.3 Evaluated SPT-N resistances for Soviet Tajik – May 1 Slide

Case History	Section	C_N	C_B	C_R	C_S	C_E	C_{fines}	N	N_{60}	$(N_1)_{60}$	$(N_1)_{60,cs}$	
Soviet Tajik – May 1 Slide	S1	0.91	-	-	-	-	1.52	2.76	2.46	4.56	6.95	6.95
	S2	0.75	-	-	-	-	1.52	2.76	2.46	4.56	6.95	

A.11.7 Evaluation of Limit Void Ratios, Void Ratio Ranges, Relative Densities and Initial Void Ratios

Since mean grain size (D_{50}), fines content (FC), and coefficient of uniformity (C_u) information were available among the required material properties for the void ratio prediction models, the arithmetic means of the limit void ratios (e_{min} and e_{max}) evaluated by Model 8 and Model 9 are considered as the representative values. The e_{max} value is slightly modified then with respect to the construction method of the case history for each prediction model.

Since the fines content value is evaluated as 100%, which is greater than 15%, it is judged that the soil of interest consists of silty soils. Therefore, the relative densities evaluated by the correlation recommended by Cubrinovski and Ishihara (1999) are directly taken as the representative relative densities of the soils. Based on these relative densities and limit void ratios, the initial void ratios (e_0) corresponding to approximately 1 kPa confining stress are estimated referring to Equation 3-68. Accordingly, the limit void ratios, void ratio ranges (without any modification for the construction method), in-situ relative densities, and initial void ratios are estimated as given in Table A.11.4.

Table A.11.4 Evaluated limit void ratios, void ratio ranges, in-situ relative densities, and initial void ratios for Soviet Tajik – May 1 Slide

Case History	Section	e_{min}	e_{max}	e_{max}-e_{min}	$RD_{C\&I}$ (%)	$RD_{K\&M}$ (%)	$RD_{overall}$ (%)	e_0
Soviet Tajik – May 1 Slide	S1	0.506	0.874	0.368	26.70	59.57	26.70	0.776
	S2	0.506	0.874	0.368	26.70	59.57	26.70	0.776

A.12 Shibecha-Cho Embankment (1993 Kushiro-Oki Earthquake, M_L=7.8)

A.12.1 Brief Summary of the Case History

Shibecha-Cho Embankment was located in Hokkaido, Japan, and the exact date of the failure was reported as September 22, 1993. The fundamental reason behind the failure was reported as the 1993 Kushiro-Oki Earthquake (M_L=7.8). The type of the structure can be classified as a poorly compacted embankment, and the maximum slope height is reported as ~ 10 m. Miura et al. (1995, 1998) are considered as the main sources of references. Olson (2001), Wang (2003) and Weber (2015) also studied this case history during their back-analyses of liquefaction failure case histories.

A.12.2 Site Geology and Critical Cross-section

Figure A.12.1 and Figure A.12.2 show the pre-failure and post-failure cross-sections of the case structure. It is decided that the idealized soil profile consists of four soil layers namely non-liquefied zone, liquefied zone, peat, and base material. The parts of the embankment remaining above and below the water table level at the time of failure are classified as non-liquefied zone and liquefied zone, respectively. The zone existing at the toe of the embankment underlying the liquefied portion is defined as peat, and the layer underlying the embankment is classified as base material.

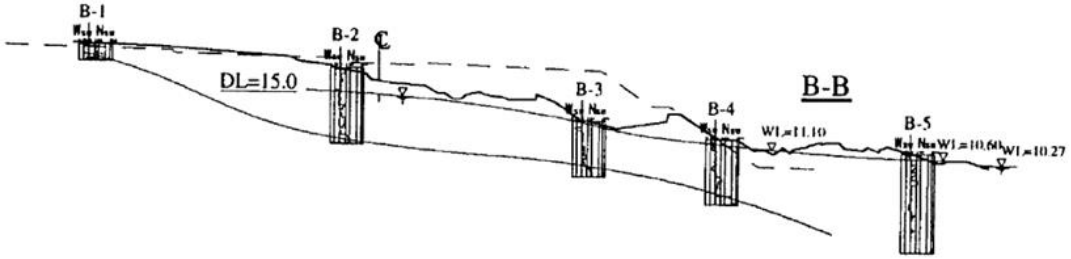

Figure A.12.1. Pre-failure and post-failure cross-sections of the Shibecha-Cho Embankment (Miura et al., 1998)

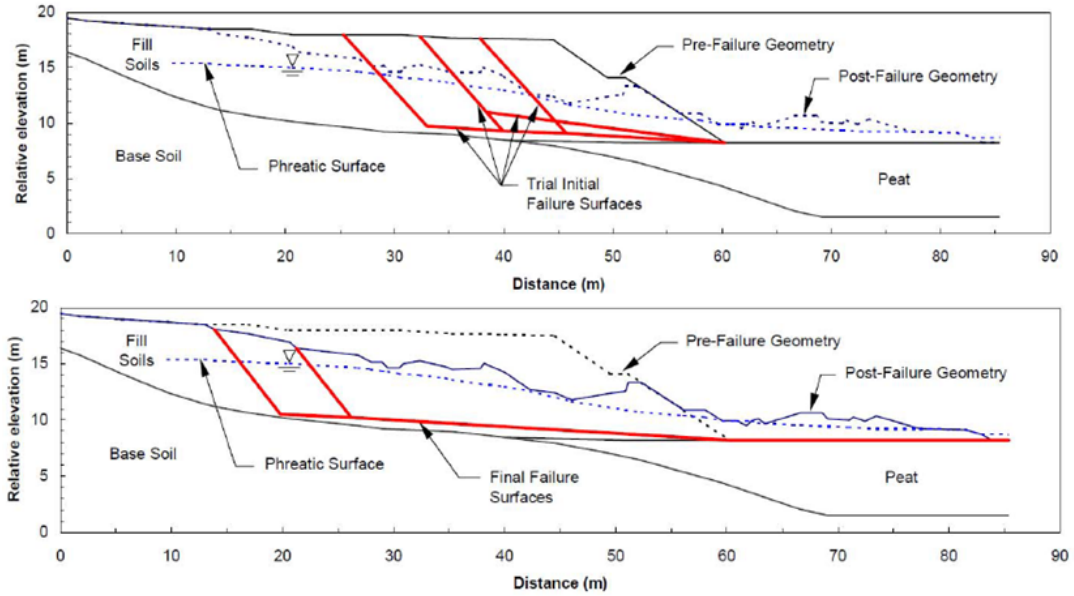

Figure A.12.2. Pre-failure and post-failure cross-sections of the Shibecha-Cho Embankment (Olson, 2001)

A.12.3 Evaluation of Material Properties

Since the grain size distribution curve of the case history was reported by the main sources of references as given in Figure A.12.3, mean grain size (D_{50}), fines content (FC) and coefficient of uniformity (C_u) values are evaluated based on this curve.

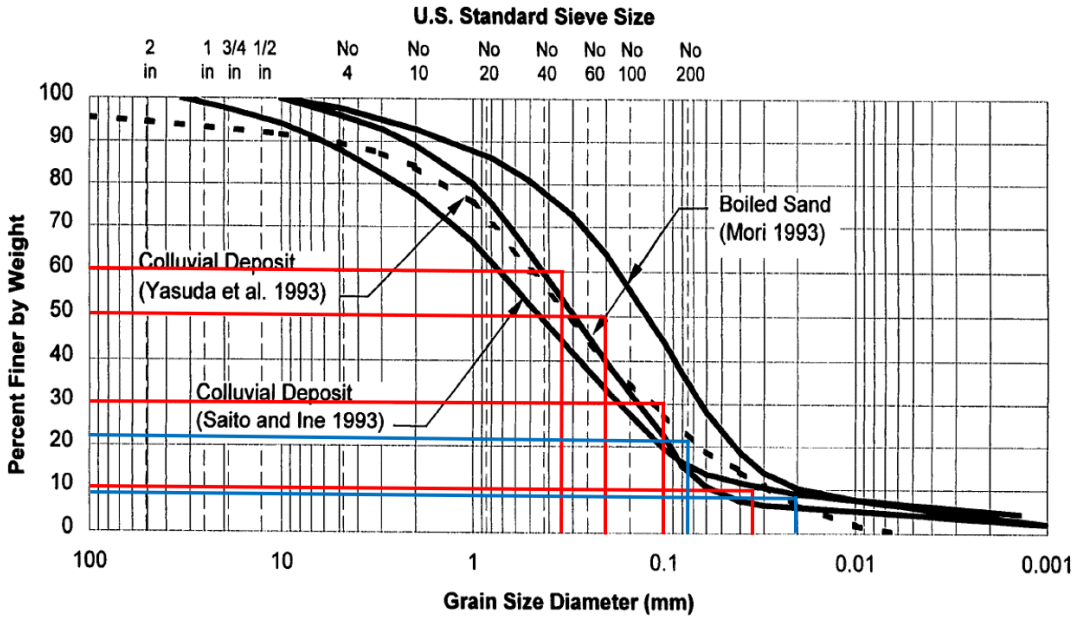

Figure A.12.3. Grain size distribution curve of the Shibecha-Cho Embankment (Miura et al., 1998)

Mean grain size (D_{50}): D_{50} = 0.200 mm is evaluated representatively based on the grain size distribution curve of the case history. Olson (2001) also suggests a range of 0.120-0.400 mm for D_{50} value with an average of 0.200 mm. Srbulov (2008) also reports D_{50} = 0.200 mm for this case history.

Fines content (FC): FC = 20% is evaluated representatively based on the grain size distribution curve of the case history. Olson (2001) also suggests a range of 12%-35% for fines content with an average of 20%. Srbulov (2008), Yasuda (1993), Saito and Ine (1993) and Mori (1993) also recommend FC = 20% for this case history.

Coefficient of uniformity (C_u): D_{10} and D_{60} values are evaluated as 0.035 mm and 0.340 mm, respectively, based on the grain size distribution curve of the case history. Therefore, the uniformity coefficient is estimated as $C_u = D_{60}/D_{10} = 0.340/0.035 = 9.71$, which indicates well-graded soil.

Roundness (R): Since no roundness value was reported by the main sources of references or other studies, no value has been set for this parameter for the evaluation

of limit void ratios and void ratio ranges. However, R = 0.50 is taken approximately as a representative value for the evaluation of liquefaction state friction angle.

Sphericity (S): Since no sphericity value was reported by the main sources of references or other studies, no value has been set for this parameter for the evaluation of limit void ratios and void ratio ranges. However, S = 0.60 is taken approximately as a representative value for the evaluation of liquefaction state friction angle.

Unit weight (γ_{dry} and γ_{sat}): As the results are not sensitive to unit weight, the dry and saturated unit weights of liquefied zone, peat layer and base material are assigned as 14.9 kN/m^3 and 15.7 kN/m^3, respectively. For the non-liquefied zone, the unit weight is defined as 14.1 kN/m^3. These values are selected accordingly to be compatible with Olson (2001) and Weber (2015).

A.12.4 Sub-sectioning of the Cross-section and Failure Plane

The exact locations of the Swedish CPT boreholes were known for this case history as presented in Figure A.12.1. Therefore, the sub-sectioning is made based on the locations of these penetration tests as shown in Figure A.12.4. Each test is assigned (names of the logs are directly assigned as the name of the sub-section) for the corresponding territory length. Two different failure planes are considered based on the information available on the main sources of references about the failure mode as presented in Figure A.12.4. While boreholes B-2, B-3 and B-5 sub-divide the larger failure plane into smaller pieces, B-4 and B-5 split the smaller failure plane.

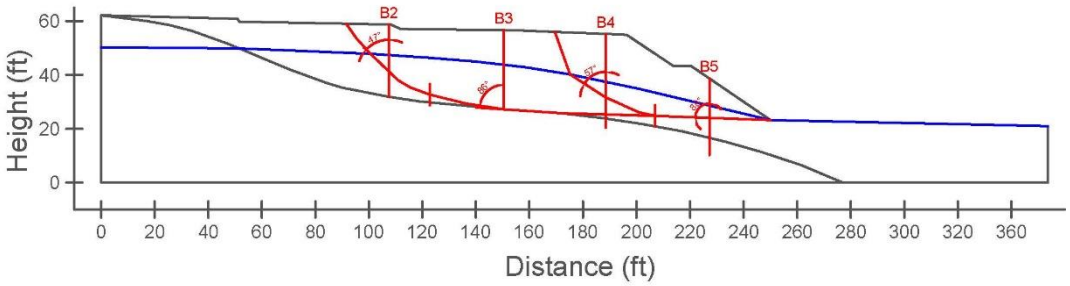

Figure A.12.4. Sub-sectioning of the cross-section and failure planes for Shibecha-Cho Embankment

The territory lengths (L_i) and inclinations (α_i) (positive sign for CCW direction) of the failure planes are evaluated as given in Table A.12.1 for each sub-section.

Table A.12.1 Sub-sections with their corresponding failure plane lengths and inclinations for Shibecha-Cho Embankment

Case History	Section	Failure plane length, L_i (m)	Total failure plane length, L_t (m)	Failure plane inclination, α_i (degrees)
Shibecha-Cho Embankment	B-2	8.32	47.32	-43
	B-3	25.85		-4
	B-5	13.14		-2
	B-4	10.87	24.02	-33
	B-5	13.14		-2

A.12.5 Elastic Modeling and Stress Rotation

All stress components are evaluated linear elastically at the points where boreholes and failure plane intersect in Figure A.12.4. The initial and deformed shape of the cross-section are presented in Figure A.12.5 and Figure A.12.6, respectively. All lengths are given in meters.

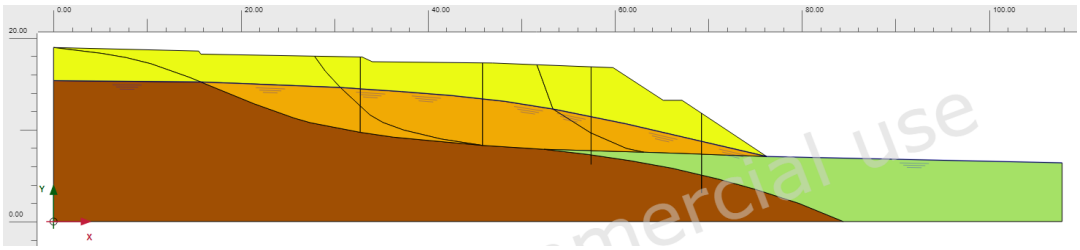

Figure A.12.5. Initial cross-section used in linear elastic modeling of Shibecha-Cho Embankment

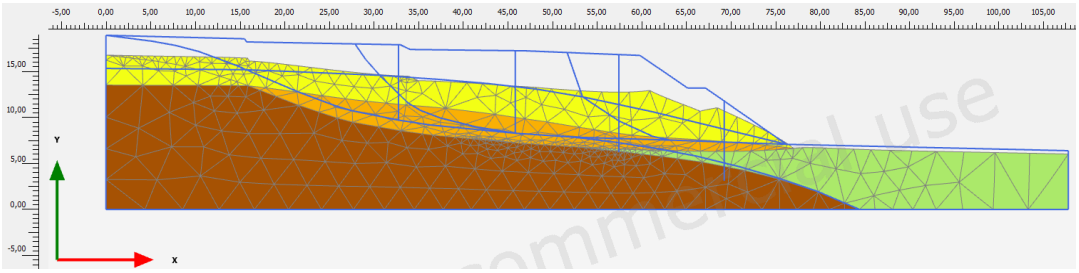

Figure A.12.6. Deformed cross-section obtained after linear elastic modeling of Shibecha-Cho Embankment

During the elastic modeling process in PLAXIS 2D Ultimate Connect Edition V22.00.00.1733 software, the Poisson's ratio values of the non-liquefied zone, liquefied zone, peat, and base material are defined as 0.30, 0.33, 0.30, and 0.30, respectively. The elastic modulus values of the same layers, on the other hand, are estimated as 10 MPa, 5 MPa, 10 MPa, and 30 MPa, respectively.

The effective normal (σ'_N) and shear (τ_{static}) stresses acting on the inclined failure plane are evaluated with corresponding Mohr's circles. The corresponding Mohr's circles and the effective stress components of the sub-sections are presented in Figure A.12.7 and Table A.12.2, respectively. All stresses are given in kilopascals.

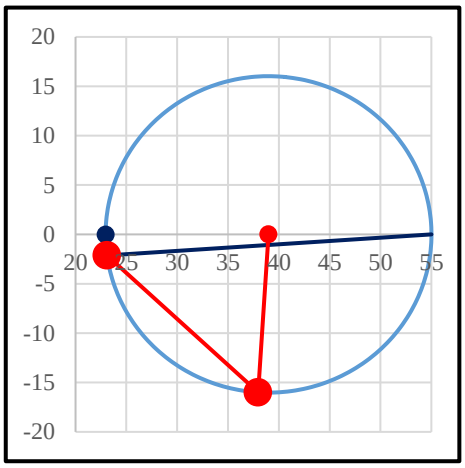

(a) B-2

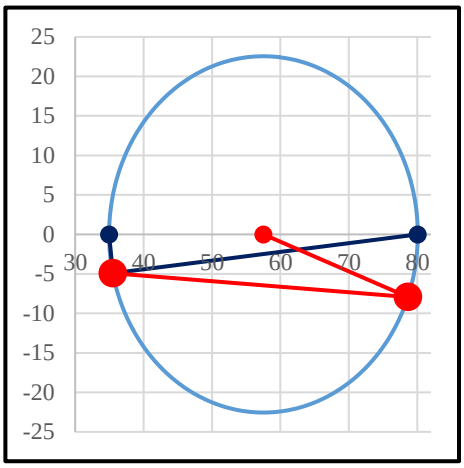

(b) B-3

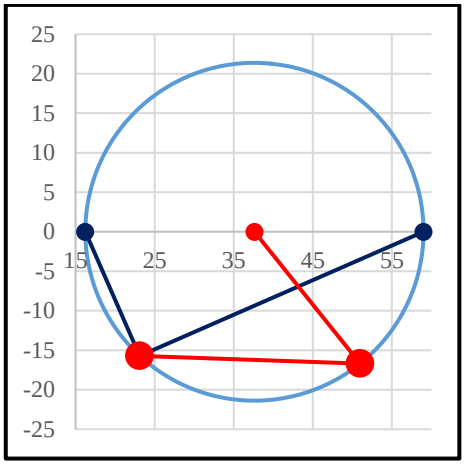

(c) B-5

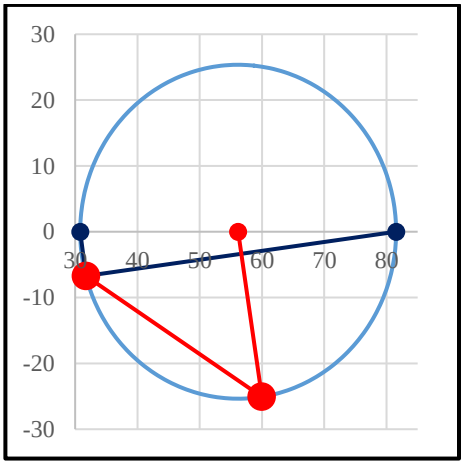

(d) B-4

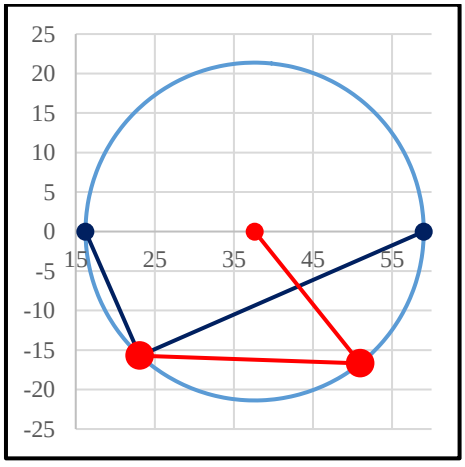

(e) B-5

Figure A.12.7. Mohr's circles for Shibecha-Cho Embankment

Table A.12.2 Evaluated stress components for Shibecha-Cho Embankment

Case History	Section	σ'_1 (kPa)	σ'_2 (kPa)	σ'_3 (kPa)	p_0' (kPa)	q (kPa)	σ'_N (kPa)	τ_{static} (kPa)	$\lvert\tau_{static}\rvert$ (kPa)
Shibecha-Cho Embankment	B-2	55.0	25.7	23.0	34.6	30.8	38.0	-16.0	16.0
	B-3	80.1	38.0	35.0	51.0	43.7	78.6	-7.9	7.9
	B-5	59.0	24.8	16.2	33.4	39.2	51.0	-16.7	16.7
	B-4	81.5	37.1	30.8	49.8	47.9	60.0	-25.1	25.1
	B-5	59.0	24.8	16.2	33.4	39.2	51.0	-16.7	16.7

A.12.6 Evaluation of SPT Resistance

The exact locations of the Swedish CPT boreholes were documented by Miura et al. (1998) as given in Figure A.12.1. One of the corresponding SCPT boreholes is presented in Figure A.12.8.

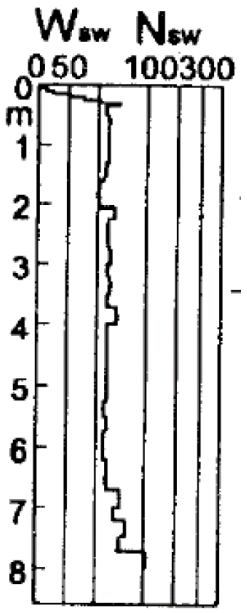

Figure A.12.8. Example SCPT borehole for Shibecha-Cho Embankment (Miura et al., 1998)

The SCPT resistances are converted to raw SPT-N values by using the correlation proposed by Inada (1982) explained in Section 3.5. These SPT-N values are assumed to be almost equal to N_{60} values as equipment, energy, and procedure corrections are

not applicable for SCPT. However, the short rod length correction factors (C_R) are still evaluated with the methods and relationships explained in Section 3.5. Similarly, the overburden stress correction factors (C_N) are again evaluated based on the effective vertical stresses estimated at the point of penetration for each recording, and average values are documented for simplicity. The fines content correction factors (C_{fines}) are also evaluated with the methods and relationships explained in Section 3.5. Accordingly, the correction factors and SPT resistances are estimated as given in Table A.12.3.

Table A.12.3 Evaluated SPT-N resistances for Shibecha-Cho Embankment

Case History	Section	C_N	C_B	C_R	C_S	C_E	C_{fines}	N	N_{60}	$(N_1)_{60}$	$(N_1)_{60,cs}$	
Shibecha-Cho Embankment	B-2	1.32	1.0	0.91	1.0	1.00	1.31	3.59	3.28	4.33	5.67	5.45
	B-3	1.10	1.0	0.91	1.0	1.00	1.36	3.59	3.28	3.59	4.88	
	B-5	1.35	1.0	0.91	1.0	1.00	1.31	3.59	3.28	4.44	5.80	
	B-4	1.09	1.0	0.91	1.0	1.00	1.36	3.59	3.28	3.57	4.86	5.33
	B-5	1.35	1.0	0.91	1.0	1.00	1.31	3.59	3.28	4.44	5.80	

A.12.7 Evaluation of Limit Void Ratios, Void Ratio Ranges, Relative Densities and Initial Void Ratios

Since mean grain size (D_{50}), fines content (FC), and coefficient of uniformity (C_u) information were available among the required material properties for the void ratio prediction models, the arithmetic means of the limit void ratios (e_{min} and e_{max}) evaluated by Model 8 and Model 9 are considered as the representative values. The e_{max} value is slightly modified then with respect to the construction method of the case history for each prediction model.

Since the fines content value is evaluated as 20%, which is greater than 15%, it is judged that the soil of interest consists of silty soils. Therefore, the relative densities evaluated by the correlation recommended by Cubrinovski and Ishihara (1999) are directly taken as the representative relative densities of the soils. Based on these

relative densities and limit void ratios, the initial void ratios (e_0) corresponding to approximately 1 kPa confining stress are estimated referring to Equation 3-68. Accordingly, the limit void ratios, void ratio ranges (without any modification for the construction method), in-situ relative densities, and initial void ratios are estimated as given in Table A.12.4.

Table A.12.4 Evaluated limit void ratios, void ratio ranges, in-situ relative densities, and initial void ratios for Shibecha-Cho Embankment

Case History	Section	e_{min}	e_{max}	e_{max}-e_{min}	$RD_{C\&I}$ (%)	$RD_{K\&M}$ (%)	$RD_{overall}$ (%)	e_0
Shibecha-Cho Embankment	B-2	0.461	0.790	0.329	23.62	31.89	23.62	0.712
	B-3	0.461	0.790	0.329	21.53	29.07	21.53	0.719
	B-5	0.461	0.790	0.329	23.93	32.31	23.93	0.711
	B-4	0.461	0.790	0.329	21.46	28.97	21.46	0.719
	B-5	0.461	0.790	0.329	23.93	32.31	23.93	0.711

A.13 Route 272 at Higashiarekinai (1993 Kushiro-Oki Earthquake, M_L=7.8)

A.13.1 Brief Summary of the Case History

Route 272 was located in Higashiarekinai, Japan, and the exact date of the failure was reported as September 22, 1993. The fundamental reason behind the failure was reported as the 1993 Kushiro-Oki Earthquake (M_L=7.8). The type of the structure can be classified as a poorly compacted embankment, and the maximum slope height is reported as ~ 8 m. Sasaki et al. (1994) and Wride et al. (1999) are considered as the main sources of references. Olson (2001), Wang (2003) and Weber (2015) also studied this case history during their back-analyses of liquefaction failure case histories.

A.13.2 Site Geology and Critical Cross-section

Figure A.13.1 shows the soil stratigraphy and pre-failure and post-failure cross-sections of the case structure. It is decided that the idealized soil profile consists of four soil layers namely non-liquefied zone, liquefied zone, dense fine sand, and foundation material. The parts of the embankment remaining above and below the water table level at the time of failure are classified as non-liquefied zone and liquefied zone, respectively. The layer underlying the embankment is classified as foundation material. A thin layer of dense fine sand is identified inside of the foundation material close to the embankment bottom.

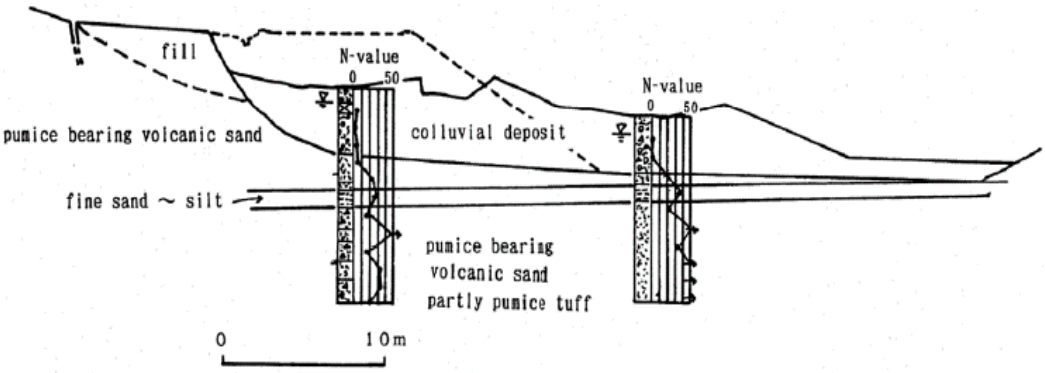

Figure A.13.1. Soil stratigraphy and pre-failure and post-failure cross-sections of the Route 272 at Higashiarekinai (Sasaki et al., 1994)

A.13.3 Evaluation of Material Properties

Since the grain size distribution curve of the case history was not reported by the main sources of references or other residual strength-related studies, mean grain size (D_{50}), fines content (FC) and coefficient of uniformity (C_u) values are estimated based on the documented representative values in those references, if available.

Mean grain size (D_{50}): The exact value of the mean grain size was reported as D_{50} = 0.200 mm in Srbulov (2008). Olson (2001) also suggests a range of 0.120-0.400 mm for D_{50} value with an average of 0.200 mm. Hence, the representative D_{50} value is also taken as 0.200 mm in this study.

Fines content (FC): The exact value of the fines content was reported as FC = 20% in Srbulov (2008). Olson (2001) also suggests a range of 12%-35% for fines content with an average of 20%. Hence, the representative FC value is also taken as 20%.

Coefficient of uniformity (C_u): Since no coefficient of uniformity value was reported by the main sources of references or other relative studies, no value has been set for this parameter.

Roundness (R): Since no roundness value was reported by the main sources of references or other studies, no value has been set for this parameter for the evaluation of limit void ratios and void ratio ranges. However, R = 0.50 is taken approximately as a representative value for the evaluation of liquefaction state friction angle.

Sphericity (S): Since no sphericity value was reported by the main sources of references or other studies, no value has been set for this parameter for the evaluation of limit void ratios and void ratio ranges. However, S = 0.60 is taken approximately as a representative value for the evaluation of liquefaction state friction angle.

Unit weight (γ_{dry} and γ_{sat}): As the results are not sensitive to unit weight, the dry and saturated unit weights of all soil layers are assigned as 16.2 kN/m^3 and 17.0 kN/m^3, respectively, to be compatible with Olson (2001) and Weber (2015).

A.13.4 Sub-sectioning of the Cross-section and Failure Plane

The exact locations of the SPT boreholes were known for this case history as presented in Figure A.13.1. Therefore, the sub-sectioning is made based on the locations of these penetration tests as presented in Figure A.13.2. Each test is assigned (names of the logs are directly assigned as the name of the sub-section) for the corresponding territory length.

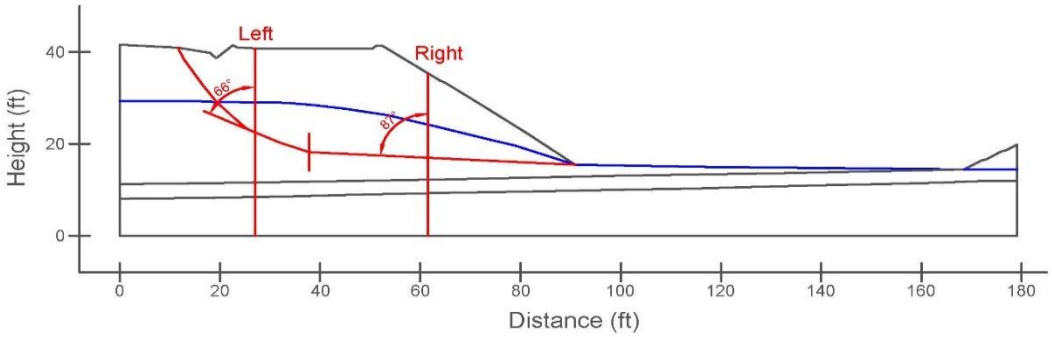

Figure A.13.2. Sub-sectioning of the cross-section and failure plane for Route 272 at Higashiarekinai

The territory lengths (L_i) and inclinations (α_i) (positive sign for CCW direction) of the failure plane are evaluated as given in Table A.13.1 for each sub-section.

Table A.13.1 Sub-sections with their corresponding failure plane lengths and inclinations for Route 272 at Higashiarekinai

Case History	Section	Failure plane length, L_i (m)	Total failure plane length, L_t (m)	Failure plane inclination, α_i (degrees)
Route 272 at Higashiarekinai	Left	6.67	22.87	-24
	Right	16.21		-3

A.13.5 Elastic Modeling and Stress Rotation

All stress components are evaluated linear elastically at the points where boreholes and failure plane intersect in Figure A.13.2. The initial and deformed shape of the cross-section are presented in Figure A.13.3 and Figure A.13.4, respectively. All lengths are given in meters.

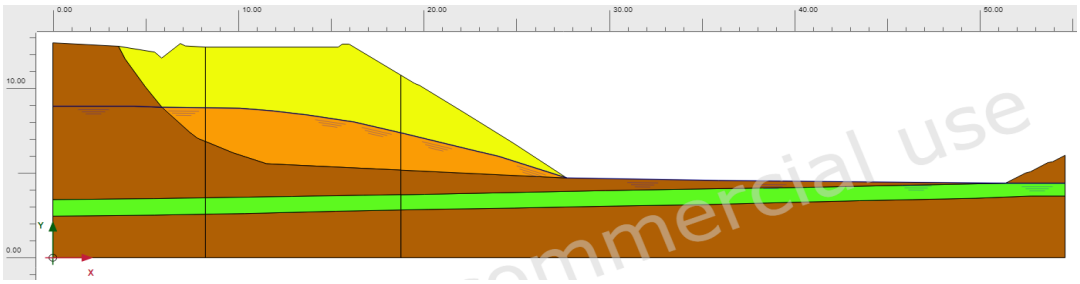

Figure A.13.3. Initial cross-section used in linear elastic modeling of Route 272 at Higashiarekinai

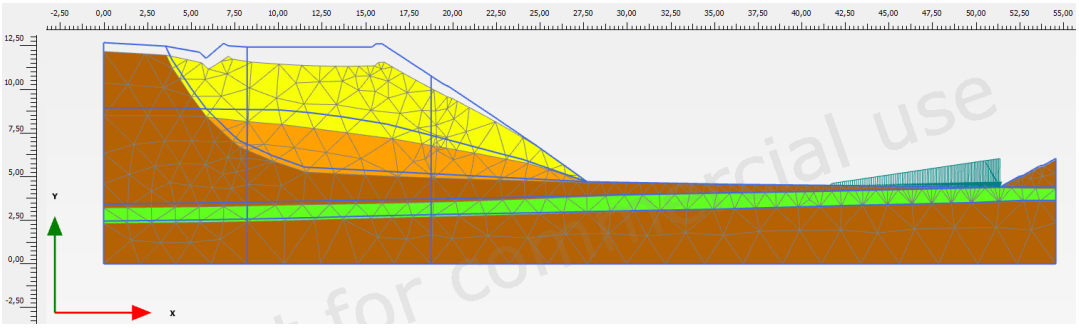

Figure A.13.4. Deformed cross-section obtained after linear elastic modeling of Route 272 at Higashiarekinai

During the elastic modeling process in PLAXIS 2D Ultimate Connect Edition V22.00.00.1733 software, the Poisson's ratio values of the non-liquefied zone, liquefied zone, dense fine sand, and foundation material are defined as 0.30, 0.33, 0.30, and 0.30, respectively. The elastic modulus values of the same layers, on the other hand, are estimated as 10 MPa, 5 MPa, 20 MPa, and 30 MPa, respectively.

The effective normal (σ'_N) and shear (τ_{static}) stresses acting on the inclined failure plane are evaluated with corresponding Mohr's circles. The corresponding Mohr's circles and the effective stress components of the sub-sections are presented in Figure A.13.5 and Table A.13.2, respectively. All stresses are given in kilopascals.

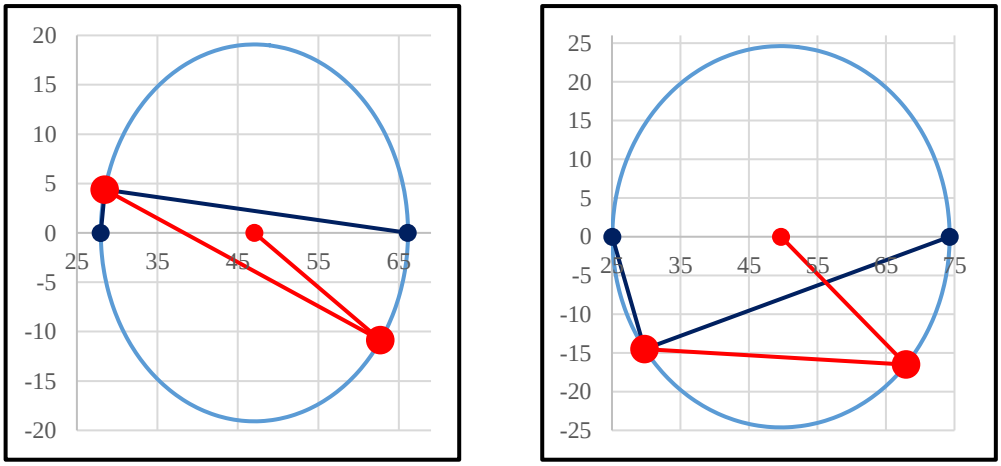

(a) Left (b) Right

Figure A.13.5. Mohr's circles for Route 272 at Higashiarekinai

Table A.13.2 Evaluated stress components for Route 272 at Higashiarekinai

Case History	Section	σ'_1 (kPa)	σ'_2 (kPa)	σ'_3 (kPa)	p_0' (kPa)	q (kPa)	σ'_N (kPa)	τ_{static} (kPa)	$\lvert\tau_{static}\rvert$ (kPa)
Route 272 at Higashiarekinai	Left	66.1	31.1	28.0	41.7	36.7	62.7	-10.9	10.9
	Right	74.3	32.8	25.1	44.0	45.9	67.9	-16.5	16.5

A.13.6 Evaluation of SPT Resistance

The exact locations of the SPT boreholes were documented by Sasaki et al. (1994) as given in Figure A.13.1. Corresponding SPT boreholes are presented in Figure A.13.6 for Left and Right logs, respectively.

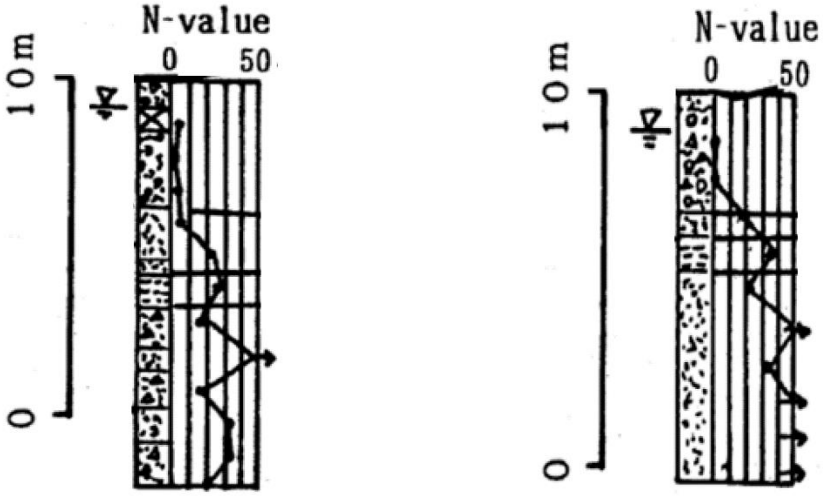

(a) Left (b) Right

Figure A.13.6. SPT boreholes for Route 272 at Higashiarekinai (Sasaki et al., 1994)

The correction factors for nonstandardized sampler configuration (C_S) and borehole diameter (C_B) are taken as 1.0 since no reliable information related to these coefficients was reported in any of the sources. The energy ratio was reported as 72% in Sasaki et al. (1994), Ishihara (1993) and Weber et al. (2015); therefore, the energy efficiency correction factor (C_E) is taken as 72/60 = 1.20. The short rod length (C_R) and fines content correction factors (C_{fines}) are evaluated with the methods and

relationships explained in Section 3.5. The overburden stress correction factors (C_N) are evaluated based on the effective vertical stresses estimated at the point of penetration for each recording, and average values are documented for simplicity. Accordingly, the correction factors and SPT resistances are estimated as given in Table A.13.3.

Table A.13.3 Evaluated SPT-N resistances for Route 272 at Higashiarekinai

Case History	Section	C_N	C_B	C_R	C_S	C_E	C_{fines}	N	N_{60}	$(N_1)_{60}$	$(N_1)_{60,cs}$	
Route 272 at Higashiarekinai	Left	1.64	1.0	0.87	1.0	1.20	1.25	3.57	3.73	5.78	7.24	7.07
	Right	1.94	1.0	0.82	1.0	1.20	1.26	3.57	3.52	5.45	6.89	

A.13.7 Evaluation of Limit Void Ratios, Void Ratio Ranges, Relative Densities and Initial Void Ratios

Since mean grain size (D_{50}) and fines content (FC) information were available among the required material properties for the void ratio prediction models, the arithmetic means of the limit void ratios (e_{min} and e_{max}) evaluated by Model 1 and Model 2 are considered as the representative values. The e_{max} value is slightly modified then with respect to the construction method of the case history for each prediction model.

Since the fines content value is evaluated as 20%, which is greater than 15%, it is judged that the soil of interest consists of silty soils. Therefore, the relative densities evaluated by the correlation recommended by Cubrinovski and Ishihara (1999) are directly taken as the representative relative densities of the soils. Based on these relative densities and limit void ratios, the initial void ratios (e_0) corresponding to approximately 1 kPa confining stress are estimated referring to Equation 3-68. Accordingly, the limit void ratios, void ratio ranges (without any modification for the construction method), in-situ relative densities, and initial void ratios are estimated as given in Table A.13.4.

Table A.13.4 Evaluated limit void ratios, void ratio ranges, in-situ relative densities, and initial void ratios for Route 272 at Higashiarekinai

Case History	Section	e_{min}	e_{max}	e_{max}-e_{min}	$RD_{C\&I}$ (%)	$RD_{K\&M}$ (%)	$RD_{overall}$ (%)	e_0
Route 272 at Higashiarekinai	Left	0.590	0.994	0.404	32.56	36.87	32.56	0.863
	Right	0.590	0.994	0.404	31.63	35.81	31.63	0.866

A.14 Zeeland - Vlietepolder (1889 High Tide)

A.14.1 Brief Summary of the Case History

Zeeland - Vlietepolder was located in Zeeland, Netherlands, and the exact date of the failure was reported as September 11, 1889. The fundamental reason behind the failure was reported as the 1889 Low Tide. The type of the structure can be classified as a delta bank constructed by water sedimentation method, and the maximum slope height is reported as ~ 3 m. Koppejan et al. (1948) is considered as the main source of reference. Olson (2001), Wang (2003) and Weber (2015) also studied this case history during their back-analyses of liquefaction failure case histories.

A.14.2 Site Geology and Critical Cross-section

Figure A.14.1 shows the soil stratigraphy of the case structure. It is decided that the idealized soil profile consists of three soil layers namely non-liquefied zone, liquefied zone, and stable foundation. The parts of the delta bank remaining above and below the water table level at the time of failure are classified as non-liquefied zone and liquefied zone, respectively. The layer underlying the liquefied zone is defined as the stable foundation.

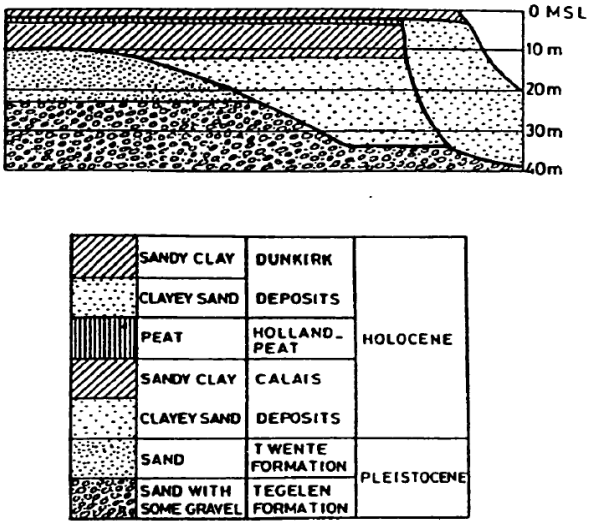

Figure A.14.1. Soil stratigraphy of the Zeeland - Vlietepolder (Silvis and de Groot, 1995)

A.14.3 Evaluation of Material Properties

Since the grain size distribution curve of the case history was reported by the main sources of references as given in Figure A.14.2, mean grain size (D_{50}), fines content (FC) and coefficient of uniformity (C_u) values are evaluated based on this curve.

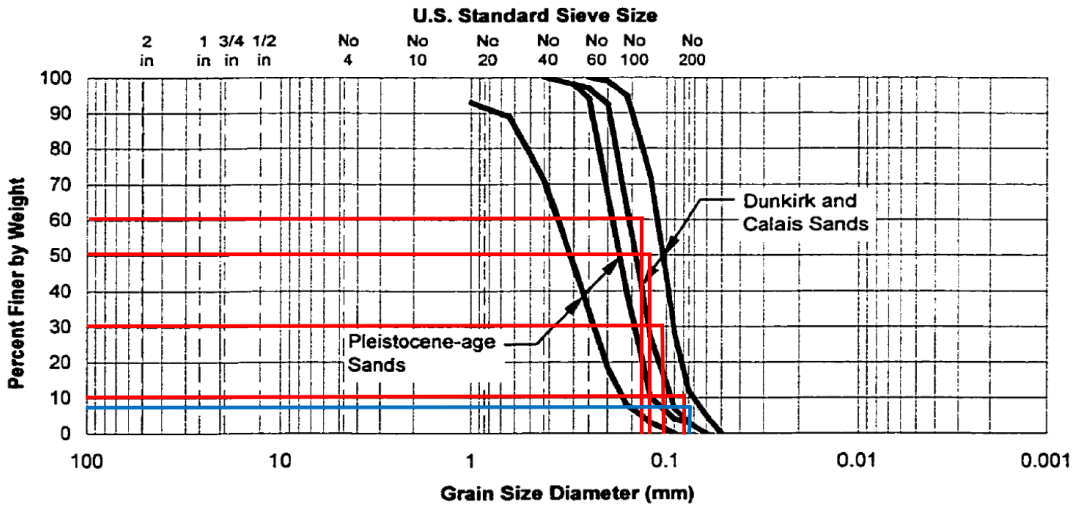

Figure A.14.2. Grain size distribution curve of the Zeeland – Vlietepolder (Olson, 2001, after Koppejan et al., 1948)

Mean grain size (D_{50}): D_{50} = 0.130 mm is evaluated representatively based on the grain size distribution curve of the case history. Olson (2001) also suggests 0.130 mm for D_{50} value of this case history.

Fines content (FC): FC = 7% is evaluated representatively based on the grain size distribution curve of the case history. Olson (2001) also suggests FC = 7%.

Coefficient of uniformity (C_u): D_{10} and D_{60} values are evaluated as 0.080 mm and 0.145 mm, respectively, based on the grain size distribution curve of the case history. Therefore, the uniformity coefficient is estimated as $C_u = D_{60}/D_{10} = 0.145/0.080 = 1.81$.

Roundness (R): Since no roundness value was reported by the main sources of references or other studies, no value has been set for this parameter for the evaluation of limit void ratios and void ratio ranges. However, R = 0.50 is taken approximately as a representative value for the evaluation of liquefaction state friction angle.

Sphericity (S): Since no sphericity value was reported by the main sources of references or other studies, no value has been set for this parameter for the evaluation of limit void ratios and void ratio ranges. However, S = 0.60 is taken approximately as a representative value for the evaluation of liquefaction state friction angle.

Unit weight (γ_{dry} and γ_{sat}): As the results are not sensitive to unit weight, the dry and saturated unit weights of non-liquefied and liquefied zones are assigned as 17.6 kN/m^3 and 18.4 kN/m^3, respectively. For the stable foundation, the unit weight is defined as 18.9 kN/m^3. These values are selected accordingly to be compatible with Olson (2001) and Weber (2015).

A.14.4 Sub-sectioning of the Cross-section and Failure Plane

The exact locations of the CPT boreholes were not known for this case history. Therefore, the sub-sectioning is made based on imaginary boreholes assigned on the cross-section. These imaginary boreholes are defined with respect to changes in

effective vertical stresses and inclination angles of the failure plane. Two different initial failure planes are considered based on the information available on the main sources of references about the failure mode as presented in Figure A.14.3. While boreholes Small-S1 and Small-S2 sub-divide the smaller failure plane into smaller pieces, Large-S1, Large-S2 and Large-S3 split the larger failure plane.

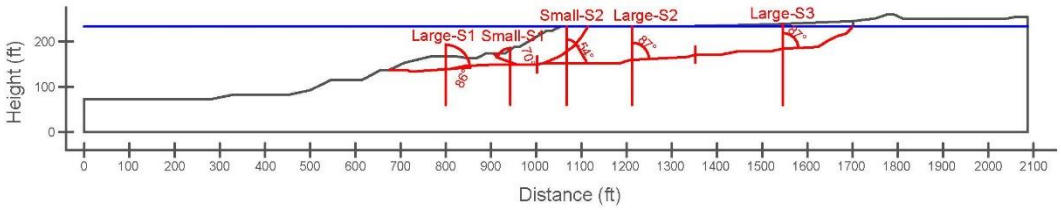

Figure A.14.3. Sub-sectioning of the cross-section and failure planes for Zeeland – Vlietepolder

The territory lengths (L_i) and inclinations (α_i) (positive sign for CCW direction) of the failure planes are evaluated as given in Table A.14.1 for each sub-section.

Table A.14.1 Sub-sections with their corresponding failure plane lengths and inclinations for Zeeland – Vlietepolder

Case History	Section	Failure plane length, L_i (m)	Total failure plane length, L_t (m)	Failure plane inclination, α_i (degrees)
Zeeland – Vlietepolder	Small-S1	31.25	75.67	-30
	Small-S2	44.42		36
	Large-S1	100.22	318.60	4
	Large-S2	107.37		3
	Large-S3	111.00		3

A.14.5 Elastic Modeling and Stress Rotation

All stress components are evaluated linear elastically at the points where boreholes and failure plane intersect in Figure A.14.3. The initial and deformed shape of the cross-section are presented in Figure A.14.4 and Figure A.14.5, respectively. All lengths are given in meters.

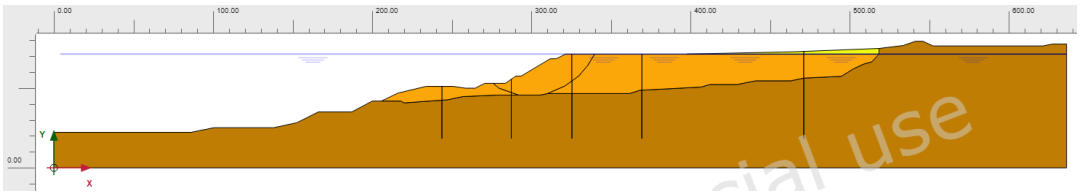

Figure A.14.4. Initial cross-section used in linear elastic modeling of Zeeland – Vlietepolder

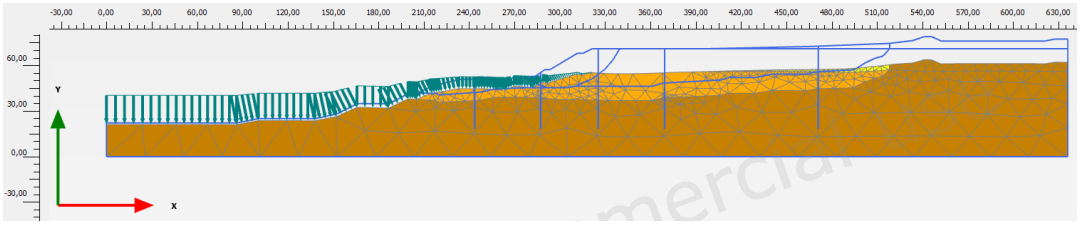

Figure A.14.5. Deformed cross-section obtained after linear elastic modeling of Zeeland – Vlietepolder

During the elastic modeling process in PLAXIS 2D Ultimate Connect Edition V22.00.00.1733 software, the Poisson's ratio values of the non-liquefied zone, liquefied zone, and stable foundation are defined as 0.30, 0.33, and 0.30, respectively. The elastic modulus values of the same layers, on the other hand, are estimated as 10 MPa, 5 MPa, and 30 MPa, respectively.

The effective normal (σ'_N) and shear (τ_{static}) stresses acting on the inclined failure plane are evaluated with corresponding Mohr's circles. The corresponding Mohr's circles and the effective stress components of the sub-sections are presented in Figure A.14.6 and Table A.14.2, respectively. All stresses are given in kilopascals.

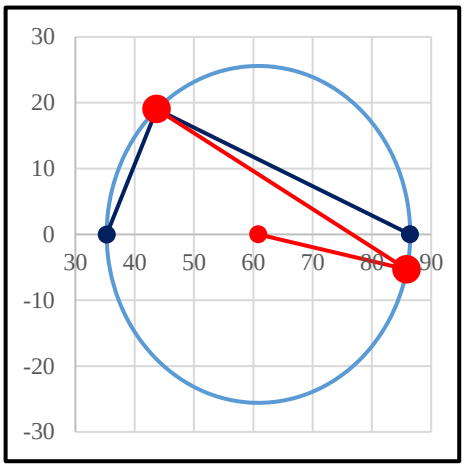

(a) Small-S1

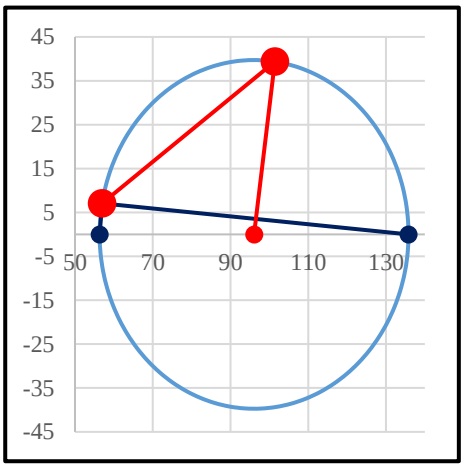

(b) Small-S2

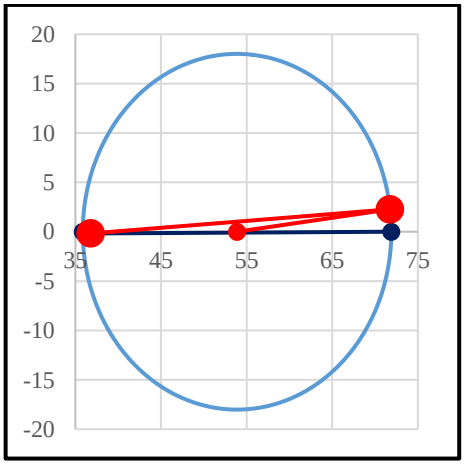

(c) Large-S1

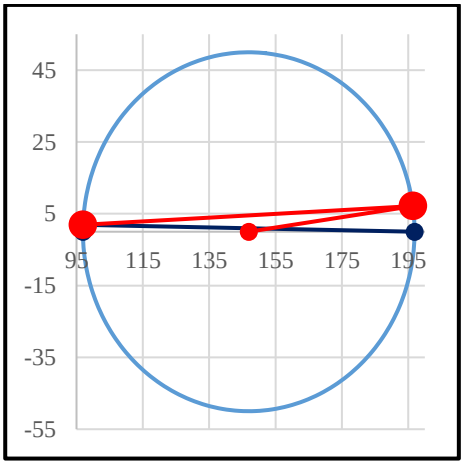

(d) Large-S2

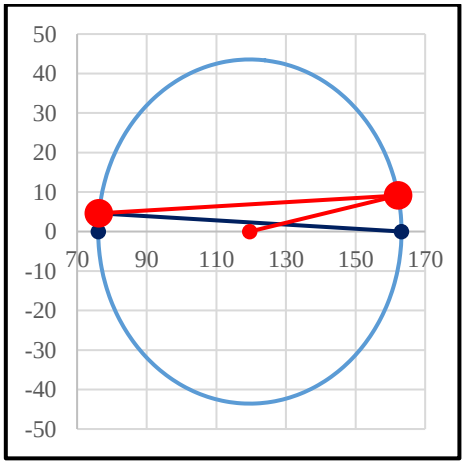

(e) Large-S3

Figure A.14.6. Mohr's circles for Zeeland – Vlietepolder

Table A.14.2 Evaluated stress components for Zeeland – Vlietepolder

Case History	Section	σ'_1 (kPa)	σ'_2 (kPa)	σ'_3 (kPa)	p_0' (kPa)	q (kPa)	σ'_N (kPa)	τ_{static} (kPa)	$\lvert\tau_{static}\rvert$ (kPa)
Zeeland – Vlietepolder	Small-S1	86.5	40.2	35.3	54.0	48.9	85.9	-5.3	5.3
	Small-S2	135.8	63.4	56.3	85.2	76.2	101.4	39.4	39.4
	Large-S1	71.9	36.8	35.9	48.2	35.6	71.8	2.3	2.3
	Large-S2	196.9	97.0	96.9	130.3	100.0	196.4	7.1	7.1
	Large-S3	163.2	79.0	76.1	106.1	85.7	162.2	9.1	9.1

A.14.6 Evaluation of SPT Resistance

The exact locations of the CPT boreholes were not documented for this case history. Therefore, imaginary boreholes are assigned along the cross-section as shown in Figure A.14.3. CPT data used for this case history is presented in Figure A.14.7.

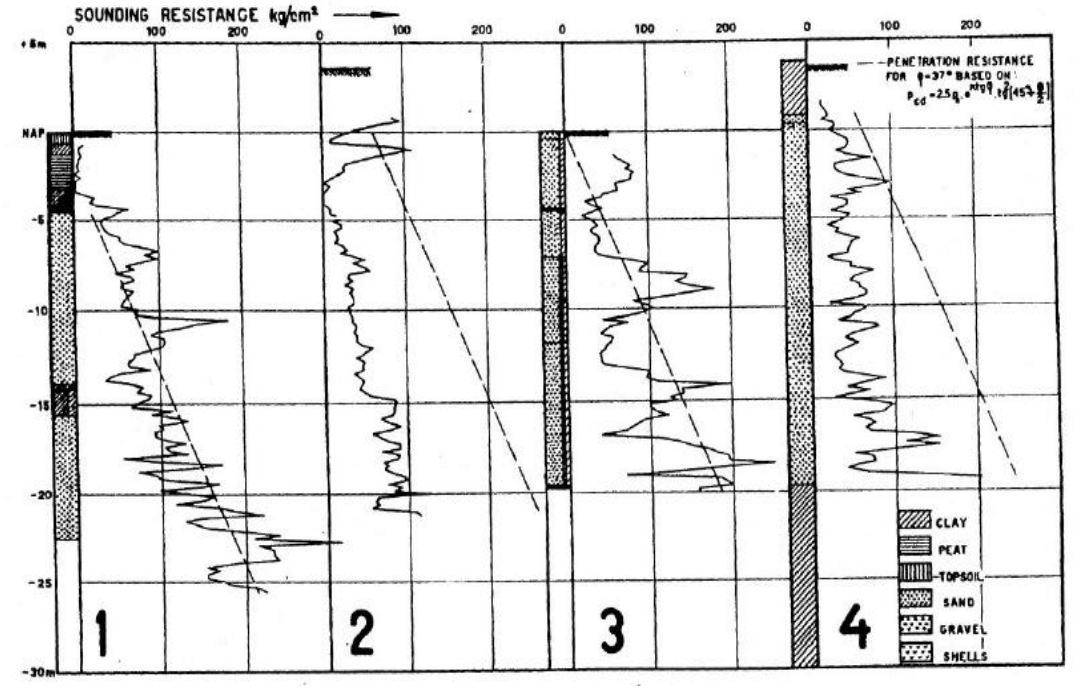

Figure A.14.7. CPT data for Zeeland – Vlietepolder (Koppejan et al., 1948)

The CPT cone tip resistances are converted to raw SPT-N and N_{60} values by using the correlations proposed by Ishihara et al. (1990) and Kulhawy and Mayne (1990), respectively, as explained in Section 3.5. Then, the overburden stress correction

factors (C_N) are again evaluated to be able to estimate $(N_1)_{60}$ values based on the effective vertical stresses estimated at the point of penetration for each recording, and average values are documented for simplicity. The fines content correction factors (C_{fines}) are also evaluated with the methods and relationships explained in Section 3.5. Accordingly, the correction factors and SPT resistances are estimated as given in Table A.14.3.

Table A.14.3 Evaluated SPT-N resistances for Zeeland – Vlietepolder

Case History	Section	C_N	C_B	C_R	C_S	C_E	C_{fines}	N	N_{60}	$(N_1)_{60}$	$(N_1)_{60,cs}$	
Zeeland – Vlietepolder	Small-S1	1.11	-	-	-	-	1.05	16.06	15.66	14.57	15.33	15.33
	Small-S2	0.84	-	-	-	-	1.05	16.06	15.66	14.57	15.33	
	Large-S1	1.15	-	-	-	-	1.05	16.06	15.66	14.57	15.33	15.33
	Large-S2	0.70	-	-	-	-	1.05	16.06	15.66	14.57	15.33	
	Large-S3	0.77	-	-	-	-	1.05	16.06	15.66	14.57	15.33	

A.14.7 Evaluation of Limit Void Ratios, Void Ratio Ranges, Relative Densities and Initial Void Ratios

Since mean grain size (D_{50}), fines content (FC), and coefficient of uniformity (C_u) information were available among the required material properties for the void ratio prediction models, the arithmetic means of the limit void ratios (e_{min} and e_{max}) evaluated by Model 8 and Model 9 are considered as the representative values. The e_{max} value is slightly modified then with respect to the construction method of the case history for each prediction model.

Since the fines content value is evaluated as 7%, which is less than 15%, it is judged that the soil of interest consists of sand type of soils. Therefore, the arithmetic mean of the relative densities evaluated by the correlations recommended by Kulhawy and Mayne (1990) and Cubrinovski and Ishihara (1999) is taken as the overall relative density of the soil. Based on these relative densities and limit void ratios, the initial void ratios (e_0) corresponding to approximately 1 kPa confining stress are estimated

referring to Equation 3-68. Accordingly, the limit void ratios, void ratio ranges (without any modification for the construction method), in-situ relative densities, and initial void ratios are estimated as given in Table A.14.4.

Table A.14.4 Evaluated limit void ratios, void ratio ranges, in-situ relative densities, and initial void ratios for Zeeland – Vlietepolder

Case History	Section	e_{min}	e_{max}	e_{max}-e_{min}	$RD_{C\&I}$ (%)	$RD_{K\&M}$ (%)	$RD_{overall}$ (%)	e_0
Zeeland – Vlietepolder	Small-S1	0.585	0.999	0.414	52.72	62.04	57.38	0.762
	Small-S2	0.585	0.999	0.414	52.72	62.04	57.38	0.762
	Large-S1	0.585	0.999	0.414	52.72	62.04	57.38	0.762
	Large-S2	0.585	0.999	0.414	52.72	62.04	57.38	0.762
	Large-S3	0.585	0.999	0.414	52.72	62.04	57.38	0.762

A.15 Sheffield Dam (1925 Santa Barbara Earthquake, M_L=6.3)

A.15.1 Brief Summary of the Case History

Sheffield Dam was located in California, USA, and the exact date of the failure was reported as June 29, 1925. The fundamental reason behind the failure was reported as the 1925 Santa Barbara Earthquake (M_L=6.3). The type of the case structure can be classified as a zoned embankment dam, and the maximum slope height is reported as ~ 8 m. Seed et al. (1969) and Engineering News Record (1925) are considered as the main sources of references. Olson (2001), Wang (2003) and Weber (2015) also studied this case history during their back-analyses of liquefaction failure case histories.

A.15.2 Site Geology and Critical Cross-section

Figure A.15.1 shows the soil stratigraphy of the case structure. It is decided that the idealized soil profile consists of five soil layers namely moist compacted sandy silt,

saturated compacted sandy silt, liquefied zone, clay blanket, and dense sandy silt. The parts of the embankment dam remaining above and below the water table level at the time of failure are classified as moist compacted sandy silt and saturated compacted sandy silt, respectively. The layer underlying the saturated compacted sandy silt is defined as the liquefied zone. Clay blanket layer is assigned to the upstream face of the embankment dam. For the layer underlying the embankment dam, dense sandy silt is defined.

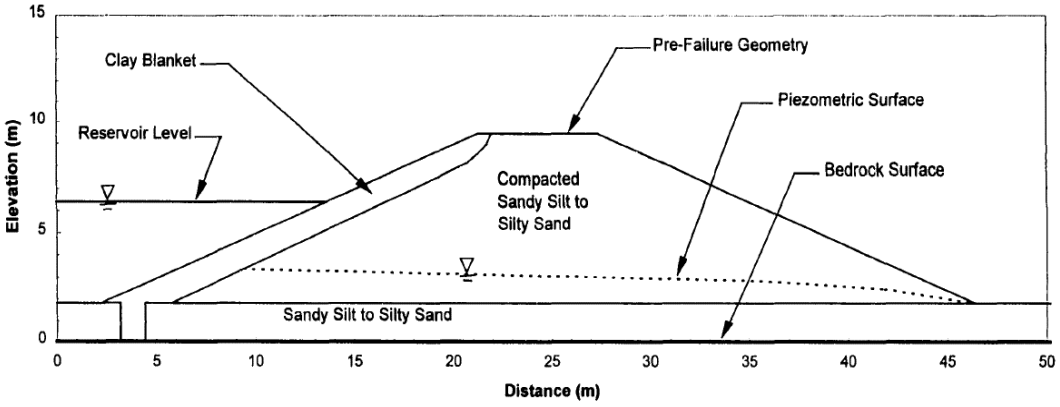

Figure A.15.1. Soil stratigraphy of the Sheffield Dam (Seed et al., 1969)

A.15.3 Evaluation of Material Properties

Since the grain size distribution curve of the case history was not reported by the main sources of references or other residual strength-related studies, mean grain size (D_{50}), fines content (FC) and coefficient of uniformity (C_u) values are estimated based on the documented representative values in those references, if available.

Mean grain size (D_{50}): The exact value of the mean grain size was reported as D_{50} = 0.100 mm in the U.S. Army Corps of Engineers (1949), Olson (2001) and Srbulov (2008). Hence, the representative D_{50} value is also taken as 0.100 mm in this study.

Fines content (FC): The exact value of the fines content was reported as FC = 40% in the U.S. Army Corps of Engineers (1949) and Srbulov (2008). Olson (2001) also

suggests a range of 33%-48% for fines content with an average of 40%. Hence, the representative FC value is also taken as 40%.

Coefficient of uniformity (C_u): Since no coefficient of uniformity value was reported by the main sources of references or other relative studies, no value has been set for this parameter.

Roundness (R): Since no roundness value was reported by the main sources of references or other studies, no value has been set for this parameter for the evaluation of limit void ratios and void ratio ranges. However, R = 0.50 is taken approximately as a representative value for the evaluation of liquefaction state friction angle.

Sphericity (S): Since no sphericity value was reported by the main sources of references or other studies, no value has been set for this parameter for the evaluation of limit void ratios and void ratio ranges. However, S = 0.60 is taken approximately as a representative value for the evaluation of liquefaction state friction angle.

Unit weight (γ_{dry} and γ_{sat}): As the results are not sensitive to unit weight, the dry and saturated unit weights of moist compacted sandy silt, saturated compacted sandy silt and liquefied zone are assigned as 18.1 kN/m^3 and 18.9 kN/m^3, respectively. For clay blanket and dense sandy silt materials, the unit weights are defined as 19.6 kN/m^3. These values are selected accordingly to be compatible with Olson (2001) and Weber (2015).

A.15.4 Sub-sectioning of the Cross-section and Failure Plane

The exact locations of the boreholes were not known for this case history. Therefore, the sub-sectioning is made based on imaginary boreholes assigned on the cross-section. These imaginary boreholes are defined with respect to changes in effective vertical stresses and inclination angles of the failure plane. Accordingly, two sub-sections are assigned for the entire failure plane, and one of them is matched with the liquefied zone as presented in Figure A.15.2.

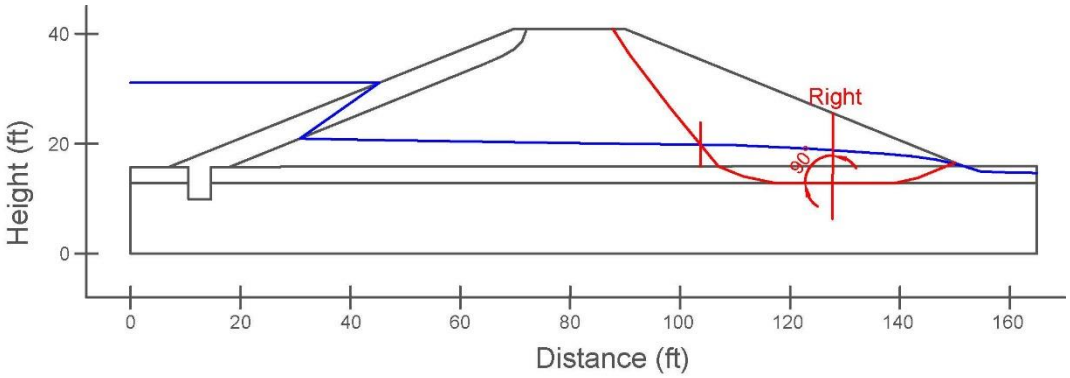

Figure A.15.2. Sub-sectioning of the cross-section and failure plane for Sheffield Dam

The territory length (L_i) and inclination (α_i) (positive sign for CCW direction) of the failure plane are evaluated as given in Table A.15.1 for the corresponding sub-section.

Table A.15.1 Sub-section with its corresponding failure plane length and inclination for Sheffield Dam

Case History	Section	Failure plane length, L_i (m)	Total failure plane length, L_t (m)	Failure plane inclination, α_i (degrees)
Sheffield Dam	Right	14.88	14.88	0

A.15.5 Elastic Modeling and Stress Rotation

All stress components are evaluated linear elastically at the points where boreholes and failure plane intersect in Figure A.15.2. The initial and deformed shape of the cross-section are presented in Figure A.15.3 and Figure A.15.4, respectively. All lengths are given in meters.

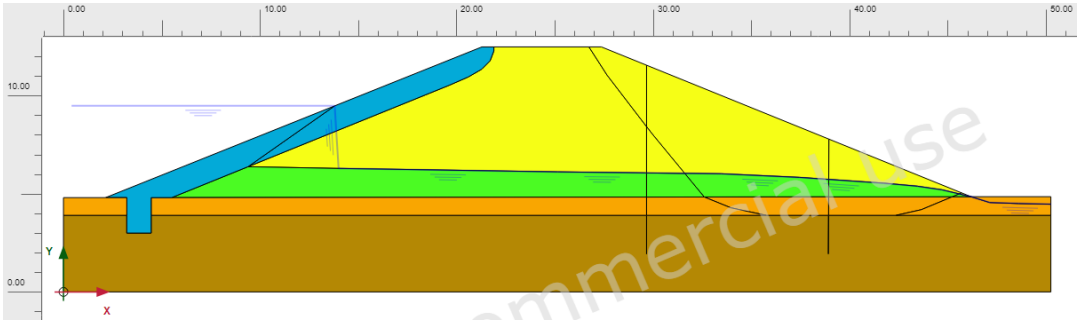

Figure A.15.3. Initial cross-section used in linear elastic modeling of Sheffield Dam

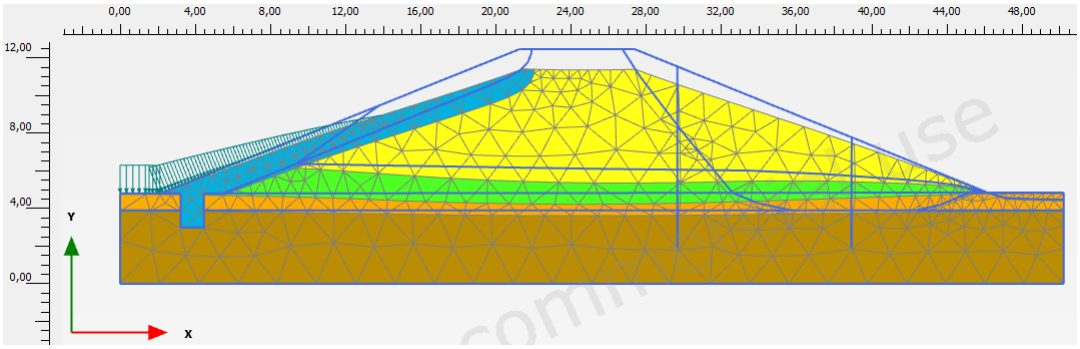

Figure A.15.4. Deformed cross-section obtained after linear elastic modeling of Sheffield Dam

During the elastic modeling process in PLAXIS 2D Ultimate Connect Edition V22.00.00.1733 software, the Poisson's ratio values of all layers other than liquefied zone are assigned as 0.30. For the liquefied zone, this value is defined as 0.33. The elastic modulus values of moist compacted sandy silt, saturated compacted sandy silt, liquefied zone, clay blanket, and dense sandy silt layers are estimated as 15 MPa, 15 MPa, 5 MPa, 20 MPa, and 30 MPa, respectively.

The effective normal (σ'_N) and shear (τ_{static}) stresses acting on the inclined failure plane are evaluated with corresponding Mohr's circle. The corresponding Mohr's circle and the effective stress components of the sub-section are presented in Figure A.15.5 and Table A.15.2, respectively. All stresses are given in kilopascals.

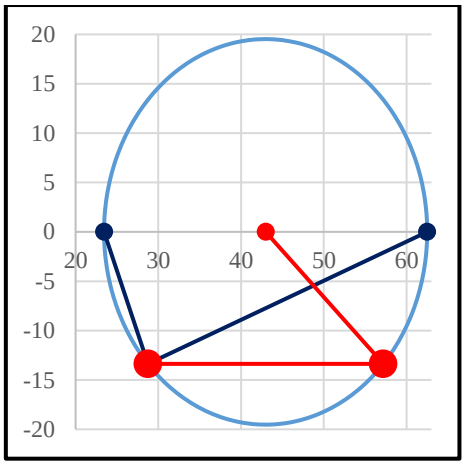

Figure A.15.5. Mohr's circle for Sheffield Dam

Table A.15.2 Evaluated stress components for Sheffield Dam

Case History	Section	σ'_1 (kPa)	σ'_2 (kPa)	σ'_3 (kPa)	p_0' (kPa)	q (kPa)	σ'_N (kPa)	τ_{static} (kPa)	$\lvert\tau_{static}\rvert$ (kPa)
Sheffield Dam	Right	62.5	28.4	23.4	38.1	36.8	57.2	-13.4	13.4

A.15.6 Evaluation of SPT Resistance

No penetration test data was available for this case history. However, the compaction ratio was evaluated as 76% by Standard Proctor Compaction Test. By using the correlations suggested by Holtz and Gibbs (1979) and Robertson and Campanella (1983), the in-situ relative density is estimated between the range of 20-40%. This relative density range indicates $(N_1)_{60}$ resistance as 4-8 blows/ft, which is also similar to the SPT resistance values recommended by previous studies. Therefore, the SPT resistance is estimated accordingly to be compatible with corresponding in-situ relative density value and SPT resistances of previous studies. The short rod length (C_R), overburden stress (C_N), and fines content correction factors (C_{fines}) are again evaluated with the methods and relationships explained in Section 3.5 by using the depth of failure plane as reference length. Accordingly, the correction factors and SPT resistances are estimated as given in Table A.15.3.

Table A.15.3 Evaluated SPT-N resistances for Sheffield Dam

Case History	Section	C_N	C_B	C_R	C_S	C_E	C_{fines}	N	N_{60}	$(N_1)_{60}$	$(N_1)_{60,cs}$	
Sheffield Dam	Right	1.29	-	0.91	-	-	1.51	4.00	3.65	4.72	7.13	7.13

A.15.7 Evaluation of Limit Void Ratios, Void Ratio Ranges, Relative Densities and Initial Void Ratios

Since mean grain size (D_{50}) and fines content (FC) information were available among the required material properties for the void ratio prediction models, the arithmetic means of the limit void ratios (e_{min} and e_{max}) evaluated by Model 1 and Model 2 are considered as the representative values. The e_{max} value is slightly modified then with respect to the construction method of the case history for each prediction model.

Since the fines content value is evaluated as 40%, which is greater than 15%, it is judged that the soil of interest consists of silty soils. Therefore, the relative densities evaluated by the correlation recommended by Cubrinovski and Ishihara (1999) are directly taken as the representative relative densities of the soils. Based on these relative densities and limit void ratios, the initial void ratios (e_0) corresponding to approximately 1 kPa confining stress are estimated referring to Equation 3-68. Accordingly, the limit void ratios, void ratio ranges (without any modification for the construction method), in-situ relative densities, and initial void ratios are estimated as given in Table A.15.4.

Table A.15.4 Evaluated limit void ratios, void ratio ranges, in-situ relative densities, and initial void ratios for Sheffield Dam

Case History	Section	e_{min}	e_{max}	e_{max}-e_{min}	$RD_{C\&I}$ (%)	$RD_{K\&M}$ (%)	$RD_{overall}$ (%)	e_0
Sheffield Dam	Right	0.610	1.041	0.431	31.04	36.72	31.04	0.907

A.16 Helsinki Harbor (1936 Fill Placement)

A.16.1 Brief Summary of the Case History

Helsinki Harbor was located in Helsinki, Finland, and the exact date of the failure was reported as November 30, 1936. The fundamental reason behind the failure was reported as the fill placement. The type of the case structure can be classified as a harbor constructed with hydraulic fill method, and the maximum slope height is reported as ~ 6 m. Anderson and Bjerrum (1968) is considered as the main source of reference. Olson (2001), Wang (2003) and Weber (2015) also studied this case history during their back-analyses of liquefaction failure case histories.

A.16.2 Site Geology and Critical Cross-section

Figure A.16.1 shows the pre-failure and post-failure cross-sections of the case structure. It is decided that the idealized soil profile consists of three soil layers namely non-liquefied zone, liquefied zone, and foundation material. The parts of the harbor remaining above and below the water table level at the time of failure are classified as non-liquefied zone and liquefied zone, respectively. The layer underlying the harbor is defined as the foundation material.

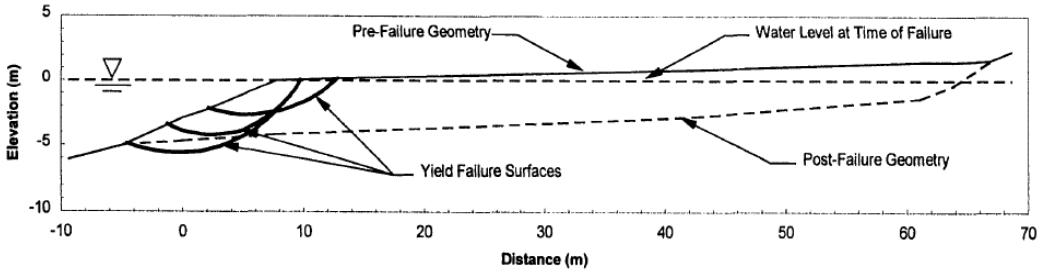

Figure A.16.1. Pre-failure and post-failure cross-sections of the Helsinki Harbor (Olson, 2001)

A.16.3 Evaluation of Material Properties

Since the grain size distribution curve of the case history was not reported by the main sources of references or other residual strength-related studies, mean grain size (D_{50}), fines content (FC) and coefficient of uniformity (C_u) values are estimated based on the documented representative values in those references, if available.

Mean grain size (D_{50}): Since no mean grain size value was reported by the main sources of references or other relative studies, D_{50} value is representatively taken as 0.100 mm in this study referring to similar type of structures and soil profiles reported in Ilgac et al. (2019) dataset.

Fines content (FC): Since no fines content value was reported by the main sources of references or other relative studies, no value has been set for this parameter.

Coefficient of uniformity (C_u): Since no coefficient of uniformity value was reported by the main sources of references or other relative studies, no value has been set for this parameter.

Roundness (R): Since no roundness value was reported by the main sources of references or other studies, no value has been set for this parameter for the evaluation of limit void ratios and void ratio ranges. However, R = 0.50 is taken approximately as a representative value for the evaluation of liquefaction state friction angle.

Sphericity (S): Since no sphericity value was reported by the main sources of references or other studies, no value has been set for this parameter for the evaluation of limit void ratios and void ratio ranges. However, S = 0.60 is taken approximately as a representative value for the evaluation of liquefaction state friction angle.

Unit weight (γ_{dry} and γ_{sat}): As the results are not sensitive to unit weight, the dry and saturated unit weights of non-liquefied and liquefied zones are assigned as 17.8 kN/m^3 and 18.5 kN/m^3, respectively. For foundation material, the unit weight is defined as 18.9 kN/m^3. These values are selected accordingly to be compatible with Olson (2001) and Weber (2015).

A.16.4 Sub-sectioning of the Cross-section and Failure Plane

The exact locations of the boreholes were not known for this case history. Therefore, the sub-sectioning is made based on imaginary boreholes assigned on the cross-section. These imaginary boreholes are defined with respect to changes in effective vertical stresses and inclination angles of the failure plane. Two different initial failure planes are considered based on the information available on the main sources of references about the failure mode as presented in Figure A.16.2. While boreholes Small-S1 and Small-S2 sub-divide the smaller failure plane into smaller pieces, Large-S1 and Large-S2 split the larger failure plane.

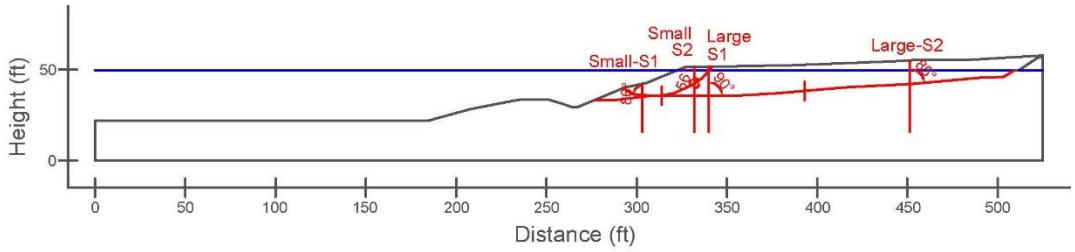

Figure A.16.2. Sub-sectioning of the cross-section and failure plane for Helsinki Harbor

The territory lengths (L_i) and inclinations (α_i) (positive sign for CCW direction) of the failure planes are evaluated as given in Table A.16.1 for each sub-section.

Table A.16.1 Sub-sections with their corresponding failure plane lengths and inclinations for Helsinki Harbor

Case History	Section	Failure plane length, L_i (m)	Total failure plane length, L_t (m)	Failure plane inclination, α_i (degrees)
Helsinki Harbor	Small-S1	6.72	15.97	-4
	Small-S2	9.25		34
	Large-S1	35.50	71.31	0
	Large-S2	35.81		5

A.16.5 Elastic Modeling and Stress Rotation

All stress components are evaluated linear elastically at the points where boreholes and failure plane intersect in Figure A.16.2. The initial and deformed shape of the cross-section are presented in Figure A.16.3 and Figure A.16.4, respectively. All lengths are given in meters.

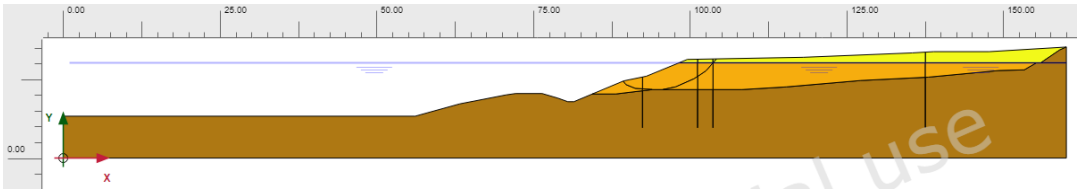

Figure A.16.3. Initial cross-section used in linear elastic modeling of Helsinki Harbor

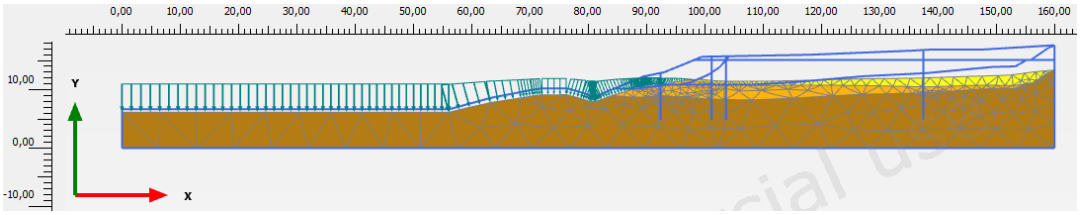

Figure A.16.4. Deformed cross-section obtained after linear elastic modeling of Helsinki Harbor

During the elastic modeling process in PLAXIS 2D Ultimate Connect Edition V22.00.00.1733 software, the Poisson's ratio values of the non-liquefied zone, liquefied zone, and foundation material are defined as 0.30, 0.33, and 0.30, respectively. The elastic modulus values of the same layers, on the other hand, are estimated as 10 MPa, 5 MPa, and 30 MPa, respectively.

The effective normal (σ'_N) and shear (τ_{static}) stresses acting on the inclined failure plane are evaluated with corresponding Mohr's circles. The corresponding Mohr's circles and the effective stress components of the sub-sections are presented in Figure A.16.5 and Table A.16.2, respectively. All stresses are given in kilopascals.

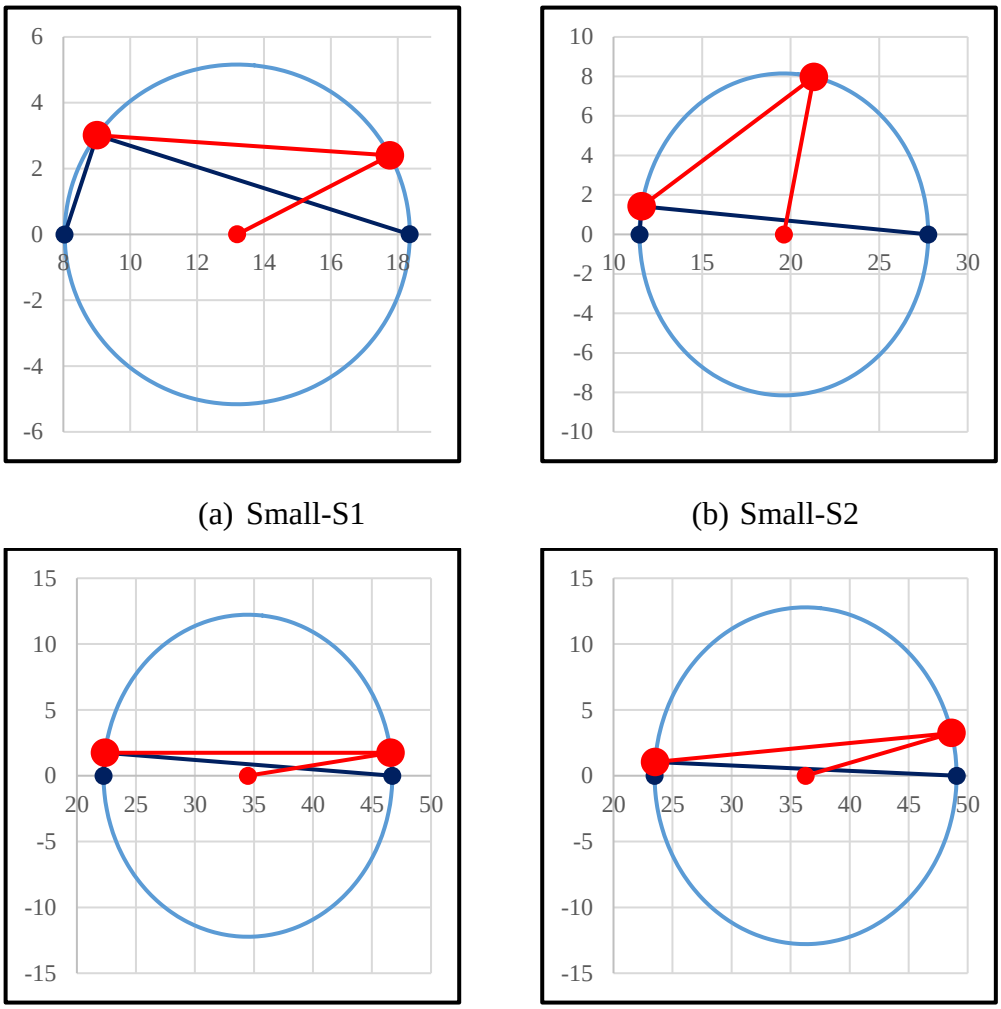

(a) Small-S1 (b) Small-S2

(c) Large-S1 (d) Large-S2

Figure A.16.5. Mohr's circles for Helsinki Harbor

Table A.16.2 Evaluated stress components for Helsinki Harbor

Case History	Section	σ'_1 (kPa)	σ'_2 (kPa)	σ'_3 (kPa)	p_0' (kPa)	q (kPa)	σ'_N (kPa)	τ_{static} (kPa)	$\lvert\tau_{static}\rvert$ (kPa)
Helsinki Harbor	Small-S1	18.4	8.7	8.0	11.7	10.0	17.8	2.4	2.4
	Small-S2	27.8	13.0	11.5	17.4	15.6	21.3	8.0	8.0
	Large-S1	46.7	22.8	22.3	30.6	24.2	46.6	1.7	1.7
	Large-S2	49.1	23.9	23.5	32.2	25.4	48.6	3.2	3.2

A.16.6 Evaluation of SPT Resistance

No penetration test data was available for this case history. However, Sladen and Hewitt (1989) reported the in-situ relative density as 40-50% for this case history. This relative density range indicates $(N_1)_{60}$ resistance as 5-8 blows/ft, which is also similar to the SPT resistance values recommended by previous studies. Therefore, the SPT resistance is estimated accordingly to be compatible with corresponding in-situ relative density value and SPT resistances of previous studies. The short rod length (C_R), overburden stress (C_N), and fines content correction factors (C_{fines}) are again evaluated with the methods and relationships explained in Section 3.5 by using the depth of failure plane as reference length. Accordingly, the correction factors and SPT resistances are estimated as given in Table A.16.3.

Table A.16.3 Evaluated SPT-N resistances for Helsinki Harbor

Case History	Section	C_N	C_B	C_R	C_S	C_E	C_{fines}	N	N_{60}	$(N_1)_{60}$	$(N_1)_{60,cs}$	
Helsinki Harbor	Small-S1	2.34	-	0.83	-	-	1.00	2.00	1.66	3.89	3.89	4.38
	Small-S2	1.86	-	0.87	-	-	1.00	3.00	2.61	4.87	4.87	
	Large-S1	1.43	-	0.94	-	-	1.00	3.50	3.28	4.70	4.70	4.59
	Large-S2	1.40	-	0.92	-	-	1.00	3.50	3.20	4.48	4.48	

A.16.7 Evaluation of Limit Void Ratios, Void Ratio Ranges, Relative Densities and Initial Void Ratios

Since only mean grain size (D_{50}) information was available among the required material properties for the void ratio prediction models, the limit void ratios (e_{min} and e_{max}) evaluated by Model 1 are directly considered as the representative values. The e_{max} value is slightly modified then with respect to the construction method of the case history for each prediction model.

Since the fines content value is unknown, the arithmetic mean of the relative densities evaluated by the correlations recommended by Kulhawy and Mayne (1990) and Cubrinovski and Ishihara (1999) is taken as the overall relative density of the

soil. Based on these relative densities and limit void ratios, the initial void ratios (e_0) corresponding to approximately 1 kPa confining stress are estimated referring to Equation 3-68. Accordingly, the limit void ratios, void ratio ranges (without any modification for the construction method), in-situ relative densities, and initial void ratios are estimated as given in Table A.16.4.

Table A.16.4 Evaluated limit void ratios, void ratio ranges, in-situ relative densities, and initial void ratios for Helsinki Harbor

Case History	Section	e_{min}	e_{max}	e_{max}-e_{min}	$RD_{C\&I}$ (%)	$RD_{K\&M}$ (%)	$RD_{overall}$ (%)	e_0
Helsinki Harbor	Small-S1	0.623	1.077	0.453	29.44	33.34	31.39	0.935
	Small-S2	0.623	1.077	0.453	32.92	37.29	35.11	0.918
	Large-S1	0.623	1.077	0.453	32.34	36.63	34.48	0.921
	Large-S2	0.623	1.077	0.453	31.57	35.76	33.67	0.924

A.17 Solfatara Canal Dike (1940 El Centro Earthquake, M=7.2)

A.17.1 Brief Summary of the Case History

Solfatara Canal Dike was located in Mexico, and the exact date of the failure was reported as May 18, 1940. The fundamental reason behind the failure was reported as the 1940 El Centro Earthquake (M=7.2). The type of the case structure can be classified as a dike constructed with water sedimentation method, and the maximum slope height is reported as ~ 3 m. Ross (1968) is considered as the main source of reference. Olson (2001), Wang (2003) and Weber (2015) also studied this case history during their back-analyses of liquefaction failure case histories.

A.17.2 Site Geology and Critical Cross-section

Figure A.17.1 presents the pre-failure cross-section, and Figure A.17.2 shows the soil stratigraphy of the case structure. It is decided that the idealized soil profile

consists of two soil layers namely non-liquefied zone and liquefied zone. The parts of the dike remaining above and below the water table level at the time of failure are classified as non-liquefied zone and liquefied zone, respectively.

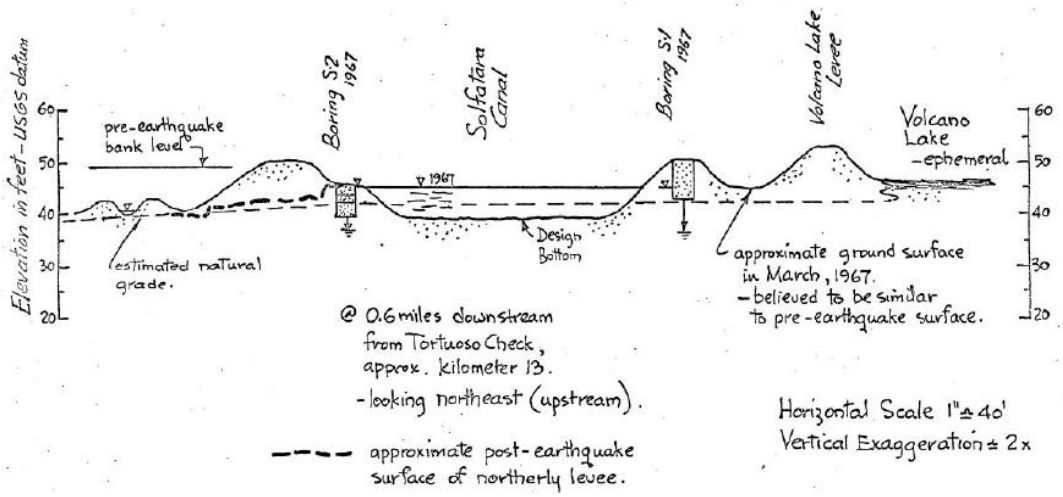

Figure A.17.1. Pre-failure cross-section of the Solfatara Canal Dike (Ross, 1968)

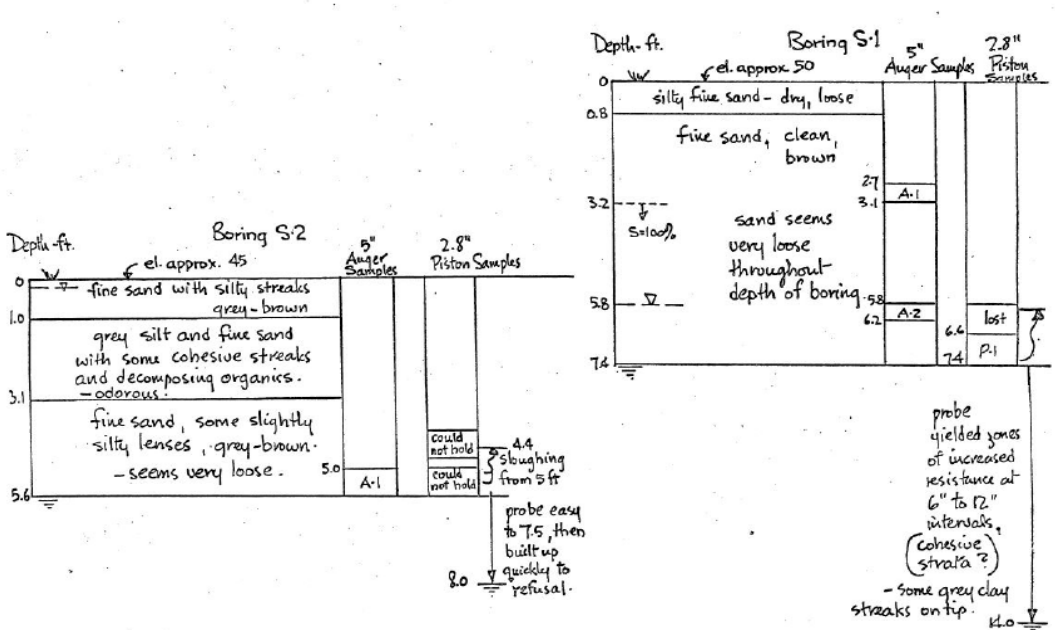

Figure A.17.2. Soil stratigraphy of the Solfatara Canal Dike (Ross, 1968)

A.17.3 Evaluation of Material Properties

Since the grain size distribution curve of the case history was reported by the main sources of references as given in Figure A.17.3, mean grain size (D_{50}), fines content (FC) and coefficient of uniformity (C_u) values are evaluated based on this curve.

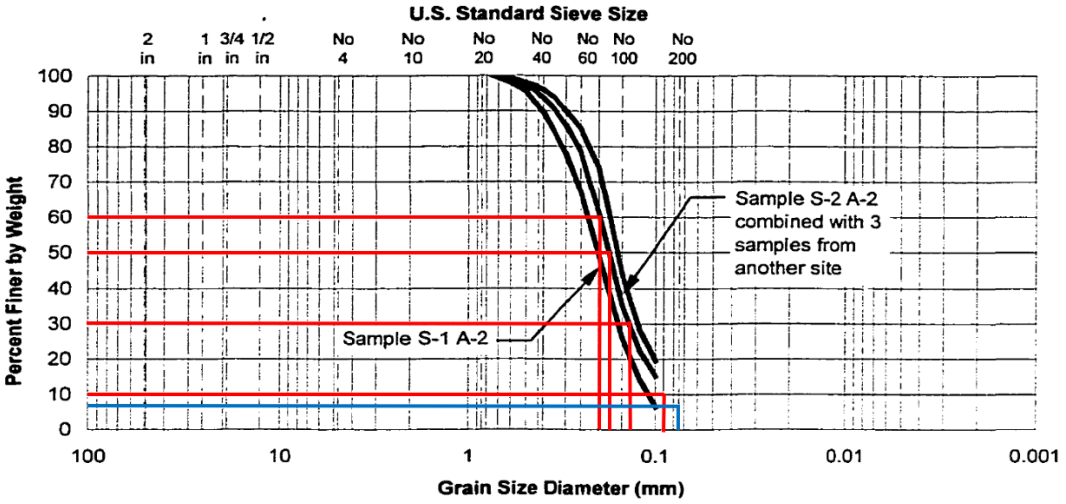

Figure A.17.3. Grain size distribution curve of the Solfatara Canal Dike (Olson, 2001, after Ross, 1968)

Mean grain size (D_{50}): D_{50} = 0.170 mm is evaluated representatively based on the grain size distribution curve of the case history. Olson (2001) also suggests a range of 0.170-0.200 mm for D_{50}. Srbulov (2008) again recommends 0.200 mm for D_{50} value by taking the Boring S-1 into account instead of Boring S-2.

Fines content (FC): FC = 7% is evaluated representatively based on the grain size distribution curve of the case history. Olson (2001) also suggests a range of 0%-8% for fines content. Srbulov (2008) again recommends 0% for FC value of this case history by taking the Boring S-1 into account instead of Boring S-2.

Coefficient of uniformity (C_u): D_{10} and D_{60} values are evaluated as 0.090 mm and 0.200 mm, respectively, based on the grain size distribution curve of the case history. Therefore, the uniformity coefficient is estimated as $C_u = D_{60}/D_{10} = 0.200/0.090 = 2.22$.

Roundness (R): Since no roundness value was reported by the main sources of references or other studies, no value has been set for this parameter for the evaluation of limit void ratios and void ratio ranges. However, R = 0.50 is taken approximately as a representative value for the evaluation of liquefaction state friction angle.

Sphericity (S): Since no sphericity value was reported by the main sources of references or other studies, no value has been set for this parameter for the evaluation of limit void ratios and void ratio ranges. However, S = 0.60 is taken approximately as a representative value for the evaluation of liquefaction state friction angle.

Unit weight (γ_{dry} and γ_{sat}): As the results are not sensitive to unit weight, the dry and saturated unit weights of both soil layers are assigned as 18.4 kN/m^3 and 19.2 kN/m^3, respectively, to be compatible with Olson (2001) and Weber (2015).

A.17.4 Sub-sectioning of the Cross-section and Failure Plane

The exact locations of the test boreholes were not known for this case history. Therefore, the sub-sectioning is made based on imaginary boreholes assigned on the cross-section. These imaginary boreholes are defined with respect to changes in effective vertical stresses and inclination angles of the failure plane. Accordingly, two sub-sections are assigned for the liquefied zone as presented in Figure A.17.4.

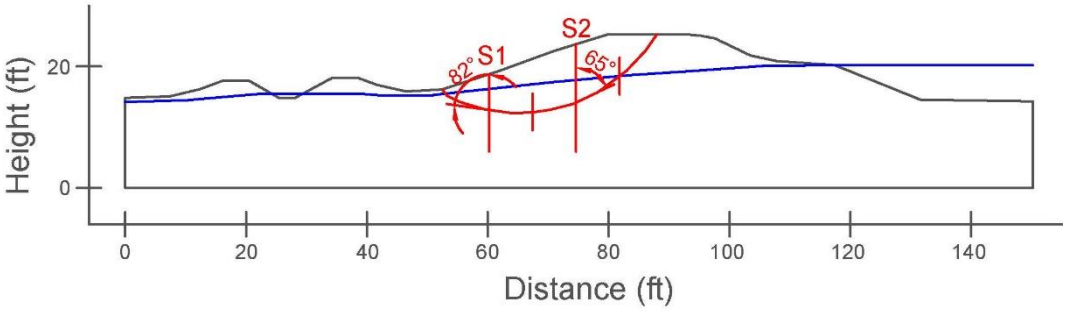

Figure A.17.4. Sub-sectioning of the cross-section and failure plane Solfatara Canal Dike

The territory lengths (L_i) and inclinations (α_i) (positive sign for CCW direction) of the failure plane are evaluated as given in Table A.17.1 for each sub-section.

Table A.17.1 Sub-sections with their corresponding failure plane lengths and inclinations for Solfatara Canal Dike

Case History	Section	Failure plane length, L_i (m)	Total failure plane length, L_t (m)	Failure plane inclination, α_i (degrees)
Solfatara Canal Dike	S1	4.58	9.41	-8
	S2	4.83		25

A.17.5 Elastic Modeling and Stress Rotation

All stress components are evaluated linear elastically at the points where boreholes and failure plane intersect in Figure A.17.4. The initial and deformed shape of the cross-section are presented in Figure A.17.5 and Figure A.17.6, respectively. All lengths are given in meters.

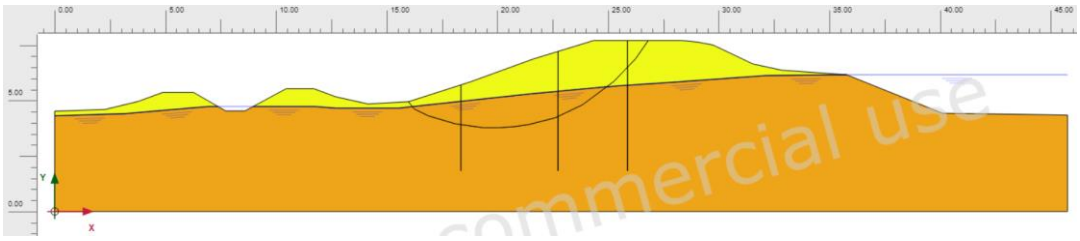

Figure A.17.5. Initial cross-section used in linear elastic modeling of Solfatara Canal Dike

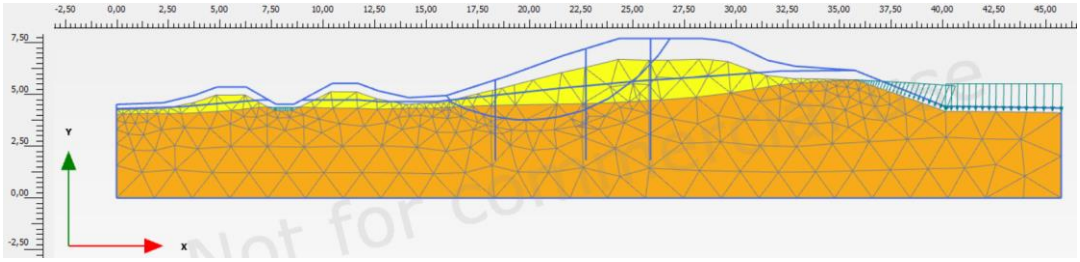

Figure A.17.6. Deformed cross-section obtained after linear elastic modeling of Solfatara Canal Dike

During the elastic modeling process in PLAXIS 2D Ultimate Connect Edition V22.00.00.1733 software, the Poisson's ratio values of the non-liquefied and

liquefied zones are defined as 0.30 and 0.33, respectively. The elastic modulus values of the same layers, on the other hand, are estimated as 10 MPa and 5 MPa, respectively.

The effective normal (σ'_N) and shear (τ_{static}) stresses acting on the inclined failure plane are evaluated with corresponding Mohr's circles. The corresponding Mohr's circles and the effective stress components of the sub-sections are presented in Figure A.17.7 and Table A.17.2, respectively. All stresses are given in kilopascals.

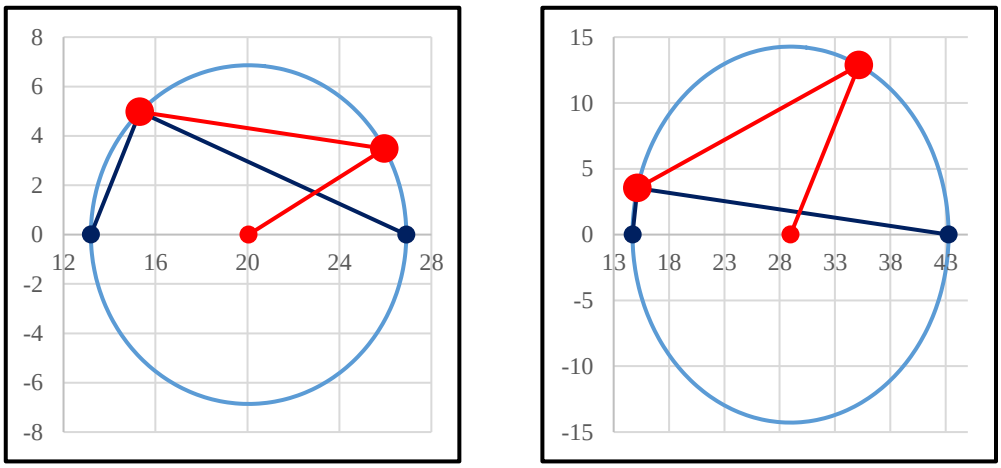

(a) S1 (b) S2

Figure A.17.7. Mohr's circles for Solfatara Canal Dike

Table A.17.2 Evaluated stress components for Solfatara Canal Dike

Case History	Section	σ'_1 (kPa)	σ'_2 (kPa)	σ'_3 (kPa)	p_0' (kPa)	q (kPa)	σ'_N (kPa)	τ_{static} (kPa)	$\lvert\tau_{static}\rvert$ (kPa)
Solfatara Canal Dike	S1	26.9	13.2	13.2	17.8	13.7	26.0	3.5	3.5
	S2	43.3	19.1	14.7	25.7	26.6	35.2	12.9	12.9

A.17.6 Evaluation of SPT Resistance

No penetration test data was available for this case history. However, Ross (1968) reported the in-situ relative density as 32% for this case history. This relative density value indicates $(N_1)_{60}$ resistance as 4-5 blows/ft, which is also similar to the SPT resistance values recommended by previous studies. Therefore, the SPT resistance

is estimated accordingly to be compatible with corresponding in-situ relative density value and SPT resistances of previous studies. The short rod length (C_R), overburden stress (C_N), and fines content correction factors (C_{fines}) are again evaluated with the methods and relationships explained in Section 3.5 by using the depth of failure plane as reference length. Accordingly, the correction factors and SPT resistances are estimated as given in Table A.17.3.

Table A.17.3 Evaluated SPT-N resistances for Solfatara Canal Dike

Case History	Section	C_N	C_B	C_R	C_S	C_E	C_{fines}	N	N_{60}	$(N_1)_{60}$	$(N_1)_{60,cs}$	
Solfatara Canal Dike	S1	1.96	-	0.82	-	-	1.10	2.90	2.39	4.70	5.18	4.72
	S2	1.49	-	0.88	-	-	1.12	2.90	2.55	3.81	4.27	

A.17.7 Evaluation of Limit Void Ratios, Void Ratio Ranges, Relative Densities and Initial Void Ratios

Since mean grain size (D_{50}), fines content (FC), and coefficient of uniformity (C_u) information were available among the required material properties for the void ratio prediction models, the arithmetic means of the limit void ratios (e_{min} and e_{max}) evaluated by Model 8 and Model 9 are considered as the representative values. The e_{max} value is slightly modified then with respect to the construction method of the case history for each prediction model.

Since the fines content value is evaluated as 7%, which is less than 15%, it is judged that the soil of interest consists of sand type of soils. Therefore, the arithmetic mean of the relative densities evaluated by the correlations recommended by Kulhawy and Mayne (1990) and Cubrinovski and Ishihara (1999) is taken as the overall relative density of the soil. Based on these relative densities and limit void ratios, the initial void ratios (e_0) corresponding to approximately 1 kPa confining stress are estimated referring to Equation 3-68. Accordingly, the limit void ratios, void ratio ranges (without any modification for the construction method), in-situ relative densities, and initial void ratios are estimated as given in Table A.17.4.

Table A.17.4 Evaluated limit void ratios, void ratio ranges, in-situ relative densities, and initial void ratios for Solfatara Canal Dike

Case History	Section	e_{min}	e_{max}	e_{max}-e_{min}	$RD_{C\&I}$ (%)	$RD_{K\&M}$ (%)	$RD_{overall}$ (%)	e_0
Solfatara Canal Dike	S1	0.576	0.981	0.405	29.41	33.94	31.68	0.853
	S2	0.576	0.981	0.405	26.50	30.59	28.55	0.865

A.18 Lake Merced Bank (1957 San Francisco Earthquake, M=5.7)

A.18.1 Brief Summary of the Case History

Lake Merced Bank was located in California, USA, and the exact date of the failure was reported as March 22, 1957. The fundamental reason behind the failure was reported as the 1957 San Francisco Earthquake (M=5.7). The type of the case structure can be classified as a lakeside bank, and the maximum slope height is reported as ~ 10 m. Ross (1968) is considered as the main source of reference. Olson (2001), Wang (2003) and Weber (2015) also studied this case history during their back-analyses of liquefaction failure case histories.

A.18.2 Site Geology and Critical Cross-section

Figure A.18.1 presents the pre-failure and post-failure cross-sections, and Figure A.18.2 shows the soil stratigraphy of the case structure. It is decided that the idealized soil profile consists of two soil layers namely non-liquefied zone and liquefied zone. The parts of the bank remaining above and below the water table level at the time of failure are classified as non-liquefied zone and liquefied zone, respectively.

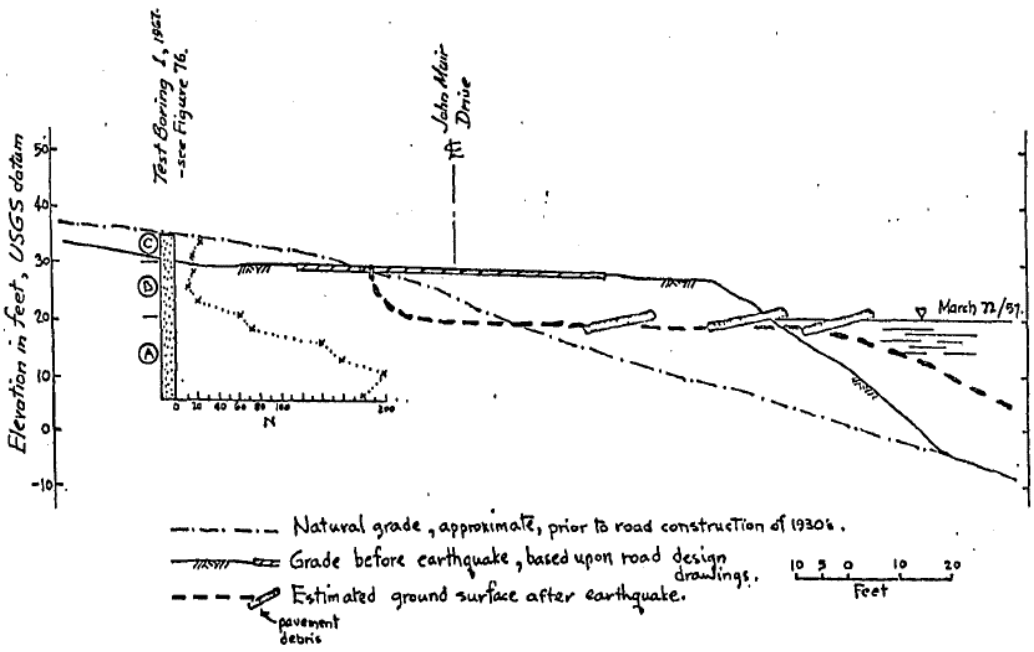

Figure A.18.1. Pre-failure and post-failure cross-sections of the Lake Merced Bank (Ross, 1968)

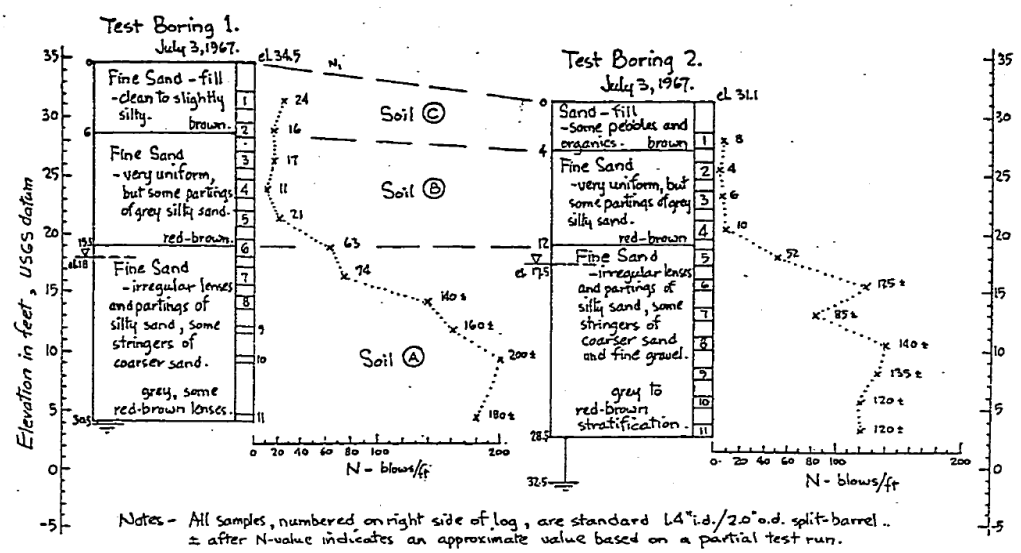

Figure A.18.2. Soil stratigraphy of the Lake Merced Bank (Ross, 1968)

A.18.3 Evaluation of Material Properties

Since the grain size distribution curve of the case history was reported by the main sources of references as given in Figure A.18.3, mean grain size (D_{50}), fines content (FC) and coefficient of uniformity (C_u) values are evaluated based on this curve.

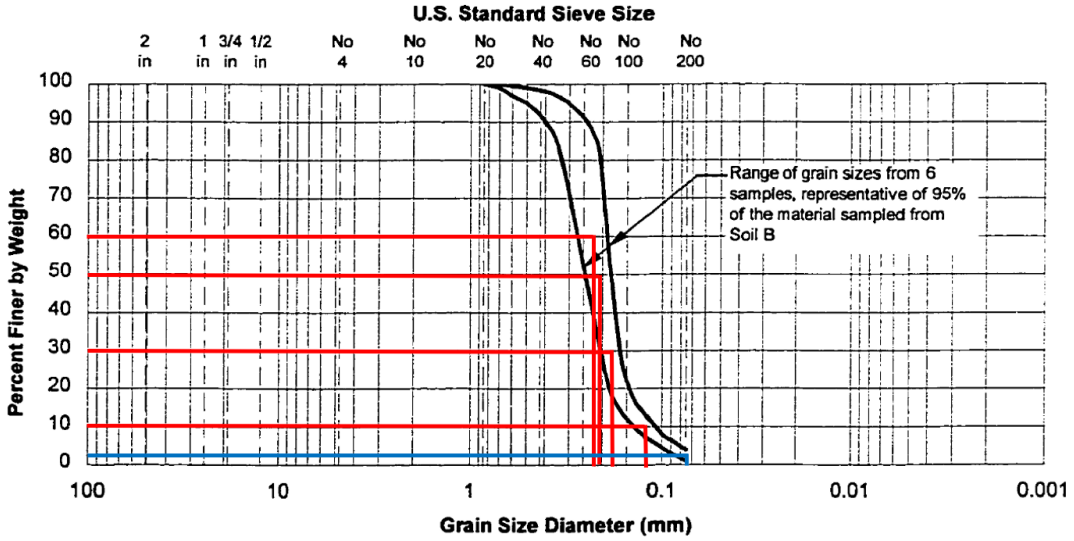

Figure A.18.3. Grain size distribution curve of the Lake Merced Bank (Olson, 2001, after Ross, 1968)

Mean grain size (D_{50}): D_{50} = 0.210 mm is evaluated representatively based on the grain size distribution curve of the case history. Olson (2001) and Srbulov (2008) also suggest 0.210 mm for D_{50} value of this case history.

Fines content (FC): FC = 3% is evaluated representatively based on the grain size distribution curve of the case history. Olson (2001) and Srbulov (2008) also suggest 3% for FC value of this case history.

Coefficient of uniformity (C_u): D_{10} and D_{60} values are evaluated as 0.120 mm and 0.230 mm, respectively, based on the grain size distribution curve of the case history. Therefore, the uniformity coefficient is estimated as $C_u = D_{60}/D_{10} = 0.230/0.120 = 1.92$.

Roundness (R): Since no roundness value was reported by the main sources of references or other studies, no value has been set for this parameter for the evaluation of limit void ratios and void ratio ranges. However, R = 0.50 is taken approximately as a representative value for the evaluation of liquefaction state friction angle.

Sphericity (S): Since no sphericity value was reported by the main sources of references or other studies, no value has been set for this parameter for the evaluation of limit void ratios and void ratio ranges. However, S = 0.60 is taken approximately as a representative value for the evaluation of liquefaction state friction angle.

Unit weight (γ_{dry} and γ_{sat}): As the results are not sensitive to unit weight, the dry and saturated unit weights of both soil layers are assigned as 16.5 kN/m^3 and 17.3 kN/m^3, respectively, to be compatible with Olson (2001) and Weber (2015).

A.18.4 Sub-sectioning of the Cross-section and Failure Plane

The exact locations of the SPT boreholes were known for this case history as presented in Figure A.18.1. Therefore, the sub-sectioning is made based on the locations of these penetration tests as presented in Figure A.18.4. Each test is assigned (names of the logs are directly assigned as the name of the sub-section) for the corresponding territory length. Accordingly, two sub-sections are assigned for the entire failure plane, and one of them is matched with the liquefied zone as presented in Figure A.18.4.

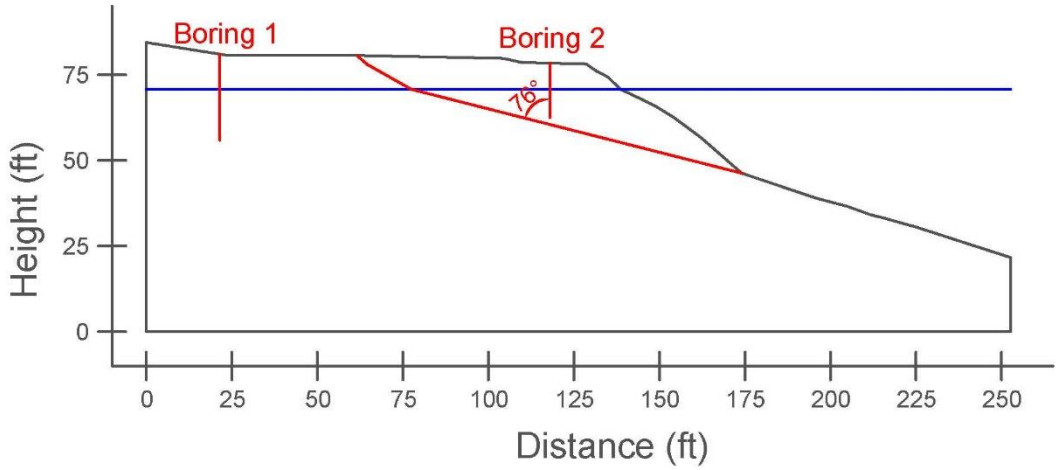

Figure A.18.4. Sub-sectioning of the cross-section and failure plane for Lake Merced Bank

The territory length (L_i) and inclination (α_i) (positive sign for CCW direction) of the failure plane are evaluated as given in Table A.18.1 for the corresponding sub-section.

Table A.18.1 Sub-section with its corresponding failure plane length and inclination for Lake Merced Bank

Case History	Section	Failure plane length, L_i (m)	Total failure plane length, L_t (m)	Failure plane inclination, α_i (degrees)
Lake Merced Bank	Boring 2	30.35	30.35	-14

A.18.5 Elastic Modeling and Stress Rotation

All stress components are evaluated linear elastically at the points where boreholes and failure plane intersect in Figure A.18.4. The initial and deformed shape of the cross-section are presented in Figure A.18.5 and Figure A.18.6, respectively. All lengths are given in meters.

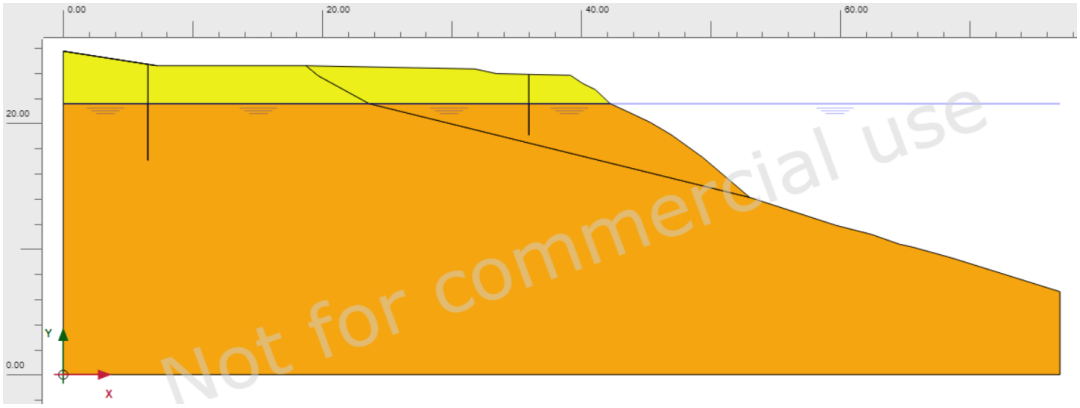

Figure A.18.5. Initial cross-section used in linear elastic modeling of Lake Merced Bank

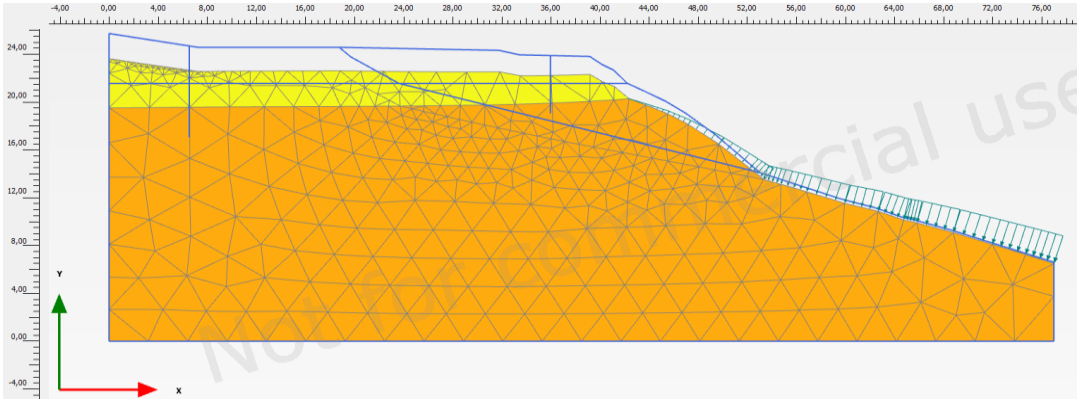

Figure A.18.6. Deformed cross-section obtained after linear elastic modeling of Lake Merced Bank

During the elastic modeling process in PLAXIS 2D Ultimate Connect Edition V22.00.00.1733 software, the Poisson's ratio values of the non-liquefied and liquefied zones are defined as 0.30 and 0.33, respectively. The elastic modulus values of the same layers, on the other hand, are estimated as 10 MPa and 5 MPa, respectively.

The effective normal (σ'_N) and shear (τ_{static}) stresses acting on the inclined failure plane are evaluated with corresponding Mohr's circle. The corresponding Mohr's circle and the effective stress components of the sub-section are presented in Figure A.18.7 and Table A.18.2, respectively. All stresses are given in kilopascals.

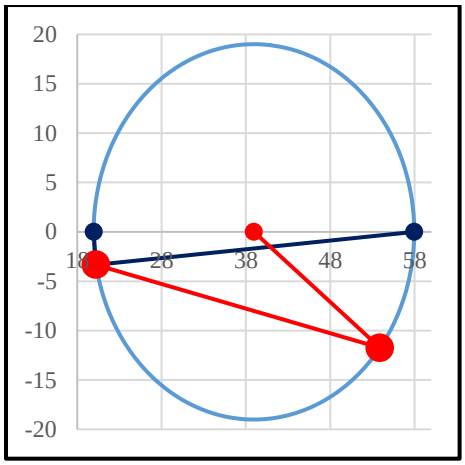

Figure A.18.7. Mohr's circle for Lake Merced Bank

Table A.18.2 Evaluated stress components for Lake Merced Bank

Case History	Section	σ'_1 (kPa)	σ'_2 (kPa)	σ'_3 (kPa)	p_0' (kPa)	q (kPa)	σ'_N (kPa)	τ_{static} (kPa)	$\lvert\tau_{static}\rvert$ (kPa)
Lake Merced Bank	Boring 2	58.0	25.7	19.9	34.5	35.5	53.9	-11.7	11.7

A.18.6 Evaluation of SPT Resistance

The exact locations of the SPT boreholes were documented by Ross (1968) as given in Figure A.18.1. Corresponding SPT boreholes are presented in Figure A.18.2 for Boring 1 and Boring 2 logs, respectively.

The correction factors for nonstandardized sampler configuration (C_S), borehole diameter (C_B), and energy efficiency (C_E) are taken as 1.0 since no reliable information related to these coefficients was reported in any of the sources. The short rod length (C_R) and fines content correction factors (C_{fines}) are evaluated with the methods and relationships explained in Section 3.5. The overburden stress correction factors (C_N) are evaluated based on the effective vertical stresses estimated at the point of penetration for the recording, and the average value is documented for simplicity. Accordingly, the correction factors and SPT resistances are estimated as given in Table A.18.3.

Table A.18.3 Evaluated SPT-N resistances for Lake Merced Bank

Case History	Section	C_N	C_B	C_R	C_S	C_E	C_{fines}	N	N_{60}	$(N_1)_{60}$	$(N_1)_{60,cs}$	
Lake Merced Bank	Boring 2	1.49	1.0	0.87	1.0	1.00	1.00	6.67	5.82	8.28	8.28	8.28

A.18.7 Evaluation of Limit Void Ratios, Void Ratio Ranges, Relative Densities and Initial Void Ratios

Since mean grain size (D_{50}), fines content (FC), and coefficient of uniformity (C_u) information were available among the required material properties for the void ratio prediction models, the arithmetic means of the limit void ratios (e_{min} and e_{max}) evaluated by Model 8 and Model 9 are considered as the representative values. The e_{max} value is slightly modified then with respect to the construction method of the case history for each prediction model.

Since the fines content value is evaluated as 3%, which is less than 15%, it is judged that the soil of interest consists of sand type of soils. Therefore, the arithmetic mean of the relative densities evaluated by the correlations recommended by Kulhawy and Mayne (1990) and Cubrinovski and Ishihara (1999) is taken as the overall relative density of the soil. Based on these relative densities and limit void ratios, the initial void ratios (e_0) corresponding to approximately 1 kPa confining stress are estimated referring to Equation 3-68. Accordingly, the limit void ratios, void ratio ranges (without any modification for the construction method), in-situ relative densities, and initial void ratios are estimated as given in Table A.18.4.

Table A.18.4 Evaluated limit void ratios, void ratio ranges, in-situ relative densities, and initial void ratios for Lake Merced Bank

Case History	Section	e_{min}	e_{max}	e_{max}-e_{min}	$RD_{C\&I}$ (%)	$RD_{K\&M}$ (%)	$RD_{overall}$ (%)	e_0
Lake Merced Bank	Boring 2	0.580	0.990	0.410	39.43	43.85	41.64	0.819

A.19 El Cobre Tailings Dam (1965 Chilean Earthquake, M_L=7.00 to 7.25)

A.19.1 Brief Summary of the Case History

El Cobre Tailings Dam was located in El Cobre, Chile, and the exact date of the failure was reported as March 28, 1965. The fundamental reason behind the failure was reported as the 1965 Chilean Earthquake (M_L=7.00 to 7.25). The type of the case structure can be classified as a tailings dam, and the maximum slope height is reported as ~ 31 m. Dobry and Alvarez (1967) is considered as the main source of reference. Olson (2001), Wang (2003) and Weber (2015) also studied this case history during their back-analyses of liquefaction failure case histories.

A.19.2 Site Geology and Critical Cross-section

Figure A.19.1 presents the pre-failure and post-failure cross-sections of the case structure. It is decided that the idealized soil profile consists of three soil layers namely non-liquefied zone, liquefied zone, and foundation. The parts of the tailings dam remaining above and below the water table level at the time of failure are classified as non-liquefied zone and liquefied zone, respectively. The layer underlying the tailings dam is defined as the foundation.

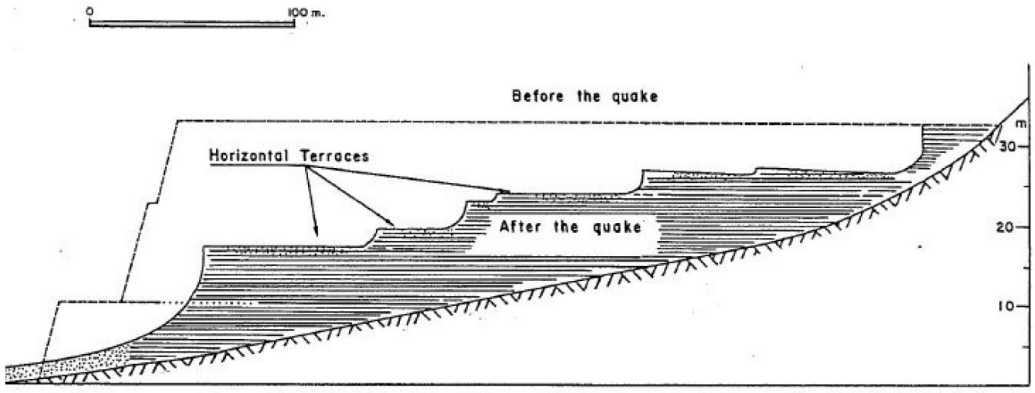

Figure A.19.1. Pre-failure and post-failure cross-sections of the El Cobre Tailings Dam (Dobry and Alvarez, 1967)

A.19.3 Evaluation of Material Properties

Since the grain size distribution curve of the case history was not reported by the main sources of references or other residual strength-related studies, mean grain size (D_{50}), fines content (FC) and coefficient of uniformity (C_u) values are estimated based on the documented representative values in those references, if available. In fact, the plot given in Figure A.19.2 was provided by Dobry and Alvarez (1967) for the distribution of SPT resistance, fines content, natural water content, and liquid limit with depth for the El Cobre Tailings Dam. Therefore, this plot is taken as reference for SPT resistance and fines content evaluations.

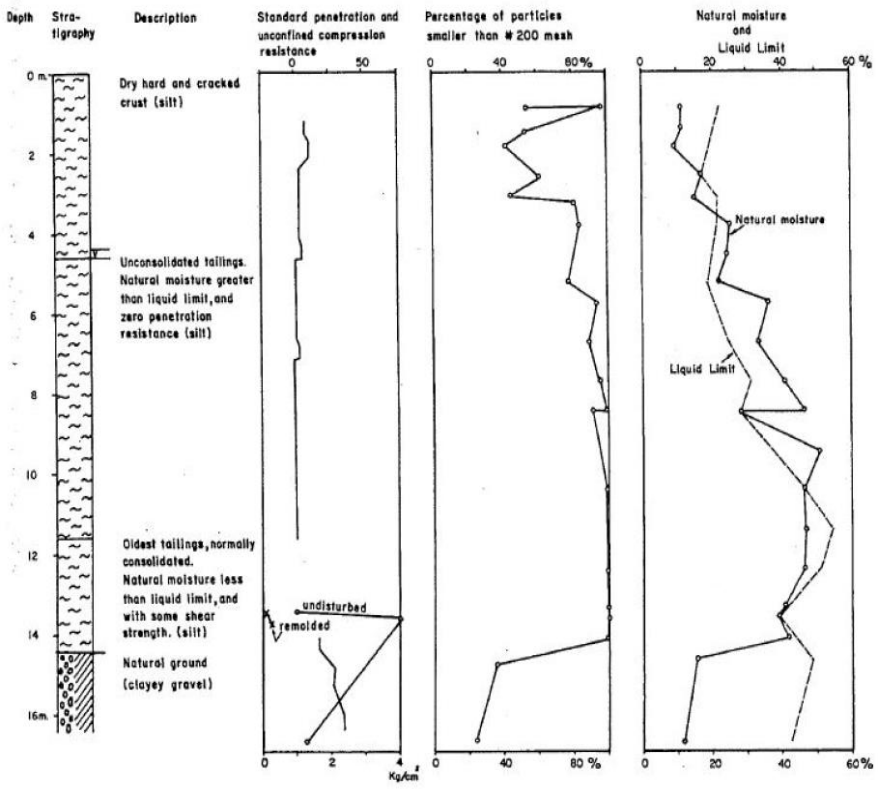

Figure A.19.2. Distribution of SPT resistance, fines content, natural water content, and liquid limit for the El Cobre Tailings Dam (Dobry and Alvarez, 1967)

Mean grain size (D_{50}): The exact value of the mean grain size was reported as D_{50} = 0.080 mm in Dobry and Alvarez (1967) and Olson (2001). Hence, the representative D_{50} value is also taken as 0.080 mm in this study.

Fines content (FC): FC = 93% is evaluated representatively based on the fines content distribution plot of the case history. Olson (2001) and Gutierrez et al. (2016) also suggest FC = 93%.

Coefficient of uniformity (C_u): Since no coefficient of uniformity value was reported by the main sources of references or other relative studies, no value has been set for this parameter.

Roundness (R): Since no roundness value was reported by the main sources of references or other studies, no value has been set for this parameter for the evaluation of limit void ratios and void ratio ranges. However, R = 0.50 is taken approximately as a representative value for the evaluation of liquefaction state friction angle.

Sphericity (S): Since no sphericity value was reported by the main sources of references or other studies, no value has been set for this parameter for the evaluation of limit void ratios and void ratio ranges. However, S = 0.60 is taken approximately as a representative value for the evaluation of liquefaction state friction angle.

Unit weight (γ_{dry} and γ_{sat}): As the results are not sensitive to unit weight, the dry and saturated unit weights of non-liquefied and liquefied zones are assigned as 12.6 kN/m^3 and 13.4 kN/m^3, respectively. For foundation, the unit weight is defined as 15.7 kN/m^3. These values are selected accordingly to be compatible with Olson (2001) and Weber (2015).

A.19.4 Sub-sectioning of the Cross-section and Failure Plane

The exact locations of the SPT boreholes were not known for this case history. Therefore, the sub-sectioning is made based on imaginary boreholes assigned on the cross-section. These imaginary boreholes are defined with respect to changes in

effective vertical stresses and inclination angles of the failure plane. Accordingly, four sub-sections are assigned for the liquefied zone as presented in Figure A.19.3.

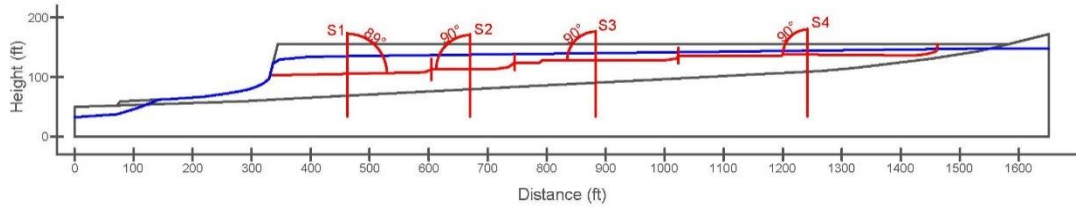

Figure A.19.3. Sub-sectioning of the cross-section and failure plane for El Cobre Tailings Dam

The territory lengths (L_i) and inclinations (α_i) (positive sign for CCW direction) of the failure plane are evaluated as given in Table A.19.1 for each sub-section.

Table A.19.1 Sub-sections with their corresponding failure plane lengths and inclinations for El Cobre Tailings Dam

Case History	Section	Failure plane length, L_i (m)	Total failure plane length, L_t (m)	Failure plane inclination, α_i (degrees)
El Cobre Tailings Dam	S1	83.71	348.12	1
	S2	43.82		0
	S3	85.77		0
	S4	134.82		0

A.19.5 Elastic Modeling and Stress Rotation

All stress components are evaluated linear elastically at the points where boreholes and failure plane intersect in Figure A.19.3. The initial and deformed shape of the cross-section are presented in Figure A.19.4 and Figure A.19.5, respectively. All lengths are given in meters.

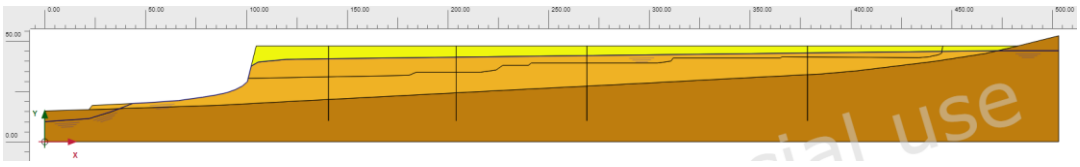

Figure A.19.4. Initial cross-section used in linear elastic modeling of El Cobre Tailings Dam

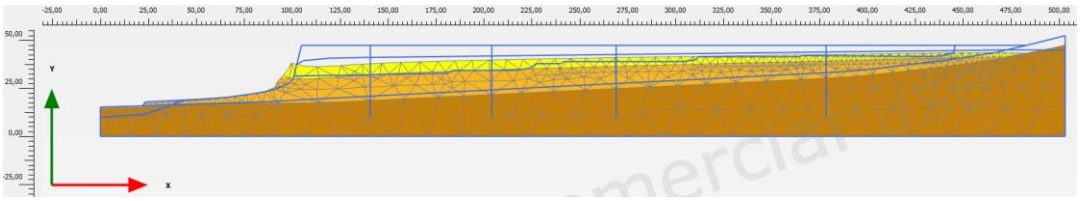

Figure A.19.5. Deformed cross-section obtained after linear elastic modeling of El Cobre Tailings Dam

During the elastic modeling process in PLAXIS 2D Ultimate Connect Edition V22.00.00.1733 software, the Poisson's ratio values of the non-liquefied zone, liquefied zone, and foundation are defined as 0.30, 0.33, and 0.30, respectively. The elastic modulus values of the same layers, on the other hand, are estimated as 10 MPa, 5 MPa, and 30 MPa, respectively.

The effective normal (σ'_N) and shear (τ_{static}) stresses acting on the inclined failure plane are evaluated with corresponding Mohr's circles. The corresponding Mohr's circles and the effective stress components of the sub-sections are presented in Figure A.19.6 and Table A.19.2, respectively. All stresses are given in kilopascals.

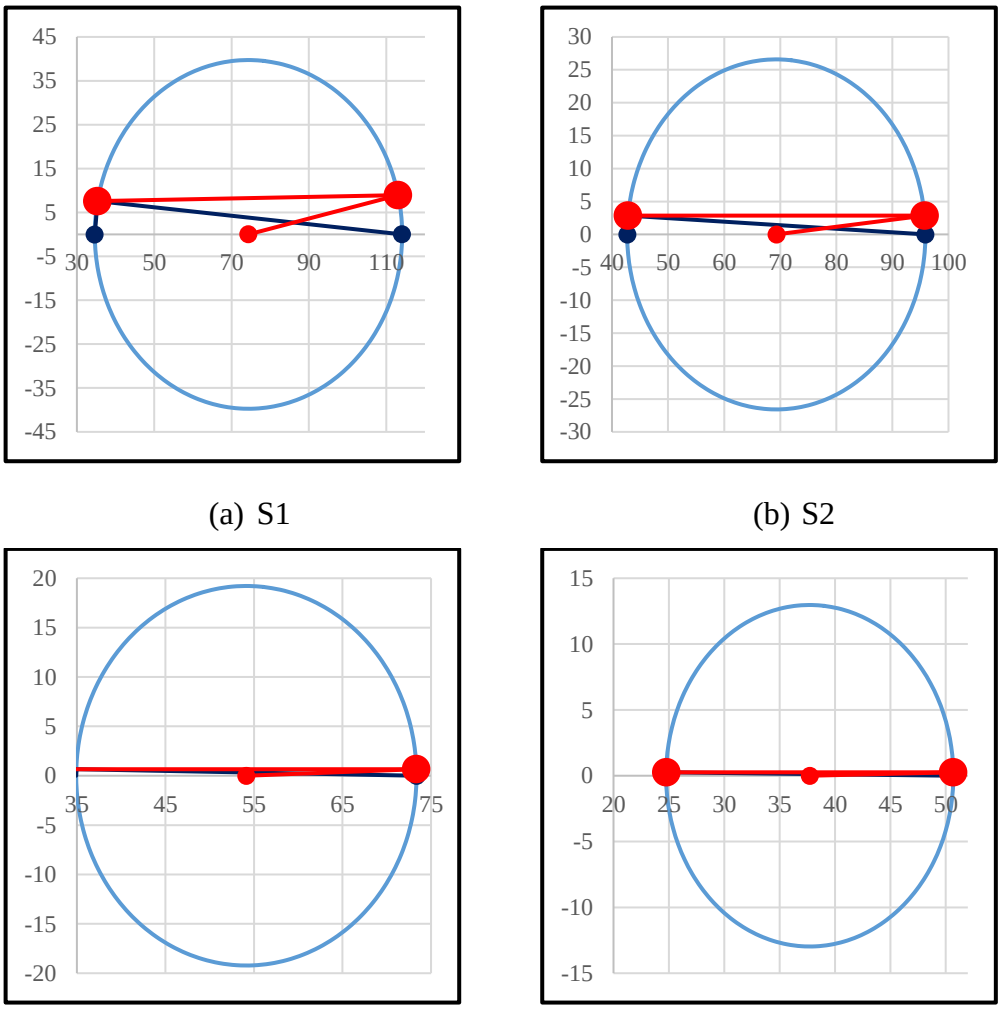

(a) S1 (b) S2

(c) S3 (d) S4

Figure A.19.6. Mohr's circles for El Cobre Tailings Dam

Table A.19.2 Evaluated stress components for El Cobre Tailings Dam

Case History	Section	σ'_1 (kPa)	σ'_2 (kPa)	σ'_3 (kPa)	p_0' (kPa)	q (kPa)	σ'_N (kPa)	τ_{static} (kPa)	$\lvert\tau_{static}\rvert$ (kPa)
El Cobre Tailings Dam	S1	114.1	49.1	34.6	66.0	73.3	113.1	8.9	8.9
	S2	95.9	45.7	42.7	61.5	51.7	95.7	2.9	2.9
	S3	73.4	35.7	34.9	48.0	38.0	73.3	0.7	0.7
	S4	50.7	24.9	24.8	33.5	25.9	50.7	0.3	0.3

A.19.6 Evaluation of SPT Resistance

The exact locations of the SPT boreholes were not documented for this case history. Therefore, imaginary boreholes are assigned along the cross-section as shown in Figure A.19.3. SPT data used for this case history is presented in Figure A.19.2.

The correction factors for nonstandardized sampler configuration (C_S), borehole diameter (C_B), and energy efficiency (C_E) are taken as 1.0 since no reliable information related to these coefficients was reported in any of the sources. The short rod length (C_R) and fines content correction factors (C_{fines}) are evaluated with the methods and relationships explained in Section 3.5. The overburden stress correction factors (C_N) are evaluated based on the effective vertical stresses estimated at the point of penetration for each recording, and average values are documented for simplicity. Accordingly, the correction factors and SPT resistances are estimated as given in Table A.19.3.

Table A.19.3 Evaluated SPT-N resistances for El Cobre Tailings Dam

Case History	Section	C_N	C_B	C_R	C_S	C_E	C_{fines}	N	N_{60}	$(N_1)_{60}$	$(N_1)_{60,cs}$	
El Cobre Tailings Dam	S1	0.92	1.0	0.98	1.0	1.00	2.19	1.46	1.43	1.67	3.66	3.66
	S2	1.00	1.0	0.98	1.0	1.00	2.19	1.46	1.43	1.67	3.66	
	S3	1.14	1.0	0.98	1.0	1.00	2.19	1.46	1.43	1.67	3.66	
	S4	1.37	1.0	0.98	1.0	1.00	2.19	1.46	1.43	1.67	3.66	

A.19.7 Evaluation of Limit Void Ratios, Void Ratio Ranges, Relative Densities and Initial Void Ratios

Since mean grain size (D_{50}) and fines content (FC) information were available among the required material properties for the void ratio prediction models, the arithmetic means of the limit void ratios (e_{min} and e_{max}) evaluated by Model 1 and Model 2 are considered as the representative values. The e_{max} value is slightly modified then with respect to the construction method of the case history for each prediction model.

Since the fines content value is evaluated as 93%, which is greater than 15%, it is judged that the soil of interest consists of silty soils. Therefore, the relative densities evaluated by the correlation recommended by Cubrinovski and Ishihara (1999) are directly taken as the representative relative densities of the soils. Based on these relative densities and limit void ratios, the initial void ratios (e_0) corresponding to approximately 1 kPa confining stress are estimated referring to Equation 3-68. Accordingly, the limit void ratios, void ratio ranges (without any modification for the construction method), in-situ relative densities, and initial void ratios are estimated as given in Table A.19.4.

Table A.19.4 Evaluated limit void ratios, void ratio ranges, in-situ relative densities, and initial void ratios for El Cobre Tailings Dam

Case History	Section	e_{min}	e_{max}	e_{max}-e_{min}	$RD_{C\&I}$ (%)	$RD_{K\&M}$ (%)	$RD_{overall}$ (%)	e_0
El Cobre Tailings Dam	S1	0.640	1.113	0.473	20.00	22.65	20.00	1.018
	S2	0.640	1.113	0.473	20.00	22.65	20.00	1.018
	S3	0.640	1.113	0.473	20.00	22.65	20.00	1.018
	S4	0.640	1.113	0.473	20.00	22.65	20.00	1.018

A.20 Metoki Road Embankment (1968 Tokachi-Oki Earthquake, M=7.9)

A.20.1 Brief Summary of the Case History

Metoki Road Embankment was located in Metoki, Japan, and the exact date of the failure was reported as March 28, 1968. The fundamental reason behind the failure was reported as the 1968 Tokachi-Oki Earthquake (M=7.9). The type of the structure can be classified as a poorly compacted embankment, and the maximum slope height is reported as ~ 5 m. Ishihara et al. (1990) is taken into account as the main source of reference. Olson (2001), Wang (2003) and Weber (2015) also studied this case history during their back-analyses of liquefaction failure case histories.

A.20.2 Site Geology and Critical Cross-section

Figure A.20.1 and Figure A.20.2 show the soil stratigraphy and pre-failure cross-section of the case structure. It is decided that the idealized soil profile consists of four soil layers namely non-liquefied zone, liquefied zone, medium-dense silty sand, and dense silty sand. The parts of the embankment remaining above and below the water table level at the time of failure are classified as non-liquefied zone and liquefied zone, respectively. The layers underlying the embankment are defined as the medium-dense silty sand and dense silty sand, from top to bottom respectively.

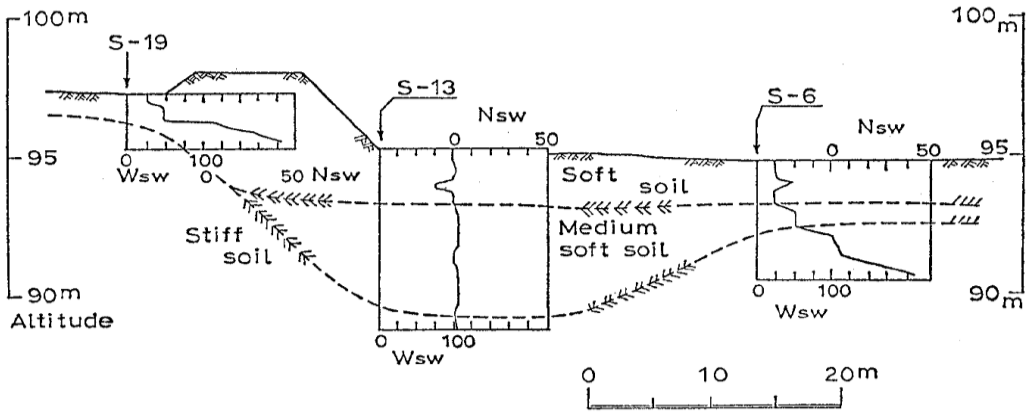

Figure A.20.1. Soil stratigraphy and pre-failure cross-section of the Metoki Road Embankment (Ishihara et al., 1990)

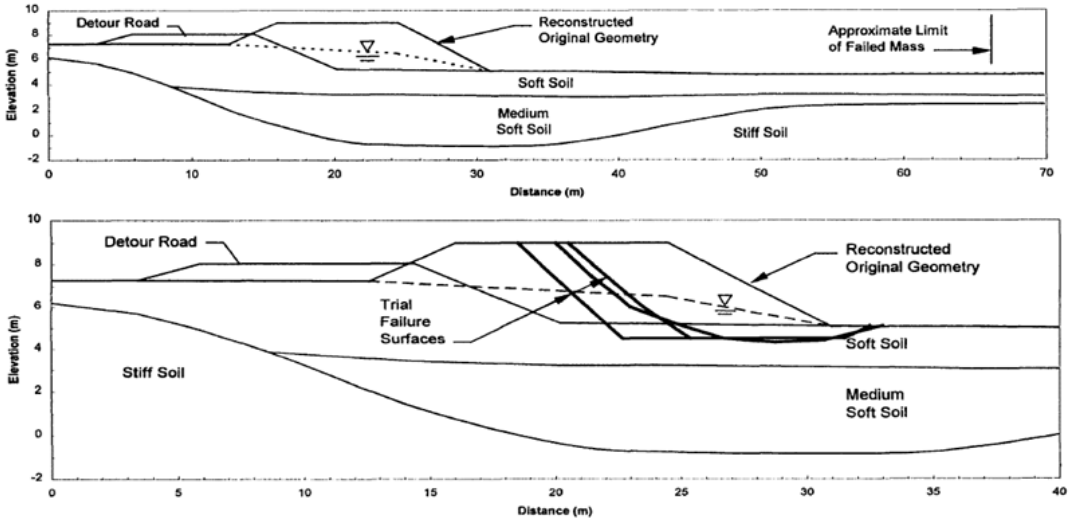

Figure A.20.2. Soil stratigraphy and pre-failure cross-section of the Metoki Road Embankment (Olson, 2001)

A.20.3 Evaluation of Material Properties

Since the grain size distribution curve of the case history was not reported by the main sources of references or other residual strength-related studies, mean grain size (D_{50}), fines content (FC) and coefficient of uniformity (C_u) values are estimated based on the documented representative values in those references, if available.

Mean grain size (D_{50}): The exact value of the mean grain size was reported as D_{50} = 0.120 mm in Olson (2001). Although there is no reliable information available regarding the mean grain size value of this case history, Olson (2001) takes D_{50} = 0.120 mm as a representative value for silty sands. Hence, the representative D_{50} value is also taken as 0.120 mm in this study.

Fines content (FC): No fines content value was reported by the main sources of references or other relative studies. However, the representative FC value is taken as 15% in this study referring to silty sand material existing in the profile.

Coefficient of uniformity (C_u): Since no coefficient of uniformity value was reported by the main sources of references or other relative studies, no value has been set for this parameter.

Roundness (R): Since no roundness value was reported by the main sources of references or other studies, no value has been set for this parameter for the evaluation of limit void ratios and void ratio ranges. However, R = 0.50 is taken approximately as a representative value for the evaluation of liquefaction state friction angle.

Sphericity (S): Since no sphericity value was reported by the main sources of references or other studies, no value has been set for this parameter for the evaluation of limit void ratios and void ratio ranges. However, S = 0.60 is taken approximately as a representative value for the evaluation of liquefaction state friction angle.

Unit weight (γ_{dry} and γ_{sat}): As the results are not sensitive to unit weight, the dry and saturated unit weights of all soil layers other than dense silty sand material are assigned as 17.3 kN/m^3 and 18.1 kN/m^3, respectively. For dense silty sand material,

the unit weight is defined as 18.9 kN/m^3. These values are selected accordingly to be compatible with Olson (2001) and Weber (2015).

A.20.4 Sub-sectioning of the Cross-section and Failure Plane

The exact locations of the Swedish CPT boreholes were known for this case history as presented in Figure A.20.1. Therefore, the sub-sectioning is made based on the locations of these penetration tests as presented in Figure A.20.3. Each test is assigned (names of the logs are directly assigned as the name of the sub-section) for the corresponding territory length.

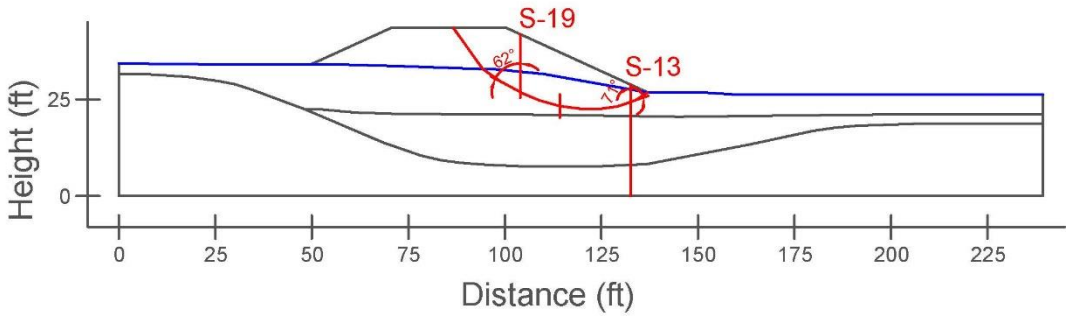

Figure A.20.3. Sub-sectioning of the cross-section and failure plane for Metoki Road Embankment

The territory lengths (L_i) and inclinations (α_i) (positive sign for CCW direction) of the failure plane are evaluated as given in Table A.20.1 for each sub-section.

Table A.20.1 Sub-sections with their corresponding failure plane lengths and inclinations for Metoki Road Embankment

Case History	Section	Failure plane length, L_i (m)	Total failure plane length, L_t (m)	Failure plane inclination, α_i (degrees)
Metoki Road Embankment	S-19	6.81	14.04	-28
	S-13	7.23		19

A.20.5 Elastic Modeling and Stress Rotation

All stress components are evaluated linear elastically at the points where boreholes and failure plane intersect in Figure A.20.3. The initial and deformed shape of the cross-section are presented in Figure A.20.4 and Figure A.20.5, respectively. All lengths are given in meters.

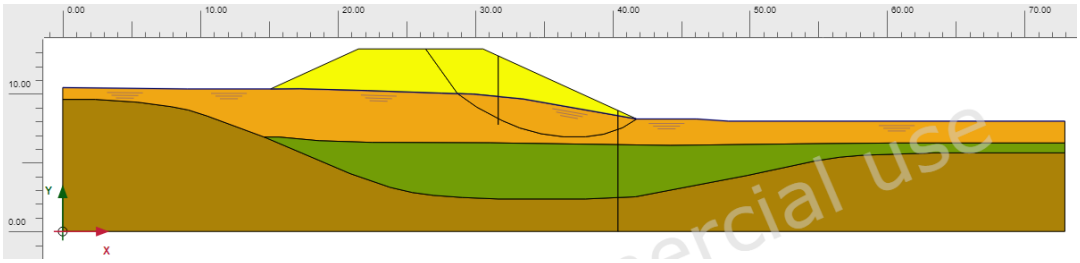

Figure A.20.4. Initial cross-section used in linear elastic modeling of Metoki Road Embankment

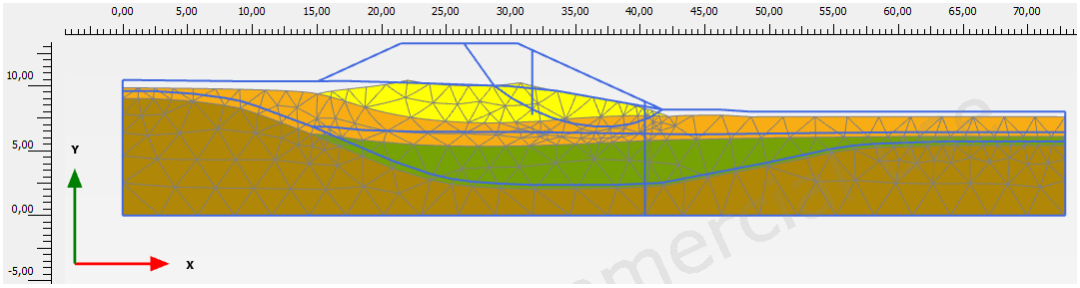

Figure A.20.5. Deformed cross-section obtained after linear elastic modeling of Metoki Road Embankment

During the elastic modeling process in PLAXIS 2D Ultimate Connect Edition V22.00.00.1733 software, the Poisson's ratio values of the non-liquefied zone, liquefied zone, medium-dense silty sand, and dense silty sand are defined as 0.30, 0.33, 0.30, and 0.30, respectively. The elastic modulus values of the same layers, on the other hand, are estimated as 10 MPa, 5 MPa, 20 MPa, and 30 MPa, respectively.

The effective normal (σ'_N) and shear (τ_{static}) stresses acting on the inclined failure plane are evaluated with corresponding Mohr's circles. The corresponding Mohr's circles and the effective stress components of the sub-sections are presented in Figure A.20.6 and Table A.20.2, respectively. All stresses are given in kilopascals.

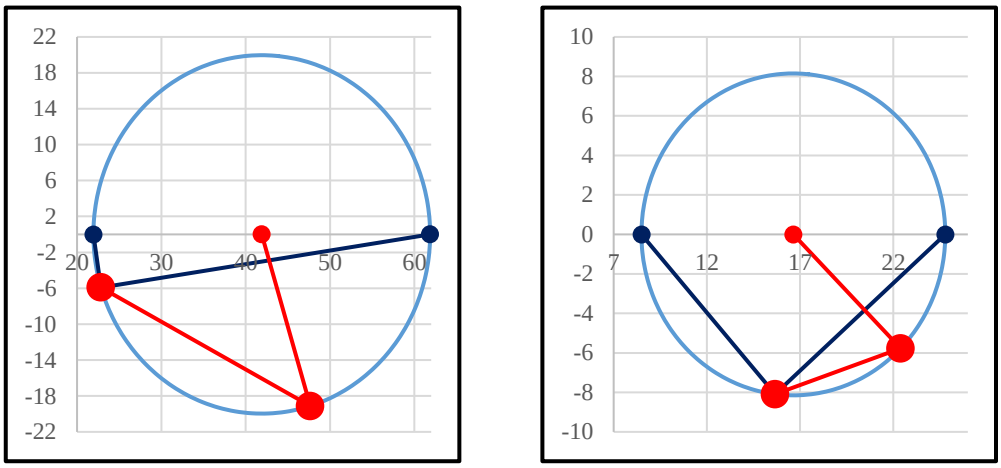

(a) S-19 (b) S-13

Figure A.20.6. Mohr's circles for Metoki Road Embankment

Table A.20.2 Evaluated stress components for Metoki Road Embankment

Case History	Section	σ'_1 (kPa)	σ'_2 (kPa)	σ'_3 (kPa)	p_0' (kPa)	q (kPa)	σ'_N (kPa)	τ_{static} (kPa)	$\lvert\tau_{static}\rvert$ (kPa)
Metoki Road Embankment	S-19	61.9	27.7	21.9	37.2	37.4	47.7	-19.1	19.1
	S-13	24.8	11.0	8.5	14.8	15.2	22.4	-5.8	5.8

A.20.6 Evaluation of SPT Resistance

The exact locations of the Swedish CPT boreholes were documented by Ishihara et al. (1990) as given in Figure A.20.1. The SCPT resistances are converted to raw SPT-N values by using the correlation proposed by Inada (1982) explained in Section 3.5. These SPT-N values are assumed to be almost equal to N_{60} values as equipment, energy, and procedure corrections are not applicable for SCPT. However, the short rod length correction factors (C_R) are still evaluated with the methods and relationships explained in Section 3.5. Similarly, the overburden stress correction factors (C_N) are again evaluated based on the effective vertical stresses estimated at the point of penetration for each recording, and average values are documented for simplicity. The fines content correction factors (C_{fines}) are also evaluated with the methods and relationships explained in Section 3.5. Accordingly, the correction factors and SPT resistances are estimated as given in Table A.20.3.

Table A.20.3 Evaluated SPT-N resistances for Metoki Road Embankment

Case History	Section	C_N	C_B	C_R	C_S	C_E	C_{fines}	N	N_{60}	$(N_1)_{60}$	$(N_1)_{60,cs}$	
Metoki Road Embankment	S-19	5.31	-	0.74	-	-	1.30	0.83	0.62	3.08	4.02	4.38
	S-13	2.11	-	0.90	-	-	1.26	2.02	1.82	3.76	4.73	

A.20.7 Evaluation of Limit Void Ratios, Void Ratio Ranges, Relative Densities and Initial Void Ratios

Since mean grain size (D_{50}) and fines content (FC) information were available among the required material properties for the void ratio prediction models, the arithmetic means of the limit void ratios (e_{min} and e_{max}) evaluated by Model 1 and Model 2 are considered as the representative values. The e_{max} value is slightly modified then with respect to the construction method of the case history for each prediction model.

Since the fines content value is evaluated as 15%, it is judged that the soil of interest consists of silty soils. Therefore, the relative densities evaluated by the correlation recommended by Cubrinovski and Ishihara (1999) are directly taken as the representative relative densities of the soils. Based on these relative densities and limit void ratios, the initial void ratios (e_0) corresponding to approximately 1 kPa confining stress are estimated referring to Equation 3-68. Accordingly, the limit void ratios, void ratio ranges (without any modification for the construction method), in-situ relative densities, and initial void ratios are estimated as given in Table A.20.4.

Table A.20.4 Evaluated limit void ratios, void ratio ranges, in-situ relative densities, and initial void ratios for Metoki Road Embankment

Case History	Section	e_{min}	e_{max}	e_{max}-e_{min}	$RD_{C\&I}$ (%)	$RD_{K\&M}$ (%)	$RD_{overall}$ (%)	e_0
Chonan Middle School	No.4	0.597	1.011	0.414	24.27	28.88	24.27	0.910
	No.3	0.597	1.011	0.414	26.79	31.88	26.79	0.900

A.21 Hokkaido Tailings Dam (1968 Tokachi-Oki Earthquake, M=7.9)

A.21.1 Brief Summary of the Case History

Hokkaido Tailings Dam was located in Hokkaido, Japan, and the exact date of the failure was reported as March 28, 1968. The fundamental reason behind the failure was reported as the 1968 Tokachi-Oki Earthquake (M=7.9). The type of the structure can be classified as a tailings dam, and the maximum slope height is reported as ~ 7 m. Ishihara et al. (1990) is taken into account as the main source of reference. Olson (2001), Wang (2003) and Weber (2015) also studied this case history during their back-analyses of liquefaction failure case histories.

A.21.2 Site Geology and Critical Cross-section

Figure A.21.1 shows the soil stratigraphy and pre-failure and post-failure cross-sections of the case structure. It is decided that the idealized soil profile consists of four soil layers namely non-liquefied zone, liquefied zone, starter dike, and foundation. The parts of the tailings dam remaining above and below the water table level at the time of failure are classified as non-liquefied zone and liquefied zone, respectively. The trapezoidal region existing at the toe of the tailings dam is assigned as starter dike. The layer underlying the tailings dam is classified as foundation.

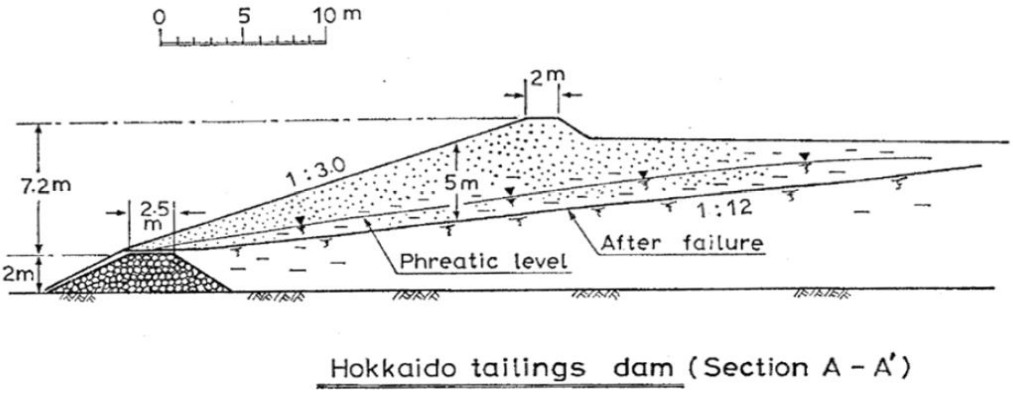

Figure A.21.1. Soil stratigraphy and pre-failure and post-failure cross-sections of the Hokkaido Tailings Dam (Ishihara et al., 1990)

A.21.3 Evaluation of Material Properties

Since the grain size distribution curve of the case history was not reported by the main sources of references or other residual strength-related studies, mean grain size (D_{50}), fines content (FC) and coefficient of uniformity (C_u) values are estimated based on the documented representative values in those references, if available.

Mean grain size (D_{50}): The exact value of the mean grain size was reported as D_{50} = 0.075 mm in Olson (2001). Although there is no reliable information available regarding the mean grain size value of this case history, Olson (2001) takes D_{50} = 0.075 mm as a representative value for typical mine tailing deposits. Hence, the representative D_{50} value is also taken as 0.075 mm in this study.

Fines content (FC): The exact value of the fines content was reported as FC = 50% in Olson (2001). It takes this value referring to typical mine tailing deposits. In fact, the exact value of the fines content was reported as FC = 48% in Bensoula et al. (2018) for this case history. Hence, the representative FC value is also taken as 50% in this study.

Coefficient of uniformity (C_u): Although no coefficient of uniformity value was reported by the main sources of references or other relative studies, C_u=1.50 is assigned representatively in this study based on typical uniformly graded mine tailing deposits.

Roundness (R): Since no roundness value was reported by the main sources of references or other studies, no value has been set for this parameter for the evaluation of limit void ratios and void ratio ranges. However, R = 0.50 is taken approximately as a representative value for the evaluation of liquefaction state friction angle.

Sphericity (S): Since no sphericity value was reported by the main sources of references or other studies, no value has been set for this parameter for the evaluation of limit void ratios and void ratio ranges. However, S = 0.60 is taken approximately as a representative value for the evaluation of liquefaction state friction angle.

Unit weight (γ_{dry} and γ_{sat}): As the results are not sensitive to unit weight, the dry and saturated unit weights of all soil layers other than foundation material are assigned as 18.5 kN/m^3 and 19.3 kN/m^3, respectively. For foundation material, the unit weight is defined as 19.6 kN/m^3. These values are selected accordingly to be compatible with Olson (2001) and Weber (2015).

A.21.4 Sub-sectioning of the Cross-section and Failure Plane

The exact locations of the Dutch CPT boreholes were not known for this case history. Therefore, the sub-sectioning is made based on imaginary boreholes assigned on the cross-section. These imaginary boreholes are defined with respect to changes in effective vertical stresses and inclination angles of the failure plane. Two different initial failure planes are considered based on the information available on the main sources of references about the failure mode as presented in Figure A.21.2. While boreholes Small-S1 and Small-S2 sub-divide the smaller failure plane into smaller pieces, Large-S1 and Large-S2 split the larger failure plane.

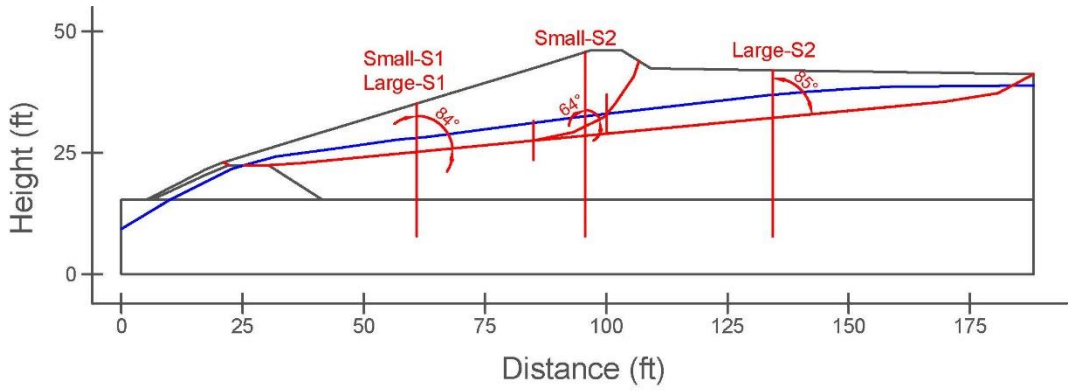

Figure A.21.2. Sub-sectioning of the cross-section and failure plane for Hokkaido Tailings Dam

The territory lengths (L_i) and inclinations (α_i) (positive sign for CCW direction) of the failure planes are evaluated as given in Table A.21.1 for each sub-section.

Table A.21.1 Sub-sections with their corresponding failure plane lengths and inclinations for Hokkaido Tailings Dam

Case History	Section	Failure plane length, L_i (m)	Total failure plane length, L_t (m)	Failure plane inclination, α_i (degrees)
Hokkaido Tailings Dam	Small-S1	18.26	23.23	6
	Small-S2	4.98		26
	Large-S1	18.26	48.61	6
	Large-S2	30.35		5

A.21.5 Elastic Modeling and Stress Rotation

All stress components are evaluated linear elastically at the points where boreholes and failure plane intersect in Figure A.21.2. The initial and deformed shape of the cross-section are presented in Figure A.21.3 and Figure A.21.4, respectively. All lengths are given in meters.

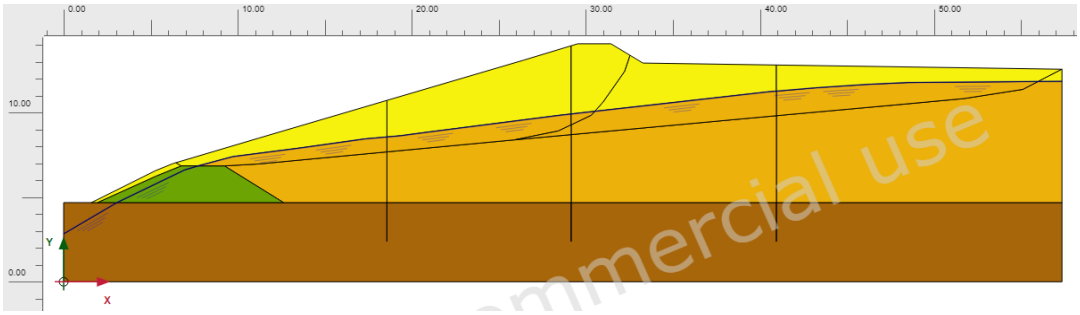

Figure A.21.3. Initial cross-section used in linear elastic modeling of Hokkaido Tailings Dam

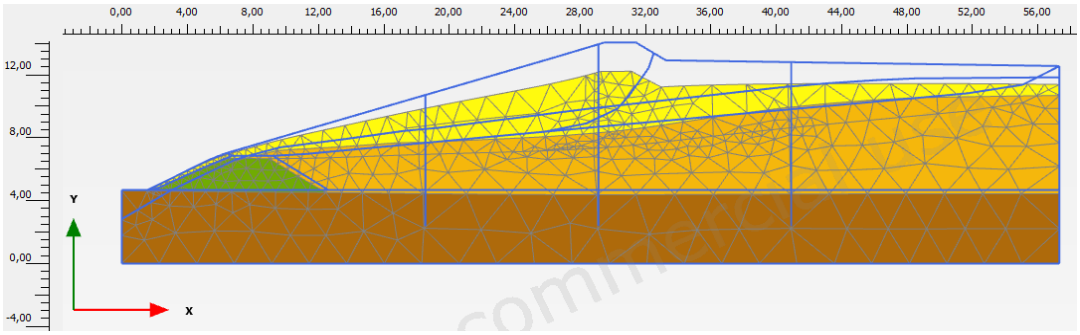

Figure A.21.4. Deformed cross-section obtained after linear elastic modeling of Hokkaido Tailings Dam

During the elastic modeling process in PLAXIS 2D Ultimate Connect Edition V22.00.00.1733 software, the Poisson's ratio values of the non-liquefied zone, liquefied zone, starter dike, and foundation material are defined as 0.30, 0.33, 0.30, and 0.30, respectively. The elastic modulus values of the same layers, on the other hand, are estimated as 10 MPa, 5 MPa, 20 MPa, and 30 MPa, respectively.

The effective normal (σ'_N) and shear (τ_{static}) stresses acting on the inclined failure plane are evaluated with corresponding Mohr's circles. The corresponding Mohr's circles and the effective stress components of the sub-sections are presented in Figure A.21.5 and Table A.21.2, respectively. All stresses are given in kilopascals.

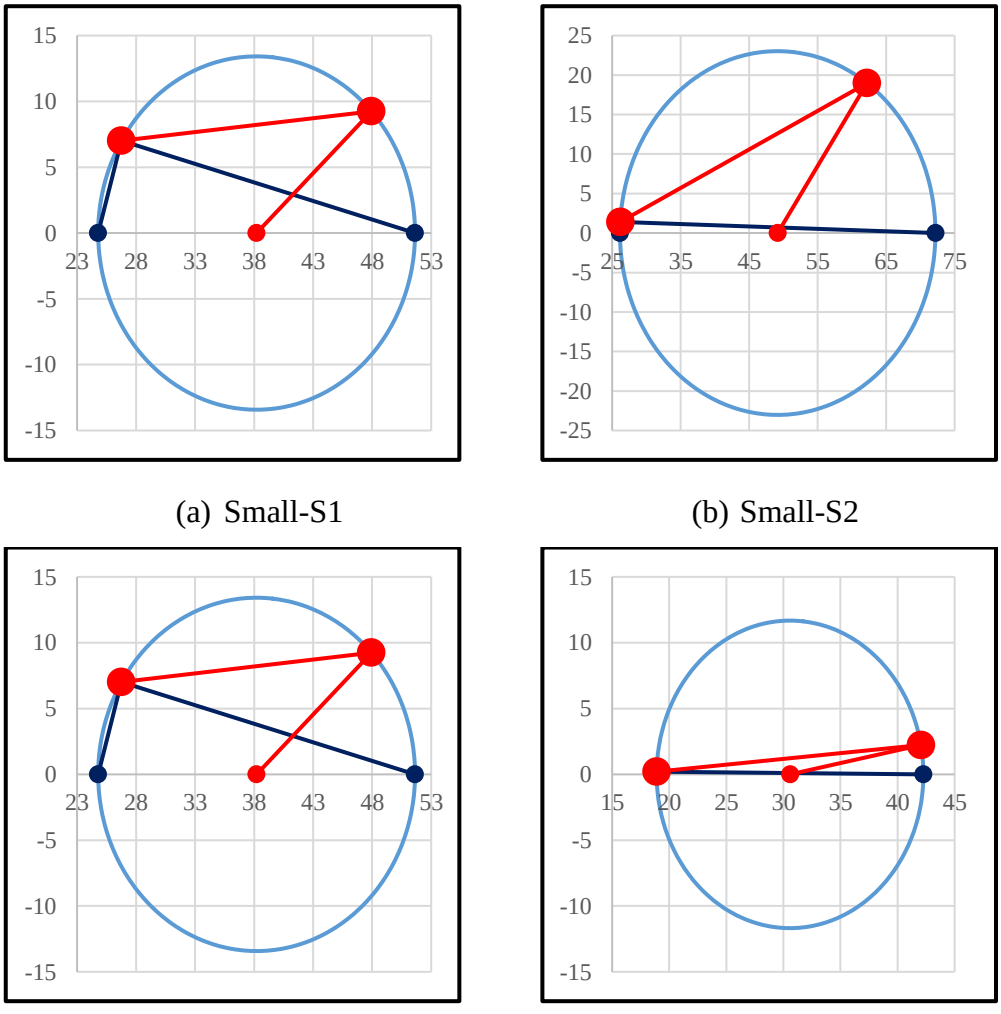

(a) Small-S1 (b) Small-S2

(c) Large-S1 (d) Large-S2

Figure A.21.5. Mohr's circles for Hokkaido Tailings Dam

Table A.21.2 Evaluated stress components for Hokkaido Tailings Dam

Case History	Section	σ'_1 (kPa)	σ'_2 (kPa)	σ'_3 (kPa)	p_0' (kPa)	q (kPa)	σ'_N (kPa)	τ_{static} (kPa)	$\lvert\tau_{static}\rvert$ (kPa)
Hokkaido Tailings Dam	Small-S1	51.6	25.2	24.8	33.9	26.6	47.9	9.2	9.2
	Small-S2	72.2	32.5	26.1	43.6	43.2	62.2	19.0	19.0
	Large-S1	51.6	25.2	24.8	33.9	26.6	47.9	9.2	9.2
	Large-S2	42.3	20.2	18.9	27.1	22.7	42.0	2.2	2.2

A.21.6 Evaluation of SPT Resistance

The exact locations of the Dutch CPT boreholes were not documented for this case. Therefore, imaginary boreholes are assigned along the cross-section as shown in Figure A.21.2. DCPT data used for this case history is presented in Figure A.21.6.

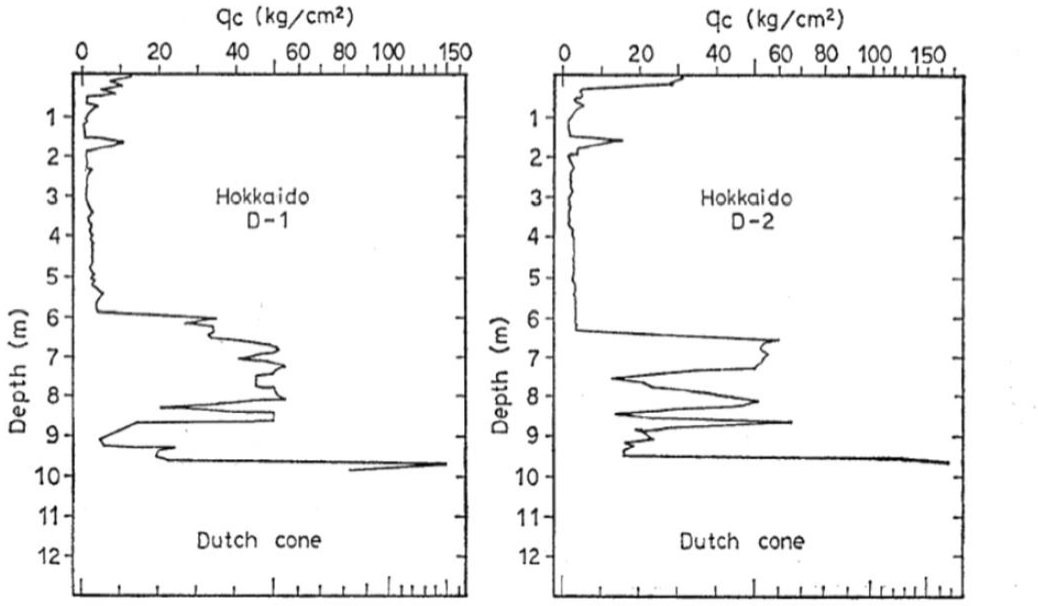

Figure A.21.6. DCPT data for Hokkaido Tailings Dam (Ishihara et al., 1990)

The DCPT cone tip resistances are converted to raw SPT-N and N_{60} values by using the correlations proposed by Ishihara et al. (1990) and Kulhawy and Mayne (1990), respectively, as explained in Section 3.5. Then, the overburden stress correction factors (C_N) are again evaluated to be able to estimate $(N_1)_{60}$ values based on the effective vertical stresses estimated at the point of penetration for each recording,

and average values are documented for simplicity. The fines content correction factors (C_{fines}) are also evaluated with the methods and relationships explained in Section 3.5. Accordingly, the correction factors and SPT resistances are estimated as given in Table A.21.3.

Table A.21.3 Evaluated SPT-N resistances for Hokkaido Tailings Dam

Case History	Section	C_N	C_B	C_R	C_S	C_E	C_{fines}	N	N_{60}	$(N_1)_{60}$	$(N_1)_{60,cs}$	
Hokkaido Tailings Dam	Small-S1	1.91	-	-	-	-	2.36	0.75	0.79	1.44	3.39	3.39
	Small-S2	1.91	-	-	-	-	2.36	0.75	0.79	1.44	3.39	
	Large-S1	1.91	-	-	-	-	2.36	0.75	0.79	1.44	3.39	3.39
	Large-S2	1.91	-	-	-	-	2.36	0.75	0.79	1.44	3.39	

A.21.7 Evaluation of Limit Void Ratios, Void Ratio Ranges, Relative Densities and Initial Void Ratios

Since mean grain size (D_{50}), fines content (FC), and coefficient of uniformity (C_u) information were available among the required material properties for the void ratio prediction models, the arithmetic means of the limit void ratios (e_{min} and e_{max}) evaluated by Model 8 and Model 9 are considered as the representative values. The e_{max} value is slightly modified then with respect to the construction method of the case history for each prediction model.

Since the fines content value is evaluated as 50%, which is greater than 15%, it is judged that the soil of interest consists of silty soils. Therefore, the relative densities evaluated by the correlation recommended by Cubrinovski and Ishihara (1999) are directly taken as the representative relative densities of the soils. Based on these relative densities and limit void ratios, the initial void ratios (e_0) corresponding to approximately 1 kPa confining stress are estimated referring to Equation 3-68. Accordingly, the limit void ratios, void ratio ranges (without any modification for the construction method), in-situ relative densities, and initial void ratios are estimated as given in Table A.21.4.

Table A.21.4 Evaluated limit void ratios, void ratio ranges, in-situ relative densities, and initial void ratios for Hokkaido Tailings Dam

Case History	Section	e_{min}	e_{max}	e_{max}-e_{min}	$RD_{C\&I}$ (%)	$RD_{K\&M}$ (%)	$RD_{overall}$ (%)	e_0
Hokkaido Tailings Dam	Small-S1	0.593	1.015	0.422	16.85	21.25	16.85	0.943
	Small-S2	0.593	1.015	0.422	16.85	21.25	16.85	0.943
	Large-S1	0.593	1.015	0.422	16.85	21.25	16.85	0.943
	Large-S2	0.593	1.015	0.422	16.85	21.25	16.85	0.943

A.22 Upper San Fernando Dam – D/S Slope (1971 San Fernando Earthquake, M_w=6.6)

A.22.1 Brief Summary of the Case History

Upper San Fernando Dam was located in California, USA, and the exact date of the failure was reported as February 9, 1971. The fundamental reason behind the failure was reported as the 1971 San Fernando Earthquake (M_w=6.6). The type of the structure can be classified as a hydraulic fill dam, and the maximum slope height is reported as ~ 20 m. Seed et al. (1973) and Lee et al. (1975) are considered as the main sources of references. Although Upper San Fernando Dam also suffered liquefaction-induced damage and displacements during the 1971 San Fernando Earthquake, it has not received as much attention as the Lower San Fernando Dam because the displacements were not sufficient to classify this case as a post-liquefaction case history. As a result, Olson (2001) and Wang (2003) did not perform back-analyses for this case history, and only Weber (2015) studied it during its back-analyses of liquefaction failure case histories.

A.22.2 Site Geology and Critical Cross-section

Figure A.22.1 shows the pre-failure and post-failure cross-sections of the case structure. Referring to this figure, it is decided that the idealized soil profile consists of many soil layers with various thickness. Basically, the layers underlying the dam

are defined as the gravelly silty sand and foundation from top to bottom, and the middle part of the dam body is classified as clay core. The upper portion of the clay core in the upstream slope is defined as rolled fill. The hydraulic fill materials at the upstream and downstream parts of the dam are classified as liquefied and moist hydraulic fill based on the location of the groundwater surface at the time of failure.

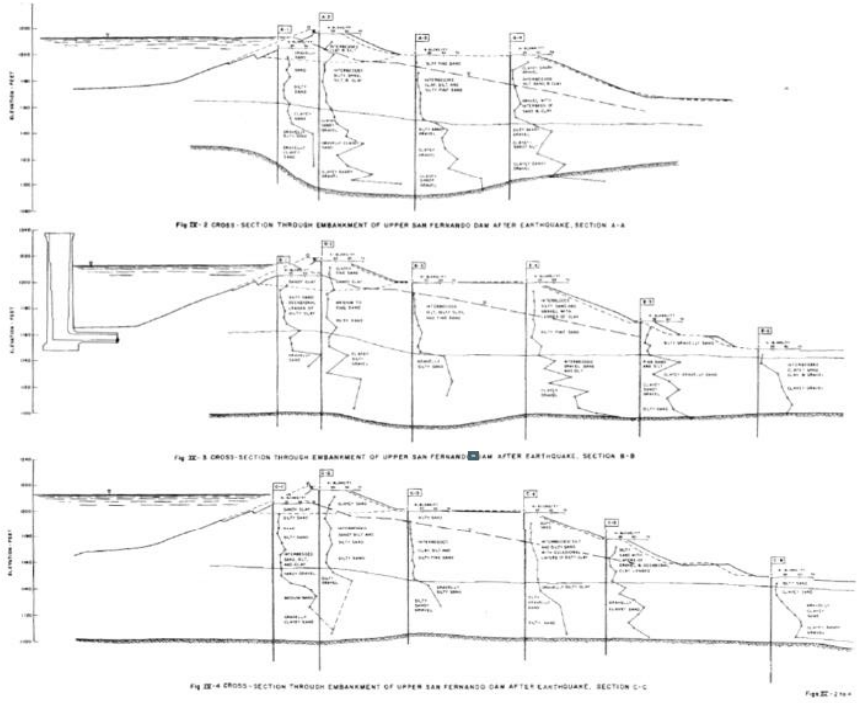

Figure A.22.1. Pre-failure and post-failure cross-sections of the Upper San Fernando Dam (Seed et al., 1973)

A.22.3 Evaluation of Material Properties

Since the grain size distribution curve of the case history was not reported by the main sources of references or other residual strength-related studies, mean grain size (D_{50}), fines content (FC) and coefficient of uniformity (C_u) values are estimated based on the documented representative values in those references, if available.

Mean grain size (D_{50}): No mean grain size value was reported by the main sources of references or other relative studies for this case history. Hence, the representative D_{50} value is taken as the same with the value reported for Lower San Fernando Dam in this study, which is D_{50} = 0.070 mm.

Fines content (FC): The exact value of the fines content was reported as FC = 47.5% in Gutierrez et al. (2016). Hence, the representative FC value is also taken as 47.5% in this study.

Coefficient of uniformity (C_u): No coefficient of uniformity value was reported by the main sources of references or other relative studies for this case history. Hence, the representative C_u value is taken as the same with the value reported for Lower San Fernando Dam in this study, which is $C_u = 31.49$ that indicates well-graded soil.

Roundness (R): Since no roundness value was reported by the main sources of references or other studies, no value has been set for this parameter for the evaluation of limit void ratios and void ratio ranges. However, R = 0.50 is taken approximately as a representative value for the evaluation of liquefaction state friction angle.

Sphericity (S): Since no sphericity value was reported by the main sources of references or other studies, no value has been set for this parameter for the evaluation of limit void ratios and void ratio ranges. However, S = 0.60 is taken approximately as a representative value for the evaluation of liquefaction state friction angle.

Unit weight (γ_{dry} and γ_{sat}): As the results are not sensitive to unit weight, the dry and saturated unit weights of hydraulic and rolled fill materials are assigned as 18.4 kN/m^3 and 19.3 kN/m^3, respectively. For gravelly silty sand and foundation layers, the unit weights are defined as 19.6 kN/m^3. For the clay core materials, the unit weights are estimated as 18.2 kN/m^3. All these values are evaluated accordingly to be compatible with Weber (2015).

A.22.4 Sub-sectioning of the Cross-section and Failure Plane

The exact locations of the SPT boreholes were known for this case history as given in Figure A.22.1. Therefore, the sub-sectioning is made based on the locations of these penetration tests as presented in Figure A.22.2. Each test is assigned (names of the logs are directly assigned as the name of the sub-section) for the corresponding territory length.

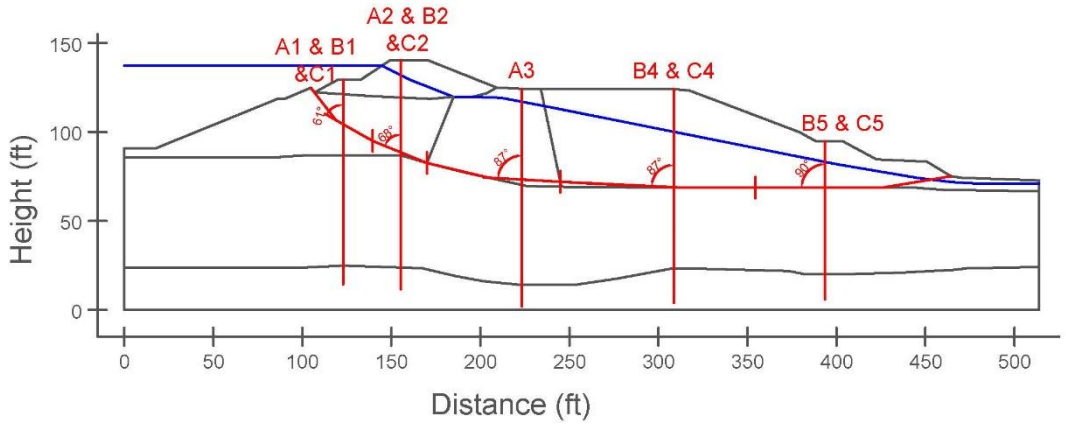

Figure A.22.2. Sub-sectioning of the cross-section and failure plane for Upper San Fernando Dam

The territory lengths (L_i) and inclinations (α_i) (positive sign for CCW direction) of the failure plane are evaluated as given in Table A.22.1 for each sub-section.

Table A.22.1 Sub-sections with their corresponding failure plane lengths and inclinations for Upper San Fernando Dam

Case History	Section	Failure plane length, L_i (m)	Total failure plane length, L_t (m)	Failure plane inclination, α_i (degrees)
Upper San Fernando Dam	A1&B1&C1	14.26	111.06	-29
	A2&B2&C2	10.02		-22
	A3	23.15		-3
	B4&C4	33.44		-3
	B5&C5	30.19		0

A.22.5 Elastic Modeling and Stress Rotation

All stress components are evaluated linear elastically at the points where boreholes and failure plane intersect in Figure A.22.2. The initial and deformed shape of the cross-section are presented in Figure A.22.3 and Figure A.22.4, respectively. All lengths are given in meters.

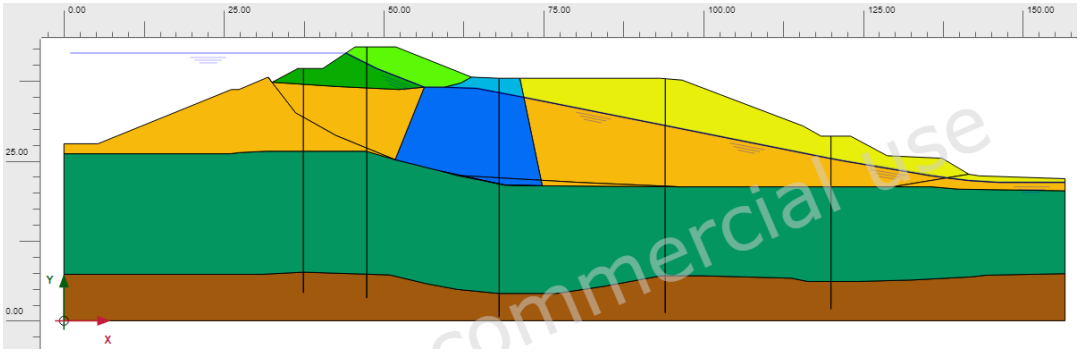

Figure A.22.3. Initial cross-section used in linear elastic modeling of Upper San Fernando Dam

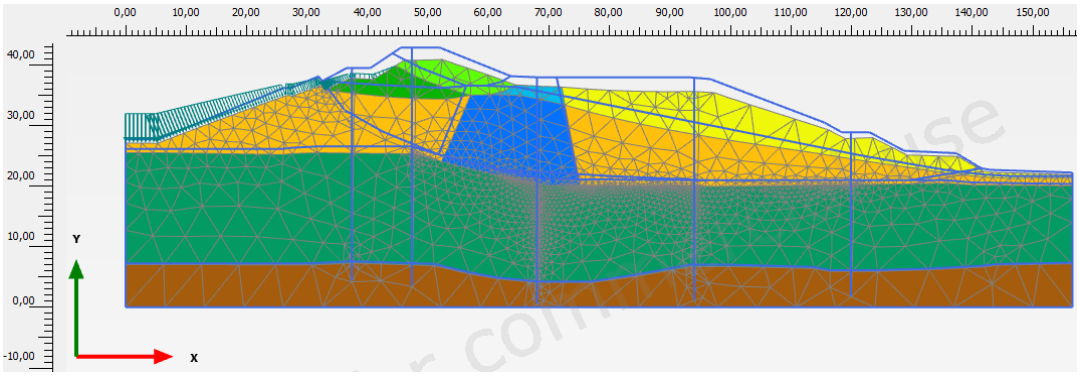

Figure A.22.4. Deformed cross-section obtained after linear elastic modeling of Upper San Fernando Dam

During the elastic modeling process in PLAXIS 2D Ultimate Connect Edition V22.00.00.1733 software, the Poisson's ratio values of the clay core, rolled fill, non-liquefied hydraulic fill, gravelly silty sand and foundation materials are defined as 0.30. For these materials, the elastic modulus values are estimated as 20 MPa, 10 MPa, 10 MPa, 20 MPa, and 30 MPa, respectively. For liquefied hydraulic fill, the Poisson's ratio and elastic modulus values are defined as 0.33 and 5 MPa, respectively.

The effective normal (σ'_N) and shear (τ_{static}) stresses acting on the inclined failure plane are evaluated with corresponding Mohr's circles. The corresponding Mohr's circles and the effective stress components of the sub-sections are presented in Figure A.22.5 and Table A.22.2, respectively. All stresses are given in kilopascals.

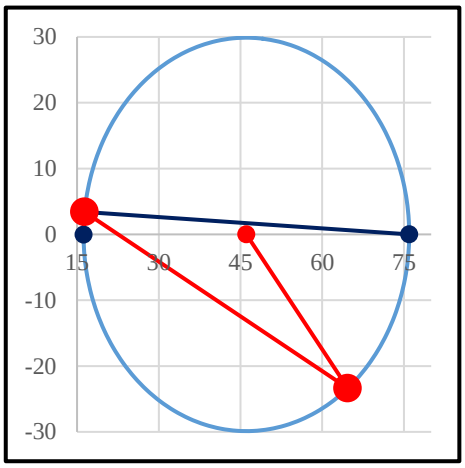

(a) A1 & B1 & C1

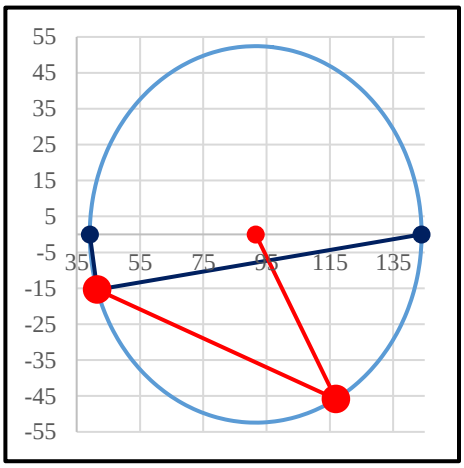

(b) A2 & B2 & C2

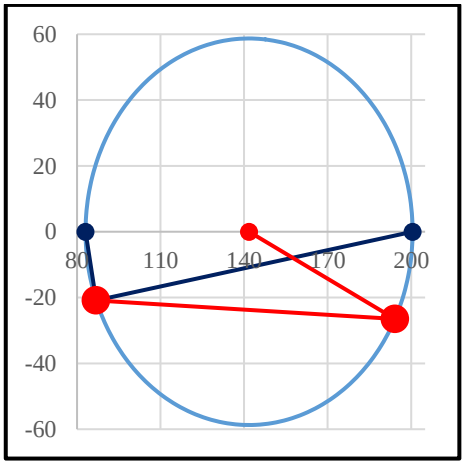

(c) A3

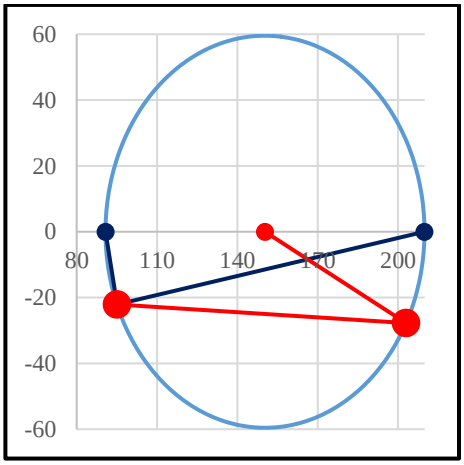

(d) B4 & C4

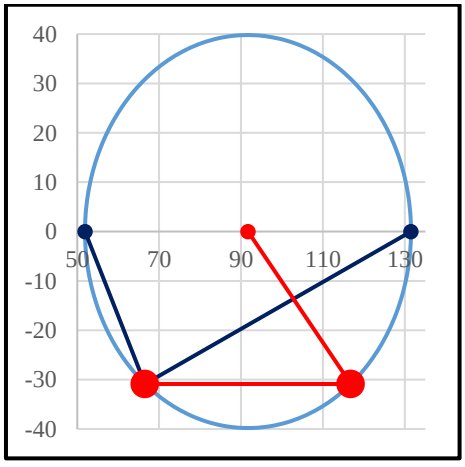

(e) B5 & C5

Figure A.22.5. Mohr's circles for Upper San Fernando Dam

Table A.22.2 Evaluated stress components for Upper San Fernando Dam

Case History	Section	σ'_1 (kPa)	σ'_2 (kPa)	σ'_3 (kPa)	p_0' (kPa)	q (kPa)	σ'_N (kPa)	τ_{static} (kPa)	$\lvert\tau_{static}\rvert$ (kPa)
Upper San Fernando Dam	A1&B1&C1	76.0	30.4	16.2	40.9	54.1	64.7	-23.4	23.4
	A2&B2&C2	144.0	60.4	39.1	81.2	96.0	116.9	-45.9	45.9
	A3	200.5	85.1	83.1	122.9	116.5	194.2	-26.5	26.5
	B4&C4	209.9	99.2	90.8	133.3	115.1	203.0	-27.8	27.8
	B5&C5	131.5	60.5	51.9	81.3	75.7	116.8	-30.9	30.9

A.22.6 Evaluation of SPT Resistance

The exact locations of the SPT boreholes were documented by Seed et al. (1973) as given in Figure A.22.1. The correction factors for nonstandardized sampler configuration (C_S), borehole diameter (C_B), and energy efficiency (C_E) are taken as 1.0 since no reliable information related to these coefficients was reported in any of the sources. The short rod length (C_R) and fines content correction factors (C_{fines}) are evaluated with the methods and relationships explained in Section 3.5. The overburden stress correction factors (C_N) are evaluated based on the effective vertical stresses estimated at the point of penetration for each recording, and average values are documented for simplicity. Accordingly, the correction factors and SPT resistances are estimated as given in Table A.22.3.

Table A.22.3 Evaluated SPT-N resistances for Upper San Fernando Dam

Case History	Section	C_N	C_B	C_R	C_S	C_E	C_{fines}	N	N_{60}	$(N_1)_{60}$	$(N_1)_{60,cs}$	
Upper San Fernando Dam	A1&B1&C1	1.07	1.0	0.97	1.0	1.00	1.33	8.32	8.09	9.15	12.18	12.31
	A2&B2&C2	0.79	1.0	0.99	1.0	1.00	1.33	8.32	8.25	9.34	12.39	
	A3	0.81	1.0	0.99	1.0	1.00	1.33	8.32	8.25	9.33	12.39	
	B4&C4	0.73	1.0	0.99	1.0	1.00	1.33	8.32	8.26	9.34	12.40	
	B5&C5	1.26	1.0	0.97	1.0	1.00	1.33	8.32	8.11	9.17	12.21	

A.22.7 Evaluation of Limit Void Ratios, Void Ratio Ranges, Relative Densities and Initial Void Ratios

Since mean grain size (D_{50}), fines content (FC), and coefficient of uniformity (C_u) information were available among the required material properties for the void ratio prediction models, the arithmetic means of the limit void ratios (e_{min} and e_{max}) evaluated by Model 8 and Model 9 are considered as the representative values. The e_{max} value is slightly modified then with respect to the construction method of the case history for each prediction model.

Since the fines content value is evaluated as 47.5%, which is greater than 15%, it is judged that the soil of interest consists of silty soils. Therefore, the relative densities evaluated by the correlation recommended by Cubrinovski and Ishihara (1999) are directly taken as the representative relative densities of the soils. Based on these relative densities and limit void ratios, the initial void ratios (e_0) corresponding to approximately 1 kPa confining stress are estimated referring to Equation 3-68. Accordingly, the limit void ratios, void ratio ranges (without any modification for the construction method), in-situ relative densities, and initial void ratios are estimated as given in Table A.22.4.

Table A.22.4 Evaluated limit void ratios, void ratio ranges, in-situ relative densities, and initial void ratios for Upper San Fernando Dam

Case History	Section	e_{min}	e_{max}	e_{max}-e_{min}	$RD_{C\&I}$ (%)	$RD_{K\&M}$ (%)	$RD_{overall}$ (%)	e_0
Upper San Fernando Dam	A1&B1&C1	0.437	0.666	0.229	25.25	54.22	25.25	0.608
	A2&B2&C2	0.437	0.666	0.229	25.51	54.76	25.51	0.608
	A3	0.437	0.666	0.229	25.51	54.76	25.51	0.608
	B4&C4	0.437	0.666	0.229	25.51	54.77	25.51	0.608
	B5&C5	0.437	0.666	0.229	25.28	54.28	25.28	0.608

A.23 Tar Island Dyke (1968 Tokachi-Oki Earthquake, M=7.9)

A.23.1 Brief Summary of the Case History

Tar Island Dyke was located in Alberta, Canada, and the exact date of the failure was reported as August 23, 1974. The fundamental reason behind the failure was reported as static flow liquefaction. The type of the structure can be classified as a tailings dike constructed by water sedimentation method, and the maximum slope height is reported as ~ 14 m. Mittal and Hardy (1977), Plewes et al. (1989) and Konrad and Watts (1995) are taken into account as the main sources of references. Olson (2001), Wang (2003) and Weber (2015) also studied this case history during their back-analyses of liquefaction failure case histories.

A.23.2 Site Geology and Critical Cross-section

Figure A.23.1 and Figure A.23.2 show the soil stratigraphy and pre-failure and post-failure cross-sections of the case structure. It is decided that the idealized soil profile consists of four soil layers namely non-liquefied zone, liquefied zone, shell material, and foundation. The parts of the tailings dike remaining above and below the water table level at the time of failure are classified as non-liquefied zone and liquefied zone, respectively. The compacted sand zone existing on the beach sand layer is defined as shell material. The layer underlying the tailings dyke is classified as foundation.

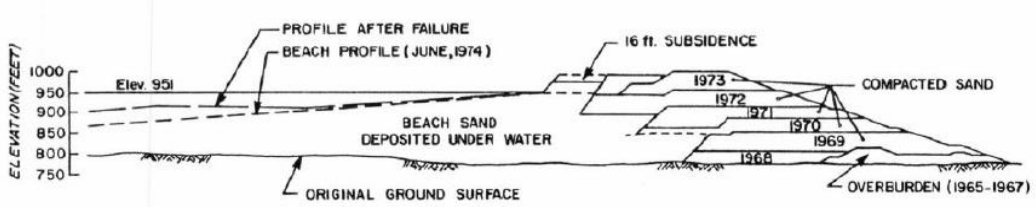

Figure A.23.1. Soil stratigraphy and pre-failure cross-section of the Tar Island Dyke (Plewes et al., 1989)

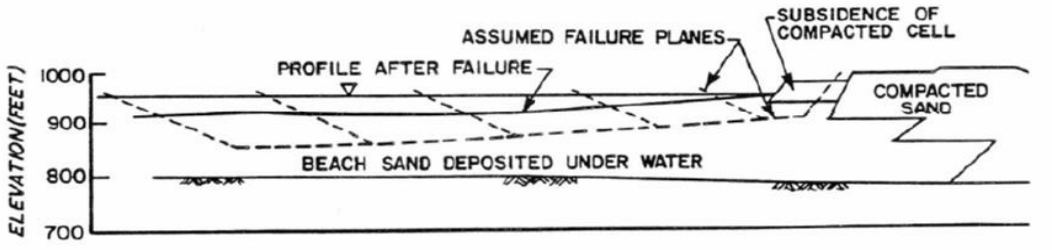

Figure A.23.2. Soil stratigraphy and pre-failure and post-failure cross-sections of the Tar Island Dyke (Plewes et al., 1989)

A.23.3 Evaluation of Material Properties

Since the grain size distribution curve of the case history was not reported by the main sources of references or other residual strength-related studies, mean grain size (D_{50}), fines content (FC) and coefficient of uniformity (C_u) values are estimated based on the documented representative values in those references, if available. Furthermore, this case is one of the two cases that some information was reported about the angularity of soil particles. Thus, the angularity parameters are also estimated based on the reported information.

Mean grain size (D_{50}): The exact value of the mean grain size was reported as D_{50} = 0.150 mm in Olson (2001). Hence, the representative D_{50} value is also taken as 0.150 mm in this study.

Fines content (FC): A range of 10-15% was reported for fines content by Mittal and Hardy (1977), Plewes et al. (1989), and Olson (2001). Therefore, the average value of this range, FC = 12.5%, is taken as the representative fines content value in this study. This value is also compatible with the one recommended by Gutierrez et al. (2016), which is FC=17.5%.

Coefficient of uniformity (C_u): Since no coefficient of uniformity value was reported by the main sources of references or other relative studies, no value has been set for this parameter.

Roundness (R): The liquefied zone was reported as consisting of mainly subangular materials in the main sources of references. Referring to common roundness values of subangular materials in literature, R = 0.30 is estimated for this case in this study.

Sphericity (S): Since no sphericity value was reported by the main sources of references or other studies, no value has been set for this parameter for the evaluation of limit void ratios and void ratio ranges. However, S = 0.60 is taken approximately as a representative value for the evaluation of liquefaction state friction angle.

Unit weight (γ_{dry} and γ_{sat}): As the results are not sensitive to unit weight, the dry and saturated unit weights of non-liquefied and liquefied zones are assigned as 18.1 kN/m^3 and 18.9 kN/m^3, respectively. For shell material and foundation layers, the unit weights are defined as 19.6 kN/m^3. All these values are evaluated accordingly to be compatible with Olson (2001) and Weber (2015).

A.23.4 Sub-sectioning of the Cross-section and Failure Plane

The exact locations of the SPT and CPT boreholes were not known for this case history. Therefore, the sub-sectioning is made based on imaginary boreholes assigned on the cross-section. These imaginary boreholes are defined with respect to changes in effective vertical stresses and inclination angles of the failure plane. Two different initial failure planes are considered based on the information available on the main sources of references about the failure mode as presented in Figure A.23.3. While boreholes Small-S1 and Small-S2 sub-divide the smaller failure plane into smaller pieces, Large-S1 and Large-S2 split the larger failure plane.

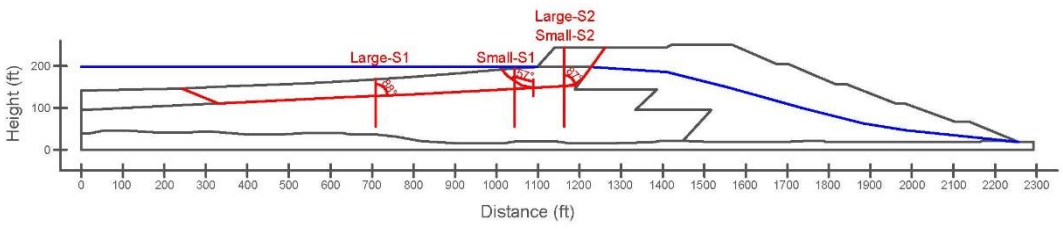

Figure A.23.3. Sub-sectioning of the cross-section and failure plane for Tar Island Dyke

The territory lengths (L_i) and inclinations (α_i) (positive sign for CCW direction) of the failure planes are evaluated as given in Table A.23.1 for each sub-section.

Table A.23.1 Sub-sections with their corresponding failure plane lengths and inclinations for Tar Island Dyke

Case History	Section	Failure plane length, L_i (m)	Total failure plane length, L_t (m)	Failure plane inclination, α_i (degrees)
Tar Island Dyke	Large-S1	260.18	308.55	2
	Large-S2	48.37		3
	Small-S1	27.62	75.99	-33
	Small-S2	48.37		3

A.23.5 Elastic Modeling and Stress Rotation

All stress components are evaluated linear elastically at the points where boreholes and failure plane intersect in Figure A.23.3. The initial and deformed shape of the cross-section are presented in Figure A.23.4 and Figure A.23.5, respectively. All lengths are given in meters.

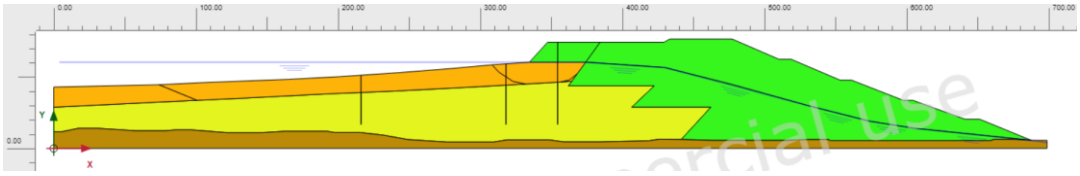

Figure A.23.4. Initial cross-section used in linear elastic modeling of Tar Island Dyke

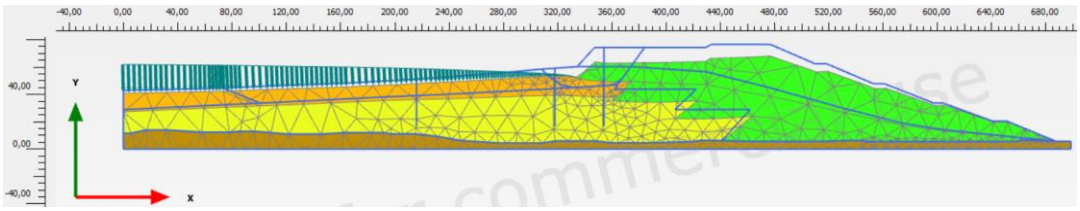

Figure A.23.5. Deformed cross-section obtained after linear elastic modeling of Tar Island Dyke

During the elastic modeling process in PLAXIS 2D Ultimate Connect Edition V22.00.00.1733 software, the Poisson's ratio values of the non-liquefied zone, liquefied zone, shell material, and foundation are defined as 0.30, 0.33, 0.30, and 0.30, respectively. The elastic modulus values of the same layers, on the other hand, are estimated as 10 MPa, 5 MPa, 20 MPa, and 30 MPa, respectively.

The effective normal (σ'_N) and shear (τ_{static}) stresses acting on the inclined failure plane are evaluated with corresponding Mohr's circles. The corresponding Mohr's circles and the effective stress components of the sub-sections are presented in Figure A.23.6 and Table A.23.2, respectively. All stresses are given in kilopascals.

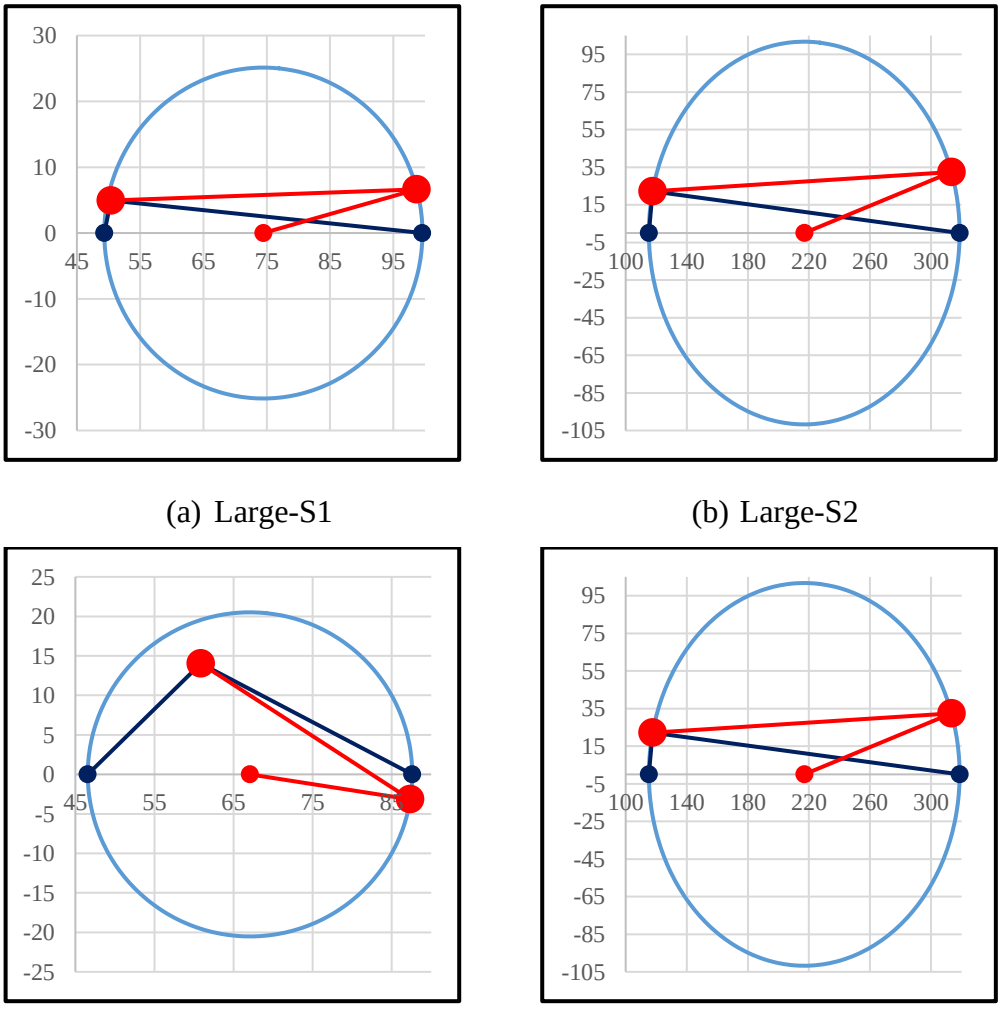

(a) Large-S1 (b) Large-S2

(c) Small-S1 (d) Small-S2

Figure A.23.6. Mohr's circles for Tar Island Dyke

Table A.23.2 Evaluated stress components for Tar Island Dyke

Case History	Section	σ'_1 (kPa)	σ'_2 (kPa)	σ'_3 (kPa)	p_0' (kPa)	q (kPa)	σ'_N (kPa)	τ_{static} (kPa)	$\lvert\tau_{static}\rvert$ (kPa)
Tar Island Dyke	Large-S1	99.6	49.9	49.3	66.3	50.0	98.7	6.6	6.6
	Large-S2	318.7	143.2	115.2	192.4	191.0	313.4	32.4	32.4
	Small-S1	87.6	53.5	46.6	62.6	38.0	87.4	-3.2	3.2
	Small-S2	318.7	143.2	115.2	192.4	191.0	313.4	32.4	32.4

A.23.6 Evaluation of SPT Resistance

The exact locations of the SPT and CPT boreholes were not documented for this case. Therefore, imaginary boreholes are assigned along the cross-section as shown in Figure A.23.3. SPT and CPT data used for this case is presented in Figure A.23.7.

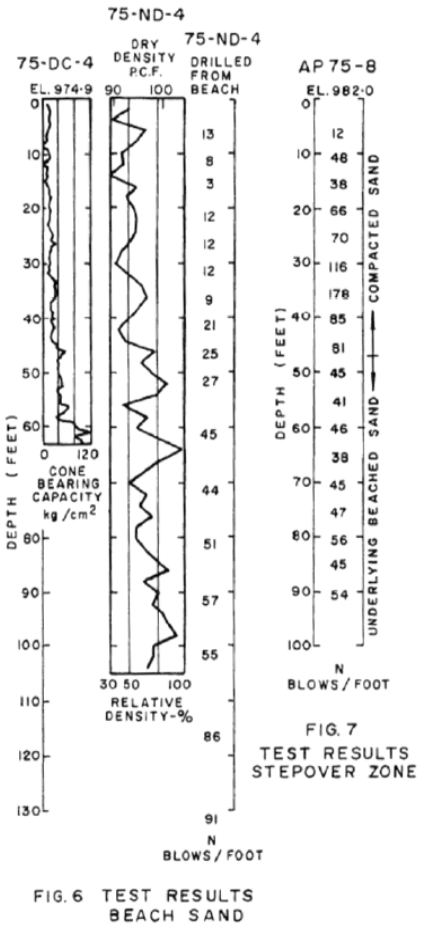

Figure A.23.7. SPT and CPT data for Tar Island Dyke (Mittal and Hardy, 1977)

Both SPT and CPT results are taken into account during the evaluation of SPT resistances of this case history. For SPT results, the correction factors for nonstandardized sampler configuration (C_S), borehole diameter (C_B), and energy efficiency (C_E) are taken as 1.0 since no reliable information related to these coefficients was reported in any of the sources. The short rod length correction factors (C_R), on the other hand, are evaluated with the methods and relationships explained in Section 3.5. For CPT results, cone tip resistances are converted to raw SPT-N and N_{60} values by using the correlations proposed by Ishihara et al. (1990) and Kulhawy and Mayne (1990), respectively, as also explained in Section 3.5. The overburden stress correction factors (C_N) are then evaluated for both SPTs and CPTs based on the effective vertical stresses estimated at the point of penetration for each recording, and average values are documented for simplicity. The fines content correction factors (C_{fines}) are also evaluated for both tests with the methods and relationships explained in Section 3.5. In the end, the arithmetic mean of the SPT resistances obtained from both tests are considered as the representative SPT resistances of the sub-sections. Accordingly, the correction factors and SPT resistances are estimated as given in Table A.23.3.

Table A.23.3 Evaluated SPT-N resistances for Tar Island Dyke

Case History	Section	C_N	C_B	C_R	C_S	C_E	C_{fines}	N	N_{60}	$(N_1)_{60}$	$(N_1)_{60,cs}$	
Tar Island Dyke	Large-S1	1.15	1.0	0.96	1.0	1.00	1.11	10.56	10.11	11.05	12.23	12.23
	Large-S2	1.15	1.0	0.96	1.0	1.00	1.11	10.56	10.11	11.05	12.23	
	Small-S1	1.15	1.0	0.96	1.0	1.00	1.11	10.56	10.11	11.05	12.23	12.23
	Small-S2	1.15	1.0	0.96	1.0	1.00	1.11	10.56	10.11	11.05	12.23	

A.23.7 Evaluation of Limit Void Ratios, Void Ratio Ranges, Relative Densities and Initial Void Ratios

Since mean grain size (D_{50}), fines content (FC), and roundness (R) information were available among the required material properties for the void ratio prediction models, the arithmetic means of the limit void ratios (e_{min} and e_{max}) evaluated by Model 1, Model 2 and Model 3 are considered as the representative values. The e_{max} value is slightly modified then with respect to the construction method of the case history for each prediction model.

Since the fines content value is evaluated as 12.5%, which is less than 15%, it is judged that the soil of interest consists of sand type of soils. Therefore, the arithmetic mean of the relative densities evaluated by the correlations recommended by Kulhawy and Mayne (1990) and Cubrinovski and Ishihara (1999) is taken as the overall relative density of the soil. Based on these relative densities and limit void ratios, the initial void ratios (e_0) corresponding to approximately 1 kPa confining stress are estimated referring to Equation 3-68. Accordingly, the limit void ratios, void ratio ranges (without any modification for the construction method), in-situ relative densities, and initial void ratios are estimated as given in Table A.23.4.

Table A.23.4 Evaluated limit void ratios, void ratio ranges, in-situ relative densities, and initial void ratios for Tar Island Dyke

Case History	Section	e_{min}	e_{max}	e_{max}-e_{min}	$RD_{C\&I}$ (%)	$RD_{K\&M}$ (%)	$RD_{overall}$ (%)	e_0
Tar Island Dyke	Large-S1	0.552	0.931	0.380	42.66	52.96	47.81	0.750
	Large-S2	0.552	0.931	0.380	42.66	52.96	47.81	0.750
	Small-S1	0.552	0.931	0.380	42.66	52.96	47.81	0.750
	Small-S2	0.552	0.931	0.380	42.66	52.96	47.81	0.750

A.24 Mochi-Koshi Tailings Dam 1 (1978 Izu-Ohshima Earthquake, M=7.0)

A.24.1 Brief Summary of the Case History

Mochi-Koshi Tailings Dam 1 was located in Izu Peninsula, Japan, and the exact date of the failure was reported as January 14, 1978. The fundamental reason behind the failure was reported as the 1978 Izu-Ohshima Earthquake (M=7.0). The type of the structure can be classified as a tailings dam constructed by water sedimentation method, and the maximum slope height is reported as ~ 14 m. Ishihara (1984) and Ishihara et al. (1990) are taken into account as the main sources of references. Olson (2001), Wang (2003) and Weber (2015) also studied this case history during their back-analyses of liquefaction failure case histories.

A.24.2 Site Geology and Critical Cross-section

Figure A.24.1 and Figure A.24.2 show the soil stratigraphy and pre-failure and post-failure cross-sections of the case structure. It is decided that the idealized soil profile consists of three soil layers namely liquefied zone, volcanic soil starter dike, and volcanic rock foundation. The trapezoidal volcanic soil zones are defined as volcanic soil starter dike, and the soil located near this starter dike is classified as liquefied zone. The layer underlying the tailings dam is classified as volcanic rock foundation.

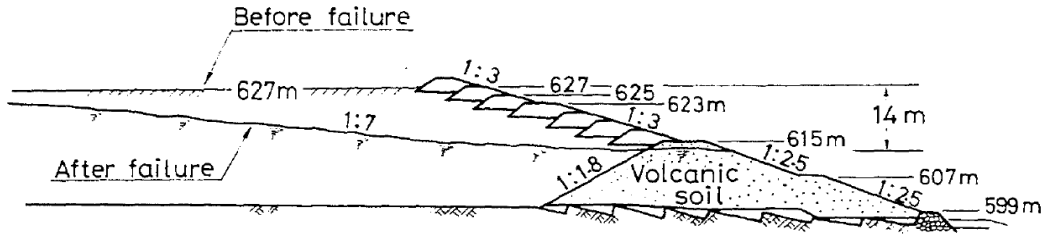

Figure A.24.1. Soil stratigraphy and pre-failure and post-failure cross-sections of the Mochi-Koshi Tailings Dam 1 (Ishihara, 1984)

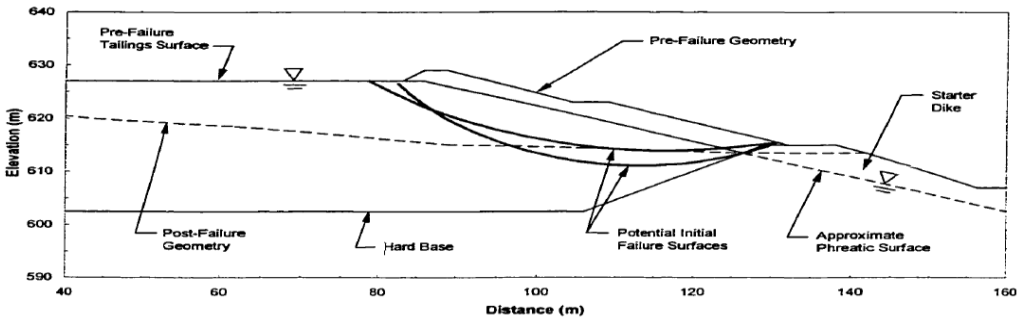

Figure A.24.2. Pre-failure and post-failure cross-sections of the Mochi-Koshi Tailings Dam 1 (Olson, 2001)

A.24.3 Evaluation of Material Properties

Since the grain size distribution curves of the case history were reported by the main sources of references as given in Figure A.24.3 and Figure A.24.4, mean grain size (D_{50}), fines content (FC) and coefficient of uniformity (C_u) values are evaluated based on these curves. Two different but similar GSD curves were documented in Ishihara (1984) and Okusa and Anma (1980); thus, the arithmetic mean of the values obtained from these two graphs are taken as the representative values.

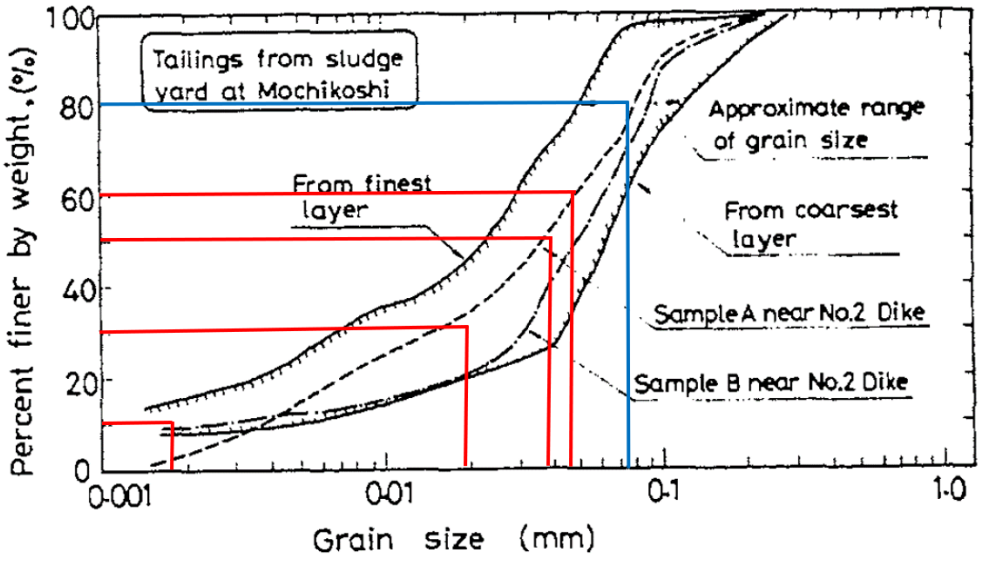

Figure A.24.3. Grain size distribution curve of the Mochi-Koshi Tailings Dam 1 (Ishihara, 1984)

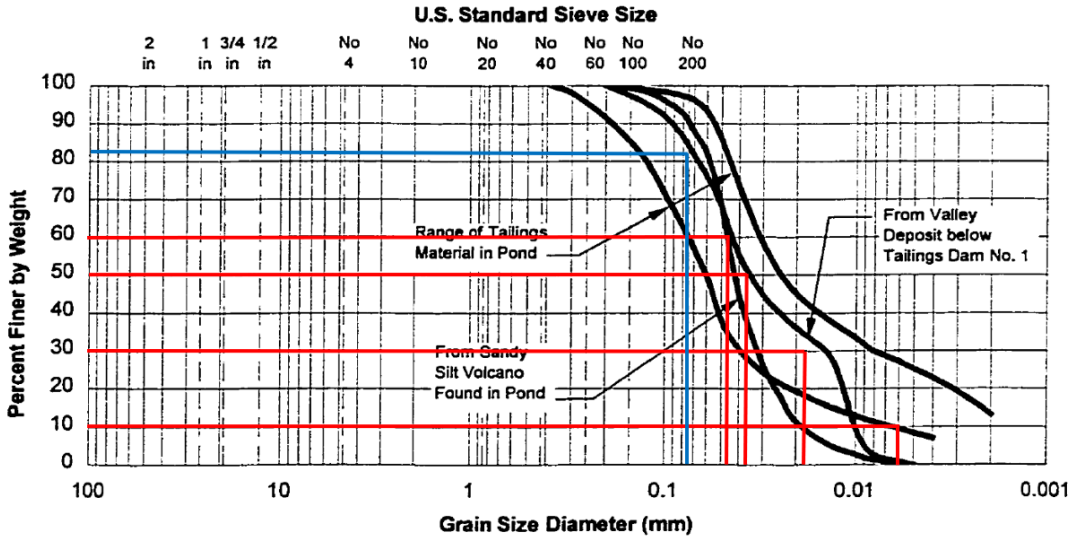

Figure A.24.4. Grain size distribution curve of the Mochi-Koshi Tailings Dam 1 (Okusa and Anma, 1980)

Mean grain size (D_{50}): D_{50} = 0.038 mm is evaluated representatively for the liquefied zone based on the grain size distribution curves of the case history. Olson (2001) also suggests 0.038 mm for D_{50} value.

Fines content (FC): FC = 81% is evaluated representatively for the liquefied zone based on the grain size distribution curves of the case history. Olson (2001) and Gutierrez et al. (2016) also suggest FC = 81% and FC = 77.5%, respectively.

Coefficient of uniformity (C_u): D_{10} and D_{60} values are evaluated as 0.0039 mm and 0.047 mm, respectively, based on the grain size distribution curves of the case history. Therefore, the uniformity coefficient is estimated as $C_u = D_{60}/D_{10}$ = 0.047/0.0039 = 16.97, which indicates well-graded soil.

Roundness (R): Since no roundness value was reported by the main sources of references or other studies, no value has been set for this parameter for the evaluation of limit void ratios and void ratio ranges. However, R = 0.50 is taken approximately as a representative value for the evaluation of liquefaction state friction angle.

Sphericity (S): Since no sphericity value was reported by the main sources of references or other studies, no value has been set for this parameter for the evaluation

of limit void ratios and void ratio ranges. However, S = 0.60 is taken approximately as a representative value for the evaluation of liquefaction state friction angle.

Unit weight (γ_{dry} and γ_{sat}): As the results are not sensitive to unit weight, the dry and saturated unit weights of liquefied zone are assigned as 17.3 kN/m^3 and 19.6 kN/m^3, respectively. For volcanic soil starter dike and volcanic rock foundation, the unit weights are defined as 18.5 kN/m^3 and 19.6 kN/m^3, respectively. All these values are evaluated accordingly to be compatible with Olson (2001) and Weber (2015).

A.24.4 Sub-sectioning of the Cross-section and Failure Plane

The exact locations of the SPT boreholes were not known for this case history. Therefore, the sub-sectioning is made based on imaginary boreholes assigned on the cross-section. These imaginary boreholes are defined with respect to changes in effective vertical stresses and inclination angles of the failure plane. Accordingly, three sub-sections are assigned for the liquefied zone as presented in Figure A.24.5.

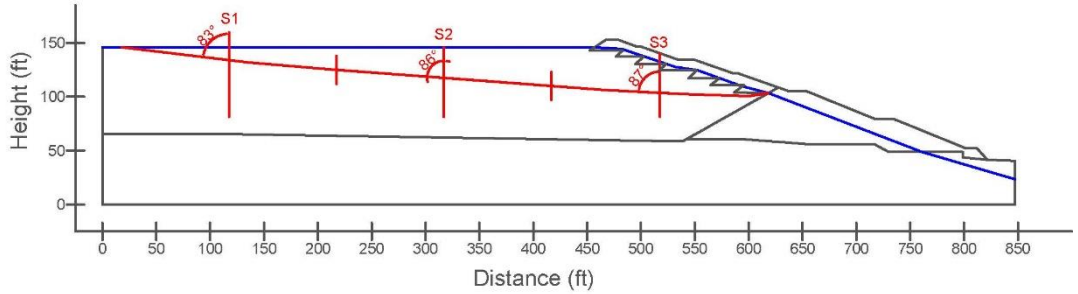

Figure A.24.5. Sub-sectioning of the cross-section and failure plane for Mochi-Koshi Tailings Dam 1

The territory lengths (L_i) and inclinations (α_i) (positive sign for CCW direction) of the failure plane are evaluated as given in Table A.24.1 for each sub-section.

Table A.24.1 Sub-sections with their corresponding failure plane lengths and inclinations for Mochi-Koshi Tailings Dam 1

Case History	Section	Failure plane length, L_i (m)	Total failure plane length, L_t (m)	Failure plane inclination, α_i (degrees)
Mochi-Koshi Tailings Dam 1	S1	61.15	183.68	-7
	S2	60.98		-4
	S3	61.55		-3

A.24.5 Elastic Modeling and Stress Rotation

All stress components are evaluated linear elastically at the points where boreholes and failure plane intersect in Figure A.24.5. The initial and deformed shape of the cross-section are presented in Figure A.24.6 and Figure A.24.7, respectively. All lengths are given in meters.

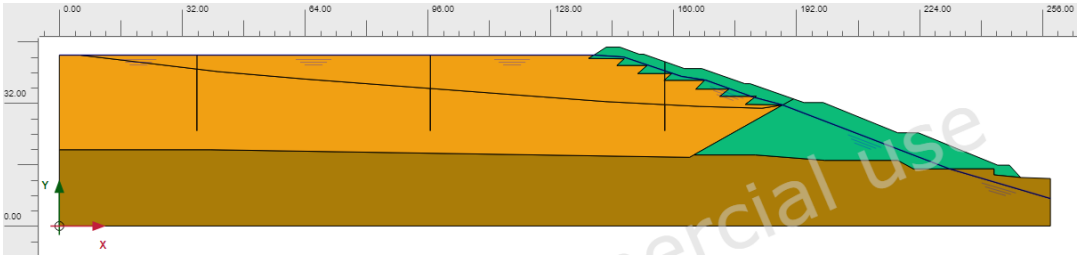

Figure A.24.6. Initial cross-section used in linear elastic modeling of Mochi-Koshi Tailings Dam 1

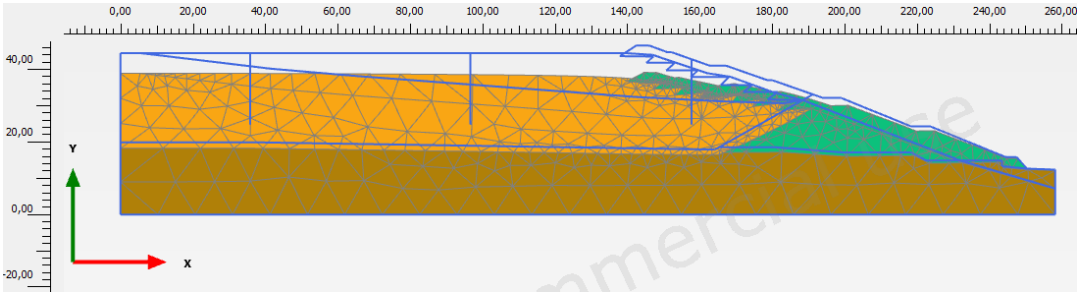

Figure A.24.7. Deformed cross-section obtained after linear elastic modeling of Mochi-Koshi Tailings Dam 1

During the elastic modeling process in PLAXIS 2D Ultimate Connect Edition V22.00.00.1733 software, the Poisson's ratio values of the liquefied zone, volcanic soil starter dike, and volcanic rock foundation are defined as 0.33, 0.30, and 0.30, respectively. The elastic modulus values of the same layers, on the other hand, are estimated as 5 MPa, 10 MPa, and 30 MPa, respectively.

The effective normal (σ'_N) and shear (τ_{static}) stresses acting on the inclined failure plane are evaluated with corresponding Mohr's circles. The corresponding Mohr's circles and the effective stress components of the sub-sections are presented in Figure A.24.8 and Table A.24.2, respectively. All stresses are given in kilopascals.

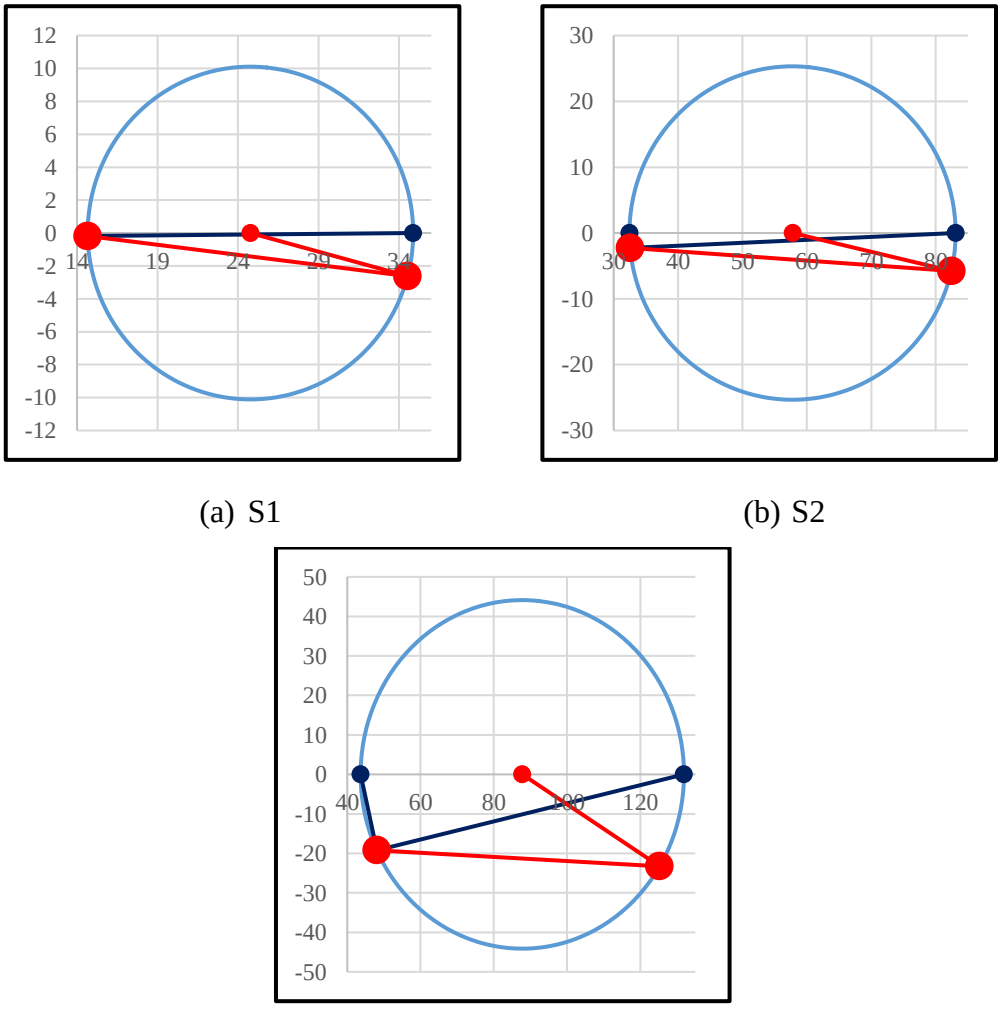

(a) S1 (b) S2

(c) S3

Figure A.24.8. Mohr's circles for Mochi-Koshi Tailings Dam 1

Table A.24.2 Evaluated stress components for Mochi-Koshi Tailings Dam 1

Case History	Section	σ'_1 (kPa)	σ'_2 (kPa)	σ'_3 (kPa)	p_0' (kPa)	q (kPa)	σ'_N (kPa)	τ_{static} (kPa)	$\lvert\tau_{static}\rvert$ (kPa)
Mochi-Koshi Tailings Dam 1	S1	34.9	16.3	14.7	22.0	19.4	34.5	-2.6	2.6
	S2	83.1	38.1	32.5	51.2	48.1	82.4	-5.8	5.8
	S3	131.9	57.9	43.7	77.8	82.0	125.3	-23.3	23.3

A.24.6 Evaluation of SPT Resistance

The exact locations of the SPT boreholes were not documented for this case history. Therefore, imaginary boreholes are assigned along the cross-section as shown in Figure A.24.5. SPT data used for this case history is presented in Figure A.24.9.

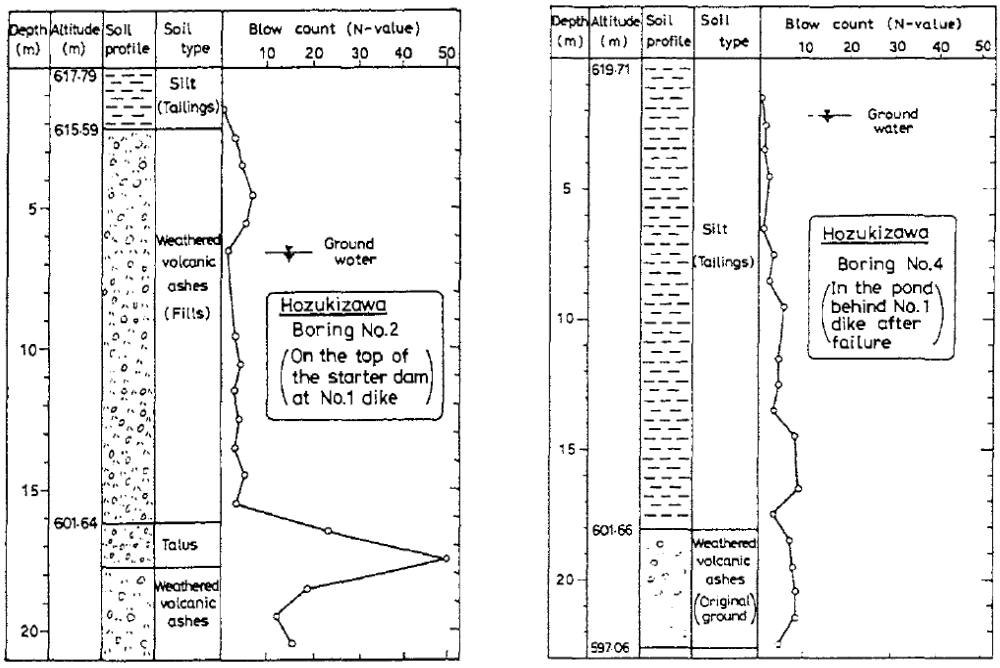

(a) Boring No.2 (b) Boring No.4

Figure A.24.9. SPT boreholes for Mochi-Koshi Tailings Dam 1 (Ishihara, 1984)

The correction factors for nonstandardized sampler configuration (C_S), borehole diameter (C_B), and energy efficiency (C_E) are taken as 1.0 since no reliable information related to these coefficients was reported in any of the sources. The short rod length (C_R) and fines content correction factors (C_{fines}) are evaluated with the

methods and relationships explained in Section 3.5. The overburden stress correction factors (C_N) are evaluated based on the effective vertical stresses estimated at the point of penetration for each recording, and average values are documented for simplicity. Accordingly, the correction factors and SPT resistances are estimated as given in Table A.24.3.

Table A.24.3 Evaluated SPT-N resistances for Mochi-Koshi Tailings Dam 1

Case History	Section	C_N	C_B	C_R	C_S	C_E	C_{fines}	N	N_{60}	$(N_1)_{60}$	$(N_1)_{60,cs}$	
Mochi-Koshi Tailings Dam 1	S1	1.15	1.0	0.99	1.0	1.00	1.57	4.26	4.21	4.04	6.36	6.36
	S2	1.15	1.0	0.99	1.0	1.00	1.57	4.26	4.21	4.04	6.36	
	S3	1.15	1.0	0.99	1.0	1.00	1.57	4.26	4.21	4.04	6.36	

A.24.7 Evaluation of Limit Void Ratios, Void Ratio Ranges, Relative Densities and Initial Void Ratios

Since mean grain size (D_{50}), fines content (FC), and coefficient of uniformity (C_u) information were available among the required material properties for the void ratio prediction models, the arithmetic means of the limit void ratios (e_{min} and e_{max}) evaluated by Model 8 and Model 9 are considered as the representative values. The e_{max} value is slightly modified then with respect to the construction method of the case history for each prediction model.

Since the fines content value is evaluated as 81%, which is greater than 15%, it is judged that the soil of interest consists of silty soils. Therefore, the relative densities evaluated by the correlation recommended by Cubrinovski and Ishihara (1999) are directly taken as the representative relative densities of the soils. Based on these relative densities and limit void ratios, the initial void ratios (e_0) corresponding to approximately 1 kPa confining stress are estimated referring to Equation 3-68. Accordingly, the limit void ratios, void ratio ranges (without any modification for the construction method), in-situ relative densities, and initial void ratios are estimated as given in Table A.24.4.

Table A.24.4 Evaluated limit void ratios, void ratio ranges, in-situ relative densities, and initial void ratios for Mochi-Koshi Tailings Dam 1

Case History	Section	e_{min}	e_{max}	e_{max}-e_{min}	$RD_{C\&I}$ (%)	$RD_{K\&M}$ (%)	$RD_{overall}$ (%)	e_0
Mochi-Koshi Tailings Dam 1	S1	0.447	0.726	0.279	19.87	40.64	19.87	0.670
	S2	0.447	0.726	0.279	19.87	40.64	19.87	0.670
	S3	0.447	0.726	0.279	19.87	40.64	19.87	0.670

A.25 Mochi-Koshi Tailings Dam 2 (1978 Izu-Ohshima Earthquake, M=7.0)

A.25.1 Brief Summary of the Case History

Mochi-Koshi Tailings Dam 2 was located in Izu Peninsula, Japan, and the exact date of the failure was reported as January 15, 1978. The fundamental reason behind the failure was reported as the 1978 Izu-Ohshima Earthquake (M=7.0). The type of the structure can be classified as a tailings dam constructed by water sedimentation method, and the maximum slope height is reported as ~ 10 m. Ishihara (1984) and Ishihara et al. (1990) are taken into account as the main sources of references. Olson (2001), Wang (2003) and Weber (2015) also studied this case history during their back-analyses of liquefaction failure case histories.

A.25.2 Site Geology and Critical Cross-section

Figure A.25.1 and Figure A.25.2 show the soil stratigraphy and pre-failure and post-failure cross-sections of the case structure. It is decided that the idealized soil profile consists of three soil layers namely liquefied zone, volcanic soil starter dike, and volcanic rock foundation. The trapezoidal volcanic soil zones are defined as volcanic soil starter dike, and the soil located near this starter dike is classified as liquefied zone. The layer underlying the tailings dam is classified as volcanic rock foundation.

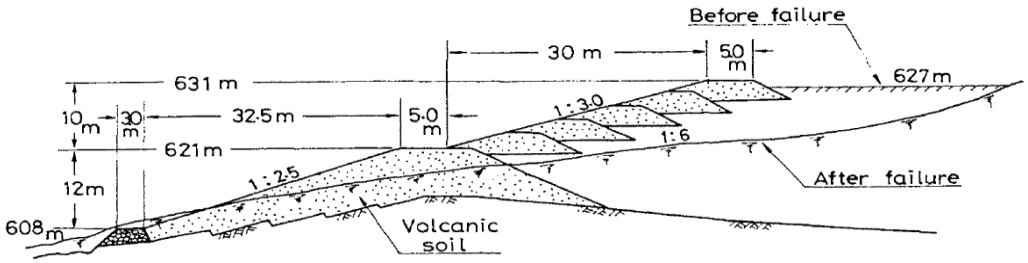

Figure A.25.1. Soil stratigraphy and pre-failure and post-failure cross-sections of the Mochi-Koshi Tailings Dam 2 (Ishihara, 1984)

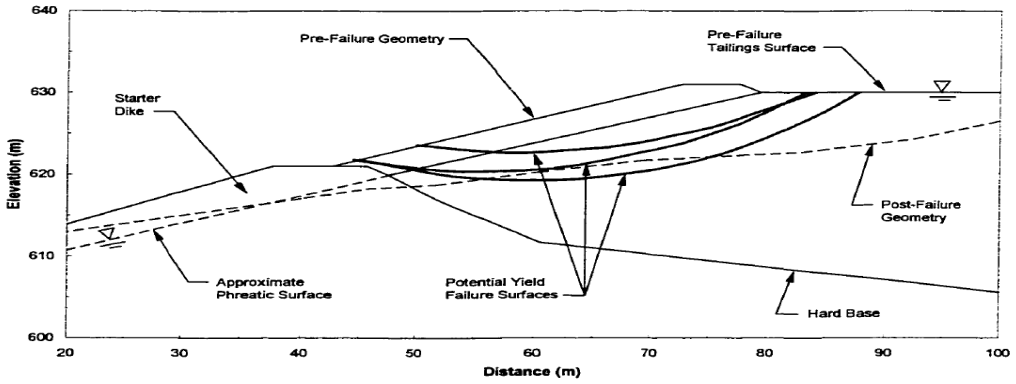

Figure A.25.2. Pre-failure and post-failure cross-sections of the Mochi-Koshi Tailings Dam 2 (Olson, 2001)

A.25.3 Evaluation of Material Properties

Since the grain size distribution curve of the case history was reported by the main sources of references as given in Figure A.25.3, mean grain size (D_{50}), fines content (FC) and coefficient of uniformity (C_u) values are evaluated based on this curve. Two different GSD curves were reported for two different samples near Dam 2 (Sample A and Sample B) in Ishihara (1984); thus, the arithmetic mean of the values obtained from these two curves are taken as the representative values.

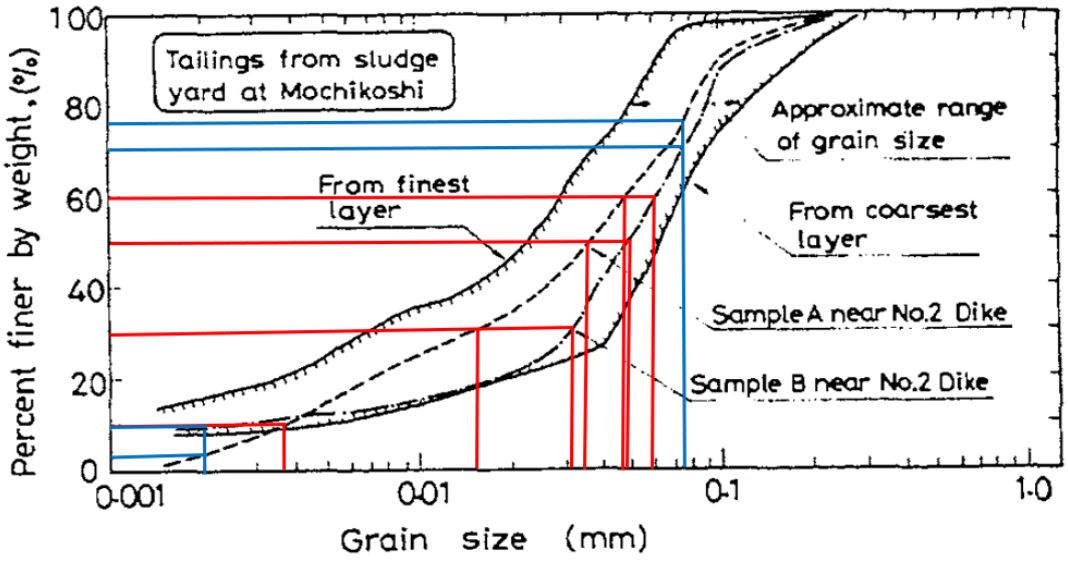

Figure A.25.3. Grain size distribution curve of the Mochi-Koshi Tailings Dam 2 (Ishihara, 1984)

Mean grain size (D_{50}): D_{50} = 0.042 mm is evaluated representatively for the liquefied zone based on the grain size distribution curve of the case history. Olson (2001) also suggests 0.038 mm for D_{50} value.

Fines content (FC): FC = 74% is evaluated representatively for the liquefied zone based on the grain size distribution curves of the case history. Olson (2001) and Gutierrez et al. (2016) also suggest FC = 82% and FC = 77.5%, respectively.

Coefficient of uniformity (C_u): D_{10} and D_{60} values are evaluated as 0.0031 mm and 0.053 mm, respectively, based on the grain size distribution curves of the case history. Therefore, the uniformity coefficient is estimated as $C_u = D_{60}/D_{10}$ = 0.053/0.0031 = 18.15, which indicates well-graded soil.

Roundness (R): Since no roundness value was reported by the main sources of references or other studies, no value has been set for this parameter for the evaluation of limit void ratios and void ratio ranges. However, R = 0.50 is taken approximately as a representative value for the evaluation of liquefaction state friction angle.

Sphericity (S): Since no sphericity value was reported by the main sources of references or other studies, no value has been set for this parameter for the evaluation

of limit void ratios and void ratio ranges. However, S = 0.60 is taken approximately as a representative value for the evaluation of liquefaction state friction angle.

Unit weight (γ_{dry} and γ_{sat}): As the results are not sensitive to unit weight, the dry and saturated unit weights of liquefied zone are assigned as 17.3 kN/m^3 and 19.6 kN/m^3, respectively. For volcanic soil starter dike and volcanic rock foundation, the unit weights are defined as 18.5 kN/m^3 and 19.6 kN/m^3, respectively. All these values are evaluated accordingly to be compatible with Olson (2001) and Weber (2015).

A.25.4 Sub-sectioning of the Cross-section and Failure Plane

The exact locations of the SPT boreholes were not known for this case history. Therefore, the sub-sectioning is made based on imaginary boreholes assigned on the cross-section. These imaginary boreholes are defined with respect to changes in effective vertical stresses and inclination angles of the failure plane. Accordingly, two sub-sections are assigned for the liquefied zone as presented in Figure A.25.4.

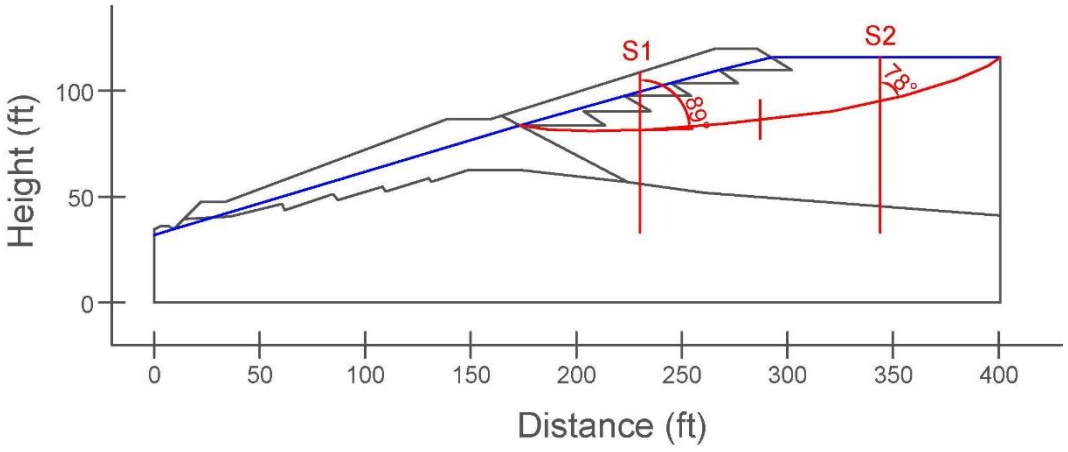

Figure A.25.4. Sub-sectioning of the cross-section and failure plane for Mochi-Koshi Tailings Dam 2

The territory lengths (L_i) and inclinations (α_i) (positive sign for CCW direction) of the failure plane are evaluated as given in Table A.25.1 for each sub-section.

Table A.25.1 Sub-sections with their corresponding failure plane lengths and inclinations for Mochi-Koshi Tailings Dam 2

Case History	Section	Failure plane length, L_i (m)	Total failure plane length, L_t (m)	Failure plane inclination, α_i (degrees)
Mochi-Koshi Tailings Dam 2	S1	34.81	70.94	1
	S2	36.13		12

A.25.5 Elastic Modeling and Stress Rotation

All stress components are evaluated linear elastically at the points where boreholes and failure plane intersect in Figure A.25.4. The initial and deformed shape of the cross-section are presented in Figure A.25.5 and Figure A.25.6, respectively. All lengths are given in meters.

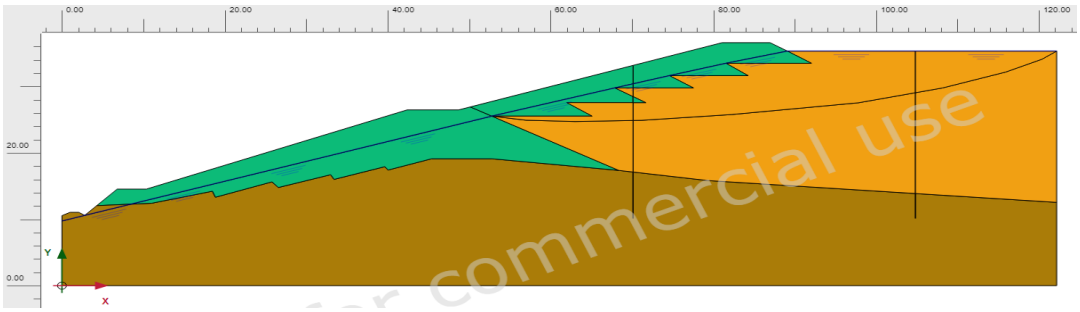

Figure A.25.5. Initial cross-section used in linear elastic modeling of Mochi-Koshi Tailings Dam 2

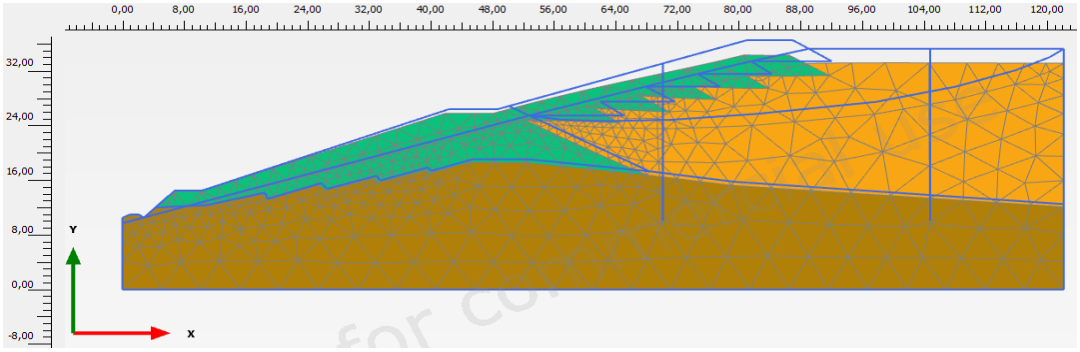

Figure A.25.6. Deformed cross-section obtained after linear elastic modeling of Mochi-Koshi Tailings Dam 2

During the elastic modeling process in PLAXIS 2D Ultimate Connect Edition V22.00.00.1733 software, the Poisson's ratio values of the liquefied zone, volcanic soil starter dike, and volcanic rock foundation are defined as 0.33, 0.30, and 0.30, respectively. The elastic modulus values of the same layers, on the other hand, are estimated as 5 MPa, 10 MPa, and 30 MPa, respectively.

The effective normal (σ'_N) and shear (τ_{static}) stresses acting on the inclined failure plane are evaluated with corresponding Mohr's circles. The corresponding Mohr's circles and the effective stress components of the sub-sections are presented in Figure A.25.7 and Table A.25.2, respectively. All stresses are given in kilopascals.

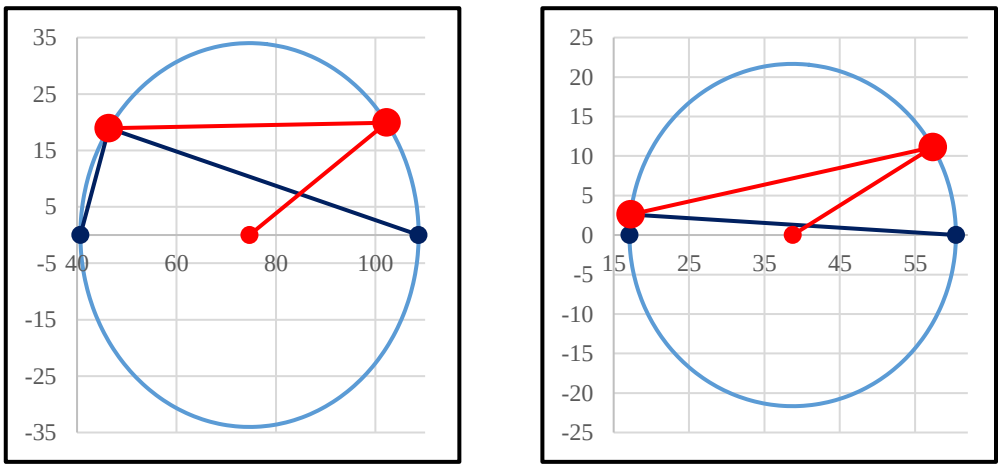

(a) S1 (b) S2

Figure A.25.7. Mohr's circles for Mochi-Koshi Tailings Dam 2

Table A.25.2 Evaluated stress components for Mochi-Koshi Tailings Dam 2

Case History	Section	σ'_1 (kPa)	σ'_2 (kPa)	σ'_3 (kPa)	p_0' (kPa)	q (kPa)	σ'_N (kPa)	τ_{static} (kPa)	$\lvert\tau_{static}\rvert$ (kPa)
Mochi-Koshi Tailings Dam 2	S1	108.7	49.3	40.7	66.2	64.2	102.3	19.9	19.9
	S2	60.4	25.6	17.1	34.4	39.8	57.3	11.1	11.1

A.25.6 Evaluation of SPT Resistance

The exact locations of the SPT boreholes were not documented for this case history. Therefore, imaginary boreholes are assigned along the cross-section as shown in Figure A.25.4. SPT data used for this case history is presented in Figure A.25.8.

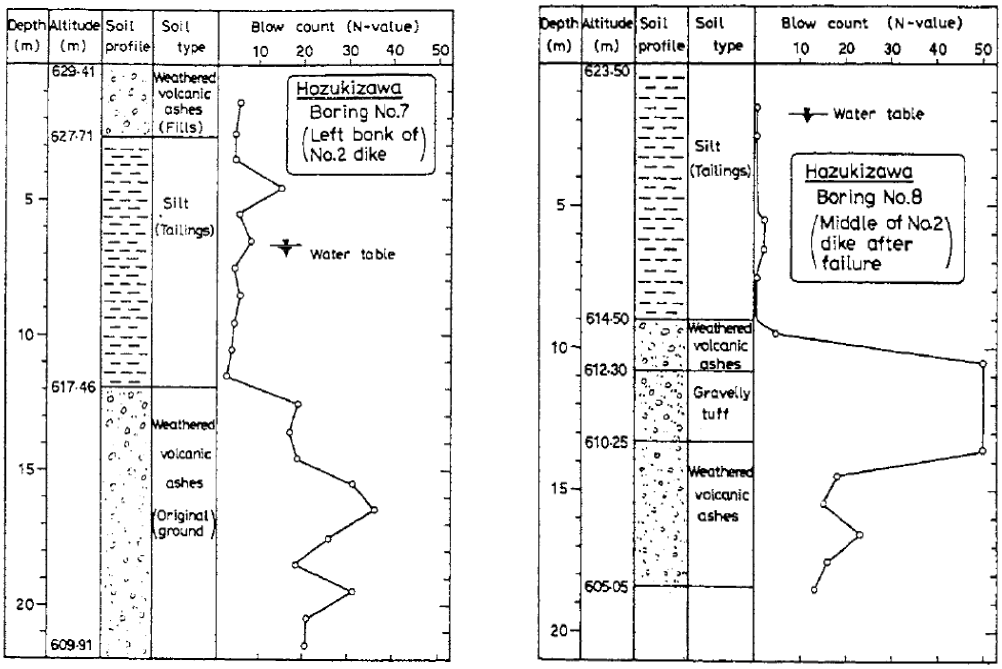

(a) Boring No.7 (b) Boring No.8

Figure A.25.8. SPT boreholes for Mochi-Koshi Tailings Dam 2 (Ishihara, 1984)

The correction factors for nonstandardized sampler configuration (C_S), borehole diameter (C_B), and energy efficiency (C_E) are taken as 1.0 since no reliable information related to these coefficients was reported in any of the sources. The short rod length (C_R) and fines content correction factors (C_{fines}) are evaluated with the methods and relationships explained in Section 3.5. The overburden stress correction factors (C_N) are evaluated based on the effective vertical stresses estimated at the point of penetration for each recording, and average values are documented for simplicity. Accordingly, the correction factors and SPT resistances are estimated as given in Table A.25.3.

Table A.25.3 Evaluated SPT-N resistances for Mochi-Koshi Tailings Dam 2

Case History	Section	C_N	C_B	C_R	C_S	C_E	C_{fines}	N	N_{60}	$(N_1)_{60}$	$(N_1)_{60,cs}$	
Mochi-Koshi Tailings Dam 2	S1	1.19	1.0	0.97	1.0	1.00	1.72	3.06	2.96	3.01	5.18	5.18
	S2	1.19	1.0	0.97	1.0	1.00	1.72	3.06	2.96	3.01	5.18	

A.25.7 Evaluation of Limit Void Ratios, Void Ratio Ranges, Relative Densities and Initial Void Ratios

Since mean grain size (D_{50}), fines content (FC), and coefficient of uniformity (C_u) information were available among the required material properties for the void ratio prediction models, the arithmetic means of the limit void ratios (e_{min} and e_{max}) evaluated by Model 8 and Model 9 are considered as the representative values. The e_{max} value is slightly modified then with respect to the construction method of the case history for each prediction model.

Since the fines content value is evaluated as 74%, which is greater than 15%, it is judged that the soil of interest consists of silty soils. Therefore, the relative densities evaluated by the correlation recommended by Cubrinovski and Ishihara (1999) are directly taken as the representative relative densities of the soils. Based on these relative densities and limit void ratios, the initial void ratios (e_0) corresponding to approximately 1 kPa confining stress are estimated referring to Equation 3-68. Accordingly, the limit void ratios, void ratio ranges (without any modification for the construction method), in-situ relative densities, and initial void ratios are estimated as given in Table A.25.4.

Table A.25.4 Evaluated limit void ratios, void ratio ranges, in-situ relative densities, and initial void ratios for Mochi-Koshi Tailings Dam 2

Case History	Section	e_{min}	e_{max}	e_{max}-e_{min}	$RD_{C\&I}$ (%)	$RD_{K\&M}$ (%)	$RD_{overall}$ (%)	e_0
Mochi-Koshi Tailings Dam 2	S1	0.445	0.718	0.273	16.81	34.39	16.81	0.672
	S2	0.445	0.718	0.273	16.81	34.39	16.81	0.672

A.26 Nerlerk Embankment Slide 1 (1983 Fill Placement)

A.26.1 Brief Summary of the Case History

Nerlerk Embankment Slide 1 was located in Beaufort Sea, Canada, and the exact date of the failure was reported as July 20, 1983. The fundamental reason behind the failure was reported as the fill placement. The type of the structure can be classified as a hydraulic embankment fill, and the maximum slope height is reported as ~ 21 m. Sladen et al. (1985, 1987), Sladen and Hewitt (1989), Mitchell (1984), Been et al. (1987), Rogers et al. (1990), and Konrad (1991) are taken into account as the main sources of references. Olson (2001), Wang (2003) and Weber (2015) also studied this case history during their back-analyses of liquefaction failure case histories.

A.26.2 Site Geology and Critical Cross-section

Figure A.26.1 presents the soil stratigraphy, and Figure A.26.2 and Figure A.26.3 show the pre-failure and post-failure cross-sections of the case structure. It is decided that the idealized soil profile consists of two soil layers namely non-liquefied zone (Ukalerk Sand) and liquefied zone (Nerlerk Sand). While the sand layer on top of the embankment is classified as the liquefied zone (Nerlerk Sand), the layer underlying it is defined as non-liquefied zone (Ukalerk Sand).

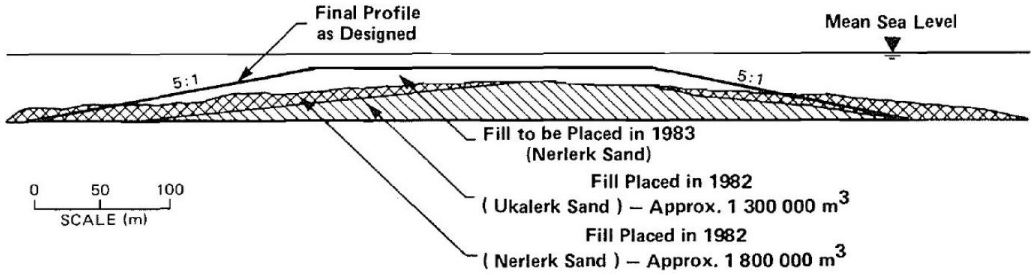

Figure A.26.1. Soil stratigraphy of the Nerlerk Embankment (Sladen et al., 1985)

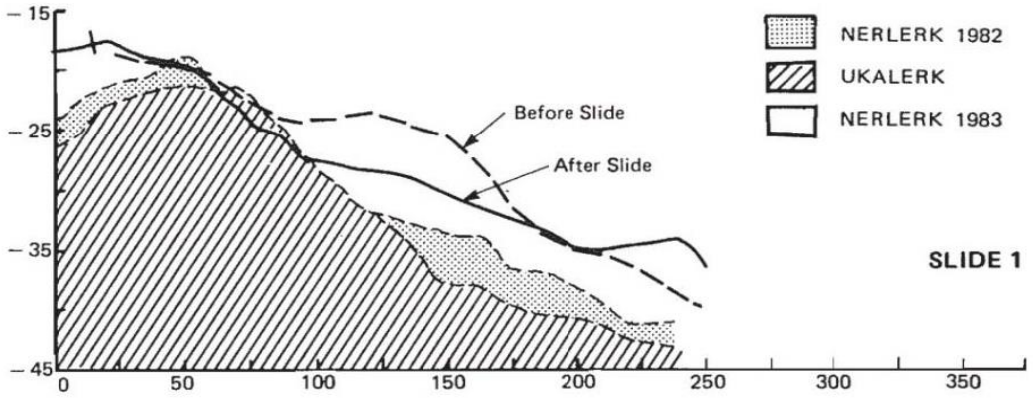

Figure A.26.2. Pre-failure and post-failure cross-sections of the Nerlerk Embankment Slide 1 (Sladen et al., 1985)

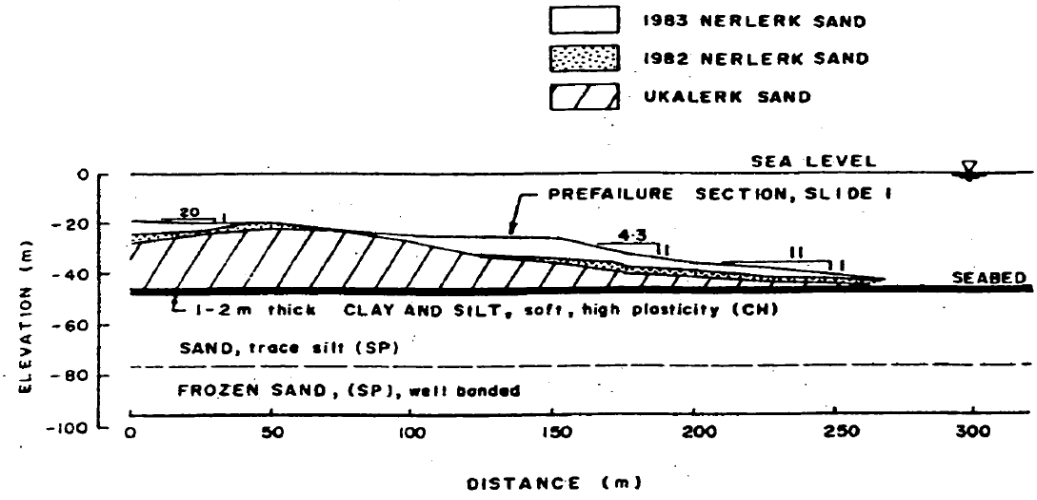

Figure A.26.3. Pre-failure and post-failure cross-sections of the Nerlerk Embankment Slide 1 (Been et al., 1987)

A.26.3 Evaluation of Material Properties

Since the grain size distribution curve of the case history was reported by the main sources of references as given in Figure A.26.4, mean grain size (D_{50}), fines content (FC) and coefficient of uniformity (C_u) values are evaluated based on this curve.

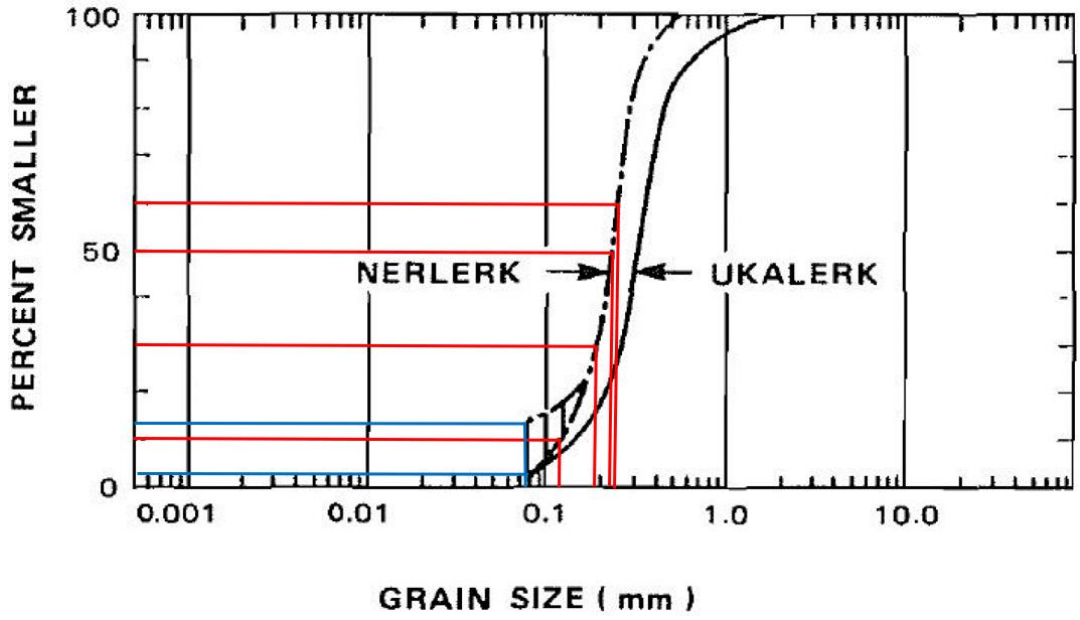

Figure A.26.4. Grain size distribution curve of the Nerlerk Embankment (Sladen et al., 1985)

Mean grain size (D_{50}): D_{50} = 0.220 mm is evaluated representatively based on the grain size distribution curve of the case history. Olson (2001) and Rogers et al. (1990) also suggest 0.220 mm and 0.280 mm for D_{50} value of this case, respectively.

Fines content (FC): FC = 7.5% is evaluated representatively based on the grain size distribution curve of the case history. Olson (2001) recommends a range of 2-12% for fines content of this case. Sladen et al. (1985) and Rogers et al. (1990) also suggest 10% and 3%, respectively, for FC value of this case history.

Coefficient of uniformity (C_u): D_{10} and D_{60} values are evaluated as 0.130 mm and 0.240 mm, respectively, based on the grain size distribution curve of the case history. Therefore, the uniformity coefficient is estimated as $C_u = D_{60}/D_{10} = 0.240/0.130 = 1.85$.

Roundness (R): Since no roundness value was reported by the main sources of references or other studies, no value has been set for this parameter for the evaluation of limit void ratios and void ratio ranges. However, R = 0.50 is taken approximately as a representative value for the evaluation of liquefaction state friction angle.

Sphericity (S): Since no sphericity value was reported by the main sources of references or other studies, no value has been set for this parameter for the evaluation of limit void ratios and void ratio ranges. However, S = 0.60 is taken approximately as a representative value for the evaluation of liquefaction state friction angle.

Unit weight (γ_{dry} and γ_{sat}): As the results are not sensitive to unit weight, the unit weights of both soil layers are assigned as 18.9 kN/m^3, to be compatible with Olson (2001) and Weber (2015).

A.26.4 Sub-sectioning of the Cross-section and Failure Plane

The exact locations of the CPT boreholes were not known for this case history. Therefore, the sub-sectioning is made based on imaginary boreholes assigned on the cross-section. These imaginary boreholes are defined with respect to changes in effective vertical stresses and inclination angles of the failure plane. Accordingly, three sub-sections are assigned for the liquefied zone as presented in Figure A.26.5.

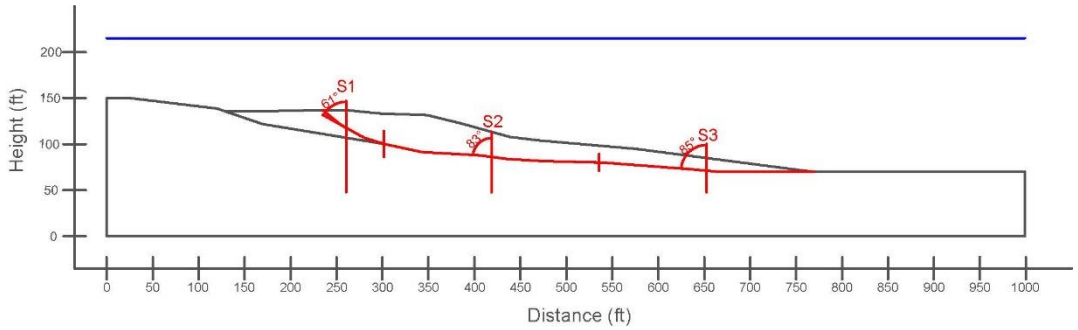

Figure A.26.5. Sub-sectioning of the cross-section and failure plane for Nerlerk Embankment Slide 1

The territory lengths (L_i) and inclinations (α_i) (positive sign for CCW direction) of the failure plane are evaluated as given in Table A.26.1 for each sub-section.

Table A.26.1 Sub-sections with their corresponding failure plane lengths and inclinations for Nerlerk Embankment Slide 1

Case History	Section	Failure plane length, L_i (m)	Total failure plane length, L_t (m)	Failure plane inclination, α_i (degrees)
Nerlerk Embankment Slide 1	S1	23.49	166.67	-29
	S2	71.73		-7
	S3	71.44		-5

A.26.5 Elastic Modeling and Stress Rotation

All stress components are evaluated linear elastically at the points where boreholes and failure plane intersect in Figure A.26.5. The initial and deformed shape of the cross-section are presented in Figure A.26.6 and Figure A.26.7, respectively. All lengths are given in meters.

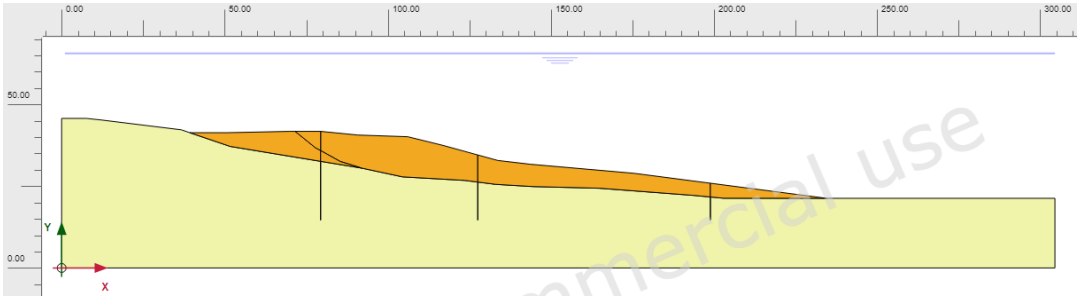

Figure A.26.6. Initial cross-section used in linear elastic modeling of Nerlerk Embankment Slide 1

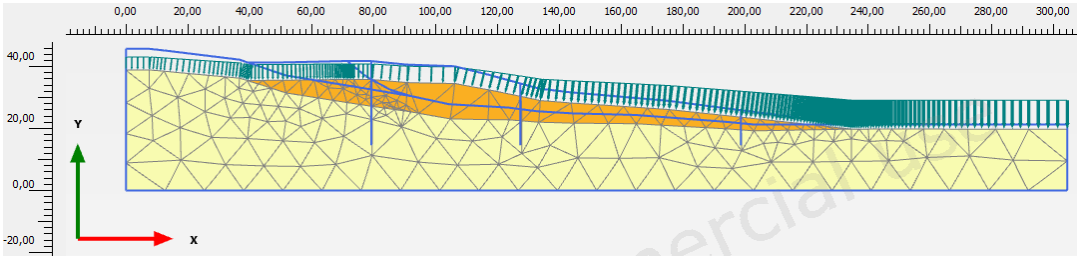

Figure A.26.7. Deformed cross-section obtained after linear elastic modeling of Nerlerk Embankment Slide 1

During the elastic modeling process in PLAXIS 2D Ultimate Connect Edition V22.00.00.1733 software, the Poisson's ratio values of the non-liquefied zone (Ukalerk Sand) and liquefied zone (Nerlerk Sand) are defined as 0.30 and 0.33, respectively. The elastic modulus values of the same layers, on the other hand, are estimated as 10 MPa and 5 MPa, respectively.

The effective normal (σ'_N) and shear (τ_{static}) stresses acting on the inclined failure plane are evaluated with corresponding Mohr's circles. The corresponding Mohr's circles and the effective stress components of the sub-sections are presented in Figure A.26.8 and Table A.26.2, respectively. All stresses are given in kilopascals.

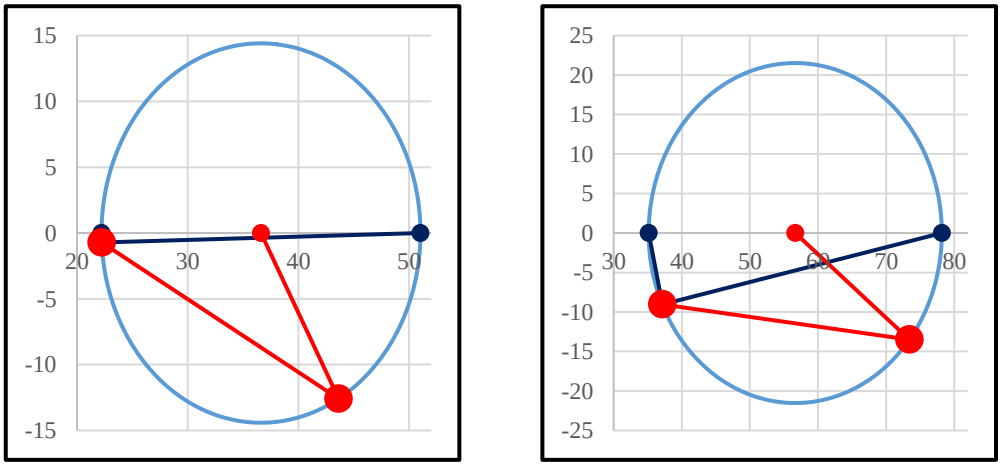

(a) S1 (b) S2

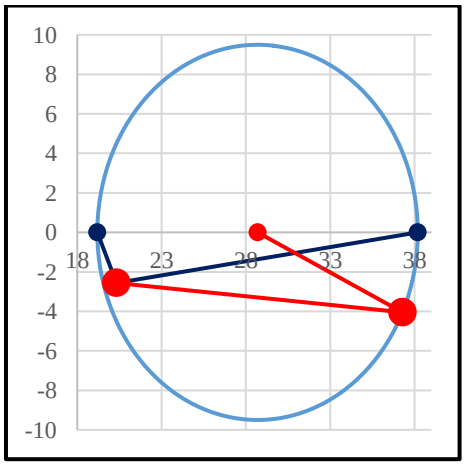

(c) S3

Figure A.26.8. Mohr's circles for Nerlerk Embankment Slide 1

Table A.26.2 Evaluated stress components for Nerlerk Embankment Slide 1

Case History	Section	σ'_1 (kPa)	σ'_2 (kPa)	σ'_3 (kPa)	p_0' (kPa)	q (kPa)	σ'_N (kPa)	τ_{static} (kPa)	$\lvert\tau_{static}\rvert$ (kPa)
Nerlerk Embankment Slide 1	S1	51.0	24.2	22.2	32.5	27.9	43.6	-12.6	12.6
	S2	78.2	37.4	35.1	50.2	42.0	73.4	-13.5	13.5
	S3	38.2	20.0	19.2	25.8	18.6	37.3	-4.0	4.0

A.26.6 Evaluation of SPT Resistance

The exact locations of the CPT boreholes were not documented for this case history. Therefore, imaginary boreholes are assigned along the cross-section as shown in Figure A.26.5. SPT data used for this case history is presented in Figure A.26.9.

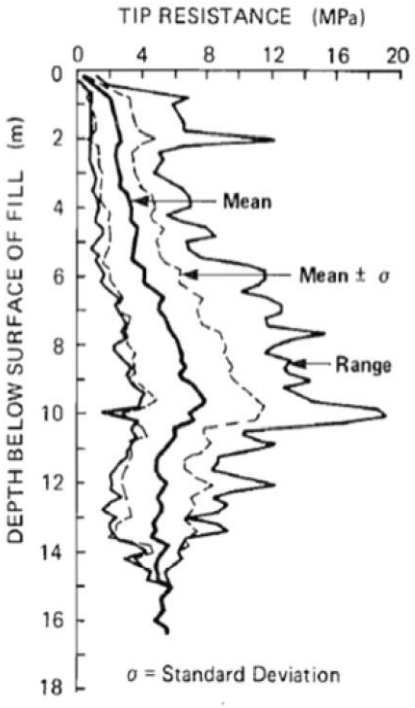

Figure A.26.9. CPT data for Nerlerk Embankment (Sladen et al., 1985)

The CPT cone tip resistances are converted to raw SPT-N and N_{60} values by using the correlations proposed by Ishihara et al. (1990) and Kulhawy and Mayne (1990), respectively, as explained in Section 3.5. Then, the overburden stress correction factors (C_N) are again evaluated to be able to estimate $(N_1)_{60}$ values based on the

effective vertical stresses estimated at the point of penetration for each recording, and average values are documented for simplicity. The fines content correction factors (C_{fines}) are also evaluated with the methods and relationships explained in Section 3.5. Accordingly, the correction factors and SPT resistances are estimated as given in Table A.26.3.

Table A.26.3 Evaluated SPT-N resistances for Nerlerk Embankment Slide 1

Case History	Section	C_N	C_B	C_R	C_S	C_E	C_{fines}	N	N_{60}	$(N_1)_{60}$	$(N_1)_{60,cs}$	
Nerlerk Embankment Slide 1	S1	1.55	-	-	-	-	1.06	6.21	8.68	13.67	14.46	14.46
	S2	1.55	-	-	-	-	1.06	6.21	8.68	13.67	14.46	
	S3	1.55	-	-	-	-	1.06	6.21	8.68	13.67	14.46	

A.26.7 Evaluation of Limit Void Ratios, Void Ratio Ranges, Relative Densities and Initial Void Ratios

Since mean grain size (D_{50}), fines content (FC), and coefficient of uniformity (C_u) information were available among the required material properties for the void ratio prediction models, the arithmetic means of the limit void ratios (e_{min} and e_{max}) evaluated by Model 8 and Model 9 are considered as the representative values. The e_{max} value is slightly modified then with respect to the construction method of the case history for each prediction model.

Since the fines content value is evaluated as 7.5%, which is less than 15%, it is judged that the soil of interest consists of sand type of soils. Therefore, the arithmetic mean of the relative densities evaluated by the correlations recommended by Kulhawy and Mayne (1990) and Cubrinovski and Ishihara (1999) is taken as the overall relative density of the soil. Based on these relative densities and limit void ratios, the initial void ratios (e_0) corresponding to approximately 1 kPa confining stress are estimated referring to Equation 3-68. Accordingly, the limit void ratios, void ratio ranges (without any modification for the construction method), in-situ relative densities, and initial void ratios are estimated as given in Table A.26.4.

Table A.26.4 Evaluated limit void ratios, void ratio ranges, in-situ relative densities, and initial void ratios for Nerlerk Embankment Slide 1

Case History	Section	e_{min}	e_{max}	e_{max}-e_{min}	$RD_{C\&I}$ (%)	$RD_{K\&M}$ (%)	$RD_{overall}$ (%)	e_0
Nerlerk Embankment Slide 1	S1	0.580	0.992	0.411	50.81	56.02	53.41	0.772
	S2	0.580	0.992	0.411	50.81	56.02	53.41	0.772
	S3	0.580	0.992	0.411	50.81	56.02	53.41	0.772

A.27 Nerlerk Embankment Slide 2 (1983 Fill Placement)

A.27.1 Brief Summary of the Case History

Nerlerk Embankment Slide 2 was located in Beaufort Sea, Canada, and the exact date of the failure was reported as July 25, 1983. The fundamental reason behind the failure was reported as the fill placement. The type of the structure can be classified as a hydraulic embankment fill, and the maximum slope height is reported as ~ 19 m. Sladen et al. (1985, 1987), Sladen and Hewitt (1989), Mitchell (1984), Been et al. (1987), Rogers et al. (1990), and Konrad (1991) are taken into account as the main sources of references. Olson (2001), Wang (2003) and Weber (2015) also studied this case history during their back-analyses of liquefaction failure case histories.

A.27.2 Site Geology and Critical Cross-section

Figure A.27.1 presents the soil stratigraphy, and Figure A.27.2 shows the pre-failure and post-failure cross-sections of the case structure. It is decided that the idealized soil profile consists of two soil layers namely non-liquefied zone (Ukalerk Sand) and liquefied zone (Nerlerk Sand). While the sand layer on top of the embankment is classified as the liquefied zone (Nerlerk Sand), the layer underlying it is defined as non-liquefied zone (Ukalerk Sand).

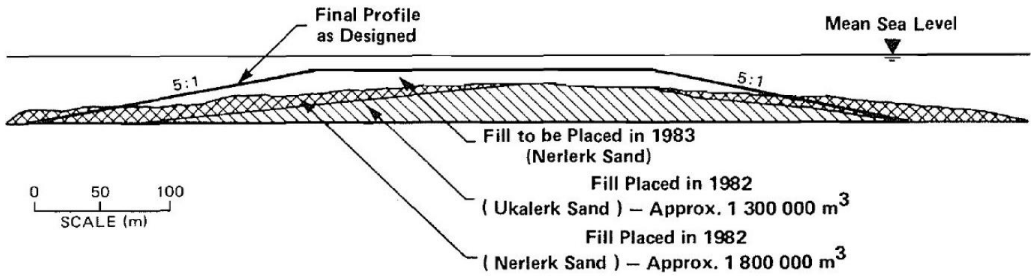

Figure A.27.1. Soil stratigraphy of the Nerlerk Embankment (Sladen et al., 1985)

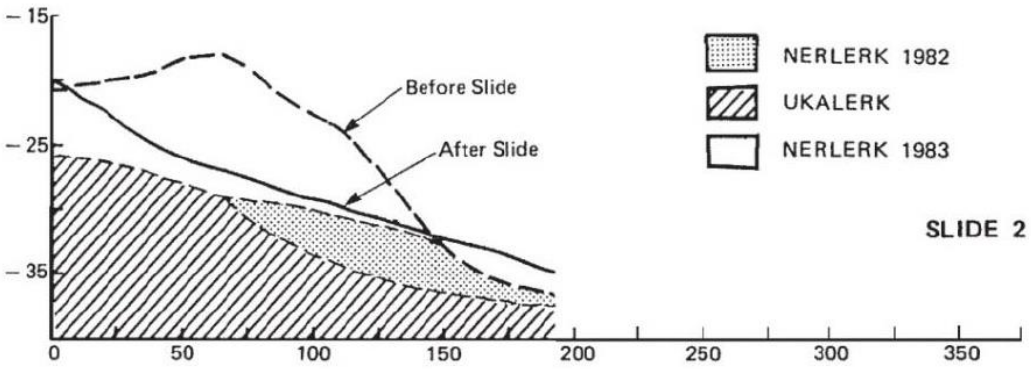

Figure A.27.2. Pre-failure and post-failure cross-sections of the Nerlerk Embankment Slide 2 (Sladen et al., 1985)

A.27.3 Evaluation of Material Properties

Since the grain size distribution curve of the case history was reported by the main sources of references as given in Figure A.27.3, mean grain size (D_{50}), fines content (FC) and coefficient of uniformity (C_u) values are evaluated based on this curve.

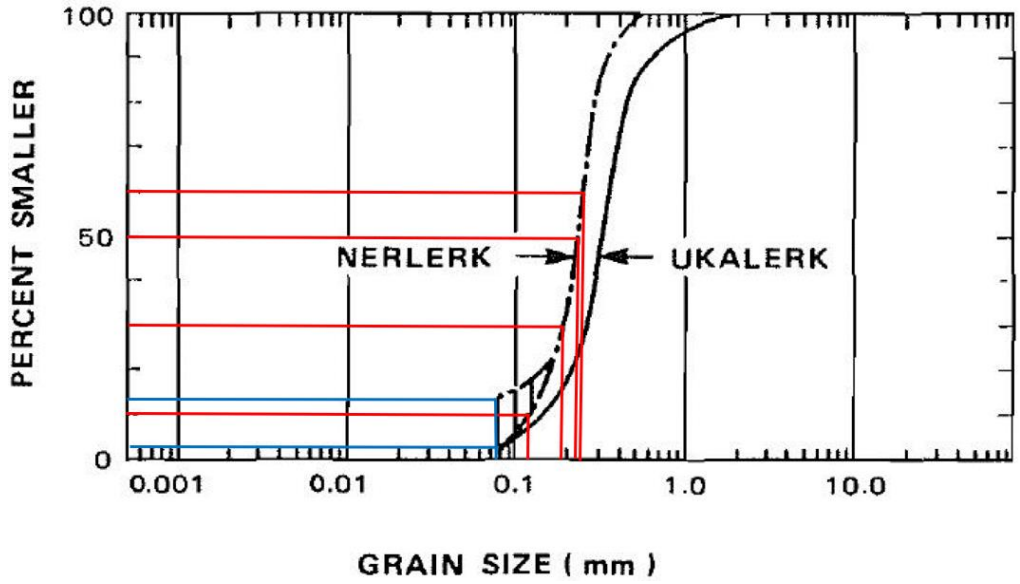

Figure A.27.3. Grain size distribution curve of the Nerlerk Embankment (Sladen et al., 1985)

Mean grain size (D_{50}): D_{50} = 0.220 mm is evaluated representatively based on the grain size distribution curve of the case history. Olson (2001) and Rogers et al. (1990) also suggest 0.220 mm and 0.280 mm for D_{50} value of this case, respectively.

Fines content (FC): FC = 7.5% is evaluated representatively based on the grain size distribution curve of the case history. Olson (2001) recommends a range of 2-12% for fines content of this case. Sladen et al. (1985) and Rogers et al. (1990) also suggest 10% and 3%, respectively, for FC value of this case history.

Coefficient of uniformity (C_u): D_{10} and D_{60} values are evaluated as 0.130 mm and 0.240 mm, respectively, based on the grain size distribution curve. Therefore, the uniformity coefficient is estimated as $C_u = D_{60}/D_{10} = 0.240/0.130 = 1.85$.

Roundness (R): Since no roundness value was reported by the main sources of references or other studies, no value has been set for this parameter for the evaluation of limit void ratios and void ratio ranges. However, R = 0.50 is taken approximately as a representative value for the evaluation of liquefaction state friction angle.

Sphericity (S): Since no sphericity value was reported by the main sources of references or other studies, no value has been set for this parameter for the evaluation

of limit void ratios and void ratio ranges. However, S = 0.60 is taken approximately as a representative value for the evaluation of liquefaction state friction angle.

Unit weight (γ_{dry} and γ_{sat}): As the results are not sensitive to unit weight, the unit weights of both soil layers are assigned as 18.9 kN/m^3, to be compatible with Olson (2001) and Weber (2015).

A.27.4 Sub-sectioning of the Cross-section and Failure Plane

The exact locations of the CPT boreholes were not known for this case history. Therefore, the sub-sectioning is made based on imaginary boreholes assigned on the cross-section. These imaginary boreholes are defined with respect to changes in effective vertical stresses and inclination angles of the failure plane. Accordingly, three sub-sections are assigned for the liquefied zone as presented in Figure A.27.4.

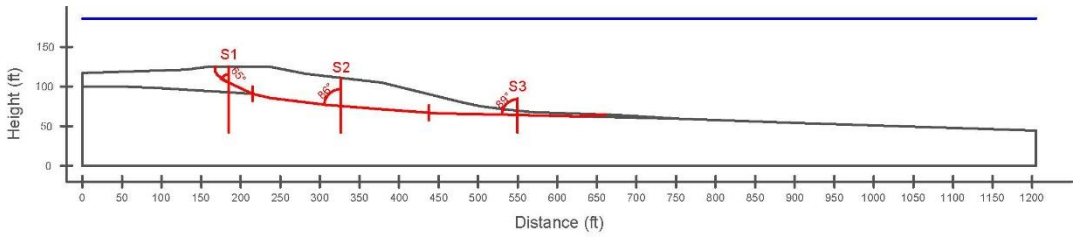

Figure A.27.4. Sub-sectioning of the cross-section and failure plane for Nerlerk Embankment Slide 2

The territory lengths (L_i) and inclinations (α_i) (positive sign for CCW direction) of the failure plane are evaluated as given in Table A.27.1 for each sub-section.

Table A.27.1 Sub-sections with their corresponding failure plane lengths and inclinations for Nerlerk Embankment Slide 2

Case History	Section	Failure plane length, L_i (m)	Total failure plane length, L_t (m)	Failure plane inclination, α_i (degrees)
Nerlerk Embankment Slide 2	S1	18.90	155.45	-25
	S2	68.49		-4
	S3	68.07		-1

A.27.5 Elastic Modeling and Stress Rotation

All stress components are evaluated linear elastically at the points where boreholes and failure plane intersect in Figure A.27.4. The initial and deformed shape of the cross-section are presented in Figure A.27.5 and Figure A.27.6, respectively. All lengths are given in meters.

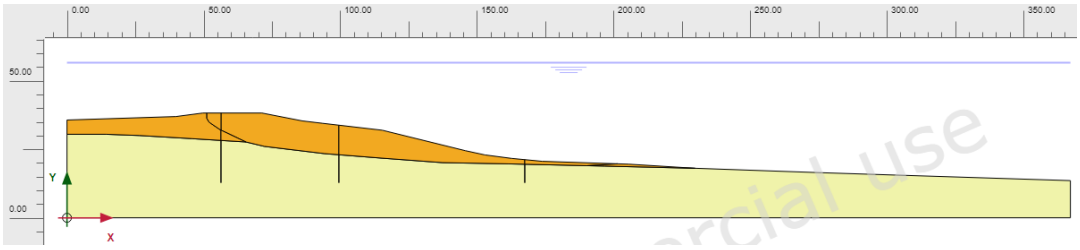

Figure A.27.5. Initial cross-section used in linear elastic modeling of Nerlerk Embankment Slide 2

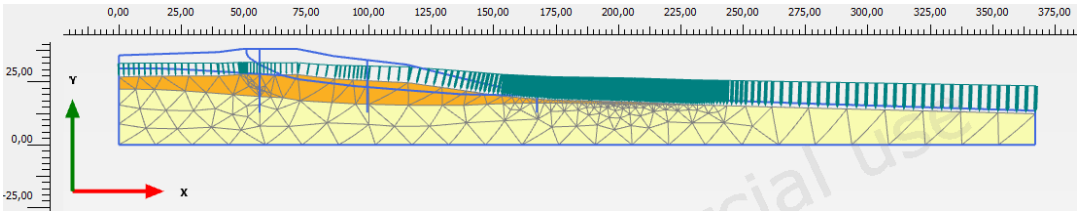

Figure A.27.6. Deformed cross-section obtained after linear elastic modeling of Nerlerk Embankment Slide 2

During the elastic modeling process in PLAXIS 2D Ultimate Connect Edition V22.00.00.1733 software, the Poisson's ratio values of the non-liquefied zone (Ukalerk Sand) and liquefied zone (Nerlerk Sand) are defined as 0.30 and 0.33, respectively. The elastic modulus values of the same layers, on the other hand, are estimated as 10 MPa and 5 MPa, respectively.

The effective normal (σ'_N) and shear (τ_{static}) stresses acting on the inclined failure plane are evaluated with corresponding Mohr's circles. The corresponding Mohr's circles and the effective stress components of the sub-sections are presented in Figure A.27.7 and Table A.27.2, respectively. All stresses are given in kilopascals.

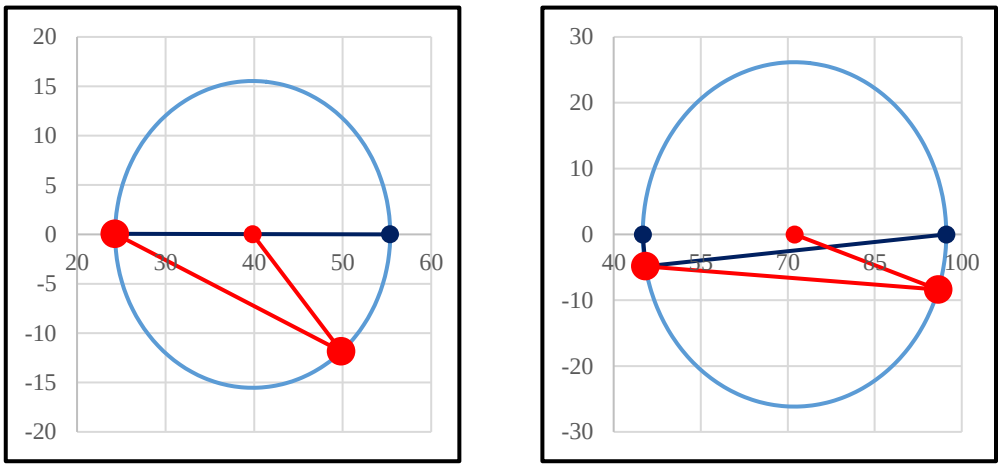

(a) S1 (b) S2

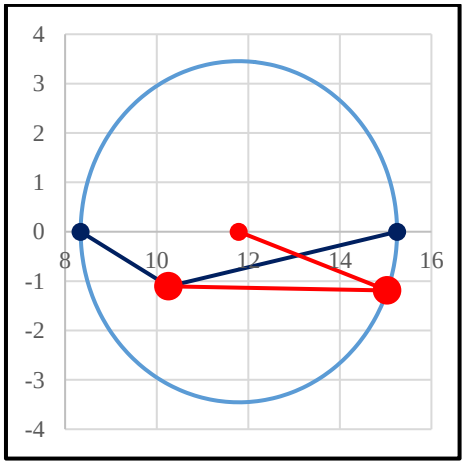

(c) S3

Figure A.27.7. Mohr's circles for Nerlerk Embankment Slide 2

Table A.27.2 Evaluated stress components for Nerlerk Embankment Slide 2

Case History	Section	σ'_1 (kPa)	σ'_2 (kPa)	σ'_3 (kPa)	p_0' (kPa)	q (kPa)	σ'_N (kPa)	τ_{static} (kPa)	$\lvert\tau_{static}\rvert$ (kPa)
Nerlerk Embankment Slide 2	S1	55.4	26.3	24.3	35.3	30.1	49.9	-11.9	11.9
	S2	97.3	47.0	45.0	63.1	51.4	96.0	-8.4	8.4
	S3	15.3	10.0	8.3	11.2	6.2	15.0	-1.2	1.2

A.27.6 Evaluation of SPT Resistance

The exact locations of the CPT boreholes were not documented for this case history. Therefore, imaginary boreholes are assigned along the cross-section as shown in Figure A.26.5. SPT data used for this case history is presented in Figure A.27.8.

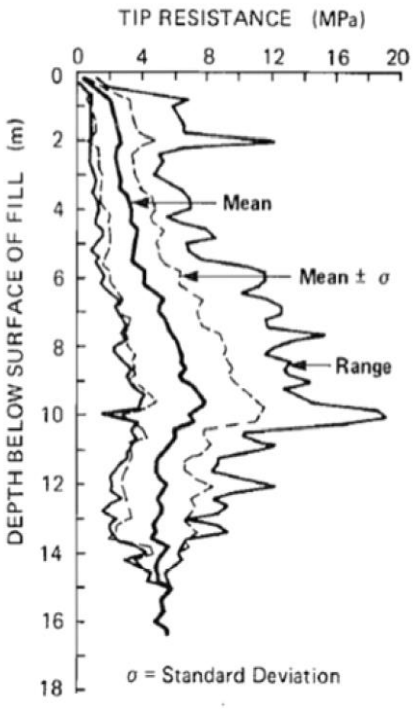

Figure A.27.8. CPT data for Nerlerk Embankment (Sladen et al., 1985)

The CPT cone tip resistances are converted to raw SPT-N and N_{60} values by using the correlations proposed by Ishihara et al. (1990) and Kulhawy and Mayne (1990), respectively, as explained in Section 3.5. Then, the overburden stress correction factors (C_N) are again evaluated to be able to estimate $(N_1)_{60}$ values based on the effective vertical stresses estimated at the point of penetration for each recording, and average values are documented for simplicity. The fines content correction factors (C_{fines}) are also evaluated with the methods and relationships explained in Section 3.5. Accordingly, the correction factors and SPT resistances are estimated as given in Table A.27.3.

Table A.27.3 Evaluated SPT-N resistances for Nerlerk Embankment Slide 2

Case History	Section	C_N	C_B	C_R	C_S	C_E	C_{fines}	N	N_{60}	$(N_1)_{60}$	$(N_1)_{60,cs}$	
Nerlerk Embankment Slide 2	S1	1.55	-	-	-	-	1.06	6.21	8.68	13.67	14.46	14.46
	S2	1.55	-	-	-	-	1.06	6.21	8.68	13.67	14.46	
	S3	1.55	-	-	-	-	1.06	6.21	8.68	13.67	14.46	

A.27.7 Evaluation of Limit Void Ratios, Void Ratio Ranges, Relative Densities and Initial Void Ratios

Since mean grain size (D_{50}), fines content (FC), and coefficient of uniformity (C_u) information were available among the required material properties for the void ratio prediction models, the arithmetic means of the limit void ratios (e_{min} and e_{max}) evaluated by Model 8 and Model 9 are considered as the representative values. The e_{max} value is slightly modified then with respect to the construction method of the case history for each prediction model.

Since the fines content value is evaluated as 7.5%, which is less than 15%, it is judged that the soil of interest consists of sand type of soils. Therefore, the arithmetic mean of the relative densities evaluated by the correlations recommended by Kulhawy and Mayne (1990) and Cubrinovski and Ishihara (1999) is taken as the overall relative density of the soil. Based on these relative densities and limit void ratios, the initial void ratios (e_0) corresponding to approximately 1 kPa confining stress are estimated referring to Equation 3-68. Accordingly, the limit void ratios, void ratio ranges (without any modification for the construction method), in-situ relative densities, and initial void ratios are estimated as given in Table A.27.4.

Table A.27.4 Evaluated limit void ratios, void ratio ranges, in-situ relative densities, and initial void ratios for Nerlerk Embankment Slide 2

Case History	Section	e_{min}	e_{max}	e_{max}-e_{min}	$RD_{C\&I}$ (%)	$RD_{K\&M}$ (%)	$RD_{overall}$ (%)	e_0
Nerlerk Embankment Slide 2	S1	0.580	0.992	0.411	50.81	56.02	53.41	0.772
	S2	0.580	0.992	0.411	50.81	56.02	53.41	0.772
	S3	0.580	0.992	0.411	50.81	56.02	53.41	0.772

A.28 Nerlerk Embankment Slide 3 (1983 Fill Placement)

A.28.1 Brief Summary of the Case History

Nerlerk Embankment Slide 3 was located in Beaufort Sea, Canada, and the exact date of the failure was reported as July 28, 1983. The fundamental reason behind the failure was reported as the fill placement. The type of the structure can be classified as a hydraulic embankment fill, and the maximum slope height is reported as ~ 21 m. Sladen et al. (1985, 1987), Sladen and Hewitt (1989), Mitchell (1984), Been et al. (1987), Rogers et al. (1990), and Konrad (1991) are taken into account as the main sources of references. Olson (2001), Wang (2003) and Weber (2015) also studied this case history during their back-analyses of liquefaction failure case histories.

A.28.2 Site Geology and Critical Cross-section

Figure A.28.1 presents the soil stratigraphy, and Figure A.28.2 shows the pre-failure and post-failure cross-sections of the case structure. It is decided that the idealized soil profile consists of two soil layers namely non-liquefied zone (Ukalerk Sand) and liquefied zone (Nerlerk Sand). While the sand layer on top of the embankment is classified as the liquefied zone (Nerlerk Sand), the layer underlying it is defined as non-liquefied zone (Ukalerk Sand).

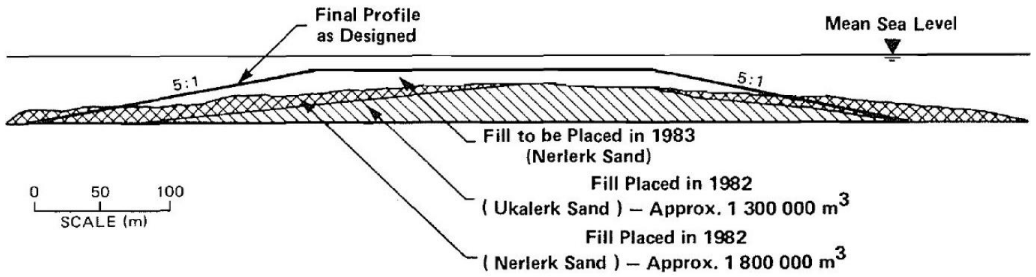

Figure A.28.1. Soil stratigraphy of the Nerlerk Embankment (Sladen et al., 1985)

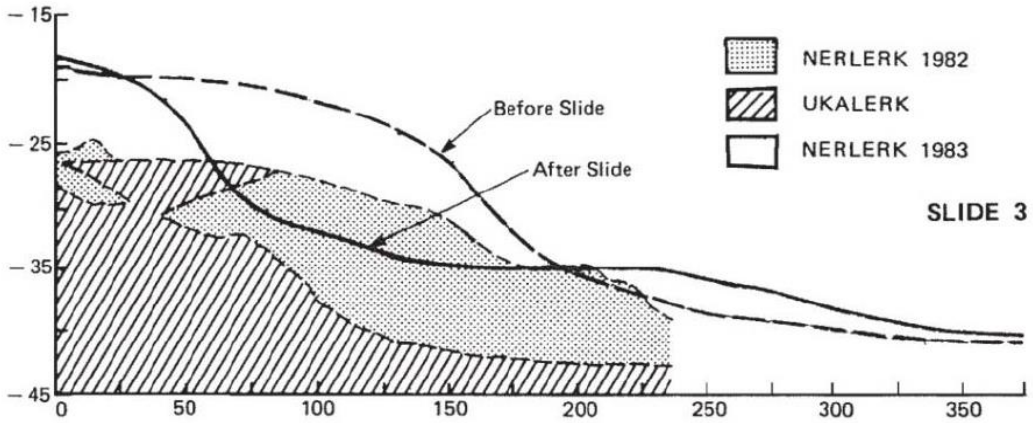

Figure A.28.2. Pre-failure and post-failure cross-sections of the Nerlerk Embankment Slide 3 (Sladen et al., 1985)

A.28.3 Evaluation of Material Properties

Since the grain size distribution curve of the case history was reported by the main sources of references as given in Figure A.28.3, mean grain size (D_{50}), fines content (FC) and coefficient of uniformity (C_u) values are evaluated based on this curve.

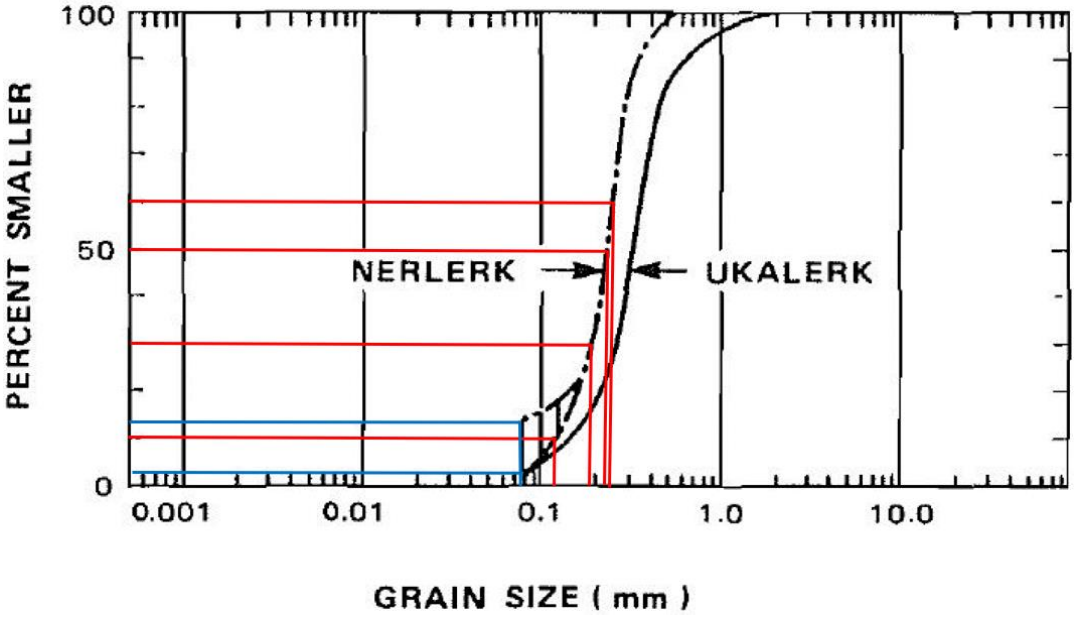

Figure A.28.3. Grain size distribution curve of the Nerlerk Embankment (Sladen et al., 1985)

Mean grain size (D_{50}): D_{50} = 0.220 mm is evaluated representatively based on the grain size distribution curve of the case history. Olson (2001) and Rogers et al. (1990) also suggest 0.220 mm and 0.280 mm for D_{50} value of this case, respectively.

Fines content (FC): FC = 7.5% is evaluated representatively based on the grain size distribution curve of the case history. Olson (2001) recommends a range of 2-12% for fines content of this case. Sladen et al. (1985) and Rogers et al. (1990) also suggest 10% and 3%, respectively, for FC value of this case history.

Coefficient of uniformity (C_u): D_{10} and D_{60} values are evaluated as 0.130 mm and 0.240 mm, respectively, based on the grain size distribution curve of the case history. Therefore, the uniformity coefficient is estimated as $C_u = D_{60}/D_{10} = 0.240/0.130 = 1.85$.

Roundness (R): Since no roundness value was reported by the main sources of references or other studies, no value has been set for this parameter for the evaluation of limit void ratios and void ratio ranges. However, R = 0.50 is taken approximately as a representative value for the evaluation of liquefaction state friction angle.

Sphericity (S): Since no sphericity value was reported by the main sources of references or other studies, no value has been set for this parameter for the evaluation of limit void ratios and void ratio ranges. However, S = 0.60 is taken approximately as a representative value for the evaluation of liquefaction state friction angle.

Unit weight (γ_{dry} and γ_{sat}): As the results are not sensitive to unit weight, the unit weights of both soil layers are assigned as 18.9 kN/m^3, to be compatible with Olson (2001) and Weber (2015).

A.28.4 Sub-sectioning of the Cross-section and Failure Plane

The exact locations of the CPT boreholes were not known for this case history. Therefore, the sub-sectioning is made based on imaginary boreholes assigned on the cross-section. These imaginary boreholes are defined with respect to changes in

effective vertical stresses and inclination angles of the failure plane. Accordingly, three sub-sections are assigned for the liquefied zone as presented in Figure A.28.4.

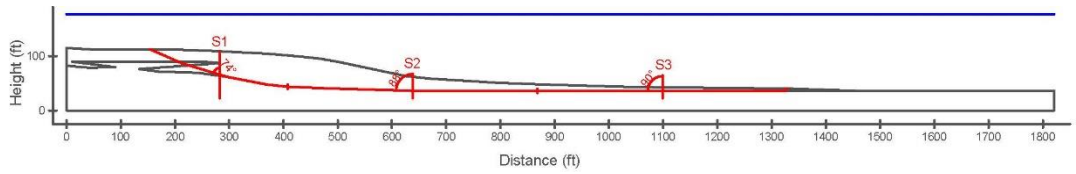

Figure A.28.4. Sub-sectioning of the cross-section and failure plane for Nerlerk Embankment Slide 2

The territory lengths (L_i) and inclinations (α_i) (positive sign for CCW direction) of the failure plane are evaluated as given in Table A.28.1 for each sub-section.

Table A.28.1 Sub-sections with their corresponding failure plane lengths and inclinations for Nerlerk Embankment Slide 3

Case History	Section	Failure plane length, L_i (m)	Total failure plane length, L_t (m)	Failure plane inclination, α_i (degrees)
Nerlerk Embankment Slide 3	S1	80.49	361.89	-16
	S2	140.49		-2
	S3	140.91		0

A.28.5 Elastic Modeling and Stress Rotation

All stress components are evaluated linear elastically at the points where boreholes and failure plane intersect in Figure A.28.4. The initial and deformed shape of the cross-section are presented in Figure A.28.5 and Figure A.28.6, respectively. All lengths are given in meters.

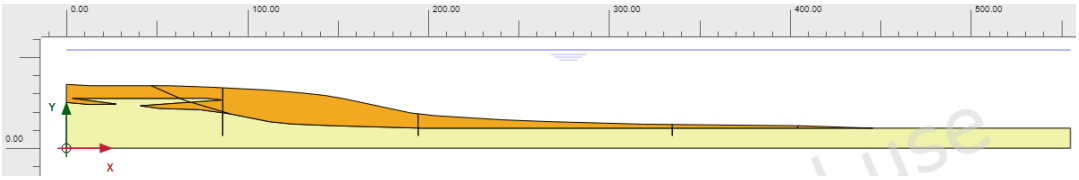

Figure A.28.5. Initial cross-section used in linear elastic modeling of Nerlerk Embankment Slide 3

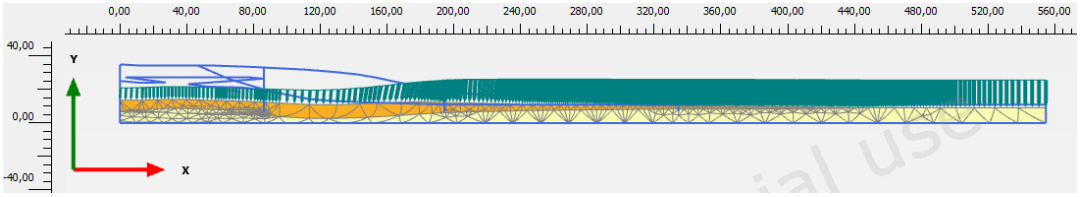

Figure A.28.6. Deformed cross-section obtained after linear elastic modeling of Nerlerk Embankment Slide 3

During the elastic modeling process in PLAXIS 2D Ultimate Connect Edition V22.00.00.1733 software, the Poisson's ratio values of the non-liquefied zone (Ukalerk Sand) and liquefied zone (Nerlerk Sand) are defined as 0.30 and 0.33, respectively. The elastic modulus values of the same layers, on the other hand, are estimated as 10 MPa and 5 MPa, respectively.

The effective normal (σ'_N) and shear (τ_{static}) stresses acting on the inclined failure plane are evaluated with corresponding Mohr's circles. The corresponding Mohr's circles and the effective stress components of the sub-sections are presented in Figure A.28.7 and Table A.28.2, respectively. All stresses are given in kilopascals.

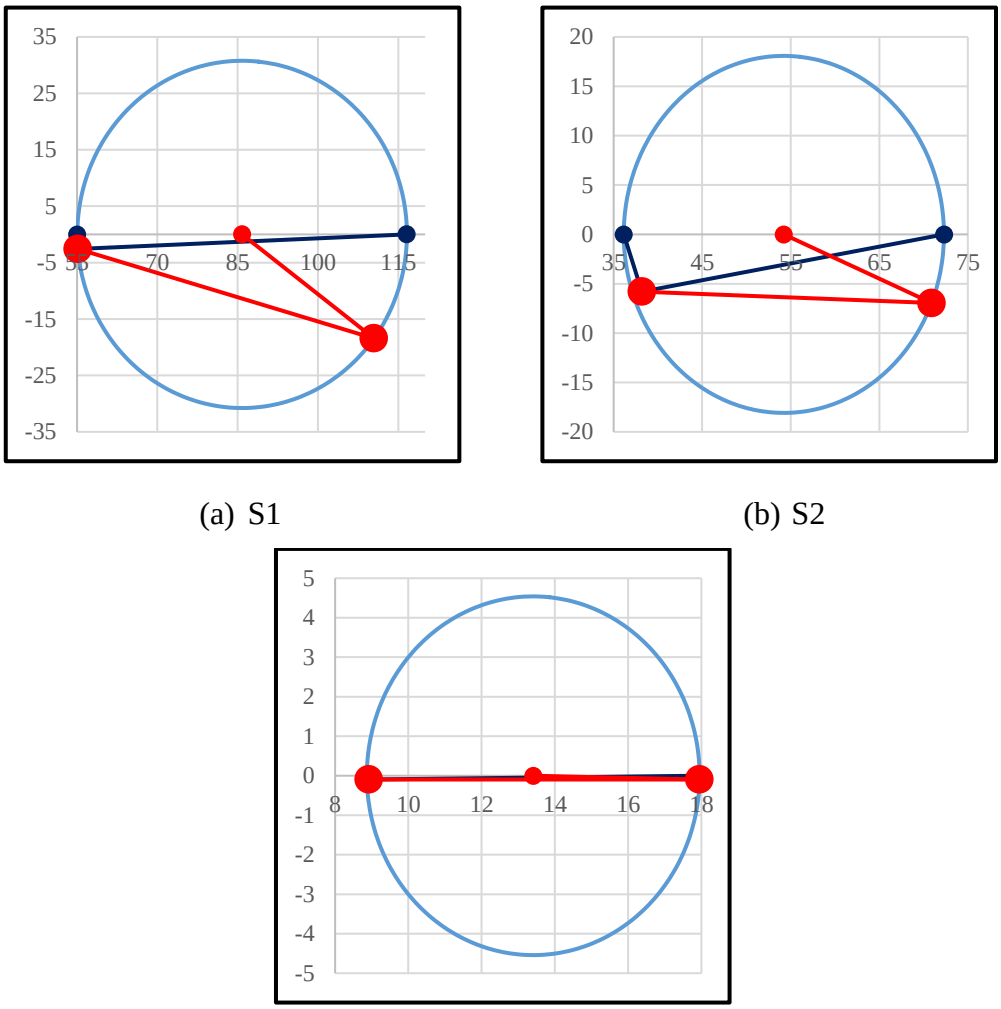

(a) S1 (b) S2

(c) S3

Figure A.28.7. Mohr's circles for Nerlerk Embankment Slide 3

Table A.28.2 Evaluated stress components for Nerlerk Embankment Slide 3

Case History	Section	σ'_1 (kPa)	σ'_2 (kPa)	σ'_3 (kPa)	p_0' (kPa)	q (kPa)	σ'_N (kPa)	τ_{static} (kPa)	$\lvert\tau_{static}\rvert$ (kPa)
Nerlerk Embankment Slide 3	S1	116.6	56.7	55.1	76.1	60.8	110.5	-18.4	18.4
	S2	72.3	37.2	36.1	48.6	35.6	70.9	-6.9	6.9
	S3	18.0	8.9	8.9	11.9	9.1	17.9	-0.1	0.1

A.28.6 Evaluation of SPT Resistance

The exact locations of the CPT boreholes were not documented for this case history. Therefore, imaginary boreholes are assigned along the cross-section as shown in Figure A.26.5. SPT data used for this case history is presented in Figure A.28.8.

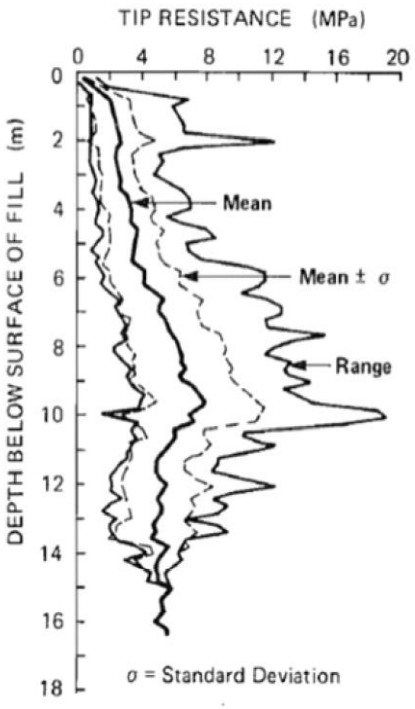

Figure A.28.8. CPT data for Nerlerk Embankment (Sladen et al., 1985)

The CPT cone tip resistances are converted to raw SPT-N and N_{60} values by using the correlations proposed by Ishihara et al. (1990) and Kulhawy and Mayne (1990), respectively, as explained in Section 3.5. Then, the overburden stress correction factors (C_N) are again evaluated to be able to estimate $(N_1)_{60}$ values based on the effective vertical stresses estimated at the point of penetration for each recording, and average values are documented for simplicity. The fines content correction factors (C_{fines}) are also evaluated with the methods and relationships explained in Section 3.5. Accordingly, the correction factors and SPT resistances are estimated as given in Table A.28.3.

Table A.28.3 Evaluated SPT-N resistances for Nerlerk Embankment Slide 3

Case History	Section	C_N	C_B	C_R	C_S	C_E	C_{fines}	N	N_{60}	$(N_1)_{60}$	$(N_1)_{60,cs}$	
Nerlerk Embankment Slide 3	S1	1.55	-	-	-	-	1.06	6.21	8.68	13.67	14.46	14.46
	S2	1.55	-	-	-	-	1.06	6.21	8.68	13.67	14.46	
	S3	1.55	-	-	-	-	1.06	6.21	8.68	13.67	14.46	

A.28.7 Evaluation of Limit Void Ratios, Void Ratio Ranges, Relative Densities and Initial Void Ratios

Since mean grain size (D_{50}), fines content (FC), and coefficient of uniformity (C_u) information were available among the required material properties for the void ratio prediction models, the arithmetic means of the limit void ratios (e_{min} and e_{max}) evaluated by Model 8 and Model 9 are considered as the representative values. The e_{max} value is slightly modified then with respect to the construction method of the case history for each prediction model.

Since the fines content value is evaluated as 7.5%, which is less than 15%, it is judged that the soil of interest consists of sand type of soils. Therefore, the arithmetic mean of the relative densities evaluated by the correlations recommended by Kulhawy and Mayne (1990) and Cubrinovski and Ishihara (1999) is taken as the overall relative density of the soil. Based on these relative densities and limit void ratios, the initial void ratios (e_0) corresponding to approximately 1 kPa confining stress are estimated referring to Equation 3-68. Accordingly, the limit void ratios, void ratio ranges (without any modification for the construction method), in-situ relative densities, and initial void ratios are estimated as given in Table A.28.4.

Table A.28.4 Evaluated limit void ratios, void ratio ranges, in-situ relative densities, and initial void ratios for Nerlerk Embankment Slide 3

Case History	Section	e_{min}	e_{max}	e_{max}-e_{min}	$RD_{C\&I}$ (%)	$RD_{K\&M}$ (%)	$RD_{overall}$ (%)	e_0
Nerlerk Embankment Slide 3	S1	0.580	0.992	0.411	50.81	56.02	53.41	0.772
	S2	0.580	0.992	0.411	50.81	56.02	53.41	0.772
	S3	0.580	0.992	0.411	50.81	56.02	53.41	0.772

A.29 Asele Road Embankment (1983 Road Pavement Repairs)

A.29.1 Brief Summary of the Case History

Asele Road Embankment was located in Sweden, and the exact date of the failure was reported as October 4, 1983. The fundamental reason behind the failure was reported as cyclic liquefaction during the repairment of road pavement. The type of the structure can be classified as an earthen embankment constructed with wet-fill method, and the maximum slope height is reported as ~ 9 m. Ekstrom and Olofsson (1985) is taken into account as the main source of reference. Olson (2001), Wang (2003) and Weber (2015) also studied this case history during their back-analyses of liquefaction failure case histories.

A.29.2 Site Geology and Critical Cross-section

Figure A.29.1 presents the soil stratigraphy of the embankment cross-section, and Figure A.29.2 shows the pre-failure and post-failure cross-sections of the case structure. It is decided that the idealized soil profile consists of three soil layers namely non-liquefied zone, liquefied zone, and firm natural till. The parts of the earthen embankment remaining above and below the water table level at the time of failure are classified as non-liquefied zone and liquefied zone, respectively. The layer underlying the earthen embankment is defined as the firm natural till.

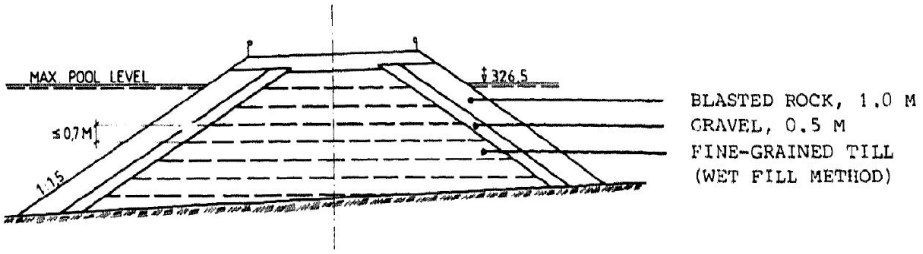

Figure A.29.1. Soil stratigraphy of the Asele Road Embankment (Ekstrom and Olofsson, 1985)

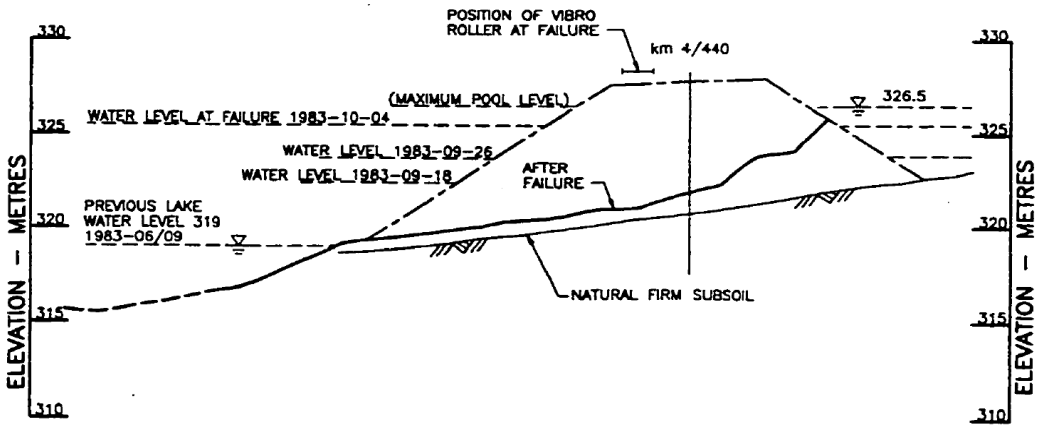

Figure A.29.2. Pre-failure and post-failure cross-sections of the Asele Road Embankment (Ekstrom and Olofsson, 1985)

A.29.3 Evaluation of Material Properties

Since the grain size distribution curve of the case history was reported by the main sources of references as given in Figure A.29.3, mean grain size (D_{50}), fines content (FC) and coefficient of uniformity (C_u) values are evaluated based on this curve.

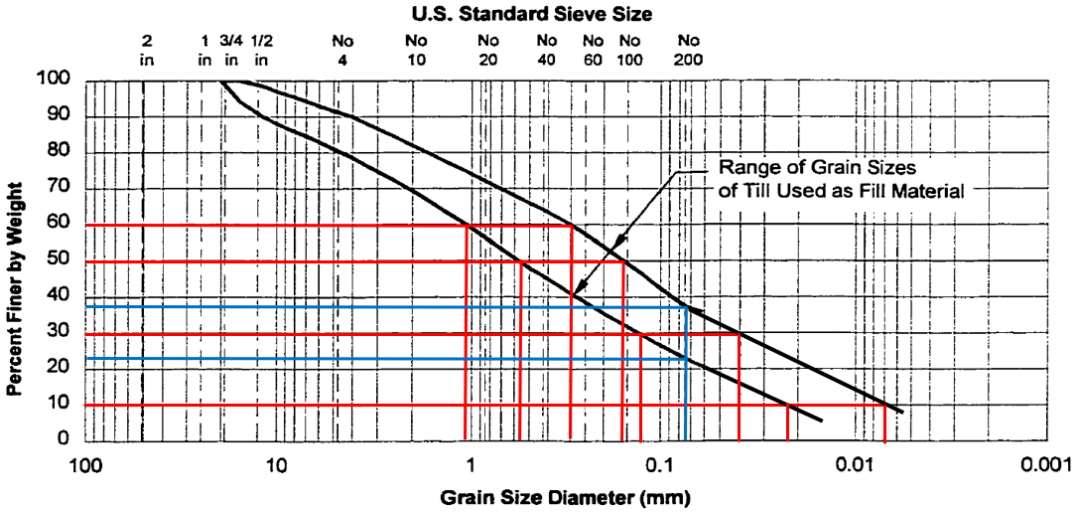

Figure A.29.3. Grain size distribution curve of the Asele Road Embankment (Olson, 2001, after Ekstrom and Olofsson, 1985)

Mean grain size (D_{50}): D_{50} = 0.276 mm is evaluated representatively based on the grain size distribution curve of the case history. Olson (2001) also suggests a range of 0.150-0.550 mm for D_{50} value of this case history with an average of 0.300 mm.

Fines content (FC): FC = 30% is evaluated representatively based on the grain size distribution curve of the case history. Ekstrom and Olofsson (1985) also recommends a range of 22-40% for FC value of this case history. Similarly, Olson (2001) also suggests a range of 23-38% for fines content.

Coefficient of uniformity (C_u): D_{10} and D_{60} values are evaluated as 0.015 mm and 0.700 mm, respectively, based on the grain size distribution curve of the case history. Therefore, the uniformity coefficient is estimated as $C_u = D_{60}/D_{10} = 0.700/0.015 = 3.51$.

Roundness (R): Since no roundness value was reported by the main sources of references or other studies, no value has been set for this parameter for the evaluation of limit void ratios and void ratio ranges. However, R = 0.50 is taken approximately as a representative value for the evaluation of liquefaction state friction angle.

Sphericity (S): Since no sphericity value was reported by the main sources of references or other studies, no value has been set for this parameter for the evaluation of limit void ratios and void ratio ranges. However, S = 0.60 is taken approximately as a representative value for the evaluation of liquefaction state friction angle.

Unit weight (γ_{dry} and γ_{sat}): As the results are not sensitive to unit weight, the dry and saturated unit weights of non-liquefied and liquefied zones are assigned as 18.1 kN/m^3 and 18.9 kN/m^3, respectively. For firm natural till layer, the unit weight is defined as 19.6 kN/m^3. All these values are evaluated accordingly to be compatible with Olson (2001) and Weber (2015).

A.29.4 Sub-sectioning of the Cross-section and Failure Plane

The exact locations of the boreholes were not known for this case history. Therefore, the sub-sectioning is made based on imaginary boreholes assigned on the cross-

section. These imaginary boreholes are defined with respect to changes in effective vertical stresses and inclination angles of the failure plane. Accordingly, two sub-sections are assigned for the liquefied zone as presented in Figure A.29.4.

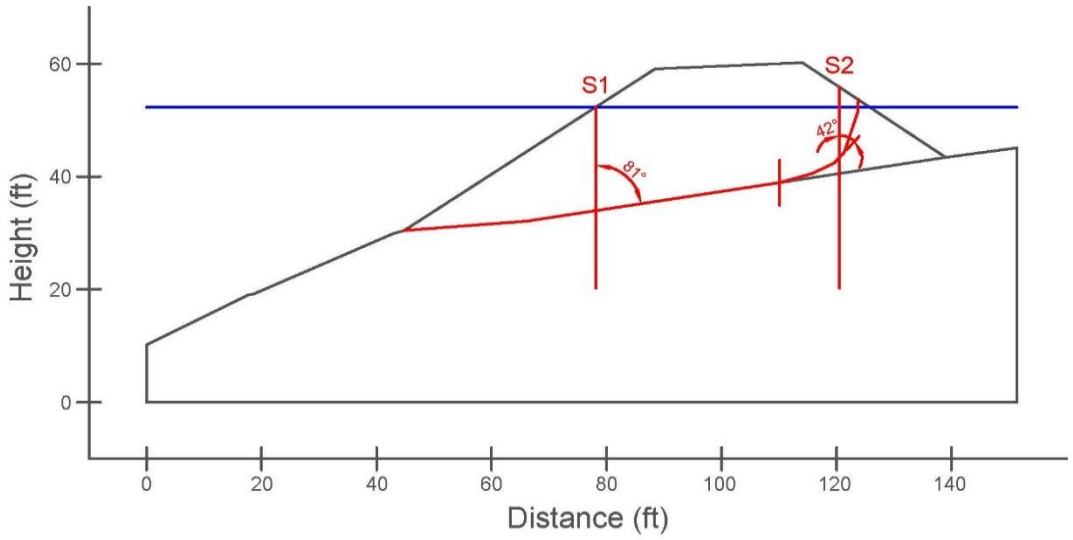

Figure A.29.4. Sub-sectioning of the cross-section and failure plane for Asele Road Embankment

The territory lengths (L_i) and inclinations (α_i) (positive sign for CCW direction) of the failure plane are evaluated as given in Table A.29.1 for each sub-section.

Table A.29.1 Sub-sections with their corresponding failure plane lengths and inclinations for Asele Road Embankment

Case History	Section	Failure plane length, L_i (m)	Total failure plane length, L_t (m)	Failure plane inclination, α_i (degrees)
Asele Road Embankment	S1	20.08	26.51	9
	S2	6.43		48

A.29.5 Elastic Modeling and Stress Rotation

All stress components are evaluated linear elastically at the points where boreholes and failure plane intersect in Figure A.29.4. The initial and deformed shape of the cross-section are presented in Figure A.29.5 and Figure A.29.6, respectively. All lengths are given in meters.

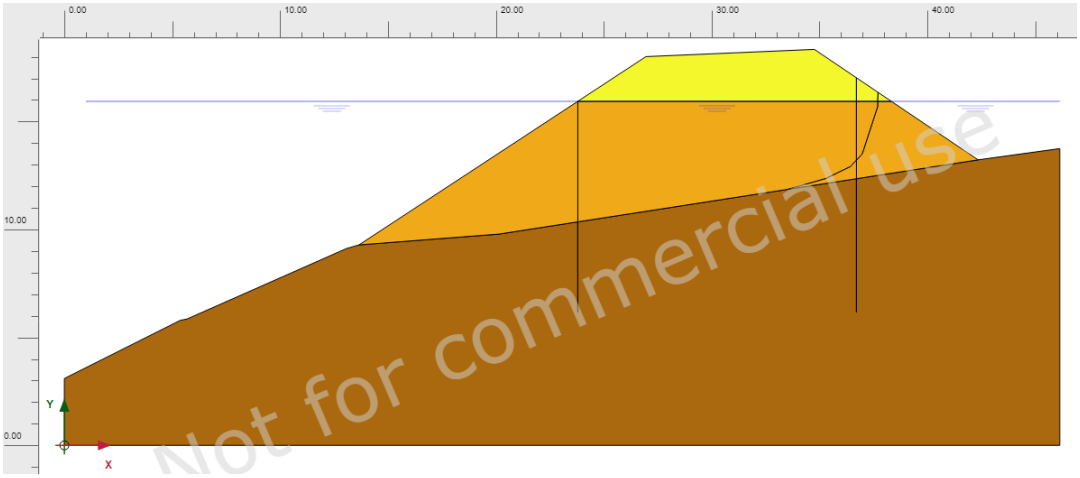

Figure A.29.5. Initial cross-section used in linear elastic modeling of Asele Road Embankment

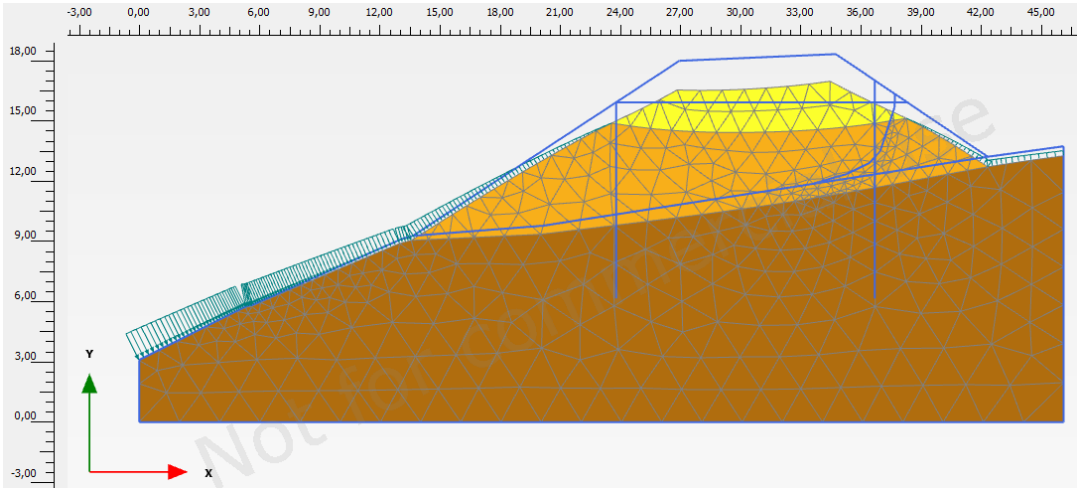

Figure A.29.6. Deformed cross-section obtained after linear elastic modeling of Asele Road Embankment

During the elastic modeling process in PLAXIS 2D Ultimate Connect Edition V22.00.00.1733 software, the Poisson's ratio values of the non-liquefied zone, liquefied zone, and firm natural till material are defined as 0.30, 0.33, and 0.30, respectively. The elastic modulus values of the same layers, on the other hand, are estimated as 10 MPa, 5 MPa, and 30 MPa, respectively.

The effective normal (σ'_N) and shear (τ_{static}) stresses acting on the inclined failure plane are evaluated with corresponding Mohr's circles. The corresponding Mohr's circles and the effective stress components of the sub-sections are presented in Figure A.29.7 and Table A.29.2, respectively. All stresses are given in kilopascals.

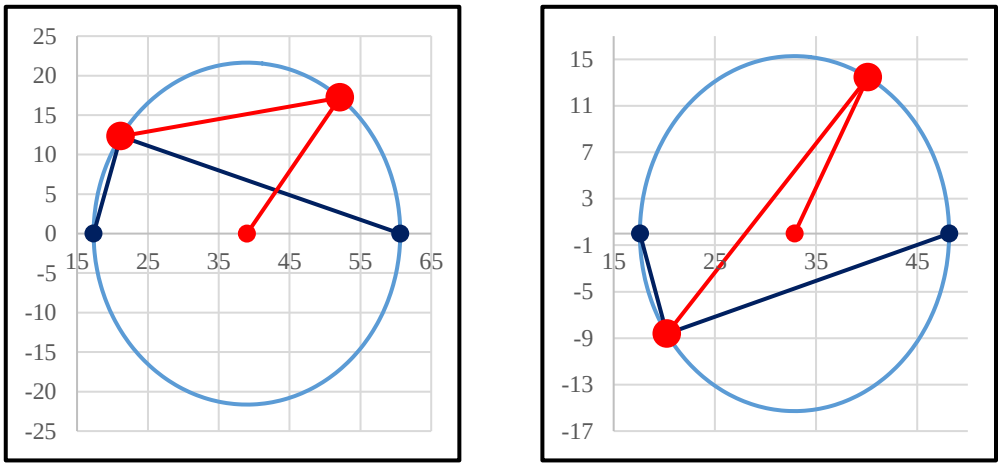

(a) S1 (b) S2

Figure A.29.7. Mohr's circles for Asele Road Embankment

Table A.29.2 Evaluated stress components for Asele Road Embankment

Case History	Section	σ'_1 (kPa)	σ'_2 (kPa)	σ'_3 (kPa)	p_0' (kPa)	q (kPa)	σ'_N (kPa)	τ_{static} (kPa)	$\lvert\tau_{static}\rvert$ (kPa)
Asele Road Embankment	S1	60.6	25.7	17.3	34.6	39.8	52.1	17.2	17.2
	S2	48.2	21.7	17.6	29.1	28.7	40.1	13.4	13.4

A.29.6 Evaluation of SPT Resistance

No penetration test data was available for this case history. However, Konrad and Watts (1995) documented a personal communication from Prof. Rainer Masarch, who conducted a post-failure investigation of the Asele Road Embankment, and reported the equipment, energy, procedure, and overburden stress corrected SPT resistance ($(N_1)_{60}$) in the range of 6-8 blows/ft for this case history. Therefore, the SPT resistance is estimated accordingly to be compatible with this personal communication information. The short rod length (C_R), overburden stress (C_N), and

fines content correction factors (C_{fines}) are again evaluated with the methods and relationships explained in Section 3.5 by using the depth of failure plane as reference length. Accordingly, the correction factors and SPT resistances are estimated as given in Table A.29.3.

Table A.29.3 Evaluated SPT-N resistances for Asele Road Embankment

Case History	Section	C_N	C_B	C_R	C_S	C_E	C_{fines}	N	N_{60}	$(N_1)_{60}$	$(N_1)_{60,cs}$	
Asele Road Embankment	S1	1.30	-	0.95	-	-	1.34	5.50	5.22	6.78	9.09	9.05
	S2	1.45	-	0.87	-	-	1.34	5.30	4.62	6.70	9.00	

A.29.7 Evaluation of Limit Void Ratios, Void Ratio Ranges, Relative Densities and Initial Void Ratios

Since mean grain size (D_{50}), fines content (FC), and coefficient of uniformity (C_u) information were available among the required material properties for the void ratio prediction models, the arithmetic means of the limit void ratios (e_{min} and e_{max}) evaluated by Model 8 and Model 9 are considered as the representative values. The e_{max} value is slightly modified then with respect to the construction method of the case history for each prediction model.

Since the fines content value is evaluated as 30%, which is greater than 15%, it is judged that the soil of interest consists of silty soils. Therefore, the relative densities evaluated by the correlation recommended by Cubrinovski and Ishihara (1999) are directly taken as the representative relative densities of the soils. Based on these relative densities and limit void ratios, the initial void ratios (e_0) corresponding to approximately 1 kPa confining stress are estimated referring to Equation 3-68. Accordingly, the limit void ratios, void ratio ranges (without any modification for the construction method), in-situ relative densities, and initial void ratios are estimated as given in Table A.29.4.

Table A.29.4 Evaluated limit void ratios, void ratio ranges, in-situ relative densities, and initial void ratios for Asele Road Embankment

Case History	Section	e_{min}	e_{max}	e_{max}-e_{min}	$RD_{C\&I}$ (%)	$RD_{K\&M}$ (%)	$RD_{overall}$ (%)	e_0
Asele Road Embankment	S1	0.543	0.929	0.386	33.90	38.37	33.90	0.798
	S2	0.543	0.929	0.386	33.69	38.14	33.69	0.799

A.30 Nalband Railway Embankment (1988 Armenian Earthquake, M_S=6.8)

A.30.1 Brief Summary of the Case History

Nalband Railway Embankment was located in Armenia, and the exact date of the failure was reported as December 7, 1988. The fundamental reason behind the failure was reported as the 1988 Armenian Earthquake (M_S=6.8). The type of the structure can be classified as a poorly compacted earthen embankment, and the maximum slope height is reported as ~ 6 m. Yegian et al. (1994) is taken into account as the main source of reference. Olson (2001), Wang (2003) and Weber (2015) also studied this case history during their back-analyses of liquefaction failure case histories.

A.30.2 Site Geology and Critical Cross-section

Figure A.30.1 presents the soil stratigraphy of the embankment cross-section, and Figure A.30.2 shows the pre-failure and post-failure cross-sections of the case structure. It is decided that the idealized soil profile consists of four soil layers namely unsaturated silty sand fill, saturated silty sand fill, liquefied zone, and volcanic tuff. The parts of the earthen embankment remaining above and below the water table level at the time of failure are classified as unsaturated silty sand fill and saturated silty sand fill, respectively. Below these sandy fill layers, liquefied zone is defined for gravelly sand with silt region. The layer underlying the earthen embankment is classified as the volcanic tuff.

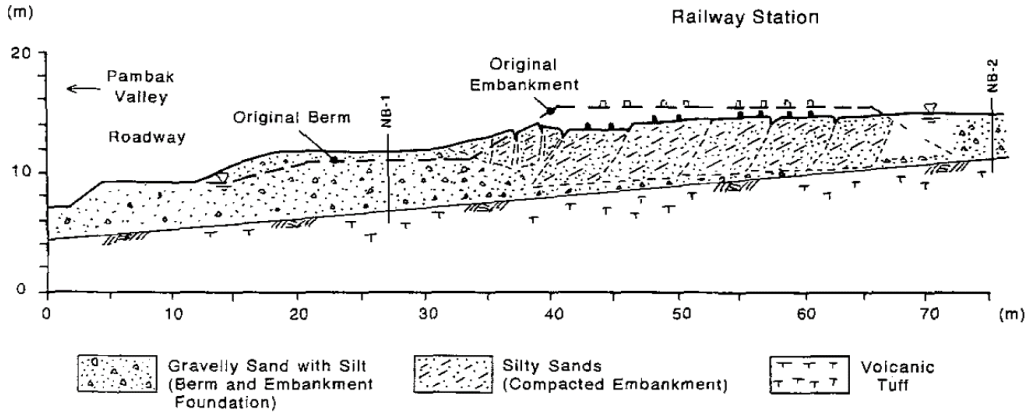

Figure A.30.1. Soil stratigraphy of the Nalband Railway Embankment (Yegian et al., 1994)

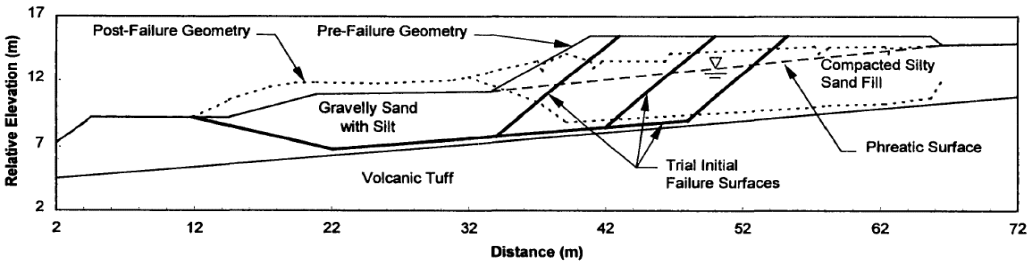

Figure A.30.2. Pre-failure and post-failure cross-sections of the Nalband Railway Embankment (Olson, 2001)

A.30.3 Evaluation of Material Properties

Since the grain size distribution curve of the case history was reported by the main sources of references as given in Figure A.30.3, mean grain size (D_{50}), fines content (FC) and coefficient of uniformity (C_u) values are evaluated based on this curve.

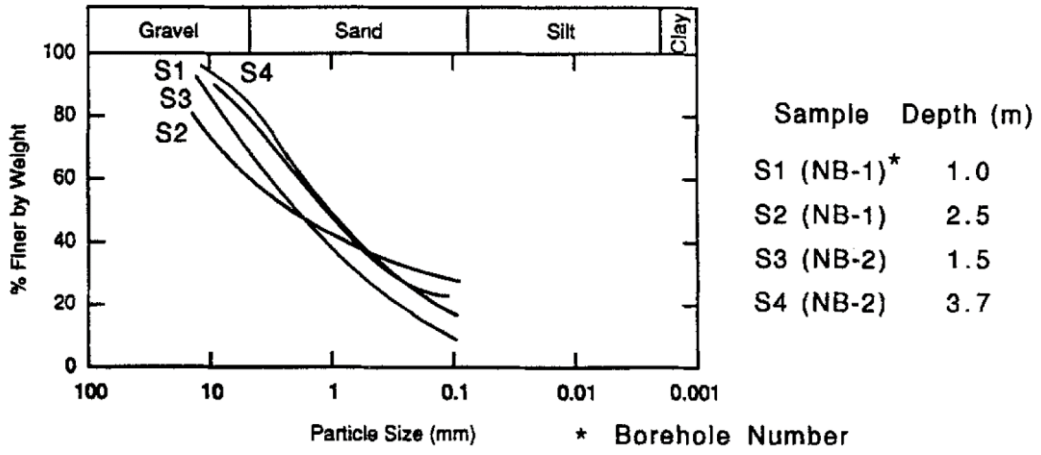

Figure A.30.3. Grain size distribution curve of the Nalband Railway Embankment (Yegian et al., 1994)

Mean grain size (D_{50}): D_{50} = 1.629 mm is evaluated representatively based on the grain size distribution curve of the case history. Olson (2001) and Srbulov (2008) also suggest 1.500 mm for D_{50} value of this case history.

Fines content (FC): FC = 28% is evaluated representatively based on the grain size distribution curve of the case history. Olson (2001) recommends a range of 10-25% for FC value of this case history. Srbulov (2008) and Gutierrez et al. (2016) also suggest 20% and 17.5% for fines content value of this case, respectively.

Coefficient of uniformity (C_u): D_{10} and D_{60} values are evaluated as 0.055 mm and 3.228 mm, respectively, based on the grain size distribution curve of the case history. Therefore, the uniformity coefficient is estimated as $C_u = D_{60}/D_{10} = 3.228/0.055 = 909.10$. Due to high gravel content of the liquefied zone, the uniformity coefficient is evaluated extremely high in average.

Roundness (R): Since no roundness value was reported by the main sources of references or other studies, no value has been set for this parameter for the evaluation of limit void ratios and void ratio ranges. However, R = 0.50 is taken approximately as a representative value for the evaluation of liquefaction state friction angle.

Sphericity (S): Since no sphericity value was reported by the main sources of references or other studies, no value has been set for this parameter for the evaluation

of limit void ratios and void ratio ranges. However, S = 0.60 is taken approximately as a representative value for the evaluation of liquefaction state friction angle.

Unit weight (γ_{dry} and γ_{sat}): As the results are not sensitive to unit weight, the dry and saturated unit weights of unsaturated silty sand fill and saturated silty sand fill layers are assigned as 20.1 kN/m^3 and 20.9 kN/m^3, respectively. For liquefied zone and volcanic tuff layers, the unit weights are defined as 19.6 kN/m^3. All these values are evaluated accordingly to be compatible with Olson (2001) and Weber (2015).

A.30.4 Sub-sectioning of the Cross-section and Failure Plane

The exact locations of the SPT boreholes were known for this case history as shown in Figure A.30.1. However, the number of boreholes was not sufficient to sub-divide the entire failure plane in reasonable sub-sections due to long failure surface length. Therefore, the sub-sectioning is made based on both actual and imaginary boreholes assigned on the cross-section. The imaginary boreholes are defined with respect to changes in effective vertical stresses and inclination angles of the failure plane. For the actual boreholes, each test is assigned (names of the logs are directly assigned as the name of the sub-section) for the corresponding territory length. Two different initial failure planes are considered based on the information available on the main sources of references about the failure mode as presented in Figure A.30.4. While boreholes NB-1, Large-S2 and Large-S3 sub-divide the larger failure plane into smaller pieces, NB-1 and Small-S2 split the smaller failure plane.

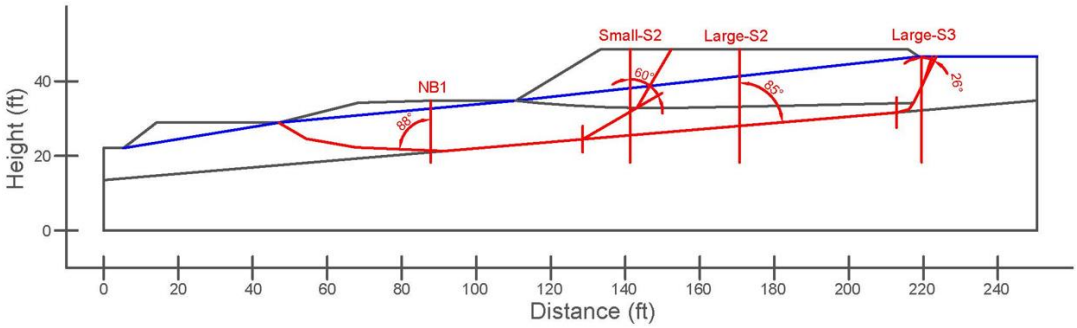

Figure A.30.4. Sub-sectioning of the cross-section and failure planes for Nalband Railway Embankment

The territory lengths (L_i) and inclinations (α_i) (positive sign for CCW direction) of the failure planes are evaluated as given in Table A.30.1 for each sub-section.

Table A.30.1 Sub-sections with their corresponding failure plane lengths and inclinations for Nalband Railway Embankment

Case History	Section	Failure plane length, L_i (m)	Total failure plane length, L_t (m)	Failure plane inclination, α_i (degrees)
Nalband Railway Embankment	NB-1	25.32	32.51	-2
	Small-S2	7.19		30
	NB-1	25.32	57.17	-2
	Large-S2	25.75		5
	Large-S3	6.09		64

A.30.5 Elastic Modeling and Stress Rotation

All stress components are evaluated linear elastically at the points where boreholes and failure plane intersect in Figure A.30.4. The initial and deformed shape of the cross-section are presented in Figure A.30.5 and Figure A.30.6, respectively. All lengths are given in meters.

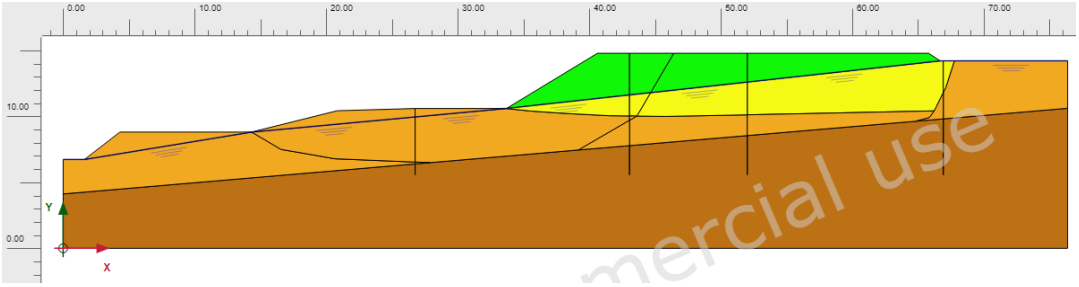

Figure A.30.5. Initial cross-section used in linear elastic modeling of Nalband Railway Embankment

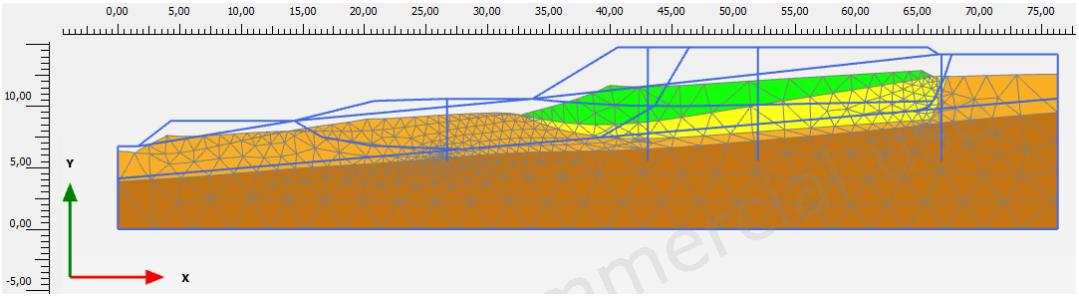

Figure A.30.6. Deformed cross-section obtained after linear elastic modeling of Nalband Railway Embankment

During the elastic modeling process in PLAXIS 2D Ultimate Connect Edition V22.00.00.1733 software, the Poisson's ratio values of the unsaturated silty sand fill, saturated silty sand fill, liquefied zone, and volcanic tuff layers are defined as 0.30, 0.30, 0.33, and 0.30, respectively. The elastic modulus values of the same layers, on the other hand, are estimated as 15 MPa, 15 MPa, 5 MPa, and 30 MPa, respectively.

The effective normal (σ'_N) and shear (τ_{static}) stresses acting on the inclined failure plane are evaluated with corresponding Mohr's circles. The corresponding Mohr's circles and the effective stress components of the sub-sections are presented in Figure A.30.7 and Table A.30.2, respectively. All stresses are given in kilopascals.

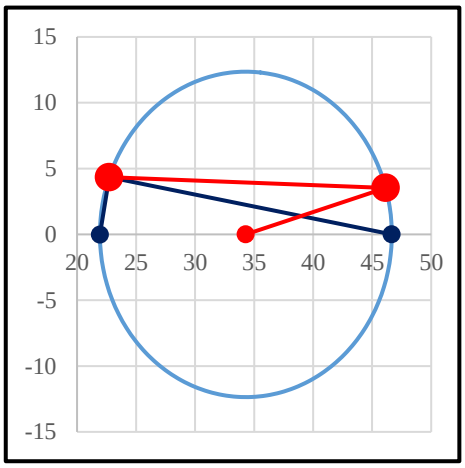

(a) NB-1

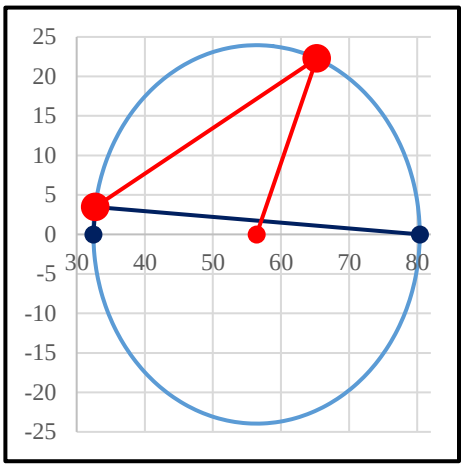

(b) Small-S2

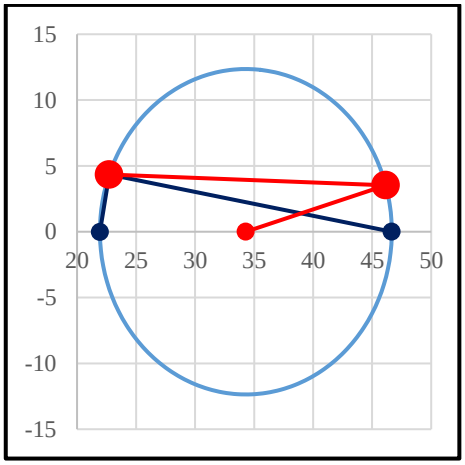

(c) NB-1

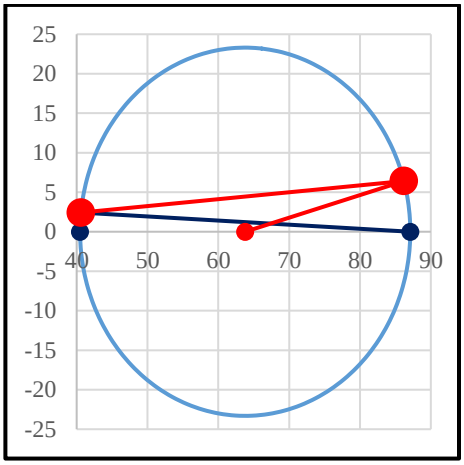

(d) Large-S2

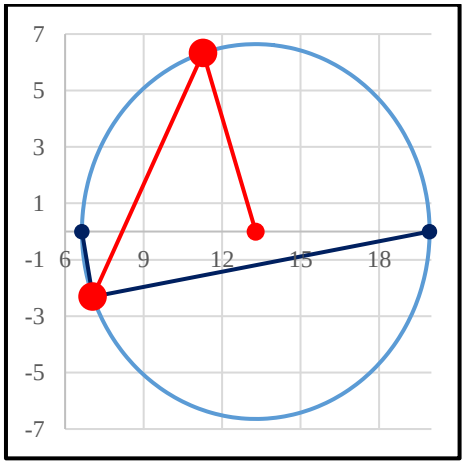

(e) Large-S3

Figure A.30.7. Mohr's circles for Nalband Railway Embankment

Table A.30.2 Evaluated stress components for Nalband Railway Embankment

Case History	Section	σ'_1 (kPa)	σ'_2 (kPa)	σ'_3 (kPa)	p_0' (kPa)	q (kPa)	σ'_N (kPa)	τ_{static} (kPa)	$\lvert\tau_{static}\rvert$ (kPa)
Nalband Railway Embankment	NB-1	46.7	22.6	21.9	30.4	24.4	46.1	3.5	3.5
	Small-S2	80.4	37.2	32.5	50.0	45.7	65.3	22.3	22.3
	NB-1	46.7	22.6	21.9	30.4	24.4	46.1	3.5	3.5
	Large-S2	87.1	42.1	40.5	56.6	45.8	86.2	6.4	6.4
	Large-S3	19.9	8.8	6.6	11.8	12.4	11.3	6.3	6.3

A.30.6 Evaluation of SPT Resistance

The exact locations of the SPT boreholes were documented by Yegian et al. (1994) as given in Figure A.30.1. Corresponding SPT boreholes are presented in Figure A.30.8 for NB-1 and NB-2 logs, respectively.

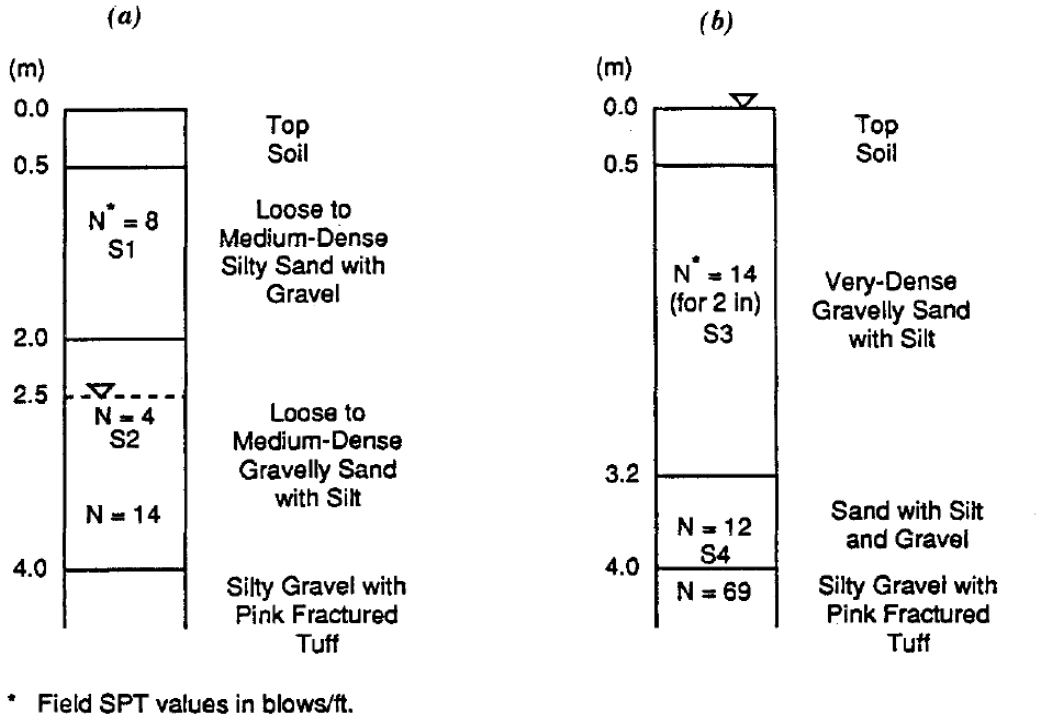

Figure A.30.8. SPT data for Nalband Railway Embankment (Yegian et al., 1994)

The correction factors for nonstandardized sampler configuration (C_S), borehole diameter (C_B), and energy efficiency (C_E) are taken as 1.0 since no reliable

information related to these coefficients was reported in any of the sources. The short rod length (C_R) and fines content correction factors (C_{fines}) are evaluated with the methods and relationships explained in Section 3.5. The overburden stress correction factors (C_N) are evaluated based on the effective vertical stresses estimated at the point of penetration for each recording, and average values are documented for simplicity. Accordingly, the correction factors and SPT resistances are estimated as given in Table A.30.3.

Table A.30.3 Evaluated SPT-N resistances for Nalband Railway Embankment

Case History	Section	C_N	C_B	C_R	C_S	C_E	C_{fines}	N	N_{60}	$(N_1)_{60}$	$(N_1)_{60,cs}$	
Nalband Railway Embankment	NB-1	1.40	1.0	0.86	1.0	1.00	1.40	4.00	3.45	4.81	6.75	6.75
	Small-S2	1.40	1.0	0.86	1.0	1.00	1.40	4.00	3.45	4.81	6.75	
	NB-1	1.40	1.0	0.86	1.0	1.00	1.40	4.00	3.45	4.81	6.75	6.75
	Large-S2	1.40	1.0	0.86	1.0	1.00	1.40	4.00	3.45	4.81	6.75	
	Large-S3	1.40	1.0	0.86	1.0	1.00	1.40	4.00	3.45	4.81	6.75	

A.30.7 Evaluation of Limit Void Ratios, Void Ratio Ranges, Relative Densities and Initial Void Ratios

Since mean grain size (D_{50}), fines content (FC), and coefficient of uniformity (C_u) information were available among the required material properties for the void ratio prediction models, the arithmetic means of the limit void ratios (e_{min} and e_{max}) evaluated by Model 8 and Model 9 are considered as the representative values. The e_{max} value is slightly modified then with respect to the construction method of the case history for each prediction model.

Since the fines content value is evaluated as 28%, which is greater than 15%, it is judged that the soil of interest consists of silty soils. Therefore, the relative densities evaluated by the correlation recommended by Cubrinovski and Ishihara (1999) are directly taken as the representative relative densities of the soils. Based on these relative densities and limit void ratios, the initial void ratios (e_0) corresponding to

approximately 1 kPa confining stress are estimated referring to Equation 3-68. Accordingly, the limit void ratios, void ratio ranges (without any modification for the construction method), in-situ relative densities, and initial void ratios are estimated as given in Table A.30.4.

Table A.30.4 Evaluated limit void ratios, void ratio ranges, in-situ relative densities, and initial void ratios for Nalband Railway Embankment

Case History	Section	e_{min}	e_{max}	e_{max}-e_{min}	$RD_{C\&I}$ (%)	$RD_{K\&M}$ (%)	$RD_{overall}$ (%)	e_0
Nalband Railway Embankment	NB-1	0.387	0.546	0.160	13.47	27.13	13.47	0.525
	Small-S2	0.387	0.546	0.160	13.47	27.13	13.47	0.525
	NB-1	0.387	0.546	0.160	13.47	27.13	13.47	0.525
	Large-S2	0.387	0.546	0.160	13.47	27.13	13.47	0.525
	Large-S3	0.387	0.546	0.160	13.47	27.13	13.47	0.525

A.31 Sullivan Tailings (1991 Dyke Raising)

A.31.1 Brief Summary of the Case History

Sullivan Tailings was located in Southeastern British Columbia, Canada, and the exact date of the failure was reported as August 23, 1991. The fundamental reason behind the failure was reported as the static flow liquefaction during dyke raising. The type of the structure can be classified as a tailings dam constructed by moist placement method, and the maximum slope height is reported as ~ 11 m. Jefferies and Been (2006) and Davies et al. (1998) are considered as the main sources of references. Olson (2001) and Wang (2003) did not perform back-analyses for this case history, and only Weber (2015) studied it during its back-analyses of liquefaction failure case histories.

A.31.2 Site Geology and Critical Cross-section

Figure A.31.1 shows the soil stratigraphy and pre-failure and post-failure cross-sections of the case structure. It is decided that the idealized soil profile consists of

five soil layers namely moist iron tailings, moist dike material, saturated dike material, liquefied zone, and glacial till foundation. The trapezoidal shaped dikes are classified as dike material, and the parts of the dikes remaining above and below the water table level at the time of failure are classified as moist dike material and saturated dike material, respectively. The unsaturated material between those dikes are defined as moist iron tailings. The layers underlying the tailings are classified as liquefied zone and glacial till foundation from top to bottom.

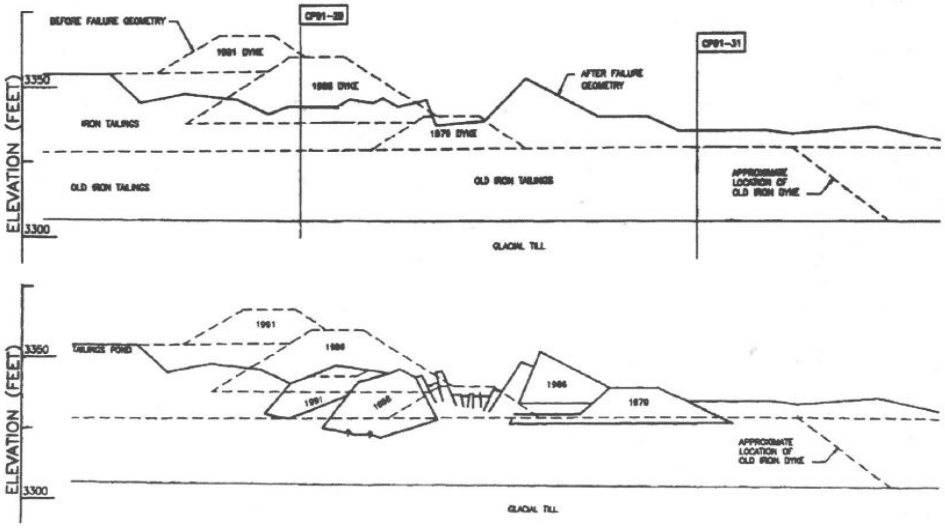

Figure A.31.1. Soil stratigraphy and pre-failure and post-failure cross-sections of the Sullivan Tailings (Jefferies and Been, 2006, after Davies et al., 1998)

A.31.3 Evaluation of Material Properties

Since the grain size distribution curve of the case history was not reported by the main sources of references or other residual strength-related studies, mean grain size (D_{50}), fines content (FC) and coefficient of uniformity (C_u) values are estimated based on the documented representative values in those references, if available.

Mean grain size (D_{50}): Since no mean grain size value was reported by the main sources of references or other relative studies, D_{50} value is representatively taken as 0.090 mm in this study referring to similar type of structures and soil profiles reported in Ilgac et al. (2019) dataset.

Fines content (FC): The exact value of the fines content was reported as FC = 50% in Jefferies and Been (2006) and Robertson (2010). Hence, the representative FC value is also taken as 50% in this study.

Coefficient of uniformity (C_u): Since no coefficient of uniformity value was reported by the main sources of references or other relative studies, no value has been set for this parameter.

Roundness (R): Since no roundness value was reported by the main sources of references or other studies, no value has been set for this parameter for the evaluation of limit void ratios and void ratio ranges. However, R = 0.50 is taken approximately as a representative value for the evaluation of liquefaction state friction angle.

Sphericity (S): Since no sphericity value was reported by the main sources of references or other studies, no value has been set for this parameter for the evaluation of limit void ratios and void ratio ranges. However, S = 0.60 is taken approximately as a representative value for the evaluation of liquefaction state friction angle.

Unit weight (γ_{dry} and γ_{sat}): As the results are not sensitive to unit weight, the dry and saturated unit weights of moist iron tailings and liquefied zones are assigned as 22.0 kN/m^3 and 22.8 kN/m^3, respectively. For moist dike material, saturated dike material, and glacial till foundation, the dry and saturated unit weights are defined as 20.4 kN/m^3 and 21.2 kN/m^3, respectively. These values are selected accordingly to be compatible with Weber (2015).

A.31.4 Sub-sectioning of the Cross-section and Failure Plane

The exact locations of the CPT boreholes were known for this case history as shown in Figure A.31.1. However, the number of boreholes was not sufficient to sub-divide the entire failure plane in reasonable sub-sections due to long failure surface length. Therefore, the sub-sectioning is made based on both actual and imaginary boreholes assigned on the cross-section. The imaginary boreholes are defined with respect to changes in effective vertical stresses and inclination angles of the failure plane. For the actual boreholes, each test is assigned (names of the logs are directly assigned as

the name of the sub-section) for the corresponding territory length. Two different initial failure planes are considered based on the information available on the main sources of references about the failure mode as presented in Figure A.31.2. While boreholes Large-S1, CP91-29 and CP91-31 sub-divide the larger failure plane into smaller pieces, Small-S1 and CP91-31 split the smaller failure plane.

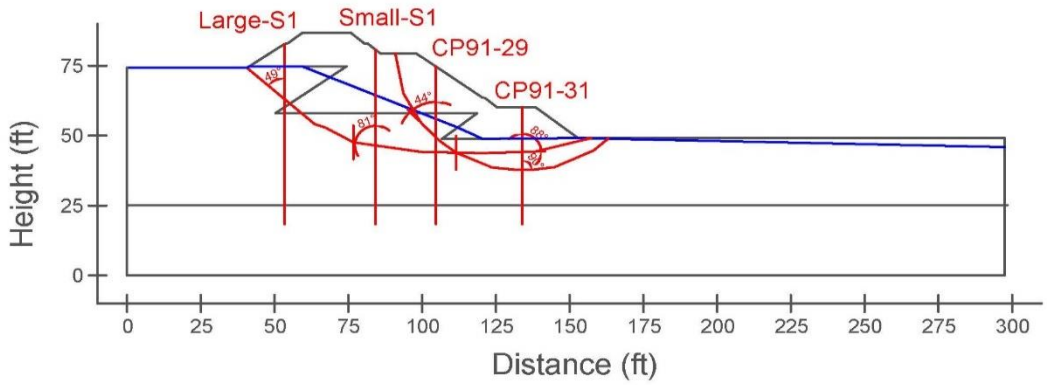

Figure A.31.2. Sub-sectioning of the cross-section and failure planes for Sullivan Tailings

The territory lengths (L_i) and inclinations (α_i) (positive sign for CCW direction) of the failure planes are evaluated as given in Table A.31.1 for each sub-section.

Table A.31.1 Sub-sections with their corresponding failure plane lengths and inclinations for Sullivan Tailings

Case History	Section	Failure plane length, L_i (m)	Total failure plane length, L_t (m)	Failure plane inclination, α_i (degrees)
Sullivan Tailings	Large-S1	13.79	38.63	-41
	CP91-29	10.68		-9
	CP91-31	14.16		2
	Small-S1	6.46	23.51	-46
	CP91-31	17.05		0

A.31.5 Elastic Modeling and Stress Rotation

All stress components are evaluated linear elastically at the points where boreholes and failure plane intersect in Figure A.31.2. The initial and deformed shape of the

cross-section are presented in Figure A.31.3 and Figure A.31.4, respectively. All lengths are given in meters.

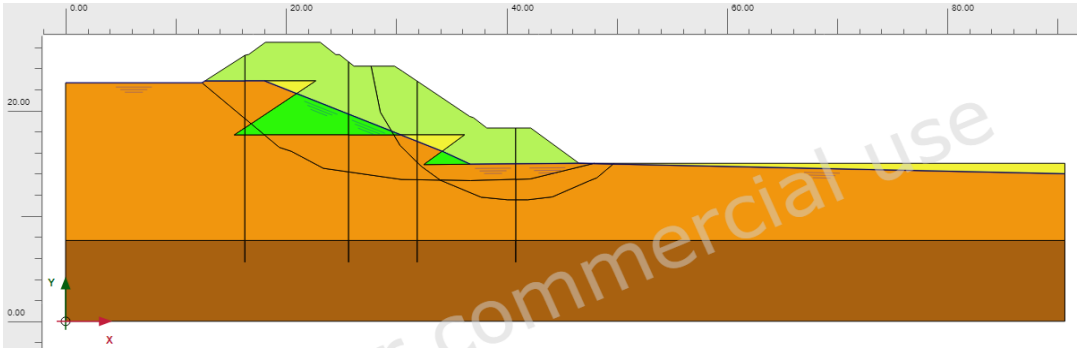

Figure A.31.3. Initial cross-section used in linear elastic modeling of Sullivan Tailings

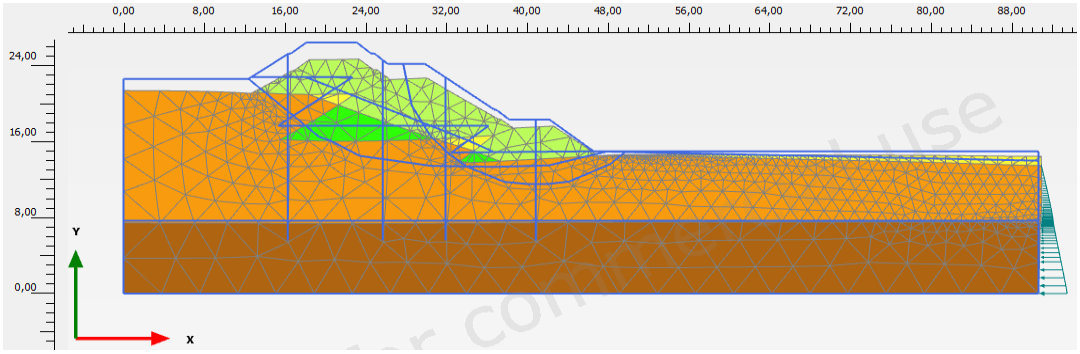

Figure A.31.4. Deformed cross-section obtained after linear elastic modeling of Sullivan Tailings

During the elastic modeling process in PLAXIS 2D Ultimate Connect Edition V22.00.00.1733 software, the Poisson's ratio values of all layers other than liquefied zone are defined as 0.30. For the liquefied zone, this value is set as 0.33. The elastic modulus values of moist iron tailings, moist dike material, saturated dike material, liquefied zone, and glacial till foundation are estimated as 10 MPa, 20 MPa, 20 MPa, 5 MPa, and 30 MPa, respectively.

The effective normal (σ'_N) and shear (τ_{static}) stresses acting on the inclined failure plane are evaluated with corresponding Mohr's circles. The corresponding Mohr's circles and the effective stress components of the sub-sections are presented in Figure A.31.5 and Table A.31.2, respectively. All stresses are given in kilopascals.

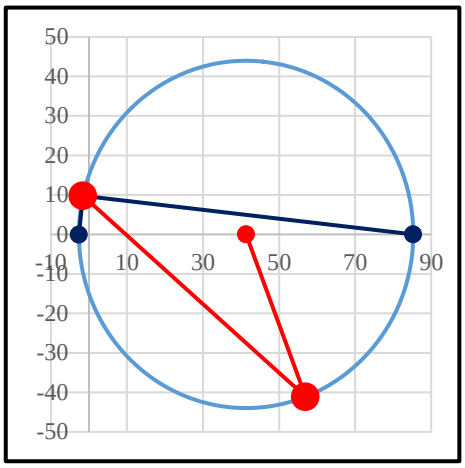

(a) Large-S1

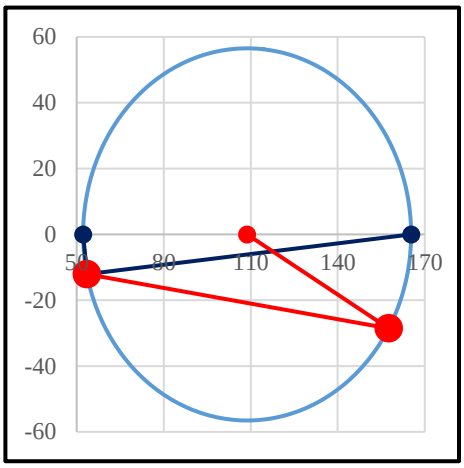

(b) CP91-29

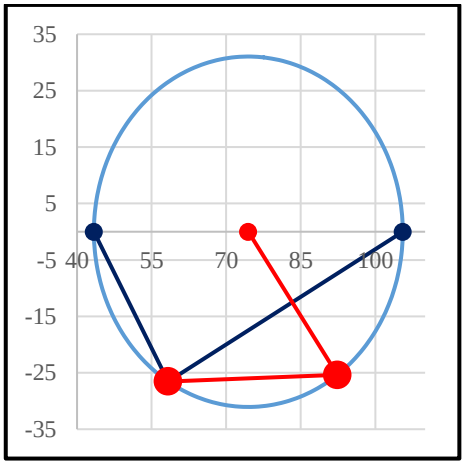

(c) CP91-31

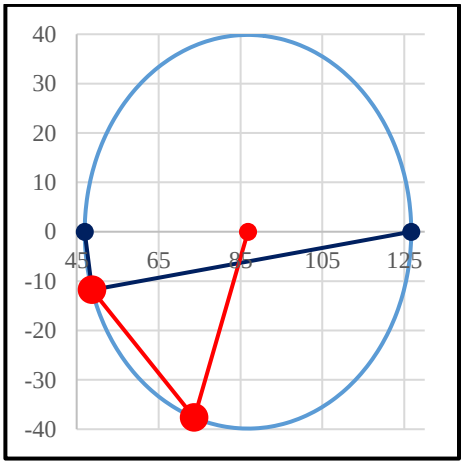

(d) Small-S1

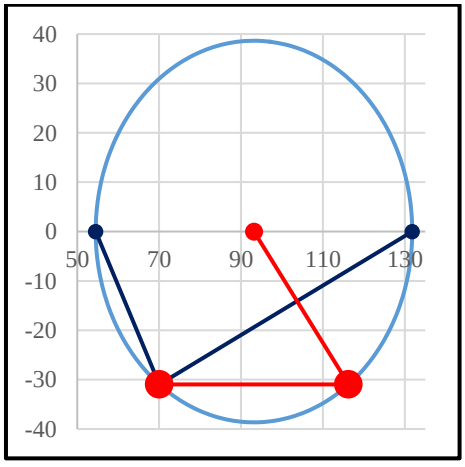

(e) CP91-31

Figure A.31.5. Mohr's circles for Sullivan Tailings

Table A.31.2 Evaluated stress components for Sullivan Tailings

Case History	Section	σ'_1 (kPa)	σ'_2 (kPa)	σ'_3 (kPa)	p_0' (kPa)	q (kPa)	σ'_N (kPa)	τ_{static} (kPa)	$\lvert\tau_{static}\rvert$ (kPa)
Sullivan Tailings	Large-S1	85.3	27.3	-2.7	36.6	77.4	57.0	-41.1	41.1
	CP91-29	165.3	71.8	52.2	96.4	104.7	157.6	-28.6	28.6
	CP91-31	105.5	49.2	43.4	66.0	59.4	92.4	-25.4	25.4
	Small-S1	126.7	57.3	47.0	77.0	75.1	73.7	-37.7	37.7
	CP91-31	131.8	61.5	54.5	82.6	74.1	116.3	-31.0	31.0

A.31.6 Evaluation of SPT Resistance

The exact locations of the CPT boreholes were documented by Jefferies and Been (2006) as given in Figure A.31.1. Corresponding CPT boreholes are presented in Figure A.31.6 for CP91-29 and CP91-31 logs, respectively.

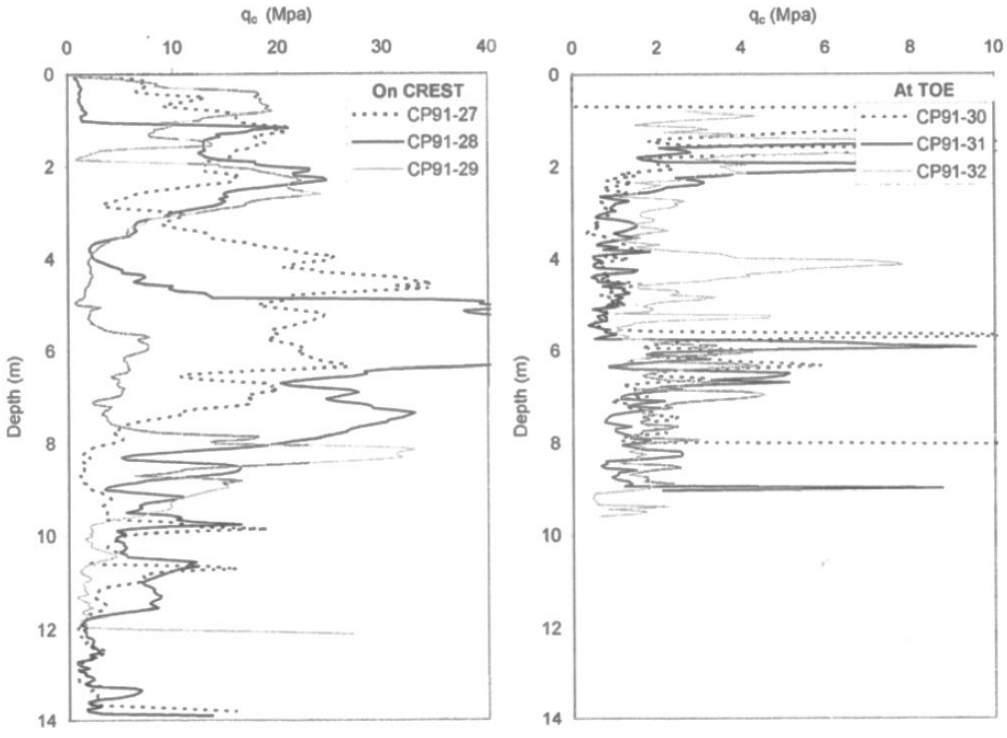

Figure A.31.6. CPT data for Sullivan Tailings (Jefferies and Been, 2006)

The CPT cone tip resistances are converted to raw SPT-N and N_{60} values by using the correlations proposed by Ishihara et al. (1990) and Kulhawy and Mayne (1990),

respectively, as explained in Section 3.5. Then, the overburden stress correction factors (C_N) are again evaluated to be able to estimate $(N_1)_{60}$ values based on the effective vertical stresses estimated at the point of penetration for each recording, and average values are documented for simplicity. The fines content correction factors (C_{fines}) are also evaluated with the methods and relationships explained in Section 3.5. Accordingly, the correction factors and SPT resistances are estimated as given in Table A.31.3.

Table A.31.3 Evaluated SPT-N resistances for Sullivan Tailings

Case History	Section	C_N	C_B	C_R	C_S	C_E	C_{fines}	N	N_{60}	$(N_1)_{60}$	$(N_1)_{60,cs}$	
Sullivan Tailings	Large-S1	1.14	-	-	-	-	1.32	7.69	7.82	9.54	12.63	12.63
	CP91-29	1.14	-	-	-	-	1.32	7.69	7.82	9.54	12.63	
	CP91-31	0.99	-	-	-	-	1.32	7.69	7.82	9.54	12.63	
	Small-S1	1.14	-	-	-	-	1.32	7.69	7.82	9.54	12.63	12.63
	CP91-31	0.99	-	-	-	-	1.32	7.69	7.82	9.54	12.63	

A.31.7 Evaluation of Limit Void Ratios, Void Ratio Ranges, Relative Densities and Initial Void Ratios

Since mean grain size (D_{50}) and fines content (FC) information were available among the required material properties for the void ratio prediction models, the arithmetic means of the limit void ratios (e_{min} and e_{max}) evaluated by Model 1 and Model 2 are considered as the representative values. The e_{max} value is slightly modified then with respect to the construction method of the case history for each prediction model.

Since the fines content value is evaluated as 50%, which is greater than 15%, it is judged that the soil of interest consists of silty soils. Therefore, the relative densities evaluated by the correlation recommended by Cubrinovski and Ishihara (1999) are directly taken as the representative relative densities of the soils. Based on these relative densities and limit void ratios, the initial void ratios (e_0) corresponding to approximately 1 kPa confining stress are estimated referring to Equation 3-68. Accordingly, the limit void ratios, void ratio ranges (without any modification for

the construction method), in-situ relative densities, and initial void ratios are estimated as given in Table A.31.4.

Table A.31.4 Evaluated limit void ratios, void ratio ranges, in-situ relative densities, and initial void ratios for Sullivan Tailings

Case History	Section	e_{min}	e_{max}	e_{max}-e_{min}	$RD_{C\&I}$ (%)	$RD_{K\&M}$ (%)	$RD_{overall}$ (%)	e_0
Sullivan Tailings	Large-S1	0.616	1.055	0.439	44.83	53.07	44.83	0.858
	CP91-29	0.616	1.055	0.439	44.83	53.07	44.83	0.858
	CP91-31	0.616	1.055	0.439	44.83	53.07	44.83	0.858
	Small-S1	0.616	1.055	0.439	44.83	53.07	44.83	0.858
	CP91-31	0.616	1.055	0.439	44.83	53.07	44.83	0.858

A.32 Jamuna Bridge (1994 Construction)

A.32.1 Brief Summary of the Case History

Jamuna Bridge was located in Bangladesh, and the date of the failure was reported as between the years 1994-1998. The fundamental reason behind the failure was reported as the static flow liquefaction during construction. The type of the structure can be classified as a bund constructed by water sedimentation method, and the maximum slope height is reported as ~ 20 m. Yoshimine et al. (1999) and Jefferies and Been (2006) are considered as the main sources of references. Olson (2001) and Wang (2003) did not perform back-analyses for this case history, and only Weber (2015) studied it during its back-analyses of liquefaction failure case histories.

A.32.2 Site Geology and Critical Cross-section

Figure A.32.1 shows the pre-failure and post-failure cross-sections of the case structure. It is decided that the idealized soil profile consists of two soil layers namely non-liquefied zone and liquefied zone. The parts of the slope remaining above and below the water table level at the time of failure are classified as non-liquefied zone and liquefied zone, respectively.

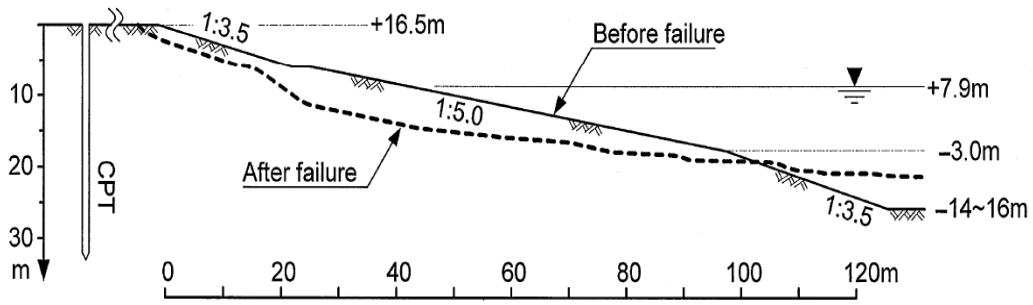

Figure A.32.1. Pre-failure and post-failure cross-sections of the Jamuna Bridge (Ishihara, 1996)

A.32.3 Evaluation of Material Properties

Since the grain size distribution curve of the case history was not reported by the main sources of references or other residual strength-related studies, mean grain size (D_{50}), fines content (FC) and coefficient of uniformity (C_u) values are estimated based on the documented representative values in those references, if available.

Mean grain size (D_{50}): A range of 0.100-0.200 mm was reported for mean grain size by Yoshimine et al. (1999). Therefore, the average value of this range, D_{50} = 0.150 mm, is taken as the representative mean grain size value in this study.

Fines content (FC): A range of 2-10% was reported for fines content by Yoshimine et al. (1999). Therefore, the average value of this range, FC = 6%, is taken as the representative fines content value in this study.

Coefficient of uniformity (C_u): Since no coefficient of uniformity value was reported by the main sources of references or other relative studies, no value has been set for this parameter.

Roundness (R): Since no roundness value was reported by the main sources of references or other studies, no value has been set for this parameter for the evaluation of limit void ratios and void ratio ranges. However, R = 0.50 is taken approximately as a representative value for the evaluation of liquefaction state friction angle.

Sphericity (S): Since no sphericity value was reported by the main sources of references or other studies, no value has been set for this parameter for the evaluation of limit void ratios and void ratio ranges. However, S = 0.60 is taken approximately as a representative value for the evaluation of liquefaction state friction angle.

Unit weight (γ_{dry} and γ_{sat}): As the results are not sensitive to unit weight, the dry and saturated unit weights of both soil layers are assigned as 18.1 kN/m^3 and 18.9 kN/m^3, respectively, to be compatible with Weber (2015).

A.32.4 Sub-sectioning of the Cross-section and Failure Plane

The exact locations of the CPT boreholes were not known for this case history. Therefore, the sub-sectioning is made based on imaginary boreholes assigned on the cross-section. These imaginary boreholes are defined with respect to changes in effective vertical stresses and inclination angles of the failure plane. Accordingly, two sub-sections are assigned for the liquefied zone as presented in Figure A.32.2.

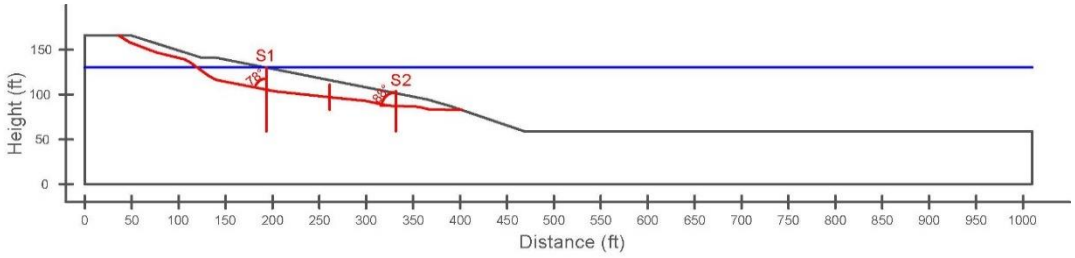

Figure A.32.2. Sub-sectioning of the cross-section and failure plane for Jamuna Bridge

The territory lengths (L_i) and inclinations (α_i) (positive sign for CCW direction) of the failure plane are evaluated as given in Table A.32.1 for each sub-section.

Table A.32.1 Sub-sections with their corresponding failure plane lengths and inclinations for Jamuna Bridge

Case History	Section	Failure plane length, L_i (m)	Total failure plane length, L_t (m)	Failure plane inclination, α_i (degrees)
Jamuna Bridge	S1	44.86	88.27	-12
	S2	43.41		-2

A.32.5 Elastic Modeling and Stress Rotation

All stress components are evaluated linear elastically at the points where boreholes and failure plane intersect in Figure A.32.2. The initial and deformed shape of the cross-section are presented in Figure A.32.3 and Figure A.32.4, respectively. All lengths are given in meters.

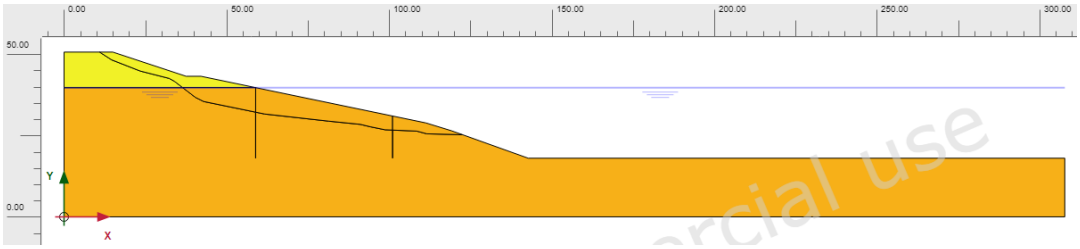

Figure A.32.3. Initial cross-section used in linear elastic modeling of Jamuna Bridge

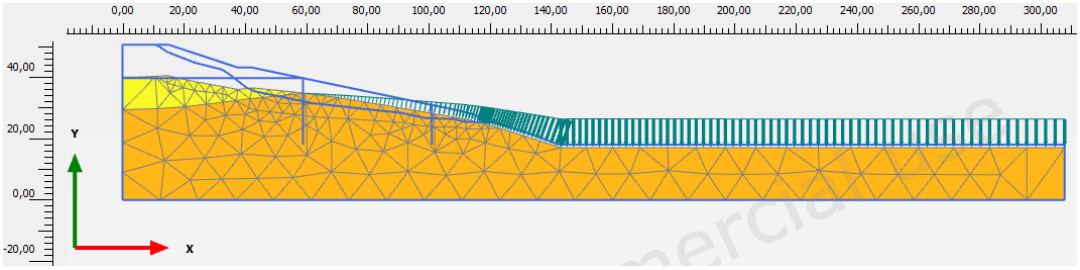

Figure A.32.4. Deformed cross-section obtained after linear elastic modeling of Jamuna Bridge

During the elastic modeling process in PLAXIS 2D Ultimate Connect Edition V22.00.00.1733 software, the Poisson's ratio values of the non-liquefied and liquefied zones are defined as 0.30 and 0.33, respectively. The elastic modulus values of the same layers, on the other hand, are estimated as 10 MPa and 5 MPa, respectively.

The effective normal (σ'_N) and shear (τ_{static}) stresses acting on the inclined failure plane are evaluated with corresponding Mohr's circles. The corresponding Mohr's circles and the effective stress components of the sub-sections are presented in Figure A.32.5 and Table A.32.2, respectively. All stresses are given in kilopascals.

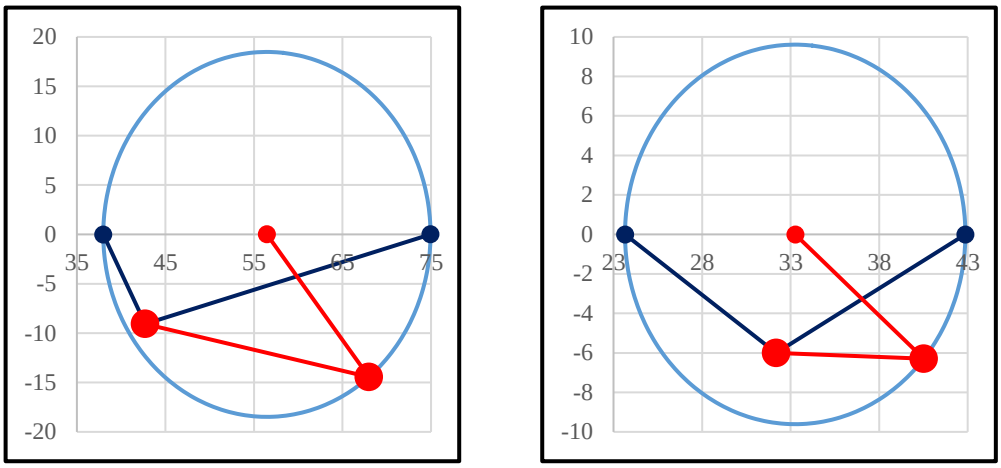

(a) S1 (b) S2

Figure A.32.5. Mohr's circles for Jamuna Bridge

Table A.32.2 Evaluated stress components for Jamuna Bridge

Case History	Section	σ'_1 (kPa)	σ'_2 (kPa)	σ'_3 (kPa)	p_0' (kPa)	q (kPa)	σ'_N (kPa)	τ_{static} (kPa)	$\lvert\tau_{static}\rvert$ (kPa)
Jamuna Bridge	S1	74.9	40.2	38.0	51.0	35.9	68.0	-14.4	14.4
	S2	42.9	28.8	23.7	31.8	17.2	40.5	-6.3	6.3

A.32.6 Evaluation of SPT Resistance

The exact locations of the CPT boreholes were not documented for this case history. Therefore, imaginary boreholes are assigned along the cross-section as shown in Figure A.32.2. CPT data used for this case history is presented in Figure A.32.6.

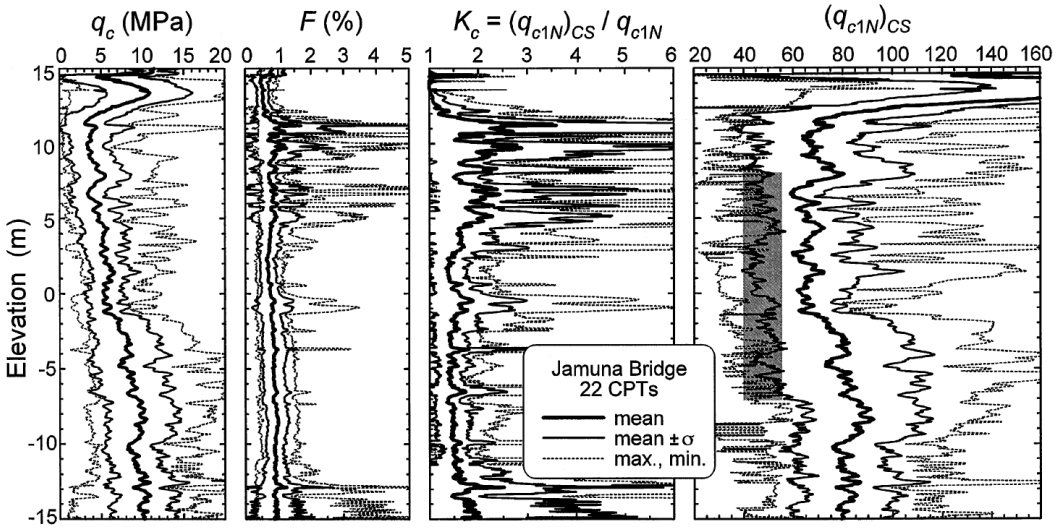

Figure A.32.6. CPT data for Jamuna Bridge (Yoshimine et al., 1999)

The CPT cone tip resistances are converted to raw SPT-N and N_{60} values by using the correlations proposed by Ishihara et al. (1990) and Kulhawy and Mayne (1990), respectively, as explained in Section 3.5. Then, the overburden stress correction factors (C_N) are again evaluated to be able to estimate $(N_1)_{60}$ values based on the effective vertical stresses estimated at the point of penetration for each recording, and average values are documented for simplicity. The fines content correction factors (C_{fines}) are also evaluated with the methods and relationships explained in Section 3.5. Accordingly, the correction factors and SPT resistances are estimated as given in Table A.32.3.

Table A.32.3 Evaluated SPT-N resistances for Jamuna Bridge

Case History	Section	C_N	C_B	C_R	C_S	C_E	C_{fines}	N	N_{60}	$(N_1)_{60}$	$(N_1)_{60,cs}$	
Jamuna Bridge	S1	0.76	-	-	-	-	1.07	9.98	16.31	6.71	7.17	7.17
	S2	0.76	-	-	-	-	1.07	9.98	16.31	6.71	7.17	

A.32.7 Evaluation of Limit Void Ratios, Void Ratio Ranges, Relative Densities and Initial Void Ratios

Since mean grain size (D_{50}) and fines content (FC) information were available among the required material properties for the void ratio prediction models, the arithmetic means of the limit void ratios (e_{min} and e_{max}) evaluated by Model 1 and Model 2 are considered as the representative values. The e_{max} value is slightly modified then with respect to the construction method of the case history for each prediction model.

Since the fines content value is evaluated as 6%, which is less than 15%, it is judged that the soil of interest consists of sand type of soils. Therefore, the arithmetic mean of the relative densities evaluated by the correlations recommended by Kulhawy and Mayne (1990) and Cubrinovski and Ishihara (1999) is taken as the overall relative density of the soil. Based on these relative densities and limit void ratios, the initial void ratios (e_0) corresponding to approximately 1 kPa confining stress are estimated referring to Equation 3-68. Accordingly, the limit void ratios, void ratio ranges (without any modification for the construction method), in-situ relative densities, and initial void ratios are estimated as given in Table A.32.4.

Table A.32.4 Evaluated limit void ratios, void ratio ranges, in-situ relative densities, and initial void ratios for Jamuna Bridge

Case History	Section	e_{min}	e_{max}	e_{max}-e_{min}	$RD_{C\&I}$ (%)	$RD_{K\&M}$ (%)	$RD_{overall}$ (%)	e_0
Jamuna Bridge	S1	0.590	0.995	0.406	35.18	41.27	38.22	0.840
	S2	0.590	0.995	0.406	35.18	41.27	38.22	0.840

A.33 Calaveras Dam (1918 Construction)

A.33.1 Brief Summary of the Case History

Calaveras Dam was located in California, USA, and the exact date of the failure was reported as March 24, 1918. The fundamental reason behind the failure was reported

as the construction. The type of the case structure can be classified as a hydraulic fill dam, and the maximum slope height is reported as ~ 61 m. Hazen (1918, 1920) and Olivia Chen Consultants (2003) are considered as the main sources of references. Olson (2001), Wang (2003) and Weber (2015) also studied this case history during their back-analyses of liquefaction failure case histories.

A.33.2 Site Geology and Critical Cross-section

Figure A.33.1 and Figure A.33.2 present the soil stratigraphy of the dam cross-section, and Figure A.33.3 and Figure A.33.4 show the pre-failure and post-failure cross-sections of the case structure. It is decided that the idealized soil profile consists of two soil layers namely liquefied zone and foundation. While the entire dam is classified as liquefied material, the layer underlying the dam is defined as the foundation.

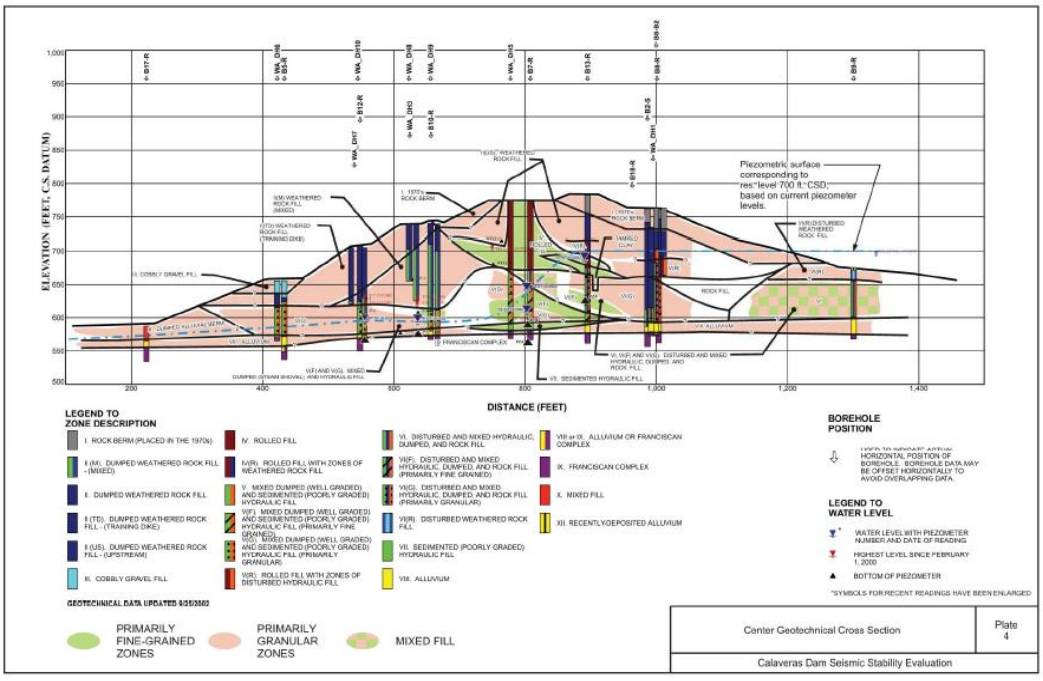

Figure A.33.1. Soil stratigraphy of the Calaveras Dam (Olivia Chen Consultants, 2003)

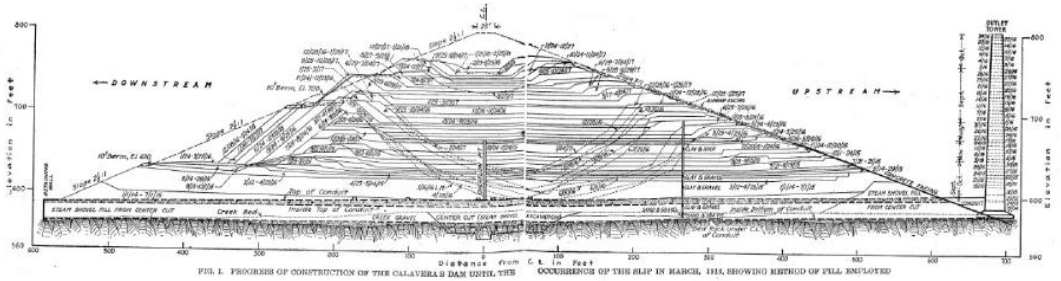

Figure A.33.2. Soil stratigraphy of the Calaveras Dam (Hazen, 1920)

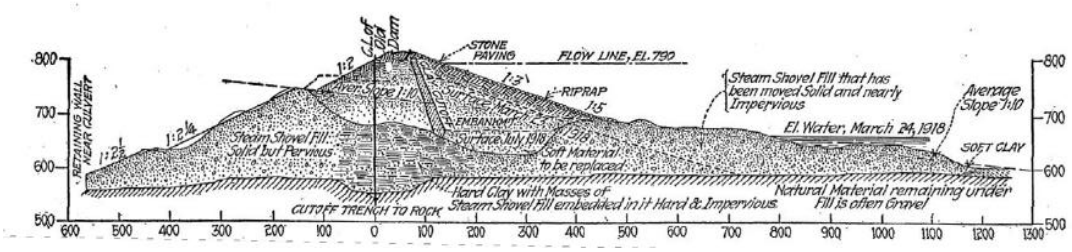

Figure A.33.3. Pre-failure and post-failure cross-sections of the Calaveras Dam (Hazen, 1920)

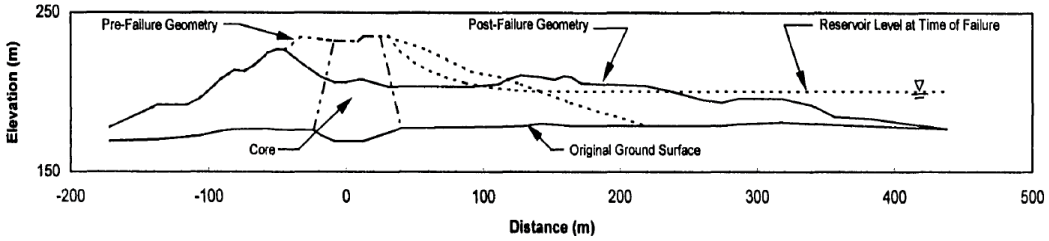

Figure A.33.4. Pre-failure and post-failure cross-sections of the Calaveras Dam (Olson 2001, after Hazen, 1918)

A.33.3 Evaluation of Material Properties

Since the grain size distribution curve of the case history was not reported by the main sources of references or other residual strength-related studies, mean grain size (D_{50}), fines content (FC) and coefficient of uniformity (C_u) values are estimated based on the documented representative values in those references, if available.

Mean grain size (D_{50}): Since no mean grain size value was reported by the main sources of references or other relative studies, D_{50} value is representatively taken as

0.732 mm in this study referring to similar type of structures and soil profiles reported in Ilgac et al. (2019) dataset.

Fines content (FC): The exact value of the fines content was reported as FC = 30% in Gutierrez et al. (2016). Similarly, a range of 10-50% was reported for fines content by Olson (2001). Therefore, the average value of this range, FC = 30%, is taken as the representative fines content value in this study.

Coefficient of uniformity (C_u): Since no coefficient of uniformity value was reported by the main sources of references or other relative studies, no value has been set for this parameter.

Roundness (R): Since no roundness value was reported by the main sources of references or other studies, no value has been set for this parameter for the evaluation of limit void ratios and void ratio ranges. However, R = 0.50 is taken approximately as a representative value for the evaluation of liquefaction state friction angle.

Sphericity (S): Since no sphericity value was reported by the main sources of references or other studies, no value has been set for this parameter for the evaluation of limit void ratios and void ratio ranges. However, S = 0.60 is taken approximately as a representative value for the evaluation of liquefaction state friction angle.

Unit weight (γ_{dry} and γ_{sat}): As the results are not sensitive to unit weight, the unit weights of liquefied zone and foundation layers are assigned as 20.1 kN/m^3 and 20.4 kN/m^3, respectively, to be compatible with Olson (2001) and Weber (2015).

A.33.4 Sub-sectioning of the Cross-section and Failure Plane

The exact locations of the SPT boreholes were not known for this case history. Therefore, the sub-sectioning is made based on imaginary boreholes assigned on the cross-section. These imaginary boreholes are defined with respect to changes in effective vertical stresses and inclination angles of the failure plane. Accordingly, two sub-sections are assigned for the liquefied zone as presented in Figure A.33.5.

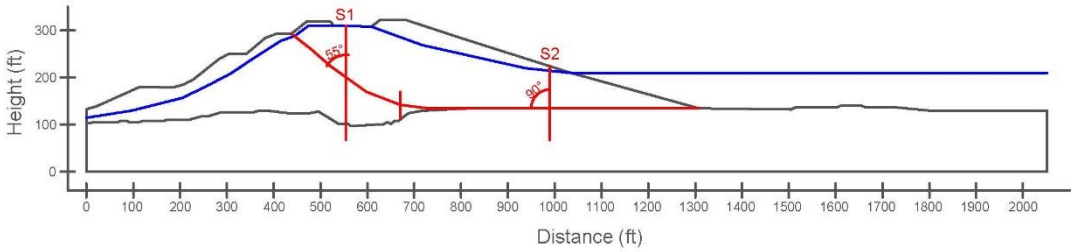

Figure A.33.5. Sub-sectioning of the cross-section and failure plane for Calaveras Dam

The territory lengths (L_i) and inclinations (α_i) (positive sign for CCW direction) of the failure plane are evaluated as given in Table A.33.1 for each sub-section.

Table A.33.1 Sub-sections with their corresponding failure plane lengths and inclinations for Calaveras Dam

Case History	Section	Failure plane length, L_i (m)	Total failure plane length, L_t (m)	Failure plane inclination, α_i (degrees)
Calaveras Dam	S1	83.00	277.27	-35
	S2	194.27		0

A.33.5 Elastic Modeling and Stress Rotation

All stress components are evaluated linear elastically at the points where boreholes and failure plane intersect in Figure A.33.5. The initial and deformed shape of the cross-section are presented in Figure A.33.6 and Figure A.33.7, respectively. All lengths are given in meters.

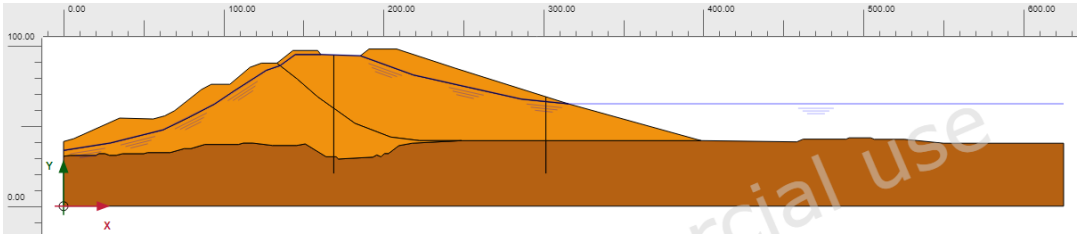

Figure A.33.6. Initial cross-section used in linear elastic modeling of Calaveras Dam

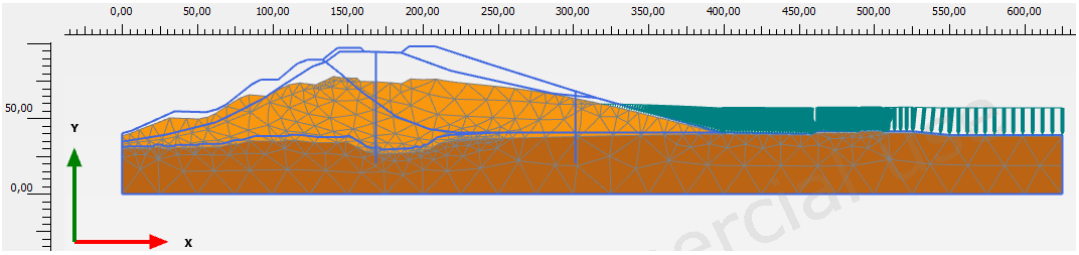

Figure A.33.7. Deformed cross-section obtained after linear elastic modeling of Calaveras Dam

During the elastic modeling process in PLAXIS 2D Ultimate Connect Edition V22.00.00.1733 software, the Poisson's ratio values of the liquefied zone and foundation layer are defined as 0.33 and 0.30, respectively. The elastic modulus values of the same layers, on the other hand, are estimated as 5 MPa and 30 MPa, respectively.

The effective normal (σ'_N) and shear (τ_{static}) stresses acting on the inclined failure plane are evaluated with corresponding Mohr's circles. The corresponding Mohr's circles and the effective stress components of the sub-sections are presented in Figure A.33.8 and Table A.33.2, respectively. All stresses are given in kilopascals.

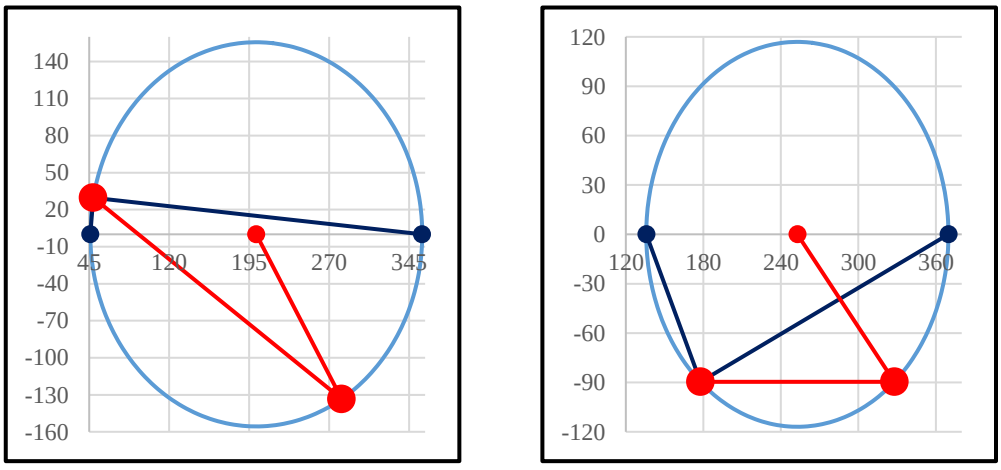

(a) S1 (b) S2

Figure A.33.8. Mohr's circles for Calaveras Dam

Table A.33.2 Evaluated stress components for Calaveras Dam

Case History	Section	σ'_1 (kPa)	σ'_2 (kPa)	σ'_3 (kPa)	p_0' (kPa)	q (kPa)	σ'_N (kPa)	τ_{static} (kPa)	$\lvert\tau_{static}\rvert$ (kPa)
Calaveras Dam	S1	357.3	133.1	46.0	178.8	278.2	281.8	-133.4	133.4
	S2	369.7	166.8	135.8	224.1	220.0	327.9	-89.6	89.6

A.33.6 Evaluation of SPT Resistance

The exact locations of the SPT boreholes were not documented for this case history. Therefore, imaginary boreholes are assigned along the cross-section as shown in Figure A.33.5. SPT data used for this case history is presented in Figure A.33.9.

Zone	Zone Description	Subzone	30th Percentile $(N_1)_{60}$ SPT	30th Percentile $(N_1)_{60}$ BPT	50th Percentile $(N_1)_{60}$ SPT	50th Percentile $(N_1)_{60}$ BPT	Representative Fines Content	ΔN_{CS} (for fines)
I	Rock Berm (Placed In The 1970s)		N/D	22	N/D	29	15 (F)	N/A
II	Dumped Weathered Rock Fill	II(M) II(TD) II(US)	17 9 23	19 (B) 8 21	21 12 22	23 8 20	14 7 10	1.5 1 1
III	Cobbly Gravel Fill		/ND	7	N/D	8	20 (F)	1.5
IV	Rolled Fill	IV IV(R)	17 24	23 (L) 12 (L)	22 (L) 32 (L)	25 16	48 12 (F)	N/A 1
V	Mixed Dumped and Sedimented Hydraulic Fill	V V(F) V(G)	13 12 17	19 17 17	16 17 20	23 23 22	20 15 (F) 19	1.5 1.5 1.5
V(R)	Mixed Hydraulic and Rolled Fill		21	14 (L)	24	18	15 (F)	1.5
VI	Disturbed and Mixed Hydraulic, Dumped, and Rock Fill	VI VI(F) VI(G)-Res VI(G)-Emb VI(R)	10 11 7 27 12 (L)	N/D 22 (L) N/D 22 N/D	17 18 8 40 12 (L)	N/D 36 (L) N/D 31 N/D	11 59 11 11 15	1 N/A 1 1 1.5
VII	Sedimented Hydraulic Fill		10	N/D	13	N/D	62	N/A
VIII	Base Alluvium		19	20	30	26	8	1
X	Mixed Fill		12	17	13	26	19 (F)	1.5
XI	Rocky Colluvium		32	36	34	43	N/D	0

(L): Limited penetration data available
(B): Based on data at bottom of zone
(F): Calibrated field-estimated fines contents were also considered
N/A: Not Applicable (High CL content)
N/D: Not Determined

Figure A.33.9. SPT data for Calaveras Dam (Olivia Chen Consultants, 2003)

The correction factors for nonstandardized sampler configuration (C_S), borehole diameter (C_B), and energy efficiency (C_E) are taken as 1.0 since no reliable

information related to these coefficients was reported in any of the sources. The short rod length (C_R) and fines content correction factors (C_{fines}) are evaluated with the methods and relationships explained in Section 3.5. The overburden stress correction factors (C_N) are evaluated based on the effective vertical stresses estimated at the point of penetration for each recording, and average values are documented for simplicity. Accordingly, the correction factors and SPT resistances are estimated as given in Table A.33.3.

Table A.33.3 Evaluated SPT-N resistances for Calaveras Dam

Case History	Section	C_N	C_B	C_R	C_S	C_E	C_{fines}	N	N_{60}	$(N_1)_{60}$	$(N_1)_{60,cs}$	
Calaveras Dam	S1	0.52	1.0	0.99	1.0	1.00	1.23	14.00	13.90	14.00	17.18	17.18
	S2	0.54	1.0	0.99	1.0	1.00	1.23	14.00	13.90	14.00	17.18	

A.33.7 Evaluation of Limit Void Ratios, Void Ratio Ranges, Relative Densities and Initial Void Ratios

Since mean grain size (D_{50}) and fines content (FC) information were available among the required material properties for the void ratio prediction models, the arithmetic means of the limit void ratios (e_{min} and e_{max}) evaluated by Model 1 and Model 2 are considered as the representative values. The e_{max} value is slightly modified then with respect to the construction method of the case history for each prediction model.

Since the fines content value is evaluated as 30%, which is greater than 15%, it is judged that the soil of interest consists of silty soils. Therefore, the relative densities evaluated by the correlation recommended by Cubrinovski and Ishihara (1999) are directly taken as the representative relative densities of the soils. Based on these relative densities and limit void ratios, the initial void ratios (e_0) corresponding to approximately 1 kPa confining stress are estimated referring to Equation 3-68. Accordingly, the limit void ratios, void ratio ranges (without any modification for the construction method), in-situ relative densities, and initial void ratios are estimated as given in Table A.33.4.

Table A.33.4 Evaluated limit void ratios, void ratio ranges, in-situ relative densities, and initial void ratios for Calaveras Dam

Case History	Section	e_{min}	e_{max}	e_{max}-e_{min}	$RD_{C\&I}$ (%)	$RD_{K\&M}$ (%)	$RD_{overall}$ (%)	e_0
Calaveras Dam	S1	0.545	0.898	0.353	45.10	49.73	45.10	0.739
	S2	0.545	0.898	0.353	45.10	49.73	45.10	0.739

A.34 Koda Numa Railway Embankment (1968 Tokachi-Oki Earthquake, M=7.9)

A.34.1 Brief Summary of the Case History

Koda Numa Railway Embankment was located in Japan, and the exact date of the failure was reported as March 28, 1968. The fundamental reason behind the failure was reported as the 1968 Tokachi-Oki Earthquake (M=7.9). The type of the structure can be classified as a poorly compacted embankment, and the maximum slope height is reported as ~ 2.5 m. Mishima and Kimura (1970) is considered as the main source of reference. Weber (2015) did not perform back-analyses for this case history, but Olson (2001) and Wang (2003) studied it during their back-analyses of liquefaction failure case histories.

A.34.2 Site Geology and Critical Cross-section

Figure A.34.1 and Figure A.34.2 show the soil stratigraphy and pre-failure and post-failure cross-sections of the case structure. It is decided that the idealized soil profile consists of three soil layers namely non-liquefied zone, liquefied zone and foundation. The parts of the poorly compacted embankment remaining above and below the water table level at the time of failure are classified as non-liquefied zone and liquefied zone, respectively. The layer underlying the embankment is defined as the foundation.

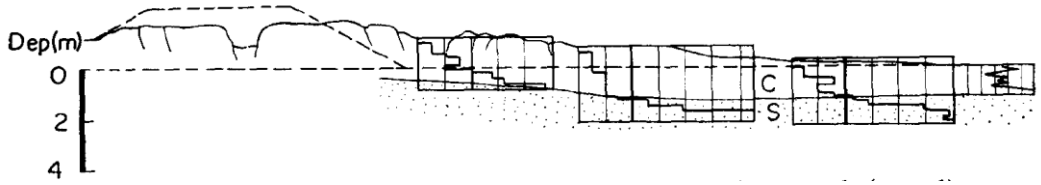

Figure A.34.1. Soil stratigraphy and pre-failure and post-failure cross-sections of the Koda Numa Railway Embankment (Mishima and Kimura, 1970)

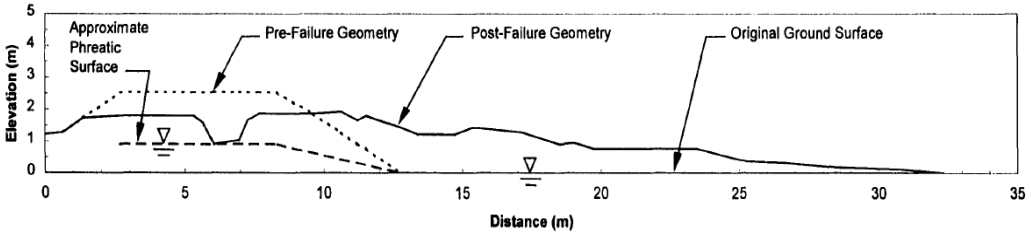

Figure A.34.2. Soil stratigraphy and pre-failure and post-failure cross-sections of the Koda Numa Railway Embankment (Olson, 2001)

A.34.3 Evaluation of Material Properties

Since the grain size distribution curve of the case history was reported by the main sources of references as given in Figure A.34.3, mean grain size (D_{50}), fines content (FC) and coefficient of uniformity (C_u) values are evaluated based on this curve.

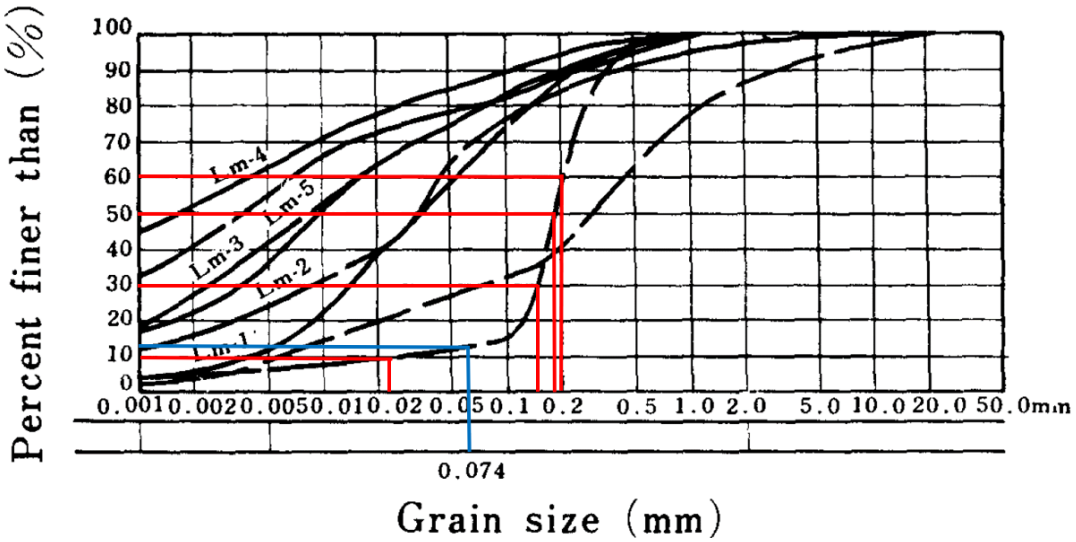

Figure A.34.3. Grain size distribution curve of the Koda Numa Railway Embankment (Mishima and Kimura, 1970)

Mean grain size (D_{50}): D_{50} = 0.180 mm is evaluated representatively based on the grain size distribution curve of the case history. Olson (2001) also suggests a range of 0.150-0.200 mm for D_{50} value of this case history.

Fines content (FC): FC = 13% is evaluated representatively based on the grain size distribution curve of the case history. Olson (2001) and Gutierrez et al. (2016) also recommend 13% for FC value of this case history.

Coefficient of uniformity (C_u): D_{10} and D_{60} values are evaluated as 0.023 mm and 0.200 mm, respectively, based on the grain size distribution curve of the case history. Therefore, the uniformity coefficient is estimated as $C_u = D_{60}/D_{10} = 0.200/0.023 = 8.70$, which indicates well-graded soil.

Roundness (R): Since no roundness value was reported by the main sources of references or other studies, no value has been set for this parameter for the evaluation of limit void ratios and void ratio ranges. However, R = 0.50 is taken approximately as a representative value for the evaluation of liquefaction state friction angle.

Sphericity (S): Since no sphericity value was reported by the main sources of references or other studies, no value has been set for this parameter for the evaluation of limit void ratios and void ratio ranges. However, S = 0.60 is taken approximately as a representative value for the evaluation of liquefaction state friction angle.

Unit weight (γ_{dry} and γ_{sat}): As the results are not sensitive to unit weight, the dry and saturated unit weights of the non-liquefied and liquefied zones are assigned as 16.0 kN/m^3 and 18.5 kN/m^3, respectively. The unit weight of the foundation, on the other hand, is defined as 18.9 kN/m^3. These values are selected to be compatible with Olson (2001).

A.34.4 Sub-sectioning of the Cross-section and Failure Plane

The exact locations of the Swedish CPT boreholes were known for this case history as presented in Figure A.34.1. Therefore, the sub-sectioning is made based on the

locations of these penetration tests as presented in Figure A.34.4. Each test is assigned (names of the logs are directly assigned as the name of the sub-section) for the corresponding territory length.

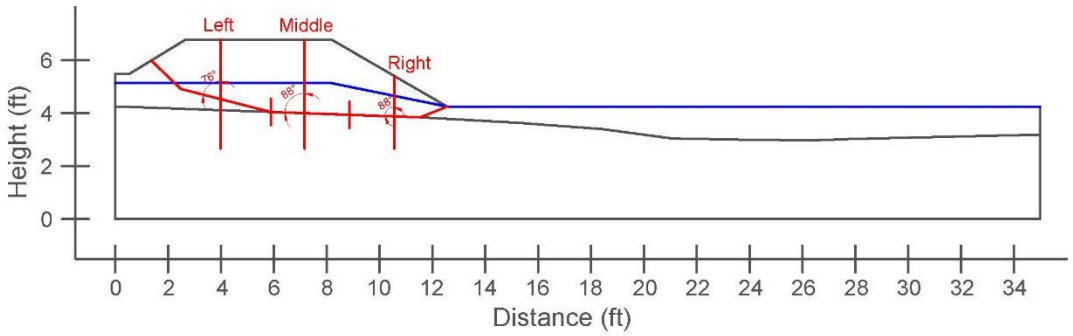

Figure A.34.4. Sub-sectioning of the cross-section and failure plane for Koda Numa Railway Embankment

The territory lengths (L_i) and inclinations (α_i) (positive sign for CCW direction) of the failure plane are evaluated as given in Table A.34.1 for each sub-section.

Table A.34.1 Sub-sections with their corresponding failure plane lengths and inclinations for Koda Numa Railway Embankment

Case History	Section	Failure plane length, L_i (m)	Total failure plane length, L_t (m)	Failure plane inclination, α_i (degrees)
Koda Numa Railway Embankment	Left	3.84	10.57	-14
	Middle	2.95		-2
	Right	3.77		-2

A.34.5 Elastic Modeling and Stress Rotation

All stress components are evaluated linear elastically at the points where boreholes and failure plane intersect in Figure A.34.4. The initial and deformed shape of the cross-section are presented in Figure A.34.5 and Figure A.34.6, respectively. All lengths are given in meters.

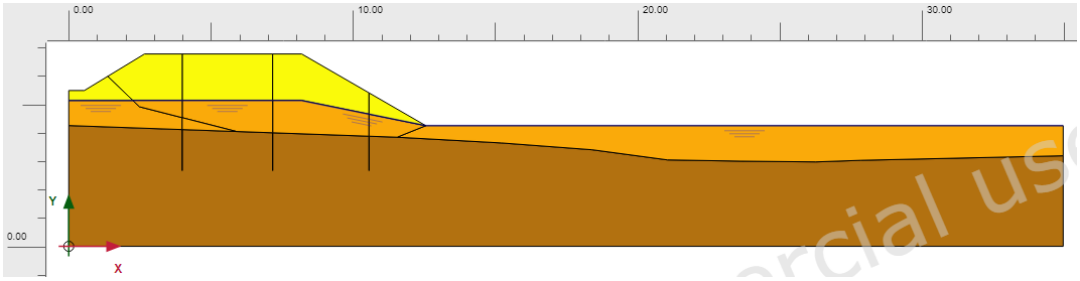

Figure A.34.5. Initial cross-section used in linear elastic modeling of Koda Numa Railway Embankment

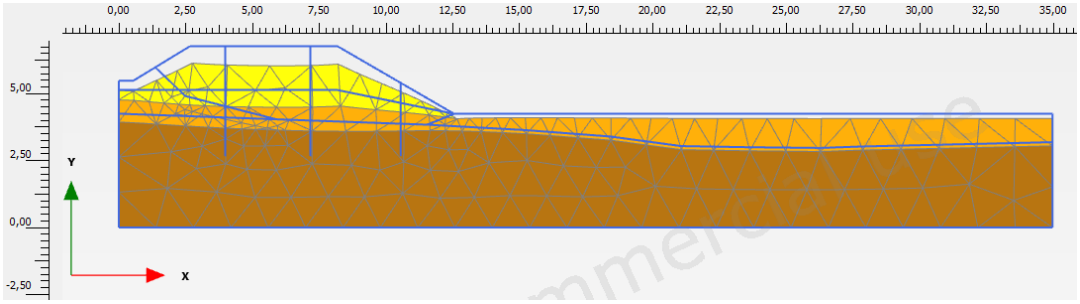

Figure A.34.6. Deformed cross-section obtained after linear elastic modeling of Koda Numa Railway Embankment

During the elastic modeling process in PLAXIS 2D Ultimate Connect Edition V22.00.00.1733 software, the Poisson's ratio values of the non-liquefied zone, liquefied zone, and foundation are defined as 0.30, 0.33, and 0.30, respectively. The elastic modulus values of the same layers, on the other hand, are estimated as 10 MPa, 5 MPa, and 20 MPa, respectively.

The effective normal (σ'_N) and shear (τ_{static}) stresses acting on the inclined failure plane are evaluated with corresponding Mohr's circles. The corresponding Mohr's circles and the effective stress components of the sub-sections are presented in Figure A.34.7 and Table A.34.2, respectively. All stresses are given in kilopascals.

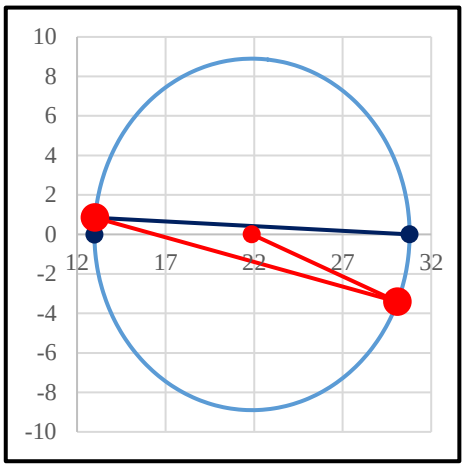

(a) Left

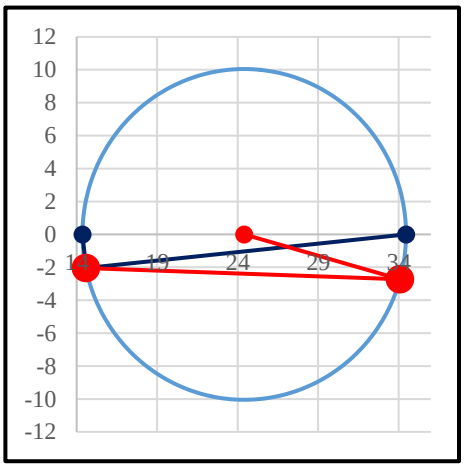

(b) Middle

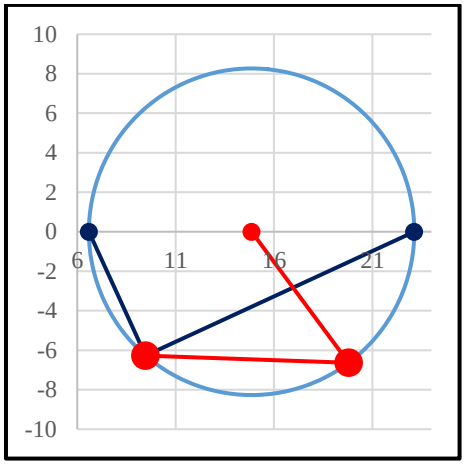

(c) Right

Figure A.34.7. Mohr's circles for Koda Numa Railway Embankment

Table A.34.2 Evaluated stress components for Koda Numa Railway Embankment

Case History	Section	σ'_1 (kPa)	σ'_2 (kPa)	σ'_3 (kPa)	p_0' (kPa)	q (kPa)	σ'_N (kPa)	τ_{static} (kPa)	$\lvert\tau_{static}\rvert$ (kPa)
Koda Numa Railway Embankment	Left	30.8	14.4	13.0	19.4	17.1	30.1	-3.4	3.4
	Middle	34.5	16.1	14.4	21.6	19.3	34.1	-2.7	2.7
	Right	23.1	9.8	6.6	13.2	15.2	19.8	-6.6	6.6

A.34.6 Evaluation of SPT Resistance

The exact locations of the Swedish CPT boreholes were documented by Mishima and Kimura (1970) as given in Figure A.34.1. The SCPT resistances are converted to raw SPT-N values by using the correlation proposed by Inada (1982) explained in Section 3.5. These SPT-N values are assumed to be almost equal to N_{60} values as equipment, energy, and procedure corrections are not applicable for SCPT. However, the short rod length correction factors (C_R) are still evaluated with the methods and relationships explained in Section 3.5. Similarly, the overburden stress correction factors (C_N) are again evaluated based on the effective vertical stresses estimated at the point of penetration for each recording, and average values are documented for simplicity. The fines content correction factors (C_{fines}) are also evaluated with the methods and relationships explained in Section 3.5. Accordingly, the correction factors and SPT resistances are estimated as given in Table A.34.3.

Table A.34.3 Evaluated SPT-N resistances for Koda Numa Railway Embankment

Case History	Section	C_N	C_B	C_R	C_S	C_E	C_{fines}	N	N_{60}	$(N_1)_{60}$	$(N_1)_{60,cs}$	
Koda Numa Railway Embankment	Left	2.93	-	0.75	-	-	1.36	1.00	0.75	2.08	2.84	2.87
	Middle	2.44	-	0.78	-	-	1.42	1.00	0.78	1.77	2.51	
	Right	2.98	-	0.77	-	-	1.31	1.13	0.87	2.48	3.25	

A.34.7 Evaluation of Limit Void Ratios, Void Ratio Ranges, Relative Densities and Initial Void Ratios

Since mean grain size (D_{50}), fines content (FC), and coefficient of uniformity (C_u) information were available among the required material properties for the void ratio prediction models, the arithmetic means of the limit void ratios (e_{min} and e_{max}) evaluated by Model 8 and Model 9 are considered as the representative values. The e_{max} value is slightly modified then with respect to the construction method of the case history for each prediction model.

Since the fines content value is evaluated as 13%, which is less than 15%, it is judged that the soil of interest consists of sand type of soils. Therefore, the arithmetic mean of the relative densities evaluated by the correlations recommended by Kulhawy and Mayne (1990) and Cubrinovski and Ishihara (1999) is taken as the overall relative density of the soil. Based on these relative densities and limit void ratios, the initial void ratios (e_0) corresponding to approximately 1 kPa confining stress are estimated referring to Equation 3-68. Accordingly, the limit void ratios, void ratio ranges (without any modification for the construction method), in-situ relative densities, and initial void ratios are estimated as given in Table A.34.4.

Table A.34.4 Evaluated limit void ratios, void ratio ranges, in-situ relative densities, and initial void ratios for Koda Numa Railway Embankment

Case History	Section	e_{min}	e_{max}	e_{max}-e_{min}	$RD_{C\&I}$ (%)	$RD_{K\&M}$ (%)	$RD_{overall}$ (%)	e_0
Koda Numa Railway Embankment	Left	0.469	0.807	0.339	16.80	22.43	19.62	0.741
	Middle	0.469	0.807	0.339	15.49	20.69	18.09	0.746
	Right	0.469	0.807	0.339	18.32	24.46	21.39	0.735

A.35 Whiskey Springs Fan (1983 Borah Peak Earthquake, M=7.3)

A.35.1 Brief Summary of the Case History

Whiskey Springs Fan was located in California, USA, and the exact date of the failure was reported as October 28, 1983. The fundamental reason behind the failure was reported as the 1983 Borah Peak Earthquake (M=7.3). The type of the structure can be classified as a springs fan, and the maximum slope height is reported as ~ 15 m. Andrus and Youd (1987), Harder (1988) and Wride et al. (1999) are considered as the main sources of references. Weber (2015), Olson (2001) and Wang (2003) did not perform back-analyses for this case history, but Seed and Harder (1990) and Stark and Mesri (1992) studied it during their back-analyses of liquefaction failure case histories.

A.35.2 Site Geology and Critical Cross-section

Figure A.35.1 presents the pre-failure and post-failure cross-sections, and Figure A.35.2 shows the soil stratigraphy of the case structure. Referring to Figure A.35.2, it is decided that the idealized soil profile consists of many horizontal soil layers with various thickness. The definitions of these layers are taken as the same with the ones reported in Figure A.35.2 by Andrus and Youd (1987). Loose and fine-grained gravelly sediment layer (Unit C) is judged to be susceptible to liquefaction.

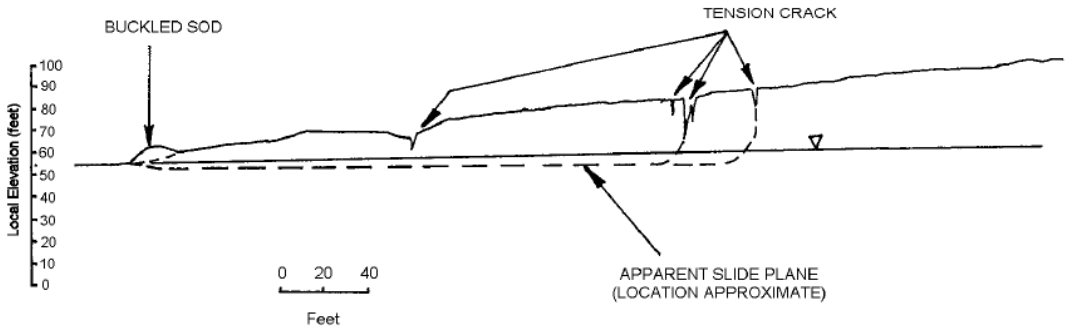

Figure A.35.1. Pre-failure and post-failure cross-sections of the Whiskey Springs Fan (Harder, 1988)

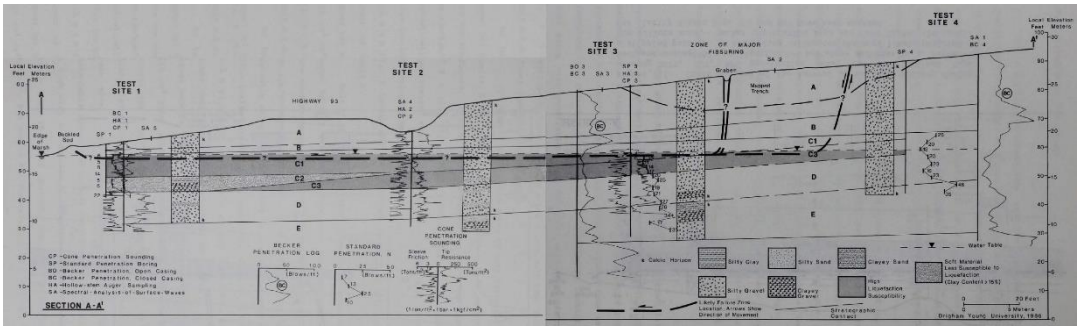

Figure A.35.2. Soil stratigraphy of the Whiskey Springs Fan (Andrus and Youd, 1987)

A.35.3 Evaluation of Material Properties

Since the grain size distribution curve of the case history was reported by the main sources of references as given in Figure A.35.3, mean grain size (D_{50}), fines content (FC) and coefficient of uniformity (C_u) values are evaluated based on this curve.

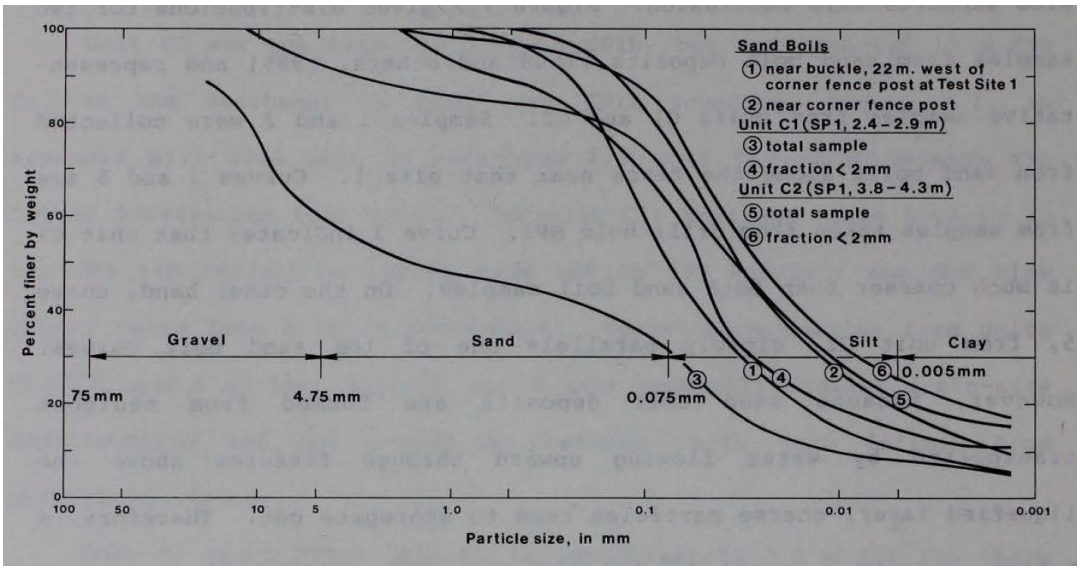

Figure A.35.3. Grain size distribution curve of the Whiskey Springs Fan (Andrus and Youd, 1987)

Mean grain size (D_{50}): D_{50} = 1.613 mm is evaluated representatively based on the grain size distribution curve of the case history. Due to high gravel content of the liquefied zone, the mean grain size is evaluated extremely high in average.

Fines content (FC): FC = 31.5% is evaluated representatively based on the grain size distribution curve of the case history. Harder (1988) and Seed and Harder (1990) also suggest 20% and 40%, respectively, for FC value of this case history.

Coefficient of uniformity (C_u): D_{10} and D_{60} values are evaluated as 0.011 mm and 4.812 mm, respectively, based on the grain size distribution curve of the case history. Therefore, the uniformity coefficient is estimated as $C_u = D_{60}/D_{10} = 4.812/0.011 = 455.33$. Due to high gravel content of the liquefied zone, the uniformity coefficient is evaluated extremely high in average.

Roundness (R): The liquefied zone was reported as consisting of mainly subangular materials in the main sources of references. Referring to common roundness values of subangular materials in literature, R = 0.30 is estimated for this case in this study.

Sphericity (S): Since no sphericity value was reported by the main sources of references or other studies, no value has been set for this parameter for the evaluation of limit void ratios and void ratio ranges. However, S = 0.60 is taken approximately as a representative value for the evaluation of liquefaction state friction angle.

Unit weight (γ_{dry} and γ_{sat}): As the results are not sensitive to unit weight, the dry and saturated unit weights of all soil layers are assigned as 17.3 kN/m^3 and 18.9 kN/m^3, respectively, to be compatible with the literature.

A.35.4 Sub-sectioning of the Cross-section and Failure Plane

The exact locations of the SPT boreholes were known for this case history as presented in Figure A.35.2. Therefore, the sub-sectioning is made based on the locations of these penetration tests as presented in Figure A.35.4. Each test is assigned (names of the logs are directly assigned as the name of the sub-section) for the corresponding territory length.

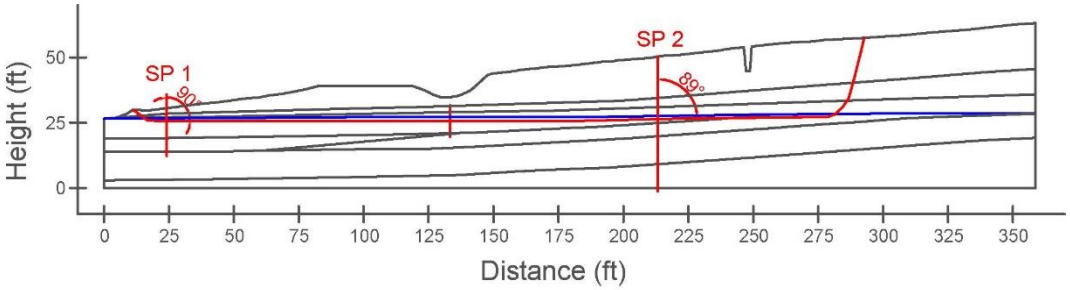

Figure A.35.4. Sub-sectioning of the cross-section and failure plane for Whiskey Springs Fan

The territory lengths (L_i) and inclinations (α_i) (positive sign for CCW direction) of the failure plane are evaluated as given in Table A.35.1 for each sub-section.

Table A.35.1 Sub-sections with their corresponding failure plane lengths and inclinations for Whiskey Springs Fan

Case History	Section	Failure plane length, L_i (m)	Total failure plane length, L_t (m)	Failure plane inclination, α_i (degrees)
Whiskey Springs Fan	SP 1	35.90	81.19	0
	SP 3	45.29		1

A.35.5 Elastic Modeling and Stress Rotation

All stress components are evaluated linear elastically at the points where boreholes and failure plane intersect in Figure A.35.4. The initial and deformed shape of the cross-section are presented in Figure A.35.5 and Figure A.35.6, respectively. All lengths are given in meters.

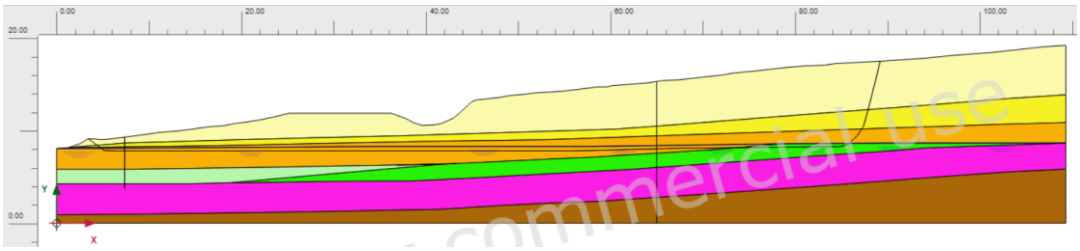

Figure A.35.5. Initial cross-section used in linear elastic modeling of Whiskey Springs Fan

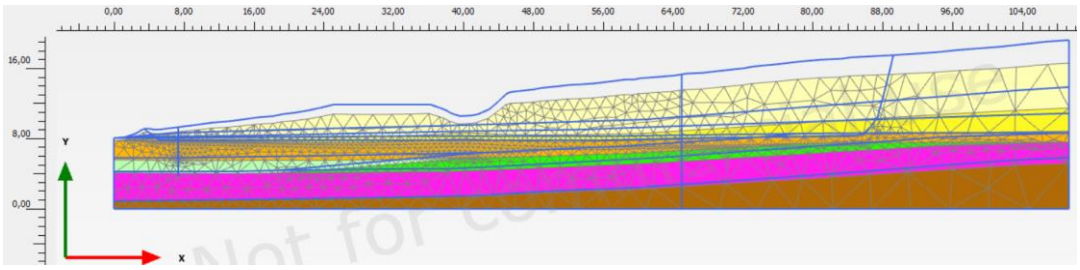

Figure A.35.6. Deformed cross-section obtained after linear elastic modeling of Whiskey Springs Fan

During the elastic modeling process in PLAXIS 2D Ultimate Connect Edition V22.00.00.1733 software, the Poisson's ratio values of all layers other than liquefied

zone are assigned as 0.30. For the liquefied zone, this value is set as 0.33. The elastic modulus values of soil layers A, B, C1 (liquefied zone), C2, C3, D and E, on the other hand, are estimated as 15 MPa, 15 MPa, 5 MPa, 10 MPa, 10 MPa, 20 MPa, and 30 MPa, respectively.

The effective normal (σ'_N) and shear (τ_{static}) stresses acting on the inclined failure plane are evaluated with corresponding Mohr's circles. The corresponding Mohr's circles and the effective stress components of the sub-sections are presented in Figure A.35.7 and Table A.35.2, respectively. All stresses are given in kilopascals.

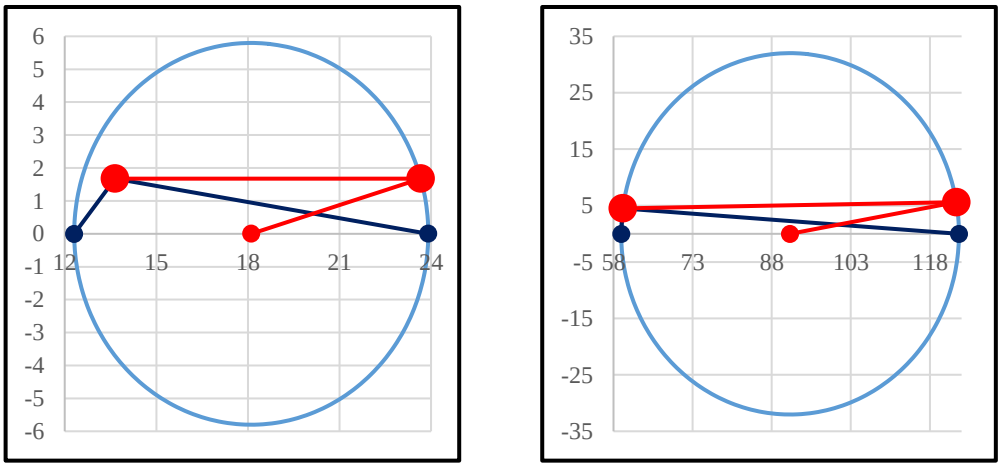

(a) SP 1 (b) SP 3

Figure A.35.7. Mohr's circles for Whiskey Springs Fan

Table A.35.2 Evaluated stress components for Whiskey Springs Fan

Case History	Section	σ'_1 (kPa)	σ'_2 (kPa)	σ'_3 (kPa)	p_0' (kPa)	q (kPa)	σ'_N (kPa)	τ_{static} (kPa)	$\lvert\tau_{static}\rvert$ (kPa)
Whiskey Springs Fan	SP 1	23.9	13.4	12.3	16.5	11.1	23.7	1.7	1.7
	SP 3	123.5	60.4	59.5	81.1	63.6	123.0	5.6	5.6

A.35.6 Evaluation of SPT Resistance

The exact locations of the SPT boreholes were documented by Andrus and Youd (1987) as given in Figure A.35.2. The correction factors for nonstandardized sampler configuration (C_S), borehole diameter (C_B), and energy efficiency (C_E) are taken as

1.0 since no reliable information related to these coefficients was reported in any of the sources. The short rod length (C_R) and fines content correction factors (C_{fines}) are evaluated with the methods and relationships explained in Section 3.5. The overburden stress correction factors (C_N) are evaluated based on the effective vertical stresses estimated at the point of penetration for each recording, and average values are documented for simplicity. Accordingly, the correction factors and SPT resistances are estimated as given in Table A.35.3.

Table A.35.3 Evaluated SPT-N resistances for Whiskey Springs Fan

Case History	Section	C_N	C_B	C_R	C_S	C_E	C_{fines}	N	N_{60}	$(N_1)_{60}$	$(N_1)_{60,cs}$	
Whiskey Springs Fan	SP 1	2.04	1.0	0.88	1.0	1.00	1.27	6.00	5.29	10.80	13.74	14.87
	SP 3	0.81	1.0	0.98	1.0	1.00	1.25	16.29	16.02	12.81	16.00	

A.35.7 Evaluation of Limit Void Ratios, Void Ratio Ranges, Relative Densities and Initial Void Ratios

Since mean grain size (D_{50}), fines content (FC), coefficient of uniformity (C_u), and roundness (R) information were available among the required material properties for the void ratio prediction models, the arithmetic means of the limit void ratios (e_{min} and e_{max}) evaluated by Model 8, Model 9 and Model 10 are considered as the representative values. The e_{max} value is slightly modified then with respect to the construction method of the case history for each prediction model.

Since the fines content value is evaluated as 31.5%, which is greater than 15%, it is judged that the soil of interest consists of silty soils. Therefore, the relative densities evaluated by the correlation recommended by Cubrinovski and Ishihara (1999) are directly taken as the representative relative densities of the soils. Based on these relative densities and limit void ratios, the initial void ratios (e_0) corresponding to approximately 1 kPa confining stress are estimated referring to Equation 3-68. Accordingly, the limit void ratios, void ratio ranges (without any modification for

the construction method), in-situ relative densities, and initial void ratios are estimated as given in Table A.35.4.

Table A.35.4 Evaluated limit void ratios, void ratio ranges, in-situ relative densities, and initial void ratios for Whiskey Springs Fan

Case History	Section	e_{min}	e_{max}	e_{max}-e_{min}	$RD_{C\&I}$ (%)	$RD_{K\&M}$ (%)	$RD_{overall}$ (%)	e_0
Whiskey Springs Fan	SP 1	0.360	0.497	0.138	17.80	40.71	17.80	0.473
	SP 3	0.360	0.497	0.138	19.38	44.33	19.38	0.471

A.36 San Fernando Valley Juvenile Hall (1971 San Fernando Earthquake, M_w=6.6)

A.36.1 Brief Summary of the Case History

San Fernando Valley Juvenile Hall was located in California, USA, and the exact date of the failure was reported as February 9, 1971. The fundamental reason behind the failure was reported as the 1971 San Fernando Earthquake (M_w=6.6). The type of the structure can be classified as a juvenile hall building, and the maximum slope height is reported as ~ 11 m. Bennett (1989) is considered as the main source of reference. Weber (2015), Olson (2001) and Wang (2003) did not perform back-analyses for this case history, but Seed and Harder (1990) and Stark and Mesri (1992) studied it during their back-analyses of liquefaction failure case histories.

A.36.2 Site Geology and Critical Cross-section

Figure A.36.1 and Figure A.36.2 show the soil stratigraphy and pre-failure cross-section of the case structure. Referring to these figures, it is decided that the idealized soil profile consists of many horizontal soil layers with various thickness. The definitions of these layers are taken as the same with the ones reported in Figure A.36.1 and Figure A.36.2 by Bennett (1989). The layer between Units B1 and B2 is judged to be susceptible to liquefaction.

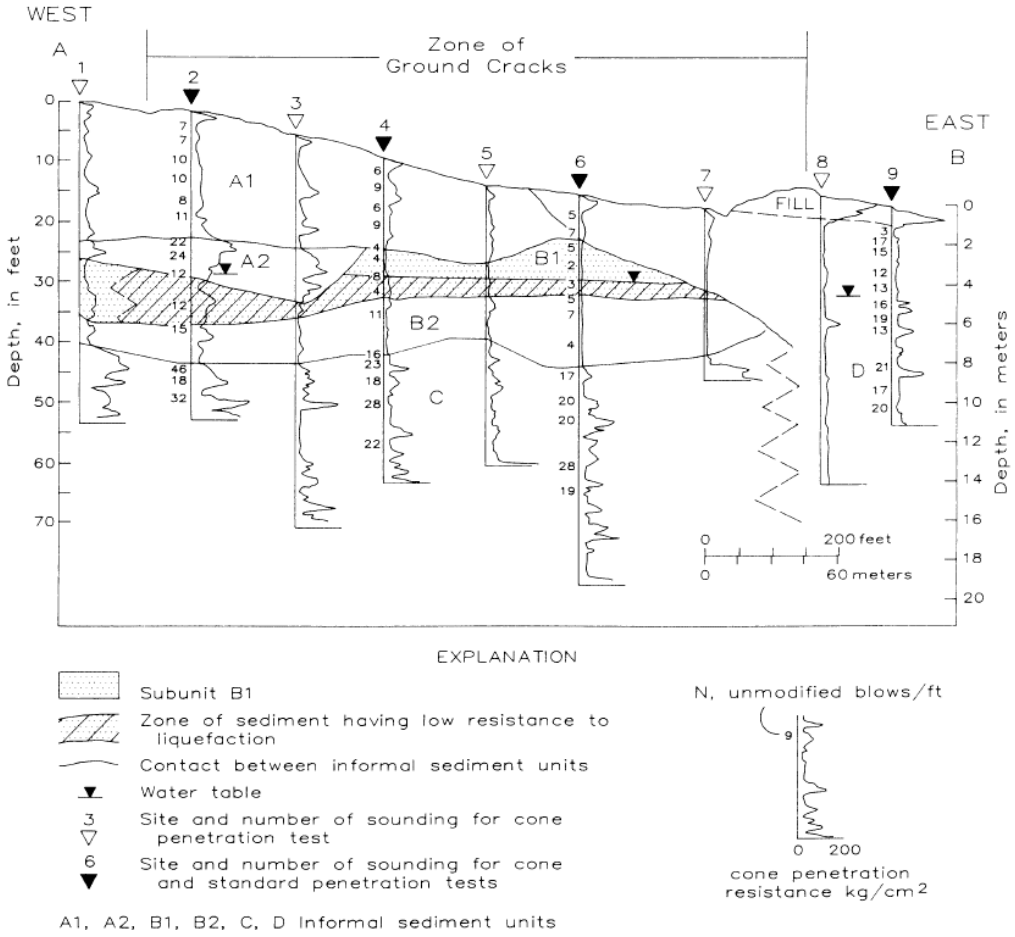

Figure A.36.1. Soil stratigraphy and pre-failure cross-section (W-E direction) of the San Fernando Valley Juvenile Hall (Bennett, 1989)

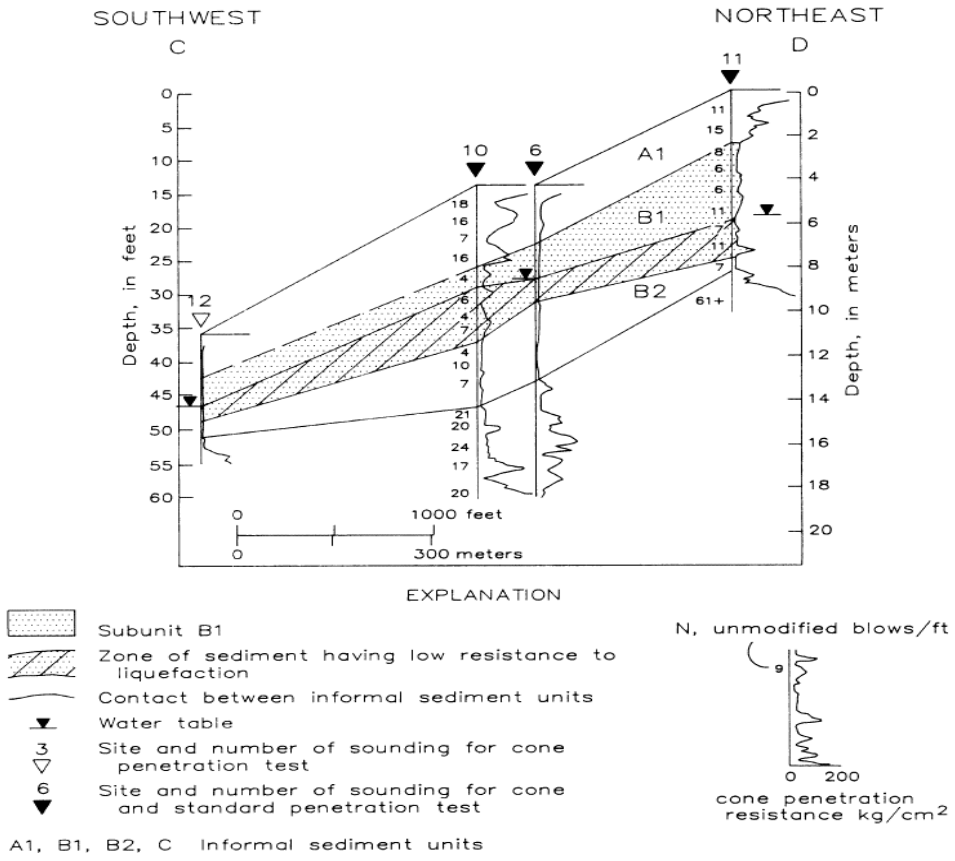

Figure A.36.2. Soil stratigraphy and pre-failure cross-section (SW-NE direction) of the San Fernando Valley Juvenile Hall (Bennett, 1989)

A.36.3 Evaluation of Material Properties

Since the grain size distribution curve of the case history was reported by the main sources of references as given in Figure A.36.3, mean grain size (D_{50}), fines content (FC) and coefficient of uniformity (C_u) values are evaluated based on this curve.

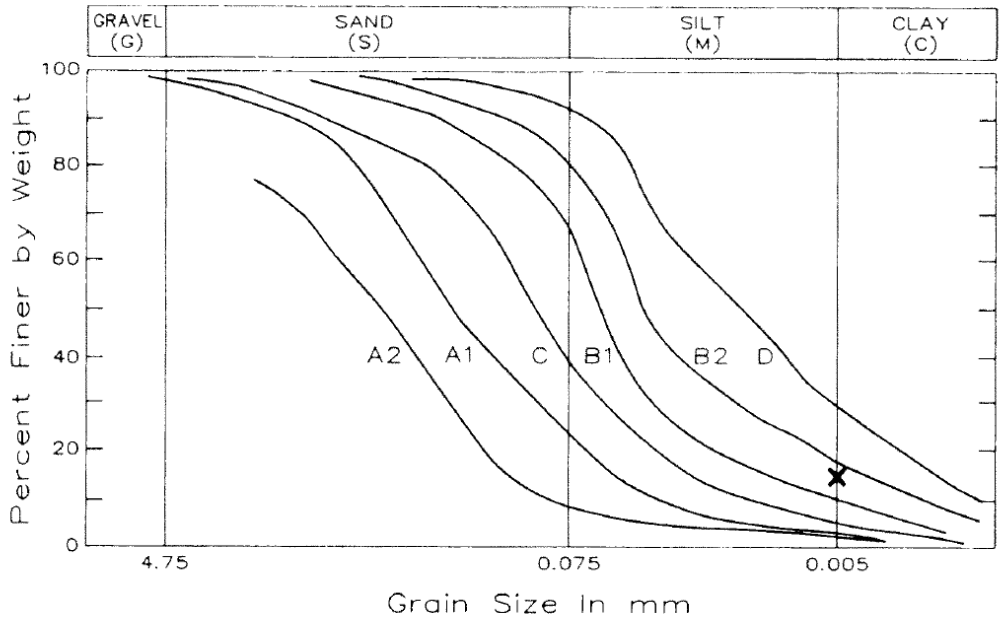

Figure A.36.3. Grain size distribution curve of the San Fernando Valley Juvenile Hall (Bennett, 1989)

Mean grain size (D_{50}): D_{50} = 0.055 mm is evaluated representatively based on the grain size distribution curve of the case history.

Fines content (FC): FC = 63% is evaluated representatively based on the grain size distribution curve of the case history. Stark and Mesri (1992) also suggests 65% for FC value of this case history.

Coefficient of uniformity (C_u): Based on the grain size distribution curve and available information of the case history, the uniformity coefficient is estimated as C_u = 17.10, which indicates well-graded soil.

Roundness (R): Since no roundness value was reported by the main sources of references or other studies, no value has been set for this parameter for the evaluation of limit void ratios and void ratio ranges. However, R = 0.50 is taken approximately as a representative value for the evaluation of liquefaction state friction angle.

Sphericity (S): Since no sphericity value was reported by the main sources of references or other studies, no value has been set for this parameter for the evaluation

of limit void ratios and void ratio ranges. However, S = 0.60 is taken approximately as a representative value for the evaluation of liquefaction state friction angle.

Unit weight (γ_{dry} and γ_{sat}): As the results are not sensitive to unit weight, the dry and saturated unit weights of all soil layers are assigned as 17.3 kN/m^3 and 18.9 kN/m^3, respectively, to be compatible with the literature.

A.36.4 Sub-sectioning of the Cross-section and Failure Plane

The exact locations of the SPT boreholes were known for this case history as presented in Figure A.36.1 and Figure A.36.2. Therefore, the sub-sectioning is made based on the locations of these penetration tests as presented in Figure A.36.4. Each test is assigned (names of the logs are directly assigned as the name of the sub-section) for the corresponding territory length.

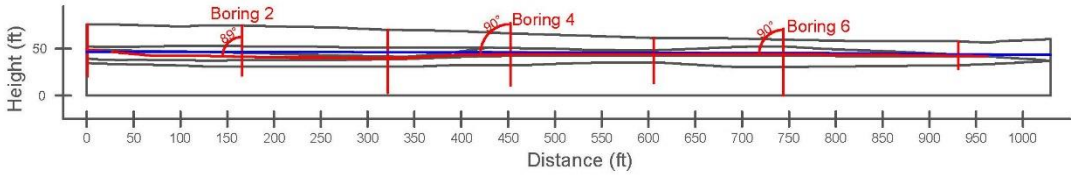

Figure A.36.4. Sub-sectioning of the cross-section and failure plane for San Fernando Valley Juvenile Hall

The territory lengths (L_i) and inclinations (α_i) (positive sign for CCW direction) of the failure plane are evaluated as given in Table A.36.1 for each sub-section.

Table A.36.1 Sub-sections with their corresponding failure plane lengths and inclinations for San Fernando Valley Juvenile Hall

Case History	Section	Failure plane length, L_i (m)	Total failure plane length, L_t (m)	Failure plane inclination, α_i (degrees)
San Fernando Valley Juvenile Hall	Boring 2	89.87	284.87	-1
	Boring 4	86.62		0
	Boring 6	108.38		0

A.36.5 Elastic Modeling and Stress Rotation

All stress components are evaluated linear elastically at the points where boreholes and failure plane intersect in Figure A.36.4. The initial and deformed shape of the cross-section are presented in Figure A.36.5 and Figure A.36.6, respectively. All lengths are given in meters.

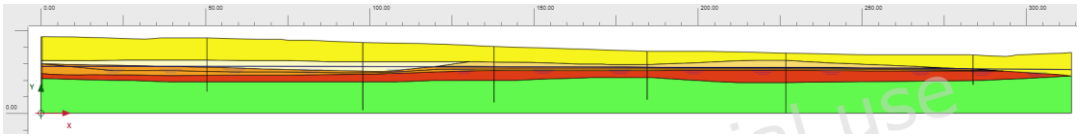

Figure A.36.5. Initial cross-section used in linear elastic modeling of San Fernando Valley Juvenile Hall

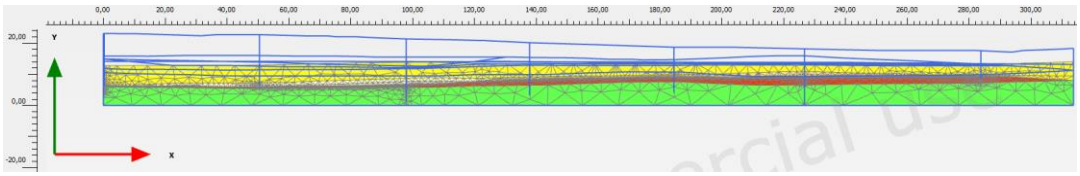

Figure A.36.6. Deformed cross-section obtained after linear elastic modeling of San Fernando Valley Juvenile Hall

During the elastic modeling process in PLAXIS 2D Ultimate Connect Edition V22.00.00.1733 software, the Poisson's ratio values of all layers other than liquefied zone are assigned as 0.30. For the liquefied zone, this value is set as 0.33. The elastic modulus values of soil layers A1, A2, B1, liquefied zone, B2, C and D are estimated as 15 MPa, 15 MPa, 10 MPa, 5 MPa, 10 MPa, 20 MPa, and 20 MPa, respectively.

The effective normal (σ'_N) and shear (τ_{static}) stresses acting on the inclined failure plane are evaluated with corresponding Mohr's circles. The corresponding Mohr's circles and the effective stress components of the sub-sections are presented in Figure A.36.7 and Table A.36.2, respectively. All stresses are given in kilopascals.

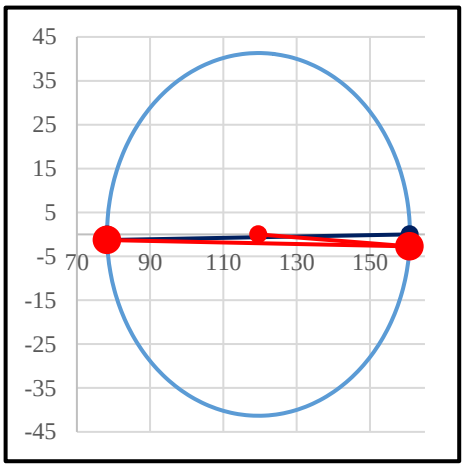

(a) Boring 2

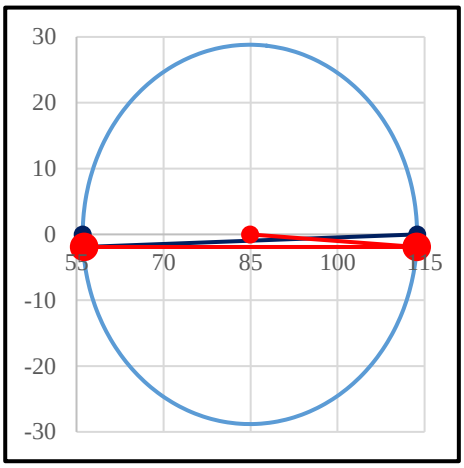

(b) Boring 4

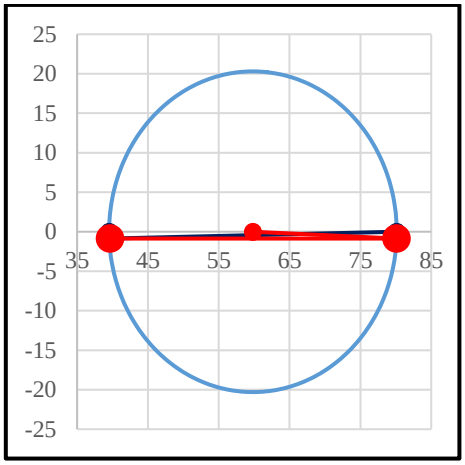

(c) Boring 6

Figure A.36.7. Mohr's circles for San Fernando Valley Juvenile Hall

Table A.36.2 Evaluated stress components for San Fernando Valley Juvenile Hall

Case History	Section	σ'_1 (kPa)	σ'_2 (kPa)	σ'_3 (kPa)	p_0' (kPa)	q (kPa)	σ'_N (kPa)	τ_{static} (kPa)	$\lvert\tau_{static}\rvert$ (kPa)
San Fernando Valley Juvenile Hall	Boring 2	160.9	78.9	78.2	106.0	82.3	160.8	-2.7	2.7
	Boring 4	113.7	56.2	56.1	75.3	57.5	113.6	-1.9	1.9
	Boring 6	80.1	39.6	39.5	53.1	40.5	80.1	-0.9	0.9

A.36.6 Evaluation of SPT Resistance

The exact locations of the SPT boreholes were documented by Bennett (1989) as given in Figure A.36.1 and Figure A.36.2. The correction factors for nonstandardized sampler configuration (C_S) and borehole diameter (C_B) are taken as 1.0 since no reliable information related to these coefficients was reported in any of the sources. The energy ratio was reported as 68% in Bennett (1989); therefore, the energy efficiency correction factor (C_E) is taken as 68/60 = 1.13. The short rod length (C_R) and fines content correction factors (C_{fines}) are evaluated with the methods and relationships explained in Section 3.5. The overburden stress correction factors (C_N) are evaluated based on the effective vertical stresses estimated at the point of penetration for each recording, and average values are documented for simplicity. Accordingly, the correction factors and SPT resistances are estimated as given in Table A.36.3.

Table A.36.3 Evaluated SPT-N resistances for San Fernando Valley Juvenile Hall

Case History	Section	C_N	C_B	C_R	C_S	C_E	C_{fines}	N	N_{60}	$(N_1)_{60}$	$(N_1)_{60,cs}$	
San Fernando Valley Juvenile Hall	Boring 2	0.79	1.0	0.98	1.0	1.13	1.29	13.00	14.49	11.45	14.80	12.59
	Boring 4	1.53	1.0	0.91	1.0	1.13	1.31	6.25	6.42	10.09	13.25	
	Boring 6	1.37	1.0	0.92	1.0	1.13	1.39	4.75	4.97	7.00	9.73	

A.36.7 Evaluation of Limit Void Ratios, Void Ratio Ranges, Relative Densities and Initial Void Ratios

Since mean grain size (D_{50}), fines content (FC), and coefficient of uniformity (C_u) information were available among the required material properties for the void ratio prediction models, the arithmetic means of the limit void ratios (e_{min} and e_{max}) evaluated by Model 8 and Model 9 are considered as the representative values. The e_{max} value is slightly modified then with respect to the construction method of the case history for each prediction model.

Since the fines content value is evaluated as 63%, which is greater than 15%, it is judged that the soil of interest consists of silty soils. Therefore, the relative densities evaluated by the correlation recommended by Cubrinovski and Ishihara (1999) are directly taken as the representative relative densities of the soils. Based on these relative densities and limit void ratios, the initial void ratios (e_0) corresponding to approximately 1 kPa confining stress are estimated referring to Equation 3-68. Accordingly, the limit void ratios, void ratio ranges (without any modification for the construction method), in-situ relative densities, and initial void ratios are estimated as given in Table A.36.4.

Table A.36.4 Evaluated limit void ratios, void ratio ranges, in-situ relative densities, and initial void ratios for San Fernando Valley Juvenile Hall

Case History	**Section**	**e_{min}**	**e_{max}**	**e_{max}-e_{min}**	**$RD_{C\&I}$ (%)**	**$RD_{K\&M}$ (%)**	**$RD_{overall}$ (%)**	**e_0**
San Fernando Valley Juvenile Hall	Boring 2	0.446	0.724	0.278	33.31	63.36	33.31	0.631
	Boring 4	0.446	0.724	0.278	31.27	59.48	31.27	0.637
	Boring 6	0.446	0.724	0.278	26.06	49.56	26.06	0.651